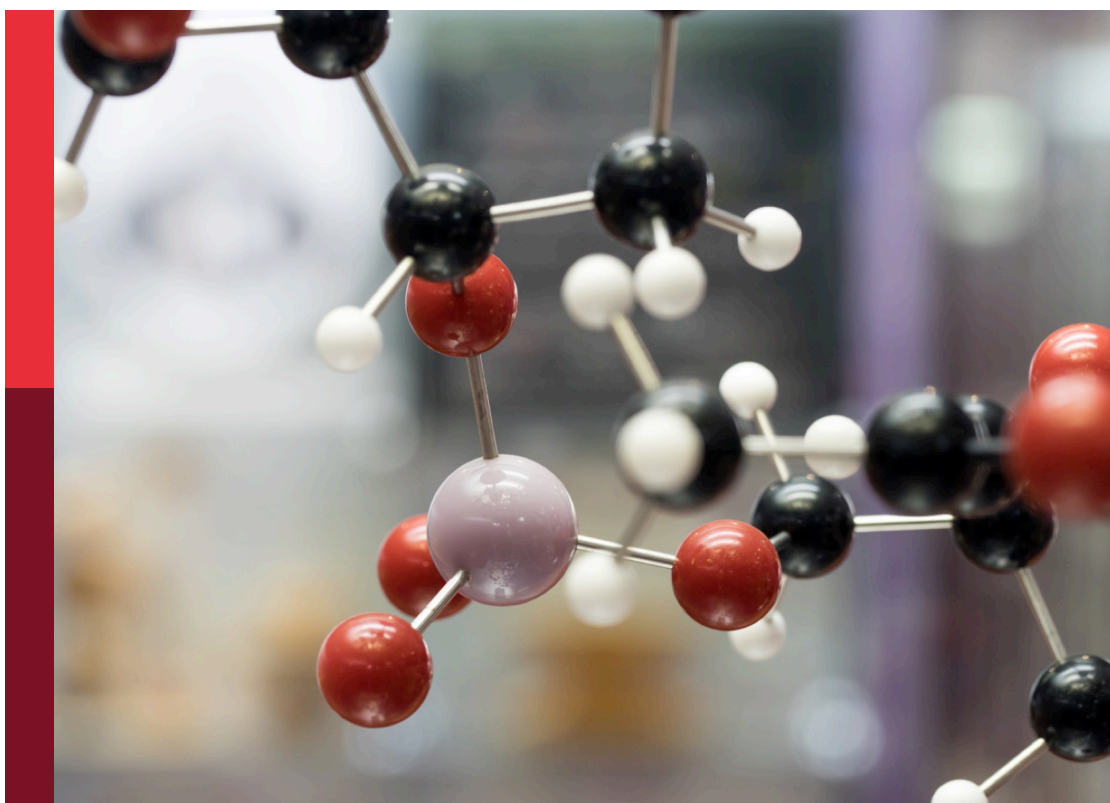# Bioactive natural products-oriented synthetic and functional studies

Edited by
Shao-Hua Wang, Xi Zheng and Xuetao Xu

Published in
Frontiers in Chemistry

About Frontiers

Frontiers is more than just an open access publisher of scholarly articles: it is a pioneering approach to the world of academia, radically improving the way scholarly research is managed. The grand vision of Frontiers is a world where all people have an equal opportunity to seek, share and generate knowledge. Frontiers provides immediate and permanent online open access to all its publications, but this alone is not enough to realize our grand goals.

Frontiers journal series

The Frontiers journal series is a multi-tier and interdisciplinary set of open-access, online journals, promising a paradigm shift from the current review, selection and dissemination processes in academic publishing. All Frontiers journals are driven by researchers for researchers; therefore, they constitute a service to the scholarly community. At the same time, the *Frontiers journal series* operates on a revolutionary invention, the tiered publishing system, initially addressing specific communities of scholars, and gradually climbing up to broader public understanding, thus serving the interests of the lay society, too.

Dedication to quality

Each Frontiers article is a landmark of the highest quality, thanks to genuinely collaborative interactions between authors and review editors, who include some of the world's best academicians. Research must be certified by peers before entering a stream of knowledge that may eventually reach the public – and shape society; therefore, Frontiers only applies the most rigorous and unbiased reviews. Frontiers revolutionizes research publishing by freely delivering the most outstanding research, evaluated with no bias from both the academic and social point of view. By applying the most advanced information technologies, Frontiers is catapulting scholarly publishing into a new generation.

What are Frontiers Research Topics?

Frontiers Research Topics are very popular trademarks of the *Frontiers journals series*: they are collections of at least ten articles, all centered on a particular subject. With their unique mix of varied contributions from Original Research to Review Articles, Frontiers Research Topics unify the most influential researchers, the latest key findings and historical advances in a hot research area.

Find out more on how to host your own Frontiers Research Topic or contribute to one as an author by contacting the Frontiers editorial office: frontiersin.org/about/contact

Bioactive natural products-oriented synthetic and functional studies

Topic editors

Shao-Hua Wang — Lanzhou University, China
Xi Zheng — The State University of New Jersey, United States
Xuetao Xu — Wuyi University, China

Table of contents

Frontiers in Chemistry

Chemistry and Bioactivity of Marine-Derived Bisabolane Sesquiterpenoids: A Review

Cheng-Shou Li, Li-Ting Liu, Lei Yang, Jing Li* and Xin Dong*

Qingdao Hospital of Traditional Chinese Medicine (Qingdao Hiser Hospital), Qingdao, China

Natural products, characterized by intriguing scaffold diversity and structural complexity, as well as significant agricultural and medicinal activities, have been a valuable source of agrochemicals/drugs development and have historically made a huge contribution to pharmacotherapy. Structurally, bisabolanes are a family of naturally occurring sesquiterpenoids that featured a hexatomic ring core incorporating with eight continuous carbons, which cause high structural variability along the alkyl side chain to form abundant functionalities. Moreover, apart from their interesting structures, bisabolanes have shown multitudinous bioactivities. Bisabolanes are distributed in a variety of marine invertebrates, terrestrial plant, and microbial sources. Interestingly, bisabolanes characterized from marine environment possess unique characteristics both structurally and biologically. A total of 296 newly-discovered bisabolanes were searched. Among them, 94 members were isolated from marine organisms. This review particularly focuses on the new bisabolanes characterized from marine organisms (covering from 2000 to 2021), including marine-derived fungi, algae, soft corals, and sponges, with emphasis on the diversity of their chemical structures as well as the novelty and differences between terrestrial and marine sources. Moreover, a wide range of bioactivities of marine-derived bisabolanes, including antimicrobial, anti-inflammatory, enzyme inhibitory, and cytotoxic properties, are presented herein, which is considered to be a promising resource for the discovery of new drug leads and agrochemicals.

Keywords: marine-derived bisabolanes, sesquiterpenoids, chemical diversity, biological activities, lead compounds

INTRODUCTION

Natural products (NPs) are secondary metabolites produced by plants, microorganisms, and animals through diversified biosynthetic pathways. NPs possess attractive structural diversity and complexity along with prominent biological properties, and hence have played an essential role in the discovery of lead compounds for new medicines (Butler, 2005). Historically, NPs and their derivatives have made a significant contribution to pharmacotherapy. The discovery of penicillin, the first broad-spectrum antibiotic, is a representative example, which, not only accelerated the course of pharmaceutical research but also saved thousands of lives (Zhang et al., 2020). NPs have been an inexhaustible reservoir for new drug development, which prove to be the cornerstone of modern pharmaceutical industry. It is estimated that approximately 60% of approved small-molecule based drugs between 1981 and 2019 are derived from NPs, indicating that there is still an urgent need to excavate more NPs with novel structures and promising bioactivities (Newman and Cragg, 2020).

Sesquiterpenoids represent structurally diverse NPs with extensive pharmacological activities, with more than 300 skeletons being reported up to now (Fraga, 2011). Bisabolanes are a family of sesquiterpenoids widely distributed in terrestrial plants, microorganisms, and marine organisms (algae, soft corals, and sponges) (Chen et al., 2021). Structurally, bisabolanes contain a hexatomic ring core that generally, but not always, features a 15-carbon skeleton. Bisabolanes appear to be among the simplest of all sesquiterpenoids, as most of them are monocyclic. However, they represent high complexity of cyclic sesquiterpenoids. These compounds incorporate an eight continuous carbons side chain, which cause high structural diversity to generate abundant functionalities including double bond, lactone, furan, pyran, and so on, by oxidation, reduction, esterification, and cyclization (Niu et al., 2020; Chen et al., 2021). Moreover, some unique members, such as norbisabolanes (Jian Li et al., 2015; Ge et al., 2021), dimers (Sun et al., 2012; Georgantea et al., 2013), glycosides (Lv et al., 2014), adducts (Xiao-Dong Li et al., 2015), have also been characterized. Chemically speaking, the findings of these fascinating molecules provide considerable chemical foundation in the course of new drugs and agricultural chemicals discovery. In addition, bisabolanes have been reported to possess extensive pharmacological activities, including but not limited to anti-inflammatory, insecticidal, antitumor, antimicrobial, and antiviral activities.

Marine environment has distinct ecological characteristics compared to terrestrial environment, such as high salinity, high pressure, extreme temperature, and low oxygen. To overcome those multiple extreme environmental stresses, marine organisms have evolved unique metabolic abilities to produce novel bioactive natural products. Marine natural products, therefore, possess unimaginable structural diversity and have brought immensely attention. A large amount of marine natural products have been discovered and reported, including polyketides, terpenoids, steroids, peptides, and nitrogen-containing compounds (Carroll et al., 2021). Compared to NPs isolated from terrestrial environment, marine natural products are often considered to be more diversiform and variable both structurally and biologically. For example, marine-derived heterocyclic alkaloids are challenging NPs possessing structurally unique skeletons arising from distinct amino acids (Zhang et al., 2020). Moreover, many of marine natural products are characterized as halogenated compounds, which are relatively few in terrestrial natural products. As for above-mentioned bisabolanes, it is believed that marine-derived bisabolanes may also have certain novelty and differences in contrast to terrestrial ones on structures and bioactivities. Therefore, to fully demonstrate the chemistry and bioactivity of newly-discovered marine-derived bisabolanes in recent years, we performed an in-depth investigation of these compounds, not only from marine sources but also from terrestrial sources. As a result, a total of 296 new bisabolanes and 93 references were searched, with 94 members isolated from marine organisms. They include 64 compounds (1–64) characterized from marine fungi, 6 compounds (65–70) from marine algae, 9 compounds (71–79) from soft corals, 15 compounds (80–94) from marine sponges.

Moreover, another 27 compounds (95–122) from terrestrial fungi, 169 compounds (123–291) from terrestrial plants, and 5 compounds (292–296) from others were presented in Supplemental Materials (Supplementary Figures S1–S3). Pharmacological studies indicated the biological potential of these compounds, exhibiting antimicrobial, anti-inflammatory, enzyme inhibitory, cytotoxic, antimicroalgal, and antifouling properties. It should be pointed out that a review regarding to the chemistry and bioactivity of bisabolanes has been published very recently (Shu et al., 2021). The previous review by Shu et al. described 356 bisabolanes in total isolated from 24 families, primarily from Compositae, Zingiberaceae, Aspergillaceae, Halichondriidae, and Aplysiidae (Shu et al., 2021). Since the authors mixed up the marine and terrestrial bisabolanes for discussion, this review gave little information on marine bisabolanes, especially their structural features. In this study, this is the first attempt to summarize the chemical diversity of marine-derived bisabolanes, highlight their novelty and differences between terrestrial and marine sources, and provide a future perspective of their potential applications as lead compounds.

CHEMICAL DIVERSITY OF THE NEWLY-DISCOVERED MARINE-DERIVED BISABOLANES
Bisabolanes Characterized From Marine-Derived Fungi

As shown in **Figure 1**, **Figure 2**, **Figure 3**, **Figure 4**, a total of 64 new bisabolanes (1–64) were characterized from marine-derived filamentous fungi. Bioassay-guided isolation of a marine-derived fungus *Aspergillus* sp. obtained from a gorgonian coral yielded three new phenolic bisabolanes, (+)-methyl sydowate (1), 7-deoxy-7,14-didehydrosydonic acid (2), and 7-deoxy-7,8-didehydrosydonic acid 3) (Wei et al., 2010). 1 possessed a 2,2,6-trimethyltetrahydro-2*H*-pyran moiety, which was proved as a natural product, rather than an artifact during the isolation process. Chemical investigation of the mangrove-derived endophytic fungus *Aspergillus* sp. xy02 resulted in the isolation of seven new phenolic bisabolanes, namely (7*R*,10*S*)-7,10-epoxysydonic acid (4), (7*S*,10*S*)-7,10-epoxysydonic acid (5), (7*R*,11*S*)-7,12-epoxysydonic acid (6), (7*S*,11*S*)-7,12-epoxysydonic acid (7), 7-deoxy-7,14-didehydro-12-hydroxysydonic acid (8), (*Z*)-7-deoxy-7,8-didehydro-12-hydroxysydonic acid (9), and (*E*)-7-deoxy-7,8-didehydro-12-hydroxysydonic acid (10) (Wang et al., 2018). Compounds 4 and 5 were elucidated as a pair of isomers of the 7,10-epoxide of sydonic acid, while compounds 6 and 7 were found to form a 7,12-epoxide. Four new phenolic bisabolanes, (*S*)-(+)-11-dehydrosydonic acid 11) and (7*S*,11*S*)-(+)-12-acetoxysydonic acid (12), and expansols A 13) and B (14), were produced by the marine fungus *Penicillium expansum* 091,006, which was endogenous with the mangrove plant *Excoecaria agallocha* (Lu et al., 2010). Compounds 13 and 14 were the first examples of adducts containing both phenolic bisabolane sesquiterpenoid and diphenyl ether units.

FIGURE 1 | Bisabolanes characterized from marine-derived fungi (1–18).

FIGURE 2 | Bisabolanes characterized from marine-derived fungi (Continued) (19–32).

FIGURE 3 | Bisabolanes characterized from marine-derived fungi (Continued) (33–53).

FIGURE 4 | Bisabolanes characterized from marine-derived fungi (Continued) (**54–64**).
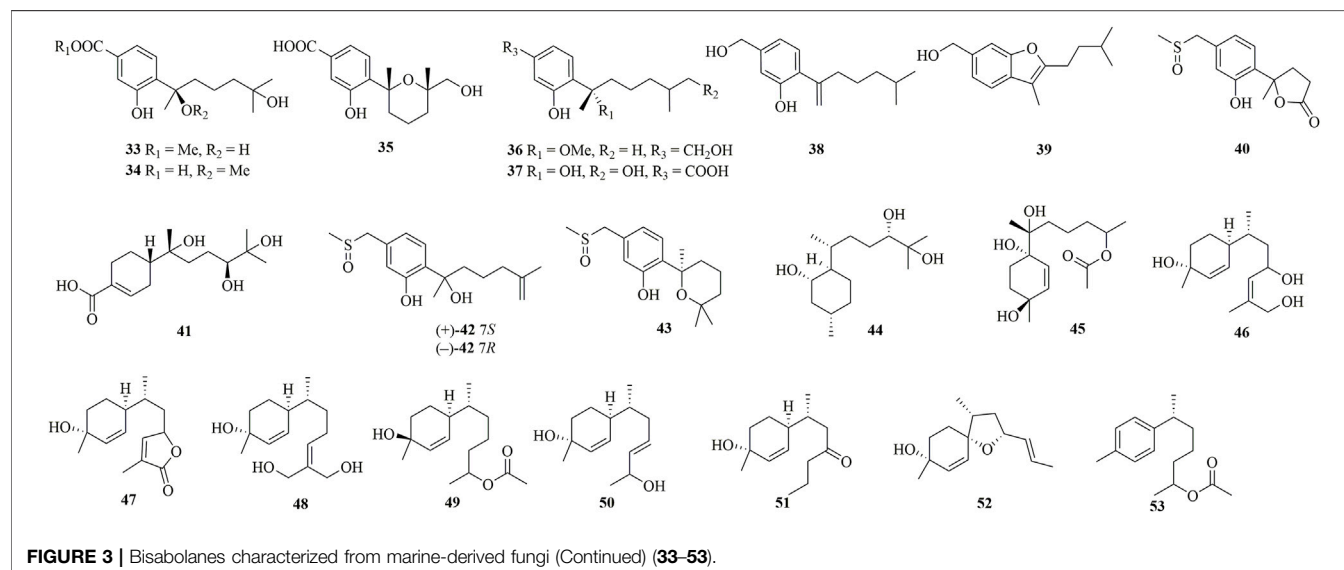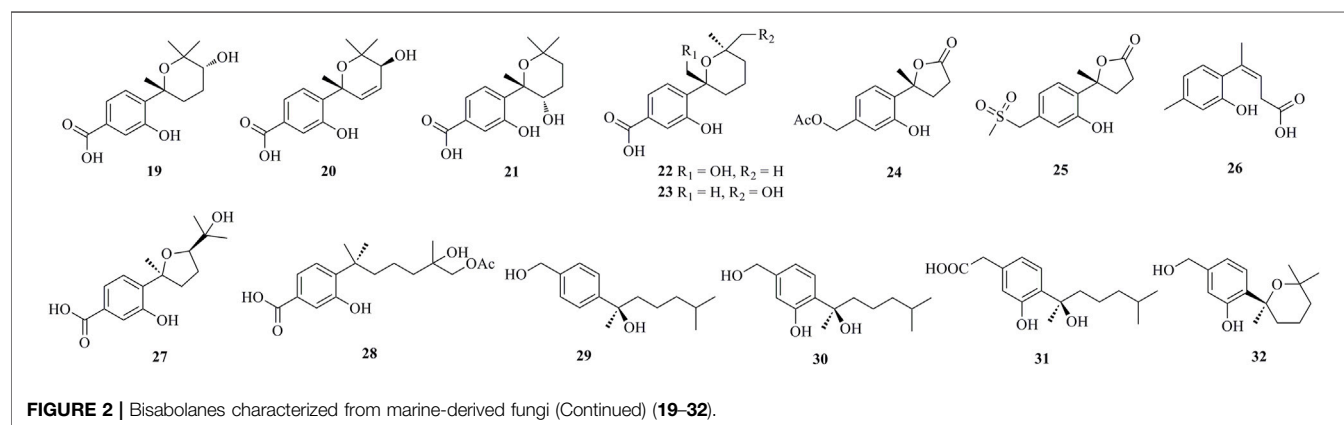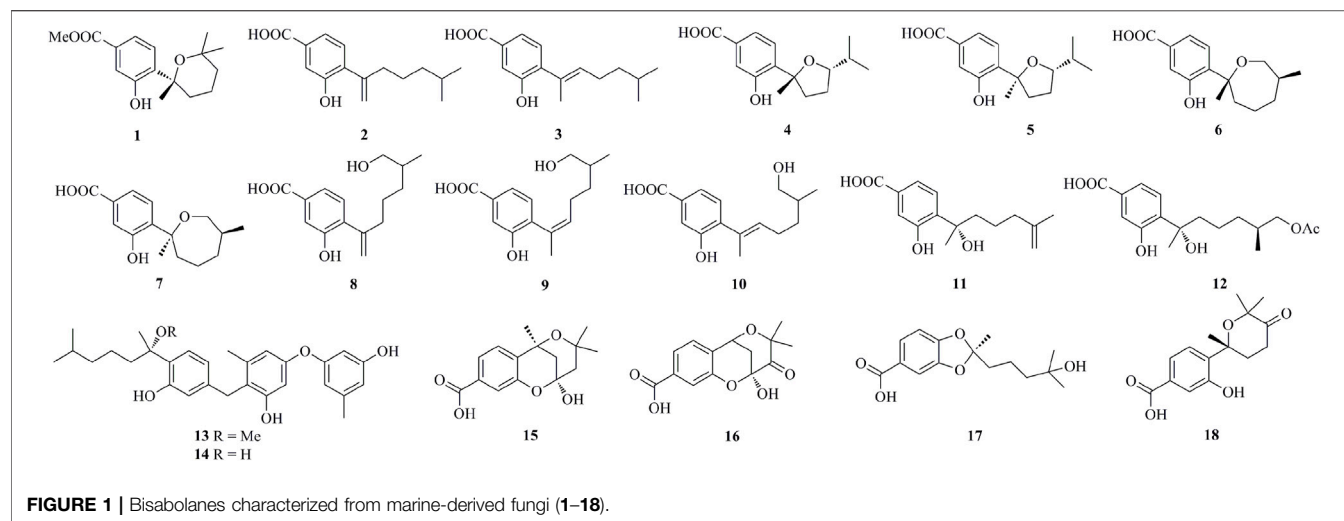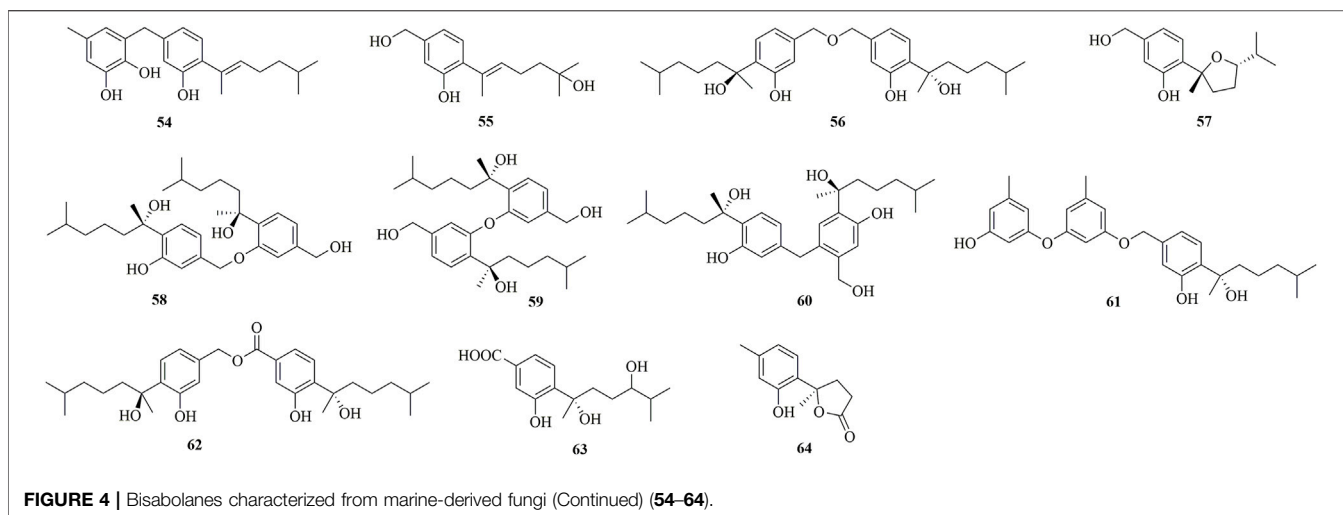
Fourteen undescribed phenolic bisabolanes with diverse structures, asperbisabolanes A−N (**15–28**), were isolated from the deep sea sediment-derived fungus *A. sydowii* MCCC 3A00324 (Niu et al., 2020). **15** and **16** represented the first bisabolanes featuring a 6/6/6 tricyclic skeleton. **17** was characterized as a novel *seco*-bisabolane containing a rare dioxolane moiety, and **25** possessed a rare methylsulfonyl group. Four new bisabolanes, including aspergiterpenoid A (**29**), (−)-sydonol (**30**), (−)-sydonic acid (**31**), and (−)-5-(hydroxymethyl)-2-(2′,6′,6′-trimethyltetrahydro-2*H*-pyran-2-yl)phenol (**32**), were characterized from a marine sponge-sourced fungus *Aspergillus* sp. (Li et al., 2012). Two new phenolic bisabolanes, *ent*-aspergoterpenin C **33**) and 7-*O*-methylhydroxysydonic acid (**34**), were obtained from the culture extracts of *A. versicolor* SD-330, a deep-sea sediment-sourced fungus (Li et al., 2019a). **33** and **34** were considered as natural products through HPLC analysis, rather than artifacts produced by esterification or methylation. Then from the same fungus, another new compound 12-hydroxysydowic acid **35**) was isolated (Li et al., 2019b). Three new bisabolanes, (7*S*)-(+)-7-*O*-methylsydonol (**36**), (7*S*,11*S*)-(+)-12-hydroxysydonic acid (**37**), and 7-deoxy-7,14-didehydrosydonol (**38**), were isolated from the fungus *A. sydowii* by the addition of a DNA methyltransferase inhibitor 5-azacytidine (Chung et al., 2013).

Through chemical epigenetic manipulation strategy, the gorgonian-derived fungus *A. versicolor* XS-20090066 was found to produce a new bisabolane aspergillusene E (**39**) with a benzofuran moiety, by the addition of histone deacetylase inhibitor, suberoylanilide hydroxamic acid, and DNA methyltransferase inhibitor, 5-azacytidine (Wu et al., 2020). A pair of new S-containing norbisabolane enantiomers methylsulfinyl-1-hydroxyboivinianin A [(±)-**40**] were produced by the marine algal-derived endophytic fungus *P. chrysogenum* LD-201810 (Ge et al., 2021). **40** was proven to possess a rare methylsulfinyl substituent, and finally afforded individual enantiomers (+)-**40** and (−)-**40** by chiral HPLC. A new polychiral bisabolane with a 10,11-diol moiety named bisabolanoic acid A **41**) was isolated from the mangrove-

derived endophytic fungus *Colletotrichum* sp. SCSIO KcB3-2 (Li et al., 2021). A pair of new bisabolanes enantiomers (±)-flavilane A (**42**), as well as a new derivative flavilane B (**43**), were isolated from the seawater-derived fungus *A. flavipes* 297 (Chen et al., 2021). **42** and **43** represented uncommon cases of phenolic bisabolanes incorporating with a methylsulfinyl group. A new bisabolane bisabolan-1,10,11-triol **44**) and a new norbisabolane 12-nor-11-acetoxybisabolen-3,6,7-triol **45**) were isolated from a marine algal-derived endophytic fungus *T. asperellum* cf44-2 (Song et al., 2018). In a systemic phytochemical investigation on a marine red alga-epiphytic isolate of *T. asperellum* Y6−2, eight new bisabolanes, trichobisabolins A−H (**46–53**), were finally obtained (Shi et al., 2019). Compounds **49–53** were rare nor-sesquiterpenes.

Four new phenolic bisabolanes **54–57** were isolated from the culture of mangrove endophytic fungus *A. flavus* QQSG-3 (Wu et al., 2018). **54** was a phenol-bisabolane adduct linked *via* a methylene, while **56** was a dimeric analogue of sydonol. Three rare phenolic bisabolane dimers, disydonols A−C (**58–60**), were acquired by the extensive investigation on a marine-derived fungus *Aspergillus* sp. (Sun et al., 2012). **58–60** were the dehydration dimeric metabolites of (*S*)-(+)-sydonol. Four new phenolic bisabolanes, peniciaulins A **61**) and B (**62**), (7*S*)-(−)-10-hydroxysydonic acid (**63**), and 1-hydroxyboivinianin A (**64**), were isolated from a deep sea sediment-derived fungus *P. aculeatum* SD-321 (Jian Li et al., 2015). **61** was a diphenyl ether-bisabolane adduct *via* an ether bond, whereas **62** represented the dimeric bisabolane with two monomers linking through an ester bond.

Bisabolanes Characterized From Marine Algae

Compounds **65–70** (**Figure 5**) were obtained from marine algae. Two new highly halogenated monocyclic bisabolanes, laurecomposins A **65**) and B (**66**), were discovered from a phytochemical investigation on the red alga *Laurencia composita* Yamada (Hu et al., 2020). Phytochemical studies on
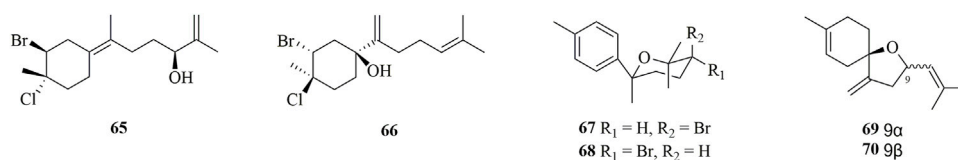
FIGURE 5 | Bisabolanes characterized from marine algae (**65**–**70**).
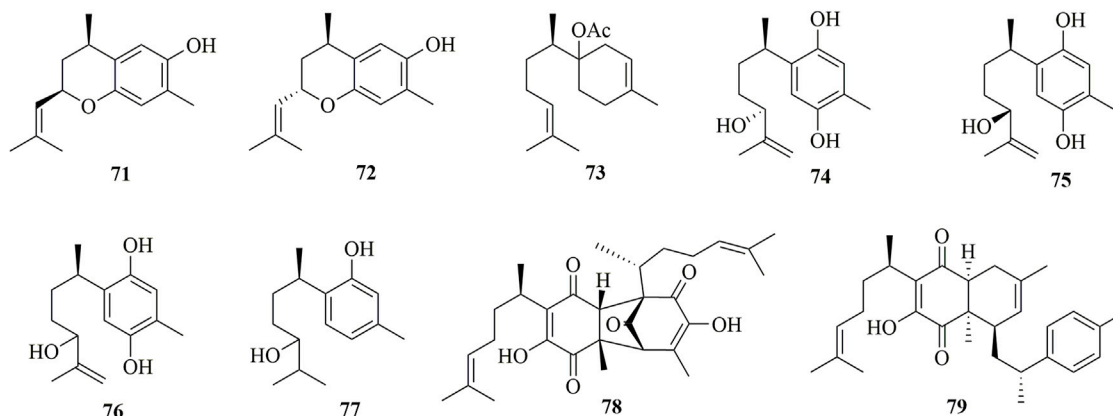
FIGURE 6 | Bisabolanes characterized from soft corals (**71**–**79**).
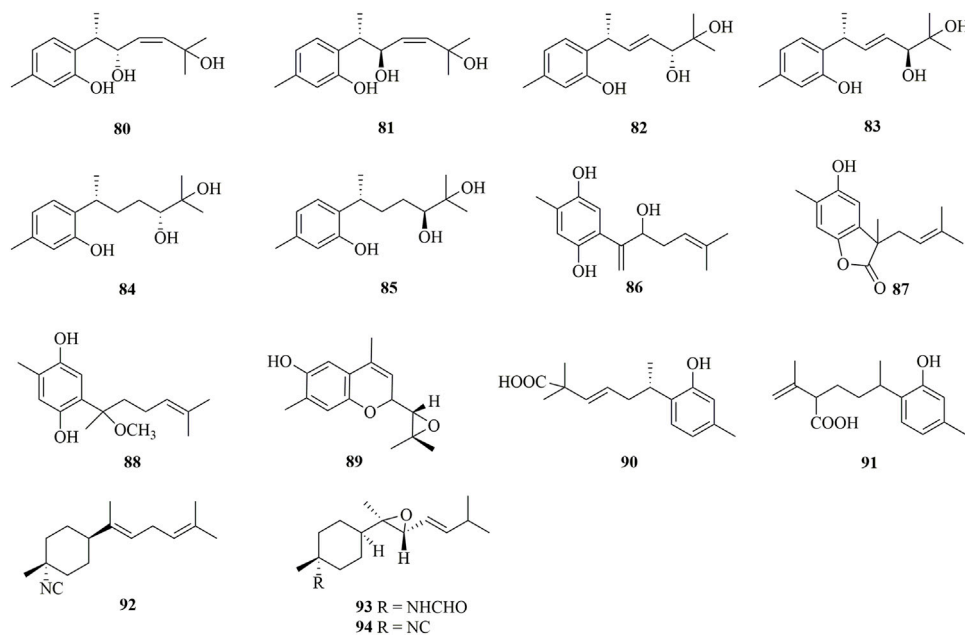
FIGURE 7 | Bisabolanes characterized from marine sponges (**80**–**94**).

L. okamurai, a marine red alga, yielded four new bisabolane sesquiterpenes, okamurenes A−D (**67**–**70**) (Liang et al., 2012). **67** and **68** were brominated isomers, and **69** and **70** were dehalogenated 6,9-epoxybisabola-2,7 (14),10-triene. In the sense of chemotaxonomy, **67** and **68** represented the first members of brominated bisabolanes possessing a phenyl moiety among sesquiterpenes isolated from algae belonging to *Laurencia*.

Bisabolanes Characterized From Soft Corals

Detailed chemical investigation of the tropical soft coral *Pseudopterogorgia rigida* led to the discovery of seven new bisabolanes **71**–**77** (**Figure 6**) (Georgantea et al., 2014). These obtained compounds belonged to phenolic bisabolanes, except for **73**, which was elucidated as acetyl-β-bisabolol. Moreover, **71** and **72** were epimers of 1,9-epoxy-4-hydroxy-α-curcumene. This species also produced minor constituents, perezoperezone **78**) and curcuperezone **79**) (Georgantea et al., 2013). **78** possessed a non-symmetrical dimeric structure through the formation of a five-membered ring, whereas **79** was a rare dimer synthesized by perezone and α-curcumene to form a tricyclic core.

Bisabolanes Characterized From Marine Sponges

As shown in **Figure 7**, 15 bisabolanes were isolated and identified from marine sponges. Six new aromatic bisabolanes, plakordiols A–D (**80**–**83**), (7*R*, 10*R*)-hydroxycurcudiol (**84**), and (7*R*, 10*S*)-hydroxycurcudiol (**85**), were isolated from the marine sponge *Plakortis simplex* (Wang et al., 2021). Another four new aromatic bisabolanes, including 6-(3-hydroxy-6-methyl-1,5-heptadien-2-yl)-3-methylbenzene-1,4-diol (**86**), 4-hydroxy-3,7-dimethyl-7-(3-methylbut-2-en-1-yl)benzofuran-15-one (**87**), 6-(2-methoxy-5-methylhept-4-en-2-yl)-3-methylbenzene-1,4-diol (**88**), and 9-(3,3-dimethyloxiran-2-yl)-1,7-dimethyl-7-chromen-4-ol (**89**), were obtained from an organic extract of the marine sponge *Myrmekioderma* sp. (Costa et al., 2019). All of the isolated compounds represented cyclic bisabolanes bearing rich oxo functionality. Furthermore, chemical investigation of the Thai marine sponge *Myrmekioderma* sp. afforded two new aromatic bisabolanes, myrmekioperoxides A (**90**) and B **91**) (Wongbundit et al., 2020). A new monocyclic bisabolane (*E*)-3-isocyanobisabolane-7,10-diene **92**) containing an isonitrile group was isolated from the Okinawan sponge of the genus *Axinyssa* (Iwashima et al., 2002). Finally, two new rare epoxy-substituted nitrogenous bisabolanes, 3-formamido-7,8-epoxy-α-bisabolane **93**) and 3-isocyano-7,8-epoxy-α-bisabolane (**94**), were produced by the Hainan sponge *Axinyssa* sp. (Sun et al., 2010). **93** and **94** were α-bisabolanes with an 7,8-epoxy ring, which also contained a formamide functional group in **93** and an isonitrile group in **94**. It is worth mentioning that, although nitrogen-bearing bisabolanes are widely encountered in marine invertebrates, epoxy-substituted nitrogenous bisabolanes are rather rare.

BIOLOGICAL ACTIVITIES OF BISABOLANES

Antimicrobial Activity

Compound **1** exerted weak antibacterial efficacy against the Gram positive strain *Staphylococcus aureus* with an inhibition zone of 11 in diameter at the concentration of 100 μg/ml (Wei et al., 2010). Compounds **5**, **6**, **8**, and **10** showed mild antibacterial effect on *S. aureus* with the IC$_{50}$ values of 32.2,

36.0, 41.9, and 31.5 μM, respectively (Wang et al., 2018). Compound **30** was active against the pathogenic bacteria *S. albus* and *Micrococcus tetragenus* with the MICs of 5.00 and 1.25 μM, while **32** on *S. albus* and *Bacillus subtilis* with the MICs of 5.00 and 2.50 μM, respectively (Li et al., 2012). Compounds **33**–**35** exhibited high antibacterial activity against zoonotic pathogenic bacteria *Escherichia coli*, *Edwardsiella tarda*, *Vibrio harveyi*, and *V. parahaemolyticus*, with MICs no higher than 8.0 μg/ml (Li et al., 2019a; Li et al., 2019b). **39** possessed activity against *S. epidermidis* and *S. aureus* with MICs of 8 and 16 μg/ml. Moreover, **39** also showed antifungal activity toward *Candida albicans* and *C. tropicalis* with MICs of 64 and 32 μg/ml, respectively (Wu et al., 2020). **44** and **45** showed weak activity against four marine pathogenic bacteria, *V. parahaemolyticus*, *V. anguillarum*, *V. harveyi*, and *V. splendidus*, with the inhibitory zone diameters of 6.3–7.5 mm at 20 μg/disk (Song et al., 2018). Compound **61** demonstrated inhibitory activity against aquatic pathogens *Micrococcus luteus* and *V. alginolyticus* with MICs of 1.0 and 2.0 μg/ml, respectively (Xiao-Dong Li et al., 2015). Moreover, the dimer **62** and norbisabolane **64** showed selective activity against *E. tarda* and *V. harveyi*, with MICs of 8.0 and 4.0 μg/ml. The halogenated bisabolanes **65** and **66** exhibited not only potent antifungal activity against *Microsporum gypseum*, with MICs of 4 and 8 μg/ml, but also considerable antibacterial activity against *S. aureus* with MICs of 26.8 and 15.4 μg/ml, respectively (Hu et al., 2020).

Cytotoxic Activity

Compound **13**, a new adduct of phenolic bisabolane and diphenyl ether, possessed moderate cytotoxicity against HL-60 tumor cells with an IC$_{50}$ value of 15.7 μM, and **14** inhibited higher activity against A549 and HL-60 cells with IC$_{50}$ values of 1.9 and 5.4 μM, respectively (Lu et al., 2010). The condensation between phenolic bisabolanes and diphenyl ethers appear to enhance cytotoxicity significantly. The sulfurated compounds **42** and **43** exhibited moderate cytotoxicity against MKN-45 and HepG2 cells, with the IC$_{50}$ values ranging from 19.8 to 30.1 μg/ml, which indicated that the methylsulfinyl group could strengthen cytotoxicity (Chen et al., 2021). The dimmers **58** and **60** showed pronounced cytotoxic activities against HepG-2 and Caski cell lines with IC$_{50}$ values of 2.91–12.40 μg/ml, whereas **59** was relatively noncytotoxic (IC$_{50}$ > 100 μg/ml) (Sun et al., 2012).

Anti-Inflammatory Activity

Compounds **15**–**28** were evaluated inhibition effects against nitric oxide (NO) secretion in LPS-activated BV-2 microglia cells. **20** and **26** possessed the inhibition rates of 46.4 and 56.8% at a concentration of 10 μM. Structure–activity relationship analysis indicated that the double bond at $\Delta^{7,8}$ in bisabolane may strengthen the inhibition of NO secretion. Molecular mechanism study revealed that **26** inhibited the NF-κB-activated pathway in a dose-dependent manner (Niu et al., 2020).

Enzyme Inhibitory Activity

The polychiral bisabolane **41** displayed moderate inhibitory activity against acetylcholinesterase (AChE) with an IC$_{50}$ value of 2.2 μM. *In*
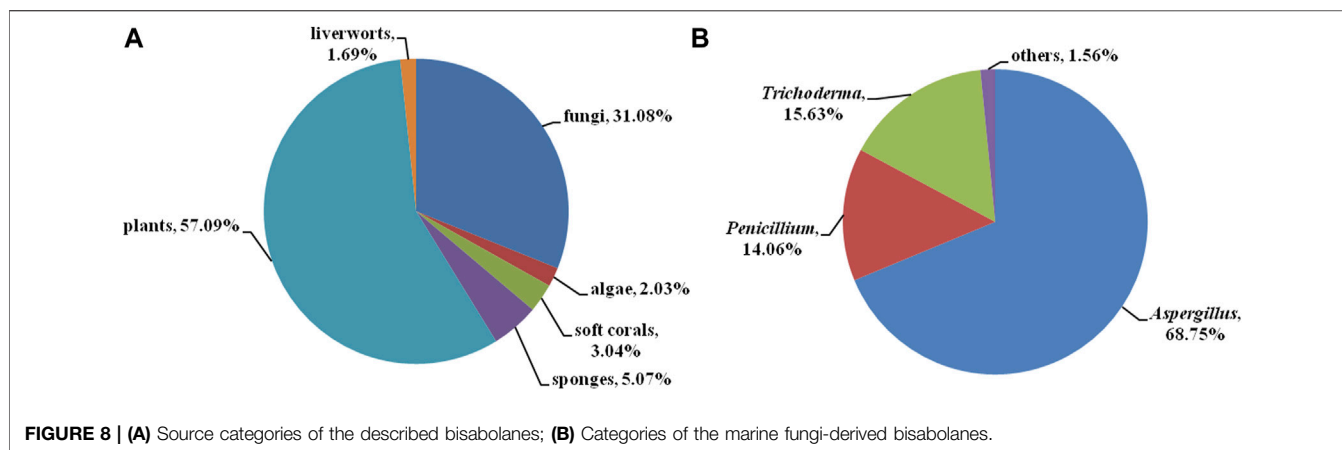
FIGURE 8 | (A) Source categories of the described bisabolanes; **(B)** Categories of the marine fungi-derived bisabolanes.

silico molecular docking analysis indicated that **41** may bind to the active site residue TYR121 by hydrogen bonds (Li et al., 2021). **54** and **56** showed strong α-glucosidase inhibitory effects with IC$_{50}$ values of 4.5 and 3.1 μM, respectively (Wu et al., 2018).

Other Activities

Compound **32** not only showed selective antibacterial activity but also possessed significant antifouling activity. **32** drastically inhibited the larval settlement of the barnacle *Balanus amphitrite* at a concentration of 25.0 μg/ml (Li et al., 2012). **36** and **37** showed anti-diabetic activity, which increased medium glucose consumption of the differentiated 3T3-L1 adipocytes in comparison with the insulin treatment (Chung et al., 2013). **39** displayed antifouling activity against bryozoan larvae of *Bugula neritina* with the EC$_{50}$ and LC$_{50}$ values of 6.25 and 25 μg/ml, respectively (Wu et al., 2020). The norbisabolane **45** possessed antimicroalgal potency against the marine phytoplankton *Heterosigma akashiwo* with an IC$_{50}$ value of 8.4 μg/ml (Song et al., 2018). Compounds **49–53** exhibited growth inhibition against four marine phytoplanktons (*H. akashiwo*, *Prorocentrum donghaiense*, *Chattonella marina*, and *Karlodinium veneficum*) with IC$_{50}$s ranging from 2.1–85 μg/ml (Shi et al., 2019). It appeared that the acetoxy group at C-11 could significantly enhance inhibitory ability against marine phytoplanktons. Zebrafish Nile red fat metabolism assay revealed that compounds **86**, **87**, and **89** had significant lipid-reducing activity with IC$_{50}$ values of 7.89, 12.61, and 1.22 μM, respectively (Costa et al., 2019). **92** containing an isonitrile group exerted strong brine shrimp lethal activity with an LC$_{50}$ of 0.1 μg/ml (Iwashima et al., 2002).

DISCUSSIONS AND CONCLUSION

The Novelty of Bisabolanes Characterized From Fungi and Differences Between Terrestrial and Marine Sources

Bisabolanes, a unique family of naturally occurring sesquiterpenoids, have been a valuable reservoir for searching for new lead compounds with medical and/or agricultural potential. These compounds are widely distributed in terrestrial plants, microorganisms, and marine organisms (algae, soft corals, and sponges) (**Figure 8A**). This review summarizes 296 newly-discovered bisabolanes in the past few years. Among them, 92 compounds, accounting for 31.08% of all described bisabolanes, were characterized from fungi [including marine-derived **1–64** (**Figure 1**, **Figure 2**, **Figure 3**, **Figure 4**) and terrestrial **95–122** (**Supplementary Figure S1** in Supplemental Materials], especially filamentous fungi. The filamentous fungi *Aspergillus*, *Penicillium*, and *Trichoderma* are dominant genera as producers of these compounds, with 44, 9, and 10 members described, respectively (**Figure 8B**). Structurally, bisabolanes characterized from fungi are mainly phenolic bisabolanes, which featured a *para*-alkylated benzene ring framework comprising a side chain with an eight consecutive carbons. Their structure variability is due to the transformation of the side chain, such as oxidation, reduction, esterification, and cyclization, to generate abundant functionalities including lactone (eg. compounds **6**, **17**, **22**, **35**), double bond (e.g., compounds **8–10**), furan (e.g., compounds **4**, **5**, **39**), pyran (e.g., compounds **1**, **32**, **43**), and so on. Moreover, fungi also produce rare bisabolane dimers. Representative examples are compounds **13** and **14**, **58–62**, and **120–122**. It should be pointed out that, the endophytic fungi, an ecological group generally resided in plants and symbiotic with their hosts, are considered as an important producer of bisabolanes. Endophytic fungi possess a complicated interaction with their host plants, thus they have evolved novel metabolic pathways to produce the same or similar secondary metabolites as the hosts. Therefore, it is a more talented pathway to isolate bisabolanes from fungal endophytes, rather than the medicinal plants.

Compared to bisabolanes isolated from terrestrial fungi, some of bisabolanes from marine-derived fungi possess unique functionalities. For example, the sulfurated bisabolanes were exclusively isolated from marine fungi, including **25** with a rare methylsulfonyl group isolated from the deep sea sediment-derived fungus *A. sydowii* MCCC 3A00324 (Niu et al., 2020), **40** and **42–43** incorporating with a rare methylsulfinyl group isolated from the marine algal-derived endophytic fungus *P. chrysogenum* LD-201810 (Ge et al., 2021) and the seawater-derived fungus *A. flavipes* 297 (Chen

et al., 2021), respectively. **52** isolated from a marine red alga-epiphytic isolate of *T. asperellum* Y6–2, represented a rare example of nor-sesquiterpenes with a spiro system (Shi et al., 2019). It is believed that marine-derived fungi suffered more survival stress than terrestrial fungi, and thus evolved more flexible metabolic pathways by producing novel secondary metabolites.

Characterization of Terrestrial and Marine-Derived Bisabolanes

Apart from marine-derived fungi, a total of 30 compounds (**65–94**) were characterized from marine organisms, including marine plants algae and marine invertebrates, soft corals and sponges. It is well-known that marine organisms, which are suffered from high salinity, high pressure, extreme temperature, and low oxygen, possess unique metabolic pathways that are quite different from that of terrestrial organisms. Accordingly, marine-derived natural products tend to have unexpected structural types. For example, compounds **78** and **79**, two unprecedented non-symmetrical tricyclic dimers were characterized from the tropical soft coral *Pseudopterogorgia rigida* (Georgantea et al., 2013). In addition, some highly halogenated bisabolanes, such as **65–68**, were isolated from the marine algae belonging to *Laurencia* (Liang et al., 2012; Hu et al., 2020). With this consideration, it is believed that marine organisms, which have emerged as a valuable frontier for the discovery of new lead compounds, continue to be a rich source of structurally diverse bisabolanes.

Most of the described bisabolanes, apparently, are isolated from terrestrial plants. As shown in **Figure 8A** and **Supplementary Figure S2**, 169 compounds (**123–291**, accounting for 57.09% of all bisabolanes) are scattered across a variety of species belonging to the genera *Ligularia*, *Parasenecio*, *Curcuma*, and so on. The chemical types of plant-derived bisabolanes are relatively common. Most of them are featured as highly oxygenated monocyclic bisabolanes bearing a cyclohexane ring. Interestingly, some bisabolanes, such as **184**, **187–190**, **196**, and **201**, are uncommon chlorinated derivatives. It is generally considered that halogenated compounds can be exclusively isolated from the marine environment. The isolation of halogenated bisabolanes from terrestrial plants indicated that terrestrial plants may also possess great potentiality in finding novel halogenated compounds.

Bioactivity Diversity and Potential Applications

Bisabolanes are also attractive for their various and potent biological activities. As shown in **Figure 9** and **Table 1**, the reported bisabolanes exhibited an extensive range of biological activities, including antimicrobial, anti-inflammatory, enzyme inhibitory, cytotoxic, antimicroalga, and other activities. Among the 94 described marine-derived bisabolanes, 43 compounds were found to possess moderate to potent biological activities. 18 compounds showed promising

FIGURE 9 | Bioactivity categories of the reported bisabolanes.
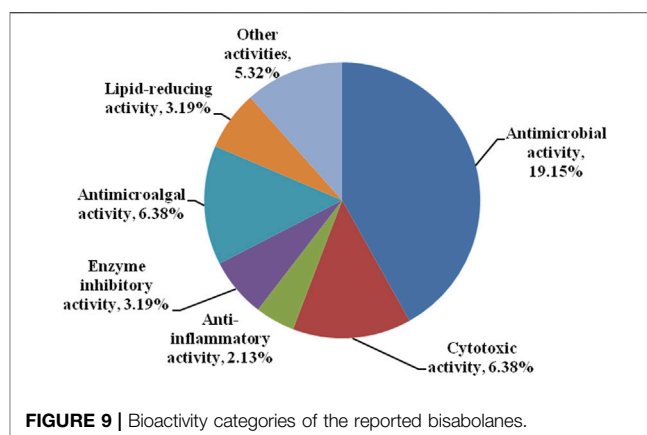
antibacterial or antifungal activity, while 6 compounds possessed various degrees of cytotoxic activity. Most importantly, some of them possessed significant bioactivities, which were higher than the positive controls. For example, **14** inhibited potent cytotoxic activity against A549 and HL-60 cells with IC_{50} values of 1.9 and 5.4 μM, respectively (Lu et al., 2010). **33–35** exhibited strong antibacterial activity against *E. coli*, *E. tarda*, *V. harveyi*, and *V. parahaemolyticus*, with MICs no higher than 8.0 μg/ml (Li et al., 2019a; Li et al., 2019b). In addition, bisabolanes characterized from terrestrial fungi and plants also possess promising activities. Compounds **118** and **119**, two dicyclic bisabolanes produced by the fungus *Pleurotus cystidiosus* were found to have significant cytotoxicity at the nM level. Especially, **119** exhibited the strongest effect on two human prostate cancer DU-145 and C42B cells, with the IC_{50}s of 28 and 52 nM. Further pharmacological studies indicated that **119** induced the apoptosis of DU-145 cells (Zheng et al., 2015). The dicyclic **141** obtained from the rhizomes of *Curcuma longa* displayed more potent anti-inflammatory activity against the LPS-activated production of NO (IC_{50}, 25.5 μM), when compared with the positive control dexamethasone (IC_{50}, 33.6 μM) (Cheng et al., 2019). The aromatic bisabolanes **182** and **183** potently inhibited α-glucosidase with the IC_{50} values of 14.9 and 19.4 μM, respectively, approximately 30 times stronger than the positive control acarbose (IC_{50}, 496 μM) (Song et al., 2021). The attractive bioactivities make many of these compounds suitable lead compounds or even candidates for the development of new medicines and agrochemicals and may trigger further pharmacological and synthesis studies.

In conclusion, bisabolane-type sesquiterpenoids, especially those isolated from marine organisms are considered to be nonnegligible natural products both structurally and biologically. This review systematically summarizes 296 newly reported bisabolanes characterized from fungi, marine algae, soft corals, marine sponges, terrestrial plants, and the others. Among them, 94 members were isolated from marine organisms. The following pharmacological studies indicated the biological potential of these compounds, which exhibited antimicrobial, anti-inflammatory, enzyme inhibitory, cytotoxic, antimicroalgal, and antifouling properties. This is the first attempt to focus on the

TABLE 1 | The environment source, producer, and biological activities of compounds **1**–**94**.

Compounds	Source	Producer	Biological activities	References
(+)-methyl sydowate (**1**), 7-deoxy-7,14-didehydrosydonic acid (**2**), and 7-deoxy-7,8-didehydrosydonic acid (**3**)	Marine fungi	*Aspergillus* sp.	Antibacterial activity	Wei et al. (2010)
(7*R*,10*S*)-7,10-epoxysydonic acid (**4**), (7*S*,10*S*)-7,10-epoxysydonic acid (**5**), (7*R*,11*S*)-7,12-epoxysydonic acid (**6**), (7*S*,11*S*)-7,12-epoxysydonic acid (**7**), 7-deoxy-7,14-didehydro-12-hydroxysydonic acid (**8**), (*Z*)-7-deoxy-7,8-didehydro-12-hydroxysydonic acid (**9**), and (*E*)-7-deoxy-7,8-didehydro-12-hydroxysydonic acid (**10**)	Marine fungi	*Aspergillus* sp. xy02	Antibacterial activity	Wang et al. (2018)
(*S*)-(+)-11-dehydrosydonic acid (**11**) and (7*S*,11*S*)-(+)-12-acetoxysydonic acid (**12**), and expansols A (**13**) and B (**14**)	Marine fungi	*Penicillium expansum*	Cytotoxic activity	Lu et al. (2010)
asperbisabolanes A–N (**15**–**28**)	Marine fungi	*A. sydowii* MCCC 3A00324	Anti-inflammatory activity	Niu et al. (2020)
aspergiterpenoid A (**29**), (–)-sydonol (**30**), (–)-sydonic acid (**31**), (–)-5-(hydroxymethyl)-2-(2′,6′,6′-trimethyltetrahydro-2*H*-pyran-2-yl)phenol (**32**)	Marine fungi	*Aspergillus* sp	Antibacterial and antifouling activity	Li et al. (2012)
ent-aspergoterpenin C (**33**), 7-*O*-methylhydroxysydonic acid (**34**)	Marine fungi	*A. versicolor* SD-330	Antibacterial activity	Li et al. (2019a)
12-hydroxysydowic acid (**35**)	Marine fungi	*A. versicolor* SD-330	Antibacterial activity	Li et al. (2019b)
(7*S*)-(+)-7-*O*-methylsydonol (**36**), (7*S*,11*S*)-(+)-12-hydroxysydonic acid (**37**), and 7-deoxy-7,14-didehydrosydonol (**38**)	Marine fungi	*A. sydowii*	Anti-diabetic and anti-inflammatory activity	Chung et al. (2013)
aspergillusene E (**39**)	Marine fungi	*A. versicolor* XS-20090066	Antimicrobial and antifouling activity	Wu et al. (2020)
methylsulfinyl-1-hydroxyboivinianin A (**40**)	Marine fungi	*P. chrysogenum* LD-201810	Antifungal activity	Ge et al. (2021)
bisabolanoic acid A (**41**)	Marine fungi	*Colletotrichum* sp. SCSIO KcB3-2	Enzyme inhibitory activity	Li et al. (2021)
(±)-flavilane A (**42**), flavilane B (**43**)	Marine fungi	*A. flavipes* 297	Cytotoxic activity	Chen et al. (2021)
bisabolan-1,10,11-triol (**44**), 12-nor-11-acetoxybisabolen-3,6,7-triol (**45**)	Marine fungi	*T. asperellum* cf44-2	Antibacterial and antimicroalgal activity	Song et al. (2018)
trichobisabolins A–H (**46**–**53**)	Marine fungi	*T. asperellum* Y6–2	Antimicroalgal activity	Shi et al. (2019)
54–**57** (names ungiven)	Marine fungi	*A. flavus* QQSG-3	Enzyme inhibitory activity	Wu et al. (2018)
disydonols A–C (**58**–**60**)	Marine fungi	*Aspergillus* sp	Cytotoxic activity	Sun et al. (2012)
peniciaculins A (**61**) and B (**62**), (7*S*)-(–)-10-hydroxysydonic acid (**63**), and 1-hydroxyboivinianin A (**64**)	Marine fungi	*P. aculeatum* SD-321	Antibacterial activity	Jian Li et al. (2015)
laurecomposins A (**65**) and B (**66**)	Algae	*Laurencia composita* Yamada	Antimicroalgal activity	Hu et al. (2020)
okamurenes A–D (**67**–**70**)	Algae	*L. okamurai*	No brine shrimp lethal activity	Liang et al. (2012)
71–**77** (names ungiven)	Soft corals	*Pseudopterogorgia rigida*	Unreported	Georgantea et al. (2014)
perezoperezone (**78**) and curcuperezone (**79**)	Soft corals	*Pseudopterogorgia rigida*	Unreported	Georgantea et al. (2013)
plakordiols A–D (**80**–**83**), (7*R*, 10*R*)-hydroxycurcudiol (**84**), and (7*R*, 10*S*)-hydroxycurcudiol (**85**)	Sponges	*Plakortis simplex*	No cytotoxic and antibacterial activity	Wang et al. (2021)
6-(3-hydroxy-6-methyl-1,5-heptadien-2-yl)-3-methylbenzene-1,4-diol (**86**), 4-hydroxy-3,7-dimethyl-7-(3-methylbut-2-en-1-yl)benzofuran-15-one (**87**), 6-(2-methoxy-5-methylhept-4-en-2-yl)-3-methylbenzene-1,4-diol (**88**), and 9-(3,3-dimethyloxiran-2-yl)-1,7-dimethyl-7-chromen-4-ol (**89**)	Sponges	*Myrmekioderma* sp	Lipid-reducing activity	Costa et al. (2019)
myrmekioperoxides A (**90**) and B (**91**)	Sponges	*Myrmekioderma* sp	Unreported	Wongbundit et al. (2020)
(*E*)-3-isocyanobisabolane-7,10-diene (**92**)	Sponges	*Axinyssa* sp	Brine shrimp lethal activity	Iwashima et al. (2002)
3-formamido-7,8-epoxy-α-bisabolane (**93**) and 3-isocyano-7,8-epoxy-α-bisabolane (**94**)	Sponges	*Axinyssa* sp	No cytotoxic activity	Sun et al. (2010)

chemistry and bioactivity of marine-derived bisabolanes, aiming to summarize the chemical diversity of marine-derived bisabolanes, highlight their novelty and differences between

terrestrial and marine sources, and provide a future perspective of their potential application prospect as lead compounds. It is believed that in the near future, the research

on these fascinating compounds will be increasingly abundant and conducive to the development of new drugs and agrochemicals.

AUTHOR CONTRIBUTIONS

Conceptualization, C-SL; Writing—original draft preparation, C-SL and L-TL; Writing—review and editing, LY, XD, and JL. All authors have read and approved the final manuscript.

REFERENCES

Butler, M. S. (2005). Natural Products to Drugs: Natural Product Derived Compounds in Clinical Trials. *Nat. Prod. Rep.* 22, 162–195. doi:10.1039/b402985m

Carroll, A. R., Copp, B. R., Davis, R. A., Keyzers, R. A., and Prinsep, M. R. (2021). Marine Natural Products. *Nat. Prod. Rep.* 38, 362–413. doi:10.1039/d0np00089b

Chen, Y., Zhu, H.-Y., Xu, L.-C., Wang, S.-P., Liu, S., Liu, G.-D., et al. (2021). Antimicrobial and Cytotoxic Phenolic Bisabolane Sesquiterpenoids from the Fungus *Aspergillus flavipes* 297. *Fitoterapia* 155, 105038. doi:10.1016/j.fitote.2021.105038

Cheng, X., Li, H., Wu, P., Xu, L., Xue, J., and Wei, X. (2019). Two New Bisabolane-type Sesquiterpenoids from the Cooking Liquid of *Curcuma Longa* Rhizomes. *Phytochemistry Lett.* 29, 169–172. doi:10.1016/j.phytol.2018.12.004

Chung, Y.-M., Wei, C.-K., Chuang, D.-W., El-Shazly, M., Hsieh, C.-T., Asai, T., et al. (2013). An Epigenetic Modifier Enhances the Production of Anti-diabetic and Anti-inflammatory Sesquiterpenes from *Aspergillus sydowii*. *Bioorg. Med. Chem.* 21, 3866–3872. doi:10.1016/j.bmc.2013.04.004

Costa, M., Coello, L., Urbatzka, R., Pérez, M., and Thorsteinsdottir, M. (2019). New Aromatic Bisabolane Derivatives with Lipid-Reducing Activity from the marine Sponge *Myrmekioderma* Sp. *Mar. Drugs* 17, 375. doi:10.3390/md17060375

Fraga, B. M. (2011). Natural Sesquiterpenoids. *Nat. Prod. Rep.* 28, 1580. doi:10.1039/c1np00046b

Ge, Y., Tang, W.-L., Huang, Q.-R., Wei, M.-L., Li, Y.-Z., Jiang, L.-L., et al. (2021). New Enantiomers of a Nor-Bisabolane Derivative and Two New Phthalides Produced by the marine-derived Fungus *Penicillium chrysogenum* LD-201810. *Front. Microbiol.* 12, 727670. doi:10.3389/fmicb.2021.727670

Georgantea, P., Ioannou, E., Vagias, C., and Roussis, V. (2013). Perezoperezone and Curcuperezone: Bisabolane Dimers from the Soft Coral *Pseudopterogorgia Rigida*. *Tetrahedron Lett.* 54, 6920–6922. doi:10.1016/j.tetlet.2013.10.041

Georgantea, P., Ioannou, E., Vagias, C., and Roussis, V. (2014). Bisabolane and Chamigrane Sesquiterpenes from the Soft Coral *Pseudopterogorgia Rigida*. *Phytochemistry Lett.* 8, 86–91. doi:10.1016/j.phytol.2014.02.006

Hu, Z.-B., Yu, X.-Q., Wang, B., Liu, A.-H., Zhao, T.-S., Guo, Y.-W., et al. (2020). Structurally Diverse Halosesquiterpenoids from the Red Alga *Laurencia Composita* Yamada. *Fitoterapia* 146, 104716. doi:10.1016/j.fitote.2020.104716

Iwashima, M., Terada, I., Iguchi, K., and Yamori, T. (2002). New Biologically Active marine Sesquiterpenoid and Steroid from the Okinawan Sponge of the Genus *Axinyssa*. *Chem. Pharm. Bull.* 50, 1286–1289. doi:10.1248/cpb.50.1286

Jian Li, J., Wang, H.-F., Chen, G., Huang, S.-D., Zhang, W.-Y., Hua, H.-M., et al. (2015). Structure Determination of Two New Bisabolane-type Sesquiterpenes from the Rhizomes of *Curcuma Longa* by NMR Spectroscopy. *Magn. Reson. Chem.* 53, 536–538. doi:10.1002/mrc.4215

Li, D., Xu, Y., Shao, C.-L., Yang, R.-Y., Zheng, C.-J., Chen, Y.-Y., et al. (2012). Antibacterial Bisabolane-type Sesquiterpenoids from the Sponge-Derived Fungus *Aspergillus* Sp. *Mar. Drugs* 10, 234–241. doi:10.3390/md10010234

Li, X.-D., Li, X.-M., Yin, X.-L., Li, X., and Wang, B.-G. (2019a). Antimicrobial Sesquiterpenoid Derivatives and Monoterpenoids from the Deep-Sea Sediment-Derived Fungus *Aspergillus versicolor* SD-330. *Mar. Drugs* 17, 563. doi:10.3390/md17100563

Li, X.-D., Li, X., Li, X.-M., Yin, X.-L., and Wang, B.-G. (2019b). Antimicrobial Bisabolane-type Sesquiterpenoids from the Deep-Sea Sediment-Derived Fungus *Aspergillus versicolor* SD-330. *Nat. Product. Res.* 35, 4265–4271. (Online ahead of print. doi:10.1080/14786419.2019.1696792

Li, K.-L., Dai, Y., She, J.-L., Zeng, Y.-B., Dai, H.-F., Ou, S.-L., et al. (2021). Bisabolanoic Acid A, a New Polychiral Sesquiterpene with AChE Inhibitory Activity from a Mangrove-Derived Fungus *Colletotrichum* Sp. *J. Asian Nat. Prod. Res.* 24, 88–95. doi:10.1080/10286020.2021.1873297

Liang, Y., Li, X.-M., Cui, C.-M., Li, C.-S., Sun, H., and Wang, B.-G. (2012). Sesquiterpene and Acetogenin Derivatives from the marine Red Alga *Laurencia Okamurai*. *Mar. Drugs* 10, 2817–2825. doi:10.3390/md10122817

Lu, Z., Zhu, H., Fu, P., Wang, Y., Zhang, Z., Lin, H., et al. (2010). Cytotoxic Polyphenols from the marine-derived Fungus *Penicillium expansum*. *J. Nat. Prod.* 73, 911–914. doi:10.1021/np100059m

Lv, J.-J., Wang, Y.-F., Zhang, J.-M., Yu, S., Wang, D., Zhu, H.-T., et al. (2014). Anti-hepatitis B Virus Activities and Absolute Configurations of Sesquiterpenoid Glycosides from *Phyllanthus Emblica*. *Org. Biomol. Chem.* 12, 8764–8774. doi:10.1039/c4ob01196a

Newman, D. J., and Cragg, G. M. (2020). Natural Products as Sources of New Drugs over the Nearly Four Decades from 01/1981 to 09/2019. *J. Nat. Prod.* 83, 770–803. doi:10.1021/acs.jnatprod.9b01285

Niu, S., Yang, L., Zhang, G., Chen, T., Hong, B., Pei, S., et al. (2020). Phenolic Bisabolane and Cuparene Sesquiterpenoids with Anti-inflammatory Activities from the Deep-Sea-Derived *Aspergillus sydowii* MCCC 3A00324 Fungus. *Bioorg. Chem.* 105, 104420. doi:10.1016/j.bioorg.2020.104420

Shi, Z.-Z., Miao, F.-P., Fang, S.-T., Yin, X.-L., and Ji, N.-Y. (2019). Trichobisabolins A-H, Eight New Bisabolane Derivatives from the marine-alga-epiphytic Fungus *Trichoderma Asperellum* Y6-2. *Fitoterapia* 134, 372–377. doi:10.1016/j.fitote.2019.03.010

Shu, H.-Z., Peng, C., Bu, L., Guo, L., Liu, F., and Xiong, L. (2021). Bisabolane-type Sesquiterpenoids: Structural Diversity and Biological Activity. *Phytochemistry* 192, 112927. doi:10.1016/j.phytochem.2021.112927

Song, Y.-P., Miao, F.-P., Fang, S.-T., Yin, X.-L., and Ji, N.-Y. (2018). Halogenated and Nonhalogenated Metabolites from the marine-alga-endophytic Fungus *Trichoderma Asperellum* Cf44-2. *Mar. Drugs* 16, 266. doi:10.3390/md16080266

Song, X.-Q., Yu, J.-H., Sun, J., Liu, K.-L., Zhang, J.-S., and Zhang, H. (2021). Bioactive Sesquiterpenoids from the Flower Buds of *Tussilago Farfara*. *Bioorg. Chem.* 107, 104632. doi:10.1016/j.bioorg.2021.104632

Sun, J.-Z., Chen, K.-S., Liu, H.-L., van Soest, R., and Guo, Y.-W. (2010). New Epoxy-Substituted Nitrogenous Bisabolene-type Sesquiterpenes from a Hainan Sponge *Axinyssa* sp. *Helvetica Chim. Acta* 93, 517–521. doi:10.1002/hlca.200900261

Sun, L.-L., Shao, C.-L., Chen, J.-F., Guo, Z.-Y., Fu, X.-M., Chen, M., et al. (2012). New Bisabolane Sesquiterpenoids from a marine-derived Fungus *Aspergillus* Sp. Isolated from the Sponge *Xestospongia Testudinaria*. *Bioorg. Med. Chem. Lett.* 22, 1326–1329. doi:10.1016/j.bmcl.2011.12.083

Wang, P., Yu, J.-H., Zhu, K., Wang, Y., Cheng, Z.-Q., Jiang, C.-S., et al. (2018). Phenolic Bisabolane Sesquiterpenoids from a Thai Mangrove Endophytic Fungus, *Aspergillus* Sp. Xy02. *Fitoterapia* 127, 322–327. doi:10.1016/j.fitote.2018.02.031

Wang, J., Liu, L., Hong, L.-L., Zhan, K.-X., Lin, Z.-J., Jiao, W.-H., et al. (2021). New Bisabolane-type Phenolic Sesquiterpenoids from the marine Sponge *Plakortis Simplex*. *Chin. J. Nat. Medicines* 19, 626–631. doi:10.1016/s1875-5364(21)60062-6

FUNDING

SUPPLEMENTARY MATERIAL

The Supplementary Material for this article can be found online at: https://www.frontiersin.org/articles/10.3389/fchem.2022.881767/full#supplementary-material

Wei, M.-Y., Wang, C.-Y., Liu, Q.-A., Shao, C.-L., She, Z.-G., and Lin, Y.-C. (2010). Five Sesquiterpenoids from a marine-derived Fungus *Aspergillus* Sp. Isolated from a Gorgonian *Dichotella Gemmacea*. *Mar. Drugs* 8, 941–949. doi:10.3390/md8040941

Wongbundit, S., Mahidol, C., Kaweetripob, W., Prachyawarakorn, V., Eurtivong, C., Sahakitpichan, P., et al. (2020). Biscurcudiols, Myrmekioperoxides, and Myrmekiodermaral from the Thai marine Sponge *Myrmekioderma* Sp. *Tetrahedron* 76, 131162. doi:10.1016/j.tet.2020.131162

Wu, Y., Chen, Y., Huang, X., Pan, Y., Liu, Z., Yan, T., et al. (2018). α-Glucosidase Inhibitors: Diphenyl Ethers and Phenolic Bisabolane Sesquiterpenoids from the Mangrove Endophytic Fungus Aspergillus flavus QQSG-3. *Mar. Drugs* 16, 307. doi:10.3390/md16090307

Wu, J.-S., Yao, G.-S., Shi, X.-H., Rehman, S. U., Xu, Y., Fu, X.-M., et al. (2020). Epigenetic Agents Trigger the Production of Bioactive Nucleoside Derivatives and Bisabolane Sesquiterpenes from the marine-derived Fungus *Aspergillus versicolor. Front. Microbiol.* 11, 85. doi:10.3389/fmicb.2020.00085

Xiao-Dong Li, X.-D., Li, X.-M., Xu, G.-M., Zhang, P., and Wang, B.-G. (2015). Antimicrobial Phenolic Bisabolanes and Related Derivatives from *Penicillium aculeatum* SD-321, a Deep Sea Sediment-Derived Fungus. *J. Nat. Prod.* 78, 844–849. doi:10.1021/acs.jnatprod.5b00004

Zhang, P., Wei, Q., Yuan, X., and Xu, K. (2020). Newly Reported Alkaloids Produced by marine-derived Penicillium Species (Covering 2014-2018). *Bioorg. Chem.* 99, 103840. doi:10.1016/j.bioorg.2020.103840

Zheng, Y., Pang, H., Wang, J., Shi, G., and Huang, J. (2015). New Apoptosis-Inducing Sesquiterpenoids from the Mycelial Culture of Chinese Edible Fungus *Pleurotus Cystidiosus. J. Agric. Food Chem.* 63, 545–551. doi:10.1021/jf504931n

Conflict of Interest: The authors declare that the research was conducted in the absence of any commercial or financial relationships that could be construed as a potential conflict of interest.

Publisher's Note: All claims expressed in this article are solely those of the authors and do not necessarily represent those of their affiliated organizations, or those of the publisher, the editors and the reviewers. Any product that may be evaluated in this article, or claim that may be made by its manufacturer, is not guaranteed or endorsed by the publisher.

Synthesis and Biological Evaluations of Betulinic Acid Derivatives With Inhibitory Activity on Hyaluronidase and Anti-Inflammatory Effects Against Hyaluronic Acid Fragment Induced Inflammation

Zhujun Luo[1,2†], Hao He[1,2,3,4†], Tiantian Tang[5,6,7†], Jun Zhou[1,2], Huifang Li[1,2,3], Navindra P. Seeram[3], Dongli Li[1,2], Kun Zhang[1,2]*, Hang Ma[1,2,3]* and Panpan Wu[1,2]*

[1]School of Biotechnology and Health Sciences, Wuyi University, Jiangmen, China, [2]International Healthcare Innovation Institute, Jiangmen, China, [3]Bioactive Botanical Research Laboratory, Department of Biomedical and Pharmaceutical Sciences, College of Pharmacy, University of Rhode Island, Kingston, NY, United States, [4]School of Chemical Engineering, Shanxi Institute of Science and Technology, Jincheng, China, [5]Laboratory of Nutrition and Development, Key Laboratory of Major Diseases in Children, Ministry of Education, Beijing, China, [6]Beijing Pediatric Research Institute, Beijing Children's Hospital, Capital Medical University, Beijing, China, [7]National Center for Children's Health, Beijing, China

***Correspondence:**
Kun Zhang
kzhang@gdut.edu.cn
Hang Ma
hang_ma@uri.edu
Panpan Wu
wyuchemwpp@126.com

[†]These authors have contributed
equally to this work

We previously reported that the structural modifications of pentacyclic triterpenoids including oleanolic acid resulted in enhanced hyaluronidase inhibitory activity but whether this applies to other pentacyclic triterpenoids such as betulinic acid (BA) is unknown. Herein, we synthesized BA derivatives with an α,β-unsaturated ketene moiety and evaluated for their: 1) hyaluronidase inhibitory activity and, 2) anti-inflammatory effects against lipopolysaccharides (LPS) induced inflammation. Compared to BA, the BA derivatives exerted improved anti-hyaluronidase activity (26.3%–72.8% vs. 22.6%) and anti-inflammatory effects by reducing nitrite production in BV2 cells (3.9%–46.8% vs. 3.4%) and RAW264.7 cells (22.7%–49.2% vs. 20.4%). BA derivatives inhibited LPS-induced production of pro-inflammatory cytokines in THP-1 cells (15.2%–22.4%). BA derivatives also exerted promising anti-inflammatory effects against hyaluronic acid fragment induced nitrite production (8.6%–35.6%) in THP-1 cells. BA derivatives showed augmented anti-hyaluronidase and anti-inflammatory effects but further biological evaluations using *in vivo* models are warranted to confirm their efficacy.

Keywords: betulinic acid, α,β-unsaturated ketene, derivative, hyaluronidase, anti-inflammatory

HIGHLIGHTS

- Novel betulinic acid (BA) derivatives with α,β-unsaturated ketene moiety
- BA derivatives exhibit augmented anti-hyaluronidase activity
- BA derivatives exert anti-inflammatory effects in murine macrophage and human monocyte cells
- BA derivatives inhibit hyaluronic acid fragment induced inflammation in human monocytes

Betulinic Acid Derivatives as Novel Inhibitors of Hyaluronidase

GRAPHICAL ABSTRACT |
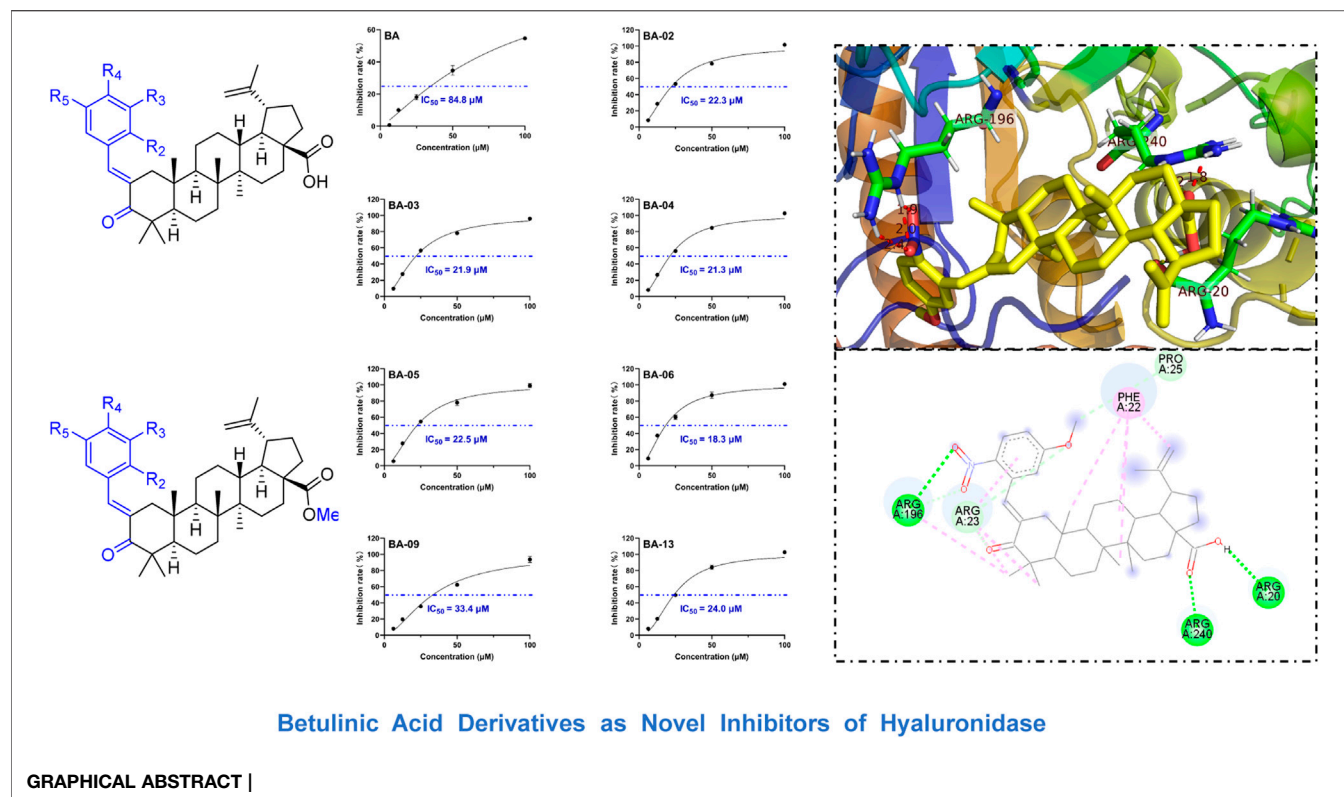
INTRODUCTION

Hyaluronic acid (HA) is a naturally occurring polysaccharide produced in the cell plasma membrane and distributed in all living organisms (Fallacara et al., 2018). HA has a linear structure with numerous repeating units consisting of anionic, nonsulfated disaccharides known as glycosaminoglycan (GAG). Each GAG disaccharide unit contains an amino sugar (N-acetyl-galactosamine or N-acetyl-glucosamine) and a uronic sugar (glucuronic acid, iduronic acid, or galactose) linked by β-1,3-glycosidic bonds (Girish and Kemparaju, 2007). The GAG two-sugar repeating units are connected by 1,3-glycosidic bonds to form a varying length of HA, which can reach to a high molecular weight (HMW) form with up to 2,50,000 GAGs (Girish and Kemparaju, 2007). HA is negatively charged in an aqueous solution, which enables it to attract water molecules and display a non-Newtonian, shear-thinning, and viscoelastic rheological profile. Due to its unique structural characteristics, HA has several critical biological functions, such as maintaining the elastoviscosity of extracellular matrix (ECM) in connective tissues and lubricating movable parts of the body (Price et al., 2007). In addition, HA plays a pivotal regulatory role in various cellular functions (e.g., cell growth, mitosis, and migration) and physiological conditions including tumor development and inflammation (Fallacara et al., 2018). Notably, HA's structural property, especially its size, and the synthesis-degradation rate, is a key factor for its modulatory effects in the development of inflammation (Jiang et al., 2011). Reported studies suggest that HA can exert both pro- and anti-inflammatory effects and this opposite effect is mediated by its length. Intact high molecular weight HA (HMWHA; $>1 \times 10^6$ Da) exerts anti-inflammatory effects by suppressing the recruitment of inflammatory cells and reducing the levels of pro-inflammatory cytokines (Quero et al., 2013; Litwiniuk et al., 2016). On the contrary, HMWHA can be degraded into smaller fragments known as low molecular weight HAs (LMWHAs; 2×10^4–1×10^6 Da), which stimulates the production of pro-inflammatory cytokines and chemokines (Litwiniuk et al., 2016; Fallacara et al., 2018) The degradation of HMWHA can be mediated by two types of mechanisms: 1) non-specific oxidative damage by reactive oxygen species (e.g., free radicals) generated during tissue injury and infection; and 2) fragmentation catalyzed by a group of enzymes named hyaluronidases (Fallacara et al., 2018). Hyaluronidase (HAase) is the key enzyme catalyzing the cleavage of the β-1,4-glycosidic bonds of HA to produce small HA fragments ($<2 \times 10^4$ Da). HA fragments can bind to a set HA cell surface receptor, such as CD44 and toll-like receptors, and subsequently triggers signaling cascades to exacerbate inflammation (Quero et al., 2013). Thus, HAase inhibitors which have the potential to suppress the generation of HA fragments are regarded as promising anti-inflammatory agents (Girish et al., 2009).

Phytochemicals including triterpenes from medicinal plants show great promise as HAase inhibitors. For instance, a group of pentacyclic triterpenoids, including a representative compound, namely, ursolic acid (UA), from *Prismatomeris tetrandra* showed inhibitory effects on the activity of HAase. Furthermore, chemical modifications (i.e., acetylation and methylation) of the UA skeleton resulted in the generation of new UA analogues with

enhanced anti-HAase activity (Abdullah et al., 2016). In addition, an extract of *Carissa carandas* leaf containing a high level of UA was reported to inhibit the activity of HAase and reduce the level of inflammatory biomarkers, such as nuclear factor kappa B, in human monocytes (Neimkhum et al., 2021). Given these previously published data, our laboratory initiated a project to screen for small molecule based HAase inhibitors from natural resources and a triterpenoid, namely, oleanolic acid (OA), as a "lead compound". We showed that chemical synthesis of OA derivatives with indole moieties led to HAase inhibitors with augmented activity (He et al., 2021). Betulinic acid (BA), another subtype of pentacyclic triterpenoid, has been reported to show anti-HAase and anti-inflammatory effects (Tsai et al., 2011; Abdullah et al., 2016; Ou et al., 2019). However, it is not clear whether the inhibitory effect of BA on HAase can be improved by chemical modifications, nor whether BA based HAase inhibitors can inhibit HA fragment induced inflammation. Herein, we initiated this study to 1) synthesize novel BA derivatives and assess their anti-HAase activity using *in vitro* and in silico methods; and 2) evaluate the anti-inflammatory effects of BA derived HAase inhibitors against HA-fragment induced inflammation using a panel of murine and human cells.

GENERAL PROCEDURES FOR THE SYNTHESIS OF BA DERIVATIVES

Preparation of BA Derivatives BA-O and BA-O-Me

BA was dissolved in acetone at 0°C; Jones reagent was added to the reaction mixture drop-wise until the solution color was a stable light brown color, which implied that the Jones reagent was in slight excess to oxidize the C-3 hydroxyl group into a ketone to produce the intermediate BA-O. Then the BA-O was dissolved in DMF. K_2CO_3 and CH_3I were added and the mixture was stirred overnight at room temperature to obtain the BA derivative BA-O-Me.

General Procedure for the Preparation of BA Derivatives (BA-01 to BA-22)

Derivatives BA-01~BA-13 could be prepared by Claisen Schmidt condensation of intermediate BA-O with corresponding aldehydes in the presence of ethanolic potassium hydroxide in good yield at room temperature. The same condition of reactions starting with BA-O-Me led to derivatives BA-14~BA-22. All the results were detailed below.

Synthesis of BA Derivative BA-01–BA-13

BA-01   *(1R,3aS,5aR,5bR,7aR,11aR,11bR,13aR,13bR)-10-((E)-3-fluorobenzylidene)-5a,5b,8,8,11a-pentamethyl-9-oxo-1-(prop-1-en-2-yl)icosahydro-3aH-cyclopenta[a]chrysene-3a-carboxylic acid* (BA-01, $C_{37}H_{49}FO_3$). According to the general procedure, derivative BA-01 was prepared by Claisen Schmidt condensation of intermediate BA-O with 3-fluorobenzaldehyde in the presence of ethanolic potassium hydroxide at room temperature. The residue was purified by flash

chromatography (eluent: petroleum ether: ethyl acetate = 10: 1) to afford BA-01 as a white solid with a yield of 90%. ^1H NMR (600 MHz, Chloroform-*d*) δ 7.32 (dd, J = 3.0, 1.5 Hz, 1H), 7.27 (td, J = 8.0, 6.0 Hz, 1H), 7.08 (d, J = 7.8 Hz, 1H), 7.00 (dt, J = 10.2, 2.1 Hz, 1H), 6.93 (td, J = 8.4, 2.6 Hz, 1H), 4.79–4.48 (m, 2H), 3.01–2.85 (m, 2H), 2.22–2.11 (m, 2H), 2.11–2.06 (m, 1H), 1.95–1.86 (m, 2H), 1.60 (d, J = 34.7 Hz, 5H), 1.47–1.29 (m, 11H), 1.24–1.11 (m, 3H), 1.04 (s, 3H), 1.02 (s, 3H), 0.93 (s, 3H), 0.87 (s, 3H), 0.69 (s, 3H). ^{13}C NMR (151 MHz, CDCl$_3$) δ 208.09, 181.99, 161.78, 150.38, 138.08, 135.92, 135.39, 129.92, 126.07, 116.57, 115.23, 109.79, 56.43, 52.82, 49.15, 48.35, 46.85, 45.24, 44.31, 42.51, 40.52, 38.43, 37.02, 36.54, 33.01, 32.05, 30.59, 29.67, 29.42, 25.54, 22.33, 21.63, 20.33, 19.47, 15.81, 15.47, 14.61. HRMS (ESI): $C_{37}H_{49}FNaO_3$ (583.3558) $[M + Na]^+$ = 583.3558.

BA-02   *(1R,3aS,5aR,5bR,7aR,11aR,11bR,13aR,13bR)-10-((E)-2-bromobenzylidene)-5a,5b,8,8,11a-pentamethyl-9-oxo-1-(prop-1-en-2-yl)icosahydro-3aH-cyclopenta[a]chrysene-3a-carboxylic acid* (BA-02, $C_{37}H_{49}BrO_3$). According to the general procedure, derivative BA-02 was prepared by Claisen Schmidt condensation of intermediate BA-O with 2-bromobenzaldehyde in the presence of ethanolic potassium hydroxide at room temperature. The residue was purified by flash chromatography (eluent: petroleum ether: ethyl acetate = 10: 1) to afford BA-02 as a white solid with a yield of 71%. ^1H NMR (600 MHz, Chloroform-*d*) δ 7.61 (dd, J = 8.0, 1.2 Hz, 1H), 7.50–7.47 (m, 1H), 7.33 (td, J = 7.5, 1.2 Hz, 1H), 7.22 (dd, J = 7.8, 1.6 Hz, 1H), 7.18 (td, J = 7.7, 1.7 Hz, 1H), 4.66 (dt, J = 71.4, 1.6 Hz, 2H), 2.99 (td, J = 10.8, 4.9 Hz, 1H), 2.81 (dd, J = 16.0, 1.5 Hz, 1H), 2.28 (dt, J = 13.0, 3.4 Hz, 1H), 2.21 (td, J = 12.3, 3.6 Hz, 1H), 2.02–1.94 (m, 3H), 1.66 (d, J = 32.6 Hz, 5H), 1.46 (tdd, J = 22.8, 16.7, 13.3 Hz, 10H), 1.32 (d, J = 10.6 Hz, 1H), 1.26–1.21 (m, 2H), 1.17 (s, 3H), 1.13 (s, 3H), 1.09–1.01 (m, 1H), 0.99 (s, 3H), 0.95 (s, 3H), 0.80 (s, 3H). ^{13}C NMR (151 MHz, CDCl$_3$) δ 208.06, 181.59, 150.48, 136.57, 136.40, 135.99, 132.86, 130.12, 129.42, 127.04, 124.81, 109.65, 56.38, 53.29, 49.13, 48.36, 46.81, 45.71, 43.36, 42.50, 40.54, 38.41, 37.00, 36.85, 33.17, 32.04, 30.56, 29.65, 28.91, 25.49, 22.42, 21.46, 20.19, 19.43, 15.73, 15.54, 14.60. HRMS (ESI): $C_{37}H_{49}{}^{79}BrNaO_3$ (643.2757) $[M + Na]^+$ = 643.2757, $C_{37}H_{49}{}^{81}BrNaO_4$ (645.2737) $[M + Na]^+$ = 645.2737.

BA-03   *(1R,3aS,5aR,5bR,7aR,11aR,11bR,13aR,13bR)-10-((E)-5-methoxy-2-nitrobenzylidene)-5a,5b,8,8,11a-pentamethyl-9-oxo-1-(prop-1-en-2-yl)icosahydro-3aH-cyclopenta[a]chrysene-3a-carboxylic acid* (BA-03, $C_{38}H_{51}NO_6$). According to the general procedure, derivative BA-03 was prepared by Claisen Schmidt condensation of intermediate BA-O with 5-methoxy-2-nitrobenzaldehyde in the presence of ethanolic potassium hydroxide at room temperature. The residue was purified by flash chromatography (eluent: petroleum ether: ethyl acetate = 10: 1) to afford BA-03 as a white solid with a yield of 79%. ^1H NMR (600 MHz, Chloroform-*d*) δ 8.20 (d, J = 9.1 Hz, 1H), 7.60 (d, J = 2.6 Hz, 1H), 6.93 (dd, J = 9.2, 2.8 Hz, 1H), 6.67 (d, J = 2.8 Hz, 1H), 4.77–4.50 (m, 2H), 3.91 (s, 3H), 2.97 (td, J = 10.8, 5.0 Hz, 1H), 2.63 (dd, J = 15.8, 1.4 Hz, 1H), 2.27 (dt, J = 12.9, 3.3 Hz, 1H), 2.20 (td, J = 12.3, 3.6 Hz, 1H), 1.97 (qd, J = 9.1, 8.0, 3.0 Hz, 2H), 1.87–1.78 (m, 1H), 1.69–1.58 (m, 5H), 1.52–1.44 (m, 3H), 1.43–1.35 (m, 5H), 1.33 (d, J = 7.0 Hz, 1H), 1.29–1.24 (m, 2H), 1.22 (dt, J = 13.2, 3.2 Hz, 2H), 1.18 (s, 3H), 1.13 (s, 3H),

1.03–0.98 (m, 1H), 0.96 (s, 3H), 0.93 (s, 3H), 0.80 (s, 3H). ^{13}C NMR (151 MHz, CDCl$_3$) δ 207.90, 181.11, 163.16, 150.59, 140.90, 135.58, 135.29, 134.92, 127.63, 115.75, 113.33, 109.58, 56.35, 56.07, 53.41, 49.07, 48.25, 46.81, 45.97, 43.04, 42.50, 40.55, 38.36, 36.98, 33.18, 32.02, 30.55, 29.71, 29.63, 28.64, 25.46, 22.41, 21.41, 20.12, 19.43, 15.73, 15.55, 14.57. HRMS (ESI): C$_{38}$H$_{51}$NNaO$_6$ (640.3609) [M + Na]$^+$ = 640.3609.

BA-04 *(1R,3aS,5aR,5bR,7aR,11aR,11bR,13aR,13bR)-10-((E)-5-fluoro-2-nitrobenzylidene)-5a,5b,8,8,11a-pentamethyl-9-oxo-1-(prop-1-en-2-yl)icosahydro-3aH-cyclopenta[a]chrysene-3a-carboxylic acid* (BA-04, C$_{37}$H$_{48}$FNO$_5$). According to the general procedure, derivative BA-04 was prepared by Claisen Schmidt condensation of intermediate BA-O with 5-fluoro-2-nitrobenzaldehyde in the presence of ethanolic potassium hydroxide at room temperature. The residue was purified by flash chromatography (eluent: petroleum ether: ethyl acetate = 10: 1) to afford BA-04 as a white solid with a yield of 88%. ^{1}H NMR (600 MHz, Chloroform-*d*) δ 8.20 (dd, *J* = 9.1, 5.0 Hz, 1H), 7.54 (d, *J* = 2.8 Hz, 1H), 7.17 (ddd, *J* = 9.5, 7.1, 2.8 Hz, 1H), 6.96 (dd, *J* = 8.5, 2.8 Hz, 1H), 4.74–4.55 (m, 2H), 2.97 (td, *J* = 10.7, 5.0 Hz, 1H), 2.66–2.52 (m, 1H), 2.27 (dt, *J* = 13.0, 3.4 Hz, 1H), 2.20 (td, *J* = 12.3, 3.6 Hz, 1H), 2.01–1.94 (m, 2H), 1.88 (dd, *J* = 15.9, 3.0 Hz, 1H), 1.64 (d, *J* = 34.2 Hz, 5H), 1.55–1.32 (m, 11H), 1.30–1.18 (m, 3H), 1.18 (s, 3H), 1.13 (s, 3H), 1.04–0.97 (m, 1H), 0.97 (s, 3H), 0.94 (s, 3H), 0.80 (s, 3H). ^{13}C NMR (151 MHz, CDCl$_3$) δ 207.43, 181.64, 163.71, 150.42, 144.10, 136.70, 135.63, 132.95, 127.83, 117.69, 115.82, 109.70, 56.36, 53.36, 49.07, 48.24, 46.82, 45.95, 43.10, 42.50, 40.55, 38.36, 37.00, 36.98, 33.13, 32.02, 30.53, 29.62, 28.67, 25.39, 22.41, 21.42, 20.11, 19.39, 15.70, 15.54, 14.56. HRMS (ESI): C$_{37}$H$_{48}$FNNaO$_5$ (628.3409) [M + Na]$^+$ = 628.3408.

BA-05 *(1R,3aS,5aR,5bR,7aR,11aR,11bR,13aR,13bR)-10-((E)-2-methoxybenzylidene)-5a,5b,8,8,11a-pentamethyl-9-oxo-1-(prop-1-en-2-yl)icosahydro-3aH-cyclopenta[a]chrysene-3a-carboxylic acid* (BA-05, C$_{38}$H$_{52}$O$_4$). According to the general procedure, derivative BA-05 was prepared by Claisen Schmidt condensation of intermediate BA-O with 2-methoxybenzaldehyde in the presence of ethanolic potassium hydroxide at room temperature. The residue was purified by flash chromatography (eluent: petroleum ether: ethyl acetate = 10: 1) to afford BA-05 as a white solid with a yield of 74%. ^{1}H NMR (600 MHz, Chloroform-*d*) δ 7.78–7.74 (m, 1H), 7.30 (ddd, *J* = 19.2, 7.7, 1.7 Hz, 2H), 6.98 (t, *J* = 7.5 Hz, 1H), 6.90 (d, *J* = 8.3 Hz, 1H), 4.68 (d, *J* = 68.0 Hz, 2H), 3.83 (s, 3H), 3.00 (ddd, *J* = 15.9, 5.7, 3.1 Hz, 2H), 2.33–2.26 (m, 1H), 2.23 (td, *J* = 12.3, 3.6 Hz, 1H), 2.11 (dd, *J* = 16.1, 3.1 Hz, 1H), 2.05–1.93 (m, 2H), 1.68 (d, *J* = 33.8 Hz, 5H), 1.56–1.47 (m, 2H), 1.49–1.39 (m, 8H), 1.25 (ddd, *J* = 16.3, 10.4, 4.1 Hz, 3H), 1.14 (s, 3H), 1.13 (s, 3H), 1.08 (dd, *J* = 13.1, 4.3 Hz, 1H), 1.01 (s, 3H), 0.96 (s, 3H), 0.79 (s, 3H). ^{13}C NMR (151 MHz, CDCl$_3$) δ 207.89, 182.06, 158.39, 150.50, 133.72, 133.24, 129.88, 129.83, 125.01, 120.02, 110.69, 109.66, 56.43, 55.49, 53.10, 49.16, 48.40, 46.83, 45.30, 43.99, 42.50, 40.53, 38.45, 37.02, 36.64, 33.17, 32.07, 30.59, 29.67, 29.29, 25.57, 22.53, 21.52, 20.29, 19.46, 15.71, 15.53, 14.61. HRMS (ESI): C$_{38}$H$_{52}$NaO$_4$ (595.3758) [M + Na]$^+$ = 595.3758.

BA-06 *(1R,3aS,5aR,5bR,7aR,11aR,11bR,13aR,13bR)-10-((E)-4-fluoro-2-nitrobenzylidene)-5a,5b,8,8,11a-pentamethyl-9-oxo-1-(prop-1-en-2-yl)icosahydro-3aH-cyclopenta[a]chrysene-3a-carboxylic acid* (BA-06, C$_{37}$H$_{48}$FNO$_5$). According to the general procedure, derivative BA-06 was prepared by Claisen Schmidt condensation of intermediate BA-O with 4-fluoro-2-nitrobenzaldehyde in the presence of ethanolic potassium hydroxide at room temperature. The residue was purified by flash chromatography eluent: petroleum ether: ethyl acetate = 10: 1) to afford BA-06 as a white solid with a yield of 69%. ^{1}H NMR (600 MHz, Chloroform-*d*) δ 7.85 (dd, *J* = 8.3, 2.7 Hz, 1H), 7.52 (d, *J* = 1.6 Hz, 1H), 7.38 (ddd, *J* = 9.9, 7.3, 2.7 Hz, 1H), 7.30–7.26 (m, 1H), 4.73–4.56 (m, 2H), 2.97 (td, *J* = 10.8, 5.1 Hz, 1H), 2.62 (dd, *J* = 15.8, 1.4 Hz, 1H), 2.27 (dt, *J* = 12.9, 3.3 Hz, 1H), 2.20 (td, *J* = 12.3, 3.6 Hz, 1H), 2.03–1.91 (m, 2H), 1.89–1.82 (m, 1H), 1.76–1.68 (m, 1H), 1.67 (s, 3H), 1.61 (t, *J* = 11.4 Hz, 1H), 1.51–1.44 (m, 3H), 1.42 (tt, *J* = 9.1, 4.9 Hz, 5H), 1.38–1.34 (m, 1H), 1.32 (d, *J* = 16.0 Hz, 1H), 1.27 (d, *J* = 17.8 Hz, 2H), 1.21 (ddt, *J* = 10.7, 8.3, 3.6 Hz, 2H), 1.18 (s, 3H), 1.13 (s, 3H), 0.97 (s, 3H), 0.94 (s, 3H), 0.79 (s, 3H).13C NMR (151 MHz, CDCl3) δ 207.58, 181.81, 150.46, 136.68, 132.88, 132.57, 132.52, 130.94, 128.86, 120.87, 120.73, 112.77, 112.59, 109.66, 77.25, 77.04, 76.83, 65.60, 56.38, 53.36, 49.08, 48.31, 46.81, 45.93, 43.21, 42.50, 40.55, 38.37, 37.01, 36.97, 33.16, 32.02, 30.58, 30.54, 29.62, 28.69, 25.42, 22.41, 21.44, 20.11, 19.42, 19.20, 15.70, 15.54, 14.57, 13.75. HRMS (ESI): C$_{37}$H$_{48}$FNNaO$_5$ (628.3409) [M + Na]$^+$ = 628.3409.

BA-07 *(1R,3aS,5aR,5bR,7aR,11aR,11bR,13aR,13bR)-10-((E)-2-fluorobenzylidene)-5a,5b,8,8,11a-pentamethyl-9-oxo-1-(prop-1-en-2-yl)icosahydro-3aH-cyclopenta[a]chrysene-3a-carboxylic acid* (BA-07, C$_{37}$H$_{49}$FO$_3$). According to the general procedure, derivative BA-07 was prepared by Claisen Schmidt condensation of intermediate BA-O with 2-fluorobenzaldehyde in the presence of ethanolic potassium hydroxide at room temperature. The residue was purified by flash chromatography (eluent: petroleum ether: ethyl acetate = 10: 1) to afford BA-07 as a white solid with a yield of 57%. ^{1}H NMR (600 MHz, Chloroform-*d*) δ 7.59–7.55 (m, 1H), 7.32 (dddd, *J* = 12.9, 7.3, 6.1, 1.8 Hz, 2H), 7.17 (td, *J* = 7.5, 1.1 Hz, 1H), 7.12–7.06 (m, 1H), 5.00–4.54 (m, 2H), 3.00 (td, *J* = 10.8, 4.9 Hz, 1H), 2.91 (d, *J* = 16.1 Hz, 1H), 2.29 (dt, *J* = 13.0, 3.3 Hz, 1H), 2.23 (td, *J* = 12.3, 3.6 Hz, 1H), 2.11 (dd, *J* = 16.5, 3.1 Hz, 1H), 1.99 (dq, *J* = 11.9, 9.2, 8.0 Hz, 2H), 1.71 (s, 4H), 1.65 (t, *J* = 11.4 Hz, 1H), 1.52 (ddd, *J* = 18.2, 8.9, 4.1 Hz, 2H), 1.47 (d, *J* = 3.4 Hz, 2H), 1.46–1.39 (m, 6H), 1.28–1.21 (m, 2H), 1.14 (s, 3H), 1.13 (s, 3H), 1.08 (dd, *J* = 13.0, 4.4 Hz, 1H), 1.01 (s, 3H), 0.96 (s, 4H), 0.79 (s, 3H). ^{13}C NMR (151 MHz, CDCl3) δ 207.69, 181.76, 160.04, 150.53, 109.65, 56.41, 53.07, 49.14, 48.36, 46.82, 45.41, 43.97, 42.51, 40.54, 38.42, 37.01, 36.64, 33.12, 32.05, 30.57, 29.66, 29.19, 25.55, 22.44, 21.53, 20.27, 19.46, 19.19, 15.77, 15.52, 14.60, 13.74. HRMS (ESI): C$_{37}$H$_{49}$FNaO$_3$ (583.3558) [M + Na]$^+$ = 583.3558.

BA-08 *(1R,3aS,5aR,5bR,7aR,11aR,11bR,13aR,13bR)-10-((E)-3-bromobenzylidene)-5a,5b,8,8,11a-pentamethyl-9-oxo-1-(prop-1-en-2-yl)icosahydro-3aH-cyclopenta[a]chrysene-3a-carboxylic acid* (BA-08, C$_{37}$H$_{49}$BrO$_3$). According to the general procedure, derivative BA-08 was prepared by Claisen Schmidt condensation of intermediate BA-O with 3-bromobenzaldehyde in the presence of ethanolic potassium hydroxide at room temperature. The residue was purified by flash chromatography (eluent: petroleum ether: ethyl acetate = 10: 1) to afford BA-08 as a white solid with a yield of 85%. ^{1}H NMR (600 MHz, Chloroform-

d) δ 7.51 (d, *J* = 1.8 Hz, 1H), 7.45 (dt, *J* = 7.9, 1.6 Hz, 1H), 7.39–7.37 (m, 1H), 7.34–7.31 (m, 1H), 7.28 (t, *J* = 7.8 Hz, 1H), 4.95–4.54 (m, 2H), 3.14–2.93 (m, 2H), 2.34–2.20 (m, 2H), 2.18–2.11 (m, 1H), 2.04–1.91 (m, 2H), 1.79–1.61 (m, 5H), 1.56–1.40 (m, 11H), 1.31–1.22 (m, 3H), 1.13 (s, 3H), 1.12 (s, 3H), 1.02 (s, 3H), 0.97 (s, 3H), 0.79 (s, 3H). ^{13}C NMR (151 MHz, CDCl3) δ 208.00, 181.84, 181.78, 167.75, 150.42, 138.10, 135.66, 133.22, 132.32, 131.25, 130.93, 129.95, 128.86, 128.09, 122.55, 109.75, 77.25, 77.03, 76.82, 65.59, 56.43, 52.91, 49.15, 48.36, 46.84, 45.31, 44.13, 42.52, 40.64, 40.54, 38.42, 37.02, 36.62, 34.99, 34.88, 33.04, 32.05, 31.52, 31.45, 30.61, 30.58, 30.33, 30.20, 30.15, 29.71, 29.69, 29.36, 25.53, 22.36, 21.63, 20.33, 19.50, 19.20, 15.82, 15.50, 14.63, 13.75, 1.05. HRMS (ESI): $C_{37}H_{50}{}^{79}BrO_3$ (621.2938) [M + H]$^+$ = 621.2938, $C_{37}H_{50}{}^{81}BrO_3$ (623.2917) [M + H]$^+$ = 623.2919.

BA-09 *(1R,3aS,5aR,5bR,7aR,11aR,11bR,13aR,13bR)-10-((E)-3-methoxybenzylidene-5a,5b,8,8,11a-pentamethyl-9-oxo-1-(prop-1-en-2-yl)icosahydro-3aH-cyclopenta[a]chrysene-3a-carboxylic acid* (BA-09, $C_{38}H_{52}O_4$). According to the general procedure, derivative BA-09 was prepared by Claisen Schmidt condensation of intermediate BA-O with 3-methoxybenzaldehyde in the presence of ethanolic potassium hydroxide at room temperature. The residue was purified by flash chromatography (eluent: petroleum ether: ethyl acetate = 10: 1) to afford BA-09 as a white solid with a yield of 87%. ^{1}H NMR (600 MHz, Chloroform-*d*) δ 7.45 (dd, *J* = 2.8, 1.5 Hz, 1H), 7.33 (t, *J* = 7.9 Hz, 1H), 7.01 (d, *J* = 7.7 Hz, 1H), 6.93 (t, *J* = 2.0 Hz, 1H), 6.88 (dd, *J* = 8.1, 2.6 Hz, 1H), 4.84–4.55 (m, 2H), 3.83 (s, 3H), 3.17–2.96 (m, 2H), 2.32–2.21 (m, 2H), 2.21–2.16 (m, 1H), 2.05–1.96 (m, 2H), 1.69 (d, *J* = 34.9 Hz, 5H), 1.57–1.38 (m, 12H), 1.27 (ddt, *J* = 16.6, 10.9, 3.8 Hz, 2H), 1.14 (s, 3H), 1.12 (s, 3H), 1.02 (s, 3H), 0.97 (s, 3H), 0.79 (s, 3H). ^{13}C NMR (151 MHz, CDCl$_3$) δ 208.24, 181.98, 159.43, 150.46, 137.32, 137.29, 134.55, 129.42, 122.39, 116.03, 113.97, 109.71, 56.44, 55.28, 52.86, 49.16, 48.39, 46.84, 45.22, 44.35, 42.50, 40.52, 38.44, 37.02, 36.52, 33.06, 32.06, 30.60, 29.68, 29.42, 25.56, 22.36, 21.63, 20.34, 19.48, 15.81, 15.49, 14.62. HRMS (ESI): $C_{38}H_{53}O_4$ (573.3938) [M + H]$^+$ = 573.3938.

BA-10 *(1R,3aS,5aR,5bR,7aR,11aR,11bR,13aR,13bR)-10-(E)-4-fluorobenzylidene-5a,5b,8,8,11a-pentamethyl-9-oxo-1-(prop-1-en-2-yl)icosahydro-3aH-cyclopenta[a]chrysene-3a-carboxylic acid* (BA-10, $C_{37}H_{49}FO_3$). According to the general procedure, derivative BA-10 was prepared by Claisen Schmidt condensation of intermediate BA-O with 4-fluorobenzaldehyde in the presence of ethanolic potassium hydroxide at room temperature. The residue was purified by flash chromatography (eluent: petroleum ether: ethyl acetate = 10: 1) to afford BA-10 as a white solid with a yield of 91%. ^{1}H NMR (600 MHz, Chloroform-*d*) δ 7.45 (t, *J* = 2.0 Hz, 1H), 7.42–7.38 (m, 2H), 7.10 (t, *J* = 8.7 Hz, 2H), 4.79–4.62 (m, 2H), 3.07–2.96 (m, 2H), 2.33–2.22 (m, 2H), 2.21–2.16 (m, 1H), 2.07–1.95 (m, 2H), 1.70 (d, *J* = 34.3 Hz, 5H), 1.58–1.39 (m, 10H), 1.34–1.24 (m, 3H), 1.13 (d, *J* = 13.8 Hz, 7H), 1.03 (s, 3H), 0.97 (s, 3H), 0.78 (s, 3H). ^{13}C NMR (151 MHz, CDCl$_3$) δ 208.09, 182.06, 161.70, 150.53, 136.22, 133.82, 132.21, 132.16, 132.09, 115.66, 115.52, 109.69, 56.44, 52.76, 49.16, 48.45, 46.83, 45.15, 44.40, 42.51, 40.52, 38.45, 37.02, 36.48, 33.04, 32.05, 30.61, 29.67, 29.48, 25.61, 22.33, 21.66, 20.34, 19.51, 15.81, 15.47, 14.61. HRMS (ESI): $C_{37}H_{49}FNaO_3$ (583.3558) [M + Na]$^+$ = 583.3558.

BA-11 *(1R,3aS,5aR,5bR,7aR,11aR,11bR,13aR,13bR)-5a,5b,8,8,11a-pentamethyl-9-oxo-1-(prop-1-en-2-yl)-10-((E)-3-(trifluoromethyl)benzylidene)icosahydro-3aH-cyclopenta[a]chrysene-3a-carboxylic acid* (BA-11, $C_{38}H_{49}F_3O_3$). According to the general procedure, derivative BA-11 was prepared by Claisen Schmidt condensation of intermediate BA-O with 3-(trifluoromethyl) benzaldehyde in the presence of ethanolic potassium hydroxide at room temperature. The residue was purified by flash chromatography (eluent: petroleum ether: ethyl acetate = 10: 1) to afford BA-11 as a white solid with a yield of 83%. ^{1}H NMR (600 MHz, Chloroform-*d*) δ 7.62 (s, 1H), 7.60–7.56 (m, 2H), 7.56–7.51 (m, 1H), 7.46 (d, *J* = 2.4 Hz, 1H), 4.90–4.61 (m, 2H), 3.23–2.83 (m, 2H), 2.34–2.28 (m, 1H), 2.25 (td, *J* = 12.3, 3.6 Hz, 1H), 2.19 (dd, *J* = 16.2, 3.0 Hz, 1H), 2.00 (dq, *J* = 12.0, 9.2, 8.0 Hz, 2H), 1.77–1.62 (m, 5H), 1.56–1.39 (m, 10H), 1.30–1.23 (m, 3H), 1.14 (d, *J* = 6.2 Hz, 7H), 1.02 (s, 3H), 0.97 (s, 3H), 0.80 (s, 3H). ^{13}C NMR (151 MHz, CDCl$_3$) δ 207.94, 181.90, 150.39, 136.72, 135.99, 135.51, 132.50, 130.84, 128.95, 127.18, 124.83, 123.03, 109.74, 56.43, 52.92, 49.13, 48.42, 46.83, 45.35, 44.16, 42.52, 40.54, 38.43, 37.01, 36.62, 33.05, 32.04, 30.59, 29.68, 29.32, 25.49, 22.36, 21.62, 20.31, 19.46, 15.84, 15.49, 14.63. HRMS (ESI): $C_{38}H_{50}F_3O_3$ (611.3707) [M + H]$^+$ = 611.3707.

BA-12 *(1R,3aS,5aR,5bR,7aR,11aR,11bR,13aR,13bR)-10-((E)-3-chlorobenzylidene)-5a,5b,8,8,11a-pentamethyl-9-oxo-1-(prop-1-en-2-yl)icosahydro-3aH-cyclopenta[a]chrysene-3a-carboxylic acid* (BA-12, $C_{37}H_{49}ClO_3$). According to the general procedure, derivative BA-12 was prepared by Claisen Schmidt condensation of intermediate 01 with 3-chlorobenzaldehyde in the presence of ethanolic potassium hydroxide at room temperature. The residue was purified by flash chromatography (eluent: petroleum ether: ethyl acetate = 10: 1) to afford BA-12 as a white solid with a yield of 79%. ^{1}H NMR (600 MHz, Chloroform-*d*) δ 7.45–7.37 (m, 1H), 7.37–7.32 (m, 2H), 7.31–7.26 (m, 2H), 4.79–4.58 (m, 2H), 3.06–2.87 (m, 2H), 2.33–2.21 (m, 2H), 2.17 (dd, *J* = 16.4, 3.1 Hz, 1H), 2.06–1.95 (m, 2H), 1.69 (d, *J* = 34.2 Hz, 5H), 1.56–1.39 (m, 12H), 1.33–1.22 (m, 2H), 1.14 (s, 3H), 1.12 (s, 3H), 1.03 (s, 3H), 0.97 (s, 3H), 0.79 (s, 3H). ^{13}C NMR (151 MHz, CDCl$_3$) δ 208.03, 181.93, 150.40, 137.79, 135.77, 135.58, 134.35, 130.20, 129.69, 128.36, 127.81, 109.74, 56.44, 52.89, 49.14, 48.34, 46.83, 45.29, 44.15, 42.51, 40.52, 38.41, 37.01, 36.60, 33.02, 32.05, 30.60, 29.68, 29.36, 25.52, 22.35, 21.62, 20.32, 19.48, 15.81, 15.49, 14.62. HRMS (ESI): $C_{37}H_{50}ClO_3$ (577.3443) [M + H]$^+$ = 577.3443.

BA-13 *(1R,3aS,5aR,5bR,7aR,11aR,11bR,13aR,13bR)-10-((E)-4-methoxybenzylidene)-5a,5b,8,8,11a-pentamethyl-9-oxo-1-(prop-1-en-2-yl)icosahydro-3aH-cyclopenta[a]chrysene-3a-carboxylic acid* (BA-13, $C_{38}H_{52}O_4$). According to the general procedure, derivative BA-13 was prepared by Claisen Schmidt condensation of intermediate BA-O with 4-methoxybenzaldehyde in the presence of ethanolic potassium hydroxide at room temperature. The residue was purified by flash chromatography (eluent: petroleum ether: ethyl acetate = 10: 1) to afford BA-13 as a white solid with a yield of 80%. ^{1}H NMR (600 MHz, Chloroform-*d*) δ 7.47 (t, *J* = 2.0 Hz, 1H), 7.44–7.36 (m, 2H), 6.97–6.92 (m, 2H), 4.81–4.60 (m, 2H), 3.85 (s, 3H), 3.11–2.94 (m, 2H), 2.33–2.23 (m, 2H), 2.23–2.18 (m, 1H), 2.07–1.96 (m, 2H), 1.71 (d, *J* = 35.7 Hz, 5H), 1.58–1.41 (m, 11H), 1.36–1.24 (m, 4H), 1.14 (s, 3H), 1.11 (s, 3H), 1.03 (s,

3H), 0.98 (s, 3H), 0.79 (s, 3H). ^{13}C NMR (151 MHz, CDCl$_3$) δ 208.12, 181.49, 159.82, 150.63, 137.29, 132.23, 132.23, 131.96, 128.67, 114.00, 114.00, 109.62, 56.43, 55.32, 52.66, 49.18, 48.51, 46.83, 45.01, 44.67, 42.51, 40.52, 38.46, 37.02, 36.40, 33.07, 32.06, 30.63, 29.69, 29.62, 25.66, 22.32, 21.68, 20.38, 19.54, 15.86, 15.48, 14.63. HRMS (ESI): C$_{38}$H$_{53}$O$_4$ (573.3938) [M + H]$^+$ = 573.3938.

Synthesis of BA Derivative BA-14~BA-22

BA-14 *methyl (1R,3aS,5aR,5bR,7aR,11aR,11bR,13aR,13bR)-10-((E)-5-methoxy-2-nitrobenzylidene)-5a,5b,8,8,11a-pentamethyl-9-oxo-1-(prop-1-en-2-yl)icosahydro-3aH-cyclopenta[a]chrysene-3a-carboxylate* (BA-14, C$_{39}$H$_{53}$NO$_6$). According to the general procedure, derivative BA-14 was prepared by Claisen Schmidt condensation of intermediate BA-O-Me with 5-methoxy-2-nitrobenzaldehyde in the presence of ethanolic potassium hydroxide at room temperature. The residue was purified by flash chromatography (eluent: petroleum ether: ethyl acetate = 10: 1) to afford BA-14 as a white solid with a yield of 66%. ^{1}H NMR (600 MHz, Chloroform-*d*) δ 8.20 (d, *J* = 9.1 Hz, 1H), 7.59 (d, *J* = 2.6 Hz, 1H), 6.93 (dd, *J* = 9.2, 2.8 Hz, 1H), 6.67 (d, *J* = 2.7 Hz, 1H), 4.84–4.48 (m, 2H), 3.91 (s, 3H), 3.66 (s, 3H), 2.97 (td, *J* = 10.7, 4.5 Hz, 1H), 2.63 (dd, *J* = 15.6, 1.4 Hz, 1H), 2.29–2.13 (m, 2H), 1.92–1.80 (m, 3H), 1.69–1.55 (m, 5H), 1.49–1.31 (m, 11H), 1.25 (s, 3H), 1.18 (s, 3H), 1.13 (s, 3H), 0.95 (s, 3H), 0.92 (s, 3H), 0.81 (s, 3H). ^{13}C NMR (151 MHz, CDCl$_3$) δ 207.93, 176.58, 163.16, 150.81, 140.89, 135.64, 135.29, 134.86, 127.63, 115.74, 113.34, 109.43, 56.55, 56.06, 53.45, 51.33, 49.31, 48.32, 46.87, 45.99, 43.03, 42.46, 40.54, 38.23, 36.99, 36.90, 33.20, 32.03, 30.62, 29.71, 29.61, 28.62, 25.50, 22.44, 21.46, 20.15, 19.45, 15.73, 15.51, 14.59. HRMS (ESI): C$_{39}$H$_{53}$NNaO$_6$ (654.3765) [M + Na]$^+$ = 654.3765.

BA-15 *methyl (1R,3aS,5aR,5bR,7aR,11aR,11bR,13aR,13bR)-10-((E)-5-fluoro-2-nitrobenzylidene)-5a,5b,8,8,11a-pentamethyl-9-oxo-1-(prop-1-en-2-yl)icosahydro-3aH-cyclopenta[a]chrysene-3a-carboxylate* (BA-15, C$_{38}$H$_{50}$FNO$_5$). According to the general procedure, derivative BA-15 was prepared by Claisen Schmidt condensation of intermediate BA-O-Me with 5-fluoro-2-nitrobenzaldehyde in the presence of ethanolic potassium hydroxide at room temperature. The residue was purified by flash chromatography (eluent: petroleum ether: ethyl acetate = 10: 1) to afford BA-15 as a white solid with a yield of 71%. ^{1}H NMR (600 MHz, Chloroform-*d*) δ 8.18 (d, *J* = 9.1 Hz, 1H), 7.58 (d, *J* = 2.5 Hz, 1H), 6.91 (dd, *J* = 9.2, 2.8 Hz, 1H), 6.64 (d, *J* = 2.7 Hz, 1H), 4.72–4.56 (m, 2H), 3.66 (s, 3H), 2.97 (td, *J* = 10.6, 4.5 Hz, 1H), 2.62 (dd, *J* = 15.7, 1.4 Hz, 1H), 2.25–2.18 (m, 2H), 1.89–1.86 (m, 1H), 1.84–1.78 (m, 1H), 1.66 (s, 3H), 1.67–1.53 (m, 2H), 1.47 (t, *J* = 7.0 Hz, 4H), 1.44–1.31 (m, 8H), 1.29–1.21 (m, 3H), 1.17 (s, 3H), 1.13 (s, 3H), 1.02 (d, *J* = 4.6 Hz, 1H), 0.95 (s, 3H), 0.92 (s, 3H), 0.80 (s, 3H). ^{13}C NMR (151 MHz, CDCl$_3$) δ 207.96, 176.58, 162.66, 150.86, 140.64, 135.52, 135.33, 135.03, 127.59, 115.88, 113.93, 109.40, 56.55, 53.44, 51.33, 49.31, 48.32, 46.86, 45.97, 43.04, 42.46, 40.54, 38.24, 36.98, 36.90, 33.20, 32.03, 30.62, 29.61, 28.63, 25.51, 22.42, 21.47, 20.15, 19.45, 15.72, 15.51, 14.56.

BA-16 *methyl (1R,3aS,5aR,5bR,7aR,11aR,11bR,13aR,13bR)-10-((E)-3-fluorobenzylidene)-5a,5b,8,8,11a-pentamethyl-9-oxo-1-(prop-1-en-2-yl)icosahydro-3aH-cyclopenta[a]chrysene-3a-carboxylate* (BA-16, C$_{38}$H$_{51}$FO$_3$). According to the general procedure, derivative BA-16 was prepared by Claisen Schmidt

condensation of intermediate BA-O-Me with 3-fluorobenzaldehyde in the presence of ethanolic potassium hydroxide at room temperature. The residue was purified by flash chromatography (eluent: petroleum ether: ethyl acetate = 10: 1) to afford BA-16 as a white solid with a yield of 76%. ^{1}H NMR (600 MHz, Chloroform-*d*) δ 7.45–7.39 (m, 1H), 7.37 (td, *J* = 8.0, 6.0 Hz, 1H), 7.17 (d, *J* = 7.7 Hz, 1H), 7.10 (dt, *J* = 10.1, 2.1 Hz, 1H), 7.02 (td, *J* = 8.4, 2.6 Hz, 1H), 4.93–4.58 (m, 2H), 3.67 (s, 3H), 3.04–2.93 (m, 2H), 2.31–2.21 (m, 2H), 2.18 (dd, *J* = 16.1, 3.3 Hz, 1H), 1.96–1.84 (m, 2H), 1.72 (s, 4H), 1.63 (t, *J* = 11.4 Hz, 1H), 1.52–1.34 (m, 11H), 1.33–1.18 (m, 2H), 1.13 (d, *J* = 18.7 Hz, 7H), 1.01 (s, 3H), 0.95 (s, 3H), 0.79 (s, 3H). ^{13}C NMR (151 MHz, CDCl$_3$) δ 208.12, 176.62, 161.79, 150.60, 138.11, 135.85, 135.49, 129.93, 126.04, 116.57, 115.22, 109.65, 56.58, 52.89, 51.34, 49.38, 48.44, 46.91, 45.27, 44.31, 42.48, 40.52, 38.29, 36.94, 36.56, 33.06, 32.08, 30.65, 29.65, 29.42, 25.60, 22.38, 21.70, 20.38, 19.49, 15.82, 15.41, 14.63. HRMS (ESI): C$_{38}$H$_{51}$FNaO$_3$ (597.3714) [M + Na]$^+$ = 597.3714.

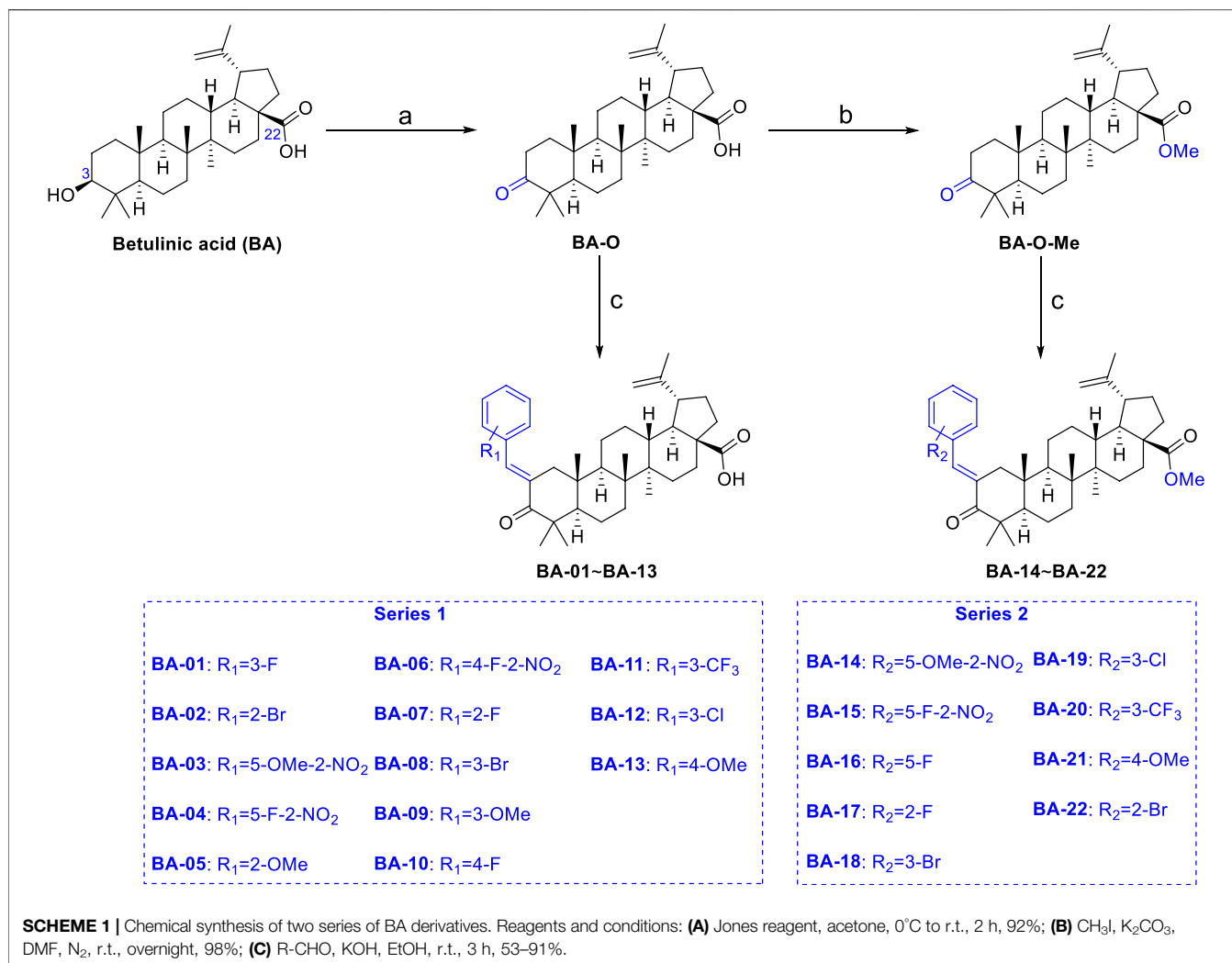**BA-17** *methyl (1R,3aS,5aR,5bR,7aR,11aR,11bR,13aR,13bR)-10-((E)-2-fluorobenzylidene)-5a,5b,8,8,11a-pentamethyl-9-oxo-1-(prop-1-en-2-yl)icosahydro-3aH-cyclopenta[a]chrysene-3a-carboxylate* (BA-17, C$_{38}$H$_{51}$FO$_3$). According to the general procedure, derivative BA-17 was prepared by Claisen Schmidt condensation of intermediate BA-O-Me with 2-fluorobenzaldehyde in the presence of ethanolic potassium hydroxide at room temperature. The residue was purified by flash chromatography (eluent: petroleum ether: ethyl acetate = 10: 1) to afford BA-17 as a white solid with a yield of 75%. ^{1}H NMR (600 MHz, Chloroform-*d*) δ 7.56 (t, *J* = 1.9 Hz, 1H), 7.32 (dtd, *J* = 12.9, 7.6, 1.8 Hz, 2H), 7.17 (td, *J* = 7.6, 1.2 Hz, 1H), 7.09 (ddd, *J* = 9.7, 8.2, 1.1 Hz, 1H), 4.82–4.52 (m, 2H), 3.67 (s, 3H), 3.05–2.95 (m, 1H), 2.91 (d, *J* = 16.3 Hz, 1H), 2.31–2.21 (m, 2H), 2.10 (dt, *J* = 16.0, 2.2 Hz, 1H), 1.90 (dddd, *J* = 13.7, 10.7, 7.5, 3.6 Hz, 2H), 1.70 (s, 4H), 1.62 (t, *J* = 11.4 Hz, 1H), 1.50–1.33 (m, 12H), 1.31–1.16 (m, 2H), 1.14 (d, *J* = 2.2 Hz, 6H), 1.00 (s, 3H), 0.95 (s, 3H), 0.80 (s, 3H). ^{13}C NMR (151 MHz, CDCl$_3$) δ 207.73, 176.61, 160.04, 150.76, 136.39, 130.34, 130.05, 129.84, 123.92, 123.82, 115.69, 109.52, 56.58, 53.13, 51.34, 49.38, 48.45, 46.89, 45.44, 43.97, 42.48, 40.54, 38.30, 36.94, 36.66, 33.16, 32.07, 30.65, 29.65, 29.18, 25.60, 22.49, 21.59, 20.31, 19.49, 15.77, 15.47, 14.63. HRMS (ESI): C$_{38}$H$_{51}$FNaO$_3$ (597.3714) [M + Na]$^+$ = 597.3714.

BA-18 *methyl (1R,3aS,5aR,5bR,7aR,11aR,11bR,13aR,13bR)-10-((E)-3-bromobenzylidene)-5a,5b,8,8,11a-pentamethyl-9-oxo-1-(prop-1-en-2-yl)icosahydro-3aH-cyclopenta[a]chrysene-3a-carboxylate* (**BA-18**, C$_{38}$H$_{51}$BrO$_3$). According to the general procedure, derivative BA-18 was prepared by Claisen Schmidt condensation of intermediate BA-O-Me with 3-bromobenzaldehyde in the presence of ethanolic potassium hydroxide at room temperature. The residue was purified by flash chromatography (eluent: petroleum ether: ethyl acetate = 10: 1) to afford BA-18 as a white solid with a yield of 89%. ^{1}H NMR (600 MHz, Chloroform-*d*) δ 7.51 (t, *J* = 1.8 Hz, 1H), 7.44 (dt, *J* = 7.9, 1.6 Hz, 1H), 7.37 (dd, *J* = 3.0, 1.5 Hz, 1H), 7.36–7.30 (m, 1H), 7.28 (t, *J* = 7.8 Hz, 1H), 4.84–4.57 (m, 2H), 3.67 (s, 3H), 2.99 (ddd, *J* = 19.9, 13.4, 3.1 Hz, 2H), 2.35–2.19 (m, 2H), 2.17–2.12 (m, 1H), 1.90 (ddt, *J* = 13.3, 10.2, 5.5 Hz, 2H), 1.77–1.57 (m, 6H), 1.51–1.35 (m, 10H), 1.31–1.16 (m, 3H), 1.14 (s, 3H), 1.12 (s, 3H), 1.01 (s,

SCHEME 1 | Chemical synthesis of two series of BA derivatives. Reagents and conditions: **(A)** Jones reagent, acetone, 0°C to r.t., 2 h, 92%; **(B)** CH$_3$I, K$_2$CO$_3$, DMF, N$_2$, r.t., overnight, 98%; **(C)** R-CHO, KOH, EtOH, r.t., 3 h, 53–91%.
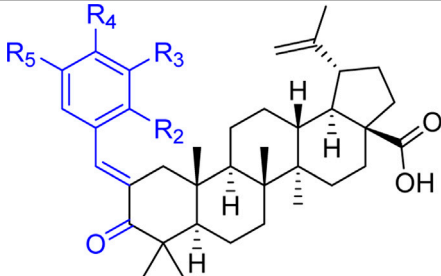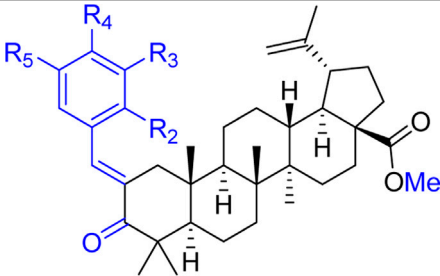
3H), 0.95 (s, 3H), 0.78 (s, 3H). ^{13}C NMR (151 MHz, CDCl$_3$) δ 208.00, 176.61, 150.62, 138.11, 135.73, 135.58, 133.21, 131.22, 129.93, 128.05, 122.53, 109.59, 56.58, 52.94, 51.33, 49.36, 48.43, 46.88, 45.31, 44.12, 42.48, 40.52, 38.27, 36.92, 36.62, 33.06, 32.06, 30.65, 29.65, 29.34, 25.56, 22.39, 21.67, 20.35, 19.50, 15.81, 15.42, 14.64. HRMS (ESI): C$_{38}$H$_{51}$^{79}BrNaO$_3$ (657.2914) [M + Na]$^+$ = 657.2914, C$_{38}$H$_{51}$^{81}BrNaO$_3$ (659.2893) [M + Na]$^+$ = 659.2894.

BA-19 *methyl (1R,3aS,5aR,5bR,7aR,11aR,11bR,13aR,13bR)-10-((E)-3-chlorobenzylidene)-5a,5b,8,8,11a-pentamethyl-9-oxo-1-(prop-1-en-2-yl)icosahydro-3aH-cyclopenta[a]chrysene-3a-carboxylate* (BA-19, C$_{38}$H$_{51}$ClO$_3$). According to the general procedure, derivative BA-19 was prepared by Claisen Schmidt condensation of intermediate BA-O-Me with 3-chlorobenzaldehyde in the presence of ethanolic potassium hydroxide at room temperature. The residue was purified by flash chromatography (eluent: petroleum ether: ethyl acetate = 10: 1) to afford BA-19 as a white solid with a yield of 53%. ^{1}H NMR (600 MHz, Chloroform-*d*) δ 7.38 (d, *J* = 2.6 Hz, 1H), 7.37–7.31 (m, 2H), 7.31–7.26 (m, 2H), 4.96–4.52 (m, 2H), 3.67 (s, 3H), 3.26–2.88 (m, 2H), 2.31–2.23 (m, 2H), 2.16 (dd, *J* = 16.3, 3.0 Hz,

1H), 1.99–1.86 (m, 2H), 1.80–1.54 (m, 6H), 1.51–1.34 (m, 11H), 1.32–1.19 (m, 3H), 1.14 (s, 3H), 1.12 (s, 3H), 1.01 (s, 3H), 0.95 (s, 3H), 0.78 (s, 3H). ^{13}C NMR (151 MHz, CDCl$_3$) δ 208.04, 176.62, 150.63, 137.82, 135.70, 135.68, 134.35, 130.21, 129.69, 128.34, 127.78, 109.61, 56.59, 52.95, 51.34, 49.38, 48.43, 46.90, 45.31, 44.16, 42.49, 40.53, 38.28, 36.93, 36.62, 33.07, 32.07, 30.66, 29.66, 29.36, 25.57, 22.40, 21.68, 20.36, 19.51, 15.81, 15.43, 14.64. HRMS (ESI): C$_{38}$H$_{51}$ClNaO$_3$ (613.3419) [M + Na]$^+$ = 613.3420.

BA-20 *methyl (1R,3aS,5aR,5bR,7aR,11aR,11bR,13aR,13bR)-5a,5b,8,8,11a-pentamethyl-9-oxo-1-(prop-1-en-2-yl)-10-((E)-3-(trifluoromethyl)benzylidene)icosahydro-3aH-cyclopenta[a]chrysene-3a-carboxylate* (BA-20, C$_{39}$H$_{51}$F$_3$O$_3$). According to the general procedure, derivative BA-20 was prepared by Claisen Schmidt condensation of intermediate BA-O-Me with 3-(trifluoromethyl)benzaldehyde in the presence of ethanolic potassium hydroxide at room temperature. The residue was purified by flash chromatography (eluent: petroleum ether: ethyl acetate = 10: 1) to afford BA-20 as a white solid with a yield of 58%. ^{1}H NMR (600 MHz, Chloroform-*d*) δ 7.62 (s, 1H), 7.59–7.56 (m, 2H), 7.55–7.50 (m, 1H), 7.46 (dd, *J* = 3.0, 1.5 Hz, 1H), 4.87–4.49 (m,

TABLE 1 | The structure and functional groups of **BA** derivatives and their inhibition rate of HAase (at a threshold concentration of 40 µM).

BA-01~BA-13   **BA-14~BA-22**

Cpd	R2=	R3=	R4=	R5=	%[a]	Cpd	R2=	R3=	R4=	R5=	%[a]
BA-01	H	F	H	H	44.1 ± 2.7	**BA-14**	NO$_2$	H	H	OMe	12.5 ± 3.4
BA-02	Br	H	H	H	65.4 ± 0.4	**BA-15**	NO$_2$	H	H	F	14.9 ± 2.1
BA-03	NO$_2$	H	H	OMe	46.5 ± 3.6	**BA-16**	H	H	H	F	1.0 ± 1.1
BA-04	NO$_2$	H	H	F	72.8 ± 0.9	**BA-17**	F	H	H	H	4.9 ± 1.9
BA-05	OMe	H	H	H	68.1 ± 6.8	**BA-18**	H	Br	H	H	6.7 ± 2.8
BA-06	NO$_2$	H	F	H	52.7 ± 1.4	**BA-19**	H	Cl	H	H	3.4 ± 2.5
BA-07	F	H	H	H	26.3 ± 2.8	**BA-20**	H	CF$_3$	H	H	8.8 ± 1.4
BA-08	H	Br	H	H	35.3 ± 6.6	**BA-21**	H	H	OMe	H	7.5 ± 2.3
BA-09	H	OMe	H	H	42.4 ± 2.1	**BA-22**	Br	H	H	H	5.5 ± 1.0
BA-10	H	H	F	H	35.5 ± 2.5						
BA-11	H	CF$_3$	H	H	31.6 ± 2.0						
BA-12	H	Cl	H	H	21.3 ± 1.1						
BA-13	H	H	OMe	H	77.7 ± 1.9						

[a]Inhibition rate against HAase of test compounds at 40 µM.

2H), 3.67 (s, 3H), 3.05–2.93 (m, 2H), 2.31–2.23 (m, 2H), 2.19–2.14 (m, 1H), 2.01–1.82 (m, 2H), 1.76–1.56 (m, 6H), 1.54–1.37 (m, 11H), 1.32–1.17 (m, 2H), 1.15 (s, 3H), 1.13 (s, 3H), 1.01 (s, 3H), 0.95 (s, 3H), 0.80 (s, 3H). ^{13}C NMR (151 MHz, CDCl$_3$) δ 207.96, 176.61, 150.60, 136.74, 136.08, 135.43, 132.47, 130.84, 128.94, 127.18, 124.80, 123.03, 109.59, 56.58, 52.97, 51.34, 49.36, 48.49, 46.89, 45.36, 44.16, 42.48, 40.53, 38.29, 36.92, 36.63, 33.08, 32.06, 30.65, 29.65, 29.31, 25.53, 22.40, 21.67, 20.34, 19.48, 15.84, 15.43. HRMS (ESI): C$_{39}$H$_{51}$F$_3$NaO$_3$ (647.3683) [M + Na]$^+$ = 647.3685.

BA-21 *methyl (1R,3aS,5aR,5bR,7aR,11aR,11bR,13aR,13bR)-10-((E)-4-methoxybenzylidene)-5a,5b,8,8,11a-pentamethyl-9-oxo-1-(prop-1-en-2-yl)icosahydro-3aH-cyclopenta[a]chrysene-3a-carboxylate* (BA-21, C$_{39}$H$_{54}$O$_4$). According to the general procedure, derivative BA-21 was prepared by Claisen Schmidt condensation of intermediate BA-O-Me with 4-methoxybenzaldehyde in the presence of ethanolic potassium hydroxide at room temperature. The residue was purified by flash chromatography (eluent: petroleum ether: ethyl acetate = 10: 1) to afford BA-21 as a white solid with a yield of 77%. ^{1}H NMR (600 MHz, Chloroform-*d*) δ 7.47 (t, *J* = 1.9 Hz, 1H), 7.32 (d, *J* = 7.9 Hz, 2H), 7.22 (d, *J* = 7.9 Hz, 2H), 4.80–4.61 (m, 2H), 3.67 (s, 3H), 3.11–2.96 (m, 2H), 2.38 (s, 3H), 2.30–2.23 (m, 2H), 2.24–2.17 (m, 1H), 1.96–1.82 (m, 2H), 1.73 (s, 3H), 1.64 (t, *J* = 11.4 Hz, 1H), 1.52–1.36 (m, 10H), 1.35–1.18 (m, 4H), 1.15 (s, 3H), 1.11 (s, 3H), 1.01 (s, 3H), 0.96 (s, 3H), 0.78 (s, 3H). ^{13}C NMR (151 MHz, CDCl$_3$) δ 208.09, 176.60, 150.71, 136.53, 136.43,

136.07, 132.86, 130.14, 129.41, 127.05, 124.80, 109.51, 56.56, 53.35, 51.33, 49.36, 48.44, 46.88, 45.74, 43.35, 42.47, 40.55, 38.27, 36.93, 36.87, 33.21, 32.06, 30.62, 29.64, 28.90, 25.54, 22.47, 21.52, 20.23, 19.46, 15.73, 15.50, 14.62.

BA-22 *methyl (1R,3aS,5aR,5bR,7aR,11aR,11bR,13aR,13bR)-10-((E)-2-bromobenzylidene)-5a,5b,8,8,11a-pentamethyl-9-oxo-1-(prop-1-en-2-yl)icosahydro-3aH-cyclopenta[a]chrysene-3a-carboxylate* (BA-22, C$_{38}$H$_{51}$BrO$_3$). According to the general procedure, derivative BA-22 was prepared by Claisen Schmidt condensation of intermediate BA-O-Me with 2-bromobenzaldehyde in the presence of ethanolic potassium hydroxide at room temperature. The residue was purified by flash chromatography (eluent: petroleum ether: ethyl acetate = 10: 1) to afford BA-22 as a white solid with a yield of 68%. ^{1}H NMR (600 MHz, Chloroform-*d*) δ 7.61 (dd, *J* = 7.9, 1.2 Hz, 1H), 7.48 (d, *J* = 2.7 Hz, 1H), 7.33 (td, *J* = 7.5, 1.2 Hz, 1H), 7.24–7.19 (m, 1H), 7.17 (td, *J* = 7.7, 1.7 Hz, 1H), 5.09–4.41 (m, 2H), 3.66 (s, 3H), 3.05–2.94 (m, 1H), 2.82 (dd, *J* = 15.9, 1.5 Hz, 1H), 2.23 (td, *J* = 12.3, 3.4 Hz, 2H), 2.03–1.81 (m, 3H), 1.68 (s, 5H), 1.49–1.34 (m, 10H), 1.30–1.18 (m, 4H), 1.16 (s, 3H), 1.14 (s, 3H), 0.97 (s, 3H), 0.94 (s, 3H), 0.81 (s, 3H). ^{13}C NMR (151 MHz, CDCl$_3$) δ 208.09, 176.60, 150.71, 136.53, 136.43, 136.07, 132.86, 130.14, 129.41, 127.05, 124.80, 109.51, 56.56, 53.35, 51.33, 49.36, 48.44, 46.88, 45.74, 43.35, 42.47, 40.55, 38.27, 36.93, 36.87, 33.21, 32.06, 30.62, 29.64, 28.90, 25.54, 22.47, 21.52, 20.23, 19.46, 15.73, 15.50, 14.62. HRMS (ESI): C$_{38}$H$_{51}$^{79}BrNaO$_3$ (657.2914) [M + Na]$^+$ = 657.2914, C$_{38}$H$_{51}$^{81}BrNaO$_3$ (659.2893) [M + Na]$^+$ = 659.2894.
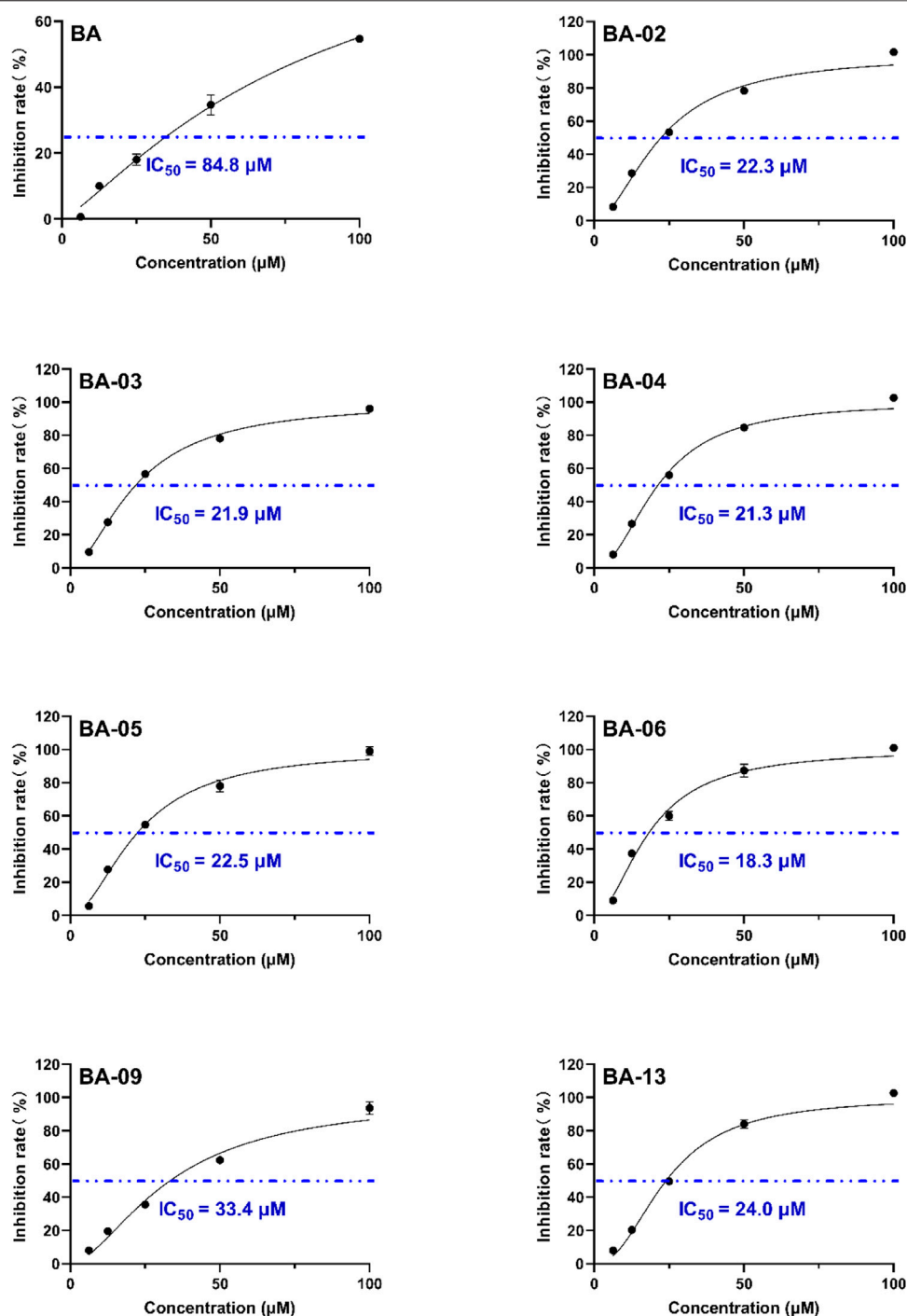
FIGURE 1 | Effects of leading BA derivatives on the activity of HAase enzyme activity. The inhibition rates (%) of each compound were measured at five concentrations (1, 5, 25, 50, and 100 μM) and an inhibition curve of each compound was constructed to calculate the IC_{50} value by analyzing the inhibition rates at different concentrations with a nonlinear regression algorithm using GraphPad Prism.

HAase Inhibition Assay

The effect of BA derivatives on HAase activity was evaluated using a previous report with some modifications (Bahadir Acikara et al., 2019; He et al., 2021). Briefly, BA derivatives were prepared to 100 mM in DMSO, then diluted with DMSO yield concentrations ranging from 6.25 to 100 μg/mL. 5 μL test samples and 95 μL HAase protein (7.5 U/mL) were dissolved in sodium phosphate buffer (20 mM) containing 0.01% BSA (pH =

TABLE 2 | Estimated free binding energy and inhibition constant of BA derivatives by molecular docking method.

Compounds	Banding energy (kcal/mol)	K_i (Inhibition constant; μM)
BA-02	−8.8	338.0
BA-03	−11.4	4.6
BA-04	−9.5	115.9
BA-05	−8.7	436.3
BA-06	−9.2	169.0
BA-09	−9.2	169.0
BA-13	−8.7	434.7

7.0) and incubated at 37°C for 10 min. Then HA (100 μl) to the mixture, followed incubation at 37°C for 45 min. Undigested HA was precipitated by adding the acidic albumin solution (1 ml; pH = 3.75) containing 0.1% BSA which dissolved in sodium acetate (24 mM) and acetic acid (79 mM) solution. After 10 min, absorbance was measured at a wavelength of 600 nm using a microplate reader (SpectraMax M2, Molecular Devices Corp., operated by SoftmaxPro v.4.6 software, Sunnyvale, CA, United States). The inhibition rate was calculated using following formula: Inhibition% = 1 − [OD (HA) − OD (sample)]/[OD (HA) − OD (HAase)]. The IC_{50} value of each sample was determined by analyzing its inhibition rates at different concentrations with a nonlinear regression algorithm by GraphPad Prism.

Molecular Docking

The molecular docking analysis was conducted on the molecular modeling station provided by the Rhode Island IDeA Network of Biomedical Research Excellence (RI-INBRE) using the Autodock 4.2 and Autodock Tools base on the Lamarckian Genetic Algorithm (LGA). The structure of compound BA derivatives was generated by Chemdraw 3D (PerkinElmer Inc.; Waltham, MA, United States). And the crystal structure of collagenase protein (PDB ID: 2PE4) was retrieved in PDB format from the RCSB protein data bank (www.rcsb.org). The HAase protein was prepared by removing water molecules and adding force field parameters and their co-crystallized ligands were used for assigning the ligand-binding domain for the docking simulations. The optimized protein structure, construction of missing side chains and loops, binding site, and the binding score of the ligands were obtained on the basis of their free banding energy and hydrogen bond. The 2D diagrams of the protein-ligand interactions were visualized by Discovery Studio (DS; BIOVIA Corp.; San Diego, CA, United States).

Cell Culture

Murine macrophage RAW264.7 cells were purchased from the American Type Culture Collection (ATCC; Rockville, MD, United States). The BV-2 murine microglial cells were a gift kindly provided by Dr. Grace Y. Sun (The University of Missouri at Columbia, MO, United States). Cells were cultured in Dulbecco's Modified Eagle's Medium (DMEM) supplemented with 10% (v/v) Fetal bovine serum (FBS) (Gibco, Life

Technologies, Gaithersburg, MD, United States) and 1% (v/v) Penicillin/Streptomycin antibiotic solution (Gibco, Life Technologies, Grand Island, NY, United States) and placed in an incubator maintained at temperature 37°C under humidified atmospheric conditions consisting of 5% CO_2. Human THP-1 monocytes were purchased from the ATCC. The cells were cultured in Roswell Park Memorial Institute (RPMI) 1640 medium supplemented with 10% (v/v) FBS and 1% (v/v) Penicillin/Streptomycin antibiotic solution, placed in an incubator maintained at a temperature of 37°C under humidified atmospheric conditions consisting of 5% CO_2. THP-1 monocytes were differentiated by incubation with phorbol 12-myristate 13-acetate (PMA from Sigma Aldridge; 25 nM) for 48 h. Then PMA was removed and cells were cultured with PMA-free medium for another 24 h.
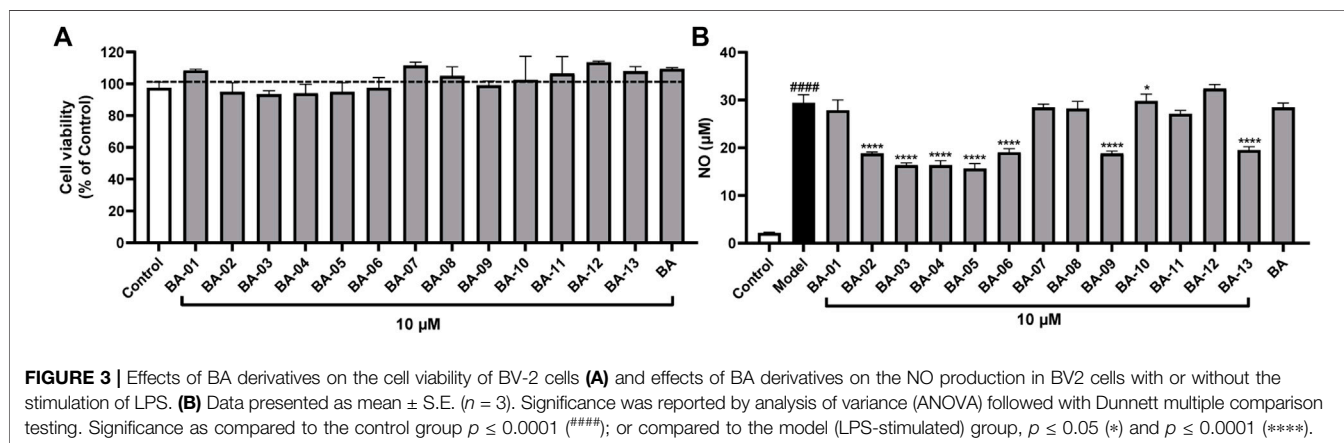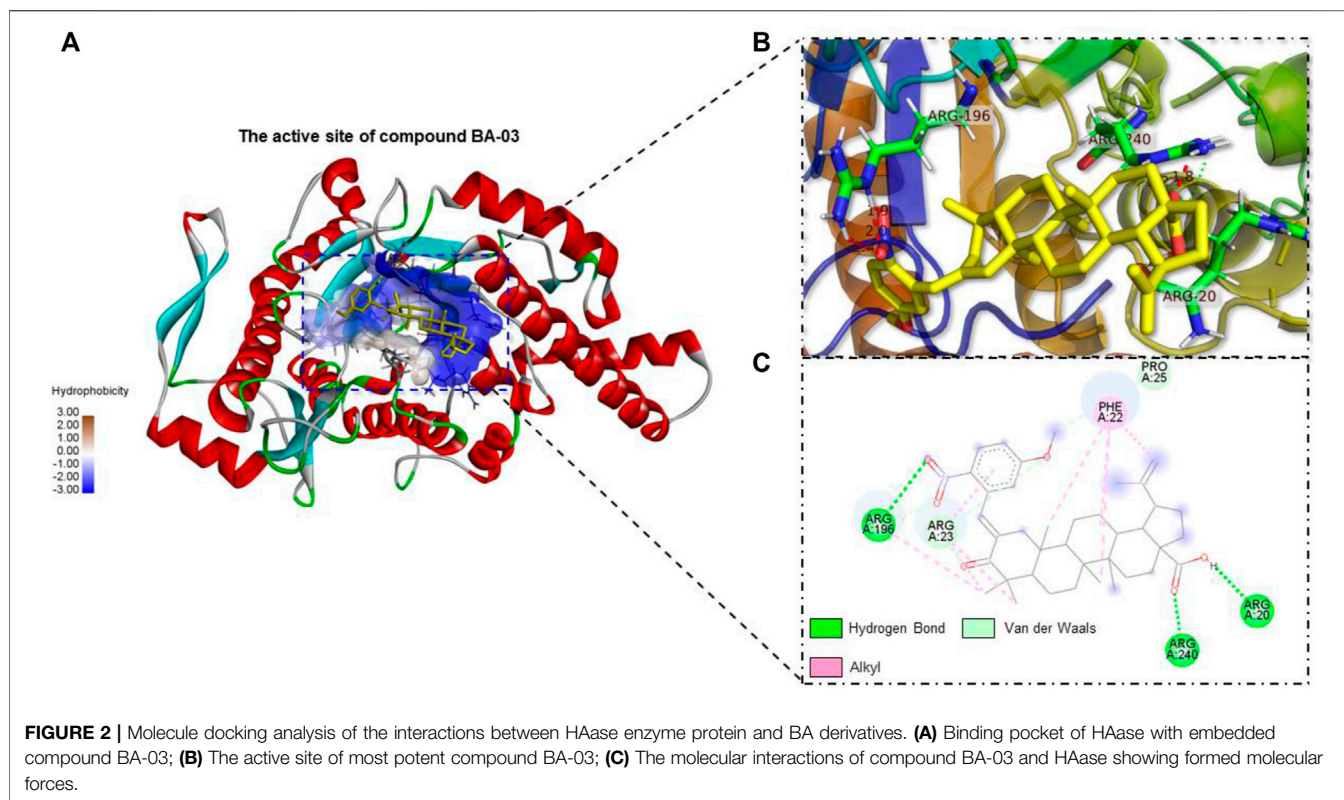
Cell Viability

The cytotoxicity of each compound was determined in BV-2 and RAW264.7 cells with the MTT assay (Li et al., 2020). Briefly, cells were seeded in 96-well plates at 20,000 cells per well. Cells were allowed to adhere for 24 h. BA derivatives were prepared to 100 mM in DMSO, then diluted in serum-free media to yield concentrations of 10 μM. After the treatment of the cells with BA derivatives for 2 h, the cells were incubated in the absence or presence of LPS (1 μg/mL) for 24 h. Cellular viability was determined as a percentage of control (DMSO) by using a Cell Proliferation Kit II (Promega, Madison, WI, United States). XTT reagent (0.3 mg/mL) was then added to each well and incubated for 4 h at 37°C and an absorbance value was measured at 492 nm using a Spectramax M2 microplate reader (Hayon et al., 2003).

NO Measurement

NO concentration was determined by the Griess assay according to a previous report (Ma et al., 2016), RAW264.7 and BV-2 cells (20,000 cells per well) were plated into 96-well plates. After an incubation period of 24 h, the cells were pre-treated with BA derivatives for 2 h and were co-treated with LPS (1 μg/mL) for 24 h. For the LMWHAFs-induced inflammation assay, THP-1 cells were pre-treated with BA derivatives for 2 h and then treated with LPS (1 μg/mL) and HA fragment (a hyaluronan oligosaccharide 6mer; 50 μg/mL) from Amsbio (Rockville, MD, United States; product code: CSR-11002) for 24 h (Campo et al., 2012; Scuruchi et al., 2016). Subsequently, the culture medium was mixed with the Griess reagent in a 1:1 ratio followed by a 15 min incubation in the dark. An absorbance value was measured at 540 nm using a Spectramax M2 microplate reader, and the NO concentration was calculated based on the standard NO curve.

Measurement of IL-6 by ELISA Assay

To evaluate the effect of BA derivatives on LPS-induced IL-6 secretion, THP-1 monocytes were seeded at a density of 50,000 cells per well in a 48-well plate and differentiated with PMA (25 ng/mL), pre-treated with the BA derivatives at concentrations of 10 μM was performed for 6 h followed by stimulation with or without 1 μg/mL LPS for 12 h. The cell culture supernatant was

FIGURE 2 | Molecule docking analysis of the interactions between HAase enzyme protein and BA derivatives. **(A)** Binding pocket of HAase with embedded compound BA-03; **(B)** The active site of most potent compound BA-03; **(C)** The molecular interactions of compound BA-03 and HAase showing formed molecular forces.

FIGURE 3 | Effects of BA derivatives on the cell viability of BV-2 cells **(A)** and effects of BA derivatives on the NO production in BV2 cells with or without the stimulation of LPS. **(B)** Data presented as mean ± S.E. ($n = 3$). Significance was reported by analysis of variance (ANOVA) followed with Dunnett multiple comparison testing. Significance as compared to the control group $p \leq 0.0001$ (####); or compared to the model (LPS-stimulated) group, $p \leq 0.05$ (∗) and $p \leq 0.0001$ (∗∗∗∗).
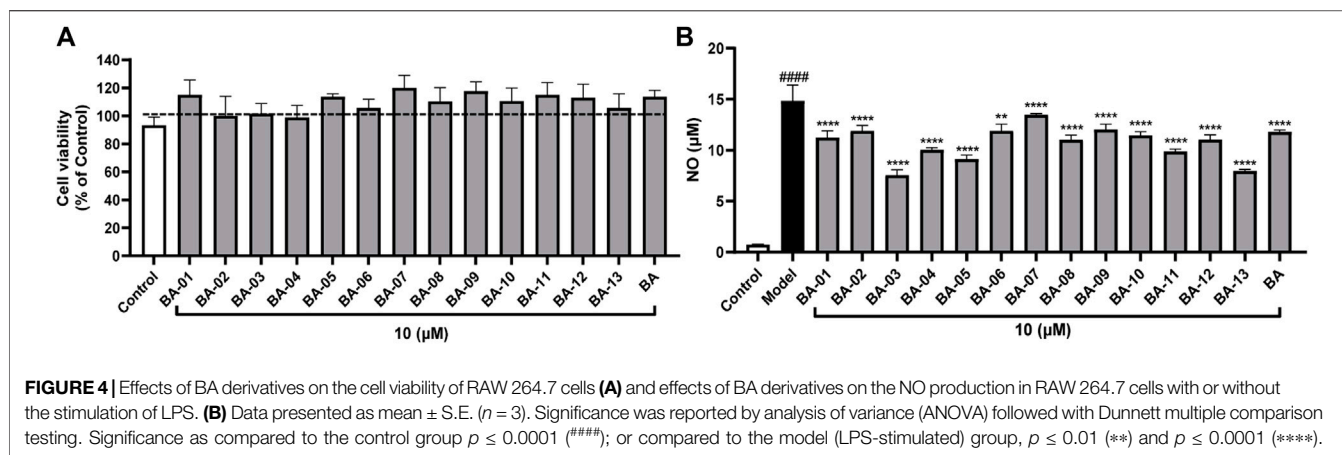
collected for the measurement of IL-6. The levels of IL-6 were determined using specific ELISA kits (BioLegend, San Diego, CA, United States) (Liu et al., 2020).

RESULTS AND DISCUSSION

Synthesis of BA Derivatives

A series of novel α,β-unsaturated BA ketene derivatives was synthesized using BA as the initial starting compound. The synthetic routes and chemical structures of two sets of BA derivatives including α,β-unsaturated ketene analogues (BA-O), and their methylated analogues (BA-O-Me) are shown in **Scheme 1**. The intermediate BA-O was synthesized by modifying the C-3 position of BA to obtain a carbonyl moiety with the Jones reagent, followed by converting it to the other intermediate BA-O-Me by modifying the -COOH group at the C-22 position via esterification with CH_3I and K_2CO_3 in DMF. Next, two series of target derivatives were generated by Claisen Schmidt condensation at the C-3 position of the ketone intermediates BA-O and BA-O-Me to obtain derivatives BA-01~BA-13 (Series 1) and BA-14~BA-22 (Series 2), respectively. All compounds

FIGURE 4 | Effects of BA derivatives on the cell viability of RAW 264.7 cells **(A)** and effects of BA derivatives on the NO production in RAW 264.7 cells with or without the stimulation of LPS. **(B)** Data presented as mean ± S.E. ($n = 3$). Significance was reported by analysis of variance (ANOVA) followed with Dunnett multiple comparison testing. Significance as compared to the control group $p \leq 0.0001$ (####); or compared to the model (LPS-stimulated) group, $p \leq 0.01$ (**) and $p \leq 0.0001$ (****).

were purified by column chromatography with yields in a range between 53% and 91%, and their chemical structures were identified by a combination of spectroscopic analyses including ^{1}H NMR, ^{13}C NMR, and HRMS.

Inhibition of BA Derivatives on HAase Activity

We first evaluated the inhibitory effects of BA derivatives on HAase enzyme at a threshold concentration of 40 μm. Compounds of Series 1 (BA-01~BA-13) showed anti-HAase activity with an inhibition rate of 21.3%–77.7% (**Table 1**). The BA-O derivatives including BA-01, BA-02, BA-03, BA-04, BA-05, BA-06, BA-09, and BA-13 showed the most potent inhibitory effect on HAase, which was superior to BA (inhibition of 44.1, 65.4, 46.5, 72.8, 68.1, 52.7, 42.4 and 77.7%, vs. 22.6%, respectively), whilst derivatives BA-14~BA-22 (Series 2) had weaker anti-HAase activity (1.0%–14.9% inhibition, respectively). Next, the inhibitory effects of BA derivatives with promising enzyme inhibition activity were further evaluated by obtaining their IC$_{50}$ inhibition value. The potency of BA-O derivatives is in an order of BA-02, BA-03, BA-04, BA-05, BA-06, BA-09, BA-13 with an IC$_{50}$ value of 22.3, 21.9, 21.3, 22.5, 18.3, 33.4 and 24.0 μM, respectively, (**Figure 1**). Oleanolic acid (OA; a pentacyclic terpenoid) was used as a positive control showing an inhibitory effect on HAase by 31.7% at a concentration of 40 μM.

Some preliminary structure and activity relationship (SAR) can be observed based on the anti-HAase activity of BA derivatives. For instance, an introduction of functional groups including halogen, nitro, methoxy, and trifluoromethyl moiety at the phenyl ring increased the anti-HAase activity of BA-O compounds as compared to their BA skeleton (by up to 400%). Our preliminary SAR analysis suggested that the phenyl ring on the BA skeleton with electron-withdrawing groups (e.g., halogen, nitro, methoxy and trifluoromethyl) is critical for the anti-HAase activity. In addition, the numbers of electron-withdrawing groups on the benzene ring seemed to be important as multiple electron-withdrawing groups had stronger HAase inhibitory activities. For instance, fluorine in the para-

position and a nitro group in the ortho position of the phenyl ring resulted in higher anti-HAase activity (IC$_{50}$ = 18.3 μM) as compared to a BA-O derivative with a single bromo group in the ortho position of the phenyl ring (IC$_{50}$ = 22.3 μM). Furthermore, induction of a methyl group *via* esterification with the -COOH group at position C-28 of BA resulted in the loss of anti-HAase activity of BA-O-Me derivatives. This may be attributed to the C-28-COOH group being critical for the maintenance of the anti-HAase activity given that this moiety can induce hydrophilic interaction with HAase enzyme. This SAR observation is in agreement with our previously reported study showing that the derivatives of OA (a triterpenoid with a carboxylic acid at the C-28 position) require the -COOH group intact to impart their HAase activity (He et al., 2021). In addition, this SAR pattern is also applicable to the triterpenoid ursolic acid (UA) and its derivatives where the carboxylic acid at the C-28 position is also essential for their inhibitory effects on HAase (Abdullah et al., 2016).

Interactions Between BA Derivatives and HAase Protein

Interactions between HAase enzyme protein and BA-O based HAase inhibitors including BA-02~BA-06, BA-09, BA-13 were investigated by molecular docking. The predicted protein-ligand complexes were evaluated on the basis of minimum free binding energy values (kcal/mol). Docking results showed that the aforementioned BA-O compounds had favorable binding energy ranging from −8.7 to −11.4 kcal/mol (**Table 2**). The predicted binding parameters were in agreement with data obtained from the enzyme inhibition assay. For instance, BA-03, which was the most active HAase inhibitor, had the lowest free binding energy (−11.4 kcal/mol) and binding constant (4.6 μM). As shown in **Figure 2**, BA-03 bound to a hydrophilic pocket on the HAase protein and interacted with several amino acid residues including Arg196, Arg240, and Arg20 via its -COOH group to form covalent bonding (i.e., hydrogen bond), which enhanced the stability of the ligand-protein complex. This conclusion is in agreement with our previously reported results showing that triterpenoid
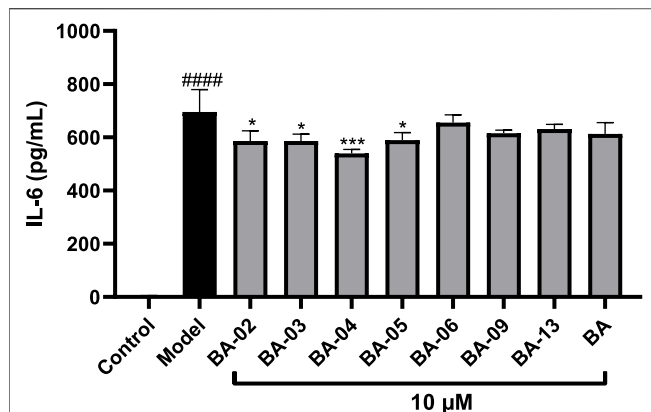
FIGURE 5 | Effect of BA derivatives on the production of IL-6 in THP-1 cells. All data expressed as mean ± standard error (n = 3), significance was reported by analysis of variance (ANOVA) followed with Dunnett multiple comparison testing. Significance as compared to the control group $p \leq 0.0001$ (####) and as compared to the model (LPS-stimulated) group, $p \leq 0.05$ (*) and $p \leq 0.001$ (***).
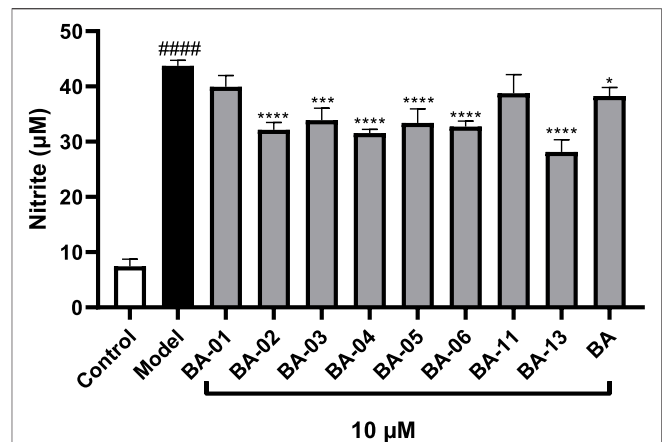

FIGURE 6 | Effect of BA derivatives on the production of IL-6 in hyaluronic acid fragment stimulated THP-1 cells. All data expressed as mean ± standard error (n = 3), significance was reported by analysis of variance (ANOVA) followed with Dunnett multiple comparison testing. Significance as compared to the control group $p \leq 0.0001$ (####) and as compared with the model group, $p \leq 0.05$ (*), $p \leq 0.001$ (***) and $p \leq 0.0001$ (****).

derivatives can bind to HAase protein via the formation of several molecular forces including hydrogen and alkyl bonds, which may contribute to their anti-HAase activity (He et al., 2021). Although data from the molecular docking experiments provide insights on possible binding modes of BA derivatives and HAase protein, further studies using biophysical methods (e.g., binding assays and the X-ray crystallography) are warranted to elucidate the binding property of BA-based ligands and HAase.

Inhibitory Effects of BA Derivatives on NO Production in LPS-Stimulated BV2 Cells

Given that the inhibition of HAase may result in less production of fragmented HAs, which is an inducing factor for inflammatory response, we further assessed whether BA based HAase inhibitors can exert anti-inflammatory effects. In this study, we first evaluated the anti-inflammatory activity of BA derivatives in LPS-stimulated murine microglial BV2 cells by measuring the production of nitrite (NO). Prior to conducting the anti-inflammatory assays, BV2 cells were treated with BA and its derivatives BA-01~13 at a concentration of 10 μM. Compounds tested at this concentration did not show any cytotoxicity with cell viability of 109.5% and 93.5%–113.5%, respectively, (**Figure 3A**). BA derivatives were further evaluated at the nontoxic concentration (10 μM). As shown in **Figure 3B**, BA derivatives including BA-02~BA-06, BA-09, BA-11, and BA-13 exerted anti-inflammatory effects by inhibiting the LPS-stimulated NO production by 35.1%–46.8%, 36.0%, 7.7%, and 33.6%, respectively. These BA derivatives showed superior NO inhibition effects as compared to their parent compound BA with a NO reduction of 3.4%.

Additionally, the NO inhibitory effects of BA and its derivatives were evaluated in murine macrophage RAW264.7 cells. All of the BA derivatives showed no cytotoxicity at a concentration of 10 μM

with cell viability no less than 99.0% (**Figure 4A**). BA showed significant anti-inflammatory effects by decreasing the LPS-stimulated NO production by 20.4% (**Figure 4B**). BA derivatives including BA-03, BA-04, BA-05, BA-13, and BA-11 showed stronger anti-inflammatory effects as compared to BA with a reduction in NO levels of 42.9%, 32.3%, 38.5%, 46.4%, and 33.4%, respectively. Compounds BA-03 and BA-13 had the most potent activities by decreasing NO production by 2.3- and 2.1-fold as compared to their parent compound BA. Other BA derivatives had comparable NO inhibition effects by reducing the NO production by 9.2%–25.6%. Given that BV2 cells are murine brain neuroglia cells and BA derivatives may not be able to penetrate the brain-blood barrier due to their molecular weight, we further evaluated the anti-inflammatory effects of BA derivatives using a human monocytic cell line (i.e., differentiated THP-1 cells).

BA Derivatives Reduce the Production of Pro-Inflammatory Cytokines in LPS-Stimulated THP-1 Cells

To further evaluate the anti-inflammatory effects of BA and its derivatives, compounds with significant inhibitory effects on NO production, namely, BA-02~BA-06, BA-09, and BA-13, were selected for the further evaluation of their inhibitory effects on the production of pro-inflammatory cytokine IL-6 in LPS-stimulated human monocyte THP-1 cells. As shown in **Figure 5**, IL-6 levels in THP-1 cells were elevated to 695.6 pg/mL after stimulation with LPS. Treatment with BA and its derivatives (BA-02, BA-03, BA-04, and BA-05) at a concentration of 10 μM significantly decreased the LPS-induced secretion of IL-6 to 613.3, 586.6, 586.0, 539.6, 589.8 pg/mL, respectively.

BA Derivatives Decreased NO Production in HA Fragment-Stimulated THP-1 Cells

Given that low molecular weight HA fragments (LMWHAFs) generated from the degradation of HA are pro-inflammatory molecules (Litwiniuk et al., 2016), it is possible that BA based HAase inhibitors may exert anti-inflammatory effects by mitigating LMWHAFs-induced inflammation. Based on the data from the anti-inflammatory assays, BA and several of its derivatives including BA-01~BA-06, BA-11, and BA-13, were selected for further anti-inflammatory effects against LMWHAFs-induced inflammation in THP-1 cells. As shown in **Figure 6**, the NO level of cells stimulated with LMWHAFs was elevated as compared to the control group (43.7 vs. 7.4 µM, respectively). The pro-inflammatory effect of LMWHAFs was counteracted by the treatment with BA and its derivatives BA-01~BA-06, BA-11, and BA-13 (at a concentration of 10 µM) by reducing the LMWHAF-stimulated NO production by 12.4%, 8.6%–27.8%, 11.3% and 35.6%, respectively). The molecular mechanisms of BA derivatives' effects against LMWHAFs-induced inflammation are still not clear but several cellular signaling pathways may be involved in the mechanisms of BA derivatives' action. For instance, LMWHAFs can be recognized by toll-like receptors (TLRs), which are a group of protein molecules in the immune system with functions of detecting bacteria and viruses and initiating early host defense against these pathogens (Scheibner et al., 2006). It has been reported that LMWHAFs can bind to the TLR-2 and -4 receptors and consequently mediate a series of signaling events, which lead to various inflammatory responses including the generation of pro-inflammatory cytokines and chemokines in immune cells (Scheibner et al., 2006; Litwiniuk et al., 2016). Notably, in a study using an animal model of collagen induced arthritis (using female albino rats), BA was reported to block the expression of TLR-2 and -4, and reduce pro-inflammatory markers including IL-1β, tumor necrosis factor-α, and interferon-γ (Mathew and Rajagopal, 2017). It is possible that BA and its derivatives can inhibit LMWHAFs-induced inflammation in THP-1 cells via the regulation of TLRs related signaling pathways but further studies are warranted to confirm this.

CONCLUSION

In summary, a series of novel BA derivatives containing an α,β-unsaturated ketene moiety were synthesized and their anti-HAase and anti-inflammatory activities were evaluated. BA derivatives with a carboxylic acid group located at the C-28 position of the BA skeleton showed enhanced inhibitory effects on HAase activity as compared to their parent compound. The preliminary SAR observation was supported by data from molecular docking assays. BA based HAase inhibitors also showed promising anti-inflammatory effects in assays using multiple cell lines. Furthermore, BA derivatives' anti-inflammatory effects against HA fragment induced inflammation were studied in a cell-based assay. Findings from the current study supported that the chemical modifications of BA yielded novel derivatives with enhanced HAase inhibitory and promising anti-inflammatory effects but further studies are warranted to elucidate their mechanism of action.

DATA AVAILABILITY STATEMENT

Publicly available datasets were analyzed in this study. This data can be found here: https://www.rcsb.org/, 2PE4.

REFERENCES

Abdullah, N., Thomas, N., Sivasothy, Y., Lee, V., Liew, S., Noorbatcha, I., et al. (2016). Hyaluronidase Inhibitory Activity of Pentacylic Triterpenoids from Prismatomeris Tetrandra (Roxb.) K. Schum: Isolation, Synthesis and QSAR Study. Ijms 17 (2), 143–163. doi:10.3390/ijms17020143

Bahadir Acikara, O., Ilhan, M., Kurtul, E., Smejkal, K., and Kupeli Akkol, E. (2019). Inhibitory Activity of Podospermum Canum and its Active Components on Collagenase, Elastase and Hyaluronidase Enzymes. Bioorg. Chem. 93, 103330–103336. doi:10.1016/j.bioorg.2019.103330

Campo, G. M., Avenoso, A., D'Ascola, A., Scuruchi, M., Prestipino, V., Calatroni, A., et al. (2012). 6-Mer Hyaluronan Oligosaccharides Increase IL-18 and IL-33 Production in Mouse Synovial Fibroblasts Subjected to Collagen-Induced Arthritis. Innate Immun. 18 (5), 675–684. doi:10.1177/1753425911435953

Fallacara, A., Baldini, E., Manfredini, S., and Vertuani, S. (2018). Hyaluronic Acid in the Third Millennium. Polymers 10 (7), 701–737. doi:10.3390/polym10070701

Girish, K., Kemparaju, K., Nagaraju, S., and Vishwanath, B. (2009). Hyaluronidase Inhibitors: a Biological and Therapeutic Perspective. Cmc 16 (18), 2261–2288. doi:10.2174/092986709788453078

Girish, K. S., and Kemparaju, K. (2007). The Magic Glue Hyaluronan and its Eraser Hyaluronidase: a Biological Overview. Life Sci. 80 (21), 1921–1943. doi:10.1016/j.lfs.2007.02.037

Hayon, T., Dvilansky, A., Shpilberg, O., and Nathan, I. (2003). Appraisal of the MTT-Based Assay as a Useful Tool for Predicting Drug Chemosensitivity in Leukemia. Leuk. Lymphoma 44 (11), 1957–1962. doi:10.1080/1042819031000116607

He, H., Li, H., Akanji, T., Niu, S., Luo, Z., Li, D., et al. (2021). Synthesis and Biological Evaluations of Oleanolic Acid Indole Derivatives as Hyaluronidase Inhibitors with Enhanced Skin Permeability. J. Enzyme Inhib. Med. Chem. 36 (1), 1665–1678. doi:10.1080/14756366.2021.1956487

Jiang, D., Liang, J., and Noble, P. W. (2011). Hyaluronan as an Immune Regulator in Human Diseases. Physiol. Rev. 91 (1), 221–264. doi:10.1152/physrev.00052.2009

Li, H., DaSilva, N. A., Liu, W., Xu, J., Dombi, G. W., Dain, J. A., et al. (2020). Thymocid, a Standardized Black Cumin (Nigella Sativa) Seed Extract, Modulates Collagen Cross-Linking, Collagenase and Elastase Activities, and Melanogenesis in Murine B16F10 Melanoma Cells. Nutrients 12 (7), 2146–2162. doi:10.3390/nu12072146

Litwiniuk, M., Krejner, A., Speyrer, M. S., Gauto, A. R., and Grzela, T. (2016). Hyaluronic Acid in Inflammation and Tissue Regeneration. Wounds 28 (3), 78–88.

Liu, C., Ma, H., Slitt, A. L., and Seeram, N. P. (2020). Inhibitory Effect of Cannabidiol on the Activation of NLRP3 Inflammasome Is Associated with its Modulation of the P2X7 Receptor in Human Monocytes. J. Nat. Prod. 83 (6), 2025–2029. doi:10.1021/acs.jnatprod.0c00138

Ma, H., DaSilva, N. A., Liu, W., Nahar, P. P., Wei, Z., Liu, Y., et al. (2016). Effects of a Standardized Phenolic-Enriched Maple Syrup Extract on β-Amyloid Aggregation, Neuroinflammation in Microglial and Neuronal Cells, and β-Amyloid Induced Neurotoxicity in Caenorhabditis elegans. Neurochem. Res. 41 (11), 2836–2847. doi:10.1007/s11064-016-1998-6

Mathew, L. E., and Rajagopal, V. (2017). Betulinic Acid and Fluvastatin Exhibits Synergistic Effect on Toll-like Receptor-4 Mediated Anti-atherogenic Mechanism in Type II Collagen Induced Arthritis. Biomed. Pharmacother. 93, 681–694. doi:10.1016/j.biopha.2017.06.053

Neimkhum, W., Anuchapreeda, S., Lin, W.-C., Lue, S.-C., Lee, K.-H., and Chaiyana, W. (2021). Effects of Carissa Carandas linn. Fruit, Pulp, Leaf, and Seed on Oxidation, Inflammation, Tyrosinase, Matrix Metalloproteinase, Elastase, and Hyaluronidase Inhibition. Antioxidants 10 (9), 1345. doi:10.3390/antiox10091345

Ou, Z., Zhao, J., Zhu, L., Huang, L., Ma, Y., Ma, C., et al. (2019). Anti-inflammatory Effect and Potential Mechanism of Betulinic Acid on λ-carrageenan-induced Paw Edema in Mice. Biomed. Pharmacother. 118, 109347–109356. doi:10.1016/j.biopha.2019.109347

Price, R. D., Berry, M. G., and Navsaria, H. A. (2007). Hyaluronic Acid: the Scientific and Clinical Evidence. J. Plast. Reconstr. Aesthet. Surg. 60 (10), 1110–1119. doi:10.1016/j.bjps.2007.03.005

Quero, L., Klawitter, M., Schmaus, A., Rothley, M., Sleeman, J., Tiaden, A. N., et al. (2013). Hyaluronic Acid Fragments Enhance the Inflammatory and Catabolic Response in Human Intervertebral Disc Cells through Modulation of Toll-like Receptor 2 Signalling Pathways. Arthritis Res. Ther. 15 (4), R94–R107. doi:10.1186/ar4274

Scheibner, K. A., Lutz, M. A., Boodoo, S., Fenton, M. J., Powell, J. D., and Horton, M. R. (2006). Hyaluronan Fragments Act as an Endogenous Danger Signal by Engaging TLR2. J. Immunol. 177 (2), 1272–1281. doi:10.4049/jimmunol.177.2.1272

Scuruchi, M., D'Ascola, A., Avenoso, A., Campana, S., Abusamra, Y. A., Spina, E., et al. (2016). 6-Mer Hyaluronan Oligosaccharides Modulate Neuroinflammation and α-Synuclein Expression in Neuron-like SH-Sy5y Cells. J. Cel. Biochem. 117 (12), 2835–2843. doi:10.1002/jcb.25595

Tsai, J. C., Peng, W. H., Chiu, T. H., Lai, S. C., and Lee, C. Y. (2011). Anti-inflammatory Effects of Scoparia Dulcis L. And Betulinic Acid. Am. J. Chin. Med. 39 (5), 943–956. doi:10.1142/S0192415X11009329

New Sesquiterpenoids From Plant-Associated *Irpex lacteus*

Huai-Zhi Luo[1,2], Huan Jiang[2], Xi-Shan Huang[3] and Ai-Qun Jia[1]*

[1]School of Pharmaceutical Sciences, Key Laboratory of Tropical Biological Resources of Ministry of Education, One Health Institute, Hainan University, Haikou, China, [2]School of Environmental and Biological Engineering, Nanjing University of Science and Technology, Nanjing, China, [3]State Key Laboratory for Chemistry and Molecular Engineering of Medicinal Resources, Collaborative Innovation Center for Guangxi Ethnic Medicine, School of Chemistry and Pharmaceutical Science, Guangxi Normal University, Guilin, China

Bacteria produce a large number of virulence factors through the quorum sensing (QS) mechanism. Inhibiting such QS system of the pathogens without disturbing their growth is a potential strategy to control multi-drug-resistant pathogens. To accomplish this, two new tremulane-type sesquiterpenoids, irpexolaceus H (**1**) and I (**2**), along with two known furan compounds, irpexlacte B (**3**) and C (**4**), were isolated from *Orychophragmus violaceus* (L.) OE Schulz endophytic fungus *Irpex lacteus* (Fr.) Fr. Their structures were elucidated by detailed spectroscopic data (NMR, HRESIMS, IR, and UV), single-crystal X-ray diffraction, and electronic circular dichroism (ECD) analysis. Furthermore, those compounds were evaluated for anti-quorum sensing (anti-QS) activity, and compound **3** was found contributing to the potential QS inhibitory activity.

Keywords: *Orychophragmus violaceus* (L.) O.E. Schulz, *Irpex lacteus* (Fr.) Fr, sesquiterpenoids, furan, quorum sensing

INTRODUCTION

Bacterial quorum sensing (QS) is a cell-density-dependent communication process by which cells measure population density and trigger appropriate responses and conduct behavioral regulation, such as luminescence, motility, secretion of virulence factors, and formation of biofilms (Papenfort and Bassler, 2016). QS inhibitor (QSI) inhibits the QS system without affecting bacteria's growth and reduces its virulence production and biofilm formation; thus, the bacteria are in a low or non-toxicity state, the growth is not inhibited, and therefore it is difficult to cause drug resistance (Jiang and Li, 2013). However, the purpose of traditional antibacterial agents is to kill or inhibit the growth of bacteria, and it is difficult to avoid bacterial resistance (Kalia, 2013). Therefore, finding new QSIs to replace traditional antibacterial agents has become a new strategy in the antibacterial field.

Irpex lacteus (Fr.) Fr. (Phanerochaetaceae) is a basidiomycete that usually colonizes on the deadwood white (i.e., white rot), and it is often used as a traditional Chinese medicine for the treatment of chronic glomerulonephritis. In our previous study on this subject, seven sesquiterpenoids, irpexolaceus A–G, and two new furan derivatives, irpexonjust A–B, were isolated from *I. lacteus* OV38 (Luo et al., 2022). Furthermore, two new tremulane-type sesquiterpenoids, irpexolaceus H (**1**) and I (**2**), were isolated in this study from fungi, as well as two furan compounds, such as irpexlacte B (**3**) and C (**4**), were also obtained (**Figure 1**). These compounds were screened for QS inhibitory activity, and compound **3** exhibited the highest QS inhibitory activity among them. The details of the isolation, structure assignment, and QS inhibitory activities of **1–4** are presented.

MATERIALS AND METHODS

General Experimental Procedures

Nuclear magnetic resonance (NMR) was obtained on a Bruker AV-400 spectrometer (Bruker Corporation, Karlsruhe, Germany). HRMSESI data were recorded on a Q-Exactive Orbitrap MS system (Thermo Fisher Scientific, Bremen, Germany). UV data were obtained on an Evolution 220 UV-vis spectrophotometer (Thermo Fisher Scientific, Madison, United States). Infrared spectroscopy (IR) spectra were obtained on a Nicolet™ iS10 FTIR spectrometer (Thermo Fisher Scientific, Madison, United States). Optical rotations were recorded on an Autopol VI automatic polarimeter (PerkinElmer, Waltham, MA, United States). The silica gel (100–200 and 200–300 mesh, Qingdao Marine Chemical Factory, Qingdao, China) and Sephadex LH-20 column (GE Healthcare Bio-Sciences AB, Uppsala, Sweden) were used for open column chromatography (CC). Fractions were monitored by TLC (HSGF 254, Yantai Jiangyou Silica Gel Development Co., Yantai, China), and spots were visualized by heating silica gel plates after soaking in methanol supplemented with 10% H_2SO_4. The preparative HPLC was performed with UltiMate 300 HPLC (Thermo Fisher Scientific, Madison, United States) equipped with a YMC-Pack ODS-A column (250 × 10 mmI.D, S-5 μm, 12 nm, and flow speed = 2–3 ml/min, YMC Co., Ltd., Kyoto, Japan).

Fungal Material and Fermentation Conditions

The strain *Irpex lacteus* was isolated from the healthy flowers and stems of *Orychophragmus violaceus* (L.) OE Schulz collected from Nanjing University of Science and Technology (NJUST) (Luo et al., 2021). The fungus *I. lacteus* was fermented in 250-ml Erlenmeyer flasks containing 100 ml Fungus No. 2 medium (2% sorbitol, 2% maltose, 1% glutamine, 1% glucose, 0.3% yeast extract, 0.05% tryptophan, 0.05% KH_2PO_4, and 0.03% $MgSO_4$, pH 6.4) at 28°C and 140 rpm for 15 d (Zhou et al., 2017).

Extraction and Purification of Secondary Metabolites

The supernatant (total 100 L) of *I. lacteus* fermentation was extracted three times by equal ethyl acetate (EtOAc) and concentrated under reduced pressure to give a crude extract (99.49 g), which was subjected to column chromatography (CC) over a silica gel (100–200 mesh) eluted with a gradient of dichloromethane/methyl alcohol (CH_2Cl_2/MeOH, 100:0-0:100) to obtain a fraction G (Fr. G) and other 13 fractions (Fr. A–F and H–M). Fr. A (19.61 g) was purified by CC over a silica gel (200–300 mesh) eluted with the gradient systems of petroleum ether/EtOAc (20:1–1:1) and EtOAc/MeOH (100:1–10:1) to yield six sub-fractions Fr. A1–A6. Fr. A6 (4.79 g) was subjected to CC over a silica gel eluted with a gradient system of CH_2Cl_2/MeOH (80:1–0:100) to yield five sub-fractions, that is, Fr. A6.1–A6.5. Fr. A6.1 (97.4 mg) was further purified by HPLC to give **3** (40.1 mg, 45% MeOH, flow speed = 2.5 ml/min, and t_R = 31.0 min) and **4** (5.0 mg, 45% MeOH, flow speed = 2.5 ml/min, and t_R = min). Fr. G (37.30 g) was continually separated by CC over a silica gel (200–300 mesh) eluted with a gradient system of CH_2Cl_2/MeOH (100:0–0:100) to give nine sub-fractions Fr. G1–G9. Fr. G2 (7.76 g) was repeatedly separated using CC over a silica gel, Sephadex LH-20 (100% MeOH), and finally purified by HPLC to give **1** (30.3 mg, 50% MeOH, flow speed = 3.0 ml/min, and t_R = 14.1 min) and **2** (4.90 mg, 50% MeOH, flow speed = 3.0 ml/min, and t_R = 25.6 min).

Irpexolaceus H (**1**). white amorphous powder; [α]18 D + 17.2 (*c* 0.19, MeOH); UV (MeOH) λ_{max} (log ε) 203 (3.99) nm and 290 (2.65) nm; IR (KBr): υ_{max} 3380.60, 2932.72, 2872.93, 1752.01, and 1027.87 cm^{-1}; ^{1}H NMR (400 MHz in MeOD) and ^{13}C NMR (100 MHz in MeOD) data are shown in **Table 1**; and HRESIMS *m/z* 311.1502 [M + COOH]$^-$ (calcd for $C_{16}H_{23}O_6$, 311.1500).

Irpexolaceus I (**2**). Yellow oil; [α]18 D + 21.6 (*c* 0.12, MeOH); UV (MeOH) λ_{max} (log ε) 205 (3.57) nm; CD (MeOH) 195 (Δε—4.72) and 215 (Δε + 8.61) nm; IR (KBr): υ_{max} 3359.87, 1564.95, 1397.66, and 1020.64 cm^{-1}; ^{1}H NMR (400 MHz in MeOD) and ^{13}C NMR (100 MHz in MeOD) data are shown in **Table 1**; and HRESIMS *m/z*, 283.1551 [M-H]$^-$ (calcd for $C_{15}H_{23}O_5$ and 283.1551).

TABLE 1 | ^{1}H (400 MHz) and ^{13}C (100 MHz) NMR spectroscopic data of **1** and **2** in CD$_3$OD.

No	1		2	
	δ_C, type	δ_H (*J* in Hz)	δ_C, type	δ_H (*J* in Hz)
1	126.8, C	–	148.0, C	–
2	139.9, C	–	134.1, C	–
3	38.7, CH	3.62, br d (14.4)	42.1, CH	3.31, m
4	30.9, CH$_2$	1.99, m and 1.84, m	40.2, CH$_2$	2.27, dd (14.0 and 7.3) and 2.11, br d (15.6)
5	73.3, CH	3.96, t (5.0)	181.5, C	–
6	39.7, CH	1.87, m	143.6, CH	5.81, m
7	40.8, CH	3.39, m	46.3, CH	3.43, m
8	40.4, CH$_2$	1.72, m; 1.40, dd (12.9 and 11.0)	43.8, CH$_2$	1.93, ddd (13.2, 8.7, and 1.4) and 1.31, dd (13.2 and 7.4)
9	44.9, C	–	44.0, C	–
10	42.1, CH$_2$	2.17, d (16.2) and 1.81, m	41.6, CH$_2$	2.57, br d (15.6) and 2.35, dd (14.0 and 7.3)
11	70.8, CH$_2$	4.82, d (13.0) and 4.73, d (13.0)	60.2, CH$_2$	4.10, d (11.6) and 4.00, d (11.6)
12	182.3, C	–	66.4, CH$_2$	3.60, dd (10.8 and 6.6); 3.50, m
13	11.8, CH$_3$	0.90, d (7.0)	114.0, CH$_2$	5.05, dt (17.1 and 1.48) and 4.94, br d (10.2)
14	23.9, CH$_3$	1.11, s	24.5, CH$_3$	1.07, s
15	68.6, CH$_2$	3.21, dd (12.2 and 11.4)	69.5, CH$_2$	3.26, d (11.0) and 3.21, d (11.0)

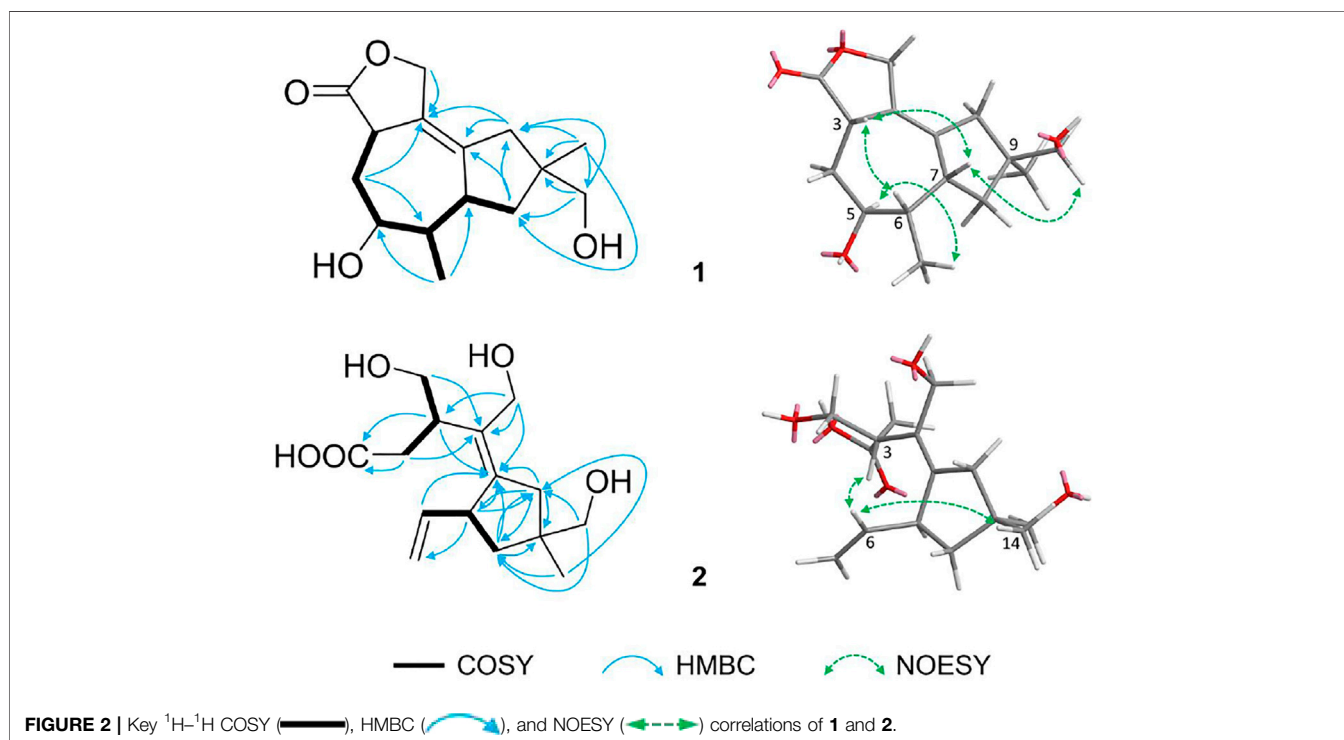**FIGURE 1 |** Chemical structures of **1–4**.
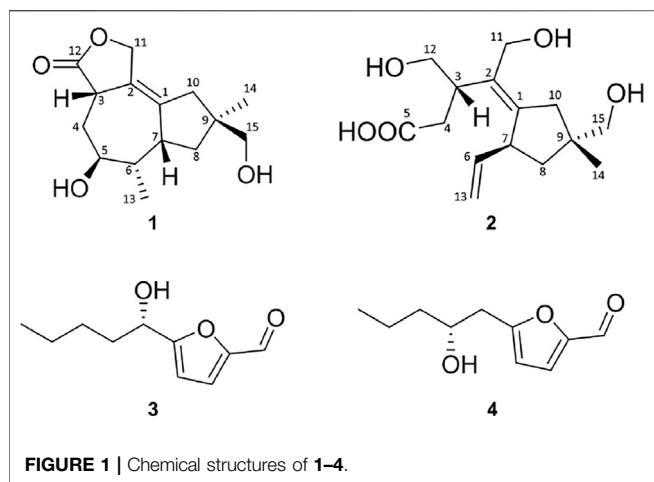
Crystallographic Data of Compound 1

Crystal data for *Cu 1_0m*. $C_{15}H_{22}O_4$, M = 266.33, a = 6.6684 (4) Å, b = 12.1018 (5) Å, c = 8.4219 (4) Å, α = 90°, β = 93.164 (4)°, γ = 90°, V = 678.61 (6) Å^3, Z = 2, T = 170.0 K, space group $P2_12_12_1$, μ(Cu Kα) = 0.760 mm^{-1}, $Dcalc$ = 1.303 g/cm^3, 10,065 reflections measured (10.520° ≤ 2θ ≤ 127.318°), and 2210 unique (R_{int} = 0.0504, R_{sigma} = 0.0357) which were used in all calculations. The final R_1 was 0.0321 [I > 2σ(I)]. The final wR_2 was 0.0752 [I > 2σ(I)]. The final R_1 was 0.0346 (all data). The final wR_2 was 0.0772 (all data). The goodness of fit on F^2 was 1.091. Flack parameter = −0.02 (12), which was determined using 1101 quotients [(I+)−(I−)]/[(I+)+(I−)]. CCDC: 2133065 (www.ccdc.cam.ac.uk).
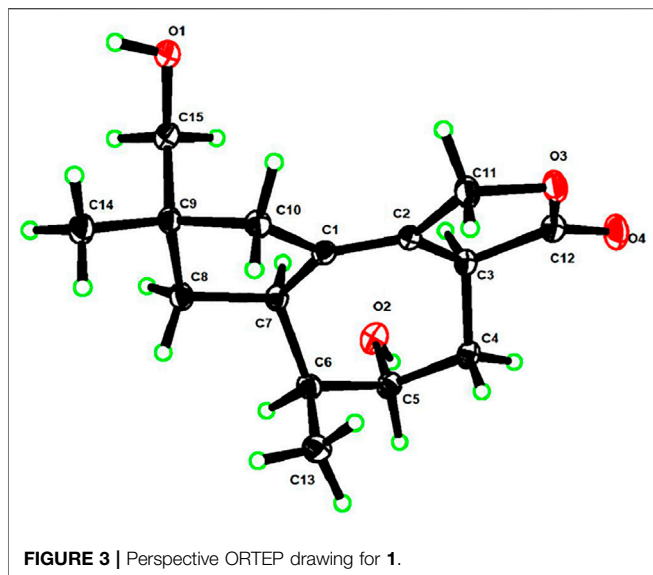
Electronic Circular Dichroism Calculation of Compound 2

The experiment was performed as previously described (Luo et al., 2022). The conformers with Boltzmann population (over 1%) were initially optimized at B3LYP/6–31+G. The ECD spectra of all conformers were conducted by time-dependent density functional theory (TD-DFT) methodology at ωB97X/def2-TZVP, CAM-B3LYP/TZVP, and M062X/def2-TZVP using IEFPCM in MeOH (Neuhaus and Loesgen, 2020). ECD spectra were generated using the program SpecDis 1.71 from dipole-length rotational strength by applying Gaussian band shapes with sigma = 0.2 eV (Bruhn et al., 2013).

Anti-Quorum Sensing Activity

The efficacy of purified compounds on inhibiting QS mechanisms was screened using indicator organisms *Chromobacterium violaceum* CV026 and *Agrobacterium tumefaciens* A136. Overnight grown *C. violaceum* CV026 culture (1 ml) (OD$_{600}$ ≈ 0.1) was added into 100 ml LB agar medium supplemented with kanamycin (20 µg/ml) and C6-HSL (5 µM), mixed, and poured into the plates (Kumar et al., 2021). After the medium was solidified, 2 µl of samples (**1–4**) (50 mg/ml) were dropped onto the plates and then incubated at 28°C for 24 h, recording the violacein changes in color. The absence of violacein production in CV026 represents compounds that inhibit the QS system. Furthermore, QS inhibitory activity-screened *A. tumefaciens* A136 was determined as described earlier (Zhu et al., 2018). X-gal (50 µg/ml) and C10-HSL (5 µM) were added into the LB agar medium supplemented with *A. tumefaciens* A136. Each experiment was repeated three times.

FIGURE 2 | Key ^{1}H–^{1}H COSY (——), HMBC (⌒▸), and NOESY (◂---▸) correlations of **1** and **2**.

FIGURE 3 | Perspective ORTEP drawing for **1**.

FIGURE 4 | Experimental and calculated ECD spectra of **2**.

RESULTS AND DISCUSSION

Structure Elucidation

Irpexolaceus H (**1**), a white amorphous powder, was assigned the molecular formula of $C_{15}H_{24}O_4$ with five degrees of unsaturation based on HRESIMS data at m/z 311.1502 [M + COOH]$^-$ (calcd for $C_{16}H_{23}O_6$, 311.1500). The ^{1}H and ^{13}C NMR spectra of **1** (**Table 1**) revealed 15 carbon resonances, including two methyls at δ_C 11.8 and 23.9, three methylene carbons at δ_C 30.9, 40.4, and 42.1, two oxygenated methylene carbons at δ_C 70.8 and 68.6, three methine carbons at δ_C 38.7, 39.7, and 40.8, one oxygenated methine carbon at δ_C 73.3, three sp^2 quaternary carbons at δ_C 126.8, 139.9, and 182.3, and one sp^3 quaternary carbon at δ_C 44.9. These data demonstrated high similarity to irpexolaceus F (Luo et al., 2022), with the main difference being that the low field at δ_C 139.9 and 126.8 (**1**) shifted downfield to δ_C 165.9 and 128.5 in irpexolaceus F, indicating differences in the position of the carbon–carbon double bonds, which was confirmed by the HMBC correlations from H$_2$-8 (δ_H 1.72, 1.40) and H$_2$-10 (δ_H 2.17, 1.81) to C-1 (δ_C 126.8) and from H$_2$-4 (δ_H 1.99, 1.84), H$_2$-10 (δ_H 2.17, 1.81), and H$_2$-11 (δ_H 4.82, 4.73) to C-2 (δ_C 139.9), in combination with the ^{1}H–^{1}H COSY correlations of H-3 (δ_H 3.62)/H$_2$-4 (δ_H 1.99, 1.84)/H-5 (δ_H 3.96)/H-6 (δ_H 1.87)/H-7 (δ_H 3.39)/H$_2$-8 (δ_H 1.72, 1.40) (**Figure 2**). The mentioned data combined with previously reported data (Luo et al., 2022) determined the planar structure of **1**. In addition, the relative configuration of **1** was determined by the NOESY correlations of H-3 (δ_H 3.62)/H-6 (δ_H 1.87)/H-7 (δ_H 3.39) and Me-13 (δ_H 0.90)/ H-5 (δ_H 3.96)/Me-14 (δ_H 1.11) (**Figure 2**). Combined with the single-crystal X-ray diffraction analysis (**Figure 3**), the absolute configuration of **1** was confirmed as 3*S*,5*S*,6*S*,7*R*,9*S*.

Irpexolaceus I (**2**), a yellow oil, was assigned the molecular formula of $C_{15}H_{24}O_5$ with four degrees of unsaturation based on HRESIMS data at m/z 283.1551 [M-H]$^-$ (calcd for $C_{15}H_{23}O_5$, 283.1551). The ^{1}H and ^{13}C NMR spectra of **2** (**Table 1**) revealed 15 carbon resonances, including one methyl at δ_C 24.5, four
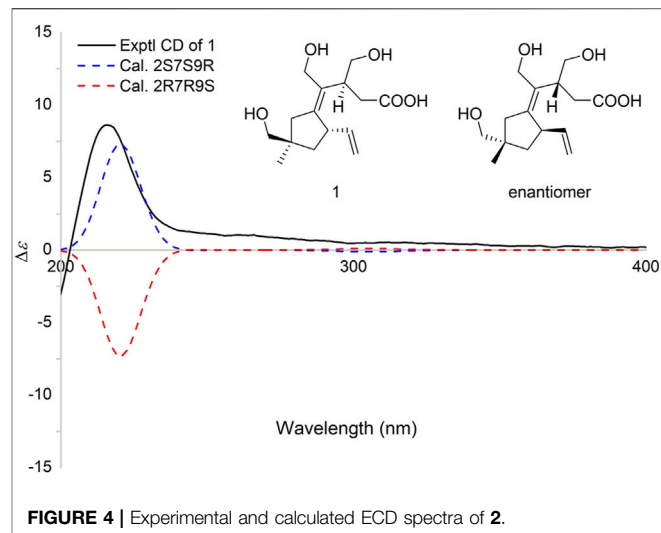
methylene carbons at δ_C 40.2, 43.8, 41.6, and 114.0, three oxygenated methylene carbons at δ_C 60.2, 66.4, and 69.5, three methine carbons at δ_C 42.1, 143.6, and 46.3, three sp^2 quaternary carbons at δ_C 148.0, 134.1, and 181.5, and one sp^3 quaternary carbon at δ_C 44.0. There were two C=C and one carbonyl group, and the remaining one unsaturation was a ring, which was confirmed by the ^{1}H-^{1}H COSY correlations of H$_2$-8 (δ_H 1.93, 1.31)/H-7 (δ_H 3.43)/H-6 (δ_H 5.81)/H$_2$-13 (δ_H 5.05, 4.94), and the HMBC correlations from H-7 (δ_H 3.43) to C-1 (δ_C 148.0) and C-10 (δ_C 41.6), from H$_2$-8 (δ_H 1.93, 1.31) to C-1 (δ_C 148.0), C-7 (δ_C 46.3), C-9 (δ_C 44.0), and C-10 (δ_C 41.6), and from H$_2$-10 (δ_H 2.57, 2.35) to C-1 (δ_C 148.0), C-7 (δ_C 46.3), C-8 (δ_C 43.8), and C-9 (δ_C 44.0). Moreover, a high-field quaternary carbon, C-9 (δ_C 44.0), was linked to C-14 (δ_C 24.5) and C-15 (δ_C 69.5). Combined with another set of ^{1}H–^{1}H COSY correlations of H-3 (δ_H 3.31)/H$_2$-4 (δ_H 2.27, 2.11)/H$_2$-12 (δ_H 3.60, 3.50), the planar structure of **2** was determined as shown in **Figure 1**, which was highly similar to ceriponol P (Ying et al., 2014), with a difference of a hydroxyl group binding to δ_C 69.5. In addition, the relative configuration of **2** was confirmed by the NOESY correlations of H-6 (δ_H 5.81)/H-3 (δ_H 3.31)/Me-14 (δ_H 1.07) (**Figure 2**). The calculated and experimental ECD spectra of **2** showed excellent fit (**Figure 4**), indicating that the absolute configuration of **2** was 2*S*,7*S*,9*R*.

In addition to the aforementioned compounds, two furans (**3** and **4**) were obtained and identified as irpexlacte B and C according to the previously reported data (Luo et al., 2022).

Proposed Biotransformation Pathway

Tremulane (**i**) and (**ii**) were biosynthesized based on the relative structures of **1** and **2** by the cyclization and rearrangement of farnesyl pyrophosphate (**FPP**) (Ayer and Browne, 1981; Ayer and Cruz, 1993). After a multi-step reaction such as esterification, cyclization, and dehydration in microbes, tremulane (**i**) was possibly converted to irpexlaceus H (**Figure 5**). Moreover, lactarane skeletons **ii-1** and **ii-2** were produced by a series of methyl migrations of tremulane (**ii**)) (Ayer and Cruz, 1993), which differed from tremulane (**i**)) in the configuration of C-1 and C-7. Lactarane skeleton **ii-2** was
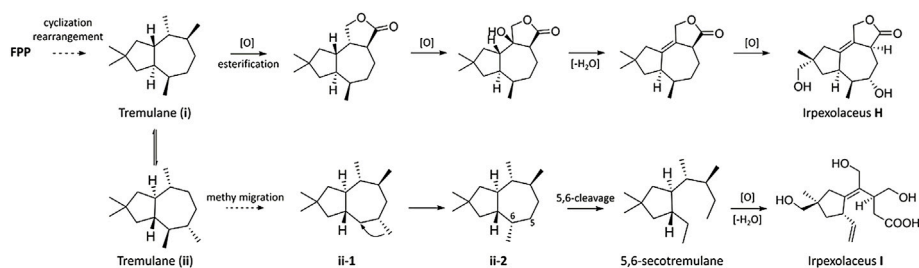
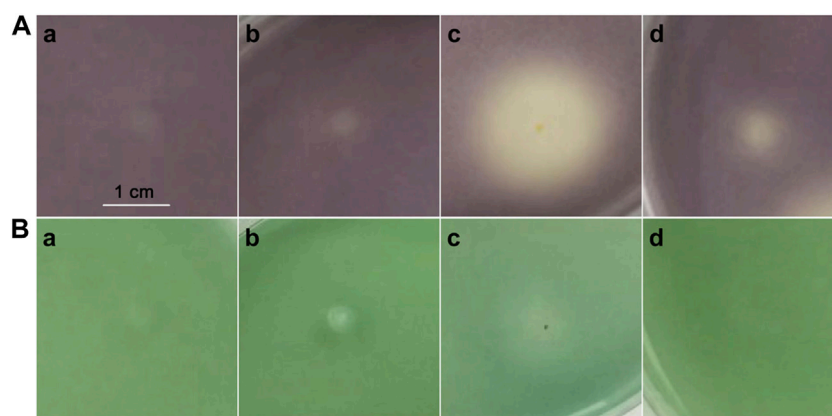**FIGURE 5 |** Proposed biosynthetic pathway for **1** and **2**.

FIGURE 6 | Screening of QS inhibitory activity by *C. violaceum* CV026 **(A)** and *A. tumefaciens* A136 **(B)**. Compounds 1 **(A)**, 2 **(B)**, 3 **(C)**, and 4 **(D)**.

transformed to 5,6-secotremulane under the 5,6-cleavage (He et al., 2020) and then possibly converted to irpexlaceus I by a series of oxidation and dehydration (**Figure 5**).

Biological Activity

Compounds **1–4** were evaluated for their QS inhibitory activities at 50 mg/ml against biomarker strains *C. violaceum* CV026 (**Figure 6A**) and *A. tumefaciens* A136 (**Figure 6B**). We assessed the inhibitory effect of the compound by assaying the inhibition of C6-HSL-induced violacein production by *C. violaceum* CV026, and C10-HSL-induced β-galactosidase expression (blue pigment) by *A. tumefaciens* A136. Compounds **1–2** showed no inhibitory activities against both QS systems of biomarker strains. However, compound **3,** in which the binding position of hydroxyl was closer to the furan ring than **4,** exhibited stronger inhibition activity against the production of violacein in *C. violaceum* CV026 than that of the latter but weaker inhibitory activity against the production of blue pigment in *A. tumefaciens* A136. The results demonstrated that the binding position of hydroxyl was vital for QS inhibitory activity.

CONCLUSION

Two new tremulane-type sesquiterpenoids, irpexolaceus H (**1**) and I (**2**), were isolated from the liquid fermentation of *I. lacteus*. Their

structures were established based on NMR, HRESIMS, IR, single-crystal X-ray diffraction, and ECD analysis. These compounds (**1–4**) were evaluated for QS inhibitory activities against *C. violaceum* CV026 and *A. tumefaciens* A136 at 50 mg/ml. The results found that compound **3** exhibited a significant QS inhibitory activity against *C. violaceum* CV026, and compound **4** showed a weaker activity. In addition, compound **3** also showed a weak QS inhibitory activity against *A. tumefaciens* A136. But interestingly, the hydroxyl binding to α-C in the furan ring showed a stronger QS inhibitory activity than that of **4** (hydroxyl binding to β-C in the furan ring), which suggested that the position of hydroxyl in the furan ring was possibly vital for QS inhibitory activity against *C. violaceum* CV026.

DATA AVAILABILITY STATEMENT

The original contributions presented in the study are publicly available. These data can be found at: https://www.ccdc.cam.ac.uk/, 2133065, 2095205, 2095201, and 2095200.

AUTHOR CONTRIBUTIONS

H-ZL contributed to the chemical and biological experiments and prepared the manuscript draft. HJ contributed to the spectra data analysis. X-SH contributed to the ECD calculation and analysis.

A-QJ contributed to the manuscript revision and financial support. All authors approved this manuscript to submit and publish.

SUPPLEMENTARY MATERIAL

The Supplementary Material for this article can be found online at: https://www.frontiersin.org/articles/10.3389/fchem.2022.905108/full#supplementary-material

REFERENCES

Ayer, W. A., and Browne, L. M. (1981). Terpenoid Metabolites of *Mushrooms* and Related *Basidiomycetes*. *Tetrahedron* 37 (12), 2197–2248. doi:10.1016/S0040-4020(01)97979-7

Ayer, W. A., and Cruz, E. R. (1993). The Tremulanes, a New Group of Sesquiterpenes from the aspen Rotting Fungus *Phellinus Tremulae*. *J. Org. Chem.* 58 (26), 7529–7534. doi:10.1021/jo00078a035

Bruhn, T., Schaumlöffel, A., Hemberger, Y., and Bringmann, G. (2013). SpecDis: Quantifying the Comparison of Calculated and Experimental Electronic Circular Dichroism Spectra. *Chirality* 25 (4), 243–249. doi:10.1002/chir.22138

He, J., Pu, C.-J., Wang, M., Li, Z.-H., Feng, T., Zhao, D.-K., et al. (2020). Conosiligins A-D, Ring-Rearranged Tremulane Sesquiterpenoids from *Conocybe Siliginea*. *J. Nat. Prod.* 83 (9), 2743–2748. doi:10.1021/acs.jnatprod.0c00681

Jiang, T., and Li, M. (2013). Quorum sensing Inhibitors: a Patent Review. *Expert Opin. Ther. Patents* 23 (7), 867–894. doi:10.1517/13543776.2013.779674

Kalia, V. C. (2013). Quorum sensing Inhibitors: an Overview. *Biotechnol. Adv.* 31 (2), 224–245. doi:10.1016/j.biotechadv.2012.10.004

Kumar, L., Brenner, N., Brice, J., Klein-Seetharaman, J., and Sarkar, S. K. (2021). Cephalosporins Interfere with Quorum Sensing and Improve the Ability of *Caenorhabditis elegans* to Survive *Pseudomonas aeruginosa* Infection. *Front. Microbiol.* 12. doi:10.3389/fmicb.2021.598498

Luo, H.-Z., Jiang, H., Sun, B., Wang, Z.-N., and Jia, A.-Q. (2022). Sesquiterpenoids and Furan Derivatives from the Orychophragmus Violaceus (L.) O.E. Schulz Endophytic Fungus Irpex Lacteus OV38. *Phytochemistry* 194, 112996. doi:10.1016/j.phytochem.2021.112996

Luo, H.-Z., Zhou, J.-W., Sun, B., Jiang, H., Tang, S., and Jia, A.-Q. (2021). Inhibitory Effect of Norharmane on *Serratia marcescens* NJ01 Quorum Sensing-Mediated Virulence Factors and Biofilm Formation. *Biofouling* 37 (2), 145–160. doi:10.1080/08927014.2021.1874942

Neuhaus, G. F., and Loesgen, S. (2020). Antibacterial Drimane Sesquiterpenes from *Aspergillus ustus*. *J. Nat. Prod.* 84 (1), 37–45. doi:10.1021/acs.jnatprod.0c00910

Papenfort, K., and Bassler, B. L. (2016). Quorum sensing Signal-Response Systems in Gram-Negative Bacteria. *Nat. Rev. Microbiol.* 14 (9), 576–588. doi:10.1038/nrmicro.2016.89

Ying, Y.-M., Tong, C.-P., Wang, J.-W., Shan, W.-G., and Zhan, Z.-J. (2014). Ceriponol P, the First Example of Monocyclic Tremulane Sesquiterpene Produced by *Ceriporia Lacerate* a Fungal Endophyte of *Huperzia Serrata*. *J. Chem. Res.* 38 (5), 304–305. doi:10.3184/174751914X13975706150476

Zhou, J., Bi, S., Chen, H., Chen, T., Yang, R., Li, M., et al. (2017). Anti-biofilm and Antivirulence Activities of Metabolites from *Plectosphaerella Cucumerina* against *Pseudomonas aeruginosa*. *Front. Microbiol.* 8, 769. doi:10.3389/fmicb.2017.00769

Zhu, S., Wu, H., Zhang, C., Jie, J., Liu, Z., Zeng, M., et al. (2018). Spoilage of Refrigerated Litopenaeus Vannamei: Eavesdropping on Acinetobacter Acyl-Homoserine Lactones Promotes the Spoilage Potential of *Shewanella Baltica*. *J. Food Sci. Technol.* 55 (5), 1903–1912. doi:10.1007/s13197-018-3108-z

Check for updates

Design, Synthesis, and Apoptosis-Promoting Effect Evaluation of Rhopaladins' Analog 4-Arylidene-5-Oxopyrrolidine Derivatives

Jun Zhu[1,2†], Ling-Qi Kong[2†], Qin-Hua Chen[3], Bin Li[1], Lun Wu[1], Feng-Ying Ran[1], Li-Na Ke[1]*, Xiao-Hua Zeng[1,2]* and Hong-Mei Wang[1,2]*

[1]Sinopharm Dongfeng General Hospital, Hubei University of Medicine, Shiyan, China, [2]Hubei Key Laboratory of Wudang Local Chinese Medicine Research, School of Pharmaceutical Sciences, Hubei University of Medicine, Hubei, China, [3]Shenzhen Baoan Authentic TCM Therapy Hospital, Shenzhen, China

Marine alkaloids have novel structures and antitumor activities. Therefore, we synthesized rhopaladins' analogs from marine alkaloids rhopaladins A-D and modified their structures to synthesize 4-benzylidene-5-pyrrolidone derivatives. Among the compounds, (2E, 4E)-4-(4-chlorobenzylidene)-2-(4-chlorostyryl)-N-cyclohexyl-1-(4-fluorophenyl)-5-oxopyrrolidine-2-carboxamide (RPDPRH) has high efficiency and less hepatotoxicity, with IC_{50} values of 4.66, 6.42, 17.66, 15.2, 12.36, 22.4, and 243.2 µM *in vitro* anti-proliferative activity testing against cervical cancer C-33A, CaSki, SiHa, and HeLa cells, human hepatocarcinoma HepG2 and 7402 cells, and human normal liver LO2 cells, respectively. In particular, RPDPRH has similar activity to cisplatin on human hepatocarcinoma cells, and cisplatin served as a positive control in our study. Next, the apoptosis of HepG2 and 7402 cells induced by RPDPRH at different concentrations was detected by Annexin V/PI flow cytometry. Moreover, the expression of apoptotic proteins was detected by Western blot analysis. Finally, the results showed that RPDPRH could induce apoptosis of hepatocarcinoma cells by regulating Bax and Bcl-2 expressions. In summary, our results indicate that RPDPRH has the potential to serve as an antitumor agent and plays a significant role in future studies.

Keywords: rhopaladins' analog, synthesis, 4-arylidene-5-oxopyrrolidine, cytotoxicity evaluation, anticancer, apoptosis

INTRODUCTION

Cancer is one of the most horrible diseases in the 20th century, which is considered as one of the primary causes of mortality and also to be a major public health problem in every country on the planet in the 21st century (Roy and Saikia, 2016; Sung et al., 2021). Primary carcinoma of the liver is the fourth leading cause of cancer-related deaths, accounting for about 840,000 new cases and more than 780,000 deaths worldwide each year (Sung et al., 2021). Hepatocellular carcinoma (HCC) is the most common primary liver cancer, accounting for about 75–85% (Lai, 2019). The treatment of tumors mainly includes surgical excision, radiotherapy, and chemotherapy. As a traditional treatment, drug therapy plays an important role in different stages of cancer cell

SCHEME 1 | Synthetic strategies leading to (2E, 4E)-4-arylidene-2-styryl-5-oxo pyrrolidines as targets.
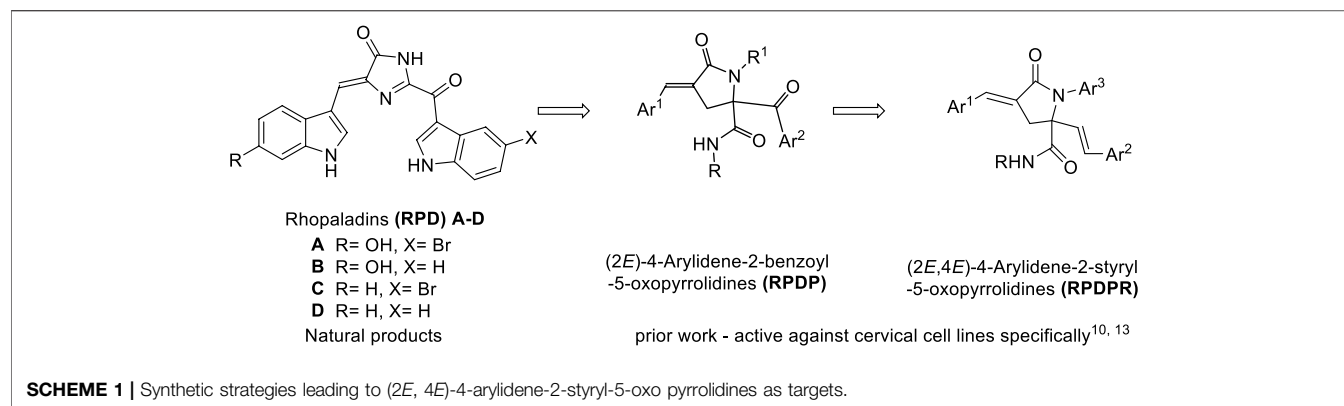
growth (Bhayani et al., 2015; An et al., 2021). Consequently, synthesizing novel and efficient compounds for cancer therapy is essential.

Compounds with a pyrrolidone structure have a wide range of applications in pharmaceutical and chemical fields, especially as basic nuclear structures for anticancer and antiviral drug syntheses (Carbone et al., 2020; Dyshlovoy et al., 2020). On the therapeutic front, the superiority of marine natural products over terrestrial natural products is because of their novelty, chemical stability, and strong biological activity (Nijampatnam et al., 2015). Marine alkaloids widely exist in marine organisms and have many physiological activities. Pyrrolidone-related natural marine compounds have a unique chemical structure and strong antifungal and antibacterial biological properties, which are favored by many chemists. Alkaloids such as rhopaladins A-D have momentous cytotoxicity to human tumor cells (Hiroyasu et al., 1998). We have previously synthesized rhopaladins' analog (E)-2-aroyl-4-arylidene-5-oxopyrrolidine (RPDP serial chemicals, *see* **Scheme 1**) from Baylis–Hillman acid (2-bromomethyl-3-*p*-fluorobenzyl-2-propenoic acid), primary amines, arylglyoxal, and isocyanide *via* a one-pot approach which is based on Ugi condensation and intramolecular S_N cyclization (Zhu et al., 2020). Moreover, the rhopaladins' analogs (E)-2-aroyl-4-arylidene-5-oxopyrrolidine inhibited CaSki human cervicocarcinoma cell proliferation, induced cell apoptosis, and downregulated the E6/E7 mRNA expression (Zeng et al., 2013; Wang et al., 2021). However, it has a high selectivity to cervical cancer cells. Hence, the novel (2E, 4E)-4-arylidene-2-styryl-5-oxopyrrolidines (Kong et al., 2021) (RPDPR serial chemicals, *see* **Scheme 1**) were designed by optimizing the rhopaladins' analog (E)-2-aroyl-4-arylidene-5-oxopyrrolidine and synthesized in the same one-pot approach by using only (E)-3-arylacrolein instead of arylglyoxal.

According to the obtained preliminary structure–activity relationship, the antitumor activities of RPDPR serial chemicals were associated with the Ar (Lai, 2019) group. The cytotoxicity of the Ar3 group is increased in the presence of halogen atoms, especially fluorine atoms, in order to obtain a more efficient and less hepatotoxic chemical and to further investigate the effect of the chemical on the apoptosis of hepatocarcinoma cells. Four RPDPR serial chemicals

(RPDPRH, RPDPRI, RPDPRK, and RPDPRO, **Scheme 2**) were synthesized and evaluated for their antitumor activities.

EXPERIMENT

Chemistry

Melting points were measured with an X-4 melting point instrument (uncorrected thermometer) produced by Beijing Ruili Analytical Instrument Co., Ltd. Mass spectrometry was performed with a Finnigan trace MS analyzer (direct injection method). Elemental analysis was determined and was performed using a vario EL III analyzer. ^{1}H NMR and ^{13}C NMR spectra were measured at 600 or 400 MHz using spectrometers. The solvent was CDCl$_3$, with TMS being the internal standard.

One-Pot Synthesis of (2E, 4E)-4-Arylidene-2-Styryl-5-Oxopyrrolidine Derivatives RPDPRH, RPDPRI, RPDPRK, and RPDPRO

First, a mixture of aromatic amine **2** (1 mol) and substituted (E)-3-arylacrolein **3** (1 mol) was stirred in methanol (5 ml) at room temperature for 30 min. After precipitation occurred, aromatic acid **1** (1 mol) and cyclohexyl isocyanide **4** (1 mol) were added successively, and the mixture was stirred at room temperature for 24 h. Then, Cs$_2$CO$_3$ (0.5 mol) was added, and the mixture was kept uniform by stirring at room temperature for 24 h. After the reaction was performed completely, the mixture was allowed to chill overnight, and the precipitate was filtered, recrystallized from ether, and four compounds were obtained as white solid. The yield, melting point, analytical data, and spectral data of each compound are given as follows.

(2E, 4E)-4-(4-chlorobenzylidene)-2-(4-chlorostyryl)-N-cyclohexyl-1-(4-fluorophenyl)-5-oxopyrrolidine-2-carboxamide (RPDPRH) (Zeng et al., 2020).

White crystals (0.50 g, yield 89%), m. p. 128–130°C; ^{1}H NMR (CDCl$_3$, 600 MHz): δ (ppm) 7.55–6.98 (m, 14H, 12Ar-H and 2=CH), 6.34 (d, J = 16.2 Hz,1H, =CH), 5.68 (s, 1H, NH), 3.74–3.72 (m, 1H, NCH), 3.45 (d, J = 16.8 Hz, 1H, CH$_2$^{a}), 3.33 (d, J = 16.8 Hz, 1H, CH$_2$^{b}), and 1.77–0.80 (m, 10H, 5CH$_2$); ^{13}C NMR (CDCl$_3$, 100 MHz): δ (ppm) 169.9, 169.0, 162.3, 135.5, 134.0, 133.1, 131.0, 129.9, 129.2, 129.0, 128.8, 127.9, 127.6, 127.5,
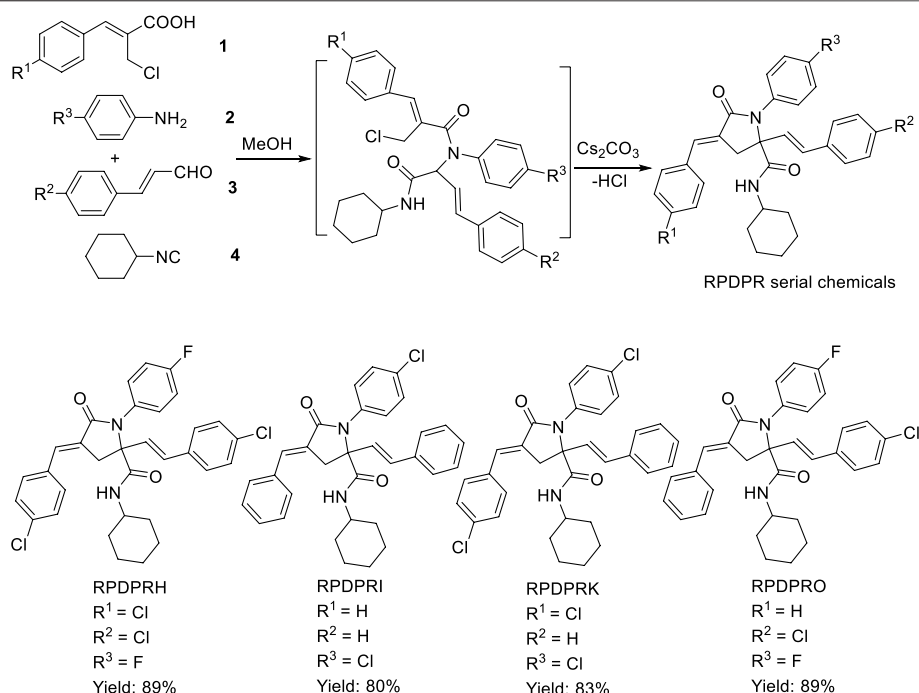
SCHEME 2 | Synthesis of (2*E*, 4*E*)-4-arylidene-2-styryl-5-oxopyrrolidine derivatives **RPDPRH, RPDPRI, RPDPRK,** and **RPDPRO**.

125.4, 124.2, 117.9, 109.8, 69.3, 48.8, 41.3, 32.3, 25.2, and 24.4; MS (m/z, %) 562 (M$^+$, 2), 466 (93), 436 (21), 341 (64), 204 (13), 95 (100), and 76 (17). Anal.Calcd for C$_{32}$H$_{29}$Cl$_2$FN$_2$O$_2$: C, 68.21; H, 5.19; and N, 4.97. Found: C, 68.13; H, 5.23; and N, 4.93.

(2*E*, 4*E*)-4-benzylidene-1-(4-chlorophenyl)-N-cyclohexyl-5-oxo-2-styrylpyrrolidine-2-carboxamide (RPDPRI).

White crystals (0.41 g, yield 80%), m. p. 209–210°C; ^{1}H NMR (CDCl$_3$, 400 MHz): δ 7.60–7.00 (m, 16H, 14Ar-H and 2=CH), 6.37 (d, *J* = 16.2 Hz,1H, =CH), 5.81 (s, 1H, NH), 3.86–3.63 (m, 1H, NCH), 3.48 (d, *J* = 16.8 Hz, 1H, CH$_2$^{a}), 3.39 (d, *J* = 16.8 Hz, 1H, CH$_2$^{b}), and 1.77–0.83 (m, 10H, 5CH$_2$); ^{13}C NMR (CDCl$_3$, 100 MHz): δ (ppm) 170.1, 169.3, 135.6, 134.8, 134.3, 131.1, 131.0, 129.8, 129.4, 129.0, 128.9, 128.8, 128.6, 128.3, 127.1, 127.0, 126.7, 124.4, 69.4, 48.7, 41.4, 32.6, 25.2, and 24.5; MS (m/z, %) 510 (M$^+$, 2), 399(13) 384 (100), 436 (21), 170 (24), 111 (43), and 76 (29). Anal.Calcd for C$_{32}$H$_{31}$ClN$_2$O$_2$: C, 75.21; H, 6.11; and N, 5.48. Found: C, 75.27; H, 6.05; and N, 5.51.

(2*E*, 4*E*)-4-(4-chlorobenzylidene)-1-(4-chlorophenyl)-*N*-cyclohexyl-5-oxo-2-styryl pyrrolidine-2-carboxamide (RPDPRK).

White crystals (0.45 g, yield 83%), m. p. 235–236°C; ^{1}H NMR (CDCl$_3$, 400 MHz): δ 7.55–6.98 (m, 15H, 13Ar-H and 2=CH), 6.37 (d, *J* = 16.2 Hz,1H, =CH), 6.00 (s, 1H, NH), 3.76–3.75 (m, 1H, NCH), 3.46 (d, *J* = 16.8 Hz, 1H, CH$_2$^{a}), 3.34 (d, *J* = 16.8 Hz, 1H, CH$_2$^{b}), and 1.81–0.89 (m, 10H, 5CH$_2$); ^{13}C NMR (CDCl$_3$, 100 MHz): δ (ppm) 170.0, 169.1, 135.5, 135.3, 133.2, 132.7, 131.2, 130.9, 129.1, 129.0, 128.9, 128.6, 128.5, 128.3, 127.8, 126.9, 126.7,

124.5, 69.4, 48.8, 41.2, 32.5, 25.2, and 24.5; MS (m/z, %) 544 (M$^+$, 2), 418 (100), 307 (13), 204 (39), 111 (73), and 77 (24). Anal.Calcd for C$_{32}$H$_{30}$Cl$_2$N$_2$O$_2$: C, 70.46; H, 5.54; and N, 5.14. Found: C, 70.50; H, 5.50; and N, 5.11.

(2*E*, 4*E*)-2-(4-chlorostyryl)-4-benzylidene-N-cyclohexyl-1-(4-fluorophenyl)-5-oxopyrrolidine-2-carboxamide   (RPDPRO) (Kong et al., 2021).

White crystals (0.47 g, yield 89%), m. p. 142–144°C; ^{1}H NMR (CDCl$_3$, 600 MHz): δ 7.54–7.26 (m, 14H, 13Ar-H and = CH), 7.00 (d, *J* = 16.2 Hz,1H, =CH), 6.37 (d, *J* = 16.2 Hz,1H, =CH), 5.74 (s, 1H, NH),3.45–3.33 (m, 1H, NCH), 3.44 (d, *J* = 16.8 Hz, 1H, CH$_2$^{a}), 3.34 (d, *J* = 16.8 Hz, 1H, CH$_2$^{b}), and 1.80–0.85 (m, 10H, 5CH$_2$); ^{13}C NMR (CDCl$_3$, 100 MHz): δ (ppm) 170.0, 169.2, 163.9, 135.5, 133.9, 133.0, 131.7, 131.0, 128.9, 128.6, 128.3, 126.9, 126.7, 126.6, 124.4, 116.1, 115.9, 101.0, 69.4, 48.7, 41.2, 32.6, 24.6, and 24.5; MS (m/z, %) 528 (M$^+$, 2), 402 (100), 307 (84), 170 (67), 111 (17), 95 (23), and 77 (24). Anal.Calcd for C$_{32}$H$_{30}$ClFN$_2$O$_2$: C, 61.55; H, 4.68; and N, 4.49. Found: C, 61.52; H, 4.71; and N, 4.53.

Biological Evaluation
Cell Lines and Cell Culture

HepG2 (human epidermoid hepatocellular carcinoma cell), 7402 (human epidermoid hepatocellular carcinoma cell), C-33A (human epidermoid cervical carcinoma cell), and HeLa (human epidermoid cervical adenocarcinoma cell) were incubated in Dulbecco's modified Eagle's medium (DMEM), which was purchased from Gibco (Grand Island, NY, United States). SiHa cells (human epidermoid cervical squamous cell carcinoma) were incubated in minimum

TABLE 1 | Anti-cancer activities *in vitro* of synthesized four compounds.

Compound	Half inhibitory concentration of various cell lines[a] (IC$_{50}$, μM)						
	C-33A	CaSki	SiHa	HeLa	HepG2	7402	LO2
RPDPRH	4.66	6.42	17.66	15.2	12.36	22.4	>100[b]
RPDPRI	>100	>100	>100	>100	>100	>100	>100
RPDPRK	89.5	46.4	67.3	44.7	>100	>100	>100
RPDPRO (Kong et al., 2021)	5.56	9.15	12.5	21.4	14.5	31.24	86.77
Cisplatin (Kong et al., 2021)	48.16	17.52	37.06	47.52	19.27	48.52	17.3

Negative control 0.1% DMSO, no activity.

[a]Cytotoxicity based on IC$_{50}$ for each cell line. IC$_{50}$ represents the concentration of the compound which is reduced by 50% of the optical density of treated cells with respect to untreated cells using MTT assay.

[b]Insignificant inhibition at the dose of 100 μM.
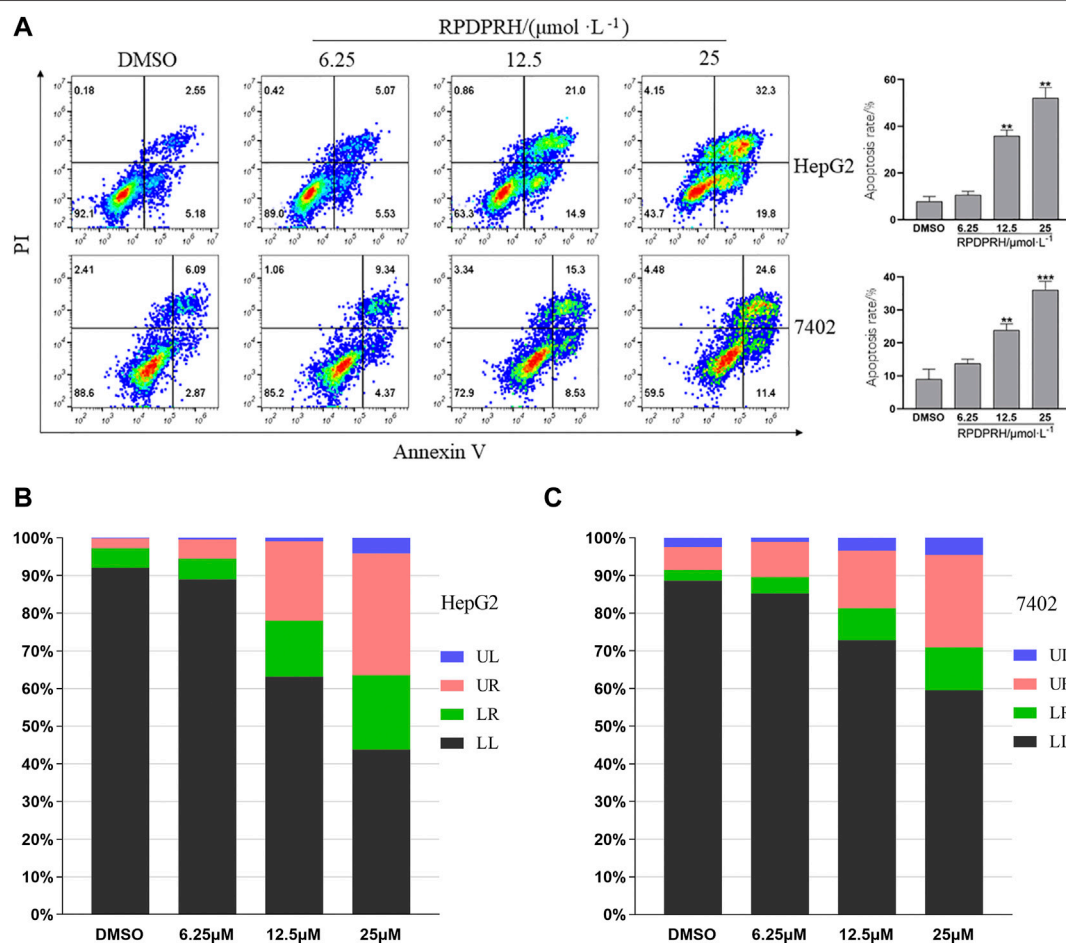
FIGURE 1 | Effect of RPDPRH on the apoptosis of HepG2 and7402 cells. Note: **(A)**: Flow cytometry analyses of apoptosis induction in HepG2 and 7402 cells after being treated by RPDPRH for 48 h and the total apoptosis rate. Compared with the DMSO control group, **$p < 0.01$ and ***$p < 0.001$, ($\bar{x} \pm s$, n=3). **(B)** and **(C)**: Living cell (LL), early apoptotic cell (LR), late apoptotic cell (UR), and necrotic cell/fragment (UL) rate of HepG2 and 7402 cells were analyzed.

essential medium (MEM, also from Gibco). CaSki (human epidermoid cervical carcinoma cell) and LO2 (human normal liver cell) were incubated in minimum essential medium (MEM, also from Gibco). All cells were maintained at 37°C in a humidified incubator with 5% carbon dioxide, and the media

contained 10% fetal bovine serum (FBS, Corning, United States) and 1% penicillin–streptomycin antibiotic solution (Corning, United States). SiHa and CaSki were bought from the China Center for Type Culture Collection (CCTCC). The other five types of cancer cell lines were obtained from the Experiment

Center of Medicine, Sinopharm Dongfeng Hospital, Hubei University of Medicine. The compounds were dissolved in dimethyl sulfoxide (DMSO, MP Biomedicals, United States), and cisplatin was purchased from Aladdin, Shanghai, China. The control (0 μM) group was treated with DMSO only in the same conditions, and the DMSO content in the medium was less than 0.1%.

Cell Viability Assay *In Vitro*
Cell viability was measured by a 3-(4,5-dimethylthiazol-2-yl)-2,5-diphenyltetrazolium bromide (MTT, MultiSciences, China) assay. The specific experimental steps referred to our previous research (Zhu et al., 2020). For each cell line, cells were digested and seeded in 96-well plates at a density of 1×10^3 cells/well. After 24 h of culture, the cells were adherent and treated with varying concentrations of RPDPRH (0, 3.125, 6.25, 12.5, 25, 50, and 100 μM). Cells without treatment were used as a solvent control group (0 μM, DMSO) and those with cisplatin treatment served as a positive control. After 48 h of treatment, MTT solution was added and incubated for 4 h. Then, the formed formazan crystals were dissolved in DMSO, and the plates were estimated in a luminescence microplate reader (BioTek Inc., Bio-Tek MQX200) at a wavelength of 490 nm. Optical density (OD) values were obtained, and the inhibition rate and IC_{50} of each compound on different cells were calculated by GraphPad Prism 8.0.1 software. Cell inhibition rate (%) = 1− [(OD experimental-OD blank)/(OD control-OD blank)] × 100%.

Cell Apoptosis Assay
The effect of RPDPRH on apoptosis was performed using the Annexin V-FITC/PI Apoptosis kit (MultiSciences, China), following the manufacturer's protocol. The cells were digested, dispersed, and plated into six-well plates with 2×10^4 cells/well and treated with RPDPRH (0, 6.25, 12.5, and 25 μM) at various concentrations for 48 h. Upon completion of the treatment, cells were harvested, washed with cool phosphate buffered solution (PBS, Gibco, United States) (0.01 M, pH=7.4), and re-suspended in a 500 μl binding buffer. Annexin V-FITC (5 μl) and PI (10 μl) were added into the cell suspension, and then, the suspension was incubated at room temperature away from light for 5 min. Cells were analyzed by using a flow cytometer (Agilent NovoCyte, China) immediately, and the results of the apoptosis were analyzed by FlowJo software.

Western Blotting Assay
The experimental steps of the Western blotting assay referred to Lin's study (Lin et al., 2020). After treatment with different concentrations of RPDPRH (0, 6.25, 12.5, and 25 μM) for 48 h, hepatocarcinoma cells were lysed with an ice-cold RIPA protein lysis buffer (Beyotime, China). Total cell lysates were prepared with RIPA lysis buffer containing phosphatase inhibitors (Roche, China) and protease inhibitors (MedChemExpress, United States). Total cell lysates were centrifuged at 10,000 g for 10 min at 4°C to obtain the supernatant. The protein concentration was detected according to the BCA Protein Assay Kit (Beyotime, China). Then, 5× SDS

loading buffer (Beyotime, China) was added to the supernatant and boiled at 100°C for 10 min. The obtained protein samples were stored at −80°C.

The protein samples (20 μg) were resolved on 4% concentration glue and 12% separating glue and prepared according to the SDS-PAGE Gel Quick Preparation Kit procedure (Beyotime, China). After electrophoresis at 80 V for 1.5–2 h, the proteins were wet-transferred onto a polyvinylidene difluoride membrane (PVDF, Millipore) at 300 mA for 1–1.5 h. The membranes were blocked in 5% skim milk on an electric rocker for 1 h, washed three times with Tris-buffered saline (TBS, Beyotime, China) containing 0.1% Tween 20 (TBS-T, Beyotime, China), incubated overnight at 4°C with primary antibodies (GAPDH, 1:2000; Bax,1:1000; Bcl-2, 1:1000; ImmunoWay, United States) in TBS-T, then washed three times with TBS-T, incubated 1 h at room temperature with secondary antibodies (1:5000; ImmunoWay, United States) in TBS-T, and washed three times with TBS-T. Finally, the signal was visualized by using enhanced chemiluminescence (ECL, Millipore, United States) reagents and photographed. ImageJ software was used to analyze the signal bands. The glyceraldehyde-3-phosphate dehydrogenase (GAPDH) antibody served as a control.

Wound Healing Assay
The experimental procedures were performed according to conventional methods (Kovaříková et al., 2014). Hepatocarcinoma cells at the logarithmic growth stage were taken and inoculated into six-well plates with 2×10^4 cells/well. When the cell density is about 80%, the cell wound was scratched with pipette tips. Cells were then washed with PBS and added to the cell culture broth containing 1% serum with varying concentrations of RPDPRH (0 μM, 6.25, 12.5, and 25 μM) for 48 h. Pictures were taken at 0 and 48 h under a microscope (100×). Wound healing rate (%) = [(0 h scratch distance−48 h scratch distance)/0 h scratch distance] × 100%.

Statistical Methods
All the experiments were repeated three times, and the data were expressed by mean ± SD. FlowJo 10.6.2 software was used to analyze the flow cytometry data. ImageJ software was used to analyze the protein gray value and measure the scratch distance. GraphPad Prism 8.0.1 software was used to process and analyze the data. The significance of difference was evaluated with one-way analysis of variance (one-way ANOVA). $p < 0.05$ was statistically significant.

RESULTS AND DISCUSSION

Chemistry
One-Pot Synthesis of (2E, 4E)-4-Arylidene-2-Styryl-5-Oxopyrrolidine Derivatives RPDPRH, RPDPRI, RPDPRK, and RPDPRO
Four (2*E*, 4*E*)-4-arylidene-2-styryl-5-oxopyrrolidine derivatives RPDPRH, RPDPRI, RPDPRK, and RPDPRO were produced in good yields around 80–89%, and the yield of the compound RPDPRH was the highest (**Scheme 2**). Spectroscopic and
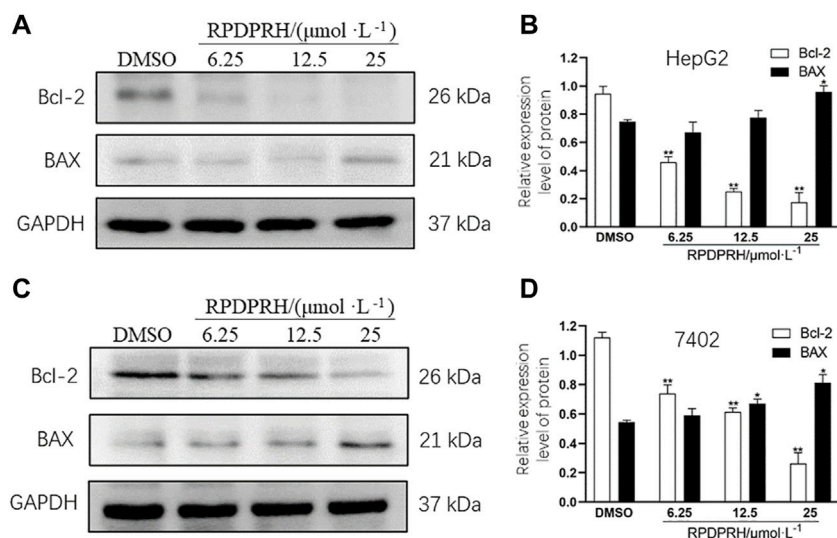
FIGURE 2 | Effect of RPDPRH on the expressions of Bax and Bcl-2. Note: **(A)** Protein expression bands of Bcl-2 and Bax in HepG2 cells. **(B)** Relative protein expressions of Bcl-2 and Bax in HepG2 cells. **(C)** Protein expression bands of Bcl-2 and Bax in 7402 cells. **(D)** Relative protein expressions of Bcl-2 and Bax in 7402 cells. Compared with the DMSO control group, $*p < 0.05$ and $**p < 0.01$, ($\bar{x} \pm s$, n=3).
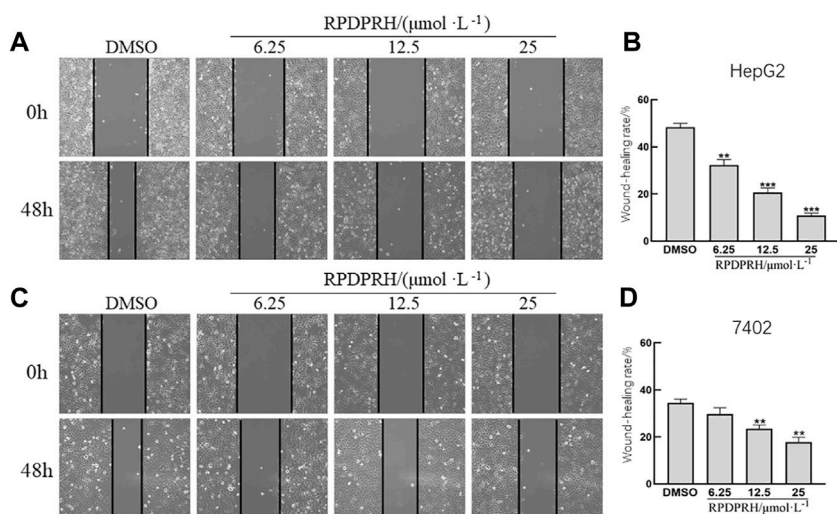

FIGURE 3 | Effect of RPDPRH on HepG2 and 7402 cell migration. Note: **(A)** Image of the wound healing assay in HepG2 cells. **(B)** Relative wound healing rate in HepG2 cells. **(C)** Image of the wound healing assay in 7402 cells. **(D)** Relative wound healing rate in 7402 cells. Compared with the DMSO control group, $**p < 0.01$ and $***p < 0.001$, ($\times 100$, $\bar{x} \pm s$, n=3).

analytical data elucidated the composition of the four synthesized compounds.

Biological Evaluation
Anticancer Activity *In Vitro*
MTT assay was used to determine the anticancer activity of four compounds in the selected six different types of cancer cells (C-33A cells, CaSki cells, SiHa cells, HeLa cells, HepG2 cells, and 7402 cells) and their cytotoxicity to a normal liver cell line (LO2 cells). Cells were treated with each compound of varying concentrations, and their IC_{50} values were calculated, using cisplatin as a positive control. All IC_{50} values are shown in **Table 1**. RPDPRH and RPDPRO have more selectivity and lower cytotoxicity than the other two compounds. Furthermore, the IC_{50} values of RPDPRH in C-33A cells, CaSki cells, SiHa cells, HeLa cells, HepG2 cells, 7402 cells, and LO2 cells were 4.66, 6.42, 17.66, 15.2, 12.36, 22.4, and 243.2 μM, respectively. The values of RPDPRO were 5.56,

9.15, 12.5, 21.4, 14.5, 31.24, and 86.77 µM. For cisplatin, the IC_{50} values were 48.16, 17.52, 37.06, 47.52, 19.27, 48.52, and 17.3 µM, respectively. The results showed that both RPDPRH and RPDPRO had obvious anticancer activities to tumor cells, but RPDPRH had lower cytotoxicity to the normal liver cell line LO2. Thus, we chose RPDPRH as the research object for subsequent studies.

RPDPRH Induce Cell Apoptosis in a Concentration-dependent Manner

According to the aforementioned research, the compound RPDPRH showed satisfactory anticancer activity among the four compounds, and more importantly, it had no significant toxicity to the normal hepatic LO2 cells. Thus, Annexin V/PI was used to detect the apoptosis of the compound RPDPRH in hepatocellular carcinoma HepG2 and 7402 cells. The results are shown in **Figure 1**; when HepG2 cells were treated with RPDPRH in 6.25, 12.5, and 25 µM for 48 h, the apoptosis of control (0 µM, DMSO) was 7.73 ± 2.18% (LR: 5.18%, UR: 2.55%, LR and UR represent early apoptotic and late apoptotic, respectively), and the apoptosis of the treated group was up to 10.6 ± 1.49% (LR: 5.53%, UR: 5.07%), 35.90 ± 2.51% (LR: 14.90%, UR: 21.00%), and 52.10 ± 4.49% (LR: 19.80%, UR: 32.30%), respectively. For 7,402 cells, compared with the control group (0 µM, DMSO), which had 8.96 ± 3.05% (LR: 2.87%, UR: 6.09%), the apoptosis rates of the treatment group increased to 13.71 ± 1.30% (LR: 4.37%, UR: 9.34%), 24.83 ± 1.91% (LR: 8.53%, UR: 15.30%), and 36.00 ± 2.67% (LR: 11.40%, UR: 24.60%), respectively. At the same time, we can *see* from **Figures 1B,C** that the apoptosis-inducing effect of RPDPRH on hepatocellular carcinoma HepG2 and 7402 cells was in a dose-dependent manner in early- and late-stage apoptosis. Moreover, RPDPRH induced HepG2 cell apoptosis better than 7402 cells. Therefore, our findings suggested that RPDPRH induced apoptosis in HepG2 and 7402 cells in a concentration-dependent manner.

RPDPRH Can Affect the Expression of Apoptosis-Associated Proteins Bcl-2 and Bax in Cancer Cells

To verify whether the death of HepG2 and 7402 cells caused by RPDPRH was induced by apoptosis, Western blot was used to analyze the expression levels of apoptosis proteins Bax and Bcl-2. The results (**Figure 2**) showed that the contents of apoptotic proteins Bax and Bcl-2 in hepatocellular carcinoma HepG2 and 7402 cells were significantly changed after 48 h treatment with RPDPRH. With the increase in the RPDPRH concentration, the expression of pro-apoptotic protein Bax was increased, while there was a decrease in anti-apoptotic protein Bcl-2 significantly. In addition, compared with the control group (0 µM, DMSO), the high treatment doses (25 µM) displayed a significant increase of Bax ($p < 0.05$) but a decrease of Bcl-2 ($p < 0.01$) in HepG2 and 7402 cells, causing the ratios of Bax/Bcl-2 to increase obviously. Therefore, the results indicated

that RPDPRH-induced HepG2 and 7402 cell death were associated with apoptosis.

RPDPRH Can Inhibit Migration of Hepatocellular Carcinoma Cells

The results of the cell wound healing assay (**Figure 3**) showed that the wound healing rate of HepG2 and 7402 cells in the concentration of RPDPRH (6.25, 12.5 and 25 µM) was significantly reduced after 48 h treatment. Compared with the control group (0 µM, DMSO), the high treatment doses (25 µM) showed a significantly decreased wound healing rate for HepG2 cells ($p < 0.001$), and the healing rate also reduced significantly for 7,402 cells ($p < 0.01$). The results indicated that RPDPRH could inhibit the migration of hepatocellular carcinoma HepG2 and 7402 cells.

CONCLUSION

Marine alkaloids are widely found in marine organisms and have diverse physiological activities, such as the antifungal activity, antimicrobial activity, anti-inflammatory activity, and cytotoxicity (Martin and Jiang, 2010; Dyshlovoy et al., 2016; Tanaka et al., 2016; and Kong et al., 2021). Studies have shown that the marine alkaloids rhopaladins A–D can inhibit the activity of cyclin-dependent kinase 4 and C-erbβ-2 kinase and promote the apoptosis of tumor cells (Janosik et al., 2002). Thus, rhopaladins' analog 4-arylidene-5-oxopyrrolidines (RPDPRH, RPDPRI, RPDPRK, and RPDPRO) were synthesized. Furthermore, the anticancer activities in C-33A cells, CaSki cells, SiHa cells, HeLa cells, HepG2 cells, and 7402 cells and their cytotoxicity to LO2 cells were evaluated. As the results of our experiment, both RPDPRH and RPDPRO could significantly inhibit the proliferation of tumor cells, while RPDPRH had a lower cytotoxicity to the normal liver cell line LO2. Thus, flow cytometry was used to evaluate the effect of RPDPRH on the apoptosis of HCC cells. We found that RPDPRH could induce HepG2 and 7402 cell apoptosis in a dose-dependent manner, and interestingly, its effect on the apoptosis of HepG2 cells is better than 7402 cells. Bax and Bcl-2 are important factors of apoptosis, and the increase in the Bax/Bcl-2 ratio may promote apoptosis. Therefore, we further detected the expression of apoptotic proteins Bax and Bcl-2. The results indicated that RPDPRH upregulated the expression of the Bax protein and downregulated the expression of the Bcl-2 protein, causing an increase in the Bax/Bcl-2 ratio, which then induced apoptosis of HepG2 and 7402 cells, thereby inhibiting cell proliferation.

In this study, four compounds RPDPRH, RPDPRI, RPDPRK, and RPDPRO were synthesized, and the anti-narcotic activities were assessed *in vitro*. Our results revealed that all target compounds demonstrated varying degrees of antitumor activities against the tested tumor cells. More importantly, we also confirmed the effects of RPDPRH on cell proliferation, migration, apoptosis, and apoptosis-related protein expressions of hepatocellular carcinoma

cells. However, this article is of preliminary nature. The exact mechanism remains to be further studied, and more basic experiments are needed to confirm this possibility. Taken together, our study provides preliminary evidence that RPDPRH has the potential to develop efficient and cost-effective antitumor agents, and it will play a significant role in our subsequent research studies.

DATA AVAILABILITY STATEMENT

The original contributions presented in the study are included in the article/**Supplementary Material**, further inquiries can be directed to the corresponding authors.

AUTHOR CONTRIBUTIONS

JZ, BL, and X-HZ contributed to the conception and design of the study. H-MW and X-HZ synthesized the compounds. JZ, L-QK, and LW wrote the manuscript, edited the manuscript, and performed experiments. JZ and Q-HC designed and performed experiments. F-YR performed the statistical analysis. L-QK and LW wrote the first draft of the manuscript. L-NK and BL wrote sections of the manuscript. All authors contributed to manuscript revision, read, and approved the submitted version.

FUNDING

SUPPLEMENTARY MATERIAL

The Supplementary Material for this article can be found online at: https://www.frontiersin.org/articles/10.3389/fchem.2022.898436/full#supplementary-material

REFERENCES

An, L., Wang, C., Zheng, Y.-G., Liu, J.-d., and Huang, T.-h. (2021). Design, Synthesis and Evaluation of Calix[4]arene-Based Carbonyl Amide Derivatives with Antitumor Activities. *Eur. J. Med. Chem.* 210, 112984. doi:10.1016/j.ejmech.2020.112984

Bhayani, N., Jiang, Y., Hamed, O., Kimchi, E., Staveley-O'Carroll, K., and Gusani, N. (2015). Advances in the Pharmacologic Treatment of Hepatocellular Carcinoma. *Ccp* 10 (4), 299–304. doi:10.2174/1574884710666151020100059

Carbone, A., Cascioferro, S., Parrino, B., Carbone, D., Pecoraro, C., Schillaci, D., et al. (2020). Thiazole Analogues of the Marine Alkaloid Nortopsentin as Inhibitors of Bacterial Biofilm Formation. *Molecules* 26 (1), 81. doi:10.3390/molecules26010081

Dyshlovoy, S. A., Kudryashova, E. K., Kaune, M., Makarieva, T. N., Shubina, L. K., Busenbender, T., et al. (2020). Urupocidin C: A New marine Guanidine Alkaloid Which Selectively Kills Prostate Cancer Cells via Mitochondria Targeting. *Sci. Rep.* 10 (1), 9764. doi:10.1038/s41598-020-66428-5

Dyshlovoy, S., Tabakmakher, K., Hauschild, J., Shchekaleva, R., Otte, K., Guzii, A., et al. (2016). Guanidine Alkaloids from the Marine Sponge Monanchora Pulchra Show Cytotoxic Properties and Prevent EGF-Induced Neoplastic Transformation In Vitro. *Mar. Drugs* 14 (7), 133. doi:10.3390/md14070133

Hiroyasu, S., Masashi, T., Kenji, W., and Rhopaladins, A. D. (1998). New Indole Alkaloids from Marine Tunicate Rhopalaea Sp. *Tetrahedron* 54 (30), 8687–8690.

Janosik, T., Johnson, A.-L., and Bergman, J. (2002). Synthesis of the Marine Alkaloids Rhopaladins A, B, C and D. *Tetrahedron* 58 (14), 2813–2819. doi:10.1016/s0040-4020(02)00171-0

Kong, L. Q., Zhu, X. L., Chen, Q. H., et al. (2021). One-Pot Synthesis and Biological Evaluation of (2E,4E)-4-Arylidene-2-Styryl-5-Oxopyrrolidine Derivatives. *J. Chem. Res.* 45 (11-12), 1042–1046. doi:10.1177/17475198211051910

Kovaříková, P., Michalova, E., Knopfova, L., et al. (2014). Methods for Studying Tumor Cell Migration and Invasiveness[J]. *Klin Onkol* 27 (Suppl. 1), S22–S27.

Lai, S. W. (2019). Risk Factors for Hepatocellular Carcinoma. *Cancer* 125 (3), 482. doi:10.1002/cncr.31802

Lin, P., Zhou, B., Yao, H., and Guo, Y.-p. (2020). Effect of Carboplatin Injection on Bcl-2 Protein Expression and Apoptosis Induction in Raji Cells. *Eur. J. Histochem.* 64 (3), 3134. doi:10.4081/ejh.2020.3134

Martin, T. A., and Jiang, W. G. (2010). Anti-Cancer Agents in Medicinal Chemistry (Formerly Current Medicinal Chemistry - Anti-Cancer Agents). *Anticancer Agents Med. Chem.* 10 (1), 1. doi:10.2174/1871520611009010001

Nijampatnam, B., Dutta, S., and Velu, S. E. (2015). Recent Advances in Isolation, Synthesis, and Evaluation of Bioactivities of Bispyrroloquinone Alkaloids of Marine Origin. *Chin. J. Nat. Medicines* 13 (8), 561–577. doi:10.1016/s1875-5364(15)30052-2

Roy, P. S., and Saikia, B. J. (2016). Cancer and Cure: A Critical Analysis. *Indian J. Cancer* 53 (3), 441–442. doi:10.4103/0019-509X.200658

Sung, H., Ferlay, J., Siegel, R. L., Laversanne, M., Soerjomataram, I., Jemal, A., et al. (2021). Global Cancer Statistics 2020: GLOBOCAN Estimates of Incidence and Mortality Worldwide for 36 Cancers in 185 Countries. *CA A. Cancer J. Clin.* 71 (3), 209–249. doi:10.3322/caac.21660

Tanaka, N., Kusama, T., Kashiwada, Y., and Kobayashi, J. i. (2016). Bromopyrrole Alkaloids from Okinawan Marine Sponges Agelas Spp. *Chemical Pharmaceutical Bulletin* 64 (7), 691–694. doi:10.1248/cpb.c16-00245

Wang, H. M., Zhu, X. L., Chen, Q. H., et al. (2021). An Efficient One-Pot Synthesis and Biological Evaluation of Novel (E)-2-Aroyl-4-Arylidene-5-Oxotetrahydrofuran Derivatives. *J. Chem. Res.* 45 (5-6), 395–399.

Zeng, X.-H., Wang, H.-M., Wu, L., and Ding, M.-W. (2013). One-Pot Synthesis of 5-Oxopyrrolidine-2-Carboxamides via a Tandem Ugi 4CC/SN Cyclization Starting from Baylis-Hillman Bromides. *Tetrahedron* 69 (19), 3823–3828. doi:10.1016/j.tet.2013.03.058

Zeng, X. H., Zhu, X. L., Wang, H. M., and Hubei University of Medicine (2020). *Cyclopolypeptide 2-Styrene-5-Pyrrolidone 2-Amide Derivatives, Preparation Method and Application*. China Patent CN 110885307A.

Zhu, X.-L., Tian, X.-Q., Xu, H.-H., Wang, H.-M., Chen, Q.-H., and Zeng, X.-H. (2020). Rhopaladins' Analogue (E)-2-Aroyl-4-(4-Fluorobenzylidene)-5-Oxopyrrolidines Inhibit Proliferation, Promote Apoptosis and Down-Regulation of E6/E7 mRNA in Cervical Cancer. *Bioorg. Med. Chem. Lett.* 30 (23), 127554. doi:10.1016/j.bmcl.2020.127554

Synthesis of Melatonin Derivatives and the Neuroprotective Effects on Parkinson's Disease Models of *Caenorhabditis elegans*

Li He[1], Jing-Jing Du[2], Jun-Jie Zhou[1], Meng-Ting Chen[1], Lu Luo[1], Bao-Qiong Li[1], Xiang-Zhi Zhang[1], Wen-Zhe Ma[2], Ai-Jun Ma[1]* and Na Feng[1]*

[1]School of Biotechnology and Health Sciences, Wuyi University, Jiangmen, China, [2]State Key Laboratory of Quality Research in Chinese Medicine, Macau University of Science and Technology, Macau, China

Melatonin (MT) is a hormone with antioxidant activity secreted by the pineal gland in the human brain, which is highly efficient in scavenging free radicals and plays an important role in the neuro-immuno-endocrine system. Emerging evidence showed that MT supplementation was a potential therapeutic strategy for Parkinson's disease (PD), which inhibits pathways associated with oxidative stress in PD. In this study, we reported a C7-selective olefination of melatonin under rhodium catalysis with the aid of P^{III}-directing groups and synthesized 10 new melatonin-C7-cinnamic acid derivatives (6a–6j). The antioxidant potential of the compounds was evaluated both by ABTS and ORAC methods. Among these newly synthesized melatonin derivatives, 6a showed significantly higher activity than MT at 10^{-5} M. In the transgenic *Caenorhabditis elegans* model of PD, 6a significantly reduces alpha-synuclein aggregation and dopaminergic neuronal damage in nematodes while reducing intracellular ROS levels and recovers behavioral dysfunction induced by dopaminergic neurodegeneration. Further study of the mechanism of action of this compound can provide new therapeutic ideas and treatment strategies for PD.

Keywords: derivative of melatonin, synthesis, antioxidant activity, *C. elegans*, Parkinson's disease

INTRODUCTION

Melatonin (MT), secreted by the midbrain pineal gland and some peripheral tissues, is a tryptophan metabolite that activates multiple intracellular signaling pathways (Pohanka et al., 2011) and has a variety of physiological effects, such as regulating circadian rhythms, scavenging free radicals, enhancing immunity, and inhibiting oxidation of biomolecules (Yu et al., 2000; Skene and Swaab., 2003; Wu et al., 2004). In addition, melatonin has protective effects against neurodegenerative diseases (Rudnitskaya et al., 2015).

Parkinson's disease (PD) is a neurodegenerative disease with motor and non-motor symptoms characterized by the loss of dopaminergic neurons in the nigrostriatal and the formation of Lewy body proteins (Calabrese et al., 2018; Bouca-Machado et al., 2019). The main features of PD are resting tremor, rigidity, and motor retardation (Mann and Yates, 1982; Smeyne and Jackson-Lewis, 2005; Jankovic and Stacy., 2007; Hirsch et al., 2012). This may be due to the selective loss of dopaminergic (DA) neurons in the substantia nigra densa (SN), resulting in neurological dysfunction (Delenclos et al., 2016). Pathologically, PD is also characterized by the formation of alpha-synuclein

(α-syn) aggregates. The pathological process of PD involves multiple pathways, including apoptosis, autophagy, oxidative stress, α-syn aggregation, and alterations in neurotransmitters (Olzmann et al., 2010; Martinez et al., 2017; Aditi and Verma, 2019; Brunetti et al., 2020).

There is emerging evidence supporting the impact of oxidative stress on PD, and therefore, drugs with antioxidant activity are expected to be a potential treatment for PD (Moosmann and Behl, 2002; Abou-Sleiman et al., 2006; Weber and Ernst, 2006; Sayre et al., 2008). Studies suggest that MT supplementation is a therapeutic approach for PD disorder. The use of MT inhibits a number of pathways associated with oxidative stress response, α-syn aggregation, and dopamine loss in PD (Chen et al., 2002; Zarranz et al., 2004; Berendse et al., 2010). MT may also improve some non-motor symptoms in PD patients.

The nematode *Caenorhabditis elegans* (*C. elegans*) is a powerful genetic model system for exploring PD and related molecular mechanisms (Nass and Chen, 2008; Anand et al., 2020). In this study, we used two well-established *C. elegans* models to assess the anti-Parkinsonian effects of melatonin derivatives and to explore their associated potential neuroprotective mechanisms.

MATERIALS AND METHODS

Materials and Strains

^{1}H NMR and ^{13}C NMR spectra were both performed on a 500 MHz Bruker NMR spectrometer using TMS as an internal standard (chloroform-*d* as the solvent). Mass spectra were carried out using a Thermo Fisher LCQ Fleet LC-MS mass spectrometer. All reagents used were of analytical grade.

Strains: Bristol N2: wild-type N2 nematode; NL5901: pkIs2386 [unc-54p:α-synuclein:YFP + unc-119 (+)], a transgenic nematode model of PD disorder expressing yellow fluorescent protein-tagged human α-synuclein in muscle; BZ555: egIs1 [dat-1p: GFP], pharmacological model of PD disorder nematode, dat-1 encodes a plasma membrane dopamine transporter protein labelled with a green fluorescent mono-white that can be observed as bright green fluorescence at the junctions between dopamine neuronal soma cells, purchased from the CGC (*Caenorhabditis* Genetics Center); *E. coli* OP50: *Escherichia coli* OP50, uracil leakage mutant strain, used as normal food for feeding *C. elegans*.

Synthesis of 6a–6j

Our group designed a P^{III}-directing group (*N*-P*t*Bu$_2$), which directed C7-H functionalization of melatonin with olefins through rhodium catalysis. (Borah and Shi, 2018). We describe the development of the decarbonylative cross-couplings (Zhao and Yu, 2008; Lei et al., 2015) of carboxylic acids with melatonin at the C7 position by P^{III}-chelation-assisted Rh^I-catalyzed C-C bond activation (Qiu et al., 2019).

The decarbonylative reaction was further optimized with substituted cinnamic acid 4 as a partner to produce the melatonin C7-olefination products. We found that the reaction achieved optimal efficiency and selectivity with 2.5 equiv. of

Boc$_2$O in the presence of 5.0 mol% Rh(cod)$_2$OTf as a catalyst. Product 5 was obtained after reaction at 120°C for 18 h under a nitrogen atmosphere. Furthermore, the directing group (P*t*Bu$_2$) could be easily removed by TBAF in THF, and N-free melatonin derivatives 6 were isolated at the yields of 47–67% (Han et al., 2019; Qiu et al., 2019) **Scheme 1**.

N-(2-(5-Methoxy-7-Styryl-1h-Indol-3-yl) ethyl)acetamide (6a)

Light yellow oil. 67% yield. ^{1}H NMR (500 MHz, Chloroform-*d*) δ: 8.47 (s, 1H), 7.60~7.49 (m, 2H), 7.44~7.35 (m, 2H), 7.35~7.27 (m, 2H), 7.18 (s, 1H), 7.09 (t, *J* = 2.0 Hz, 2H), 7.03 (d, *J* = 2.3 Hz, 1H), 5.62 (s, 1H), 3.92 (s, 3H), 3.62 (q, *J* = 6.5 Hz, 2H), 2.97 (t, *J* = 6.8 Hz, 2H), and 1.94 (s, 3H); ^{13}C NMR (125 MHz, chloroform-*d*) δ: 170.2, 154.4, 137.2, 130.5, 129.8, 128.8, 128.5, 127.9, 126.5, 124.3, 122.9, 122.3, 113.2, 109.9, 100.7, 56.1, 39.8, 25.3, and 23.4; LC-MS (ESI) *m/z*: calcd. for C$_{21}$H$_{22}$N$_2$O$_2$ {[M + Na]$^+$} 357.1573, found 357.1572.

The details of compounds 6b–6j can be found in the **Supplementary Material S1**.

ABTS Method

The ABTS assay was performed in accordance with a previously reported procedure (Schaich et al., 2015; Sommer et al., 2022). A volume of 5 ml of 7 mmol/L ABTS and 88 μL of 140 mmol/L potassium persulfate were mixed and left for 12 h at room temperature in the dark to form an ABTS$^+$ free radical reserve solution. The reserve liquid was relatively stable at room temperature away from the light. Before use, it was diluted into the working liquid with ultra-pure water, and its absorbance was required to be 0.7 ± 0.02 at 30°C and a wavelength of 734 nm. The samples were prepared with DMSO into 5, 10, 20, and 40 μg/ml sample solutions for later use. During the determination, 100 μL of ABTS working solution was added to each well of the 96-well microtitration plate, and then 100 μL of sample solution at different concentrations was added to shake and mix. After 10 min, the absorbance at 734 nm was determined, and 100 μL of ABTS working solution mixed with 100 μL of DMSO was used to determine the blank absorbance A$_0$. The absorbance of a 100 μL sample mixed with 100 μL of DMSO was defined as Ar. For each determination, experiments were performed in triplicate.

The radical scavenging rate of ABTS is calculated using the following formula: ABTS free radical scavenging rate (%) = [1 − (At − Ar)/A$_0$] × 100%.

ORAC Method

The ORAC method was performed as described previously (Huang et al., 2002; Ou et al., 2002) with slight modification. The reaction was carried out in 75 mM phosphate buffer (pH 7.4), while the addition of antioxidant substances produced more stable fluorescent signal that could reflect the antioxidant capacity.

A volume of 50 μL of samples to be tested or different concentrations of Trolox working solution (0.10, 0.08, 0.06, 0.04, and 0.02 mmol/L) were added to a 96-well plate, followed by the addition of 100 μL of FL working solution (8.4 × 10^{-8} mol/L) and shaking for 30 s. The fluorescence value F0 was
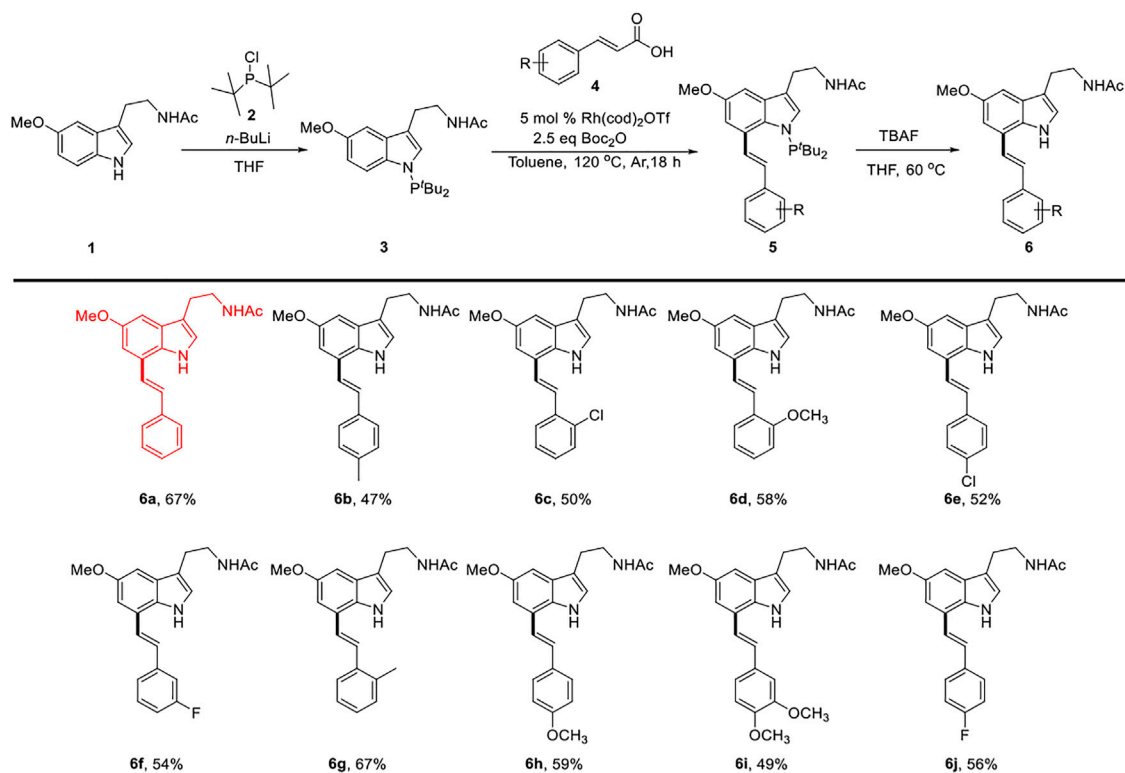
SCHEME 1 | Synthesis route for compounds 6a~ 6j.

recorded immediately, and then the reaction was shaken for 3 min and incubated at 37°C for 10 min. A volume of 50 μL of AAPH working fluid was added to induce the reaction. The excitation wavelength and emission wavelength were 485 and 535 nm, respectively, and the fluorescence value Fn was recorded every 2.5 min. The reaction was considered to be over when the fluorescence decrease slowed. The initial fluorescence value (F0) is the pore fluorescence intensity reading without AAPH. fn = fluorescence value (Fn)/initial fluorescence value (F0); AUC = 2 × (f0 + f1 +...+ fn) − f0 − fn; NetAUC (ORAC value) = AUC$_{sample}$ − AUC$_{AAPH}$⁺. NetAUC was used to determine the capacity for absorbing free radicals. Here, AUC is the area under the fluorescence decay curve, and NetAUC is the protected area. In addition to the tested sample group, a blank group and an AAPH + group (for which 50 μL of 75 mM phosphate-buffered saline (PBS) solution was used as the sample substitution) were also tested. To create a standard curve, different concentrations of Trolox solution were used for the abscissa and NetAUC was used for the ordinate, and the absorption capacity of the sample was expressed as μmol TE/g DW. For each determination, experiments were performed in triplicate.

Measurement of Reactive Oxygen Species (ROS)

2′,7′-Dichlorofluorescein diacetate (H$_2$DCFDA), a universal oxidative stress indicator, was used as a probe for the

detection of intracellular ROS. H$_2$DCFDA was oxidized by ROS to form the fluorescent dye dichlorofluorescein (DCF) (Jia et al., 2021). The fluorescence intensity was proportional to the ROS level in *C. elegans*.

Briefly, age-matched L3 larvae were treated with 10 μM MT or **6a** for 24 h. Subsequently, 2000 nematodes per group were collected and washed three times with M9 buffer. The nematodes were suspended in 400 μL of PBS with 1% Tween-20 and homogenized to obtain worm lysate. The protein concentration of the lysate was determined using the BCA protein assay kit. A volume of 50 μL of nematode lysate was transferred into a 96-well black microplate and incubated with 50 μL of 50 μM H$_2$DCFDA. Fluorescence intensity (485 nm excitation and 590 nm emission) was monitored using an enzyme plate reader (Wu et at., 2006; Liu et al., 2015; Zhao et al., 2018).

α-Synuclein Accumulation Assay

PD pathology usually showed an accumulation of the α-syn. We used strain NL5901 to test the effect of MT and 6a on α-syn aggregation. The synchronized nematodes were immersed in M9 buffer containing 10 μM melatonin and 6a for 48 h at 20°C. L1 worms were transferred to OP50/NGM plates at 20°C for 65 h (L3 stage), and then the nematodes were transferred to plates containing OP50/NGM/5-fluorodeoxyuridine (FUDR, 0.04 mg/ml) and incubated at 20°C for 3 days. The young adults were washed three times with M9 buffer, then anesthetized with 10% sodium azide, and fixed on slides. The worms were observed
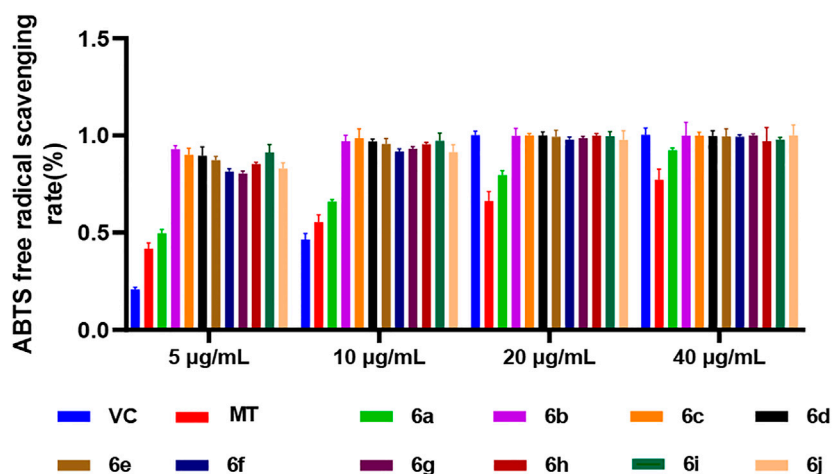
FIGURE 1 | ABTS method for measuring the antioxidant activity of 6a~ 6j.
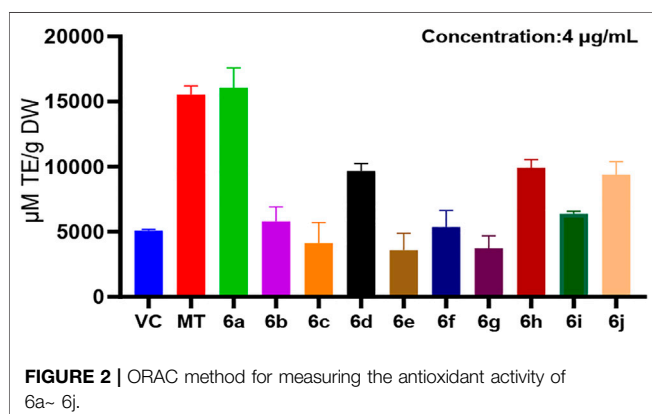

FIGURE 2 | ORAC method for measuring the antioxidant activity of 6a~ 6j.

using an Olympus BX63 fluorescent microscope to monitor the YFP expression (α-syn aggregation). The fluorescence intensity of each nematode was quantified using ImageJ software (Jadiya et al., 2011; Govindan et al., 2018; Anjaneyulu et al., 2020).

6-OHDA-Induced Damage to Dopaminergic Neurons

Dopaminergic neuron degeneration was induced by 50 mM 6-OHDA in *C. elegans* as described previously (Tucci et al., 2011). Briefly, the synchronized nematodes were immersed in M9 buffer containing MT or 6a for 48 h at 20°C, and then L1 worms were transferred to OP50/NGM plates at 20°C for 65 h (L3 stage), after which they were exposed to 50 mM 6-OHDA for 1 h. After exposure, the worms were washed with M9 buffer and transferred to OP50/NGM plates containing 0.04 mg/ml FUDR for 3 days at 20 °C for various assays (Chalorak et al., 2021; Ma et al., 2021).

Behavior Assay

In general, N₂ nematodes were treated with 50 mM 6-OHDA to induce degenerative lesions in dopamine neurons.

For thrashing assay, synchronized L4 stage nematodes were transferred to a 3-cm diameter Petri dish, 1 ml of M9 buffer was added, and after the nematodes were stabilized for 30 s, a Leica M205 FA microscope was used to continuously capture the worms for 10 s. The number of thrashing of the nematodes was counted (Lee et al., 2021).

For travel distance assay, nematodes of the synchronized L4 stage were transferred from food-containing dishes to non-food dishes and washed three times repeatedly in M9 buffer to remove the remaining food. The distance (mm) and speed (μm/sec) of the nematode's movement in 20 s were calculated using the Leica M205 FA microscope and finally analyzed using GraphPad Prism software (Sawin et al., 2000).

Statistical Analysis

All the experiments were performed in triplicate. The significance of differences between control and treated groups was analyzed by one-way analysis of variance (ANOVA), followed by Bonferroni's method. p-values < 0.05 were accepted as statistically significant. Graphs were constructed using GraphPad Prism version 8.00.

RESULTS AND DISCUSSION

Antioxidant Activity of Melatonin Derivatives *In Vitro*

In the ABTS method, the antioxidant activity of the 10 derivatives of melatonin at the C7 position, 6a–6j, increased in a concentration-dependent manner, and the antioxidant activity of 6a–6j was higher than that of melatonin at the same concentration, while the ABTS radical scavenging rate of the 10 derivatives, 6a–6j, was higher than that of vitamin C (VC) and MT at low concentrations of 5 and 10 μg/ml (**Figure 1**). These results indicated that the derivatization of melatonin at the C7 position could improve its antioxidant activity.

In the ORAC method, at the same concentration (4 μg/ml), the antioxidant activity of derivatives 6b–6j at the C7 position of
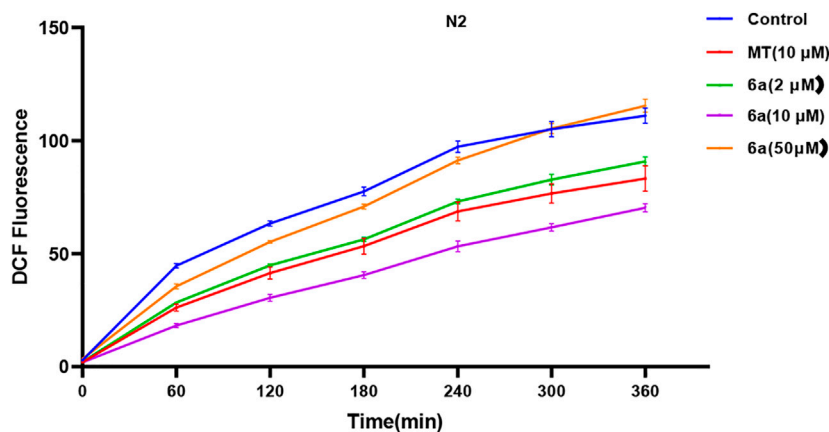
FIGURE 3 | Effect of 6a on the ROS level in wild-type.
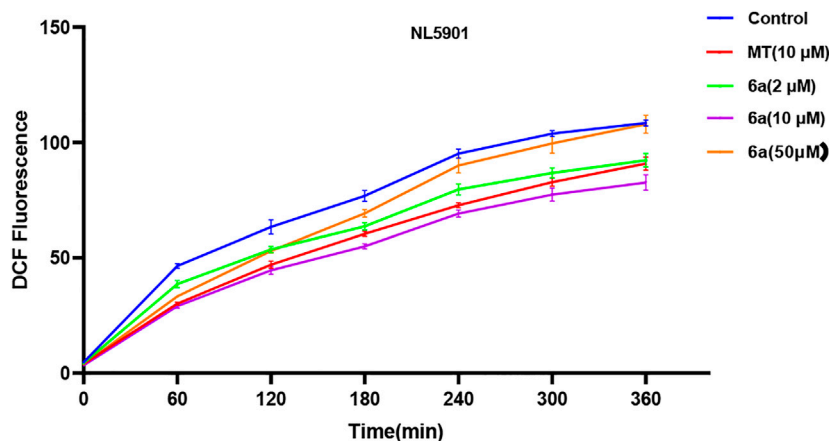
FIGURE 4 | Effect of 6a on the ROS level of the transgenic nematode NL5901.

melatonin was lower than that of melatonin, whereas the antioxidant activity of 6a was higher than that of MT (**Figure 2**). This suggested that the derivatization of melatonin at the C7 position may increase its antioxidant activity.

In this study, the antioxidant activity of melatonin derivatives was assessed by two *in vitro* assays, the ABTS method and the ORAC method. Comparing the results of these two methods, we found that the antioxidant activity of 6a, a derivative of melatonin at position C7, was higher than that of MT and the positive control VC as well.

6a Decreased the ROS Level in *C. elegans*

To further confirm the antioxidant effect of 6a, we tested the intracellular ROS level in *C. elegans*. We first examined the effect of 6a on the ROS levels in wild-type N2 nematodes. As shown in **Figure 3**, compared with the untreated group, after treatment with 6a at different concentrations (2, 10, and 50 μM), the levels of ROS in the nematodes decreased, and 10 μM of 6a achieved a significant decrease compared with the

level in the untreated group ($p < 0.001$). Additionally, the ROS levels clearly declined in the 6a group compared with those in the MT group ($p < 0.05$). These results are consistent with the *in vitro* antioxidant assay, further demonstrating the antioxidant capacity of 6a. The excellent antioxidant activity of 6a suggests its potential as a therapeutic agent for PD disorders.

To test this hypothesis, we first examined the effect of 6a on the ROS level in the transgenic nematode model of PD. As shown in **Figure 4**, compared with the untreated group, after treatment with different concentrations (2, 10, and 50 μM) of 6a, the levels of ROS in NL5901 worms reduced, and 10 μM of 6a achieved a significant decrease compared with the level in the untreated group ($p < 0.001$), along with a clear decline compared with that in the MT group ($p < 0.05$). These results are consistent with the findings in the ROS levels in N2 worms. The regulation of ROS levels in wild-type and NL590 animals by **6a** confirmed its ability to regulate ROS *in vivo*, suggesting that it could reduce ROS-induced acute oxidative damage.
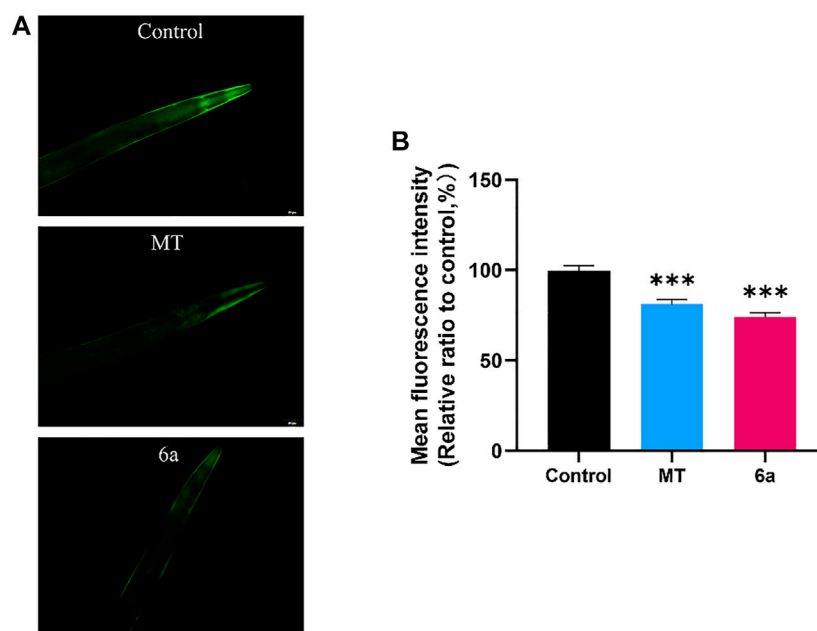
FIGURE 5 | α-syn aggregation in NL5901 was decreased by treatment of MT and 6a. **(A)** Representative images of α-syn accumulation in different groups of head muscles. **(B)** Quantification of fluorescence intensity in NL5901 using ImageJ software (***$p < 0.001$).
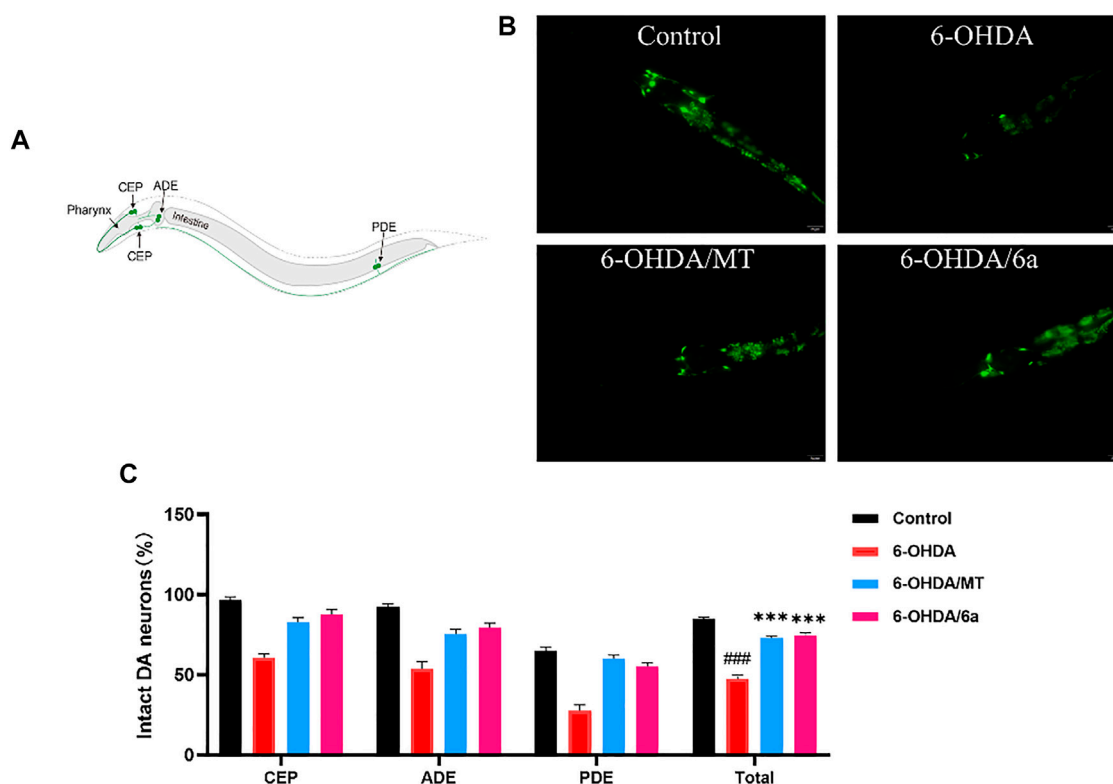
FIGURE 6 | Effect of MT and 6a on restoration of 6-OHDA-induced DA neurodegeneration in the BZ555 strain. **(A)** Neuronal circuits in *C. elegans.* **(B)** GFP expression patterns of CEP and ADE in BZ555. **(C)** Quantification of the fluorescence intensity of all eight DA neurons of BZ555. (###$p < 0.001$, compared with the control; ***$p < 0.001$, compared with the 6-OHDA-treated group).
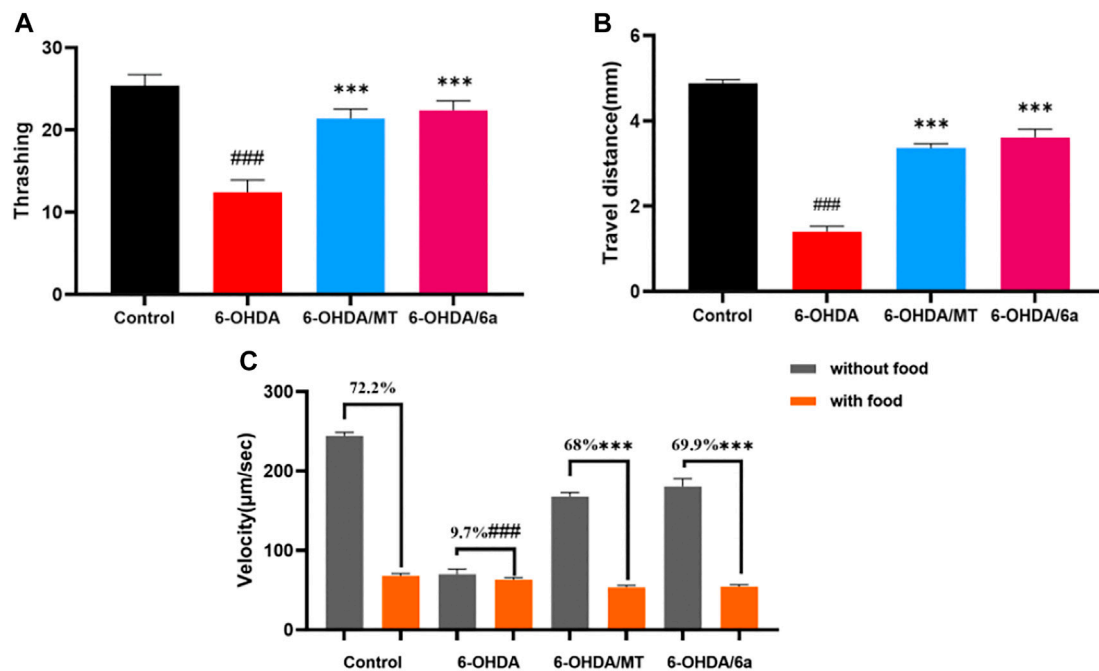
FIGURE 7 | Effect of MT and 6a on DA neuronal function. **(A)** Thrashing behavior of N2. **(B)** Travel distances of N2. **(C)** Velocity of N2 in NGM plates with and without food and basal slowing response. (###$p < 0.001$, compared with the control; ***$p < 0.001$, compared with the 6-OHDA-treated group).

6a Reduced α-Synuclein Aggregation in the Transgenic Nematode NL5901

One of the typical features of PD patients is the formation of Lewy bodies in the brain. The accumulation of Lewy bodies exacerbates the neurodegenerative progression in PD. Aggregated α-syn, which is known as a major component of Lewy bodies, can be measured in the transgenic NL5901 strain of *C. elegans*. In this strain, human α-syn is expressed in muscle cells with a YFP reporter. The fluorescence intensity at the anterior end of the worms indicates the accumulation of α-syn. To further confirm the therapeutic effect of 6a on PD, we examined its effect on α-syn aggregation. The results showed that, in the group treated with 10 μM 6a, the YFP fluorescence intensity in NL5901 was reduced compared with that in the untreated control group (**Figure 5A**). Quantitative analysis of the fluorescence intensity using ImageJ software showed that, in worms treated with 10 μM 6a (73.92 ± 1.80), the fluorescence intensity was lowered by 25.65% ($p < 0.001$) compared with that in untreated worms (99.45 ± 2.03). In addition, the 6a-treated group had lower fluorescence intensity than the MT-treated group (81.04 ± 2.74, $p < 0.05$; **Figure 5B**). These results indicate that the protective effect of 6a occurs by reducing the aggregation of α-syn in the PD model.

6a Is Protective Against 6-OHDA-Induced Dopaminergic Neuronal Damage

C. elegans contains exactly eight dopaminergic neurons, including two ADEs, four CEPs, and two PDEs (**Figure 6A**). In the BZ555 strain, all the eight DA neurons were tagged with

GFP. Upon exposure to 50 mM 6-OHDA, the BZ555 strain showed selective damage in DA neurons. To examine the efficacy of 6a, the viability of the DA neurons was assessed by measuring the loss of expression of the GFP reporter. We found that CEP, ADE, and PDE neurons showed partial GFP loss after 6-OHDA treatment (**Figure 6B**). When nematodes were pretreated with MT or 6a for 48 h at L1, the GFP expression loss was remarkably restored in CEP and ADE neurons (**Figure 6B**). We further measured the fluorescence intensity in DA neurons using ImageJ software. In nematodes treated with 50 mM 6-OHDA (47.41 ± 2.53), the mean fluorescence (GFP) intensity decreased by about 56% ($p < 0.001$) compared with that of untreated nematodes (84.71 ± 1.25), whereas dopaminergic neurons of nematodes exposed to 6-OHDA after treatment with 10 μM 6a recovered to 74.28 ± 1.87 ($p < 0.001$), and the mean fluorescence intensity was higher in the 6a-treated group than in the MT-treated group (72.94 ± 1.09, $p < 0.05$; **Figure 6C**), suggesting that 6a is protective against 6-OHDA-induced dopaminergic neuronal damage and that this protective effect is stronger than that of MT.

6a Recovers Behavioral Dysfunction Induced by DA Neurodegeneration

We next investigated whether 6a improves the functions of DA neurons. The locomotion of worms slows down when they encounter food, referred to as the basal slowing response, which is mediated by mechanosensory DA neurons. In this study, we found that N2 nematodes showed a 72.2% decrease in

speed when on NGM plates with food and a 9.7% decrease in basal deceleration induced by 50 mM 6-OHDA ($p < 0.001$), in terms of food perception behavior. Meanwhile, there was significant recovery from this decline to 69.9% after treatment with 10 μM 6a ($p < 0.001$), and the 6a-treated group showed a better basal deceleration response than the melatonin-treated group ($p < 0.05$) (**Figure 7C**). Similarly, in wild-type N2 nematodes, supplementation with 6a also restored 6-OHDA-induced deficits in DA neuron-associated motor activity, such as increasing the distance traveled and thrashing behavior (**Figures 7A, B**). These results suggest that 6a recovers the behavioral dysfunction induced by DA neurodegeneration.

CONCLUSION

We successfully synthesized 10 melatonin derivatives 6a–6j, and their activities were tested using *in vitro* antioxidant assays, ABTS and ORAC. The results showed that the antioxidant activity of melatonin derivative 6a was higher than that of MT. Subsequently, we evaluated the effect of 6a on ROS levels in *C. elegans*. The results showed that 10 μM 6a significantly reduced the ROS levels in wild-type N2. We also used two PD models of *C. elegans* to investigate the therapeutic effect of 6a on PD. We found that 10 μM 6a significantly reduced the ROS levels and α-syn aggregation in NL5901. Treatment of BZ555 with 50 mM 6-OHDA reduced the fluorescence intensity of their dopaminergic neuronal cells, which was increased by supplementation with 10 μM 6a. Finally, we evaluated the capacity of 6a to improve behavioral deficits caused by DA neurodegeneration. The results showed that 10 μM 6a improved the nematode's behavior in perceiving food and increased its basal rate compared with the findings in the control.

Our conclusions prove that melatonin derivative 6a significantly reduces α-syn aggregation and dopaminergic neuronal damage in PD by reducing oxidative stress-induced ROS levels and improves the behavioral impairment caused by DA neurodegeneration. Further study of the mechanism of action of this compound could provide new therapeutic ideas and treatment strategies for PD.

DATA AVAILABILITY STATEMENT

The original contributions presented in the study are included in the article/**Supplementary Material**; further inquiries can be directed to the corresponding authors.

AUTHOR CONTRIBUTIONS

NF, A-JM, and W-ZM designed the work and wrote the manuscript. LH, J-JD, J-JZ, M-TC, and LL carried out the experiments. All authors reviewed the manuscript and agreed to its publication.

SUPPLEMENTARY MATERIAL

The Supplementary Material for this article can be found online at: https://www.frontiersin.org/articles/10.3389/fchem.2022.918116/full#supplementary-material

REFERENCES

Abou-Sleiman, P. M., Muqit, M. M. K., and Wood, N. W. (2006). Expanding Insights of Mitochondrial Dysfunction in Parkinson's Disease. *Nat. Rev. Neurosci.* 7, 207–219. doi:10.1038/nrn1868

Anand, N., Holcom, A., Broussalian, M., Schmidt, M., Chinta, S. J., Lithgow, G. J., et al. (2020). Dysregulated Iron Metabolism in *C. elegans* catp-6/ATP13A2 Mutant Impairs Mitochondrial Function. *Neurobiol. Dis.* 139, 104786. doi:10.1016/j.nbd.2020.104786

Anjaneyulu, J., R, V., and Godbole, A. (2020). Differential Effect of Ayurvedic Nootropics on *C. elegans* Models of Parkinson's Disease. *J. Ayurveda Integr. Med.* 11, 440–447. doi:10.1016/j.jaim.2020.07.006

Berendse, H. W., Booij, J., Francot, C. M. J. E., Bergmans, P. L. M., Hijman, R., Stoof, J. C., et al. (2001). Subclinical Dopaminergic Dysfunction in Asymptomatic Parkinson's Disease Patients' Relatives with a Decreased Sense of Smell. *Ann. Neurol.* 50, 34–41. doi:10.1002/ana.1049

Borah, A. J., and Shi, Z. (2018). Rhodium-Catalyzed, Remote Terminal Hydroarylation of Activated Olefins through a Long-Range Deconjugative Isomerization. *J. Am. Chem. Soc.* 140, 6062–6066. doi:10.1021/jacs.8b03560

Bouça-Machado, R., Duarte, G. S., Patriarca, M., Castro Caldas, A., Alarcão, J., Fernandes, R. M., et al. (2019). Measurement Instruments to Assess Functional Mobility in Parkinson's Disease: A Systematic Review. *Mov. Disord. Clin. Pract.* 7, 129–139. doi:10.1002/mdc3.12874

Brunetti, G., Di Rosa, G., Scuto, M., Leri, M., Stefani, M., Schmitz-Linneweber, C., et al. (2020). Healthspan Maintenance and Prevention of Parkinson's-like Phenotypes with Hydroxytyrosol and Oleuropein Aglycone in *C. elegans*. *Ijms* 21, 2588. doi:10.3390/ijms21072588

Calabrese, V., Santoro, A., Monti, D., Crupi, R., Di Paola, R., Latteri, S., et al. (2018). Aging and Parkinson's Disease: Inflammaging, Neuroinflammation and Biological Remodeling as Key Factors in Pathogenesis. *Free Radic. Biol. Med.* 115, 80–91. doi:10.1016/j.freeradbiomed.2017.10.379

Chalorak, P., Sanguanphun, T., Limboonreung, T., and Meemon, K. (2021). Neurorescue Effects of Frondoside A and Ginsenoside Rg3 in *C. elegans* Model of Parkinson's Disease. *Molecules* 26, 4843. doi:10.3390/molecules26164843

Chen, S. T., Chuang, J. I., Hong, M. H., and Li, E. I.-C. (2002). Melatonin Attenuates MPP+ -induced Neurodegeneration and Glutathione Impairment in the Nigrostriatal Dopaminergic Pathway. *J. Pineal Res.* 32, 262–269. doi:10.1034/j.1600-079X.2002.01871.x

Delenclos, M., Jones, D. R., Mclean, P. J., and Uitti, R. J. (2016). Biomarkers in Parkinson's Disease: Advances and Strategies. *Park. Relat. Disord.* 22, s106–s110. doi:10.1016/j.parkreldis.2015.09.048

Govindan, S., Amirthalingam, M., Duraisamy, K., Govindan, T., Sundararaj, N., and Palanisamy, S. (2018). Phytochemicals-induced Hormesis Protects *Caenorhabditis elegans* against α-synuclein Protein Aggregation and Stress through Modulating HSF-1 and SKN-1/Nrf2 Signaling Pathways. *Biomed. Pharmacother.* 102, 812–822. doi:10.1016/j.biopha.2018.03.128

Han, X., Yuan, Y., and Shi, Z. (2019). Rhodium-Catalyzed Selective C-H Trideuteromethylation of Indole at C7 Position Using Acetic-D6 Anhydride. *J. Org. Chem.* 84, 12764–12772. doi:10.1021/acs.joc.9b01114

Hirsch, E. C., Jenner, P., and Przedborski, S. (2012). Pathogenesis of Parkinson's Disease. *Mov. Disord.* 28, 24–30. doi:10.1002/mds.25032

Huang, D., Ou, B., Hampsch-Woodill, M., Flanagan, J. A., and Prior, R. L. (2002). High-throughput Assay of Oxygen Radical Absorbance Capacity (ORAC) Using a Multichannel Liquid Handling System Coupled with a Microplate Fluorescence Reader in 96-well Format. *J. Agric. Food Chem.* 50, 4437–4444. doi:10.1021/jf0201529

Jadiya, P., Khan, A., Sammi, S. R., Kaur, S., Mir, S. S., and Nazir, A. (2011). Anti-Parkinsonian Effects of Bacopa Monnieri: Insights from Transgenic and Pharmacological *Caenorhabditis elegans* Models of Parkinson's Disease. *Biochem. Biophysical Res. Commun.* 413, 605–610. doi:10.1016/j.bbrc.2011.09.010

Jankovic, J., and Stacy, M. (2007). Medical Management of Levodopa-Associated Motor Complications in Patients with Parkinson?s Disease. *Cns Drugs* 21, 677–692. doi:10.2165/00023210-200721080-00005

Jia, W., Su, Q., Cheng, Q., Peng, Q., Qiao, A., Luo, X., et al. (2021). Neuroprotective Effects of Palmatine via the Enhancement of Antioxidant Defense and Small Heat Shock Protein Expression in Aβ-Transgenic *Caenorhabditis elegans*. *Oxidative Med. Cell. Longev.* 2021, 1–18. doi:10.1155/2021/9966223

Lee, S. H., Han, Y. T., and Cha, D. S. (2021). Neuroprotective Effect of Damaurone D in a *C. elegans* Model of Parkinson's Disease. *Neurosci. Lett.* 747, 135623. doi:10.1016/j.neulet.2021.135623

Lei, Z.-Q., Pan, F., Li, H., Li, Y., Zhang, X.-S., Chen, K., et al. (2015). Group Exchange between Ketones and Carboxylic Acids through Directing Group Assisted Rh-Catalyzed Reorganization of Carbon Skeletons. *J. Am. Chem. Soc.* 137, 5012–5020. doi:10.1021/ja512003d

Liu, J., Banskota, A., Critchley, A., Hafting, J., and Prithiviraj, B. (2015). Neuroprotective Effects of the Cultivated Chondrus Crispus in a *C. elegans* Model of Parkinson's Disease. *Mar. Drugs* 13, 2250–2266. doi:10.3390/md13042250

Ma, J., Wang, R., Chen, T., Jiang, S., and Xu, A. (2021). Protective Effects of Baicalin in a *Caenorhabditis elegans* Model of Parkinson's Disease. *Toxicol. Res.* 10, 409–417. doi:10.1093/toxres/tfaa107

Mann, D. M. A., and Yates, P. O. (1982). Pathogenesis of Parkinson's Disease. *Archives Neurology* 39, 545–549. doi:10.1001/archneur.1982.00510210015004

Martinez, B. A., Caldwell, K. A., and Caldwell, G. A. (2017). C . Elegans as a Model System to Accelerate Discovery for Parkinson Disease. *Curr. Opin. Genet. Dev.* 44, 102–109. doi:10.1016/j.gde.2017.02.011

Moosmann, B., and Behl, C. (2002). Antioxidants as Treatment for Neurodegenerative Disorders. *Expert Opin. Investigational Drugs* 11, 1407–1435. doi:10.1517/13543784.11.10.1407

Nass, R., and Chen, L. (2008). *Caenorhabditis elegans* Models of Human Neurodegenerative Diseases. *Humana Press* 6615, 91–101. 978-1-58829-933-8. doi:10.1007/978-1-59745-285-4_12

Olzmann, J. A., Bordelon, J. R., Muly, E. C., Rees, H. D., Levey, A. I., Li, L., et al. (2007). Selective Enrichment of DJ-1 Protein in Primate Striatal Neuronal Processes: Implications for Parkinson's Disease. *J. Comp. Neurol.* 500, 585–599. doi:10.1002/cne.21191

Ou, B., Huang, D., Hampsch-Woodill, M., Flanagan, J. A., and Deemer, E. K. (2002). Analysis of Antioxidant Activities of Common Vegetables Employing Oxygen Radical Absorbance Capacity (ORAC) and Ferric Reducing Antioxidant Power (FRAP) Assays: a Comparative Study. *J. Agric. Food Chem.* 50, 3122–3128. doi:10.1021/jf0116606

Pohanka, M. (2011). Alzheimer's Disease and Related Neurodegenerative Disorders: Implication and Counteracting of Melatonin. *Jab* 9, 185–196. doi:10.2478/v10136-011-0003-6

Qiu, X., Wang, P., Wang, D., Wang, M., Yuan, Y., and Shi, Z. (2019). PIII -Chelation-Assisted Indole C7-Arylation, Olefination, Methylation, and Acylation with Carboxylic Acids/Anhydrides by Rhodium Catalysis. *Angew. Chem. Int. Ed.* 58, 1504–1508. doi:10.1002/anie.201813182

Rudnitskaya, E. A., Maksimova, K. Y., Muraleva, N. A., Logvinov, S. V., Yanshole, L. V., Kolosova, N. G., et al. (2015). Beneficial Effects of Melatonin in a Rat Model of Sporadic Alzheimer's Disease. *Biogerontology* 16, 303–316. doi:10.1007/s10522-014-9547-7

Sawin, E. R., Ranganathan, R., and Horvitz, H. R. (2000). *C. elegans* Locomotory Rate Is Modulated by the Environment through a Dopaminergic Pathway and by Experience through a Serotonergic Pathway. *Neuron* 26, 619–631. doi:10.1016/S0896-6273(00)81199-X

Sayre, L. M., Perry, G., and Smith, M. A. (2008). Oxidative Stress and Neurotoxicity. *Chem. Res. Toxicol.* 21, 172–188. doi:10.1021/tx700210j

Schaich, K. M., Tian, X., and Xie, J. (2015). Hurdles and Pitfalls in Measuring Antioxidant Efficacy: A Critical Evaluation of ABTS, DPPH, and ORAC Assays. *J. Funct. Foods* 14, 111–125. doi:10.1016/j.jff.2015.01.043

Skene, D., and Swaab, D. F. (2003). Melatonin Rhythmicity: Effect of Age and Alzheimer's Disease. *Exp. Gerontol.* 38, 199–206. doi:10.1016/S0531-5565(02)00198-5

Smeyne, R. J., and Jackson-Lewis, V. (2005). The MPTP Model of Parkinson's Disease. *Mol. Brain Res.* 134, 57–66. doi:10.1016/j.molbrainres.2004.09.017

Sommer, J., Kunzmann, A., Stuthmann, L. E., and Springer, K. (2022). The Antioxidative Potential of Sea Grapes (Caulerpa Lentillifera, Chlorophyta) Can Be Triggered by Light to Reach Comparable Values of Pomegranate and Other Highly Nutritious Fruits. *Plant Physiol. Rep.* 27, 186–191. doi:10.1007/s40502-021-00637-6

Tucci, M. L., Harrington, A. J., Caldwell, G. A., and Caldwell, K. A. (2011). Modeling Dopamine Neuron Degeneration in *Caenorhabditis elegans*. *Humana Press* 793, 129–148. doi:10.1007/978-1-61779-328-8_9

Verma, A., and Ravindranath, V. (2019). CaV1.3 L-type Calcium Channels Increase the Vulnerability of Substantia Nigra Dopaminergic Neurons in MPTP Mouse Model of Parkinson's Disease. *Front. Aging Neurosci.* 11, 382. doi:10.3389/fnagi.2019.00382

Weber, C. A., and Ernst, M. E. (2006). Antioxidants, Supplements, and Parkinson's Disease. *Ann. Pharmacother.* 40, 935–938. doi:10.1345/aph.1G551

Wu, Y.-H., Feenstra, M. G. P., Zhou, J.-N., Liu, R.-Y., Torano̅, J. S., Van Kan, H. J. M., et al. (2003). Molecular Changes Underlying Reduced Pineal Melatonin Levels in Alzheimer Disease: Alterations in Preclinical and Clinical Stages. *J. Clin. Endocrinol. Metabolism* 88, 5898–5906. doi:10.1210/jc.2003-030833

Wu, Y., Wu, Z., Butko, P., Christen, Y., Lambert, M. P., Klein, W. L., et al. (2006). Amyloid- -Induced Pathological Behaviors Are Suppressed by Ginkgo Biloba Extract EGb 761 and Ginkgolides in Transgenic *Caenorhabditis elegans*. *J. Neurosci.* 26, 13102–13113. doi:10.1523/JNEUROSCI.3448-06.2006

Yu, C.-X., Zhu, C.-B., Xu, S.-F., Cao, X.-D., and Wu, G.-C. (2000). Selective MT2 Melatonin Receptor Antagonist Blocks Melatonin-Induced Antinociception in Rats. *Neurosci. Lett.* 282, 161–164. doi:10.1016/S0304-3940(00)00883-1

Zarranz, J. J., Alegre, J., Gómez-Esteban, J. C., Lezcano, E., Ros, R., Ampuero, I., et al. (2004). The New Mutation, E46K, of α-synuclein Causes Parkinson and Lewy Body Dementia. *Ann. Neurol.* 55, 164–173. doi:10.1002/ana.10795

Zhao, S., Cheng, Q., Peng, Q., Yu, X., Yin, X., Liang, M., et al. (2018). Antioxidant Peptides Derived from the Hydrolyzate of Purple Sea Urchin (Strongylocentrotus Nudus) Gonad Alleviate Oxidative Stress in *Caenorhabditis elegans*. *J. Funct. Foods* 48, 594–604. doi:10.1016/j.jff.2018.07.060

Zhao, X., and Yu, Z. (2008). Rhodium-Catalyzed Regioselective C–H Functionalization via Decarbonylation of Acid Chlorides and C–H Bond Activation under Phosphine-free Conditions. *J. Am. Chem. Soc.* 130, 8136–8137. doi:10.1021/ja803154h

Check for updates

Investigation of the Structural, Thermal, and Physicochemical Properties of Nanocelluloses Extracted From Bamboo Shoot Processing Byproducts

Tong Lin[1], Qi Wang[2,3], Xuan Zheng[1], Yu Chang[1], Hui Cao[4,5] and Yafeng Zheng[1,2]*

[1]College of Food Science, Fujian Agriculture and Forestry University, Fuzhou, China, [2]Institute of Agricultural Engineering, Fujian Academy of Agriculture Sciences, Fuzhou, China, [3]Fujian Key Laboratory of Agricultural Product (Food) Processing, Fuzhou, China, [4]Institute of Chinese Medical Sciences, University of Macau, Macau SAR, China, [5]Faculty of Food Science and Technology, University of Vigo, Pontevedra, Spain

Nanocellulose has gained increasing interest due to its excellent properties and great potential as a functional component or carrier in food and pharmaceutical industries. This study investigated the structural, thermal, and physicochemical properties of nanofibrillated cellulose (NFC) and nanocrystalline cellulose (CNC) extracted from bamboo shoot (*Leleba oldhami* Nakal) processing byproducts. NFCs were prepared through low concentration acid hydrolysis combined with ultrasonic treatment. CNCs were further isolated from NFCs using sulfuric acid hydrolysis treatment. TEM images showed that NFC and CNC exhibited typical long-chain and needle-like structures, respectively. CNC suspension was stable due to its zeta potential of -34.3 ± 1.23 mV. As expected, both NFC and CNC displayed high crystallinity indexes of 68.51 and 78.87%, and FTIR analysis confirmed the successful removal of lignin and hemicellulose during the treatments. However, the thermogravimetric analysis indicated that sulfuric acid hydrolysis decreased the thermal stability of CNCs. The improved physicochemical properties of NFC and CNC suggested their potential in various applications.

Keywords: nanofibrillated cellulose, nanocrystalline cellulose, bamboo shoot, acid hydrolysis, physicochemical property

1 INTRODUCTION

Cellulose, the main component of plant cell walls, is the most abundant biomaterial in the world with its biodegradability and renewability (Eichhorn et al., 2010). Recently, to increase the value of cellulose-rich processing residues, effective conversion of cellulose from various plant-derived residues into nanocellulose, mainly nanofibrillated cellulose (NFC) or cellulose nanocrystals (CNCs), has received increasing attention due to their great potential on biomedical and food applications (Kaushik and Singh 2011; Pelissari et al., 2013; Chen et al., 2016; Perumal et al., 2022; Sainorudin et al., 2022). NFC is a novel nanomaterial with soft and long-chain structures (typical diameter of 4–20 nm and length of 500–2000 nm) with a high aspect ratio, which is produced based on a fibrillation process (Yan et al., 2018). CNC is a spherical "rod" or "needle" with a highly crystalline structure with a diameter of 3–10 nm and a length of 100–1,000 nm (Marett et al., 2017).

The physical dimensions and related properties of nanocellulose could be varied based on the source of cellulose and the applied preparation conditions (Mishra et al., 2019; Holilah et al., 2022).

In recent years nanocellulose has attracted intensive research attention and been used in many industrial applications, which can be attributed to its special properties, including high specific strength and stiffness, high reinforcing potential, large specific surface area, and biocompatibility (Ghaderi et al., 2014; Reshmy et al., 2020; Almashhadani et al., 2022). Moreover, non-toxic nanocellulose also exhibits promising potential in the food industry, such as biodegradable food packaging, novel delivery systems, food stabilizer, and functional food ingredients (Mu et al., 2019). It was reported that the rising demand and the novel applications of nanocellulose have driven the industry to build a number of new manufacturing facilities (Mariano et al., 2014; Coelho et al., 2018).

Bamboo shoots have been traditionally consumed as delicious forest vegetables and healthcare food worldwide, especially in Asian countries (Choudhury et al., 2012). As fresh bamboo shoots have short shell life, most of them are dried, canned, or fermented into various food products for consumption during off-seasons (Satya et al., 2010; Choudhury et al., 2012). However, only the tender top part (around 50% w/w) of bamboo shoots can be utilized; therefore, the fast-growing bamboo shoot processing industry in China creates a huge amount of processing byproducts. Some research achievements have been made on the innovative utilization of bamboo shoot byproducts (Zhang et al., 2017a; Zhang et al., 2017b), but most of those still have been discarded directly resulting in waste of resources and environmental problems (Chen et al., 2018; Chen et al., 2019). Bamboo shoot processing byproducts consist of a considerable amount of cellulose (Peng and She 2014), representing an abundant and cheap source for production of nanocellulose, such as NFC or CNC based on different application purposes. To increase the marketability of nanocellulose, numerous agricultural or processing byproducts, such as banana peel (Pelissari et al., 2013; Khawas and Deka 2016), cassava bagasse (Travalini et al., 2017), cotton stalks (Soni et al., 2015), and rice husk (Johar et al., 2012), have been investigated as new sources for the nanocellulose production. In a previous study, nanocrystalline cellulose with a length of 200–500 nm and a diameter less than 20 nm was prepared from bamboo pulp through chemical treatment (Yu et al., 2012). However, to the best of our knowledge, bamboo shoot (*Leleba oldhami* Nakal) processing byproducts have not been investigated as a source for NFC and CNC production.

In this study, bamboo shoot NFC was prepared through low concentration acid hydrolysis combined with ultrasonic treatment, which is a relatively green method with the reduced use of chemical reagents. Thereafter, the NFC is subjected to sulfuric acid hydrolysis to further remove the amorphous region in the fiber to obtain CNC. Multiple analysis methods were applied to determine the morphological, structural, and thermal properties of the as-prepared samples. Moreover, to estimate their potential in the food application, the physicochemical properties, including water/oil binding and swell capacities were investigated and compared.

2 MATERIALS AND METHODS

2.1 Materials
Bamboo shoot (*Leleba oldhami* Nakal) processing byproducts (basal parts of the bamboo shoot) were obtained from a local bamboo shoot processing company in Fujian province, China. Sulfuric acid, hydrochloric acid, ethyl acetate, and hydrogen peroxide were purchased from Fuyu Fine Chemical Co., Ltd. (Tianjin, China). Sodium hydroxide (tablet) and anhydrous ethanol were purchased from Wokai Biotechnology Co., Ltd. (Shanghai, China). All other chemicals were of analytical grade.

2.2 Isolation of Insoluble Fiber
The isolation procedure of bamboo shoot insoluble dietary fiber (IDF) was adapted from Luo et al. (2018) with modifications. The bamboo shoot byproducts were cut into small pieces (3–5 cm), dried, and ground into fine powder. The resulting powder was soaked in ethyl acetate at a ratio of 1:4 (w/v) for 1 h and then washed with distilled water to obtain a degreased sample. Then, it was added to distilled water at a ratio of 1:30 (w/v), leached at 80°C for 2 h, then washed with 78% ethanol, and dried for 24 h to obtain IDF (100 mesh).

2.3 Preparation of NFC
The preparation of NFC from IDF was carried out according to the reported methods with modifications (Kaushik and Singh 2011; Leite et al., 2017). IDF powder was pretreated with 5% (w/v) NaOH solution at a ratio of 1:20 (w/v) at 50°C, and the suspension was stirred for 4 h. The mixture was centrifuged to achieve the residue, which was then washed with distilled water. The procedure was repeated until the fiber was free of alkali. To remove the residual lignin and hemicellulose, the alkali-treated fiber was then bleached with 8% (v/v) hydrogen peroxide (H_2O_2) at room temperature for 24 h, then washed and centrifuged (2 times, 10,000 rpm/15°C/10 min). The bleached fiber was subjected to low concentration acid hydrolysis combined with ultrasonic treatment to isolate NFC. The fiber was mixed with 5% (v/v) HCl solution at a ratio of 1:30 (w/v), and treated with an ultrasonic transducer (KQ2200DE, Ultrasonic Instrument, Kunshan, China) at the ultrasonic power of 170 W at 56°C for 80 min. The procedure was repeated under the same conditions except for the increased HCl concentration (10%, v/v). The resulting mixture was neutralized with NaOH and washed with distilled water. The precipitate was freeze-dried to obtain NFC powders.

2.4 Preparation of CNC
The sulfuric acid hydrolysis was conducted on NFC powders to prepare CNC (Johar et al., 2012). Briefly, NFC powder was mixed with a preheated sulfuric acid solution (62%, w/v) at a ratio of 1:20 (w/v) at 37°C for 80 min under continuous stirring of 600 rpm. The hydrolyzed material was washed and centrifuged (4,000 rpm, 10 min) several times to remove residual sulfuric acid. The suspension was dialyzed against distilled water and homogenized for 5 min. The suspension was lyophilized to obtain CNC, and kept refrigerated for further analysis.

2.5 Surface Morphology Analysis

To observe the surface morphology and determine the dimensions of NFC and CNC, 1.0 mg of sample powder was dispersed in 10 ml of deionized water and sonicated for 15 min to disperse the agglomerated fibers. After sonication, a drop of dispersion was deposited on the carbon-coated copper grid and allowed to dry at room temperature. Transmission electron microscope (TEM) images were obtained under an acceleration voltage of 200 kV using a transmission electron microscope (THS-117, Tecnai, United States). The dimension and aspect ratio of samples were measured according to the TEM images using the software (Nano Measurer 1.2).

2.6 Zeta Potential Analysis

The samples were diluted with deionized water at a fiber/liquid ratio of 1:5. The surface charge (zeta potential) of diluted fiber suspensions was measured at 25°C using a Zetasizer Nano ZS90 analyzer (Malvern, United Kingdom).

2.7 Fourier Transform Infrared Spectroscopy

To analyze and compare the functional groups of nanocellulose samples, each sample was finely ground and mixed with KBr. The mixture was then pressed into a transparent film and analyzed by a Fourier transform infrared spectroscopy (Vertex 70/70 v, Bruker, Germany). FTIR spectra were recorded in a measurement range of 300–4,000 cm^{-1} with a resolution of 4 cm^{-1}.

2.8 X-Ray Diffraction

To examine the crystallinity of the fiber samples, XRD images were scanned in the range 2θ = 5–50° and recorded at a speed of 5°/min using an X-ray diffractometer (D8 Rigaku9000, BrukerAXS, Karlsruhe, Germany). The crystallinity index (CrI) is calculated according to **Eq. 1**.

$$CrI\,(\%) = \left(1 - \frac{I_{(am)}}{I_{(200)}}\right) \times 100\% \tag{1}$$

where $I_{(am)}$ is the diffraction intensity of the only amorphous regions at around 2θ = 18°, and $I_{(200)}$ represents the maximum diffraction intensity of both crystalline and amorphous regions at around 2θ = 22.6° (Travalini et al., 2017).

2.9 Thermogravimetric Analysis

The dried samples (5.0 mg) were subjected to thermal stability analysis using a thermogravimetric analyzer (4F3, NETZSCH, Germany). The mass change in the range of 30–790°C was measured at a constant heating rate of 10°C/min under a nitrogen atmosphere, and the sample was kept at 790°C for 5 min.

2.10 Physicochemical Properties

2.10.1 Swelling Capacity

Accurately weigh 0.5 g of sample (W_d) in a 10 ml calibrated tube and its initial bed volume was recorded as V_1, and mixed with 5.0 ml of distilled water and shaken well. The tube was placed in a 25°C water bath for 24 h, and the bed volume of fiber in the liquid was carefully measured and recorded as V_2. SC was calculated according to **Eq. 2**:

$$SC\,(mL/g) = \frac{V_2 - V_1}{W_d} \tag{2}$$

2.11 Water Holding Capacity

The dried sample (0.5 g, M_d) was transferred into a 50 ml centrifuge tube, mixed with 25 ml of deionized water, and then placed in a 37°C water bath for 30 min with continuous stirring. The mixture was centrifuged at 4,000 rpm for 15 min, and the supernatant was discarded. The precipitated wet powder (M_w) was collected and weighed. WHC was calculated according to **Eq. 3**:

$$WHC\,(g/g)\frac{M_w - M_d}{M_d} \tag{3}$$

2.12 Oil Binding Capacity

The dried sample (1.0 g, M_1) was mixed with 20 ml of edible blend oil in a 50 ml centrifuge tube and stirred for 30 s every 5 min. After 1 h, the tube was centrifuged at 4,000 rpm for 15 min, and the upper layer of oil was decanted. The residue (M_2) was blotted with filter paper to dry the free oil and weighed. OBC was calculated according to **Eq. 4**:

$$OBC\,(g/g)\frac{M_2 - M_1}{M_1} \tag{4}$$

2.13 Statistical Analyses

All results are expressed as mean ± SD. p values less than 0.05 were considered to indicate a significant difference between treatments. Data were analyzed using SPSS/11.5 software.

3 RESULTS AND DISCUSSION

3.1 Morphology, Dimension and Surface Charge

The images of the IDF, NFC, and CNC isolated from bamboo shoot processing byproducts and their suspensions are shown in **Figure 1**. The color of the bamboo shoot IDF is brown due to the presence of non-cellulosic materials and other impurities, including main lignin, hemicelluloses, and pectin (Johar et al., 2012). Obviously different from IDF, the color of NFC and CNC powders appear completely white, indicating the presence of almost pure cellulosic material and the successful removal of non-cellulosic materials and other impurities during the chemical and physical treatments. The dispersibility of the samples was observed by dispersing the powder (50 mg) in 10 ml of water and setting it aside at room temperature for 24 h. Compared to IDF and NFC, CNC exhibited a significantly stronger ability to disperse in water and provided a more stable suspension. One of the main reasons was due to the sulfuric acid hydrolysis used for the

FIGURE 1 | Photographs of IDF, NFC, and CNC powders and their aqueous suspensions after setting aside at room temperature for 24 h.
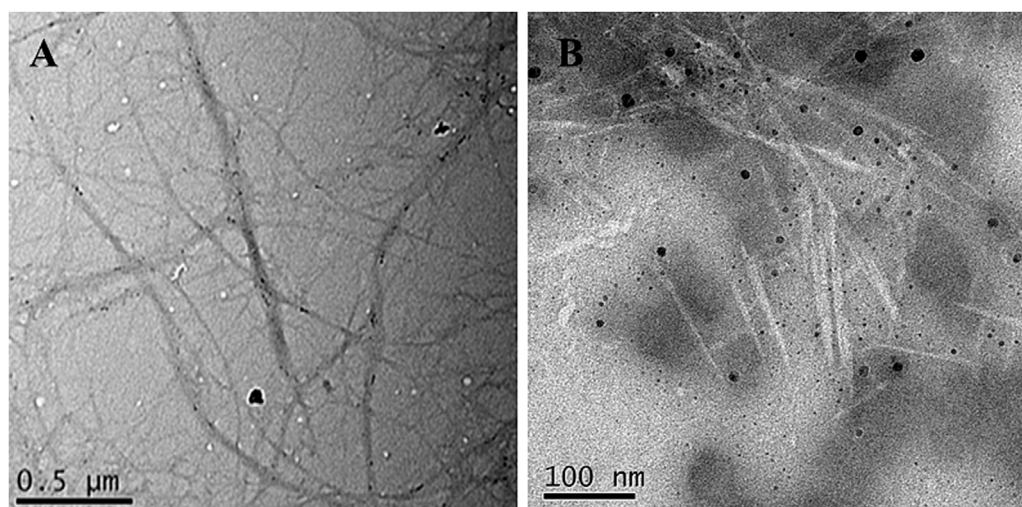
FIGURE 2 | TEM images of bamboo shoot NFC **(A)** and CNC **(B)**.

isolation of CNC. As the most popular and effective method for CNC production, sulfuric acid is able to react with the surface hydroxyl groups to form negatively charged sulfate ester groups randomly distributed on the surface of CNC, promoting their dispersion in water (Mariano et al., 2014).

As shown in **Figure 2**, after pretreatment and low concentration acid hydrolysis combined with ultrasonic treatment, raw insoluble fiber was broken and crushed into individualized NFCs with a soft and long-chain structure. NFC was then subjected to sulfuric acid hydrolysis, which further

TABLE 1 | Dimensions and zeta potential of NFC and CNC isolated from bamboo shoot processing byproducts.

Sample	Length (nm)	Diameter (nm)	Aspect Ratio	Zeta Potential (mV)
NFC	952.45 ± 38.53[a]	69.97 ± 3.21[a]	13.64 ± 1.61[b]	-15.5 ± 0.87[a]
CNC	124.50 ± 51.94[b]	7.23 ± 2.07[b]	18.19 ± 2.45[a]	-34.3 ± 1.23[b]

[a,b] *Different letter superscripts in the same column indicate a statistically significant difference (p < 0.05).*
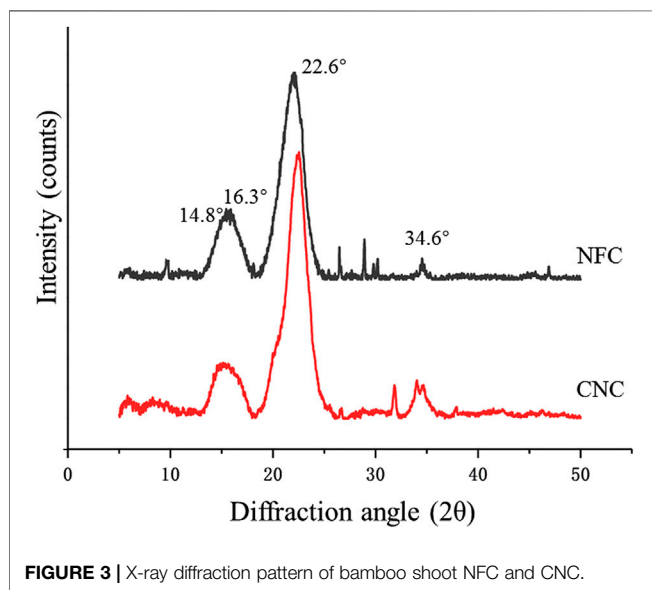
FIGURE 3 | X-ray diffraction pattern of bamboo shoot NFC and CNC.
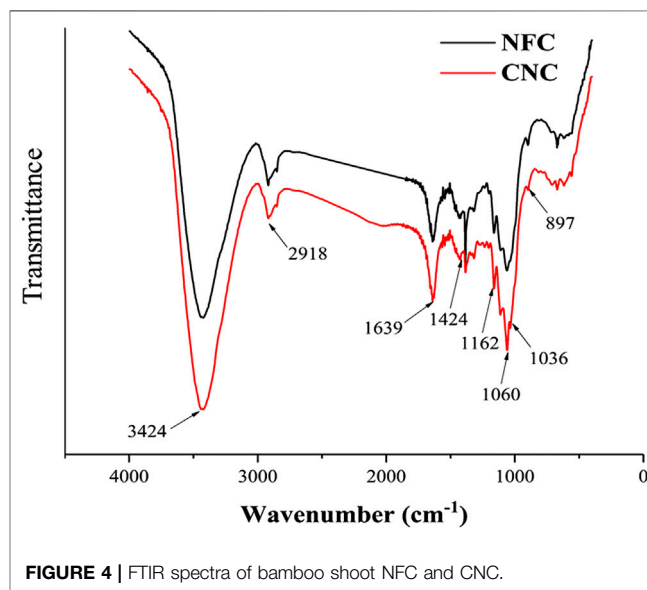
FIGURE 4 | FTIR spectra of bamboo shoot NFC and CNC.

destroyed the long-chain structure of NFCs into the typical needle-like structure of CNC. The results from **Table 1** revealed that the average length and diameter of NFC were 952.45 ± 38.53 nm and 69.97 ± 3.21 nm, respectively. Thus, its aspect ratio was 13.64 ± 1.61. It is notable that the width of NFC is higher than the nanofibrillated cellulose obtained in other studies (Winuprasith and Suphantharika 2013; Yan et al., 2018), suggesting that the method applied in this study was relatively green but also less efficient due to low concentration acid applied. The diameter and length of CNC were 7.23 ± 2.07 nm and 124.50 ± 51.94 nm, with an aspect ratio of 18.19 ± 2.45. Bamboo shoot CNC with a high aspect ratio is useful to enhance and improve the mechanical properties of composite materials under low loads (Liu et al., 2017).

3.2 Zeta Potential Analysis

As shown in **Table 1**, both NFC and CNC aqueous suspensions exhibited negative zeta potential (surface charge), and CNC presented a significantly lower zeta potential value of −34.3 ± 1.23 mV than that of NFC (−15.5 ± 0.87 mV). Electrostatic repulsion of the CNC suspension was enhanced due to the connection of negatively charged sulfate groups to the nanofiber surface during the sulfuric acid hydrolysis. It has been reported that if the absolute value of nanofiber's zeta potential is higher than 30, the nanofiber aggregation will be greatly minimized, which could be desirable for many applications (Leite et al., 2017).

3.3 X-Ray Diffraction

X-ray diffraction (XRD) analysis was used to evaluate XRD patterns and changes in the crystallinity of bamboo shoot NFC and CNC (**Figure 3**). It was noticed that both NFC and CNC had diffraction peaks at 2θ = 14.8°, 16.3°, 22.6°, and 34.6°, indicating that the cellulose was in the form of cellulose I (Marett et al., 2017). The peak position of the nanocelluloses was not obviously different, suggesting that the crystalline structure of CNC did not change after subjecting NFC to sulfuric acid hydrolysis. Meanwhile, the diffraction peak of CNC at 22.6° was sharper than that of NFC, and the intensity of the diffraction peak of the amorphous region is significantly decreased, indicating an increase in crystallinity. The calculated crystallinity indexes of NFC and CNC were 68.51 and 78.87%, respectively. The high crystallinity was strongly related to the different treatments of fiber samples. NFC was prepared from IDF through low concentration acid hydrolysis combined with ultrasonic treatment, which effectively destroyed the amorphous lignin and hemicellulose to release the nanofibrillated cellulose. Sulfuric acid hydrolysis further dissolved the remained amorphous regions (mainly hemicellulose) in NFC, releasing more individual needle-like crystallites by promoting the hydrolytic cleavage of glycosidic bonds. The crystallinity of CNC prepared from bamboo shoot residue was higher than that of cellulose nanocrystalline isolated from the bamboo pulp (Yu et al., 2012) or other agricultural wastes (Liu et al., 2017; Rohaizu and Wanrosli 2017). Therefore,

FIGURE 5 | TG **(A)** and DTG **(B)** curves of bamboo shoot CNC and NFC.
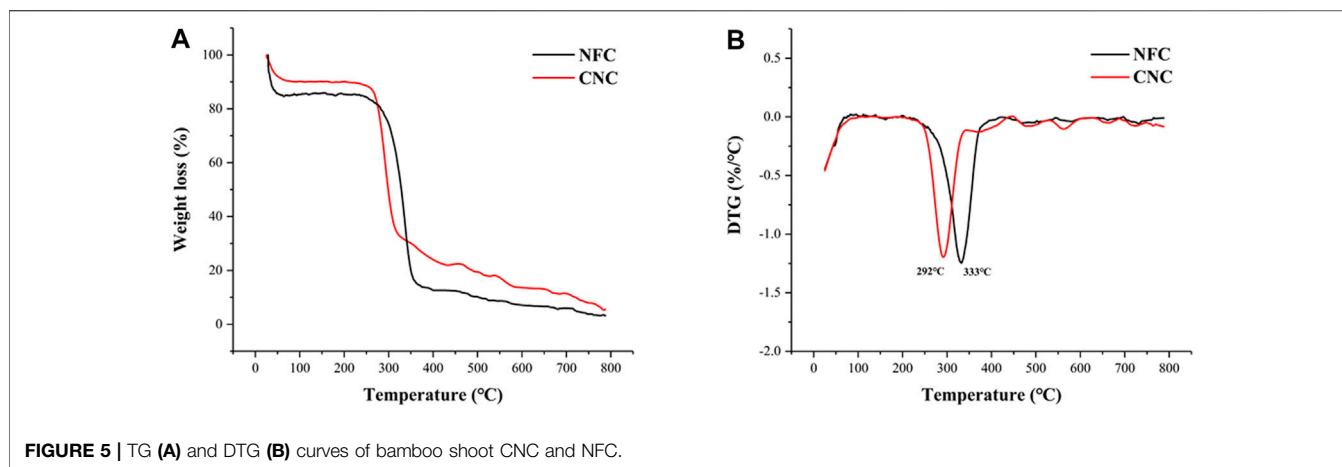
CNC prepared in this study could provide promising reinforcement potential for promising the composite materials (Marett et al., 2017).

3.4 Fourier Transform Infrared Spectroscopy

The FTIR spectra of NFC and CNC (**Figure 4**) could be used to provide direct information on chemical changes that occur during the different treatments for the isolation of NFC and CNC from bamboo shoot byproducts. According to the literature, there are several characteristic bands related to the chemical structure of the non-cellulosic materials, mainly lignin and hemicellulose. The bands between 1,600 and 1,500 cm^{-1} correspond to the vibrations of the aromatic rings of lignin. The peak at 1730 cm^{-1} in the FTIR spectrum is attributed to the ester groups in hemicellulose or carboxylic group in the ferulic and *p*-coumaric acids of lignin (Mandal and Chakrabarty 2011). Likewise, the peak at around 1,240 cm^{-1} stand for the elongation of the ether linkages in the lignin (Travalini et al., 2017). All these mentioned bands have disappeared in the FTIR spectra of NFC and CNC, meaning the successful removal of non-cellulosic material upon the treatments.

The main absorption peak located near 3,424 cm^{-1} in the spectrum is formed by the free O-H stretching vibrations of the OH groups in the cellulose molecule (Alemdar and Sain 2008; Johnson et al., 2011). Moreover, the absorption peaks at 2,918 cm^{-1}, 1,639 cm^{-1}, and 1,424 cm^{-1} are attributed to the characteristic C-H stretching vibration, the O-H bending of the adsorbed water, and the CH$_2$ bending vibration of the crystalline region in cellulose (Mandal and Chakrabarty 2011; Wang et al., 2017). The absorption peak at 1,162 cm^{-1} is derived from the stretching of the glycosidic bond anti-symmetric C-O-C (Pereira et al., 2017). In both samples, the observed peaks at 1,060 and 897 cm^{-1} refer to the C-O vibration and C-H stretching in the cellulose chains (Johar et al., 2012). These results indicate that the cellulose component was not destroyed or removed after the chemical treatments carried out on the bamboo shoot residues and remained as dominating material presented in both samples, which is consistent with the result

from the XRD analysis. Additionally, the absorption peaks at 1,060 and 1,036 cm^{-1} of CNC were shapers than those of NFC, which could be due to that the C-O bond stretching of CNC was affected by the sulfonic acid groups after the sulfuric acid hydrolysis (Li et al., 2018).

3.5 Thermogravimetric Analysis

Thermogravimetric (TG) and derivative thermogravimetric (DTG) curves obtained for NFC and CNC are shown in **Figure 5**. It was observed that both NFC and CNC had two decomposition stages. The initial weight loss starting at 30°C and continuing up to around 100°C could be attributed to the evaporation of loosely bound moisture on the fiber surface and the intermolecularly H-bonded water (Khawas et al., 2016), which had been confirmed by the characteristic peak of FTIR spectra at 1,639 cm^{-1}. In the next stage, the sharp decomposition peaks at around 300°C were noticed and corresponded to cellulose decomposition (Kaushik and Singh 2011). Meanwhile, it was notable that there were no characteristic peaks attributing to the thermal decomposition of lignin and hemicellulose were found, which was consistent with the XRD and FTIR results. In the second decomposition stage, NFC started to degrade at around 235°C, and the rate of degradation reached a maximum at 333°C. However, obviously different from the degradation behavior of NFC, CNC showed lower start and main degradation temperatures at around 224 and 292°C, respectively. The decreased thermal stability of CNC might be corresponded to its high surface area to volume ratio and the introduced sulfated groups in the cellulose crystals (Mandal and Chakrabarty 2011; Lu et al., 2013). Compared to NFC, a greater surface area of CNC exposed to heat contributes to diminishing its thermal stability. Moreover, the highly sulfated regions presented on the surface of cellulose crystals after sulfuric acid hydrolysis are more accessible and degradable. As shown in the TG curve, CNC showed a slower weight loss rate than that of NFC after the temperature of 350°C, which could be explained by the fact that the unsulfated crystal interior of CNC is dense and compact. Subsequent slow decomposition at the temperature range of 400–530°C corresponds to the oxidative decomposition of carbon (Nada and Hassan 2000).
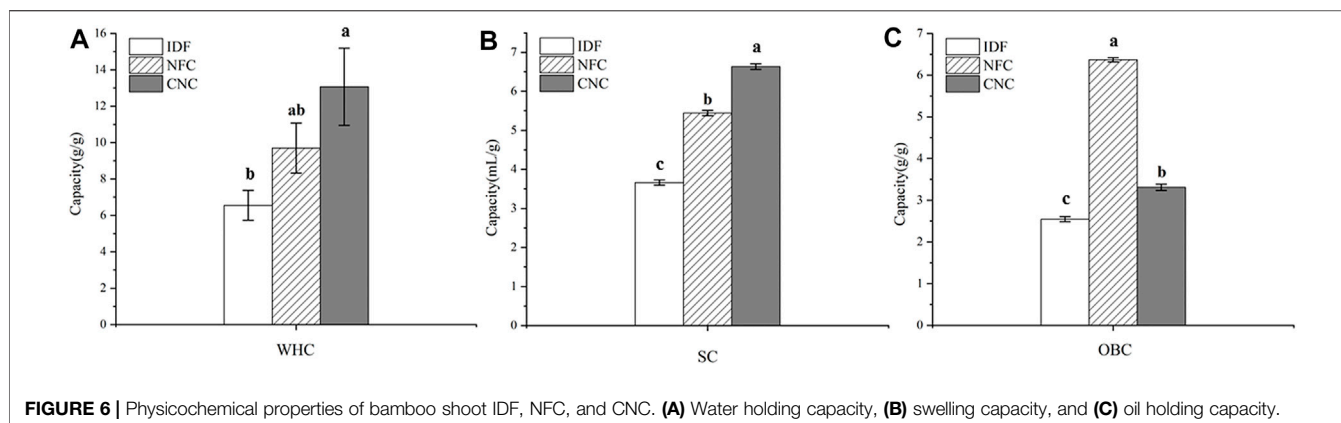
FIGURE 6 | Physicochemical properties of bamboo shoot IDF, NFC, and CNC. **(A)** Water holding capacity, **(B)** swelling capacity, and **(C)** oil holding capacity.

3.6 Physicochemical Properties

Hydration properties, including swelling capacity (SC) and water holding capacity (WHC), are one of the important factors influencing the success of the incorporation of fiber ingredients into foods requiring moisture retention. As shown in **Figure 6**, after different chemical and physical treatments, SC values of NFC (5.44 ml/g) and CNC (6.63 ml/g) were significantly ($p < 0.05$) increased by 48.6 and 81.1%, compared with that of IDF (3.66 ml/g). Similarly, WHC values of NFC (9.70 g/g) and CNC (13.07 g/g) also significantly ($p < 0.05$) increased by 48.1 and 99.5%, compared with that of IDF (6.55 g/g). The improved hydration properties of NFC and CNC could be explained by the decreased particle size after the removal of lignin and hemicellulose, and therefore the increased surface area provides more binding sites for water molecules. Moreover, the broken cellulose chain structure in NFC and CNC also contributed to the increased space-enlarging effects and thus swelling capacity (Lu et al., 2013). The sulfated regions in the surface of CNC might also provide enhanced interchain spaces for the entrapment of moisture, which further contribute to its hydration properties (Mandal and Chakrabarty 2011).

OBC is an important factor for the dietary fibers to adsorb or bind the lipid components and thus be appropriate for the stabilization of foods with a high content of fat, and emulsions. Bamboo shoot dietary fiber has been proven to be effective on oil binding, which contributes to its weight control function (Park and Jhon 2009; Luo et al., 2017). In this study, IDF extracted from bamboo shoot residue exhibited a promising OBC value of 2.55 g/g, which is significantly higher than that of fruit dietary fibers ranging from 0.7 to 1.6 g/g (Martinez et al., 2012). After low concentration acid hydrolysis combined with ultrasonic treatment, the OBC of NFC significantly increased by 2.5-fold–6.37 g/g ($p < 0.05$). Considering its greater surface area, CNC prepared from NFC by sulfuric acid hydrolysis is expected to exhibit a great capacity to bind the oil molecules. However, CNC showed a decreased OBC (3.31 g/g), compared with that NFC. This opposite result might be related to the fact that a large amount of CNC powder suspended in the upper layer of oil could not be precipitated, thus greatly lowering the OBC value.

4 CONCLUSION

This study investigated the morphological, crystal, thermal, and physicochemical properties of bamboo shoot NFC and CNC. CNC had a high-zeta potential of −34.3 mV, contributing to its suspension stability. The crystal type of NFC and CNC retained a type of cellulose I pattern with the crystallinity indexes of 68.51 and 78.87%, respectively. FTIR spectra evidenced about the successful removal of lignin and hemicellulose during the treatments. Thermogravimetric analysis indicated that CNC had lower thermal stability than that of NFC, which might be corresponded to its high surface area and the introduced sulfated groups in the cellulose crystals. NFC and CNC exhibited promising physicochemical properties, indicating that they are suitable to be incorporated into various foods with different purposes. However, a thorough toxicity assessment of these novel nanocelluloses needs to be carried out before their applications in the food industry.

DATA AVAILABILITY STATEMENT

The original contributions presented in the study are included in the article/Supplementary Material; further inquiries can be directed to the corresponding author.

AUTHOR CONTRIBUTIONS

TL: investigation, data curation, writing–original draft. QW: investigation, conceptualization, writing–original draft. XZ: formal analysis, visualization. YC: resources, software. HC: writing–review and editing. YZ: funding acquisition, writing–review and editing, supervision. All authors agree to be accountable for the content of the work.

FUNDING

REFERENCES

Alemdar, A., and Sain, M. (2008). Isolation and Characterization of Nanofibers from Agricultural Residues Wheat Straw and Soy Hulls. *Bioresour. Technol.* 99 (6), 1664–1671. doi:10.1016/j.biortech.2007.04.029

Almashhadani, A. Q., Leh, C. P., Chan, S.-Y., Lee, C. Y., and Goh, C. F. (2022). Nanocrystalline Cellulose Isolation via Acid Hydrolysis from Non-woody Biomass: Importance of Hydrolysis Parameters. *Carbohydr. Polym.* 286, 119285. doi:10.1016/j.carbpol.2022.119285

Chen, G., Chen, K., Zhang, R., Chen, X., Hu, P., and Kan, J. (2018). Polysaccharides from Bamboo Shoots Processing By-Products: New Insight into Extraction and Characterization. *Food Chem.* 245, 1113–1123. doi:10.1016/j.foodchem.2017.11.059

Chen, G., Li, C., Wang, S., Mei, X., Zhang, H., and Kan, J. (2019). Characterization of Physicochemical Properties and Antioxidant Activity of Polysaccharides from Shoot Residues of Bamboo (Chimonobambusa Quadrangularis): Effect of Drying Procedures. *Food Chem.* 292, 281–293. doi:10.1016/j.foodchem.2019.04.060

Chen, Y. W., Lee, H. V., Juan, J. C., and Phang, S.-M. (2016). Production of New Cellulose Nanomaterial from Red Algae Marine Biomass Gelidium Elegans. *Carbohydr. Polym.* 151, 1210–1219. doi:10.1016/j.carbpol.2016.06.083

Choudhury, D., Sahu, J. K., and Sharma, G. D. (2012). Value Addition to Bamboo Shoots: a Review. *J. Food Sci. Technol.* 49 (4), 407–414. doi:10.1007/s13197-011-0379-z

Coelho, C. C. S., Michelin, M., Cerqueira, M. A., Gonçalves, C., Tonon, R. V., Pastrana, L. M., et al. (2018). Cellulose Nanocrystals from Grape Pomace: Production, Properties and Cytotoxicity Assessment. *Carbohydr. Polym.* 192, 327–336. doi:10.1016/j.carbpol.2018.03.023

Eichhorn, S. J., Dufresne, A., Aranguren, M., Marcovich, N. E., Capadona, J. R., Rowan, S. J., et al. (2010). Review: Current International Research into Cellulose Nanofibres and Nanocomposites. *J. Mater. Sci.* 45 (1), 1–33. doi:10.1007/s10853-009-3874-0

Ghaderi, M., Mousavi, M., Yousefi, H., and Labbafi, M. (2014). All-cellulose Nanocomposite Film Made from Bagasse Cellulose Nanofibers for Food Packaging Application. *Carbohydr. Polym.* 104, 59–65. doi:10.1016/j.carbpol.2014.01.013

Holilah, H., Bahruji, H., Ediati, R., Asranudin, A., Jalil, A. A., Piluharto, B., et al. (2022). Uniform Rod and Spherical Nanocrystalline Celluloses from Hydrolysis of Industrial Pepper Waste (*Piper Nigrum* L.) Using Organic Acid and Inorganic Acid. *Int. J. Biol. Macromol.* 204, 593–605. doi:10.1016/j.ijbiomac.2022.02.045

Johar, N., Ahmad, I., and Dufresne, A. (2012). Extraction, Preparation and Characterization of Cellulose Fibres and Nanocrystals from Rice Husk. *Industrial Crops Prod.* 37 (1), 93–99. doi:10.1016/j.indcrop.2011.12.016

Johnson, R. K., Zink-Sharp, A., and Glasser, W. G. (2011). Preparation and Characterization of Hydrophobic Derivatives of TEMPO-Oxidized Nanocelluloses. *Cellulose* 18 (6), 1599–1609. doi:10.1007/s10570-011-9579-y

Kaushik, A., and Singh, M. (2011). Isolation and Characterization of Cellulose Nanofibrils from Wheat Straw Using Steam Explosion Coupled with High Shear Homogenization. *Carbohydr. Res.* 346 (1), 76–85. doi:10.1016/j.carres.2010.10.020

Khawas, P., Das, A. J., and Deka, S. C. (2016). Production of Renewable Cellulose Nanopaper from Culinary Banana (Musa ABB) Peel and its Characterization. *Industrial Crops Prod.* 86, 102–112. doi:10.1016/j.indcrop.2016.03.028

Khawas, P., and Deka, S. C. (2016). Isolation and Characterization of Cellulose Nanofibers from Culinary Banana Peel Using High-Intensity Ultrasonication Combined with Chemical Treatment. *Carbohydr. Polym.* 137, 608–616. doi:10.1016/j.carbpol.2015.11.020

Leite, A. L. M. P., Zanon, C. D., and Menegalli, F. C. (2017). Isolation and Characterization of Cellulose Nanofibers from Cassava Root Bagasse and Peelings. *Carbohydr. Polym.* 157, 962–970. doi:10.1016/j.carbpol.2016.10.048

Li, T.-F., Shen, C., Zhang, H.-X., Wang, X.-Q., Jiao, J., Wang, W., et al. (2018). Transesterification of Pistacia Chinensis Seed Oil Using a Porous Cellulose-Based Magnetic Heterogeneous Catalyst. *Int. J. Green Energy* 16 (3), 228–235. doi:10.1080/15435075.2018.1555759

Liu, Z., Li, X., Xie, W., and Deng, H. (2017). Extraction, Isolation and Characterization of Nanocrystalline Cellulose from Industrial Kelp (*Laminaria Japonica*) Waste. *Carbohydr. Polym.* 173, 353–359. doi:10.1016/j.carbpol.2017.05.079

Lu, H., Gui, Y., Zheng, L., and Liu, X. (2013). Morphological, Crystalline, Thermal and Physicochemical Properties of Cellulose Nanocrystals Obtained from Sweet Potato Residue. *Food Res. Int.* 50 (1), 121–128. doi:10.1016/j.foodres.2012.10.013

Luo, X., Wang, Q., Fang, D., Zhuang, W., Chen, C., Jiang, W., et al. (2018). Modification of Insoluble Dietary Fibers from Bamboo Shoot Shell: Structural Characterization and Functional Properties. *Int. J. Biol. Macromol.* 120 (Pt B), 1461–1467. doi:10.1016/j.ijbiomac.2018.09.149

Luo, X., Wang, Q., Zheng, B., Lin, L., Chen, B., Zheng, Y., et al. (2017). Hydration Properties and Binding Capacities of Dietary Fibers from Bamboo Shoot Shell and its Hypolipidemic Effects in Mice. *Food Chem. Toxicol.* 109, 1003–1009. doi:10.1016/j.fct.2017.02.029

Mandal, A., and Chakrabarty, D. (2011). Isolation of Nanocellulose from Waste Sugarcane Bagasse (SCB) and its Characterization. *Carbohydr. Polym.* 86 (3), 1291–1299. doi:10.1016/j.carbpol.2011.06.030

Marett, J., Aning, A., and Foster, E. J. (2017). The Isolation of Cellulose Nanocrystals from Pistachio Shells via Acid Hydrolysis. *Industrial Crops Prod.* 109, 869–874. doi:10.1016/j.indcrop.2017.09.039

Mariano, M., El Kissi, N., and Dufresne, A. (2014). Cellulose Nanocrystals and Related Nanocomposites: Review of Some Properties and Challenges. *J. Polym. Sci. Part B Polym. Phys.* 52 (12), 791–806. doi:10.1002/polb.23490

Martínez, R., Torres, P., Meneses, M. A., Figueroa, J. G., Pérez-Álvarez, J. A., and Viuda-Martos, M. (2012). Chemical, Technological and *In Vitro* Antioxidant Properties of Mango, Guava, Pineapple and Passion Fruit Dietary Fibre Concentrate. *Food Chem.* 135 (3), 1520–1526. doi:10.1016/j.foodchem.2012.05.057

Mishra, S., Kharkar, P. S., and Pethe, A. M. (2019). Biomass and Waste Materials as Potential Sources of Nanocrystalline Cellulose: Comparative Review of Preparation Methods (2016 - till Date). *Carbohydr. Polym.* 207, 418–427. doi:10.1016/j.carbpol.2018.12.004

Mu, R., Hong, X., Ni, Y., Li, Y., Pang, J., Wang, Q., et al. (2019). Recent Trends and Applications of Cellulose Nanocrystals in Food Industry. *Trends Food Sci. Technol.* 93, 136–144. doi:10.1016/j.tifs.2019.09.013

Nada, A. M. A., and Hassan, M. L. (2000). Thermal Behavior of Cellulose and Some Cellulose Derivatives. *Polym. Degrad. Stab.* 67 (1), 111–115. doi:10.1016/S0141-3910(99)00100-7

Park, E.-J., and Jhon, D.-Y. (2009). Effects of Bamboo Shoot Consumption on Lipid Profiles and Bowel Function in Healthy Young Women. *Nutrition* 25 (7–8), 723–728. doi:10.1016/j.nut.2009.01.007

Pelissari, F. M., Sobral, P. J. d. A., and Menegalli, F. C. (2013). Isolation and Characterization of Cellulose Nanofibers from Banana Peels. *Cellulose* 21 (1), 417–432. doi:10.1007/s10570-013-0138-6

Peng, P., and She, D. (2014). Isolation, Structural Characterization, and Potential Applications of Hemicelluloses from Bamboo: a Review. *Carbohydr. Polym.* 112, 701–720. doi:10.1016/j.carbpol.2014.06.068

Pereira, P. H. F., Waldron, K. W., Wilson, D. R., Cunha, A. P., Brito, E. S. d., Rodrigues, T. H. S., et al. (2017). Wheat Straw Hemicelluloses Added with Cellulose Nanocrystals and Citric Acid. Effect on Film Physical Properties. *Carbohydr. Polym.* 164, 317–324. doi:10.1016/j.carbpol.2017.02.019

Perumal, A. B., Nambiar, R. B., Moses, J. A., and Anandharamakrishnan, C. (2022). Nanocellulose: Recent Trends and Applications in the Food Industry. *Food Hydrocoll.* 127, 107484. doi:10.1016/j.foodhyd.2022.107484

Reshmy, R., Philip, E., Paul, S. A., Madhavan, A., Sindhu, R., Binod, P., et al. (2020). Nanocellulose-based Products for Sustainable Applications-Recent Trends and Possibilities. *Rev. Environ. Sci. Biotechnol.* 19 (4), 779–806. doi:10.1007/s11157-020-09551-z

Rohaizu, R., and Wanrosli, W. D. (2017). Sono-assisted TEMPO Oxidation of Oil Palm Lignocellulosic Biomass for Isolation of Nanocrystalline Cellulose. *Ultrason. Sonochemistry* 34, 631–639. doi:10.1016/j.ultsonch.2016.06.040

Sainorudin, M. H., Abdullah, N. A., Rani, M. S. A., Mohammad, M., Abd Kadir, N. H., Razali, H., et al. (2022). Investigation of the Structural, Thermal and Morphological Properties of Nanocellulose Synthesised from Pineapple Leaves and Sugarcane Bagasse. *Cnano* 18 (1), 68–77. doi:10.2174/1573413717666210216115609

Satya, S., Bal, L. M., Singhal, P., and Naik, S. N. (2010). Bamboo Shoot Processing: Food Quality and Safety Aspect (A Review). *Trends Food Sci. Technol.* 21 (4), 181–189. doi:10.1016/j.tifs.2009.11.002

Soni, B., Hassan, E. B., and Mahmoud, B. (2015). Chemical Isolation and Characterization of Different Cellulose Nanofibers from Cotton Stalks. *Carbohydr. Polym.* 134, 581–589. doi:10.1016/j.carbpol.2015.08.031

Travalini, A. P., Prestes, E., Pinheiro, L. A., and Demiate, I. M. (2017). Extraction and Characterization of Nanocrystalline Cellulose from Cassava Bagasse. *J. Polym. Environ.* 26 (2), 789–797. doi:10.1007/s10924-017-0983-8

Wang, L.-F., Shankar, S., and Rhim, J.-W. (2017). Properties of Alginate-Based Films Reinforced with Cellulose Fibers and Cellulose Nanowhiskers Isolated from Mulberry Pulp. *Food Hydrocoll.* 63, 201–208. doi:10.1016/j.foodhyd.2016.08.041

Winuprasith, T., and Suphantharika, M. (2013). Microfibrillated Cellulose from Mangosteen (Garcinia Mangostana L.) Rind: Preparation, Characterization, and Evaluation as an Emulsion Stabilizer. *Food Hydrocoll.* 32 (2), 383–394. doi:10.1016/j.foodhyd.2013.01.023

Yan, J., Hu, J., Yang, R., Zhang, Z., and Zhao, W. (2018). Innovative Nanofibrillated Cellulose from Rice Straw as Dietary Fiber for Enhanced Health Benefits Prepared by a Green and Scale Production Method. *ACS Sustain. Chem. Eng.* 6 (3), 3481–3492. doi:10.1021/acssuschemeng.7b03765

Yu, M., Yang, R., Huang, L., Cao, X., Yang, F., and Liu, D. (2012). Preparation and Characterization of Bamboo Nanocrystalline Cellulose. *Bioresources* 7 (2), 1802–1812. doi:10.15376/biores.7.2.1802-1812

Zhang, J.-G., Li, Q.-L., and Wei, Z.-J. (2017a). Degradation of Bamboo-Shoot Shell Powder by a Fungal Consortium: Changes in Chemical Composition and Physical Structure. *Int. Biodeterior. Biodegrad.* 116, 205–210. doi:10.1016/j.ibiod.2016.11.002

Zhang, J.-G., Li, Q.-M., Thakur, K., Faisal, S., and Wei, Z.-J. (2017b). A Possible Water-Soluble Inducer for Synthesis of Cellulase in Aspergillus niger. *Bioresour. Technol.* 226, 262–266. doi:10.1016/j.biortech.2016.12.028

Synthesis and Biological Activity Evaluation of 2-Cyanopyrrole Derivatives as Potential Tyrosinase Inhibitors

Ya-Guang Hu[1†], Zhu-Peng Gao[1†], Ying-Ying Zheng[2], Chun-Mei Hu[2], Jing Lin[2], Xiao-Zheng Wu[2], Xin Zhang[2], Yong-Sheng Zhou[3], Zhuang Xiong[2*] and Dao-Yong Zhu[1*]

[1]School of Pharmacy and State Key Laboratory of Applied Organic Chemistry, Lanzhou University, Lanzhou, China, [2]School of Biotechnology and Health Sciences, Wuyi University, Jiangmen, China, [3]Guangzhou Yuming Biologival Technology Co, LTD, Guangzhou, China

In order to find potential inhibitors of tyrosinase, two series of pyrrole derivatives A (1–17) and B (1–8) were synthesized and screened for their inhibitory activities on tyrosinase. Most of the 2-cyanopyrrole derivatives exhibited effective inhibitory activities. In particular, A12 exhibited the strongest inhibitory activities, with the IC_{50} values of 0.97 μM, which is ~30 times stronger than the reference inhibitor kojic acid (IC_{50}: 28.72 μM). The inhibitory mechanism analysis results revealed that A12 was a reversible and mixed-type inhibitor. Molecular docking experiments clarified the interaction between A12 with tyrosinase. Furthermore, A12 (100 μM) presented effective inhibitory effect on tyrosinase in B16 melanoma cells with inhibition of 33.48%, which was equivalent to that of Kojic acid (39.81%). Accordingly, compound A12 may serve as the lead structure for the further design of potent tyrosinase inhibitors. Molecular docking studies confirmed the interaction between the compound and tyrosinase.

Keywords: tyrosinase, reversible inhibitor, mixed-type inhibitor, 2-cyanopyrrole, molecular docking

INTRODUCTION

The browning of food including fruits, vegetables, and beverages seriously threats the development of agriculture and the food industry (Chai et al., 2018). Recently, quality loss of food during postharvest handling and processing occur frequently in the food industry (Zhu et al., 2011). The recognized mechanism of the corresponding browning includes two types of procedures, namely, enzymatic and non-enzymatic browning (Todaro et al., 2011). Tyrosinase, a metalloenzyme containing dinuclear copper ions, is one of the key catalytic proteins in the process of enzymatic browning (Liu et al., 2012; Asthana et al., 2015; Chai et al., 2015; Xie et al., 2016). It is widely distributed in animals, insects, plants, and microorganisms and is a rate-limiting enzyme involved in two-step oxidation reactions including mono phenols into diphenols and o-diphenols into o-quinones, followed by further transformations into dark brown pigments (Ullah et al., 2016; Cai et al., 2019; Ielo et al., 2019; Zolghadri et al., 2019). For plant-derived foods, enzymatic browning would result in abnormal variations of color, flavor, and nutritional quality (Larik et al., 2017). In addition, it has been believed that excessively active tyrosinase leads to the accumulation of melanin in the human skin, which results in various common skin diseases, such as freckles, melasma, and melanosis (Ullah et al., 2019a; Ullah et al., 2019b; Butt et al., 2019; Haldys and Latajka, 2019; Huang et al., 2019; Lee et al., 2019). In the

biosynthesis pathway of melanin, tyrosinase oxidizes L-tyrosine into L-3,4-dihydroxyphenylalanine (L-DOPA), and L-DOPA into o-quinones (Akın et al., 2019; Ashooriha et al., 2019; Santi et al., 2019). Tyrosinase is also proven to be related to Parkinson's and other neurodegenerative diseases (Ali et al., 2019). Moreover, tyrosinase plays a key role in the processes of cuticle formation in insects (Yu, 2003). Hence, developing tyrosinase inhibitors is very important in the agriculture and food industry, medicine, and cosmetic products.

Although hundreds of tyrosinase inhibitors have been obtained in the laboratory, only a few are sufficiently potent for practical use, such as arbutin, kojic acid, and ascorbic acid (Demirkiran et al., 2013; Crespo et al., 2019; Rodriguez et al., 2020; Wang et al., 2020). However, they still exhibit the defect of undesirable side effects, including cytotoxicity, dermatitis, and neurodegenerative disorders. Therefore, it is extremely urgent to develop alternatively safe and effective tyrosinase inhibitors.

Pyrrole, aromatic five-membered heterocyclic compounds containing nitrogen, have gotten increased attention due to their extensive biological, agrochemical, and pharmaceutical activities, as well as reactivity and stability (Deibl et al., 2015; Liao et al., 2015; Qin et al., 2015). Moreover, heterocyclic compounds containing nitrogen exhibit good water solubility and salt formation ability. Until now, more and more biologically active molecules were designed based on the pyrrole skeleton (Insuasty et al., 2010; Jamwal et al., 2013; Kumar et al., 2013; Ansari et al., 2017). Also, for searching tyrosinase inhibitors, N-heterocycle derivatives have received much attention.

Recently, we have reported some efficient synthetic methodologies of N-heterocycles, which are the key skeleton of many bioactive molecules (Mou et al., 2016; Zhang et al., 2017). As the systematic continuation of aforementioned research results, we synthesized two series of pyrrole derivatives and screened their tyrosinase inhibitory activity.

MATERIALS AND METHODS

Materials

Mushroom tyrosinase (EC 1.14.18.1), L-3,4-dihydroxy phenylalanine (L-DOPA), and kojic acid were obtained from Sigma (St. Louis, MO, United States). Dimethyl sulfoxide (DMSO) of molecular biological grade was purchased from J&K Chemical Co., Ltd. (Shanghai, China). Fetal bovine serum (FBS) and Dulbecco's Modified Eagle's Medium (DMEM) were obtained from Gibco (Grand Island, NY, United States). The 3-(4,5-Dimethythiazol-2-yl)-2,5-diphenyl-tetra-zoliumbromide (MTT) dye was supplied by Sigma-Aldrich (St. Louis, MO, United States). All other reagents were of analytical grade.

Instruments

^{1}H and ^{13}C NMR spectra were recorded in CDCl$_3$ on 400/300 MHz instruments, and spectral data were reported in ppm. High-resolution mass spectral analysis (HRMS) data were measured on Apex II by means of the ESI technique.

Synthesis of 2-Cyanopyrrole Derivatives A (1–17)

2-Cyanopyrrole derivatives A (1–17) were synthesized according to our previous article (Mou et al., 2016).

The general synthetic procedure for derivative A (1–12) is as follows. To a stirred mixture of aromatic olefin or alkyne (0.5 mmol, 1 equiv), DMF (15 equiv), TMSCN (trimethylsilanecarbonitrile, 5 equiv), and Cu(OTf)$_2$ (0.2 equiv), was added DDQ (2 equiv) through a batch-wise mode (the first equiv was added 0.2 equiv/2 h for 5 times, and the second equiv of DDQ was then introduced at once) at 80°C under an argon atmosphere. Then, the reaction mixture was stirred for an additional 14 h. Upon the completion of the reaction (monitored by TLC), the mixture was quenched by the addition of water. The aqueous layer was extracted three times with EtOAc, and the combined organic layers were washed with brine, dried over sodium sulfate, evaporated to dryness, and purified by column chromatography to afford desired products A (1–12).

The general synthetic procedure for derivative A (13–17) is as follows. To a mixed solvent of n-heptane and N,N-diethylacetamide (v/v = 6:1, 1 ml), aromatic olefin (0.5 mmol, 1 equiv), N,N-disubstituted formamide (3 equiv), TMSCN (6 equiv), and Cu(OTf)$_2$ (0.2 equiv) were successively added at 80°C under an argon atmosphere. Next, DDQ was added through a batch-wise mode (the first equiv was added 0.2 equiv/2 h five times, and the second equiv of DDQ was then introduced at once) at the same temperature. The reaction mixture was refluxed for an additional 14 h. Upon completion of the reaction (monitored by TLC), the reaction mixture was quenched by the addition of water. The aqueous layer was extracted three times with EtOAc, and the combined organic layers were washed with brine, dried over sodium sulfate, evaporated to dryness, and purified by column chromatography to afford desired products A (13–17).

Synthesis of N-Heterocycle Derivatives B (1–8)

The general synthetic procedure for derivative B (1–2) is as follows. To a stirred mixture of A5 or A6 (1 mmol) in DMSO (10 ml), K$_2$CO$_3$ (2 mmol) and hydrogen peroxide (30% aqueous, 30 ml) were added. The mixture was stirred at room temperature for 8 h. When the substrate was completely disappeared (monitored by TLC), the reaction mixture was extracted with ether and dichloromethane (2: 1) three times. The combined organic layers were washed with saturated brine (50 ml), dried over sodium sulfate, filtered, and concentrated in vacuo. The residue was purified by column chromatography to give B (1–2).

The general synthetic procedure for derivative B (3–8) is as follows. To a stirred mixture of A6, A3, A5, A1, A9, or A2 (1 mmol) in ether (10 ml), lithium aluminum tetrahydride (1.2 mmol) was added slowly at 0°C. Then, the mixture was stirred at reflux for 3 h and quenched with water (10 ml). The mixture was extracted with ether three times. The combined organic layers were washed with brine (50 ml), dried over magnesium sulfate, and concentrated in vacuo to give crude primary amine 2. Then, the crude primary

amine 2 (1 mmol), (Boc)$_2$O (1.3 mmol), and Et$_3$N (5 mmol) were added into methanol (10 ml) and refluxed for 20 min. The mixture was quenched with saturated aqueous ammonium chloride solution and extracted with diethyl ether three times. The combined organic layers were washed with brine (50 ml), dried over magnesium sulfate, and concentrated in vacuo. The crude residue was purified by column chromatography to afford B (3–8).

3-(3-Bromophenyl)-1-methyl-1H-pyrrole-2-carboxamide (B1). Amorphous solid; 39% yield; ^{1}H NMR (400 MHz, CDCl$_3$) δ 7.53–7.52 (m, 1H), 7.52–7.49 (m, 1H), 7.31–7.30 (m, 1H), 7.29–7.28 (m, 1H), 6.74 (d, J = 2.4 Hz, 1H), 6.09 (d, J = 2.4 Hz, 1H), 5.43–5.29 (m, 2H), 3.93 (s, 3H); ^{13}C NMR (100 MHz, CDCl$_3$) δ 163.45, 134.99, 131.81, 131.07, 127.98, 127.14, 121.46, 109.32, 109.28, 98.48, 37.31, and 37.27; HRMS (ESI) calcd for C$_{12}$H$_{11}$BrN$_2$O [M + H]$^+$: 279.0128, found 279.0124.

3-(4-Bromophenyl)-1-methyl-1H-pyrrole-2-carboxamide (B2). White solid; mp 172–174°C; 33% yield; ^{1}H NMR (400 MHz, CDCl$_3$) δ 7.52 (d, J = 8.4 Hz, 2H), 7.30 (d, J = 8.4 Hz, 2H), 6.73 (d, J = 2.4 Hz, 1H), 6.09 (d, J = 2.4 Hz, 2H), 5.48 (d, J = 9.6 Hz, 2H), 3.92 (s, 3H); ^{13}C NMR (100 MHz, CDCl$_3$) δ 163.52, 134.94, 131.79, 131.06, 127.95, 127.13, 121.44, 109.28, and 37.31; HRMS (ESI) calcd for C$_{12}$H$_{11}$BrN$_2$O [M + H]$^+$:279.0128, found 279.0123.

tert-Butyl ((3-(4-bromophenyl)-1-methyl-1H-pyrrol-2-yl)methyl)carbamate (B3). White solid; mp 109–113°C; 29% yield; ^{1}H NMR (400 MHz, CDCl$_3$) δ 7.48 (d, J = 8.4 Hz, 2H), 7.19 (d, J = 8.4 Hz, 2H), 6.64 (d, J = 2.4 Hz, 1H), 6.19 (d, J = 2.8 Hz, 1H), 4.59 (s, 1H), 4.39 (d, J = 5.2 Hz, 2H), 3.65 (s, 3H), and 1.46 (s, 9H); ^{13}C NMR (100 MHz, CDCl$_3$) δ 155.25, 135.28, 131.54, 129.55, 125.03, 123.82, 122.73, 119.67, 107.40, 79.65, 34.57, 34.10, and 28.33; HRMS (ESI) calcd for C$_{17}$H$_{21}$BrN$_2$O$_2$ [M + H]$^+$: 365.0859, found 365.0853.

tert-Butyl ((3-(3-fluorophenyl)-1-methyl-1H-pyrrol-2-yl)methyl)carbamate (B4). White solid; mp 103–104°C; 44% yield; ^{1}H NMR (400 MHz, CDCl$_3$) δ 7.35–7.29 (m, 1H), 7.10–7.08 (m, 1H), 6.95–6.91 (m, 1H), 6.64 (d, J = 2.4 Hz, 1H), 6.21 (d, J = 2.4 Hz, 1H), 4.63 (s, 1H), 4.42–4.41 (m, 2H), 3.66 (s, 3H), and 1.47 (s, 9H); ^{13}C NMR (100 MHz,CDCl$_3$) δ 162.93 (d, J = 243 Hz), 155.28, 138.62 (d, J = 7.9 Hz), 129.85 (d, J = 8.6 Hz), 125.19, 123.89, 123.53, 122.71, 114.68 (d, J = 21.4 Hz), 112.54 (d, J = 21 Hz), 107.50, 79.64, 34.55, 34.07, and 28.32; HRMS (ESI) calcd for C$_{17}$H$_{21}$FN$_2$O$_2$ [M + Na]$^+$: 327.1479, found 324.1472.

tert-Butyl ((3-(3-bromophenyl)-1-methyl-1H-pyrrol-2-yl)methyl)carbamate (B5). White solid; mp 124–127°C; 40% yield; ^{1}H NMR (400 MHz, CDCl$_3$) δ 7.46 (s, 1H), 7.35–7.32 (m, 1H), 7.23–7.20 (m, 2H), 6.61 (d, J = 2.8 Hz, 1H), 6.17 (d, J = 2.8 Hz, 1H), 4.59 (s, 1H), 4.37 (d, J = 5.2 Hz, 2H), 3.62 (s, 3H), and 1.44 (s, 9H); ^{13}C NMR (100 MHz, CDCl$_3$) δ 155.25, 138.53, 130.89, 129.94, 128.70, 126.49, 125.23, 123.57, 122.75, 122.54, 107.50, 79.65, 34.52, 34.09, and 28.33; HRMS (ESI) calcd for C$_{17}$H$_{21}$BrN$_2$O$_2$ [M + H]$^+$: 365.0859, found 365.0857.

tert-Butyl ((1-methyl-3-phenyl-1H-pyrrol-2-yl)methyl) carbamate (B6). White solid; mp 87–90°C; 46% yield; ^{1}H NMR (400 MHz, CDCl$_3$) δ 7.37–7.30 (m, 4H), 7.24–7.20 (m, 1H), 6.61 (d, J = 2.4 Hz, 1H), 6.20 (d, J = 2.4 Hz, 1H), 4.67 (s, 1H), 4.40 (d, J = 4.8 Hz, 2H), 3.62 (s, 3H), and 1.45 (s, 9H); ^{13}C NMR (100 MHz,CDCl$_3$) δ 155.26, 136.30, 128.41, 127.98, 125.73,

124.92, 122.43, 107.46, 79.40, 34.56, 33.91, and 28.24; HRMS (ESI) calcd for C$_{17}$H$_{22}$N$_2$O$_2$ [M + H]$^+$: 287.1754, found 287.1750.

tert-Butyl ((1-methyl-3-(4-(trifluoromethyl)phenyl)-1H-pyrrol-2-yl)methyl)carbamate (B7). White solid; mp 120–122°C; 37% yield; ^{1}H NMR (400 MHz, CDCl$_3$) δ 7.62 (d, J = 8 Hz, 2H), 7.43 (d, J = 8.0 Hz, 2H), 6.67 (d, J = 2.8 Hz, 1H), 6.25 (d, J = 2.8 Hz, 1H), 4.66 (s, 1H), 4.42 (d, J = 4.8 Hz, 2H), 3.68 (s, 3H), and 1.47 (s, 9H); ^{13}C NMR (100 MHz,CDCl$_3$) δ 155.27, 140.06, 127.99, 127.74 (q, J = 32.3 Hz), 125.56, 125.43 (q, J = 3.8 Hz), 124.41 (q, J = 270 Hz), 123.70, 122.98, 107.63, 79.75, 34.64, 34.12, and 28.34; HRMS (ESI) calcd for C$_{18}$H$_{21}$F$_3$N$_2$O$_2$ [M + H]$^+$: 355.1628, found 355.1623.

tert-Butyl ((3-(2-fluorophenyl)-1-methyl-1H-pyrrol-2-yl) methyl)carbamate (B8). White solid; mp 81–84°C; 39% yield; ^{1}H NMR (400 MHz, CDCl$_3$) δ 7.31–7.27 (m, 1H), 7.25–7.21 (m, 1H), 7.17–7.08 (m, 2H), 6.68 (d, J = 2.4 Hz, 1H), 6.17 (d, J = 2.8 Hz, 1H), 4.81 (s, 1H), 4.29 (d, J = 5.6 Hz, 2H), 3.68 (s, 3H), and 1.45 (s, 9H); ^{13}C NMR (100 MHz, CDCl$_3$) δ 159.50 (d, J = 241.7 Hz), 155.45, 131.63 (d, J = 3.7 Hz), 127.78 (d, J = 8.3 Hz), 126.72, 124.19 (d, J = 3.5 Hz), 124.05 (d, J = 15.3 Hz), 122.71, 117.68, 115.60 (d, J = 23.3 Hz), 108.39, 79.36, 34.81, 34.21, and 28.35; HRMS (ESI) calcd for C$_{17}$H$_{21}$FN$_2$O$_2$ [M + H]$^+$: 305.1660, found 305.1657.

Tyrosinase Inhibitory Assay

The mushroom tyrosinase activity assays of synthetic compounds were carried out according to the previously reported modification (Qin et al., 2015). L-DOPA was used as the substrate. Briefly, 800 μl of phosphate buffer (50 mM, pH 6.8), 50 μl of mushroom tyrosinase (666.67 U/ml, dissolved in PBS), and 50 μl of inhibitor (dissolved in DMSO) were placed in the plastic centrifuge tube. Then, 100 μl of L-DOPA (5 mM, dissolved in PBS) was added. Subsequently, its change in absorbance at 475 nm was measured in a time-dependent manner using a Beckman UV-650 spectrophotometer. The percentage inhibition was calculated by using [(OD$_0$ - OD$_1$)/OD$_0$] × 100%, where OD$_0$ was the absorbance without inhibitor, and OD$_1$ was the absorbance with the inhibitor. The IC$_{50}$ value of the potential compound was calculated from dose-response curves of percentage inhibition. Kojic acid was used as a standard control for comparison. All experiments were performed in duplicate.

Inhibition Mechanism and Kinetic Analysis

Experiments were performed to analyze the inhibitory mechanism by the following method. For the text, the mushroom tyrosinase at a final concentration of 16.67–100.00 U/ml and L-DOPA at a final concentration of 0.5 mM were chosen. Then, the mushroom tyrosinase activity was measured in the presence of the inhibitor.

The inhibition type of the inhibitor on mushroom tyrosinase was evaluated by the Lineweaver–Burk plot, and the inhibition constants were obtained from the second plots of the apparent 1/V$_{max}$ and K$_m$/V$_{max}$ against the inhibitor concentration. In this assay, mushroom tyrosinase at a final concentration of 33.33 U/ml and L-DOPA at a final concentration of 0.25–2 mM were used. The equation for the Lineweaver–Burk plot can be written as follows:
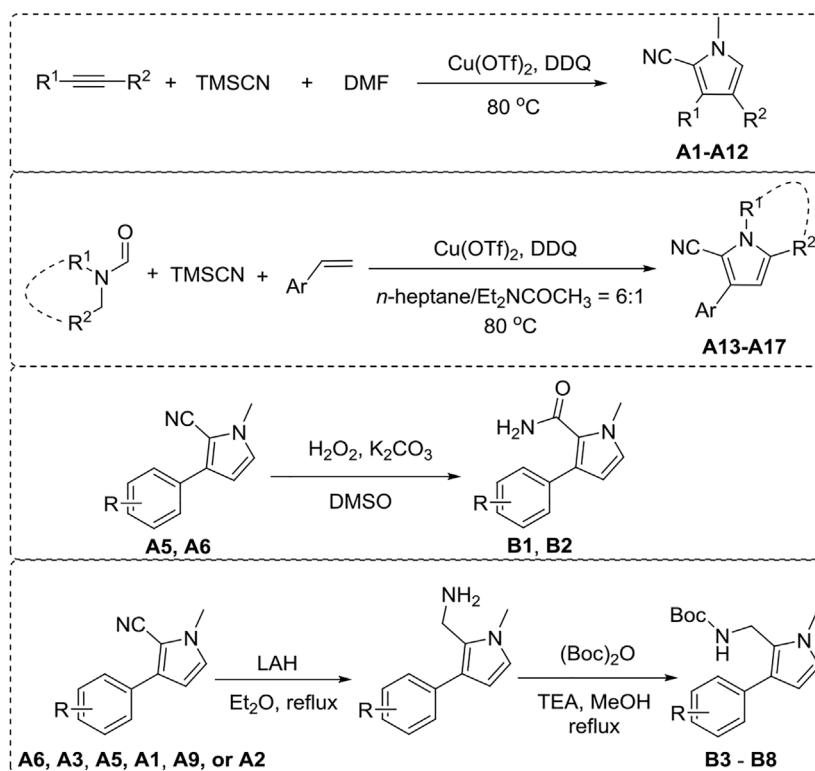
Scheme 1 | General synthesis of A (1–17) and B (1–8).

$$\frac{1}{v} - \frac{K_m}{V_m}\left(1 + \frac{[I]}{K_I}\right) + \frac{1}{V_m}\left(1 + \frac{[I]}{K_{IS}}\right)$$

where v is the reaction velocity, K_m is the Michaelis constant, V_m is the maximal velocity, [I] is the concentration of the inhibitor, [S] is the concentration of the substrate, K_I is the constant for the inhibitor binding with the free enzyme, and K_{IS} is the constant for the inhibitor binding with the enzyme-substrate complex. K_I and K_{IS} were obtained from the slope or the vertical intercept vs. the inhibitor concentration, respectively.

Molecular Docking Study

Sybyl 2.1.1 (Tripos, United States) was used for the docking simulations between mushroom tyrosinase and the inhibitor. First, compound A12 was prepared by the energy minimization using the MM2 program, with energy termination of 0.01 kcal/mol, iteration of 1,000 times, and charges of Gasteiger-Hückle. Second, the crystal structure of mushroom tyrosinase (PDB ID: 2Y9X) was prepared by extracting ligands, removing H_2O, termini treatment, and adding hydrogens. The active pocket of tyrosinase was generated using the ligand mode. Finally, the docking simulation between tyrosinase and compound A12 was carried out in the default format. PyMOL software was used to draw the view based on the Sybyl results.

Cell Culture

B16 mouse melanoma cells were cultured in Dulbecco's modified Eagle's medium (DMEM) containing 10% fetal bovine serum and 1% penicillin/streptomycin at 37°C in a 5% CO_2 incubator.

MTT Assay

B16 cells (100 µl) were plated in a 96-well plate (5×10^3 cells/well) for 24 h and then treated with a 100 µl complete medium containing A12 or kojic acid for 24 h. MTT solution (0.5 mg/ml, final concentration) was added to each well, and plates were incubated at 37°C for another 3 h. The absorbance was measured at 490 nm using a multi-detection microplate reader.

Cellular Tyrosinase Activity
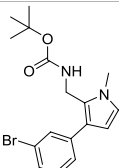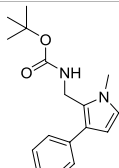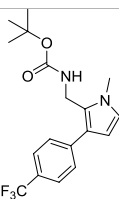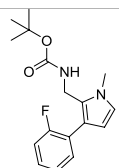
The inhibitory activity of A12 on tyrosinase in B16 cells was evaluated. B16 cells (5×10^4 cells/well) were plated in 96-well plates and incubated for 24 h. A measure of 100 µl of complete medium including A12 or kojic acid was added for further incubation of 48 h. Then, cells were added to 50 µl Triton X-100 (1%) and allowed for freezing for 1 h at −80°C. After thawing at room temperature, 10 µl L-DOPA solutions (0.1%, w/v) were added and co-incubated for 1 h at 37°C. The absorbance at 405 nm was measured.

TABLE 1 | Inhibitory activity of N-heterocycle derivatives on tyrosinase.

Compound	Structure	IC$_{50}$ (μM)	Compound	Structure	IC$_{50}$ (μM)
A1		7.42	A2		8.72
A3		21.43	A4		8.47
A5		16.52	A6		8.17
A7		23.57	A8		89.15
A9		12.44	A10		4.83
A11		2.11	A12		0.97
A13		4.46	A14		80.46
A15		87.32	A16		5.06
A17		5.57			
B1		>200	B2		>200
B3		>200	B4		>200

(Continued on following page)

TABLE 1 | (*Continued*) Inhibitory activity of N-heterocycle derivatives on tyrosinase.

Compound	Structure	IC$_{50}$ (µM)	Compound	Structure	IC$_{50}$ (µM)
B5		>200	B6		>200
B7		>200	B8		>200
Kojic acid		28.72			

FIGURE 1 | Plots of ν vs. [E] and the Lineweavere–Burk plot of compound A12 (concentrations: (a) 0, (b) 0.75, (c) 1 µM, and (d) 1.5 µM).

FIGURE 2 | Representative tyrosinase inhibitors.
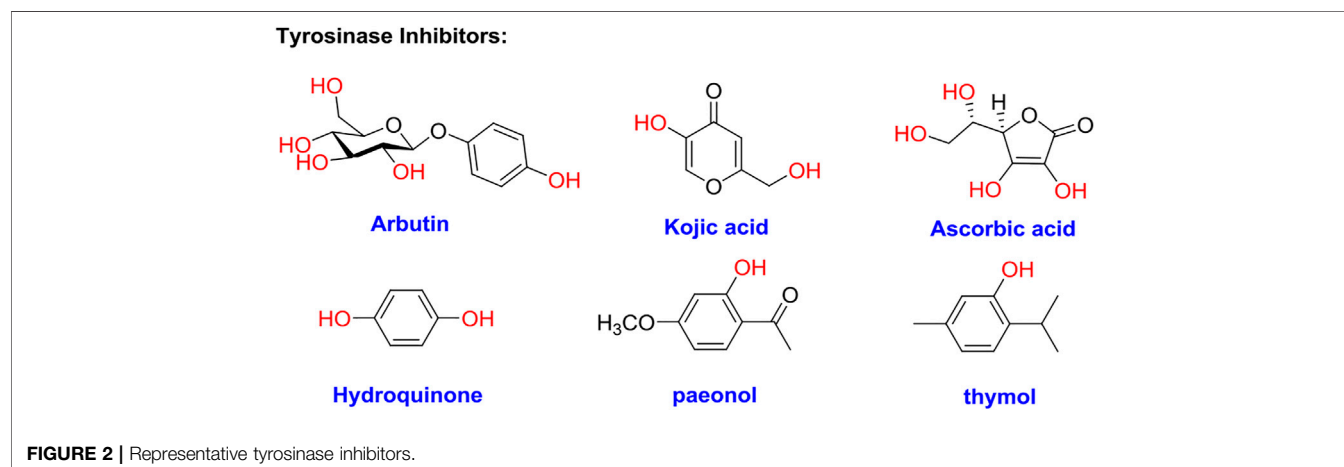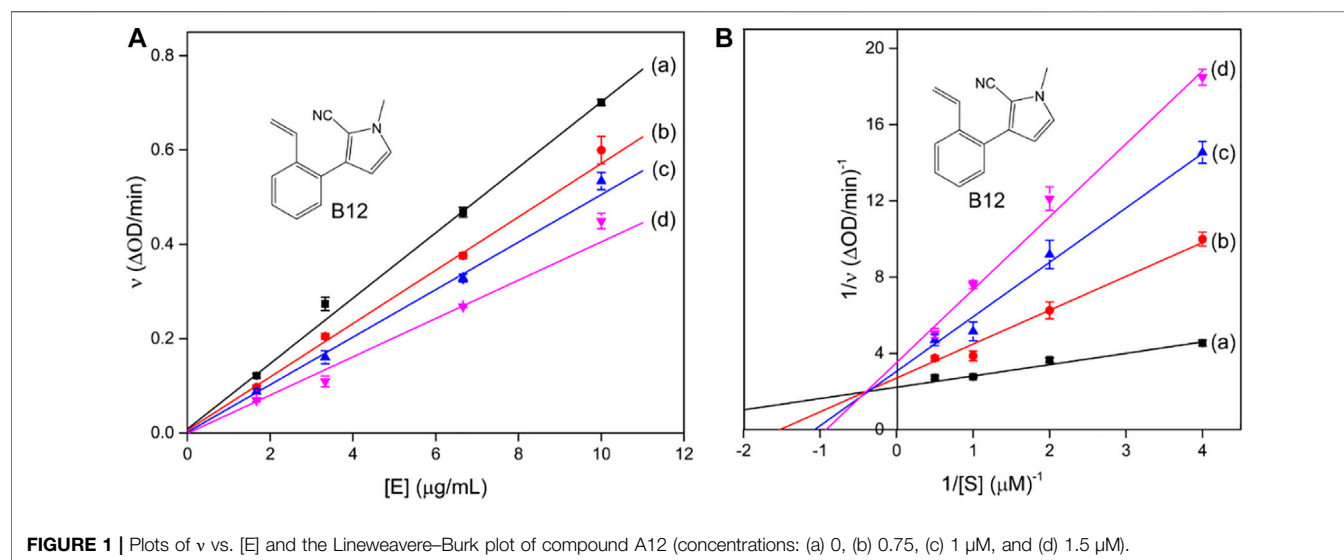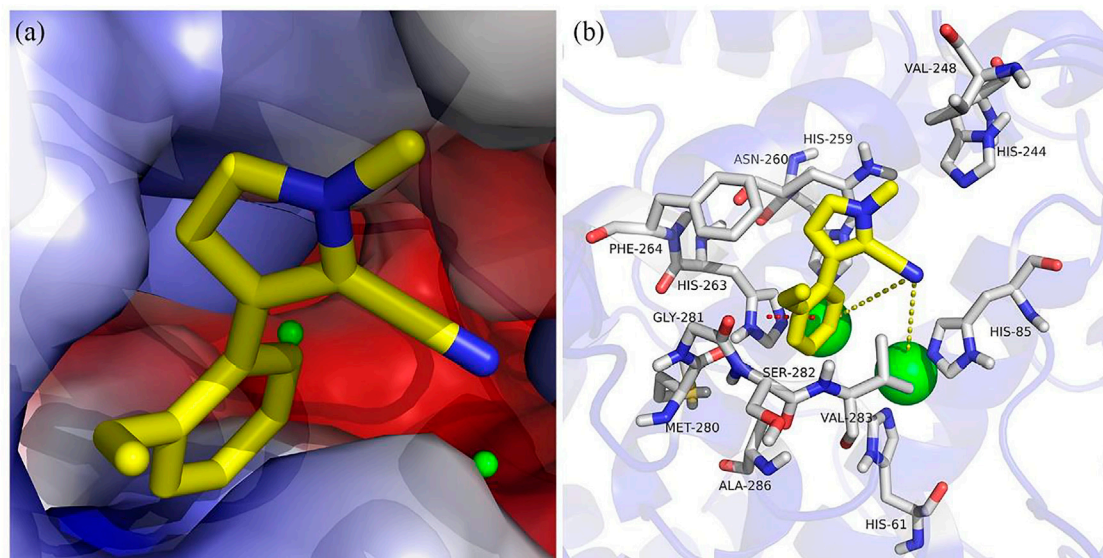
FIGURE 3 | Molecular docking of compound A12 with tyrosinase: (A) in the active pocket; (B) interactions with amino acid residues.
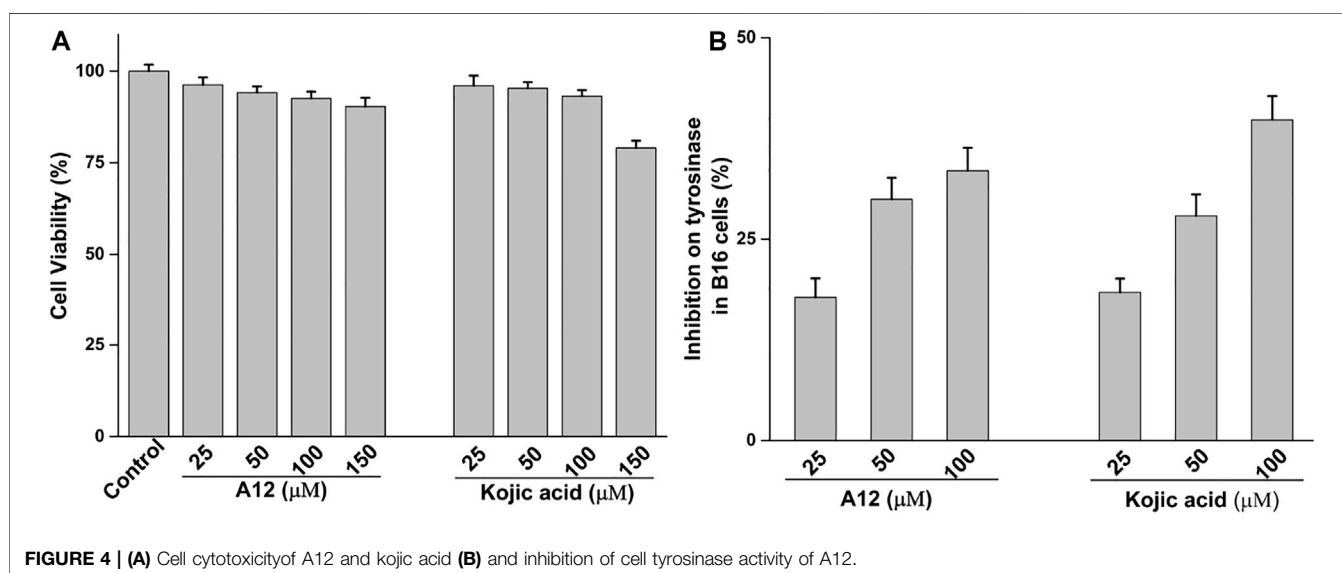
FIGURE 4 | (A) Cell cytotoxicity of A12 and kojic acid (B) and inhibition of cell tyrosinase activity of A12.

RESULTS AND DISCUSSION

Chemistry

Pyrrole derivatives A (1–17) and B (1–8) were synthesized according to the synthetic route shown in **Scheme 1**. A1–A12 were obtained using aromatic olefin or alkyne, DMF, and TMSCN as starting materials under the catalysis of Cu(OTf)$_2$ and DDQ. A (13–17) were synthesized from aromatic olefin, N,N-disubstituted formamide, and TMSCN with Cu(OTf)$_2$ as the catalyst and DDQ as additive. B 1–2 could be synthesized from compound A5 or A6 through a hydrolysis reaction. Meanwhile, the reduction of compounds A6, A3, A5, A1, A9, or A2 by LAH with subsequent amine derivatization

by (Boc)$_2$O would produce B (3–8). ^{1}H NMR, ^{13}C NMR, and HRMS were applied to confirm their structures.

Tyrosinase Inhibitory Activity Assay and SAR Analysis

Tyrosinase inhibitory assay of all synthesized pyrrole derivatives A (1–17) and B (1–8) was performed using L-DOPA as the substrate. As shown in **Table 1**, compounds A (1–17) exhibited moderate to excellent inhibitory activities against tyrosinase, with IC$_{50}$ values ranging from 0.97 to 89.15 µM. In particular, A12 (IC$_{50}$ = 0.97 µM) showed the strongest inhibitory

activities, which were ~30 times stronger than the reference inhibitor kojic acid (IC_{50} = 28.72 µM).

Based on the data displayed in **Table 1**, the SAR of the tested compounds against tyrosinase was analyzed. For compounds A (1–17), compound A1 (IC_{50} = 7.24 µM) with no substitute group was selected as the template compound. It was clear that the introduction of a substituent on the phenyl ring at the 3-position of the pyrrole skeleton did show the clear influence of the corresponding inhibition potency. Among them, compound A2 with the 2-fluorine group on the benzene ring (IC_{50} = 8.72 µM), A3 with the 3-fluorine group (IC_{50} = 21.43 µM), A4 with the 2-bromine group (IC_{50} = 8.47 µM), A5 with the 3-bromine group (IC_{50} = 16.52 µM), A6 with the 4-bromine group (IC_{50} = 8.17 µM), A7 with the 2-methoxy group (IC_{50} = 23.57 µM), A8 with the 4-methoxy group (IC_{50} = 89.15 µM), and A9 with the 4-trifluoromethyl group (IC_{50} = 12.44 µM) all presented lower inhibitory activities than compound A1. These results indicated that the introduction of fluorine, bromine, methoxy and trifluoromethyl alone might cause a decrease in tyrosinase inhibitory activity. In contrast, two compounds A10 and A11 with dual substituents on the benzene ring provided better inhibitory results than compound A1 and showed an IC_{50} value of 4.83 and 2.11 µM, respectively. Moreover, A12 with a 2-vinyl group on the benzene ring (IC_{50} = 0.97 µM) also appeared to have much higher inhibitory activities than compound A1. This result revealed the special property of the 2-vinyl group during the interaction between A12 and tyrosinase. As for the substituent on the 1- and 5-positions of the pyrrole ring, additional five compounds A (13–17) were further tested. Based on the results, it is obvious that the presence of an untethered benzyl at 1-position (A14) or the phenyl group at 5-position (A15) would dramatically affect the inhibitory activities. On the contrary, A13 with the ethyl group on nitrogen of the pyrrole ring (IC_{50} = 4.46 µM), A16, and A17 with the pyrrole as a part of a fused ring system showed higher inhibitory activities (IC_{50} = 5.06 and 5.57 µM, respectively) than compound A1, which revealed that the alkyl group at 1-position or a planar type of the molecule might increase the inhibitory activity against tyrosinase. Therefore, based on the previous SAR results of all compounds, further derivatization of A1 with other ring systems at 3-position of the pyrrole ring or other fused ring systems will be designed and screened.

For investigating the effect of the cyano group on the inhibitory activities, it was transformed into an amide group (B1, B2) or carbamate group (B3 ~ 8), and the inhibitory activities of corresponding derivatives were obviously reduced. These results indicated that the cyano group of compounds A1-A17 was crucial for tyrosinase inhibition.

Inhibition Mechanism

Compound A12 with the best inhibition activity was selected as the lead compound to ascertain the inhibition mechanism of mushroom tyrosinase. **Figure 1A** shows the plots of initial velocity vs. tyrosinase concentrations at different concentrations of compound A12. As can be seen, the plots gave a family of straight lines, respectively, which

passed through the origin point. Moreover, the slopes of the lines extended a descent with the increase of concentrations of compound A12. These results revealed that the presence of compound A12 did not bring down the amount of active enzyme but just resulted in the reduction of the enzyme activity. Hence, the tyrosinase inhibition of compound A12 was reversible.

To further explore the inhibition kinetic behavior of the most promising compound A12 on mushroom tyrosinase, the tyrosinase activity was determined under different concentrations of L-DOPA in the presence or absence of an inhibitor. The results were analyzed using Lineweaver–Burk double reciprocal plots. For compound A12 (**Figure 2B**), the results presented that the plots of 1/ν vs. 1/[S] gave straight lines with different slopes intersecting one another in the second quadrant. The values of V_m and K_m all descended with the increase in concentration of A12, which suggested that compound A12 induced mixed-type inhibition of mushroom tyrosinase. In other words, compound A12 could bind with both free enzyme and the enzyme-substrate complex, which was similar to the inhibition type of kojic acid. Hence, we determined the equilibrium constant for inhibitor binding with free enzyme (K_I) and the enzyme-substrate complex (K_{IS}) through the second plots of the apparent K_m/V_{max} and $1/V_{max}$ vs. inhibitor concentrations. The K_I and K_{IS} values of the compound A12 were calculated as 1.11 and 1.00 µM.

Molecular Docking

To better understand the inhibitory activity of compound A12, Sybyl and PyMOL software were conducted to understand the interaction pattern between the A12 and the active site of tyrosinase. Mushroom tyrosinase (PDB: 2Y9X) from the RCSB Protein Data Bank was selected as the target protein for simulation. The docking simulation results showed that A12 was well accommodated and bound in the active pocket of tyrosinase (**Figure 3A**) and had in-depth interactions with the active site residues (**Figure 3B**). The cyano group of A12 resided adjacent to the dicopper nucleus, indicating that there was a potential metal-ligand interaction, which was considered to be one of the key interactions between tyrosinase and the ligand compound. The pyrrole ring formed a π-π interaction with His263. Furthermore, A12 formed hydrophobic interactions with Ala286, Asn260, Gly281, His244, His259, Met280, Phe264, Ser282, Val248, and Val283.

Effect of Compound A12 on Cellular Tyrosinase Activity

For evaluating the effect of compound A12 on cellular tyrosinase activity, its cell cytotoxicity was first tested. The results showed that compound A12 and kojic acid showed no cytotoxicity on B16 melanoma cells under a concentration of 100 µM (**Figure 4A**). Thence, the concentration of A12 (under 100 µM) was selected for the assay of the cellular tyrosinase activity. A12 could effectively inhibit the tyrosinase activity in B16 melanoma cells in a dose-dependent manner (**Figure 4B**) and present an effective

inhibitory of 33.48% at a concentration of 100 μM, which was equivalent to that of Kojic acid (39.81%).

CONCLUSION

To conclude, the inhibitory activities of two series of pyrrole derivatives A (1–17) and B (1–8) were screened against tyrosinase. Compound A12 showed the highest inhibition activity with reversible and mixed-type inhibition types. Compound A12 (IC_{50}: 0.97 μM) showed ~30 times stronger inhibition activity than the reference inhibitor kojic acid (IC_{50}: 28.72 μM). Molecular docking studies showed that the metal–ligand interaction, π-π interaction, and hydrophobic interactions played important roles in the interaction between tyrosinase and A12. Furthermore, A12 (100 μM) presented effective inhibitory on tyrosinase in B16 melanoma cells with an inhibition rate of 33.48%, which was equivalent to that of kojic acid (39.81%). Our studies have indicated that these pyrrole derivatives have the potential to be developed as anti-tyrosinase agents for use in medicine, agriculture and food industry, and cosmetic products.

DATA AVAILABILITY STATEMENT

The original contributions presented in the study are included in the article/**Supplementary Material**; further inquiries can be directed to the corresponding authors.

AUTHOR CONTRIBUTIONS

Y-GH and Z-PG carried out the synthetic work. ZX and D-YZ were responsible for the initial study design and overall supervision. All the authors participated in the writing of the manuscript.

SUPPLEMENTARY MATERIAL

The Supplementary Material for this article can be found online at: https://www.frontiersin.org/articles/10.3389/fchem.2022.914944/full#supplementary-material

REFERENCES

Akın, Ş., Demir, E. A., Colak, A., Kolcuoglu, Y., Yildirim, N., and Bekircan, O. (2019). Synthesis, Biological Activities and Molecular Docking Studies of Some Novel 2,4,5-Trisubstituted-1,2,4-Triazole-3-One Derivatives as Potent Tyrosinase Inhibitors. *J. Mol. Struct.* 1175, 280–286.

Ali, A., Ashraf, Z., Rafiq, M., Kumar, A., Jabeen, F., Lee, G. J., et al. (2019). Novel Amide Derivatives as Potent Tyrosinase Inhibitors; *In-Vitro*, *In-Vivo* Antimelanogenic Activity and Computational Studies. *Mc* 15, 715–728. doi:10.2174/1573406415666190319101329

Ansari, A., Ali, A., Asif, M., and Shamsuzzaman, S. (2017). Review: Biologically Active Pyrazole Derivatives. *New J. Chem.* 41 (1), 16–41. doi:10.1039/c6nj03181a

Ashooriha, M., Khoshneviszadeh, M., Khoshneviszadeh, M., Moradi, S. E., Rafiei, A., Kardan, M., et al. (2019). 1,2,3-Triazole-based Kojic Acid Analogs as Potent Tyrosinase Inhibitors: Design, Synthesis and Biological Evaluation. *Bioorg. Chem.* 82, 414–422. doi:10.1016/j.bioorg.2018.10.069

Asthana, S., Zucca, P., Vargiu, A. V., Sanjust, E., Ruggerone, P., and Rescigno, A. (2015). Structure-Activity Relationship Study of Hydroxycoumarins and Mushroom Tyrosinase. *J. Agric. Food Chem.* 63 (32), 7236–7244. doi:10.1021/acs.jafc.5b02636

Butt, A. R. S., Abbasi, M. A., Aziz-ur-Rehman, R., Siddiqui, S. Z., Raza, H., Hassan, M., et al. (2019). Synthesis and Structure-Activity Relationship of Tyrosinase Inhibiting Novel Bi-heterocyclic Acetamides: Mechanistic Insights through Enzyme Inhibition, Kinetics and Computational Studies. *Bioorg. Chem.* 86, 459–472. doi:10.1016/j.bioorg.2019.01.036

Cai, P., Xiong, Y., Yao, Y., Chen, W., and Dong, X. (2019). Synthesis, Screening and Biological Activity of Potent Thiosemicarbazone Compounds as a Tyrosinase Inhibitor. *New J. Chem.* 43 (35), 14102–14111. doi:10.1039/c9nj02360g

Chai, W.-M., Huang, Q., Lin, M.-Z., Ou-Yang, C., Huang, W.-Y., Wang, Y.-X., et al. (2018). Condensed Tannins from Longan Bark as Inhibitor of Tyrosinase: Structure, Activity, and Mechanism. *J. Agric. Food Chem.* 66 (4), 908–917. doi:10.1021/acs.jafc.7b05481

Chai, W.-M., Wei, M.-K., Wang, R., Deng, R.-G., Zou, Z.-R., and Peng, Y.-Y. (2015). Avocado Proanthocyanidins as a Source of Tyrosinase Inhibitors: Structure Characterization, Inhibitory Activity, and Mechanism. *J. Agric. Food Chem.* 63 (33), 7381–7387. doi:10.1021/acs.jafc.5b03099

Crespo, M. I., Chabán, M. F., Lanza, P. A., Joray, M. B., Palacios, S. M., Vera, D. M. A., et al. (2019). Inhibitory Effects of Compounds Isolated from Lepechinia Meyenii on Tyrosinase. *Food Chem. Toxicol.* 125, 383–391. doi:10.1016/j.fct.2019.01.019

Deibl, N., Ament, K., and Kempe, R. (2015). A Sustainable Multicomponent Pyrimidine Synthesis. *J. Am. Chem. Soc.* 137 (40), 12804–12807. doi:10.1021/jacs.5b09510

Demirkiran, O., Sabudak, T., Ozturk, M., and Topcu, G. (2013). Antioxidant and Tyrosinase Inhibitory Activities of Flavonoids fromTrifolium nigrescensSubsp.Petrisavi. *J. Agric. Food Chem.* 61 (51), 12598–12603. doi:10.1021/jf403669k

Haldys, K., and Latajka, R. (2019). Thiosemicarbazones with Tyrosinase Inhibitory Activity. *Medchemcomm* 10 (3), 378–389.

Huang, H.-W., Cheng, M.-C., Chen, B.-Y., and Wang, C.-Y. (2019). Effects of High Pressure Extraction on the Extraction Yield, Phenolic Compounds, Antioxidant and Anti-tyrosinase Activity of Djulis Hull. *J. Food Sci. Technol.* 56 (9), 4016–4024. doi:10.1007/s13197-019-03870-y

Ielo, L., Deri, B., Germanò, M. P., Vittorio, S., Mirabile, S., Gitto, R., et al. (2019). Exploiting the 1-(4-fluorobenzyl)piperazine Fragment for the Development of Novel Tyrosinase Inhibitors as Anti-melanogenic Agents: Design, Synthesis, Structural Insights and Biological Profile. *Eur. J. Med. Chem.* 178, 380–389. doi:10.1016/j.ejmech.2019.06.019

Insuasty, B., Tigreros, A., Orozco, F., Quiroga, J., Abonía, R., Nogueras, M., et al. (2010). Synthesis of Novel Pyrazolic Analogues of Chalcones and Their 3-Aryl-4-(3-Aryl-4,5-Dihydro-1h-Pyrazol-5-Yl)-1-Phenyl-1h-Pyrazole Derivatives as Potential Antitumor Agents. *Bioorg. Med. Chem.* 18 (14), 4965–4974. doi:10.1016/j.bmc.2010.06.013

Jamwal, A., Javed, A., and Bhardwaj, V. A. (2013). Review on Pyrazole Derivatives of Pharmacological Potential. *J. Pharm. Biosci.* 3, 114–123.

Kumar, V., Kaur, K., Gupta, G. K., and Sharma, A. K. (2013). Pyrazole Containing Natural Products: Synthetic Preview and Biological Significance. *Eur. J. Med. Chem.* 69, 735–753. doi:10.1016/j.ejmech.2013.08.053

Larik, F. A., Saeed, A., Channar, P. A., Muqadar, U., Abbas, Q., Hassan, M., et al. (2017). Design, Synthesis, Kinetic Mechanism and Molecular Docking Studies of Novel 1-Pentanoyl-3-Arylthioureas as Inhibitors of Mushroom Tyrosinase and Free Radical Scavengers. *Eur. J. Med. Chem.* 141, 273–281. doi:10.1016/j.ejmech.2017.09.059

Lee, S., Ullah, S., Park, C., Won Lee, H., Kang, D., Yang, J., et al. (2019). Inhibitory Effects of N-(acryloyl)benzamide Derivatives on Tyrosinase and Melanogenesis. *Bioorg. Med. Chem.* 27 (17), 3929–3937. doi:10.1016/j.bmc.2019.07.034

Liao, J.-Y., Shao, P.-L., and Zhao, Y. (2015). Catalytic Divergent Synthesis of 3H or 1H Pyrroles by [3 + 2] Cyclization of Allenoates with Activated Isocyanides. *J. Am. Chem. Soc.* 137 (2), 628–631. doi:10.1021/ja511895q

Liu, J., Wu, F., Chen, L., Zhao, L., Zhao, Z., Wang, M., et al. (2012). Biological Evaluation of Coumarin Derivatives as Mushroom Tyrosinase Inhibitors. *Food Chem.* 135 (4), 2872–2878. doi:10.1016/j.foodchem.2012.07.055

Mou, X.-Q., Xu, Z.-L., Xu, L., Wang, S.-H., Zhang, B.-H., Zhang, D., et al. (2016). The Synthesis of Multisubstituted Pyrroles via a Copper-Catalyzed Tandem Three-Component Reaction. *Org. Lett.* 18 (16), 4032–4035. doi:10.1021/acs.orglett.6b01883

Qin, H.-L., Shang, Z.-P., Jantan, I., Tan, O. U., Hussain, M. A., Sher, M., et al. (2015). Molecular Docking Studies and Biological Evaluation of Chalcone Based Pyrazolines as Tyrosinase Inhibitors and Potential Anticancer Agents. *RSC Adv.* 5 (57), 46330–46338. doi:10.1039/c5ra02995c

Rodriguez, R., Escobedo, B., Lee, A. Y., Thorwald, M., Godoy-Lugo, J. A., Nakano, D., et al. (2020). Simultaneous Angiotensin Receptor Blockade and Glucagon-like Peptide-1 Receptor Activation Ameliorate Albuminuria in Obese Insulin-resistant Rats. *Clin. Exp. Pharmacol. Physiol.* 47 (3), 422–431. doi:10.1111/1440-1681.13206

Santi, M. D., Bouzidi, C., Gorod, N. S., Puiatti, M., Michel, S., Grougnet, R., et al. (2019). *In Vitro* biological Evaluation and Molecular Docking Studies of Natural and Semisynthetic Flavones from Gardenia Oudiepe (Rubiaceae) as Tyrosinase Inhibitors. *Bioorg. Chem.* 82, 241–245. doi:10.1016/j.bioorg.2018.10.034

Todaro, A., Cavallaro, R., Argento, S., Branca, F., and Spagna, G. (2011). Study and Characterization of Polyphenol Oxidase from Eggplant (Solanum Melongena L.). *J. Agric. Food Chem.* 59 (20), 11244–11248. doi:10.1021/jf201862q

Ullah, S., Park, C., Ikram, M., Kang, D., Lee, S., Yang, J., et al. (2019). Tyrosinase Inhibition and Anti-melanin Generation Effect of Cinnamamide Analogues. *Bioorg. Chem.* 87, 43–55. doi:10.1016/j.bioorg.2019.03.001

Ullah, S., Park, Y., Park, C., Lee, S., Kang, D., Yang, J., et al. (2019). Antioxidant, Anti-tyrosinase and Anti-melanogenic Effects of (E)-2,3-diphenylacrylic Acid Derivatives. *Bioorg. Med. Chem.* 27 (11), 2192–2200. doi:10.1016/j.bmc.2019.04.020

Ullah, S., Son, S., Yun, H. Y., Kim, D. H., Chun, P., and Moon, H. R. (2016). Tyrosinase Inhibitors: a Patent Review (2011-2015). *Expert Opin. Ther. Pat.* 26 (3), 347–362. doi:10.1517/13543776.2016.1146253

Wang, Y., Hao, X., Wang, Z., Dong, M., and Cui, L. (2020). Facile Fabrication of Mn 2+ -doped ZnO Photocatalysts by Electrospinning. *R. Soc. open Sci.* 7 (4), 191050. doi:10.1098/rsos.191050

Xie, J., Dong, H., Yu, Y., and Cao, S. (2016). Inhibitory Effect of Synthetic Aromatic Heterocycle Thiosemicarbazone Derivatives on Mushroom Tyrosinase: Insights from Fluorescence, 1 H NMR Titration and Molecular Docking Studies. *Food Chem.* 190, 709–716. doi:10.1016/j.foodchem.2015.05.124

Yu, L. (2003). Inhibitory Effects of (S)- and (R)-6-Hydroxy-2,5,7,8-tetramethylchroman-2-carboxylic Acids on Tyrosinase Activity. *J. Agric. Food Chem.* 51, 2344–2347. doi:10.1021/jf0208379

Zhang, B.-H., Lei, L.-S., Liu, S.-Z., Mou, X.-Q., Liu, W.-T., Wang, S.-H., et al. (2017). Zinc-promoted Cyclization of Tosylhydrazones and 2-(dimethylamino) malononitrile: an Efficient Strategy for the Synthesis of Substituted 1-Tosyl-1h-Pyrazoles. *Chem. Commun.* 53 (61), 8545–8548. doi:10.1039/c7cc04610c

Zhu, Y.-J., Zhou, H.-T., Hu, Y.-H., Tang, J.-Y., Su, M.-X., Guo, Y.-J., et al. (2011). Antityrosinase and Antimicrobial Activities of 2-phenylethanol, 2-phenylacetaldehyde and 2-phenylacetic Acid. *Food Chem.* 124 (1), 298–302. doi:10.1016/j.foodchem.2010.06.036

Zolghadri, S., Bahrami, A., Hassan Khan, M. T., Munoz-Munoz, J., Garcia-Molina, F., Garcia-Canovas, F., et al. (2019). A Comprehensive Review on Tyrosinase Inhibitors. *J. Enzyme Inhibition Med. Chem.* 34 (1), 279–309. doi:10.1080/14756366.2018.1545767

Check for updates

Inclusion Complex of Isoliquiritigenin With Sulfobutyl Ether-β-Cyclodextrin: Preparation, Characterization, Inclusion Mode, Solubilization, and Stability

Xiaozheng Wu[†], Jiamin Li[†], Chunmei Hu, Yingying Zheng, Yufei Zhang, Jianping Li, Mengyue Li, Di Xiao, Li Lu, Yuechang Huang, Xingmin Zhang and Chen Li*

School of Biotechnology and Health Sciences, Wuyi University, Jiangmen, China

Isoliquiritigenin (ISL) possesses a wide variety of pharmacological properties, however, its poor solubility and oral bioavailability pose a significant barrier to its application. In present studies, the ISL inclusion complex was prepared with sulfobutyl ether-β-cyclodextrin (SBE-β-CD). The physicochemical characterizations of ISL-SBE-β-CD were performed with Fourier transform infrared (FT-IR) spectroscopy and X-ray powder diffraction (XRD). Phase solubility study suggested a 1:1 formation of ISL-SBE-β-CD complexes. The water solubility of ISL rose from 13.6 μM to 4.05 mM by the inclusion of SBE-β-CD. The antioxidant activities (IC50) of ISL-SBE-β-CD reached 42.2 μg/ml, which was significantly lower than that of ISL (60.5 μg/ml). Its stability in biological environments was also enhanced.

Keywords: isoliquiritigenin, sulfobutyl ether-β-cyclodextrin, inclusion complex, preparation, characterization

INTRODUCTION

Isoliquiritigenin (ISL; **Figure 1**), a flavonoid, is the major bioactive constituent isolated from the food plants such as licorice, shallot, and bean sprouts (Cao et al., 2004; Cho et al., 2011; Tan et al., 2022). Numerous pharmacological studies have suggested that ISL exhibited various pharmacological properties including anti-inflammatory, antioxidant, analgesic, anticancer, antiplatelet aggregation, anti-angiogenic effect, and cytoprotective effects (Chin et al., 2007; Lee et al., 2009; Sun et al., 2022). Although many pharmacological activities of ISL have been recognized, its water solubility is relatively poor (Kakegawa et al., 1992; Kang et al., 2010). The poor water solubility of ISL would result in a slow dissolution and low absorption rate in the gastrointestinal tract, hence reducing oral bioavailability, which hinders its wide applications in pharmaceutical and functional foods (Jang et al., 2008). Microencapsulation is an effective method to maintain its bioactivity.

Cyclodextrins (CDs) are cyclic oligosaccharides equipped with a hydrophilic surface and a hydrophobic cavity, which can encapsulate hydrophobic molecules to prepare water-soluble complexes (Gotsev and Ivanov, 2009; Nguyen et al., 2013). Notably, when hydrophobic molecules were encapsulated in CDs, their biological activities were improved compared to free molecules (Fuchs et al., 1993; Irie and Uekama, 1997). Sulfobutylether-β-cyclodextrin (SBE-β-CD), a negatively charged derivative of β-CD, is prepared with SBE groups substituting the secondary hydroxyls of β-CD (Wu et al., 2013; Zhou et al., 2020). Hence, SBE-β-CD shows an extremely hydrophilic exterior surface and an extended hydrophobic cavity (Kucerova et al., 2016; Jafari et al.,

FIGURE 1 | The chemical structure of isoliquiritigenin.

FIGURE 2 | XRD patterns of ISL, SBE-β-CD, and ISL-SBE-β-CD.
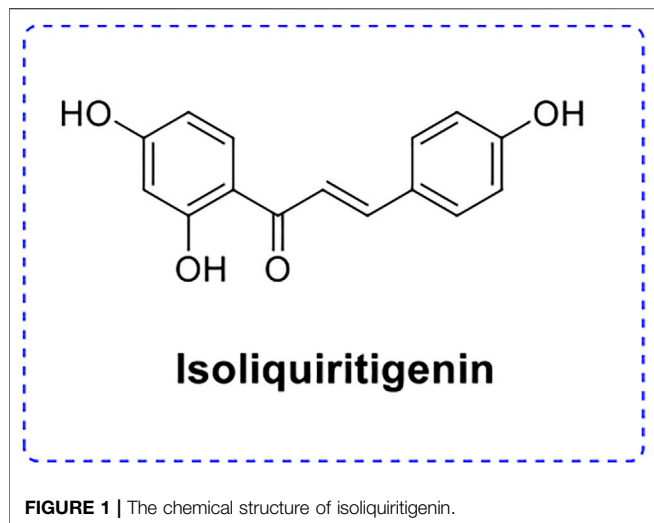
2022). Especially, SBE-β-CD presents relatively low toxicity and high water-solubility than β-CD (Merzlikine et al., 2011; Shen et al., 2013). The formation of natural product molecules with inclusion complex with SBE-β-CD is of great interest in various fields (Fulop et al., 2015; Zhang et al., 2017; Zhao et al., 2020; Wang and Zhang, 2022). Although Li et al. (2015) reported the inclusion complex of isoliquiritigenin and 6-*o*-α-D-maltosyl-β-cyclodextrin. However, the ISL inclusion complex with SBE-β-CD has not been described.

Thus, the aim of the study is to investigate the inclusion complex of ISL with SBE-β-CD as a potential method to increase bioavailability. First, the interactions between the ISL and SBE-β-CD are determined by a phase solubility analysis. Then, the ISL-SBE-β-CD is characterized by Fourier transform infrared (FT-IR) spectroscopy and X-ray powder diffraction (XPRD). Finally, the bioavailability of the ISL complex with SBE-β-CD is evaluated.

EXPERIMENTAL

Instruments and Reagents

ISL was purchased from Xi'an Kai Lai Biological Engineering Co., Ltd. SBE-β-CD with an average molecular weight of 1,410 was provided by Nanjing Dulai Biotechnology Co., Ltd. All other reagents used were of analytical grade.

Preparation of Isoliquiritigenin-Sulfobutyl Ether-β-Cyclodextrin Inclusion Complex

The ISL-SBE-β-CD inclusion complex was prepared by the method of an aqueous solution according to the previous method (Mohan et al., 2012; Mura, 2015). In brief, SBE-β-CD (6.50 mmol) was dissolved in 100 ml of distilled water at 60°C with continuous stirring for 1 h. The ISL solution containing 3.25 mmol of ISL in ethanol was added. Then the suspension solution was stirred at 60°C for 4 h. After removing ethanol, the solution was freeze-dried for 24 h and the ISL-SBE-β-CD inclusion complex was obtained.
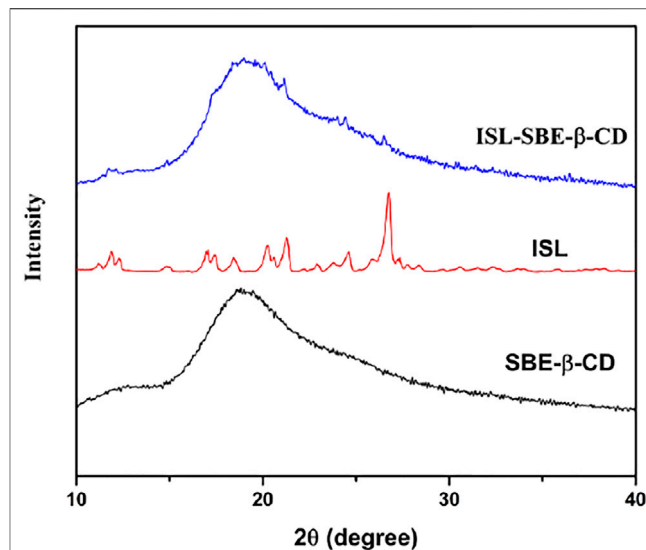
X-ray Powder Diffraction Assay

The X-ray powder diffraction patterns of ISL, SBE-β-CD, and ISL-SBE-β-CD were recorded on a Rigaku powder X-ray diffraction system (Siemens D5000, Germany). Powders were scanned at a diffraction angle of 2θ from 2 to 40°, with 40 KV and 30 mA under Cu Kα radiation (Qiu et al., 2014).

Fourier Transform Infrared Spectroscopy Assay

The FT-IR spectra of ISL, SBE-β-CD, and ISL-SBE-β-CD were recorded using a Nicolet 6700 spectrophotometer (Thermo Fisher Scientific, United States). The FT-IR measurements of samples were performed in the scanning range of 4,000 cm^{-1} ~400 cm^{-1} (Volobuef et al., 2012).

Concentration–Absorbance Calibration Curve of Isoliquiritigenin

ISL (10 mg) was accurately weighed and dissolved into 100 ml ethanol–water solution (v: v = 1:1). ISL ethanol–water solution with concentrations of 1, 2, 3, 4, 5, 6, 7, 8, 9, and 10 μg/ml were prepared. The UV spectra of samples were measured with a UV-8000S from 200 to 600 nm. Also, then the concentration–absorbance calibration curve of ISL was made (Yang et al., 2009).

Phase Solubility Study

Phase solubility study of ISL in the aqueous solution of SBE-β-CD was conducted according to the previous method (Chen et al., 2007; Aleem et al., 2008). An excess amount of ISL (8 mg) was added to 10 ml of SBE-β-CD solution with different concentrations (0–9 mM). The samples were shaken for 48 h at 25°C. After equilibrium, the samples were filtered through 0.22 μm PTFE filters to remove the excess ISL. Then, the UV
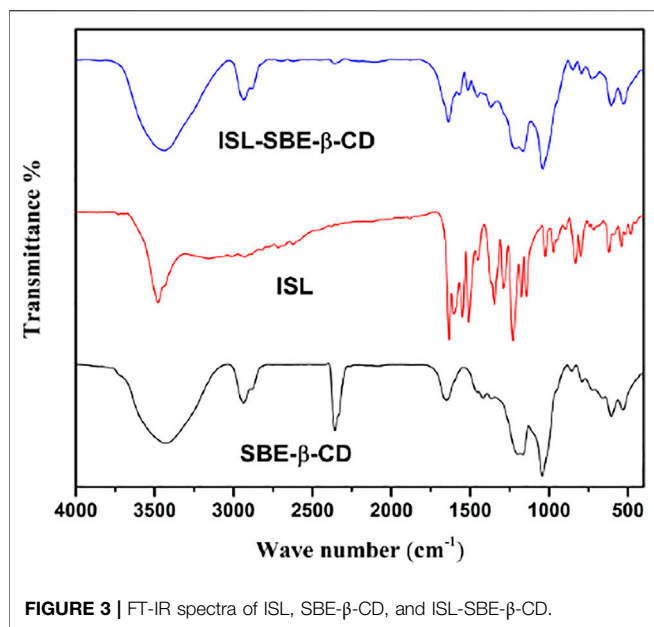
FIGURE 3 | FT-IR spectra of ISL, SBE-β-CD, and ISL-SBE-β-CD.

absorption of ISL in each aqueous solution was determined at 374 nm, and the concentration of ISL in each aqueous solution was accounted for against the concentration–absorbance standard curve of ISL. The phase solubility profiles of ISL were obtained by plotting the solubility of ISL as a function of SBE-β-CD concentration.

The stability constants, K_c, were calculated from the phase solubility diagram according to the Higuchi–Connors equation: $K_c = \text{slope}/[S_o \times (1 - \text{slope})]$, where S_o is the ISL solubility in the absence of SBE-β-CD.

Solubility Study

Solubility determination of pure ISL and ISL-SBE-β-CD was carried out in the aqueous solution according to the previous references. An access amount of ISL was added to a 5 ml aqueous solution, and then the suspension was shaken for 48 h at 25°C. After filtering through 0.22 μm PTFE filters, the UV absorption of ISL in each aqueous solution was determined at 374 nm, and the

concentration was accounted for. The solubility of ISL-SBE-β-CD in an aqueous solution was measured using a similar method.

Antioxidant Capacity

The DPPH radical scavenging assay was used to assay the antioxidant capacity (García-Padial et al., 2013). The samples were resolved in methanol and diluted to different concentrations, respectively. First, 1.5 ml sample solution was added to DPPH methanolic solution (1.5 ml, 0.1 mM) and laid in the dark for 30 min. Then, their absorbance was determined at 517 nm, respectively, and 50% inhibitory concentration (IC$_{50}$) was obtained from the scavenging results.

RESULTS AND DISCUSSION

X-ray Powder Diffraction Assay

The XRD spectra of ISL, SBE-β-CD, and ISL-SBE-β-CD are shown in **Figure 2**. The diffractogram of ISL showed various characteristic peaks at 12.3°, 17.1°, 18.4°, 20.2°, 21.3°, 24.6°, and 26.7°, indicating a highly crystalline structure. In contrast, the absence of characteristic peaks in the spectrum of SBE-β-CD reveals its amorphous state. Compared with ISL and SBE-β-CD, the diffraction of ISL-SBE-β-CD was similar to that of SBE-β-CD and showed no characteristic peaks of ISL. The XRD results showed that ISL was cocooned ion into the SBE-β-CD cavity, resulting in the self-lattice arrangement change of ISL from crystalline to amorphous state. These results were consistent with Li's report (Li et al., 2015) that the inclusion complex form changed the self-lattice arrangement.

Fourier Transform Infrared Assay

The FT-IR spectra of ISL, SBE-β-CD, and ISL-SBE-β-CD are shown in **Figure 3**. The spectrum of ISL consisted of mainly significant groups including 3,479 cm^{-1} (O–H stretching vibration); 1,631 cm^{-1} (C=O group); and 1,600, 1,550, 1,510, and 1,450 cm^{-1} (aromatic nucleus). The FT-IR spectrum SBE-β-CD shows the main absorption bands at 3,490 cm^{-1} (O-H); 2,938 cm^{-1} (C-H)$^{--}$; 1,677 cm^{-1} (O-H); and 1,217 and 1,050 cm^{-1} (C-H and C-O). But in FT-IR spectra of ISL-SBE-β-CD, its FT-IR spectra are close to that of SBE-β-CD, and

FIGURE 4 | Concentration–absorbance calibration curve of ISL.

FIGURE 5 | A phase solubility diagram of the ISL-SBE-β-CD system.

FIGURE 6 | Antioxidant activities of ISL and ISL-SBE-β-CD system.

the characteristic absorption band of ISL at $400–1600 \text{ cm}^{-1}$ are overshadowed by corresponding ones of SBE-β-CD. These changes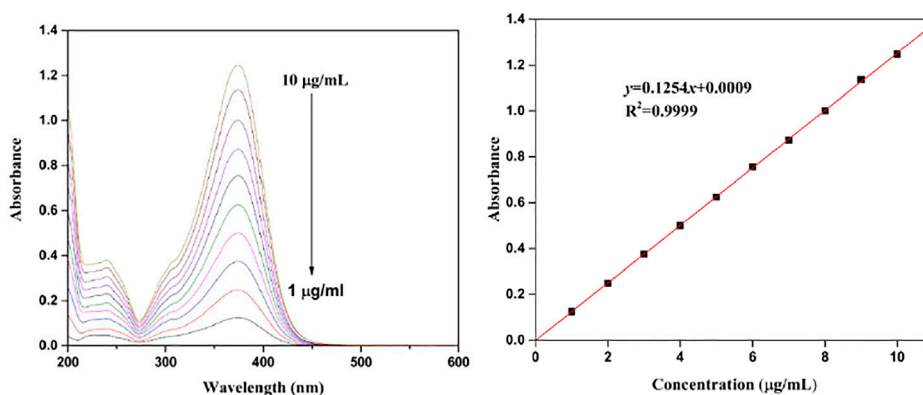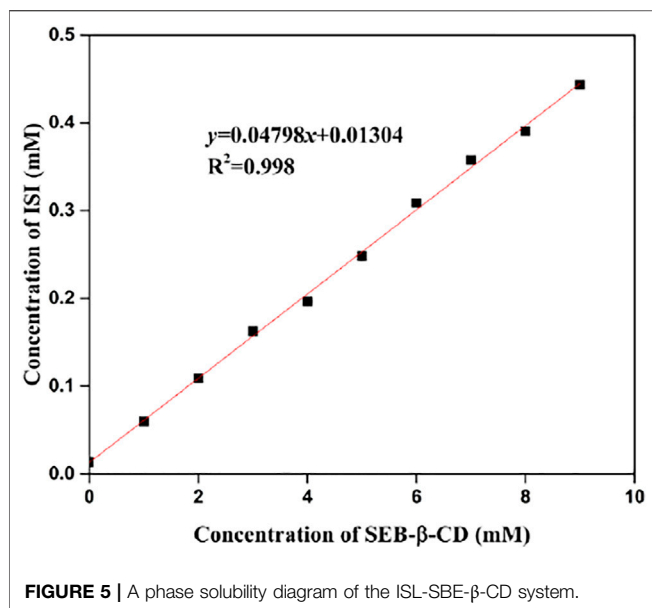 suggested that ISL got into the SBE-β-CD cavity and formed intra-molecular hydrogen bonds in the inclusion process of ISL and SBE-β-CD. The results were verified with XRD results.

Concentration–Absorbance Calibration Curve of Isoliquiritigenin

The UV spectra of ISL with different concentrations are illustrated in **Figure 4**. The characteristic absorption peak of ISL was found at 374 nm. The absorption intensity enhanced with the increase of ISL concentration, resulting in the concentration–absorbance calibration curve ($y = 0.1254x+0.0009$, $R^2 = 0.999$).

Phase Solubility Study

The phase solubility profiles of ISL-SBE-β-CD are presented in **Figure 5**. It could be seen that the concentration of ISL in water was obviously solubilized by the presence of SBE-β-CD. Moreover, the solubility curve was a straight line ($R^2 = 0.998$). According to Higuchi and Connors, this profile could be described as an AL type, suggesting a 1:1 formation of ISL-SBE-β-CD complexes. The molar ratio of ISL to SBE-β-CD in this complex might be determined by the characteristics of ISL. Also, the stability constants, Kc, of ISL-SBE-β-CD were calculated as 3864 M^{-1} according to the phase solubility diagram. The high K_c value verified a high tendency of ISL to enter the SBE-β-CD cavity.

Effect of Sulfobutyl Ether-β-Cyclodextrin on Aqueous Solubility of Isoliquiritigenin

SBE-β-CD is usually used to enhance the aqueous solubility of drugs due to the large number of hydroxyl groups. SBE-β-CD could provide the lipophilic microenvironment for hydrophobic drug molecules. ISL was encapsulated into the hydrophobic cavity
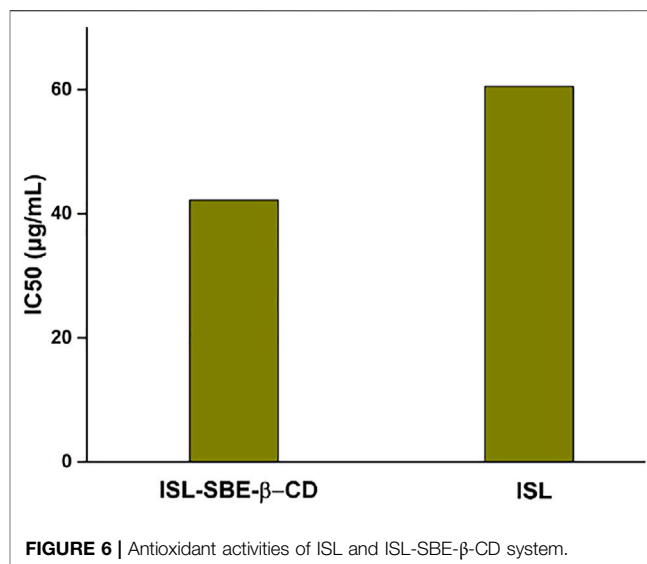
of SBE-β-CD interiors, leading to the form of non-covalent dynamic inclusion complexes. The aqueous solubility of ISL and ISL-SBE-β-CD was assessed. The water solubility of ISL was only 13.6 μM, while complexation led to a notable increase to 4.05 mM in water. A 298-fold increase in water solubility was achieved by the solubilizing effect of SBE-β-CD. Hence, SBE-β-CD could be used as an effective inclusion agent with a solubilizing effect.

Stability in Biological Environments

To evaluate the stability of ISL-SBE-β-CD in biological environments, the absorbance changes of ISL and ISL-SBE-β-CD in a simulated gastric acid environment (ca. pH 1.5) and simulated intestinal fluid environment (ca. pH 7.6) were tracked. ISL and ISL-SBE-β-CD were dissolved in the buffer solution, respectively, and the absorbance at 374 nm was recorded. At pH 1.5 solution, the absorbance of ISL tapered off to 13.5 and 22.4% at 24 and 60 h, respectively. However, the absorbance of ISL-SBE-β-CD dwindled to only 6.8 and 14.2% at 24 and 60 h. At pH 7.6 solution, the absorbance of ISL and ISL-SBE-β-CD was similarly changed before 60 h, tapered off to 95.3 and 96.8%. These results showed that ISL-SBE-β-CD was more stable than ISL at both pH 1.5 and pH 7.6. Thence, SBE-β-CD could improve the stability of the included compounds.

Antioxidant Capacity

The DPPH assay results of ISL and ISL-SBE-β-CD are shown in **Figure 6**. The antioxidant activity (IC_{50}) of ISL-SBE-β-CD was 42.2 μg/ml, which was significantly higher than that of ISL (60.5 μg/ml). The results showed that the ISL-SBE-β-CD presented a much higher antioxidant capacity than ISL. Thence, the antioxidant capacity of compounds can be optimized by the presence of cyclodextrins.

CONCLUSION

The inclusion complexation behavior and characterization of isoliquiritigenin with sulfobutyl ether-β-cyclodextrin were

investigated. The results showed that sulfobutyl ether-β-cyclodextrin could enhance the water solubility and stability of isoliquiritigenin. Moreover, inclusion complexation presented a much higher antioxidant capacity than isoliquiritigenin. Given the shortage of applications for isoliquiritigenin, the inclusion complexation would be regarded as an effective step in the development of a novel formulation of isoliquiritigenin for medicine or healthcare products.

DATA AVAILABILITY STATEMENT

The original contributions presented in the study are included in the article/Supplementary Material; further inquiries can be directed to the corresponding author.

REFERENCES

AUTHOR CONTRIBUTIONS

XW and JL contributed to the synthesis. CH, YZ, YZ, JL, ML, DX, LL, YH, and XZ contributed to the characterization and analysis, and CL supervised the work and prepared the manuscript.

Aleem, O., Kuchekar, B., Pore, Y., and Late, S. (2008). Effect of β-cyclodextrin and Hydroxypropyl β-cyclodextrin Complexation on Physicochemical Properties and Antimicrobial Activity of Cefdinir. *J. Pharm. Biomed. Analysis* 47, 535–540. doi:10.1016/j.jpba.2008.02.006

Cao, Y., Wang, Y., Ji, C., and Ye, J. (2004). Determination of Liquiritigenin and Isoliquiritigenin in *Glycyrrhiza Uralensis* and its Medicinal Preparations by Capillary Electrophoresis with Electrochemical Detection. *J. Chromatogr. A* 1042, 203–209. doi:10.1016/j.chroma.2004.05.049

Chen, X., Chen, R., Guo, Z., Li, C., and Li, P. (2007). The Preparation and Stability of the Inclusion Complex of Astaxanthin with β-cyclodextrin. *Food Chem.* 101, 1580–1584. doi:10.1016/j.foodchem.2006.04.020

Chin, Y.-W., Jung, H.-A., Liu, Y., Su, B.-N., Castoro, J. A., Keller, W. J., et al. (2007). Anti-oxidant Constituents of the Roots and Stolons of Licorice (*Glycyrrhiza Glabra*). *J. Agric. Food Chem.* 55, 4691–4697. doi:10.1021/jf0703553

Cho, S., Kim, S., Jin, Z., Yang, H., Han, D., Baek, N.-I., et al. (2011). Isoliquiritigenin, a Chalcone Compound, Is a Positive Allosteric Modulator of GABAA Receptors and Shows Hypnotic Effects. *Biochem. Biophysical Res. Commun.* 413, 637–642. doi:10.1016/j.bbrc.2011.09.026

Fuchs, R., Habermann, N., and Klüfers, P. (1993). Multinuclear Sandwich-type Complexes of Deprotonatedβ-Cyclodextrin and Copper(II) Ions. *Angew. Chem. Int. Ed. Engl.* 32, 852–854. doi:10.1002/anie.199308521

Fülöp, Z., Balogh, A., Saokham, P., Jansook, P., and Loftsson, T. (2015). Formation and Stability Assessment of Self-Assembled Nanoparticles from Large Mw Chitosan and Sulfobutylether-β-Cyclodextrin. *J. Drug Deliv. Sci. Technol.* 30, 478–485. doi:10.1016/j.jddst.2015.03.001

García-Padial, M., Martínez-Ohárriz, M. C., Navarro-Blasco, I., and Zornoza, A. (2013). The Role of Cyclodextrins in ORAC-Fluorescence Assays. Antioxidant Capacity of Tyrosol and Caffeic Acid with Hydroxypropyl-β-Cyclodextrin. *J. Agric. Food Chem.* 61, 12260–12264. doi:10.1021/jf403265b

Gotsev, M. G., and Ivanov, P. M. (2009). Molecular Dynamics of Large-Ring Cyclodextrins: Principal Component Analysis of the Conformational Interconversions. *J. Phys. Chem. B* 113, 5752–5759. doi:10.1021/jp805446w

Irie, T., and Uekama, K. (1997). Pharmaceutical Applications of Cyclodextrins. III. Toxicological Issues and Safety Evaluation. *J. Pharm. Sci.* 86, 147–162. doi:10.1021/js960213f

Jafari, G., Raissi, H., and Shahabi, M. (2022). Assessment of Sulfobutylether-Beta-Cyclodextrin as a Promising Fluorometholone Molecule Container: DFT, Docking, Molecular Dynamics and MM-PBSA Free Energy Calculations. *Mol. Simul.* 48, 168–175. doi:10.1080/08927022.2021.1996575

Jang, E. Y., Choe, E. S., Hwang, M., Kim, S. C., Lee, J. R., Kim, S. G., et al. (2008). Isoliquiritigenin Suppresses Cocaine-Induced Extracellular Dopamine Release in Rat Brain through GABAB Receptor. *Eur. J. Pharmacol.* 587, 124–128. doi:10.1016/j.ejphar.2008.03.054

Kakegawa, H., Matsumoto, H., and Satoh, T. (1992). Inhibitory Effects of Some Natural Products on the Activation of Hyaluronidase and Their Antiallergic Actions. *Chem. Pharm. Bull.* 40, 1439–1442. doi:10.1248/cpb.40.1439

Kang, S.-W., Choi, J.-S., Choi, Y.-J., Bae, J.-Y., Li, J., Kim, D. S., et al. (2010). Licorice Isoliquiritigenin Dampens Angiogenic Activity via Inhibition of MAPK-Responsive Signaling Pathways Leading to Induction of Matrix Metalloproteinases. *J. Nutr. Biochem.* 21, 55–65. doi:10.1016/j.jnutbio.2008.10.004

Kucerova, G., Prochazkova, H., Kalikova, K., and Tesarova, E. (2016). Sulfobutylether-beta-cyclodextrin as a Chiral Selector for Separation of Amino Acids and Dipeptides in Chromatography. *J. Chromatogr. A* 1467, 356. doi:10.1016/j.chroma.2016.07.061

Lee, S. H., Kim, J. Y., Seo, G. S., Kim, Y.-C., and Sohn, D. H. (2009). Isoliquiritigenin, from *Dalbergia Odorifera*, Up-Regulates Anti-inflammatory Heme Oxygenase-1 Expression in RAW264.7 Macrophages. *Inflamm. Res.* 58, 257–262. doi:10.1007/s00011-008-8183-6

Li, B., Liu, B., Li, J., Xiao, H., Wang, J., and Liang, G. (2015). Experimental and Theoretical Investigations on the Supermolecular Structure of Isoliquiritigenin and 6-O-α-D-Maltosyl-β-Cyclodextrin Inclusion Complex. *Int. J. Mol. Sci.* 16, 17999–18017. doi:10.3390/ijms160817999

Merzlikine, A., Abramov, Y. A., Kowsz, S. J., Thomas, V. H., and Mano, T. (2011). Development of Machine Learning Models of β-cyclodextrin and Sulfobutylether-β-Cyclodextrin Complexation Free Energies. *Int. J. Pharm.* 418, 207–216. doi:10.1016/j.ijpharm.2011.03.065

Mohan, P. R. K., Sreelakshmi, G., Muraleedharan, C. V., and Joseph, R. (2012). Water Soluble Complexes of Curcumin with Cyclodextrins: Characterization by FT-Raman Spectroscopy. *Vib. Spectrosc.* 62, 77–84. doi:10.1016/j.vibspec.2012.05.002

Mura, P. (2015). Analytical Techniques for Characterization of Cyclodextrin Complexes in the Solid State: A Review. *J. Pharm. Biomed. Analysis* 113, 226–238. doi:10.1016/j.jpba.2015.01.058

Nguyen, T. A., Liu, B., Zhao, J., Thomas, D. S., and Hook, J. M. (2013). An Investigation into the Supramolecular Structure, Solubility, Stability and Antioxidant Activity of Rutin/cyclodextrin Inclusion Complex. *Food Chem.* 136, 186–192. doi:10.1016/j.foodchem.2012.07.104

Qiu, N., Cheng, X., Wang, G., Wang, W., Wen, J., Zhang, Y., et al. (2014). Inclusion Complex of Barbigerone with Hydroxypropyl-β-Cyclodextrin: Preparation and *In Vitro* Evaluation. *Carbohydr. Polym.* 101, 623–630. doi:10.1016/j.carbpol.2013.09.035

Shen, M., Wu, M., Tan, X., and Song, Z. (2013). Study on the Inclusion Interaction between Sulfobutylether-B-Cyclodextrin and Clozapine by Flow Injection Chemiluminescence. *Instrum. Sci. Technol.* 42, 46–58. doi:10.1080/10739149.2013.834449

Sun, L. M., Yang, Z., Zhang, J. Y., and Wang, J. (2022). Isoliquiritigenin Attenuates Acute Renal Injury through Suppressing Oxidative Stress, Fibrosis and JAK2/STAT3 Pathway in Streptozotocin-Induced Diabetic Rats. *Bioengineered* 12, 11188. doi:10.1080/21655979.2021.2006978

Tan, R. Z., Xie, K. H., Liao, Y., Lin, X., Zhu, B. W., Liu, T. T., et al. (2022). Renoprotective Effect of Isoliquiritigenin on Cisplatin-Induced Acute Kidney Injury through Inhibition of FPR2 in Macrophage. *J. Pharmacol. Sci.* 148 (1), 56–64. doi:10.1016/j.jphs.2021.10.001

Volobuef, C., Moraes, C. M., S. Nunes, L. A., S. Cereda, C. M., Yokaichiya, F., K. D. Franco, M. K., et al. (2012). Sufentanil-2-Hydroxypropyl-β-Cyclodextrin

Inclusion Complex for Pain Treatment: Physicochemical, Cytotoxicity, and Pharmacological Evaluation. *J. Pharm. Sci.* 101, 3698–3707. doi:10.1002/jps.23234

Wang, L., and Zhang, Z. (2022). Comment about the Safety of Intravenous Voriconazole Formulated with Sulfobutylether Beta-Cyclodextrin. *Expert Opin. Drug Saf.* 21, 133–134. doi:10.1080/14740338.2021.1978976

Wu, J., Shen, Q., and Fang, L. (2013). Sulfobutylether-β-cyclodextrin/chitosan Nanoparticles Enhance the Oral Permeability and Bioavailability of Docetaxel. *Drug Dev. Industrial Pharm.* 39, 1010–1019. doi:10.3109/03639045.2012.694588

Yang, B., Lin, J., Chen, Y., and Liu, Y. (2009). Artemether/hydroxypropyl-β-cyclodextrin Host-Guest System: Characterization, Phase-Solubility and Inclusion Mode. *Bioorg. Med. Chem.* 17, 6311–6317. doi:10.1016/j.bmc.2009.07.060

Zhang, S., Zhang, H., Xu, Z., Wu, M., Xia, W., and Zhang, W. (2017). Chimonanthus Praecox Extract/cyclodextrin Inclusion Complexes: Selective Inclusion, Enhancement of Antioxidant Activity and Thermal Stability. *Industrial Crops Prod.* 95, 60–65. doi:10.1016/j.indcrop.2016.09.033

Zhao, L., Tang, B., Tang, P., Sun, Q., Suo, Z., Zhang, M., et al. (2020). Chitosan/Sulfobutylether-β-Cyclodextrin Nanoparticles for Ibrutinib Delivery: A Potential Nanoformulation of Novel Kinase Inhibitor. *J. Pharm. Sci.* 109, 1136–1144. doi:10.1016/j.xphs.2019.10.007

Zhou, L., Liu, B., Guan, J., Jiang, Z., and Guo, X. (2020). Preparation of Sulfobutylether β-cyclodextrin-silica Hybrid Monolithic Column, and its Application to Capillary Electrochromatography of Chiral Compounds. *J. Chromatogr. A* 1620, 460932. doi:10.1016/j.chroma.2020.460932

Check for updates

Synthesis and Biological Evaluation of 5-Fluoro-2-Oxindole Derivatives as Potential α-Glucosidase Inhibitors

Jing Lin[†], Qi-Ming Liang[†], Yuan-Na Ye, Di Xiao, Li Lu, Meng-Yue Li, Jian-Ping Li, Yu-Fei Zhang, Zhuang Xiong*, Na Feng* and Chen Li*

School of Biotechnology and Health Sciences, Wuyi University, Jiangmen, China

α-Glucosidase inhibitors are known to prevent the digestion of carbohydrates and reduce the impact of carbohydrates on blood glucose. To develop novel α-glucosidase inhibitors, a series of 5-fluoro-2-oxindole derivatives (**3a ~ 3v**) were synthesized, and their α-glucosidase inhibitory activities were investigated. Biological assessment results showed that most synthesized compounds presented potential inhibition on α-glucosidase. Among them, compounds **3d**, **3f**, and **3i** exhibited much better inhibitory activity with IC_{50} values of 49.89 ± 1.16 μM, 35.83 ± 0.98 μM, and 56.87 ± 0.42 μM, respectively, which were about 10 ~ 15 folds higher than acarbose (IC_{50} = 569.43 ± 43.72 μM). A kinetic mechanism study revealed that compounds **3d**, **3f**, and **3i** inhibited the α-glucosidase in a reversible and mixed manner. Molecular docking was carried out to simulate the affinity between the compound and α-glucosidase.

Keywords: oxindole, α-glucosidase, inhibition, docking, kinetics

1 INTRODUCTION

Diabetes is a chronic metabolic disorder disease that increases the risk of cancer, stroke, peripheral arterial disease, cardiovascular disease, retinopathy, and kidney disease. (Wang et al., 2017; Sonia et al., 2019; Proença et al., 2019; Proença et al., 2017; Proença et al., 2018; Rocha et al., 2019; Santos et al., 2018; Wu et al., 2014; Wu et al., 2017). The prevalence of diabetes at all ages worldwide is rising. It is estimated that by 2030, the prevalence of diabetes may rise from 2.8% (171 million) in 2000 to 4.4% (366 million) (Zhong et al., 2019). Type 2 diabetes, which is characterized by insulin resistance, is the most common, which accounts for approximately 90% of all diabetic patients (Taha et al., 2015; Leong et al., 2019; Settypalli et al., 2019).
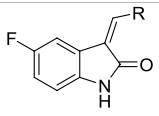
α-Glucosidase is an indispensable enzyme in the sugar metabolism pathway of organisms, and its main function is to hydrolyze glycosidic bonds into glucose (Chaudhry et al., 2019; Dan et al., 2019; Gollapalli et al., 2019; Krishna et al., 2019; Mendieta-Moctezuma et al., 2019; Spasov et al., 2019; Ye et al., 2019). Thus inhibiting the α-glucosidase would obviously control the postprandial hyperglycemia. α-Glucosidase inhibitors can block the hydrolysis of 1, 4-glycosidic bonds and delay the hydrolysis of carbohydrates into glucose, resulting in the effective reduction of postprandial blood sugar (Al-Salahi, et al., 2018; Qamar, et al., 2018; Shah, et al., 2018; Wang, et al., 2018). Up to now, a great number of naturally occurring and synthetic α-glucosidase inhibitors have been reported. However, only several well-known inhibitors, such as acarbose, voglibose, and miglitol, are used clinically as first-line drugs. Moreover, these drugs have uncomfortable side effects (e.g., flatulence, abdominal pain, and diarrhea) (Taha et al., 2018a; Kasturi et al., 2018; Prachumart et al., 2018). These prompt us to develop effective and safe α-glucosidase inhibitors from natural sources.

SCHEME 1 | Synthetic route to 5-fluoro-2-oxindole derivatives (**3a ~ 3u**). Reagents and conditions: 5-fluoro-2-oxindole (1.0 mmol, 1.0 equiv), substituted aldehydes (1.5 mmol, 1.5 equiv), KOH (6.0 mmol, 6.0 equiv), and EtOH, r. t., 3 h.
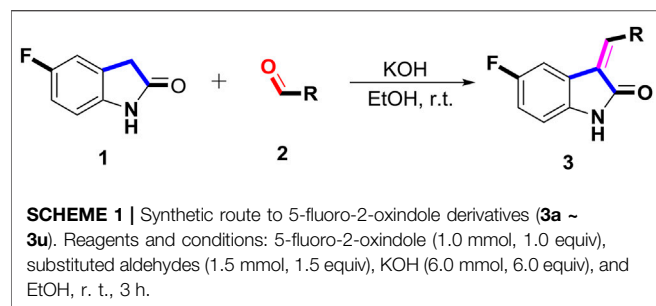
Lots of compounds from natural sources have shown potential inhibitory activity on α-glucosidase. Oxindoles, the important indole-based derivatives, widely exist in many natural alkaloids. It was reported that oxindoles have the ability to inhibit the α-glucosidase (Khan et al., 2014; Asadollahi-Baboli and Dehnavi, 2018; Taha et al., 2018b). Moreover, oxindoles have attracted much attention due to their broad-spectrum biological activity, such as anti-inflammatory, anti-bacterial, and anti-tumor. (Yang et al., 2014; Xu et al., 2016; Alvarez et al., 2018; Bao et al., 2018; Huang et al., 2019). In addition, fluorine, a key atom in medicine, might enhance metabolic stability, improve the pharmacodynamic effect, and eliminate active metabolic intermediates (Johnson et al., 2020). Hence, 5-fluoro-2-oxindole was selected as the leading structure to synthesize the title compounds (**3a ~ 3u**) through the condensation with the substituted aromatic aldehydes, followed by the screening on α-glucosidase inhibitory activities and the molecular docking studies.
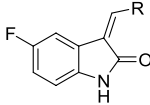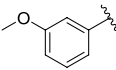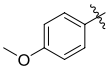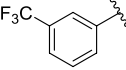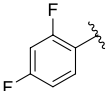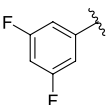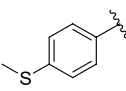
TABLE 1 | α-Glucosidase inhibitory activities of compounds (**3a ~ 3v**).

Compound	R	Inhibition rate at a concentration of 100 μM (%)	IC$_{50}$ (μM)
3a	2-F-phenyl	7.29 ± 0.16	>100[a]
3b	3-F-phenyl	5.19 ± 0.79	>100[a]
3c	4-F-phenyl	9.55 ± 0.13	>100[a]
3d	2-Cl-phenyl	89.19 ± 0.14	49.89 ± 1.16
3e	3-Cl-phenyl	21.64 ± 0.78	>100[a]
3f	4-Cl-phenyl	90.52 ± 0.27	35.83 ± 0.98
3g	2-Br-phenyl	53.71 ± 0.47	95.68 ± 0.28
3h	3-Br-phenyl	31.61 ± 0.21	>100[a]
3i	4-Br-phenyl	92.86 ± 0.32	56.87 ± 0.42

(Continued on following page)

TABLE 1 | (*Continued*) α-Glucosidase inhibitory activities of compounds **(3a ~ 3v)**.

3j		19.17 ± 1.21	>100[a]
3k		27.25 ± 1.47	>100[a]
3l		15.70 ± 0.71	>100[a]
3m		8.43 ± 1.14	>100[a]
3n		52.79 ± 1.68	96.78 ± 0.72
3o		18.78 ± 1.15	>100[a]
3p		55.89 ± 1.71	92.62 ± 0.45
3q		10.01 ± 1.75	>100[a]
3r		60.8 ± 1.27	90.56 ± 1.87
3s		4.49 ± 1.88	>100[a]
3t		5.67 ± 1.11	>100[a]
3u		3.77 ± 1.35	>100[a]
3v		3.99 ± 1.28	>100[a]
5-Fluoro-2-oxindole			(7.51 ± 0.17) × 10³
Acarbose			569.43 ± 43.72

[a]*The inhibitory activity of test compounds at 100 µM is less than 50%.*

FIGURE 1 | Inhibition mechanism determination of compound **3f** on α-glucosidase.
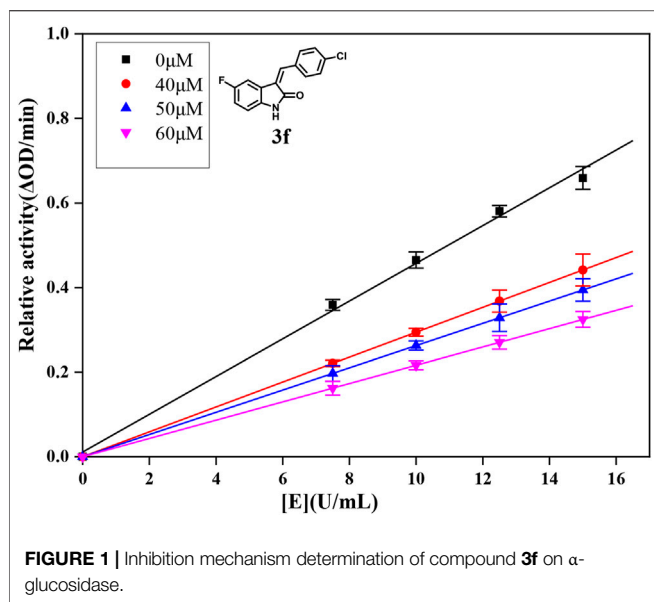
2 RESULTS AND DISCUSSION

2.1 Chemistry

The 5-fluoro-2-oxindole derivatives (**3a ~ 3v**) were prepared according to the synthetic route shown in **Scheme 1**. As the starting material, 5-fluoro-2-oxindole (**1**) was condensed with the substituted aromatic aldehydes (**2a ~ 2v**) in the presence of KOH to produce the title compounds (**3a ~ 3v**). The structures of compounds **3a ~ 3v** were characterized by ^{1}H NMR, MS, and melting point.

2.2 α-Glucosidase Inhibition Assay

α-Glucosidase from *Saccharomyces cerevisiae* (EC 3.2.1.20) was widely accepted and used to evaluate the inhibitory activity against α-glucosidase. Then, the inhibitory activity of compounds (**3a ~ 3v**) on α-glucosidase from *S. cerevisiae* was investigated using *p*-NPG as the substrate. First, the inhibitory activities of compounds (**3a ~ 3v**) were screened at a concentration of 100 μM. As shown in **Table 1**, compounds **3d**, **3f**, and **3i** presented better activities, with inhibition of ~90% at a concentration of 100 μM and those of compounds (**3g**, **3n**, **3p**, and **3r**) were ~50% at a concentration of 100 μM, while those of other compounds were below 50% at a concentration of 100 μM. Then, IC$_{50}$ values of compounds **3d**, **3f**, **3i**, **3n**, **3p**, and **3r** were measured due to their better inhibitory activities. The IC$_{50}$ values are summarized in **Table 1**, and the inhibitory activities of compounds **3d**, **3f**, and **3i** on α-glucosidase are presented in **Figure 1**. For analyzing the inhibitory activities of compounds (**3a ~ 3v**), the inhibitory activities of 5-fluoro-2-oxindole and acarbose were investigated. Among all compounds, compounds **3d**, **3f**, and **3i** exhibited much better potent inhibitory activity with IC$_{50}$ values of 56.87 ± 0.42 μM, 49.89 ± 1.16 μM, and 35.83 ± 0.98 μM, respectively, which were about 10 ~ 15 folds higher than that of acarbose (IC$_{50}$ = 569.43 ± 43.72 μM) and significantly better than that of 5-fluoro-2-oxindole (IC$_{50}$ = (7.51 ± 0.17)×10^3 μM).

2.3 Structure–Activity Relationships

Then, the structure–activity relationships of compounds (**3a ~ 3v**) were analyzed according to the experimental data in **Table 1**. First, the steric effect of substituents at aldehydes was investigated based on the inhibitory activities of compounds **3a/3b/3c**, **3d/3e/3f**, **3g/3h/3i**, and **3m/3n**, with -F, -Cl, -Br, and -CF$_3$ at ortho-, meta- and para-positions of the benzene ring, and the order of the inhibitory activities is 4- > 2- > 3-. When the substituent was OCH$_3$ (**3j/3k/3l**), it turned out just the opposite. Second, the electronic effect of substituents was considered. The introduction of -F, -Cl, -Br, -CF$_3$, and -OCH$_3$ at phenyl para-position (compounds **3c**, **3f**, **3i**, **3l**, and **3r**) could enhance the inhibitory activities with the inhibitory activity order of -Cl > -Br > -SCH$_3$ > -OCH$_3$ > -F. It could be seen that the inhibitory activity has no correlation with the steric and electronic effects of substituents at aldehydes. Furthermore, the introduction of various heterocycles (compounds **3s**, **3t**, **3u**, and **3v**) presented a negative effect on inhibitory activity. It could be concluded that the introduction of the substituents at the benzyl para-position of substituted aldehydes is beneficial to the improvement of the inhibitory activity. Therefore, the further derivatization of title compounds might be focused on the screening of substituents at the benzyl para-position of substituted aldehydes.

2.4 Inhibitory Mechanism Analysis

For further understanding the interaction mechanism of title compounds with α-glucosidase, compounds **3d**, **3f**, and **3i** were selected to investigate the inhibition mechanism of α-glucosidase through revealing the linkage between enzyme activity and the enzyme concentration in the presence of test compounds (figures for the inhibitory mechanism analysis of compounds **3f** was shown in **Figure 2** and figures for the inhibitory mechanism analysis of compounds **3d** and **3i** have been shown in the supporting information). The increasing concentrations of compounds **3d**, **3f**, or **3i** reduced the slope of the lines and the plots of the enzyme activity vs. the enzyme concentration at different concentrations of compounds **3d**, **3f**, or **3i** gave a group of straight lines, which all passed through the origin, indicating that the inhibitor reduces the activity of the enzyme and the inhibition of compounds **3d**, **3f**, or **3i** against α-glucosidase was reversible.

In order to obtain the inhibition kinetics type of compounds **3d**, **3f**, and **3i**, the Lineweaver–Burk plot analysis method was carried out with different concentrations of test compounds and substrates. For compounds **3d**, **3f**, and **3i**, the plots of 1/ν vs. 1/[S] gave a group of straight lines with different slopes that intersected the same point at the second quadrant, indicating that compounds **3d**, **3f**, and **3i** were mixed-type inhibitors. Then, the K_I values were calculated as 14.96, 33.85, and 22.72 μM, respectively, and the K_{IS} values were calculated as 453.85, 58.31, and 24.74 μM, respectively, which are summarized in **Table 2**. These results showed that compounds **3d**, **3f**, and **3i** could bind with the free enzyme as well as the enzyme–substrate complex of α-glucosidase. In addition, the inhibition types of compounds **3d**, **3f**, and **3i**, different from that of acarbose, are the competitive inhibition type.
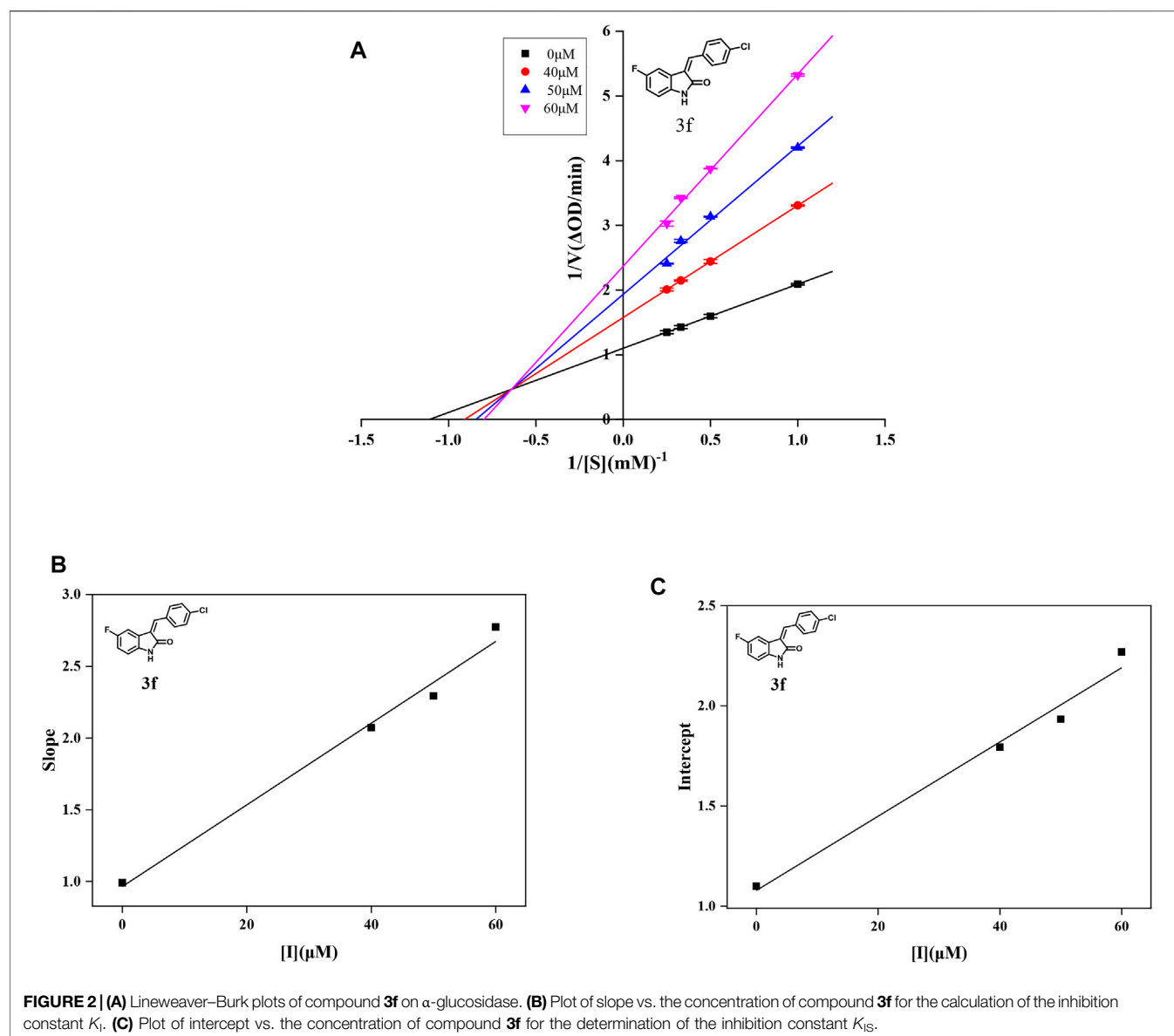
FIGURE 2 | (A) Lineweaver–Burk plots of compound **3f** on α-glucosidase. (B) Plot of slope vs. the concentration of compound **3f** for the calculation of the inhibition constant K_I. (C) Plot of intercept vs. the concentration of compound **3f** for the determination of the inhibition constant K_{IS}.

TABLE 2 | Type of inhibition mechanism and K_I and K_{IS} values of compounds **3d**, **3f**, and **3i**.

Compound	Inhibition mechanism	K_I (µM)	K_{IS} (µM)
3d	Mixed type	14.96	453.85
3f	Mixed type	33.85	58.31
3i	Mixed type	22.72	24.74

2.5 Molecular Docking Studies

With the purpose of acquiring a better comprehension of the mutual effects between compounds **3d**, **3f**, and **3i** and α-glucosidase, molecular docking studies were implemented using Sybyl tools. The 3D structures of *S. cerevisiae* α-glucosidase (EC 3.2.1.20) are unavailable, and oligo-1, 6-glucosidase from *S. cerevisiae* (PDB: 1UOK) was selected as the target protein. Also, the sequence similarity is about 62.0% and the sequence identity is about 38.0%, as compared with α-glucosidase. As demonstrated in **Figure 3A**, compounds **3d**, **3f**, and **3i** were well inserted into the active pocket of α-glucosidase, with similar angles and positions. A hydrogen bond between carbonyl of compounds **3d**, **3f**, and **3i** and amino acid sequences of GLN330 was formed to increase the affinity with α-glucosidase (**Figure 3B**). These similar integrated situations of compounds **3d**, **3f**, and **3i** with α-glucosidase indicated the same inhibition mechanism. In addition, the lipophilic potential interaction between **3d**, **3f**, and **3i** and the active pocket was investigated. As shown in **Figure 3C**, the active pocket external is more lipophilic than the interior. Then, in **Figure 3D**, the fluorophenyl as the lipophilic fraction of **3d**, **3f**, and **3i** was close to the lipophilic potential region, while the pyrrole ring as the hydrophilic fraction was near to the hydrophilic region.
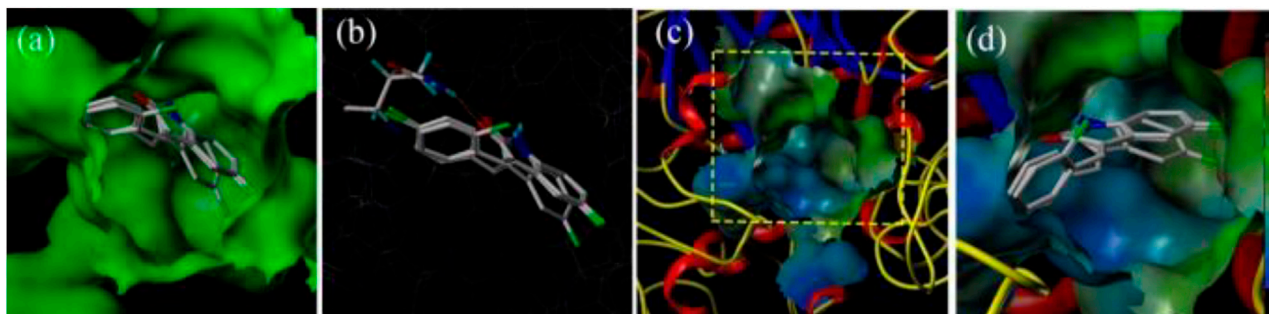
FIGURE 3 | (A) The insertion of compounds **3d**, **3f**, and **3i** into the active pocket of α-glucosidase; **(B)** The hydrogen-bond interaction between carbonyl of the compounds (**3d**, **3f**, and **3i**) and α-glucosidase; **(C)** The lipophilic interaction between the compounds (**3d**, **3f**, and **3i**) and α-glucosidase; **(D)** The fluorophenyl as the lipophilic fraction of compounds **3d**, **3f**, and **3i** binding to α-glucosidase.

3 EXPERIMENTAL

3.1 Chemicals

α-Glucosidase from *S. cerevisiae* (EC 3.2.1.20) and 4-nitrophenyl-β-D-galactopyranoside (*p*-NPG) were supplied by Sigma-Aldrich. All other reagents were of analytical grade. The water used was re-distilled and ion-free.

3.2 Instruments

^{1}H NMR was recorded by using a NMR spectrometer (DPX-500 MHz) in chloroform-*d* or DMSO-d_6, with chemical shifts (d) given in parts per million (ppm) relative to TMS as internal standard and recorded. Mass spectrometry was determined on a (LCQTM) LC-MS supplied by Thermo Fisher Scientific (Shanghai) Co., Ltd. Melting points were measured on a micro melting point instrument, which was supplied by Shanghai Yidian Physical Optical Instrument Co., Ltd. The absorbance was recorded using a microplate reader supplied by Thermo Fisher Scientific (Shanghai) Co., Ltd.

3.3 Synthesis of Compounds 3a ~ 3v

To a solution of 1 (1.0 mmol, 1.0 equiv.) and **2a ~ 2v** in 10 ml absolute ethanol was added KOH (6 mmol, 6.0 equiv.), followed by the addition of the corresponding substituted aldehydes. Then, the mixture was stirred at room temperature for 3 h and detected to be complete by TLC. The mixture was adjusted to the pH value between 2.0 and 3.0, followed by the evaporation of ethanol, and extraction with ethyl acetate. The ethyl acetate layer was washed with saturated NaHCO$_3$ and brine and then was concentrated under vacuum to give the crude product, subsequently by the recrystallization with ethanol to give compounds **3a ~ 3v**.

(Z)-5-Fluoro-3-(2-Fluorobenzylidene) Indolin-2-One (3a). Orange-yellow crystal; yield 65.0%; m p.: 228.3–230.2°C; ^{1}H NMR (500 MHz, DMSO-d_6) δ 10.73 (s, 1H), 7.77 (td, *J* = 7.7, 1.7 Hz, 1H), 7.65–7.55 (m, 2H), 7.47–7.36 (m, 2H), 7.13 (td, *J* = 9.0, 2.6 Hz, 1H), 6.94 (dd, *J* = 9.0, 2.6 Hz, 1H), and 6.88 (dd, *J* = 8.5, 4.6 Hz, 1H); HRMS (ESI) calculated for C$_{15}$H$_9$F$_2$NO [M - H]$^-$: m/z = 256.24, found 255.85.

(Z)-5-Fluoro-3-(3-Fluorobenzylidene) Indolin-2-One (3b). Orange-yellow crystal; yield 41.2%; m p.: 191.4–192.2°C; ^{1}H NMR (500 MHz, chloroform-*d*) δ 7.81 (s, 1H), 7.49 (td, *J* = 8.0, 5.7 Hz, 1H), 7.42 (dp, *J* = 7.6, 0.9 Hz, 1H), 7.30 (ddd, *J* = 8.9, 6.8, 2.4 Hz, 2H), 7.20–7.15 (m, 1H), 6.97 (td, *J* = 8.7, 2.5 Hz, 1H), 6.82 (dd, *J* = 8.6, 4.4 Hz, 1H); HRMS (ESI) calculated for C$_{15}$H$_9$F$_2$NO [M - H]$^-$: m/z = 256.24, found 256.09.

(Z)-5-Fluoro-3-(4-Fluorobenzylidene) Indolin-2-One (3c). Orange-yellow crystal; yield 55.7%; mp.: 217.0–219.6°C; ^{1}H NMR (500 MHz, chloroform-*d*) δ 8.10 (s, 1H), 7.82 (s, 1H), 7.64 (dd, *J* = 8.5, 5.4 Hz, 2H), 7.32 (dd, *J* = 9.1, 2.5 Hz, 1H), 7.20 (t, *J* = 8.4 Hz, 2H), 6.96 (td, *J* = 8.8, 2.6 Hz, 1H), and 6.83 (dd, *J* = 8.5, 4.4 Hz, 1H); HRMS (ESI) calculated for C$_{15}$H$_9$F$_2$NO [M-H]$^-$: m/z = 256.24, found 256.17.

(Z)-3-(2-Chlorobenzylidene)-5-Fluoroindolin-2-One (3d). Orange-yellow crystal; yield 82.4%; m p.: 219.7–221.9°C; ^{1}H NMR (500 MHz, chloroform-*d*) δ 8.12 (s, 1H), 7.92 (s, 1H), 7.68 (dd, *J* = 7.5, 1.8 Hz, 1H), 7.54 (dd, *J* = 7.9, 1.4 Hz, 1H), 7.40 (dtd, *J* = 20.5, 7.5, 1.6 Hz, 2H), 7.04 (dd, *J* = 8.9, 2.6 Hz, 1H), 6.94 (td, *J* = 8.8, 2.6 Hz, 1H), and 6.82 (dd, *J* = 8.5, 4.3 Hz, 1H); HRMS (ESI) calculated for C$_{15}$H$_9$ClFNO [M-H]$^-$: m/z = 272.69, found 271.96.

(Z)-3-(3-Chlorobenzylidene)-5-Fluoroindolin-2-One (3e). Orange-yellow crystal; yield 47.8%; mp: 237.4–238.9°C; ^{1}H NMR (500 MHz, chloroform-*d*) δ 7.97 (s, 1H), 7.79 (s, 1H), 7.58 (dd, *J* = 2.1, 1.1 Hz, 1H), 7.54–7.50 (m, 1H), 7.46–7.43 (m, 2H), 7.25 (d, *J* = 2.5 Hz, 1H), 6.97 (td, *J* = 8.7, 2.6 Hz, 1H), and 6.82 (dd, *J* = 8.5, 4.4 Hz, 1H); HRMS (ESI) calculated for C$_{15}$H$_9$ClFNO [M-H]$^-$: m/z = 272.69, found 272.10.

(Z)-3-(4-Chlorobenzylidene)-5-Fluoroindolin-2-One (3f). Orange-yellow crystal; yield 44.2%; mp: 200.6–202.5°C; ^{1}H NMR (500 MHz, chloroform-*d*) δ 7.80 (s, 1H), 7.58 (d, *J* = 8.3 Hz, 2H), 7.51–7.45 (m, 2H), 7.30 (dd, *J* = 8.9, 2.5 Hz, 1H), 6.96 (td, *J* = 8.7, 2.6 Hz, 1H), and 6.82(dd, *J* = 8.5, 4.4 Hz, 1H); HRMS (ESI) calculated for C$_{15}$H$_9$ClFNO [M-H]$^-$: m/z = 272.69, found 272.39.

(Z)-3-(2-Bromobenzylidene)-5-Fluoroindolin-2-One (3g). Orange-yellow crystal; yield 69.7%; mp: 194.9–197.1°C; ^{1}H NMR (500 MHz, chloroform-*d*) δ 7.90–7.82 (m, 1H), 7.73 (dd, *J* = 8.1, 1.1 Hz, 1H), 7.66 (dt, *J* =

7.7, 1.9 Hz, 1H), 7.44 (td, J = 7.4, 1.1 Hz, 1H), 7.34 (td, J = 7.7, 1.6 Hz, 1H), 7.00 (dd, J = 8.9, 2.6 Hz, 1H), and 6.94 (td, J = 8.7, 2.6 Hz, 1H); HRMS (ESI) calculated for $C_{15}H_9BrFNO$ [M + Na]$^+$: m/z = 340.15, found 340.59.

(Z)-3-(3-Bromobenzylidene)-5-Fluoroindolin-2-One (3h). Orange-yellow crystal; yield 70.4%; mp: 222.6–223.8°C; ^{1}H NMR (500 MHz, chloroform-*d*) δ 8.31 (s, 1H), 7.86–7.67 (m, 2H), 7.66–7.48 (m, 2H), 7.38 (t, J = 7.9 Hz, 1H), 7.24 (d, J = 2.6 Hz, 1H), 6.97 (td, J = 8.7, 2.6 Hz, 1H), and 6.84 (dd, J = 8.5, 4.4 Hz, 1H); HRMS (ESI) calculated for $C_{15}H_9BrFNO$ [M + Na]$^+$: m/z = 357.15, found 357.97.

(Z)-3-(4-Bromobenzylidene)-5-Fluoroindolin-2-One (3i). Orange-yellow crystal; yield 65.7%; mp: 249.3–251.6°C; ^{1}H NMR (500 MHz, chloroform-*d*) δ 7.77 (s, 1H), 7.67–7.61 (m, 2H), 7.51 (d, J = 8.4 Hz, 2H), 7.30 (dd, J = 9.0, 2.6 Hz, 1H), 6.96 (td, J = 8.7, 2.6 Hz, 1H), and 6.81 (dd, J = 8.5, 4.4 Hz, 1H); HRMS (ESI) calculated for $C_{15}H_9BrFNO$ [M + Na]$^+$: m/z = 341.15, found 340.97.

(Z)-5-Fluoro-3-(2-Methoxybenzylidene) Indolin-2-One (3j). Orange-yellow crystal; yield 52.7%; mp: 227.1–227.8°C; ^{1}H NMR (500 MHz, chloroform-*d*) δ 8.02 (s, 1H), 7.97 (s, 1H), 7.67 (dd, J = 7.7, 1.7 Hz, 1H), 7.49–7.42 (m, 1H), 7.28 (dd, J = 9.2, 2.7 Hz, 1H), 7.06 (td, J = 7.5, 1.0 Hz, 1H), 7.00 (dd, J = 8.3, 1.0 Hz, 1H), 6.91 (td, J = 8.8, 2.6 Hz, 1H), 6.80 (dd, J = 8.5, 4.4 Hz, 1H), and 3.89 (s, 3H); HRMS (ESI) calculated for $C_{16}H_{12}FNO_2$ [M-H]$^-$: m/z = 268.28, found 268.19.

(Z)-5-Fluoro-3-(3-Methoxybenzylidene) Indolin-2-One (3k). Orange-yellow crystal; yield 73.3%; mp: 200.1–202.1°C; ^{1}H NMR (500 MHz, chloroform-*d*) δ 7.86 (s, 1H), 7.45–7.38 (m, 2H), 7.23 (d, J = 7.5 Hz, 1H), 7.14 (t, J = 2.0 Hz, 1H), 7.04–6.90 (m, 2H), 6.82 (dd, J = 8.6, 4.4 Hz, 1H), and 3.86 (s, 3H); HRMS (ESI) calculated for $C_{16}H_{12}FNO_2$ [M-H]$^-$: m/z = 268.28, found 268.01.

(Z)-5-Fluoro-3-(4-Methoxybenzylidene) Indolin-2-One (3l). Orange-yellow crystal; yield 42.8%; mp: 358.8–359.9°C; ^{1}H NMR (500 MHz, chloroform-*d*) δ 7.84 (s, 1H), 7.68–7.62 (m, 2H), 7.49 (dd, J = 9.3, 2.6 Hz, 1H), 7.04–7.00 (m, 2H), 6.93 (dd, J = 8.8, 2.6 Hz, 1H), 6.83 (dt, J = 9.0, 3.6 Hz, 1H), and 3.91 (s, 3H); HRMS (ESI) calculated for $C_{16}H_{12}FNO_2$ [M-H]$^-$: m/z = 268.28, found 268.11.

(Z)-5-Fluoro-3-[2-(Trifluoromethyl) Benzylidene) Indolin-2-One (3m). Orange-yellow crystal; yield 53.1%; mp: 235.2–236.4°C; ^{1}H NMR (500 MHz, chloroform-*d*) δ 8.33–8.22 (m, 1H), 8.01 (q, J = 2.5 Hz, 1H), 7.83 (d, J = 7.8 Hz, 1H), 7.70–7.65 (m, 2H), 7.63–7.55 (m, 1H), 6.93 (td, J = 8.8, 2.6 Hz, 1H), 6.83 (dd, J = 8.5, 4.3 Hz, 1H), and 6.66 (dd, J = 8.7, 2.6 Hz, 1H); HRMS (ESI) calculated for $C_{16}H_9F_4NO$ [M-H]$^-$: m/z = 306.25, found 305.91.

(Z)-5-Fluoro-3-[3-(Trifluoromethyl) Benzylidene] Indolin-2-One (3n). Orange-yellow crystal; yield 42.9%; mp: 199.7–200.5°C; ^{1}H NMR (500 MHz, chloroform-*d*) δ 7.87 (s, 1H), 7.85 (s, 1H), 7.81 (d, J = 7.7 Hz, 1H), 7.73 (d, J = 7.8 Hz, 1H), 7.64 (t, J = 7.8 Hz, 1H), 7.18 (dd, J = 8.9, 2.6 Hz, 1H), 6.97 (td, J = 8.7, 2.6 Hz, 1H), and 6.83 (dd, J = 8.6, 4.3 Hz, 1H); HRMS (ESI) calculated for $C_{16}H_9F_4NO$ [M-H]$^-$: m/z = 306.25, found 306.01.

(Z)-3-(2,4-Difluorobenzylidene)-5-Fluoroindolin-2-One (3o). Orange-yellow crystal; yield 55.3%; mp: 221.1–224.3°C; ^{1}H NMR (500 MHz, chloroform-*d*) δ 8.31–8.21 (s, 1H), 8.01 (s, 1H), 7.83 (d, J = 7.8 Hz, 1H), 7.68–7.65 (m, 2H), 7.62–7.58 (m, 1H), 6.93 (td, J = 8.8, 2.6 Hz, 1H), 6.83 (dd, J = 8.5, 4.3 Hz, 1H), and 6.66 (dd, J = 8.7, 2.6 Hz, 1H); HRMS (ESI) calculated for $C_{16}H_9F_4NO$ [M + H]$^+$: m/z = 276.23, found 278.01.

(Z)-3-(3,4-Difluorobenzylidene)-5-Fluoroindolin-2-One (3p). Orange-yellow crystal; yield 44.6%; mp: 189.2–190.2°C; ^{1}H NMR (500 MHz, chloroform-*d*) δ 8.99 (dd, J = 10.1, 2.7 Hz, 1H), 8.91 (ddd, J = 4.6, 2.0, 0.8 Hz, 1H), 7.83 (td, J = 7.7, 1.9 Hz, 1H), 7.73 (s, 1H), 7.63 (dd, J = 7.7, 1.1 Hz, 1H), 7.36 (ddd, J = 7.7, 4.7, 1.1 Hz, 1H), 7.01 (td, J = 8.6, 2.7 Hz, 1H), and 6.80 (dd, J = 8.5, 4.4 Hz, 1H); HRMS (ESI) calculated for $C_{15}H_8F_3NO$ [M-H]$^-$: m/z = 274.23, found 274.02.

(Z)-3-Benzylidene-5-Fluoroindolin-2-One (3q). Orange-yellow crystal; yield 76.3%; mp: 198.9–199.7°C; ^{1}H NMR (500 MHz, chloroform-*d*) δ 8.93 (s, 1H), 7.90 (s, 1H), 7.67–7.62 (m, 2H), 7.53–7.46 (m, 3H), 7.36 (dd, J = 9.1, 2.6 Hz, 1H), 6.94 (td, J = 8.7, 2.5 Hz, 1H), and 6.86 (dd, J = 8.5, 4.5 Hz, 1H); HRMS (ESI) calculated for $C_{15}H_8F_3NO$ [M-H]$^-$: m/z = 238.25, found 237.99.

(Z)-5-Fluoro-3-[4-(Methylthio) Benzylidene] Indolin-2-One (3r). Orange-yellow crystal; yield 41.8%; mp: 246.1–247.1°C; ^{1}H NMR (500 MHz, chloroform-*d*) δ 8.13 (s, 1H), 7.81 (s, 1H), 7.61–7.55 (m, 2H), 7.44 (dd, J = 9.0, 2.6 Hz, 1H), 7.36–7.31 (m, 2H), 6.94 (td, J = 8.7, 2.5 Hz, 1H), 6.82 (dd, J = 8.5, 4.4 Hz, 1H), and 2.56 (s, 3H); HRMS (ESI) calculated for $C_{16}H_{12}FNOS$ [M-H]$^-$: m/z = 284.34, found 284.13.

(Z)-5-Fluoro-3-(Furan-2-ylmethylene) Indolin-2-One (3s). Orange-yellow crystal; yield 72.5%; mp: 237.9–238.8°C; ^{1}H NMR (500 MHz, chloroform-*d*) δ 7.76 (s, 1H), 7.41 (s, 1H), 7.24–7.16 (m, 2H), 6.88 (td, J = 8.8, 2.5 Hz, 1H), 6.82 (dd, J = 8.5, 4.2 Hz, 2H), and 6.42 (dt, J = 4.0, 2.1 Hz, 1H); HRMS (ESI) calculated for $C_{16}H_{12}FNOS$ [M-H]$^-$: m/z = 228.21, found 227.95.

(Z)-5-Fluoro-3-(Thiophen-2-ylmethylene) Indolin-2-One (3t). Orange-yellow crystal; yield 44.6%; mp: 219.0–223.4°C; ^{1}H NMR (500 MHz, chloroform-*d*) δ 8.01 (dd, J = 9.4, 2.5 Hz, 1H), 7.97 (s, 1H), 7.85 (s, 1H), 7.65 (dd, J = 23.4, 4.4 Hz, 2H), 7.23 (dd, J = 5.1, 3.7 Hz, 1H), 6.99 (td, J = 8.7, 2.5 Hz, 1H), and 6.84 (dd, J = 8.5, 4.5 Hz, 1H); HRMS (ESI) calculated for $C_{16}H_{12}FNOS$ [M-H]$^-$: m/z = 244.27, found 244.14.

(Z)-3-[(1H-Pyrrol-2-yl)methylene]-5-Fluoroindolin-2-One (3u). Orange-yellow crystal; yield 54.4%; mp: 198.9–201.6°C; ^{1}H NMR (500 MHz, chloroform-*d*) δ 13.30 (s, 1H), 7.76 (s, 1H), 7.41 (s, 1H), 7.22 (s, 1H), 7.19 (dd, J = 8.7, 2.5 Hz, 1H), 6.88 (td, J = 8.8, 2.5 Hz, 1H), 6.82 (d, J = 4.2 Hz, 2H), and 6.42 (dt, J = 4.0, 2.1 Hz, 1H); HRMS (ESI) calculated for $C_{13}H_9FN_2O$ [M-H]$^-$: m/z = 227.23, found 227.02.

(Z)-5-Fluoro-3-(Pyridin-2-ylmethylene) Indolin-2-One (3v). Orange-yellow crystal; yield 47.9%; mp: 248.5–251.2°C; ^{1}H NMR (500 MHz, chloroform-*d*) δ 8.99 (dd, J = 10.1, 2.7 Hz, 1H), 8.91 (ddd, J = 4.6, 2.0, 0.8 Hz, 1H), 7.83 (td, J = 7.7, 1.9 Hz, 1H), 7.73 (s, 1H), 7.63 (dd, J = 7.7, 1.1 Hz, 1H), 7.36 (ddd, J = 7.7, 4.7, 1.1 Hz, 1H), 7.01 (td, J = 8.6, 2.7 Hz, 1H), and 6.80 (dd, J = 8.5, 4.4 Hz, 1H); HRMS (ESI) calculated for $C_{13}H_9FN_2O$ [M-H]$^-$: m/z = 239.24, found 238.93.

3.4 α-Glucosidase Inhibitory Assay

The α-glucosidase inhibition of synthetic compounds was performed as previously reported methods with minor modification (Deng et al., 2022) which is as follows: briefly, 130 μl of phosphate buffer (10 mM, pH 6.8), 10 μl of α-glucosidase (1 U/ml), and 10 μl of test compound solution were added into the wells of a 96-well plate, followed by incubation for 10 min at 37°C. Then, 50 μl of *p*-NPG (1 mM) was added, and the plate was further incubated for 30 min at 37°C. Finally, the absorbance of each well was recorded at 405 nm using a microplate reader. Acarbose was used as the reference. The inhibition of the test compound on α-glucosidase was calculated as follows: inhibition ratio (%) = [(A− B)/A] × 100, where A is the absorbance of blank and B is the absorbance of the test compound. Each concentration was experimented four times in parallel. Half inhibitory concentration (IC$_{50}$) was obtained from the fitting curve of inhibition ratio vs. test compound with different concentrations.

3.5 Kinetics Mechanism Analysis

Compounds **3d**, **3f**, and **3i** with much better α-glucosidase inhibitory activity were selected for kinetic analysis. The experiments were performed to investigate the kinetics mechanism of compounds **3d**, **3f**, and **3i** by the previously reported method (Xu et al., 2019). To determine the inhibition mechanism, the final concentrations for **3d** were 0, 40, 50, 60 μM, for 3f were 0, 40, 50, 60 μM, and for **3i** were 0, 30, 40, 50 μM, the final substrate *p*-NPG concentration was 0.25 mM, and the final concentrations for α-glucosidase were 3.75×10^{-2}, 5.00×10^{-2}, 6.25×10^{-2}, and 7.50×10^{-2} U/ml. Then, the inhibition rates were measured by the aforementioned method.

To analyze the inhibition type, the final concentrations for **3d** were 0, 40, 50, and 60 μM, for **3f** were 0, 40, 50, and 60 μM, and for **3i** were 0, 30, 40, and 50 μM, the final α-glucosidase concentration was 5.00×10^{-2} U/ml, and final concentrations for substrate *p*-NPG concentration were 0.25, 0.50, 0.75, and 1.00 mM. The inhibition rates were obtained by the aforementioned method. The inhibition type on α-glucosidase was analyzed by using Lineweaver–Burk plots of the inverse of velocities (1/v) vs. the inverse of substrate concentration 1/[S]. The K_I and K_{IS} were obtained from the slope and the vertical intercept vs. the inhibitor concentration, respectively.

3.6 Molecular Docking

The molecular docking between compounds **3d**, **3f**, and **3i** and α-glucosidase were simulated with Sybyl-2.1.1 (Tripos, Shanghai, China) (Hu et al., 2021). First, compounds **3d**, **3f**, and **3i** were prepared by hydrogenation and energy minimization using the MM2 program. In the energy minimization program, the energy convergence criterion was revised to 0.001 kcal/mol, optimizing the energy gradient that was revised to 2,500 times, and the charge was run with the Gasteiger–Huckle charges method. Next, after being retrieved from the RCSB Protein Database (PDB: 1UOK), the α-glucosidase structure was prepared, followed by the procedure of removing water, termini treatment, adding

hydrogens, adding charges with the MMFF94, fixing side chain amides, and staged minimization. The active pocket of α-glucosidase was generated with the automatic mode. Then, the molecular docking between compounds **3d**, **3f**, and **3i** and α-glucosidase were operated in the default format.

4 CONCLUSION

In summary, a series of α-glucosidase inhibitors based on 5-fluoro-2-oxindole have been synthesized and evaluated. Most synthesized compounds presented better potential inhibitory on α-glucosidase than the parent compound. Among them, compounds **3d**, **3f**, and **3i** exhibited much better inhibitory activity with IC$_{50}$ values of 49.89 ± 1.16, 35.83 ± 0.98 and 56.87 ± 0.42 μM, respectively, which were about 10 ~ 15 folds higher activities than acarbose (IC$_{50}$ = 569.43 ± 43.72 μM) that was used as reference. The kinetics mechanism study revealed that compounds **3d**, **3f**, and **3i** inhibited the α-glucosidase in a reversible and mixed manner. Molecular docking confirmed that compounds could effectively integrate with α-glucosidase. These results indicated that these synthesized compounds could be used as the leading structure in the research and development of α-glucosidase inhibitors for the prevention and treatment of type 2 diabetes.

DATA AVAILABILITY STATEMENT

The original contributions presented in the study are included in the article/**Supplementary Material**; further inquiries can be directed to the corresponding authors.

AUTHOR CONTRIBUTIONS

JL, Q-ML, and Y-NY contributed to the synthesis and inhibitory activity evaluation. DX, LL, M-YL, J-PL, and Y-Z contributed to the characterization and analysis of ^{1}H NMR, ^{13}C NMR, and MS. ZX, NF, and CL supervised the work and prepared the manuscript.

SUPPLEMENTARY MATERIAL

The Supplementary Material for this article can be found online at: https://www.frontiersin.org/articles/10.3389/fchem.2022.928295/full#supplementary-material

REFERENCES

Al-Salahi, R., Ahmad, R., Anouar, E., Iwana Nor Azman, N. I., Marzouk, M., and Abuelizz, H. A. (2018). 3-Benzyl(phenethyl)-2-thioxobenzo[g]quinazolines as a New Class of Potent α-glucosidase Inhibitors: Synthesis and Molecular Docking Study. *Future Med. Chem.* 10, 1889–1905. doi:10.4155/fmc-2018-0141

Álvarez, R., Gajate, C., Puebla, P., Mollinedo, F., Medarde, M., and Peláez, R. (2018). Substitution at the Indole 3 Position Yields Highly Potent Indolecombretastatins against Human Tumor Cells. *Eur. J. Med. Chem.* 158, 167–183. doi:10.1016/j.ejmech.2018.08.078

Asadollahi-Baboli, M., and Dehnavi, S. (2018). Docking and QSAR Analysis of Tetracyclic Oxindole Derivatives as α-glucosidase Inhibitors. *Comput. Biol. Chem.* 76, 283–292. doi:10.1016/j.compbiolchem.2018.07.019

Bao, W., Wang, J.-Q., Xu, X.-T., Zhang, B.-H., Liu, W.-T., Lei, L.-S., et al. (2018). Copper-catalyzed Cyclization of 2-cyanobenzaldehydes and 2-isocyanoacetates: an Efficient Strategy for the Synthesis of Substituted 1-aminoisoquinolines. *Chem. Commun.* 54, 8194–8197. doi:10.1039/c8cc04733b

Chaudhry, F., Naureen, S., Ashraf, M., Al-Rashida, M., Jahan, B., Munawar, M. A., et al. (2019). Imidazole-pyrazole Hybrids: Synthesis, Characterization and *In-Vitro* Bioevaluation against α-glucosidase Enzyme with Molecular Docking Studies. *Bioorg. Chem.* 82, 267–273. doi:10.1016/j.bioorg.2018.10.047

Dan, W.-J., Zhang, Q., Zhang, F., Wang, W.-W., and Gao, J.-M. (2019). Benzonate Derivatives of Acetophenone as Potent α-glucosidase Inhibitors: Synthesis, Structure-Activity Relationship and Mechanism. *J. Enzyme Inhibition Med. Chem.* 34, 937–945. doi:10.1080/14756366.2019.1604519

Deng, X. Y., Ke, J. J., Zheng, Y. Y., Li, D. L., Zhang, K., Zheng, X., et al. (2022). Synthesis and Bioactivities Evaluation of Oleanolic Acid Oxime Ester Derivatives as α-glucosidase and α-amylase Inhibitors. *J. Enzyme Inhib. Med. Chem.* 37, 451–461. doi:10.1080/14756366.2021.2018682

Gollapalli, M., Taha, M., Javid, M. T., Almandil, N. B., Rahim, F., Wadood, A., et al. (2019). Synthesis of Benzothiazole Derivatives as a Potent α-glucosidase Inhibitor. *Bioorg. Chem.* 85, 33–48. doi:10.1016/j.bioorg.2018.12.021

Hu, C. M., Wang, W. J., Ye, Y. N., Kang, Y., Lin, J., Wu, P. P., et al. (2021). Novel Cinnamic Acid Magnolol Derivatives as Potent α-glucosidase and α-amylase Inhibitors: Synthesis, *In Vitro* and In Silico Studies. *Bioorgan. Chem.* 116, 105435. doi:10.1016/j.bioorg.2021.105291

Huang, Y., Zhang, B., Li, J., Liu, H., Zhang, Y., Yang, Z., et al. (2019). Design, Synthesis, Biological Evaluation and Docking Study of Novel Indole-2-Amide as Anti-inflammatory Agents with Dual Inhibition of COX and 5-LOX. *Eur. J. Med. Chem.* 180, 41–50. doi:10.1016/j.ejmech.2019.07.004

Johnson, B. M., Shu, Y.-Z., Zhuo, X., and Meanwell, N. A. (2020). Metabolic and Pharmaceutical Aspects of Fluorinated Compounds. *J. Med. Chem.* 63, 6315–6386. doi:10.1021/acs.jmedchem.9b01877

Kasturi, S. P., Surarapu, S., Uppalanchi, S., Dwivedi, S., Yogeeswari, P., Sigalapalli, D. K., et al. (2018). Synthesis, Molecular Modeling and Evaluation of α-glucosidase Inhibition Activity of 3,4-dihydroxy Piperidines. *Eur. J. Med. Chem.* 150, 39–52. doi:10.1016/j.ejmech.2018.02.072

Khan, M., Yousaf, M., Wadood, A., Junaid, M., Ashraf, M., Alam, U., et al. (2014). Discovery of Novel Oxindole Derivatives as Potent α-glucosidase Inhibitors. *Bioorg. Med. Chem.* 22, 3441–3448. doi:10.1016/j.bmc.2014.04.033

Leong, S. W., Awin, T., Mohd Faudzi, S. M., Maulidiani, M., Shaari, K., and Abas, F. (2019). Synthesis and Biological Evaluation of Asymmetrical Diarylpentanoids as Antiinflammatory, Anti-α-glucosidase, and Antioxidant Agents. *Med. Chem. Res.* 28, 2002–2009. doi:10.1007/s00044-019-02430-5

Mendieta-Moctezuma, A., Rugerio-Escalona, C., Villa-Ruano, N., Gutierrez, R. U., Jiménez-Montejo, F. E., Fragoso-Vázquez, M. J., et al. (2019). Synthesis and Biological Evaluation of Novel Chromonyl Enaminones as α-glucosidase Inhibitors. *Med. Chem. Res.* 28, 831–848. doi:10.1007/s00044-019-02320-w

Prachumrat, P., Kobkeatthawin, T., Ruanwas, P., Boonnak, N., Laphookhieo, S., Kassim, M. B., et al. (2018). Synthesis, Crystal Structure, Antioxidant, and α-Glucosidase Inhibitory Activities of Methoxy-Substituted Benzohydrazide Derivatives. *Crystallogr. Rep*+ 63, 405–411. doi:10.1134/s1063774518030227

Proença, C., Freitas, M., Ribeiro, D., Oliveira, E. F. T., Sousa, J. L. C., Tomé, S. M., et al. (2017). α-Glucosidase Inhibition by Flavonoids: an *In Vitro* and In Silico Structure-Activity Relationship Study. *J. Enzyme Inhibition Med. Chem.* 32, 1216–1228. doi:10.1080/14756366.2017.1368503

Proença, C., Freitas, M., Ribeiro, D., Sousa, J. L. C., Carvalho, F., Silva, A. M. S., et al. (2018). Inhibition of Protein Tyrosine Phosphatase 1B by Flavonoids: A Structure - Activity Relationship Study. *Food Chem. Toxicol.* 111, 474–481. doi:10.1016/j.fct.2017.11.039

Proença, C., Freitas, M., Ribeiro, D., Tomé, S. M., Oliveira, E. F. T., Viegas, M. F., et al. (2019). Evaluation of a Flavonoids Library for Inhibition of Pancreatic α-amylase towards a Structure-Activity Relationship. *J. Enzyme Inhibition Med. Chem.* 34, 577–588. doi:10.1080/14756366.2018.1558221

Qamar, R., Saeed, A., Saeed, M., Shah, B. H., Ashraf, Z., Abbas, Q., et al. (2018). Synthesis and Enzyme Inhibitory Kinetics of Some Novel 3-(substituted Benzoyl)-2-Thioxoimidazolidin-4-One Derivatives as α-glucosidase/α-amylase Inhibitors. *Med. Chem. Res.* 27, 1528–1537. doi:10.1007/s00044-018-2170-4

Rama Krishna, B., Ramakrishna, S., Rajendra, S., Madhusudana, K., and Mallavadhani, U. V. (2019). Synthesis of Some Novel Orsellinates and Lecanoric Acid Related Depsides as α-glucosidase Inhibitors. *J. Asian Nat. Prod. Res.* 21, 1013–1027. doi:10.1080/10286020.2018.1490274

Rocha, S., Sousa, A., Ribeiro, D., Correia, C. M., Silva, V. L. M., Santos, C. M. M., et al. (2019). A Study towards Drug Discovery for the Management of Type 2 Diabetes Mellitus through Inhibition of the Carbohydrate-Hydrolyzing Enzymes α-amylase and α-glucosidase by Chalcone Derivatives. *Food Funct.* 10, 5510–5520. doi:10.1039/C9FO01298B

Santos, C. M. M., Freitas, M., and Fernandes, E. (2018). A Comprehensive Review on Xanthone Derivatives as α-glucosidase Inhibitors. *Eur. J. Med. Chem.* 157, 1460–1479. doi:10.1016/j.ejmech.2018.07.073

Settypalli, T., Chunduri, V. R., Maddineni, A. K., Begari, N., Kotha, P., Chippada, A. R., et al. (2019). Design, Synthesis, In Silico Docking Studies and Biological Evaluation of Novel Quinoxaline-Hydrazide Hydrazone-1,2,3-Triazole Hybrids as α-glucosidase Inhibitors and Antioxidants. *New J. Chem.* 43, 15435–15452. doi:10.1039/c9nj02580d.

Shah, S., ArshiaJavaid, K., Zafar, H., Mohammed Khan, K., Khalil, R., et al. (2018). Synthesis, and *In Vitro* and *In Silico* α-Glucosidase Inhibitory Studies of 5-Chloro-2-Aryl Benzo[d]thiazoles. *Bioorg. Chem.* 78, 269–279. doi:10.1016/j.bioorg.2018.02.013

Sonia, R., Daniela, R., Eduarda, F., and Marisa, F. (2019). Meet Our Editorial Board Member. *Curr. Med. Chem.* 26, 1–64. doi:10.2174/092986732601190314143611

Spasov, A. A., Babkov, D. A., Osipov, D. V., Klochkov, V. G., Prilepskaya, D. R., Demidov, M. R., et al. (2019). Synthesis, *In Vitro* and *In Vivo* Evaluation of 2-Aryl-4h-Chromene and 3-Aryl-1h-Benzo[f]chromene Derivatives as Novel α-glucosidase Inhibitors. *Bioorg. Med. Chem. Lett.* 29, 119–123. doi:10.1016/j.bmcl.2018.10.018

Taha, M., Imran, S., Rahim, F., Wadood, A., and Khan, K. M. (2018b). Oxindole Based Oxadiazole Hybrid Analogs: Novel α-glucosidase Inhibitors. *Bioorg. Chem.* 76, 273–280. doi:10.1016/j.bioorg.2017.12.001

Taha, M., Ismail, N. H., Imran, S., Wadood, A., Rahim, F., Ali, M., et al. (2015). Novel Quinoline Derivatives as Potent *In Vitro* α-glucosidase Inhibitors: In Silico Studies and SAR Predictions. *Med. Chem. Commun.* 6, 1826–1836. doi:10.1007/s00044-019-02430-510.1039/c5md00280j

Taha, M., Shah, S. A. A., Afifi, M., Imran, S., Sultan, S., Rahim, F., et al. (2018a). Synthesis, α-glucosidase Inhibition and Molecular Docking Study of Coumarin Based Derivatives. *Bioorg. Chem.* 77, 586–592. doi:10.1016/j.bioorg.2018.01.033

Wang, G.-c., Peng, Y.-p., Xie, Z.-z., Wang, J., and Chen, M. (2017). Synthesis, α-glucosidase Inhibition and Molecular Docking Studies of Novel Thiazolidine-2,4-Dione or Rhodanine Derivatives. *Med. Chem. Commun.* 8, 1477–1484. doi:10.1039/C7MD00173H

Wang, M.-Y., Cheng, X.-C., Chen, X.-B., Li, Y., Zang, L.-L., Duan, Y.-Q., et al. (2018). Synthesis and Biological Evaluation of novelN-Aryl-ω-(benzoazol-2-Yl)-Sulfanylalkanamides as Dual Inhibitors of α-glucosidase and Protein Tyrosine Phosphatase 1B. *Chem. Biol. Drug Des.* 92, 1647–1656. doi:10.1111/cbdd.13331

Wu, P.-P., Zhang, B.-J., Cui, X.-P., Yang, Y., Jiang, Z.-Y., Zhou, Z.-H., et al. (2017). Synthesis and Biological Evaluation of Novel Ursolic Acid Analogues as Potential α-glucosidase Inhibitors. *Sci. Rep.* 7, 45578. doi:10.1038/srep45578

Wu, P.-P., Zhang, K., Lu, Y.-J., He, P., and Zhao, S.-Q. (2014). *In Vitro* and *In Vivo* Evaluation of the Antidiabetic Activity of Ursolic Acid Derivatives. *Eur. J. Med. Chem.* 80, 502–508. doi:10.1016/j.ejmech.2014.04.073

Xu, X.-T., Mou, X.-Q., Xi, Q.-M., Liu, W.-T., Liu, W.-F., Sheng, Z.-J., et al. (2016). Anti-inflammatory Activity Effect of 2-Substituted-1,4,5,6-

Tetrahydrocyclopenta[b]pyrrole on TPA-Induced Skin Inflammation in Mice. *Bioorg. Med. Chem. Lett.* 26, 5334–5339. doi:10.1016/j.bmcl.2016.09.034

Xu, X. T., Deng, X. Y., Chen, J., Liang, Q. M., Zhang, K., Li, D. L., et al. (2019). Synthesis and Biological Evaluation of Coumarin Derivatives as α-glucosidase Inhibitors. *Eur. J. Med. Chem.* 189, 112013. doi:10.1016/j.ejmech.2019.112013

Yang, C., Yu, Y., Sun, W., and Xia, C. (2014). Indole Derivatives Inhibited the Formation of Bacterial Biofilm and Modulated Ca2+ Efflux in Diatom. *Mar. Pollut. Bull.* 88, 62–69. doi:10.1016/j.marpolbul.2014.09.027

Ye, G.-J., Lan, T., Huang, Z.-X., Cheng, X.-N., Cai, C.-Y., Ding, S.-M., et al. (2019). Design and Synthesis of Novel Xanthone-Triazole Derivatives as Potential Antidiabetic Agents: α-Glucosidase Inhibition and Glucose Uptake Promotion. *Eur. J. Med. Chem.* 177, 362–373. doi:10.1016/j.ejmech.2019.05.045

Zhong, Y., Yu, L., He, Q., Zhu, Q., Zhang, C., Cui, X., et al. (2019). Bifunctional Hybrid Enzyme-Catalytic Metal Organic Framework Reactors for α-Glucosidase Inhibitor Screening. *ACS Appl. Mat. Interfaces* 11, 32769–32777. doi:10.1021/acsami.9b11754

Synthesis and Anticancer Activity of Rhopaladins' Analog RPDPD Against the HeLa Human Cervical Cancer Cell Line

Feng Chen[1,2†], Hong-Mei Wang[2†], Ling-Qi Kong[2†], Qin-Hua Chen[3], Li-Na Ke[1]*, He-Liu Dai[1]* and Xiao-Hua Zeng[1,2]*

[1]Sinopharm Dongfeng General Hospital, Hubei University of Medicine, Shiyan, China, [2]Hubei Key Laboratory of Wudang Local Chinese Medicine Research, School of Pharmaceutical Sciences, Hubei University of Medicine, Shiyan, China, [3]Shenzhen Baoan Authentic TCM Therapy Hospital, Shenzhen, China

Heterocyclic compounds were widely used in many domains; pyrrolidone is a derivative of heterocycles that can be used to synthesize anticancer drugs. A new fluorine-containing rhopaladins' analog(*E*)-2-(4-bromobenzoyl)-*N*-(tert-butyl)-4-(4-fluoro benzylidene)-5-oxo-1-propylpyrrolidine-2-carboxamide (RPDPD for short) of 2-aroyl-4-arylidene-5-oxopyrrolidine derivative was synthesized by the one-pot synthesis method and evaluated for its anti-tumor activity *in vitro via* CCK8 assay and annexin V/propidium iodide (PI) staining of HeLa cells. The results exhibited that compound RPDPD has inhibited the proliferation of HeLa in a dose-dependent manner with an IC_{50} of 24.23 µmol/L ($p < 0.05$) and has low hepatotoxicity with an IC_{50} of 235.6 µmol/L ($p < 0.05$) to normal hepatocyte LO2 cells. The apoptotic assay demonstrated that compound RPDPD has induced apoptosis in HeLa cells (from 14.26 to 23.4%, $p < 0.05$). qRT-PCR results showed that the compound RPDPD could inhibit the expression of oncogene E6/E7 mRNA ($p < 0.05$) of human papillomavirus (HPV). The results of Western blot showed that the compound RPDPD promoted the expression of TIMP3 protein and inhibited the expression of MMP3 ($p < 0.05$). In conclusion, the compound RPDPD can inhibit the proliferation of cervical cancer cells and induce the apoptosis of cervical cancer cells, and its mechanism may be related to the inhibition of E6 mRNA and E7 mRNA expressions, and the anticancer effect of the compound RPDPD on cervical cancer is closely related to the TIMP3/MMP3 signaling axis.

Keywords: rhopaladins' analog, synthesis, 2-aroyl-4-arylidene-5-oxopyrrolidine, cytotoxicity evaluation, HPV E6/E7 mRNA, TIMP3/MMP3 pathway

INTRODUCTION

Heterocyclic compounds are extensively used in plenty of fields and are favored by many drug researchers. Pyrrolidone, one of the heterocyclic compounds, can be used as an antiviral (Nilsson et al., 1990), antiepileptic (Kenda et al., 2004), and anti-HIV (Kraus et al., 2000) agent. It has been reported that pyrrolidone can be used as an inhibitor of ceramide (Atigadda et al., 1999) and a selective inhibitor of matrix metalloproteinase (Wu and Feldkamp, 1961).

The incidence and development of cancer seriously threaten human health. The incidence rate of cervical cancer ranks fourth among cancer in women. In 2018, the incidence of new cases was about
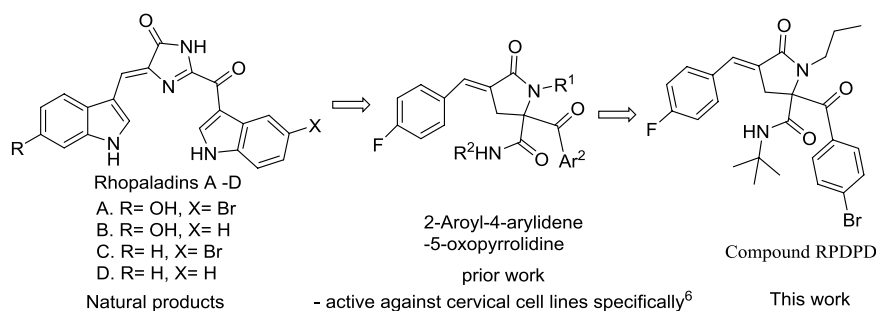
SCHEME 1 | Design strategy of rhopaladins' analog RPDPD as the target.
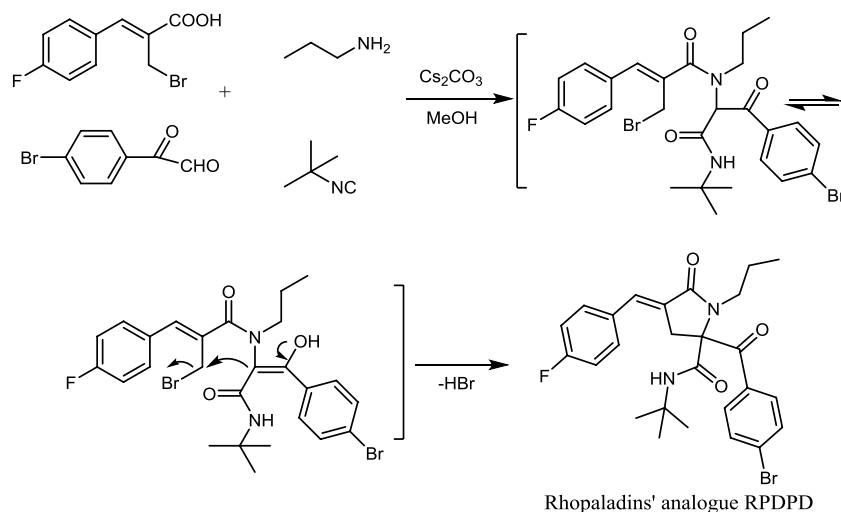
SCHEME 2 | Synthesis of rhopaladins' analog RPDPD.

570,000, and the death toll was about 310,000 for cervical cancer in the world (Freddie et al., 2018). The pathogenic factor of cervical cancer is human papillomavirus (HPV) (Ijang et al., 2019). HPV is a small enveloped DNA virus, which can be divided into two kinds of "low risk" or "high risk", with the inherent disorder area; it is the most common route of transmission for sexually transmitted disease (STD) (Kaushiki, et al., 2018). The common high-risk HPV viruses are HPV 16 and HPV 18. HeLa belongs to HPV 18 cells.

The studies have shown that marine alkaloids rhopaladins A–D have significant cytotoxicity to human tumor cell lines. Rhopaladin B has inhibitory activity against CDK4 and c-erbB-2 kinases (IC$_{50}$ of 12.5 and 7.4 μg/ml, respectively) (Hiroyasu et al., 1998; Zhu et al., 2019.). We have previously synthesized rhopaladins' analogs 2-aroyl-4-arylidene-5-oxopyrrolidine derivatives (see **Scheme 1**) via a tandem Ugi 4CC/S$_N$ cyclization and studied their cytotoxicity to HeLa cells (Wang et al., 2020). According to the existing structure–activity relationship analysis (Wang et al., 2020), in order to obtain a compound with good anti-cervical cancer activity (fluorine-containing) and low hepatotoxicity (bromine-containing), a new rhopaladins' analog(E)-2-(4-bromobenzoyl)-N-(tert-butyl)-4-(4-fluorobenzylidene) -5-oxo-1-propylpyrrolidine-2-carboxamide

(RPDPD for short) of 2-aroyl-4-arylidene-5-oxopyrrolidine derivative was synthesized by a similar method (see **Scheme 2**). We investigated the cytotoxic and apoptotic effects of compound RPDPD on HeLa cell lines and preliminarily explored the relationship between RPDPD and TIMP3/MMP3 signaling axis.

We used a one-pot Ugi 4CC/S$_N$ cyclization method to synthesize 5-oxopyrrolidine -2-carboxamide. The advantages of this synthesis method lie in mild reaction conditions, high yield, and easy availability of raw materials. This new rhopaladins' analog RPDPD can inhibit the proliferation of the HeLa cell line. Moreover, RPDPD induced HeLa cell apoptosis at early apoptosis. We believed that this synthesis method has potential application prospects in the synthesis of natural products and their analogs, and this compound RPDPD has an important application value as a potential bioactive compound or pharmaceutical.

MATERIALS AND METHODS

The melting point was determined by the x-4 model apparatus without correction. The Finnigan trace MS spectrometer was
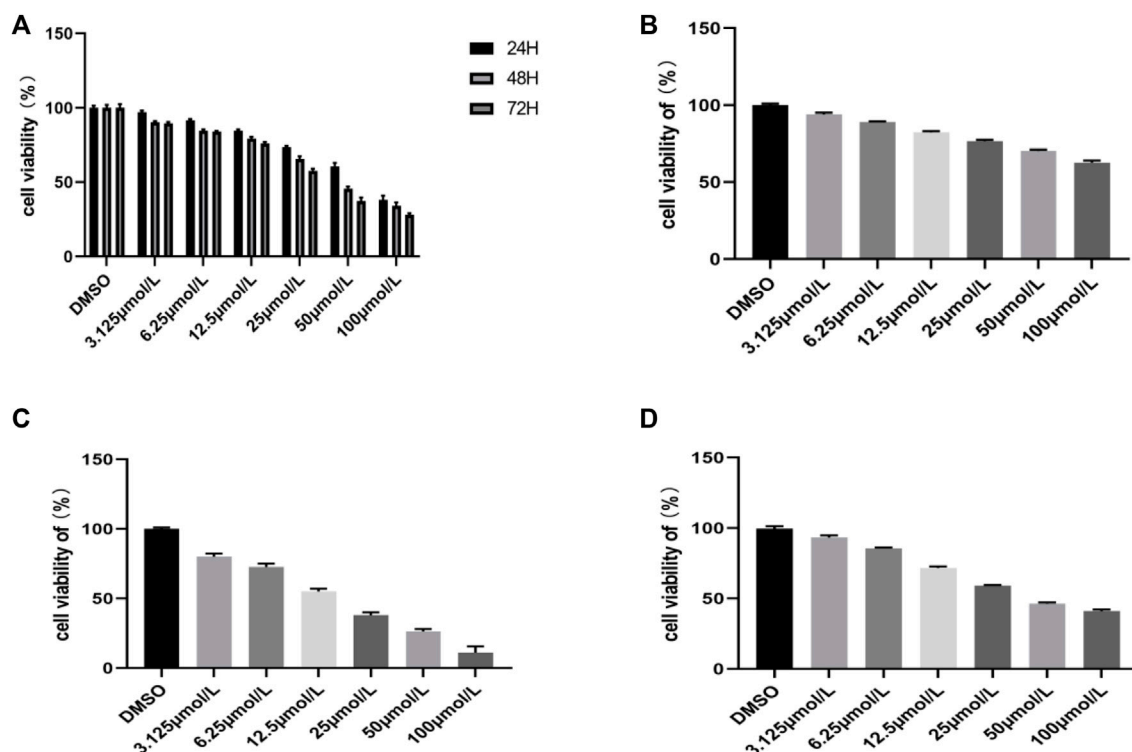
FIGURE 1 | Inhibitory effects of the compound RPDPD on HeLa cells. **(A)** Cell viability of HeLa cells treated with different concentrations of compound RPDPD for 24, 48, and 72 h. **(B)** Cell viability of normal hepatocyte LO2 cells treated with different concentrations of compound RPDPD for 48 h. **(C)** Cell viability of LO2 cells incubated with different concentrations of cisplatin for 48 h. **(D)** Cell viability of HeLa cells incubated with different concentrations of cisplatin for 48 h.

used to detect the compound structure. The infrared absorption of KBr pellets in cm^{-1} was recorded using a PE-983 infrared spectrometer. A Varian mercury 600 spectrometer was used to record NMR in $CDCl_3$, which was related to TMS. Elemental analysis was carried out on the Vario-ELIII element analyzer.

The cervical carcinoma cell line HeLa was stemmed from the Chinese Medicine Experiment Center, Affiliated Dongfeng Hospital, Hubei University of Medicine, and maintained in RPMI 1640 medium which contained FBS (10%). The cells were grown in an incubator at 37°C with 5% CO_2 content.

One-Pot Synthesis of Rhopaladins' Analog RPDPD

First, 2-(bromomethyl)-3-phenyl-2-acrylic acid (0.26 g, 1 mmol) was dissolved in methanol (5 ml), and n-propylamine was added (0.06 g, 1 mmol) and was stirred at room temperature for 10 min. Then, 4-bromophenylglyoxal (0.21 g, 1 mmol) and tertbutyl thiocyanate (0.08 g, 1 mmol) were added. The reaction was carried out at room temperature, and the pH value of the reaction system was adjusted to 6 by Cs_2CO_3 during the stirring process. After stirring the reaction system for 12 h, the mixture was cooled and filtered with a paper filter. The resulting

solid was recrystallized with ether to obtain rhopaladins' analog RPDPD.

CCK8 Assay

Seeded in a 96-well plate at a density of 2×10^4 cells/well, the original medium was removed after the cells adhered the next day, and the compound RPDPD (0 μmol/L, 3.125 μmol/L, 6.25 μmol/L, 12.5 μmol/L, 25 μmol/L, 50 μmol/L, and 100 μmol/L) medium was added and cultured for 24, 48, and 72 h, respectively. With DMSO as the control group, cisplatin treatment was used as a positive control, and normal hepatocytes were used for cytotoxicity experiments, and CCK8 (TargetMol, Shanghai, China) was incubated for 2 h. Also, the plate was evaluated in a luminescence microplate reader (BioTEK INC, Biotek MQX200) at 450 nm wavelength. The optical density (OD) values were obtained. The inhibition rate and IC_{50} of each compound on different cells were calculated by GraphPad Prism 8.0.1 software. Cell survival rate (%) = [(A (experimental group)-A (blank)]/[(A (DMSO)-A (blank)]× 100%.

Apoptotic Assay

The effect of RPDPRH on apoptosis was performed using the Annexin V-FITC/PI Apoptosis kit (MultiSciences, China) following the manufacturer's protocol. The cells were digested, dispersed, and plated into 6-well plates with 2 ×
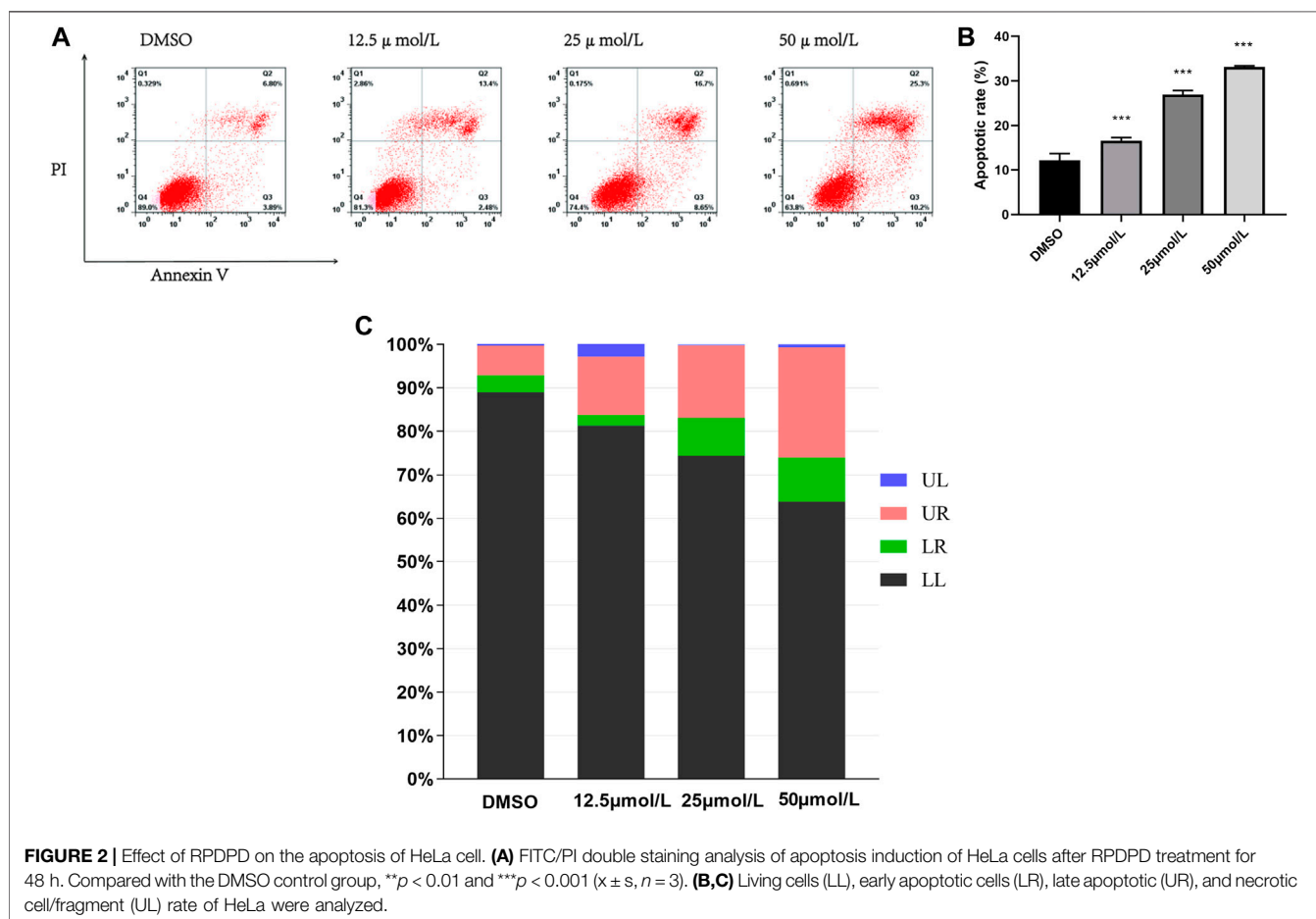
FIGURE 2 | Effect of RPDPD on the apoptosis of HeLa cell. **(A)** FITC/PI double staining analysis of apoptosis induction of HeLa cells after RPDPD treatment for 48 h. Compared with the DMSO control group, $**p < 0.01$ and $***p < 0.001$ (x ± s, $n = 3$). **(B,C)** Living cells (LL), early apoptotic cells (LR), late apoptotic (UR), and necrotic cell/fragment (UL) rate of HeLa were analyzed.

104 cells/well and treated with RPDPRH (0 μmol/L, 6.25 μmol/L, 12.5 μmol/L, and 25 μmol/L) at various concentrations for 48 h. Upon completion of the treatment, the cells were harvested and washed with cool phosphate buffered solution (PBS, Gibco, United States) (0.01M, pH = 7.4) and resuspended in 500 μl binding buffer. Annexin V-FITC (5 μl) and PI (10 μl) were added to the cell suspension, and then the suspension was incubated at room temperature away from light for 5 min. The cells were analyzed using a flow cytometer (Agilent NovoCyte, China) immediately, and the results of apoptosis were analyzed by Flow J software (Zhu et al., 2020). Set 3 has duplicate holes in each group.

qRT-PCR Assay

The HeLa cells were treated with the compound **RPDPD** (0 μmol/L, 12.5 μmol/L, 25 μmol/L, and 50 μmol/L) for 48 h. The total RNA was extracted and reverse transcribed into double-stranded cDNA according to the cell processing manual. The amplification procedure for amplifying E6/E7 mRNA was as follows: pre-denaturation at 95°C for 1 min, denaturation at 95°C for 15 s, annealing at 55°C for 15 s, and extension at 72°C for 45 s, a total of 40 cycles. $2^{-\Delta\Delta Ct}$ was used to calculate the relative expression of genes. The primer sets were as follows: E6 F: 5′-TTGCTTTTCGGGATTTATGC-3′, R:5′-CAGGACACAGTGGCTTTTGA-3'; E7 F: 5′-GAACCGGAC AGAGCCCATTA-3′, R: 5′-AGAACAGATGGGGCACAC AAT-3′. Set 3 has duplicate holes in each group.

Western Blot Assay

The cells were inoculated into 6-well plates at a cell density of 2 × 10⁴/well, and the supernatant medium was removed after the cells adhered the next day, and 2 ml of the compound RPDPD (0 μmol/L, 12.5 μmol/L, 25 μmol/L, and 50 μmol/L) medium of different concentrations were added to each well and incubated for 48 h. The rabbit anti-TIMP3 antibody (1:1000, Abcam, United Kingdom) and rabbit anti-MMP3 (1:1000, Abcam, United Kingdom) were used for Western blotting. The gray value of protein was analyzed using ImageJ software, and the relative expression of the protein was calculated. Set 3 has duplicate holes in each group.

Statistical Methods

The statistical software used was SPSS 22.0. The data were expressed as mean ± standard deviation (Mean ± SD), and the data were in line with normal distribution and were compared by one-way ANOVA between groups, and further pairwise comparisons were performed by LSD-t test. $p < 0.05$ indicated that the difference was statistically significant.

RESULTS AND DISCUSSION

Synthesis of the Compound RPDPD

We used a one-pot Ugi 4CC/S_N cyclization reaction to obtained rhopaladins' analog RPDPD, a white solid, with a yield of 0.42 g, 80% in w/w. The spectral data of RPDPD are as follows. Mp: 197–198°C. 1H NMR (CDCl3, 600 MHz): δ 7.73 (d, J = 8.4 Hz, 2H, Ar-H), 7.61 (d, J = 9.2 Hz, 2H, Ar-H), 7.40 (d, J = 5.2 Hz, 2H, Ar-H), 7.36 (s, 1H, = CH), 7.07 (d, J = 9.2 Hz, 2H, Ar-H), 6.14 (s, 1H, NH), 3.76 (d, J = 17.6 Hz, 1H, CH2a), 3.63–3.55 (m, 1H, NCH2a), 3.28 (d, J = 17.6 Hz, 1H, CH2b), 3.18–3.12 (m, 1H, NCH2b), 1.72–1.51 (m, 2H, CH2), 1.35 (s, 9H, 3CH3), and 0.87 (t, J = 7.2 Hz, 3H, CH3). 13C NMR (CDCl3, 100 MHz): δ 196.1, 169.7, 167.4, 159.4, 132.5, 132.1, 131.5, 130.7, 129.2, 126.1, 124.4, 116.0, 115.8, 74.7, 52.6, 46.1, 35.4, 28.3, 21.3, and 11.6. EI-MS m/z (%): 516 (M++2, 4), 514 (M+, 4), 414 (22), 332 (53), 233 (55), and 183 (100). Anal. Calcd for C26H28BrFN2O3: C, 60.59; H, 5.48; N, 5.44. Found: C, 60.45; H, 5.59; and N, 5.31.

In the experimental process, the reaction conditions were mild, the yield was high, and the raw materials were easy to obtain. The synthetic route of the new fluorine-containing compound RPDPD is outlined in **Scheme 2**.

Inhibitory Effects of the Compound RPDPD on HeLa Cell Viability

The antiproliferative effect of the compound RPDPD was investigated by CCK8 assay against the cervical carcinoma HeLa tumor cell line. The result exhibited that the compound RPDPD at a varying concentration could inhibit cell growth. We can see that the rate of surviving cells decreased with the increasing drug concentrations and also with time (**Figure 1A**). The IC_{50} values of compound RPDPD on HeLa cells for 24, 48, and 72 h were 59.56 μmol/L, 39.64 μmol/L, and 24.23 μmol/L, respectively, and the IC_{50} of cisplatin on HeLa cells for 48 h was 17.36 μmol/L. The IC_{50} of compound RPDPD on normal hepatocyte LO2 cells for 48 h was 235.6 μmol/L, but the IC_{50} of cisplatin on normal hepatocyte LO2 cells for 48 h was just 21.32 μmol/L. The results showed that rhopaladins' analog RPDPD has good anti-cervical cancer activity and low hepatotoxicity, and the inhibition of RPDPD on cell growth

was different with varying concentrations, i.e., the higher the concentration, the higher the inhibition rate of the cells. It can be seen from the experimental result that the inhibitory effect of the compound RPDPD on the growth of HeLa cells was exerted in concentration-dependent and time-dependent manners.

Induction of Apoptosis in HeLa Cells

To determine the type of cell death by the compound RPDPD, it was measured by FITC/PI double staining, which can give a differential analysis of apoptosis cells. The results showed that the survival rate of HeLa cells treated with IC_{50} of the compound RPDPD was decreased after 48 h. After the cells were treated with the compound RPDPD, the apoptosis rate of the cells was increased. The FACS flow cytometry analysis showed that HeLa cells were treated with the compound RPDPD at its IC_{50} concentration for 48 h, and the percentage of apoptosis cells was increased in a concentration-dependent manner (**Figure 2**). There was an increase in percentage of annexin-V-positive cells occurred indicating early apoptosis, and the apoptosis was from 10.67% in control to 35.5% for the compound RPDPD.

Inhibition of E6 mRNA and E7 mRNA Expressions in HeLa Cells

E6/E7 are the main oncogenes of HPV and are involved in various pathological processes in the occurrence and development of cervical cancer. The expression levels of E6 mRNA and E7 mRNA genes were analyzed by qRT-PCR. After RPDPD treatment of HeLa cells for 48 h, the expression levels of E6 mRNA and E7 mRNA genes were significantly decreased in a concentration-dependent manner ($p < 0.05$, **Figure 3**). The results showed that RPDPD could regulate the expression level of E6/E7 in HeLa cells.

RPDPD Regulates the TIMP3/MMP3 Signaling Pathway in Cervical Cancer Cells

To further explore whether the effect of the compound RPDPD on the proliferation, migration, and invasion of cervical cancer cells is mediated by inhibiting TIMP3, the expression levels of TIMP3 and MMP3 were analyzed by Western blot. The Western

FIGURE 3 | Effect of RPDPD on the expressions of E6 mRNA and E7 mRNA. **(A)** Relative expression levels in E6 mRNA cells. **(B)** Relative expression levels in E7 mRNA cells. *$p < 0.05$ and **$p < 0.01$ (x ± s, n = 3).

FIGURE 4 | Effect of RPDPRH on the expression levels of TIMP3 and MMP3 proteins. **(A)** Protein expression bands of TIMP3 and MMP3 proteins in HeLa cells. **(B)** Relative protein profiles of TIMP3 and MMP3 proteins in HeLa cells. Compared with the DMSO control group, $*p < 0.05$ and $**p < 0.01$ (x ± s, $n = 3$).

blot analysis showed that compared with the control group DMSO, the expression of TIMP3 protein in HeLa cells treated with 12.5 μmol/L, 25.0 μmol/L, and 50.0 μmol/L RPDPD was significantly increased in a concentration-dependent manner after the compound RPDPD intervention for 48 h. The expression was significantly downregulated with the increase in drug concentration, and the difference was statistically significant ($p < 0.05$, **Figure 4**). The results indicated that TIMP3/MMP3 was involved in the tumor suppressor effect of the compound on cervical cancer.

DISCUSSION AND CONCLUSION

We used a one-pot Ugi 4CC/S_N cyclization method to synthesize Rhopaladins' analog RPDPD which can inhibit proliferation and promote apoptosis in HeLa cell lines. We performed an *in vitro* cell assay for the first time to evaluate the anticancer effect of testing a new compound on cervical cancer.

The integration of high-risk HPV into the DNA of cells and long-term persistent infection are the main causes of cervical cancer, of which HPV 16 is considered to be the main risk factor for squamous cervical lesions and squamous cervical cancer (Wang et al., 2021). In our study, we selected high-risk HPV 16-positive HeLa cells for *in vitro* cell experiments. The results of cell proliferation experiments showed that the compound RPDPD could significantly inhibit the viability of cervical cancer HeLa cells in a time- and dose-dependent manner. However, the toxicity of the compound RPDPD to LO2 in normal hepatocytes was weak. Our further study found that RPDPD not only inhibited cell proliferation but also induced cell apoptosis in a dose-dependent manner. These experimental results suggest that this new fluorine-containing compound RPDPD may have significant anti-cervical cancer effects.

The studies have shown that the oncogenic potential of high-risk HPV 16 genotypes is determined by the E6 and E7 oncogenes. These two viral oncogenes are often co-expressed in cervical cancer cells and regulate the occurrence and maintenance of cervical cancer (Hu et al., 2022). Their open reading frames are directly involved in regulating the growth of cervical cancer cells, play a key role in the proliferation of cervical cancer cells, and are closely related to the apoptosis of cervical cancer cells (Wen et al., 2021; Zhang et al., 2021). In this study, we found that RPDPD could inhibit the expression of E6 mRNA and E7 mRNA, which further proved

that the anticancer effect of the compound RPDPD on cervical cancer was closely related to the oncogenes E6 and E7.

The endogenous inhibitors of matrix metalloproteinases (MMPs) play an important role in extracellular matrix (ECM) homeostasis and are involved in tumorigenesis and development, angiogenesis, apoptosis, and tumor metastasis (Deryugina and Quigley, 2006), such as cervical cancer and breast cancer (Duffy et al., 2000; Xie et al., 2016). MMPs are natural factor regulators of tissue inhibitors of metalloproteinases (TIMPs). The studies have shown that TIMP3 can inhibit tumor proliferation and angiogenesis by inhibiting MMP3 protein (Zhang et al., 2018; Sun et al., 2019). The study showed that this study was the first to investigate the effect of RPDPD on the TIMP3/MMP3 signaling axis after treatment of HeLa cells. The results showed that the expression of TIMP3 protein in cells was enhanced, and the expression of MMP3 protein in cells was decreased. It is suggested that the anticancer effect of compound RPDPD may also depend on the TIMP3/MMP3 signaling axis. We demonstrate for the first time that RPDPD may alter cervical cancer progression through TIMP3/MMP3.

In conclusion, our study confirmed that rhopaladins' analog RPDPD affects the proliferation and apoptosis of cervical cancer cells, inhibits the expression of oncogenes E6 mRNA and E7 mRNA, and its anticancer activity may be related to the TIMP3/MMP3 signaling axis. This study is only the first time to explore its anticancer activity, and we will continue to conduct more in-depth research on the mechanism of the compound RPDPD in the future, so as to provide effective experimental data for the development and application of the compound RPDPD in the clinical treatment of cervical cancer.

DATA AVAILABILITY STATEMENT

The datasets presented in this study can be found in online repositories. The names of the repository/repositories and accession number(s) can be found in the article/**Supplementary Material**.

AUTHOR CONTRIBUTIONS

Q-HC and X-HZ contributed to the conception and design of the study. H-MW and X-HZ synthesized the compounds. FC and L-QK wrote the manuscript, edited the manuscript, and performed

experiments. and designed and performed experiments. H-LD performed the statistical analysis. FC and L-NK wrote the first draft of the manuscript. All authors contributed to manuscript revision and read and approved the submitted version.

SUPPLEMENTARY MATERIAL

The Supplementary Material for this article can be found online at: https://www.frontiersin.org/articles/10.3389/fchem.2022.921276/full#supplementary-material

REFERENCES

Atigadda, V. R., Brouillette, W. J., Duarte, F., Ali, S. M., Babu, Y. S., Bantia, S., et al. (1999). Potent Inhibition of Influenza Sialidase by a Benzoic Acid Containing a 2-pyrrolidinone Substituent. *J. Med. Chem.* 42, 2332–2343. doi:10.1021/jm980707k

Deryugina, E. I., and Quigley, J. P. (2006). Matrix Metalloproteinases and Tumor Metastasis. *Cancer Metastasis Rev.* 25 (1), 9–34. doi:10.1007/s10555-006-7886-9

Duffy, M. J., Maguire, T. M., Hill, A., McDermott, E., and O'Higgins, N. (2000). Metalloproteinases: Role in Breast Carcinogenesis, Invasion and Metastasis. *Breast Cancer Res.* 2 (4), 252–257. doi:10.1186/bcr65

Freddie, B., Jacques, F., Isabelle, S., Rebecca, L. S., Lindsey, A. T., and Ahmedin, J. (2018). Global Cancer Statistics 2018: GLOBOCAN Estimates of Incidence and Mortality Worldwide for 36 Cancers in 185 Countries. *CA A Cancer J. Clin.* 68, 394–424. doi:10.3322/caac.21492

Hiroyasu, S., Masashi, T., Kenji, W., and Rhopaladins, A. D. (1998). New Indole Alkaloids from Marine Tunicate Rhopalaea Sp. *Tetrahedron* 54 (30), 8687–8690.

Hu, C., Liu, T., Han, C., Xuan, Y., Jiang, D., Sun, Y., et al. (2022). HPV E6/E7 Promotes Aerobic Glycolysis in Cervical Cancer by Regulating IGF2BP2 to Stabilize m6A-MYC Expression. *Int. J. Biol. Sci.* 18 (2), 507–521. doi:10.7150/ijbs.67770

Ijang, Y. P., Cumber, S. N. N., Nkfusai, C. N., Venyuy, M. A., Bede, F., and Tebeu, P. M. (2019). Awareness and Practice of Birth Preparedness and Complication Readiness Among Pregnant Women in the Bamenda Health District, Cameroon. *BMC Pregnancy Childbirth* 19, 371. doi:10.1186/s12884-019-2511-4

Kaushiki, C., Dina, A. S., Christina, M., Palwasha, S., Mohamed Al, S., and Jimmie, E. S. (2018). Resveratrol and Pterostilbene Exhibit Anticancer Properties Involving the Downregulation of HPv Oncoprotein e6 in Cervical Cancer Cells. *Nutrients* 10, 24. doi:10.3390/nu10020243

Kenda, B. M., Matagne, A. C., Talaga, P. E., Pasau, P. M., Edmond, D., Benedicte, I. L., et al. (2004). Discovery of 4-Substituted Pyrrolidone Butanamides as New Agents with Significant Antiepileptic Activity. *J. Med. Chem.* 47, 530–549. doi:10.1021/jm030913e

Kraus, J. L., Bouygues, M., Courcambeck, J., and Chermann, J. C. (2000). Use of Proline Bioisosteres in Potential HIV Protease Inhibitors: Phenylalanine-2-Thiophenoxy-3-Pyrrolidinone: Synthesis and Anti-HIV Evaluation. *Bioorg Med. Chem. Lett.* 10, 2023–2026. doi:10.1016/s0960-894x(00)00393-0

Nilsson, B. M., Ringdahl, B., and Hacksell, U. (1990). beta.-Lactam Analogs of Oxotremorine. 3- and 4-Methyl-Substituted 2-azetidinones. *J. Med. Chem.* 33, 580–584. doi:10.1021/jm00164a018

Sun, Q., Yang, Z., Li, P., Wang, X., Sun, L., Wang, S., et al. (2019). A Novel miRNA Identified in GRSF1 Complex Drives the Metastasis via the PIK3R3/AKT/NF-κB and TIMP3/MMP9 Pathways in Cervical Cancer Cells. *Cell. Death Dis.* 10 (9), 636. doi:10.1038/s41419-019-1841-5

Wang, H. M., Zhu, X. L., and Deng, S. H. (2020). Synthesis and Cytotoxic Effects on HeLa Cervical Cancer Cells of (E)-2-aroyl-4-(4-fluorobenzylidene)-5-oxopyrrolidine. *J. Chem. Res.* 44, 9. In press. doi:10.1177/1747519820911849

Wang, L., Wang, F., Fu, S., Zhang, C., Zhe, X., Li, H., et al. (2021). Analysis of Genetic Variation in Human Papillomavirus Type 16 E1 and E2 in Women with Cervical Infection in Xinjiang, China. *BMC Med. Genomics* 14 (1), 268. doi:10.1186/s12920-021-01120-9

Wen, N., Bian, L., Gon, J., and Meng, Y. (2021). RPRD1B Is a Potentially Molecular Target for Diagnosis and Prevention of Human Papillomavirus E6/E7 Infection-induced Cervical Cancer: A Case-control Study. *Asia-Pac J. Clin. Oncol.* 17 (3), 230–237. doi:10.1111/ajco.13439

Wu, Y.-H., and Feldkamp, R. F. (1961). Pyrrolidines. I. 1-Substituted 3-Pyrrolidinylmethyl Alcohols and Chlorides1. *J. Org. Chem.* 26, 1519–1524. doi:10.1021/jo01064a051

Xie, B., Zhang, Z., Wang, H., Chen, Z., Wang, Y., Liang, H., et al. (2016). Genetic Polymorphisms in MMP 2, 3, 7, and 9 Genes and the Susceptibility and Clinical Outcome of Cervical Cancer in a Chinese Han Population. *Tumor Biol.* 37 (4), 4883–4888. doi:10.1007/s13277-015-4204-6

Zhang, X., ZHang, A., ZHang, X., Hu, S., Bao, Z., Zhang, Y., et al. (2021). ERa-36 Instead of ERa Mediates the Stimulatory Effects of Estrogen on the Expression of Viral Oncogenes HPV E6/E7 and the Malignant Phenotypes in Cervical Cancer Cells. *Virus Res.* 306, 198602. doi:10.1016/j.virusres.2021.198602

Zhang, Z., Wang, J., Wang, X., Song, W., Shi, Y., and Zhang, L. (2018). MicroRNA-21 Promotes Proliferation, Migration, and Invasion of Cervical Cancer through Targeting TIMP3. *Arch. Gynecol. Obstet.* 297 (2), 433–442. doi:10.1007/s00404-017-4598-z

Zhu, J., Kong, L-Q., and Chen, Q-H.(2019). Design, Synthesis, and Apoptosis-Promoting Effect Evaluation of Rhopa Ladins' Analog 4-Arylidene-5-Oxopyrrolidine Derivatives. *Front. Chem.* 10, 898436. doi:10.3389/fchem.2022.898436

Zhu, X. L., Tian, X. Q., Xu, H. H., Wang, H. M., Chen, Q. H., and Zeng, X. H. (2020). Rhopaladins' Analogue (E)-2-aroyl-4-(4-fluorobenzylidene)-5-oxopyrrolidines Inhibit Proliferation, Promote Apoptosis and Down-Regulation of E6/E7 mRNA in Cervical Cancer. *Bioorg Med. Chem. Lett.* 30, 127554. doi:10.1016/j.bmcl.2020.127554

Synthesis and Evaluation of Coumarin-Chalcone Derivatives as α-Glucosidase Inhibitors

Chun-Mei Hu[†], Yong-Xin Luo[†], Wen-Jing Wang, Jian-Ping Li, Meng-Yue Li, Yu-Fei Zhang, Di Xiao, Li Lu, Zhuang Xiong*, Na Feng* and Chen Li*

School of Biotechnology and Health Sciences, Wuyi University, Jiangmen, China

Coumarin and chalcone, two important kinds of natural product skeletons, both exhibit α-glucosidase inhibitory activity. In this work, coumarin-chalcone derivatives 3 (**a~v**) were synthesized, and their α-glucosidase inhibitory activity was screened. The results showed that all synthetic derivatives (IC$_{50}$: 24.09 ± 2.36 to 125.26 ± 1.18 μM) presented better α-glucosidase inhibitory activity than the parent compounds 3-acetylcoumarin (IC$_{50}$: 1.5 × 10^5 μM) and the positive control acarbose (IC$_{50}$: 259.90 ± 1.06 μM). Among them, compound **3t** displayed the highest α-glucosidase inhibitory activity (IC$_{50}$: 24.09 ± 2.36 μM), which was approximately 10 times stronger than that of acarbose. The kinetic assay of **3t** (K_I = 18.82 μM, K_{IS} = 59.99 μM) revealed that these compounds inhibited α-glucosidase in a mixed-type manner. Molecular docking was used to simulate the interaction between α-glucosidase and compound **3t**.

Keywords: coumarin, chalcone, α-glucosidase, enzyme inhibitor, docking

INTRODUCTION

Type 2 diabetes mellitus (T2DM) is a metabolic disease characterized by hyperglycemia resulting from insulin resistance and insufficient insulin secretion by pancreatic β-cells. One of the key reasons for the hyperglycemia is the enzymatic hydrolysis of carbohydrates. α-Glucosidase (EC 3.2.1.20) plays an important role in carbohydrate digestion, in which the oligosaccharides and disaccharides from dietary carbohydrates are broken down into monosaccharides. The α-glucosidase inhibitors suppress the absorption and assimilation of monosaccharides and delay the digestion of carbohydrates (Cohen and Goedert, 2004; Proença et al., 2017; Xu et al., 2019; Zhong et al., 2019). Some commercially available α-glucosidase inhibitors, including miglitol, voglibose, and acarbose, have been used in the clinical treatment of T2DM, but they still show several adverse effects (Chai et al., 2015; Khursheed et al., 2019; Rocha et al., 2019). In addition, α-glucosidase is closely related to hepatitis, cancer, and Pompe disease (Kasturi et al., 2018; Gulcin et al., 2019). Therefore, it is always beneficial in medicinal chemistry to develop potent α-glucosidase inhibitors.

Coumarin is an important natural product skeleton with various pharmacological properties; among these, its anti-hyperglycemic activity is the focus of our research (Kontogiorgis et al., 2012; Katsori and Litina, 2014; Adib et al., 2018). Previous studies have shown that natural products containing the coumarin moiety and synthesized coumarin derivatives exhibit anti-hyperglycemic activity through the inhibition of α-glucosidase (Adib et al., 2018). For instance, Wang et al. (2016) reported on a series of coumarin-thiazoles with the highest α-glucosidase inhibitory activity (IC$_{50}$ = 6.2 μM). Salar et al. (2016) developed 3-thiazolyl coumarins with the most potent α-glucosidase inhibitory activity (IC$_{50}$ = 0.12 μM) (Salar et al., 2016)). Ibrar *et al.* designed coumarinyl iminothiazolidinones with the most effective inhibitory activity (IC$_{50}$ = 0.09 μM) (Ibrar et al.,
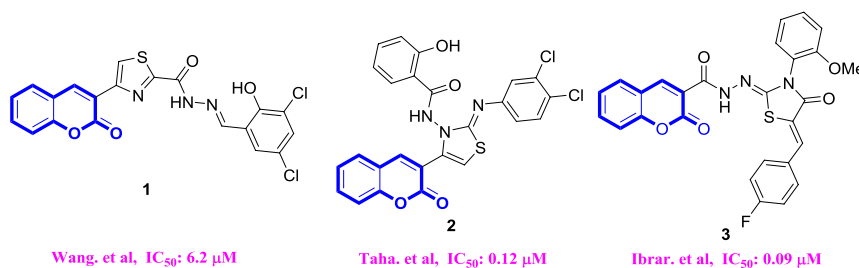
FIGURE 1 | α-glucosidase inhibitors containing coumarin.

SCHEME 1 | The synthetic route to coumarin-chalcone derivatives 3 (a~v). Reagents and conditions: **(A)** ethyl acetoacetate, piperidine, ethanol, 65°C, 20 min **(B)** substituted aldehydes, piperidine, ethanol, reflux, 24 h.
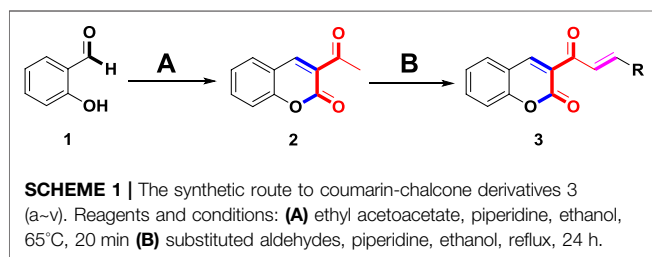
2017). (**Figure 1**) Chalcone, an important sub-structure widely existing in many natural products, has the ability to bind to a variety of targets, resulting in many biological activities (Bak et al., 2011; Feng et al., 2014; Kang et al., 2018; Djemoui et al., 2020; Rocha et al., 2020; Dorn et al., 2010).

In medicinal chemistry, the hybrid of pharmacophore and skeleton is an effective strategy for obtaining active lead compounds. Until now, many coumarin-chalcone derivatives had been synthesized with many biological properties, such as antioxidant, anti-cancer, antibacterial, and anti-inflammatory properties (Pingaew et al., 2014; Seidel et al., 2014; Lee et al., 2018). However, there were few reports on the application of α-glucosidase inhibitors. Therefore, we synthesized coumarin-chalcone derivatives **3a~v** and screened their inhibitory activity against α-glucosidase.

RESULTS AND DISCUSSION

Chemistry

Coumarin-chalcone derivatives **3(a~v)** were prepared according to a well-known method (Roussel and Fraser, 1993; Vazquez-Rodriguez et al., 2015; Shang et al., 2018; Wang et al., 2019). In the presence of piperidine, salicylaldehyde **1**) reacted with ethyl acetoacetate to produce 3-acetylcoumarin (**2**). Then 3-acetylcoumarin **2**) and the substituted aldehydes underwent the aldol condensation reaction under the catalysis of piperidine to give coumarin-chalcone derivatives **3(a~v)** (**Scheme 1**). Compounds **3(a~v)** had been reported previously and the title compounds were characterized by ^{1}H NMR.

α-Glucosidase Inhibition Assay

Coumarin-chalcone derivatives **3(a~v)** were screened for their inhibitory activities against α-glucosidase using 4-nitrophenyl-α-

D-galactopyranoside (*p*-NPG) as a substrate and the results are summarized in **Table 1**. The parent compounds 3-acetylcoumarin only showed low inhibitory activity with IC$_{50}$ values of 1.5×10^5. Interestingly, all synthetic derivatives showed moderate to good inhibitory activity towards α-glucosidase with IC$_{50}$ values ranging from 24.09 ± 2.36 to 125.26 ± 1.18 μM. The results revealed that the inhibitory activities of synthetic compounds were significantly enhanced by hybridizing the two molecular skeletons. Furthermore, all the title compounds presented higher inhibitory activity than that of the positive control acarbose (IC$_{50}$: 259.90 ± 1.06 μM). Among them, compounds **3j**, **3q** and **3t** demonstrated the highest inhibitory activity (IC$_{50}$: 30.30 ± 2.53, 29.74 ± 2.68, and 24.09 ± 2.36 μM, respectively): 10 times stronger than that of acarbose.

Structure Activity Relationships

The structure activity relationships (SARs) of compounds **3(a~v)** was analyzed based on their α-glucosidase inhibitory activities. Compound **3a** (IC$_{50}$: 125.26 ± 1.18 μM) without any substituent was selected as the template compound. It could be seen that the introduction of various substituents resulted in an obvious change in inhibitory activity. For compound **3b** (IC$_{50}$: 95.23 ± 1.35 μM) with a 4-methyl group, its inhibitory activity slightly increased compared to **3a**. For compounds **3(g~i)** with the fluorine group, **3(l~n)** with the trifluoromethyl group, **3(o~q)** with the chlorine group, and **3(r~t)** with the bromine group, all presented stronger inhibitory activity than compound **3a**, indicating that electron-withdrawing groups such as fluorine, trifluoromethyl, chlorine, and bromine could lead to an increase in inhibitory activity. Among them, **3i** with the 4-fluorine group (IC$_{50}$: 35.68 ± 0.28 μM), **3n** with the 4-trifluoromethyl group (IC$_{50}$: 53.58 ± 1.95 μM), **3q** with the 4-chlorine group (IC$_{50}$: 29.74 ± 2.68 μM), and **3t** with the 4-bromine group (IC$_{50}$: 24.09 ± 2.36 μM) showed higher inhibitory activity than the 2- and 3-position groups. For compounds **3j** and **3k** with difluoro groups, the introduction of 2,4-difluoro groups (**3j**, IC$_{50}$: 30.30 ± 2.53) resulted in the stronger inhibitory activities. While for compounds **3(c~e)** with methoxy group, the 2-position group (**3c**, IC$_{50}$: 60.89 ± 2.74) was better than 3-position group and 4-position group.

Furthermore, the sequencing of inhibitory activity was identified: **3t** (with 4-bromine group) > **3q** (with 4-chlorine group) > **3i** (with 4-fluorine group) > **3n** (with 4-trifluoromethyl group), predicting that stronger electron-withdrawing groups led to weaker inhibitory activity as for the compounds with electron-withdrawing groups. In addition, in the electron-withdrawing groups, inhibitory activity was

TABLE 1 | α-Glucosidase inhibitory activities of compounds **3** (**a~v**).

Compound	R	IC$_{50}$ (μM)	Compound	R	IC$_{50}$ (μM)
3a		125.26 ± 1.18	3b		95.23 ± 1.35
3c		60.89 ± 2.74	3d		96.39 ± 1.37
3e		105.18 ± 1.98	3f		75.53 ± 0.98
3g		48.36 ± 1.42	3h		45.68 ± 1.28
3i		35.68 ± 0.28	3j		30.30 ± 2.53
3k		49.68 ± 3.28	3l		71.52 ± 2.14
3m		64.71 ± 1.82	3n		53.58 ± 1.95
3o		59.68 ± 1.73	3p		52.62 ± 2.45
3q		29.74 ± 2.68	3r		38.56 ± 1.87
3s		35.56 ± 2.18	3t		24.09 ± 2.36
3u		109.23 ± 2.69	3v		103.31 ± 1.45
3-Acetylcoumarin		1.5 × 105			
Acarbose		259.90 ± 1.06			

related to the substituted position as follows: the inhibitory activity of compounds with the withdrawing groups at para-position was superior to that at meta-position, which is better than that at ortho-position. The introduction of thiophene (**3u**) or indole (**3v**) ring only slightly improved the inhibitory activity compared with compound **3a**.

Inhibitory Mechanism Analysis

Generally, according to the type of inhibition, enzyme inhibitors can be divided into reversible inhibitors and irreversible inhibitors (Abuelizz et al., 2019). In order to obtain the principle of the combination of enzyme inhibitors and enzymes, it is necessary to study the interaction between enzyme inhibitors and enzymes. Compounds **3j, 3q** and **3t** with strongest inhibitory activity were chosen for the research of inhibition kinetics against α-glucosidase (the inhibitory mechanism analysis of compound **3t** was shown in **Figure 2** and figures for the inhibitory mechanism analysis of compounds **3j** and **3q** have been shown in the supporting information). A series of plots of enzymatic reaction rate (v) vs. α-glucosidase

FIGURE 2 | Inhibition mechanism determination of compounds **3t** on α-glucosidase.

TABLE 2 | Type of inhibition mechanism, as well as K_I and K_{IS} values of compounds **3j**, **3q** and **3t**.

Compound	Inhibition mechanism	K_I (μM)	K_{IS} (μM)
3j	Mixed type	19.53	25.94
3q	Mixed type	16.13	20.34
3t	Mixed type	11.02	20.71

but reduced the enzyme activity, which indicated that their inhibition mechanisms on α-glucosidase were reversible.

The inhibit type of inhibitors on α-glucosidase include four types, named competitive inhibition, non-competitive inhibition, mixed inhibition, and anti-competitive inhibition (Abuelizz et al., 2019). The inhibition modes of compounds **3j**, **3q** and **3t** against α-glucosidase were investigated using Lineweaver-Burk double reciprocal plot. As shown in **Figure 3**, the straight lines of 1/v vs. 1/(S) in the presence of compounds **3j**, **3q** and **3t** intersected at a point in the second quadrant respectively, illustrating that the inhibit type of **3j**, **3q** and **3t** was mixed-type inhibition. Subsequently, the K_I values and K_{IS} values of **3j**, **3q** and **3t** were calculated based on the slope or intercept vs. PNPG concentration and summarized in **Table 2**. The higher K_{IS} values compared to K_I values indicated

concentration in the presence of inhibitors were generated to identify the type of inhibition that is listed in **Figure 1**. The presence of **3j**, **3q** and **3t** did not change the number of enzymes

FIGURE 3 | Lineweaver-Burk plots of compounds **3t** on α-glucosidase **(A)**. Plot of slope vs. the concentration of compounds for the calculation of the inhibition constant K_I **(B)**. Plot of intercept vs. the concentration of compounds for the determination of the inhibition constant K_{IS} **(C)**.

FIGURE 4 | Molecular docking of compounds **3d**, **3f** and **3i** with α-glucosidase. **(A)** Compound **3q** in the active pocket **(B)**; Compound **3t** in the active pocket **(C)**; compounds **3j**, **3q** and **3t** in the active pocket of α-glucosidase **(D)**; 2D view of **3j** with α-glucosidase **(E)**; 2D view of **3q** with α-glucosidase **(F)**; 2D view of **3t** with α-glucosidase **(G)**.

that the affinity of compounds **3j**, **3q** and **3t** with free enzyme was higher than that with enzyme-substrate complex.

Molecular Docking Simulation

To better understand the inhibition mechanism of compounds **3j**, **3q** and **3t**, the binding modes of α-glucosidase with **3j**, **3q** and **3t** were simulated using Sybyl 2.1.1 (United States) and Pymol software. The crystal structure of *Saccharomyces cerevisiae* isomaltase (PDB: 3AJ7) with 72.4% of sequence identity with α-glucosidase was chosen as the target protein (Wang et al., 2017; Asgari et al., 2019; Morocho et al., 2019; Salar et al., 2016). As can be seen in **Figures 4A–D**, compounds **3j**, **3q** and **3t** had the similar interaction with the active pocket of α-glucosidase.. **Figures 4E–G** show that the carbonyl group of coumarin of **3j**, **3q** and **3t** all formed two hydrogen bonds with Thr310 and Arg315, respectively. Compounds **3j**, **3q** and **3t** all made an π-π interaction with Phe303; and all established hydrophobic interactions with Pro310, Asp307, Asp352, Gln353, and Asn350.

CONCLUSION

In summary, the α-glucosidase inhibitory activity of coumarin-chalcone derivatives **3(a~v)** was evaluated. The results showed that all compounds presented outstanding α-glucosidase inhibitory activities (IC$_{50}$: 24.09 ± 2.36 to 125.26 ± 1.18 μM) than the positive control acarbose and parent compounds 3-acetylcoumarin and benzaldehyde. Compounds **3j**, **3q**, **3t** displayed the highest α-glucosidase inhibitory activity (IC$_{50}$: 30.30 ± 2.53, 29.74 ± 2.68, 24.09 ±

2.36μM, respectively), which was approximately 10 times stronger than acarbose. Inhibition mechanism results revealed that these compounds inhibited α-glucosidase in a mixed-type manner. Molecular docking verified the interactions of α-glucosidase with compounds **3j**, **3q**, and **3t**.

EXPERIMENT

Chemicals and Instruments

Ethyl acetoacetate, salicylaldehyde and absolute ethanol were analytical pure grade and purchased from Aladdin (Shanghai) Reagent Co., Ltd. Piperidine; glacial acetic acid, petroleum ether and ethyl acetate were supplied by Titan (Shanghai) Technology Co., Ltd.; α-Glucosidase from *Saccharomyces cerevisiae* (EC 3.2.1.20), 4-nitrophenyl-α-D-galactopyranoside (*p*-NPG), and Dimethyl sulfoxide (DMSO) were supported by Sigma-Aldrich (United States) Chemical Co., Ltd. Melting points were tested on a micro melting-point instrument. ^{1}H NMR spectra were measured (CDCl$_3$) by Bruker DPX-500 MHz AVANCE with TMS as an internal standard. Mass spectroscopy was performed on a (LCQTM). The absorbance was recorded by a micro-plate reader.

Synthesis of 3-Acetylcoumarin

To a solution of Salicylaldehyde **1** (1.0 mmol) in ethanol (10 ml), ethyl acetoacetate (1.0 mmol) and piperidine (1.0 mmol) were added and the mixture was stirred at 65˚C for 20 min. When the reaction was judged to be complete by TLC, the crude product was obtained by filtration, followed by washing with petroleum ether to produce 3-acetylcoumarin **2**.

Yellow solid; yield 72.3%; ^{1}H NMR (500 MHz, Chloroform-*d*) δ 8.54 (s, ^{1}H), 7.70–7.66 (m, 2H), 7.42–7.36 (m, 2H) 2.76 (s, 3H).

Synthesis of Coumarin-Chalcone Derivatives 3(a~v)

To a solution of 3-acetylcoumarin **2** (1.0 mmol) in ethanol (10 ml) substituted aromatic aldehydes (1.0 mmol) and piperidine (1.0 mmol) were added, and then the mixture was refluxed for 24 h. The crude product was obtained by filtration, and subsequently by recrystallization by ethanol to give the title compounds **3(a~v)**.

(E)-3-cinnamoyl-2H-chromen-2-one (3a). Yellow solid; yield 51.7%; ^{1}H NMR (500 MHz, Chloroform-*d*) δ 8.60 (s, ^{1}H), 7.92 (dd, *J* = 40, 20 Hz, 2H), 7.71–7.65 (m, 4H), 7.44–7.39 (m, 4H), 7.35 (t, *J* = 8, 7.5 Hz, ^{1}H).

(E)-3-[3-(p-tolyl) acryloyl]-2H-chromen-2-one (3b). Yellow solid; yield 45.9%; ^{1}H NMR (500 MHz, Chloroform-*d*) δ 8.58 (s, ^{1}H), 7.84 (dd, *J* = 20, 15 Hz, 2H), 7.69–7.62 (m, 4H), 7.39 (d, *J* = 5 Hz, ^{1}H), 7.35 (td, *J* = 7.5, 1 Hz, ^{1}H), 6.93 (dt, *J* = 10, 3 Hz, 2H), 3.85 (s, 3H).

(E)-3-[3-(2-methoxyphenyl) acryloyl]-2H-chromen-2-one (3c). Yellow solid; yield 37.7%; ^{1}H NMR (500 MHz, Chloroform-*d*) δ 8.56 (s, ^{1}H), 8.22 (d, *J* = 15 Hz, ^{1}H), 7.98 (d, *J* = 15 Hz, ^{1}H), 7.73–7.62 (m, 3H), 7.42–7.32 (m, 3H), 6.99 (t, *J* = 10, 10 Hz, ^{1}H), 6.93 (d, *J* = 10 Hz, ^{1}H), 3.92 (s, 3H).

(E)-3-[3-(3-methoxyphenyl) acryloyl]-2H-chromen-2-one (3d). yellow solid; yield 42.1%; ^{1}H NMR (500 MHz, Chloroform-*d*) δ 8.59 (s, ^{1}H), 7.93 (d, *J* = 20 Hz, ^{1}H), 7.71–7.65 (m, 2H), 7.41 (d, *J* = 5 Hz, ^{1}H), 7.39–7.31 (m, 2H), 7.28 (d, *J* = 10 Hz, ^{1}H), 7.19 (t, *J* = 5, 2 Hz, ^{1}H), 6.97 (ddd, *J* = 8, 2.5, 1 Hz, ^{1}H), 3.86 (s, 3H).

(E)-3-[3-(4-methoxyphenyl) acryloyl]-2H-chromen-2-one (3e). Yellow solid; Yield 49.7%; ^{1}H NMR (500 MHz, Chloroform-*d*) δ 8.58 (s, ^{1}H), 7.88 (dd, *J* = 30, 15 Hz, 2H), 7.69–7.64 (m, 2H), 7.58 (d, *J* = 10 Hz, 2H), 7.40 (d, *J* = 10 Hz, ^{1}H), 7.35 (t, *J* = 10, 5 Hz, ^{1}H), 7.22 (d, *J* = 10 Hz, 2H), 2.39 (s, 3H).

(E)-3-{3-[4-(methylthio)phenyl] acryloyl}-2H-chromen-2-one (3f). Yellow solid; yield 55.2%; ^{1}H NMR (500 MHz, Chloroform-*d*) δ 8.59 (s, ^{1}H), 7.87 (dd, *J* = 40, 20 Hz, 2H), 7.70–7.64 (m, 2H), 7.61–7.57 (m, 2H), 7.40 (d, *J* = 10 Hz, ^{1}H), 7.35 (td, *J* = 10, 1.5 Hz, ^{1}H), 7.24 (d, *J* = 10 Hz, 2H), 2.52 (s, 3H).

(E)-3-[3-(2-fluorophenyl) acryloyl]-2H-chromen-2-one (3g). Yellow solid; yield 45.0%; ^{1}H NMR (500 MHz, Chloroform-*d*) δ 8.60 (s, ^{1}H), 8.01 (dd, *J* = 30, 15 Hz, 2H), 7.74 (t, *J* = 10, 10 Hz, ^{1}H), 7.71–7.65 (m, 2H), 7.42–7.34 (m, 3H), 7.19 (t, *J* = 10, 10 Hz, ^{1}H), 7.12 (t, *J* = 10, 10 Hz, ^{1}H).

(E)-3-[3-(3-fluorophenyl) acryloyl]-2H-chromen-2-one (3h). Yellow solid; yield 35.3%; ^{1}H NMR (500 MHz, Chloroform-*d*) δ 8.61 (s, ^{1}H), 7.95 (d, *J* = 20 Hz, ^{1}H), 7.81 (d, *J* = 15 Hz, ^{1}H), 7.71–7.66 (m, 2H), 7.45–7.36 (m, 5H), 7.19 (tdd, *J* = 8.2, 2.6, 1 Hz, ^{1}H).

(E)-3-[3-(4-fluorophenyl) acryloyl]-2H-chromen-2-one (3i). Yellow solid; yield 44.9%; ^{1}H NMR (500 MHz, Chloroform-*d*) δ 8.61 (s, ^{1}H), 7.90 (d, *J* = 20 Hz, ^{1}H), 7.84 (d, *J* = 20 Hz, ^{1}H), 7.71–7.65 (m, 4H), 7.41 (d, *J* = 10 Hz, ^{1}H), 7.37 (td, *J* = 8.1, 0.4 Hz, ^{1}H), 7.14–7.08 (m, 2H).

(E)-3-[3-(2,4-difluorophenyl) acryloyl]-2H-chromen-2-one (3j). Yellow solid; yield 44.7%; ^{1}H NMR (500 MHz, Chloroform-*d*) δ 8.61 (s, ^{1}H), 7.96 (d, *J* = 15 Hz, 2H), 7.78–7.71 (m, ^{1}H), 7.71–7.65 (m, 2H), 7.41 (d, *J* = 10 Hz, ^{1}H), 7.39–7.35 (m, ^{1}H), 6.98–6.92 (m, ^{1}H), 6.91–6.84 (m, ^{1}H).

(E)-3-[3-(3,4-difluorophenyl) acryloyl]-2H-chromen-2-one (3k). Yellow solid; yield 37.3%; ^{1}H NMR (500 MHz, Chloroform-*d*) δ 8.64 (s, ^{1}H), 7.91 (d, *J* = 15 Hz, ^{1}H), 7.78 (d, *J* = 15 Hz, ^{1}H), 7.70 (dd, *J* = 10, 5 Hz, ^{1}H), 7.56–7.50 (m, ^{1}H), 7.45–7.38 (m, 4H), 7.23 (dt, *J* = 10, 10 Hz, ^{1}H).

(E)-3-{3-[2-(trifluoromethyl) phenyl]acryloyl}-2H-chromen-2-one (3l). Yellow solid; yield 39.8%; ^{1}H NMR (500 MHz, Chloroform-*d*) δ 8.63 (s, ^{1}H), 7.94 (dd, *J* = 10, 5 Hz, 2H), 7.74–7.58 (m, 4H), 7.53–7.48 (m, ^{1}H), 7.45–7.34 (m, 3H).

(E)-3-{3-[3-(trifluoromethyl) phenyl]acryloyl}-2H-chromen-2-one (3m). Yellow solid; yield 39.9%; ^{1}H NMR (500 MHz, Chloroform-*d*) δ 8.62 (s, ^{1}H), 7.86 (dd, *J* = 10, 5 Hz, 3H), 7.71–7.65 (m, 3H), 7.57–7.53 (m, ^{1}H), 7.44–7.34 (m, 3H).

(E)-3-{3-[4-(trifluoromethyl) phenyl]acryloyl}-2H-chromen-2-one (3n). Yellow solid; yield 41.4%; ^{1}H NMR (500 MHz, Chloroform-*d*) δ 8.63 (s, ^{1}H), 7.86 (d, *J* = 15 Hz, ^{1}H), 7.78 (d, *J* = 10 Hz, 2H), 7.72–7.65 (m, 3H), 7.44–7.36 (m, 3H).

(E)-3-[3-(2-chlorophenyl) acryloyl]-2H-chromen-2-one (3o). Yellow solid; yield 51.2%; ^{1}H NMR (500 MHz, Chloroform-*d*) δ 8.61 (s, ^{1}H), 8.03 (d, *J* = 15 Hz, ^{1}H), 7.79 (d, *J* = 15 Hz, ^{1}H), 7.70–7.66 (m, 3H), 7.58 (d, *J* = 10 Hz, ^{1}H), 7.46–7.35 (m, 4H).

(E)-3-[3-(3-chlorophenyl) acryloyl]-2H-chromen-2-one (3p). Yellow solid; yield 36.4%; ^{1}H NMR (500 MHz, Chloroform-*d*) δ 8.61 (s, ^{1}H), 7.95 (d, *J* = 15 Hz, ^{1}H), 7.78 (d, *J* = 15 Hz, ^{1}H), 7.71–7.64 (m, 3H), 7.55 (d, *J* = 10 Hz, ^{1}H), 7.43–7.34 (m, 4H).

(E)-3-[3-(4-chlorophenyl)acryloyl]-2H-chromen-2-one (3q). Yellow solid; yield 45.2%; ^{1}H NMR (500 MHz, Chloroform-*d*) δ 8.61 (s, ^{1}H), 7.93 (d, *J* = 15 Hz, ^{1}H), 7.81 (d, *J* = 15 Hz, ^{1}H), 7.70–7.65 (m, 2H), 7.63 (dt, *J* = 8.5, 2.5 Hz, 2H), 7.42–7.34 (m, 4H).

(E)-3-[3-(2-bromophenyl)acryloyl]-2H-chromen-2-one (3r). Yellow solid; yield 40.8%; ^{1}H NMR (500 MHz, Chloroform-*d*) δ 8.62 (s, ^{1}H), 8.24 (d, *J* = 15 Hz, ^{1}H), 7.90 (d, *J* = 15 Hz, ^{1}H), 7.83 (dd, *J* = 10, 5 Hz, ^{1}H), 7.72–7.66 (m, 2H), 7.63 (dd, *J* = 10, 5 Hz, ^{1}H), 7.41 (d, *J* = 10 Hz, ^{1}H), 7.39–7.34 (m, 2H), 7.28–7.22 (m, ^{1}H).

(E)-3-[3-(3-bromophenyl)acryloyl]-2H-chromen-2-one (3s). Yellow solid; yield 41.8%; ^{1}H NMR (500 MHz, Chloroform-*d*) δ 8.61 (s, ^{1}H), 7.94 (d, *J* = 15 Hz, ^{1}H), 7.82–7.75 (m, 2H), 7.70–7.65 (m, 2H), 7.59 (d, *J* = 10 Hz, ^{1}H), 7.53 (ddd, *J* = 3, 1.5, 1 Hz, ^{1}H), 7.43–7.35 (m, 2H), 7.29 (t, *J* = 10, 10 Hz, ^{1}H).

(E)-3-[3-(4-bromophenyl)acryloyl]-2H-chromen-2-one (3t). Yellow solid; yield 44.5%; ^{1}H NMR (500 MHz, Chloroform-*d*) δ 8.61 (s, ^{1}H), 7.95 (d, *J* = 15 Hz, ^{1}H), 7.79 (d, *J* = 15 Hz, ^{1}H), 7.70–7.65 (m, 2H), 7.54 (s, 4H), 7.41 (d, *J* = 10 Hz, ^{1}H), 7.36 (td, *J* = 5, 1 Hz, ^{1}H).

(E)-3-[3-(thiophen-2-yl)acryloyl]-2H-chromen-2-one (3u).
Yellow solid; yield 40.7%; ^{1}H NMR (500 MHz, DMSO-d_6) δ
12.00 (s, ^{1}H), 8.68 (s, ^{1}H), 8.01 (d, J = 15 Hz, ^{1}H), 8.10–8.04
(m, 2H), 7.98 (td, J = 10, 3.5 Hz, 2H), 7.78–7.73 (m, ^{1}H), 7.69 (d,
J = 15 Hz, ^{1}H), 7.54–7.49 (m, 2H), 7.44 (td, J = 10, 1.5 Hz, ^{1}H),
7.30–7.22 (m, 2H).

(E)-3-[3-(^{1}H-indol-2-yl)acryloyl]-2H-chromen-2-one (3v).
Yellow solid; yield 51.7%; ^{1}H NMR (500 MHz, Chloroform-d)
δ 8.60 (s, ^{1}H), 7.92 (dd, J = 40, 20 Hz, 2H), 7.71–7.65 (m, 4H),
7.44–7.39 (m, 4H), 7.35 (t, J = 8, 7.5 Hz, ^{1}H).

α-Glucosidase Inhibition and Kinetics Mechanism Analysis Assay

The α-glucosidase inhibitory activity assay of coumarin-chalcone
derivatives 3 (a~v) was conducted using *p*-NPG as a substrate.
(Pogaku et al., 2019; Saeedi et al., 2019; Xu et al., 2019). 10 μl of the
test compound and 10 μl of the enzyme (final concentration 0.1 U/
ml) were added to 130 μl of PBS (0.1 M phosphate, pH 6.8), and
incubated at 37°C for 10 min. Then *p*-NPG (final concentration
0.25 mM) was added and the absorbance change was measured by a
micro-plate reader at 405 nm. All experiments were assayed four
times. The percentage of inhibition was obtained using the formula:
Inhibition (%) = [(OD$_1$ - OD$_0$)/OD$_0$] × 100%, where OD$_1$ and OD$_0$
represent the absorbance value of the experimental group and the
blank group respectively. Acarbose as a positive sample was also
tested. The IC$_{50}$ value of each compound was obtained from the
fitting curve of inhibition vs. compound concentration.

The type of inhibition was identified by the plots of enzymatic
reaction rate (V) vs. α-glucosidase concentration. The test
method was similar to the above enzyme activity assay. In the
presence of different concentrations of compounds **3j**, **3q** and **3t**,
respectively (0, 25, 30, and 40 μM), the absorbance change was
detected under different concentrations of α-glucosidase (0.075,
0.1, 0.125, and 0.15 U/mL).

The inhibition mode was also detected using a similar method
to that described above. In the presence of different concentrations
of compounds **3j**, **3q** and **3t**, respectively (0, 25, 30 and 40 μM), the
absorbance change was measured under different concentrations
of *p*-NPG (0.25, 0.5, 0.75, 1 mM). The inhibition mode of the
inhibitor was obtianed using Lineweaver-Burk plots. The constant
K$_I$ was obtained by secondary plots of the derivatives concentration
(I) vs. Slope, constant K$_{IS}$ was obtained by secondary plots of the
derivatives concentration (I) vs. Intercept.

Molecular Docking

The molecular docking of α-glucosidase with compounds **3d**,
3f, and **3i** was simulated with Sybyl 2.1.1 (United States) and
Pymol software. First, compounds **3d**, **3f**, and **3i** were prepared
by energy minimization with the Tripos force field by the
Powell gradient algorithm with Gasteiger-Hückel charges. The

maximum iterations for the minimization were set to 10 000.
The minimization was terminated when an energy gradient
convergence criterion of 0.005 kcal mol−1 Å−1 was reached.
The energy convergence criterion of 0.01 kcal/mol and the
maximum iterations for the minimization of 1,000 times were
reached. Next, the crystal structure of *Saccharomyces cerevisiae*
isomaltase (PDB: 3AJ7) was downloaded from the RCSB
Protein Data Bank. The protein was prepared by
biopolymer and implemented following the procedure of
removing water molecules, adding hydrogen atoms, and
repairing end residues. The active pocket of protein was
generated with the automatic mode. Then the molecular
docking of protein with **3d**, **3f**, and **3i** was operated in the
default format. The Pymol software was used to draw the view
of protein with **3d**, **3f**, and **3i**.

DATA AVAILABILITY STATEMENT

The original contributions presented in the study are included in
the article/**Supplementary Material**, further inquiries can be
directed to the corresponding authors.

AUTHOR CONTRIBUTIONS

C-MH, Y-XL, W-JW, J-PL, and M-YL dedicated to the synthesis
of compounds; C-MH, Y-XL, Y-FZ, DX, and LL dedicated to the
characterization of compounds and analysis of data. C-MH,
Y-XL, W-JW, J-PL, and LL dedicated to the enzyme inhibition
assay and enzyme kinetics assay; C-MH and Y-XL carried out the
molecular docking simulation. ZX and NF designed and managed
the experiments. CL supervised the work and prepared the
manuscript.

FUNDING

SUPPLEMENTARY MATERIAL

The Supplementary Material for this article can be found online at:
https://www.frontiersin.org/articles/10.3389/fchem.2022.926543/
full#supplementary-material

REFERENCE

Abuelizz, H. A., Anouar, E. H., Ahmad, R., Azman, N. I. I. N., Marzouk, M., and Al-
     Salahi, R. (2019). Triazoloquinazolines as a New Class of Potent α-glucosidase

Inhibitors: *In Vitro* Evaluation and Docking Study. *PLoS One* 14, e0220379.
     doi:10.1371/journal.pone.0220379
Adib, M., Peytam, F., Rahmanian-Jazi, M., Mohammadi-Khanaposhtani, M.,
     Mahernia, S., Bijanzadeh, H. R., et al. (2018). Design, Synthesis and *In Vitro*
     α-glucosidase Inhibition of Novel Coumarin-Pyridines as Potent

Antidiabetic Agents. *New J. Chem.* 42, 17268–17278. doi:10.1039/C8NJ02495B

Asgari, M. S., Mohammadi-Khanaposhtani, M., Kiani, M., Ranjbar, P. R., Zabihi, E., Pourbagher, R., et al. (2019). Biscoumarin-1,2,3-triazole Hybrids as Novel Antidiabetic Agents: Design, Synthesis, *In Vitro* α-glucosidase Inhibition, Kinetic, and Docking Studies. *Bioorg. Chem.* 92, 103206. doi:10.1016/j.bioorg.2019.103206

Bak, E.-J., Park, H.-G., Lee, C.-H., Lee, T.-I., Woo, G.-H., Na, Y.-H., et al. (2011). Effects of Novel Chalcone Derivatives on α-glucosidase, Dipeptidyl Peptidase-4, and Adipocyte Differentiation *In Vitro*. *BMB Rep.* 44, 410–414. doi:10.5483/BMBRep.2011.44.6.410

Chai, T.-T., Kwek, M.-T., Ong, H.-C., and Wong, F.-C. (2015). Water Fraction of Edible Medicinal Fern *Stenochlaena palustris* Is a Potent α-glucosidase Inhibitor with Concurrent Antioxidant Activity. *Food Chem.* 186, 26–31. doi:10.1016/j.foodchem.2014.12.099

Cohen, P., and Goedert, M. (2004). GSK3 Inhibitors: Development and Therapeutic Potential. *Nat. Rev. Drug Discov.* 3, 479–487. doi:10.1038/nrd1415

Djemoui, A., Naouri, A., Ouahrani, M. R., Djemoui, D., Lahcene, S., Lahrech, M. B., et al. (2020). A Step-by-step Synthesis of Triazole-Benzimidazole-Chalcone Hybrids: Anticancer Activity in Human Cells. *J. Mol. Struct.* 1204, 127487. doi:10.1016/j.molstruc.2019.127487

Dorn, C., Kraus, B., Motyl, M., Weiss, T. S., Gehrig, M., Schölmerich, J., et al. (2010). Xanthohumol, a Chalcon Derived from Hops, Inhibits Hepatic Inflammation and Fibrosis. *Mol. Nutr. Food Res.* 54 (Suppl. 2), S205–S213. doi:10.1002/mnfr.200900314

Feng, L., Maddox, M. M., Alam, M. Z., Tsutsumi, L. S., Narula, G., Bruhn, D. F., et al. (2014). Synthesis, Structure-Activity Relationship Studies, and Antibacterial Evaluation of 4-Chromanones and Chalcones, as Well as Olympicin A and Derivatives. *J. Med. Chem.* 57, 8398–8420. doi:10.1021/jm500853v

Gulcin, I., Kaya, R., Goren, A. C., Akincioglu, H., Topal, M., Bingol, Z., et al. (2019). Anticholinergic, Antidiabetic and Antioxidant Activities of Cinnamon (Cinnamomum Verum) Bark Extracts: Polyphenol Contents Analysis by LC-MS/MS. *Int. J. Food Prop.* 22, 1511–1526. doi:10.1080/10942912.2019.1656232

Ibrar, A., Zaib, S., Khan, I., Shafique, Z., Saeed, A., and Iqbal, J. (2017). New Prospects for the Development of Selective Inhibitors of α-glucosidase Based on Coumarin-Iminothiazolidinone Hybrids: Synthesis, *In-Vitro* Biological Screening and Molecular Docking Analysis. *J. Taiwan Inst. Chem. Eng.* 81, 119–133. doi:10.1016/j.jtice.2017.09.041

Kang, L., Gao, X.-H., Liu, H.-R., Men, X., Wu, H.-N., Cui, P.-W., et al. (2018). Structure-activity Relationship Investigation of Coumarin-Chalcone Hybrids with Diverse Side-Chains as Acetylcholinesterase and Butyrylcholinesterase Inhibitors. *Mol. Divers.* 22, 893–906. doi:10.1007/s11030-018-9839-y

Kasturi, S. P., Surarapu, S., Uppalanchi, S., Dwivedi, S., Yogeeswari, P., Sigalapalli, D. K., et al. (2018). Synthesis, Molecular Modeling and Evaluation of α-glucosidase Inhibition Activity of 3,4-dihydroxy Piperidines. *Eur. J. Med. Chem.* 150, 39–52. doi:10.1016/j.ejmech.2018.02.072

Katsori, A.-M., and Hadjipavlou-Litina, D. (2014). Coumarin Derivatives: an Updated Patent Review (2012 - 2014). *Expert Opin. Ther. Pat.* 24, 1323–1347. doi:10.1517/13543776.2014.972368

Khursheed, R., Singh, S. K., Wadhwa, S., Kapoor, B., Gulati, M., Kumar, R., et al. (2019). Treatment Strategies against Diabetes: Success So Far and Challenges Ahead. *Eur. J. Pharmacol.* 862, 172625. doi:10.1016/j.ejphar.2019.172625

Kontogiorgis, C., Detsi, A., and Hadjipavlou-Litina, D. (2012). Coumarin-based Drugs: a Patent Review (2008 - Present). *Expert Opin. Ther. Pat.* 22, 437–454. doi:10.1517/13543776.2012.678835

Lee, S. Y., Chiu, Y. J., Yang, S. M., Chen, C. M., Huang, C. C., Lee-Chen, G. J., et al. (2018). Novel Synthetic Chalcone-coumarin Hybrid for Aβ Aggregation Reduction, Antioxidation, and Neuroprotection. *CNS Neurosci. Ther.* 24, 1286–1298. doi:10.1111/cns.13058

Morocho, V., Sarango, D., Cruz-Erazo, C., Cumbicus, N., Cartuche, L., and Suárez, A. I. (2019). Chemical Constituents of Croton Thurifer Kunth as α-Glucosidase Inhibitors. *Rec. Nat. Prod.* 14, 31–41. doi:10.25135/rnp.136.18.11.1069

Pingaew, R., Saekee, A., Mandi, P., Nantasenamat, C., Prachayasittikul, S., Ruchirawat, S., et al. (2014). Synthesis, Biological Evaluation and Molecular Docking of Novel Chalcone-Coumarin Hybrids as Anticancer and Antimalarial Agents. *Eur. J. Med. Chem.* 85, 65–76. doi:10.1016/j.ejmech.2014.07.087

Pogaku, V., Gangarapu, K., Basavoju, S., Tatapudi, K. K., and Katragadda, S. B. (2019). Design, Synthesis, Molecular Modelling, ADME Prediction and Anti-hyperglycemic Evaluation of New Pyrazole-Triazolopyrimidine Hybrids as Potent α-glucosidase Inhibitors. *Bioorg. Chem.* 93, 103307. doi:10.1016/j.bioorg.2019.103307

Proença, C., Freitas, M., Ribeiro, D., Oliveira, E. F. T., Sousa, J. L. C., Tomé, S. M., et al. (2017). α-Glucosidase Inhibition by Flavonoids: an *In Vitro* and In Silico Structure-Activity Relationship Study. *J. Enzyme Inhibition Med. Chem.* 32, 1216–1228. doi:10.1080/14756366.2017.1368503

Rocha, S., Ribeiro, D., Fernandes, E., and Freitas, M. (2020). A Systematic Review on Anti-diabetic Properties of Chalcones. *Curr. Med. Chem.* 27, 2257–2321. doi:10.2174/0929867325666181001112226

Rocha, S., Sousa, A., Ribeiro, D., Correia, C. M., Silva, V. L. M., Santos, C. M. M., et al. (2019). A Study towards Drug Discovery for the Management of Type 2 Diabetes Mellitus through Inhibition of the Carbohydrate-Hydrolyzing Enzymes α-amylase and α-glucosidase by Chalcone Derivatives. *Food Funct.* 10, 5510–5520. doi:10.1039/C9FO01298B

Roussel, M. R., and Fraser, S. J. (1993). Global Analysis of Enzyme Inhibition Kinetics. *J. Phys. Chem.* 97, 8316–8327. doi:10.1021/j100133a031

Saeedi, M., Mohammadi-Khanaposhtani, M., Asgari, M. S., Eghbalnejad, N., Imanparast, S., Faramarzi, M. A., et al. (2019). Design, Synthesis, *In Vitro*, and In Silico Studies of Novel Diarylimidazole-1,2,3-Triazole Hybrids as Potent α-glucosidase Inhibitors. *Bioorg. Med. Chem.* 27, 115148. doi:10.1016/j.bmc.2019.115148

Salar, U., Taha, M., Khan, K. M., Ismail, N. H., Imran, S., Perveen, S., et al. (2016). Syntheses of New 3-thiazolyl Coumarin Derivatives, *In Vitro* α -glucosidase Inhibitory Activity, and Molecular Modeling Studies. *Eur. J. Med. Chem.* 122, 196–204. doi:10.1016/j.ejmech.2016.06.037

Seidel, C., Schnekenburger, M., Zwergel, C., Gaascht, F., Mai, A., Dicato, M., et al. (2014). Novel Inhibitors of Human Histone Deacetylases: Design, Synthesis and Bioactivity of 3-alkenoylcoumarines. *Bioorg. Med. Chem. Lett.* 24, 3797–3801. doi:10.1016/j.bmcl.2014.06.067

Shang, Y.-j., Wei, Q., and Sun, Z.-b. (2018). Studying the Cytotoxicity of Coumarin-Chalcone Hybrids by a Prooxidant Strategy in A549 Cells. *Monatsh Chem.* 149, 2287–2292. doi:10.1007/s00706-018-2273-0

Vazquez-Rodriguez, S., Lama López, R., Matos, M. J., Armesto-Quintas, G., Serra, S., Uriarte, E., et al. (2015). Design, Synthesis and Antibacterial Study of New Potent and Selective Coumarin-Chalcone Derivatives for the Treatment of Tenacibaculosis. *Bioorg. Med. Chem.* 23, 7045–7052. doi:10.1016/j.bmc.2015.09.028

Wang, G., He, D., Li, X., Li, J., and Peng, Z. (2016). Design, Synthesis and Biological Evaluation of Novel Coumarin Thiazole Derivatives as α-glucosidase Inhibitors. *Bioorg. Chem.* 65, 167–174. doi:10.1016/j.bioorg.2016.03.001

Wang, G., Wang, J., Xie, Z., Chen, M., Li, L., Peng, Y., et al. (2017). Discovery of 3,3-Di(indolyl)indolin-2-One as a Novel Scaffold for α-glucosidase Inhibitors: In Silico Studies and SAR Predictions. *Bioorg. Chem.* 72, 228–233. doi:10.1016/j.bioorg.2017.05.006

Wang, Y.-H., Jiang, S.-C., Chen, Y., Guo, T., Xia, R.-J., Tang, X., et al. (2019). Synthesis and Antibacterial Activity of Novel Chalcone Derivatives Bearing a Coumarin Moiety. *Chem. Pap.* 73, 2493–2500. doi:10.1007/s11696-019-00802-0

Xu, X. T., Deng, X. Y., Chen, J., Liang, Q. M., Zhang, K., Li, D. L., et al. (2019). Synthesis and Biological Evaluation of Coumarin Derivatives as α-glucosidase Inhibitors. *Eur. J. Med. Chem.* 189, 112013. doi:10.1016/j.ejmech.2019.112013

Zhong, Y., Yu, L., He, Q., Zhu, Q., Zhang, C., Cui, X., et al. (2019). Bifunctional Hybrid Enzyme-Catalytic Metal Organic Framework Reactors for α-Glucosidase Inhibitor Screening. *ACS Appl. Mat. Interfaces* 11, 32769–32777. doi:10.1021/acsami.9b11754

Conflict of Interest: The authors declare that the research was conducted in the absence of any commercial or financial relationships that could be construed as a potential conflict of interest.

Publisher's Note: All claims expressed in this article are solely those of the authors and do not necessarily represent those of their affiliated organizations, or those of the publisher, the editors and the reviewers. Any product that may be evaluated in this article, or claim that may be made by its manufacturer, is not guaranteed or endorsed by the publisher.

Responsive Fluorescent Coumarin–Cinnamic Acid Conjugates for α-Glucosidase Detection

Dong Luo[1†], Xin Zhang[1†], Xiaoying Li[1], Yi-Yu Zhen[1], Xingyi Zeng[1], Zhuang Xiong[1]*, Yinghui Zhang[1,2]* and Hongguang Li[1,2]*

[1]School of Biotechnology and Health Science, Wuyi University, Jiangmen, China, [2]Guangdong Provincial Key Laboratory of Large Animal Models for Biomedicine, South China Institute of Large Animal Models for Biomedicine, Wuyi University, Jiangmen, China

α-Glucosidase is a potent drug target for treating type II diabetes mellitus. A great number of α-glucosidase inhibitors have been developed based on the molecular skeletons of bioactive natural products. However, efficient fluorescent probes for α-glucosidase detection are still limited, not to mention the probes with additional inhibitory functions. In this work, aiming for the enzyme's highly specific detection, we designed and synthesized two environmentally sensitive fluorescent probes, namely, LD01 and LD02, respectively, based on conjugates of coumarin and cinnamic acid derivatives. We found a significant responsive emission enhancement upon LD02's binding to α-glucosidase. These newly designed probes can act as a simple but efficient tool to evaluate the binding affinity of α-glucosidase to their inhibitors.

Keywords: α-glucosidase, fluorescent probe, responsive probe, coumarin, environmentally sensitive dyes, cinnamic acid

INTRODUCTION

Diabetes mellitus (DM) can be categorized into three types (type I, type II, and gestational diabetes), with type II DM accounting for ninety percent of the total number of patients (Chen et al., 2015). Pathological features of type II DM are characterized by hyperglycemia arising from various causes such as a relative deficiency of insulin secretion, insulin resistance, or other malfunctioning factors on carbohydrate metabolism (Teng and Chen, 2017). Long-term high blood glucose levels in human bodies can lead to various complications, such as kidney disease, cataract, and vascular diseases (Prattichizzo et al., 2019). α-Glucosidase is a membrane-bound enzyme in small intestinal epithelial cells, playing a pivotal role in the digestion of carbohydrates by direct participation in the metabolic pathway of glycogen and starch (Tang et al., 2017). Biochemically, in the last step of glycolysis, it can breakdown the α-1,4 glycosidic bonds from the non-reducing saccharide chains' end, hydrolyzing the long oligosaccharide chains into single glucose. Then the digested glucose can be absorbed by the small intestine and transported to the blood. When this physiological process overacts due to excessive ingestion of carbohydrates, hyperglycemia occurs, leading to the development of DM (Guo et al., 2021).

Because of the biological and pharmacological importance of α-glucosidase, a great number of natural products and synthetic compounds were developed for α-glucosidase-targeting inhibition (Liu and Ma, 2017; Dhameja and Gupta, 2019; Gutiérrez-González et al., 2021; Trang et al., 2021). However, efficient probes targeting α-glucosidase and the corresponding detection methods are still very rare. Up to now, only limited examples were reported in recent years about α-glucosidase's molecular detection (Zhang et al., 2015; Ao et al., 2017; Kong et al., 2017; Li et al., 2018; Cheng et al.,
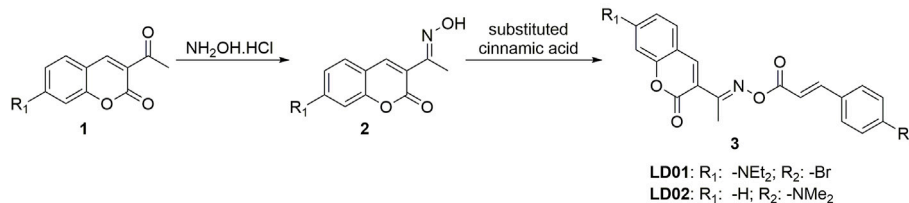
SCHEME 1 | Synthetic route of LD01 and LD02.
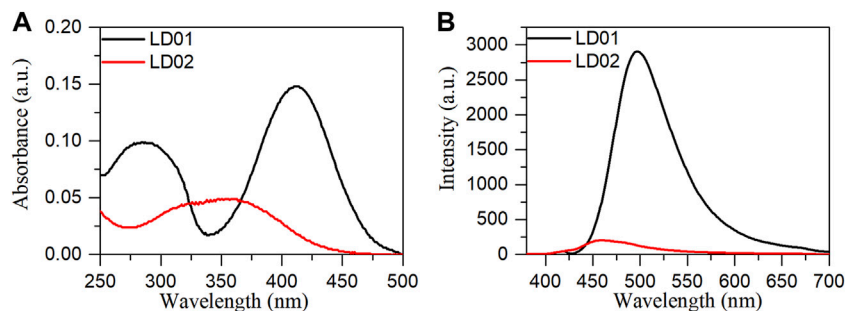
FIGURE 1 | Absorption **(A)** and emission **(B)** spectra of **LD01** (λ_{ex} = 410 nm) and LD02 (λ_{ex} = 365 nm) in PBS buffer (10 mM, pH = 7.4).

2019), which are all focused on the catalytic function of α-glucosidase. Because this type of technical system involved multiple steps in the sensing protocol, the quantitative detection of α-glucosidase cannot be satisfactorily acquired.

Environmentally sensitive fluorescent probes are widely used for protein detection and imaging, whose responsive emissions are highly sensitive to the microenvironmental properties, such as polarity, pH, or viscosity of the surrounding medium where the dyes are located (Shvadchak et al., 2017; Dong et al., 2020; Zhou et al., 2020). Intramolecular charge transfer (ICT)-based donor-π-acceptor dyes were found to exhibit strong emission in non-polar environments but fail to do so in highly polar solvents (Dai et al., 2020; Pal. et al., 2020). Theoretically, the binding pocket of a specific target protein for such fluorescent probes may be more hydrophobic than that in aqueous solutions.

Coumarin and cinnamic acid are two types of typical natural products widely distributed in nature, harboring typical useful motifs in medicinal chemistry (Gaudino et al., 2016; Adisakwattana, 2017; Annunziata et al., 2020; Ruwizhi and Aderibigbe, 2020). Recently, Xu et al. reported that the conjugates of coumarin and cinnamic acid derivatives are potent inhibitors against α-glucosidase (Xu et al., 2019). In this work, we designed and synthesized two fluorescent conjugates of dialkyl-substituted coumarin and cinnamic acid, LD01 and LD02, featuring donor-π-acceptor structures as two environmentally sensitive probes for α-glucosidase-targeting detection. We hypothesized the binding pocket inside α-glucosidase may provide a relatively non-polar environment for the fluorescent probes so that intense fluorescence emission will be activated when

bound to α-glucosidase. Comprehensive photophysical studies and enzyme inhibitory assays demonstrated newly designed fluorescent probe LD02 can act as a fluorescent indicator for α-glucosidase, which can also serve as a potential tool for evaluating the binding affinity between α-glucosidase and its inhibitors.

EXPERIMENTAL

Instruments and Reagents

All chemicals and solvents were obtained from commercial suppliers without further purification. α-Glucosidase from *Saccharomyces cerevisiae* (EC 3.2.1.20) was purchased from Sigma-Aldrich. p-Nitrophenyl-α-D-galactopyranoside (PNPG) was obtained from Abcam. Nuclear magnetic resonance (NMR) spectra of new compounds were recorded in DMSO-d_6 using a Bruker Advance 500 MHz spectrometer. High-resolution mass spectrometry (HRMS) was measured on a Thermo Fisher Scientific Q Exactive Orbitrap mass spectrometer. UV–Vis absorption spectra were measured using an Hitachi 3,900 absorption spectrophotometer (Tokyo, Japan). Fluorescence spectra were recorded using an Edinburgh FLS1000 fluorescence spectrophotometer (Edinburgh, UK).

Synthesis of LD01 and LD02

The substituted 3-acetyl-aminocoumarin derivatives (1.0 mmol) were added to a solution of hydroxylamine hydrochloride (3.0 mmol) and pyridine (0.04 mmol) in ethanol (10.0 ml), and

FIGURE 2 | Fluorescence spectra of LD01 (λ$_{ex}$ = 410 nm) and LD02 (λ$_{ex}$ = 365 nm) in different solvents **(A, B)** and in mixed solvents of dioxane and water **(E, F)**. Scatterplots of the most intense fluorescence emission by LD01 **(C, G)** and LD02 **(D, H)** in **(A, B, E, and F)**, respectively.
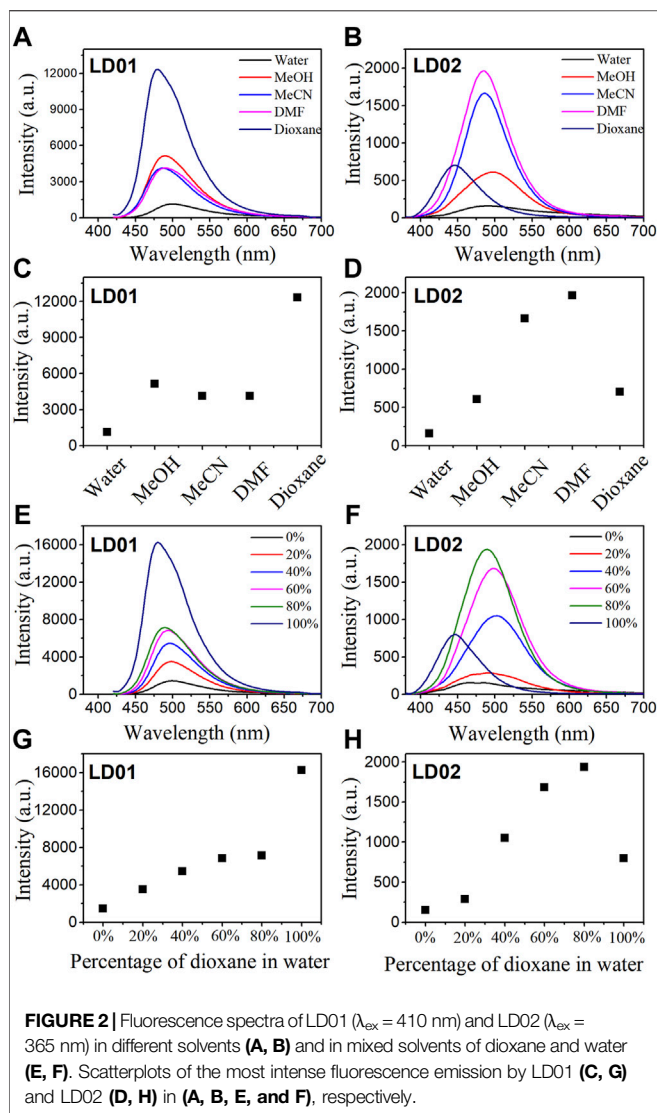
the mixture was stirred for 20 h at room temperature. When the reaction ended, the mixture was filtered to obtain precipitate which was then washed with ethanol to generate the substituted coumarin-based oxime product. DCC (1.1 mmol) and DMAP (0.2 mmol) were added to the solution of the substituted cinnamic acid at 0°C, and the mixture was stirred for 15 min; subsequently, the coumarin-based oxime compounds were added into the mixture and thoroughly stirred for another 12 h at room temperature. The mixture was quenched with water and extracted three times with DCM, washed with brine, and dried with magnesium sulfate. The crude product could be obtained under vacuum, and then purified by column chromatography to give the title product.

Compound LD01. Orange, sold; yield 70%; m.p. 196–198°C; ^{1}H NMR (500 MHz, DMSO-d_6) δ 7.86 (s, 1H), 7.64 (d, J = 8.6 Hz, 2H), 7.60 – 7.57 (m, 3H), 7.49 (d, J = 8.8 Hz, 1H), 6.69 (dd, J = 8.9, 2.5 Hz, 1H), 6.56 (d, J = 16.0 Hz, 1H), 6.52 (d, J = 2.6 Hz, 1H), 3.42 (q, J = 7.0 Hz, 4H), 2.05 (s, 3H), 1.11 (t, J =

7.0 Hz, 6H); ^{13}C NMR (126 MHz, DMSO-d_6) δ 167.89, 160.51, 156.73, 152.69, 151.18, 143.08, 141.91, 133.99, 132.31, 130.61, 130.44, 123.99, 120.58, 117.64, 109.66, 108.03, 96.61, 44.57, 14.10, 12.77; HRMS (+ESI) [M + H]$^+$ calcd. For $C_{24}H_{23}BrN_2O_4$: 483.0930; found: 483.0967.

Compound LD02. Yellow, sold; yield 65%; m.p. 167–168°C; ^{1}H NMR (500 MHz, DMSO-d_6) δ 8.63 (s, 1H), 7.93 (dd, J = 7.8, 1.6 Hz, 1H), 7.73 (ddd, J = 8.7, 7.3, 1.7 Hz, 1H), 7.46 (dt, J = 10.6, 6.8 Hz, 4H), 7.40 (td, J = 7.6, 1.1 Hz, 1H), 6.67 (d, J = 8.9 Hz, 2H), 6.20 (d, J = 15.9 Hz, 1H), 2.95 (s, 6H), 2.58 (s, 3H); ^{13}C NMR (126 MHz, DMSO-d_6) δ 195.51, 168.67, 158.90, 155.06, 152.02, 147.52, 145.12, 134.92, 131.24, 130.16, 125.37, 124.81, 121.99, 118.61, 116.56, 113.35, 112.20, 40.14, 30.52; HRMS (+ESI) [M + H]$^+$ calcd. For $C_{22}H_{20}N_2O_4$: 377.1509; found: 377.1533.

Photophysical Properties' Measurements

All solvents used for spectroscopic studies are spectrum pure grade. The stock solution of each sample was prepared in DMSO (1 mM), and the working solution was obtained by diluting 30 μL of stock solutions into 3 ml of PBS buffer (10 mM, pH = 7.4) or other solvents in a quartz cuvette (1 cm × 1 cm). The absorption and emission spectra were measured at room temperature. The widths of the slits for both excitation and emission were 2 nm for all experiments.

pH-Dependent Emission

The emission spectra of the probes in PBS buffer (pH from 3.0 to 8.0) were determined at room temperature. The pKa value was calculated using the Henderson–Hosslbalch equation (Finikova et al., 2003):

$$pH = pKa + \lg\left(\frac{[A]}{[HA]}\right).$$

Fluorescence Titration of The Probes With α-Glucosidase

α-Glucosidase protein was titrated to the solution of the testing probe (LD01 or LD02) (10 μM), and the fluorescence emission spectra were recorded from 380 to 700 nm under excitation of 365 nm. The binding constants of Ka were obtained from a double logarithm regression curve (Wei et al., 2010):

$$\lg[(I - I_0)/I_0] = \lg Ka + n \lg[G],$$

where I and I_0 are the current and initial fluorescence intensity, respectively, K_a is the binding constant, n is the number of binding sites for each α-glucosidase, and [G] is the total concentration of the α-glucosidase protein.

Fluorescence Competitive Binding Assay

The binding complexes of α-glucosidase with LD02 were prepared by adding α-glucosidase (final concentration = 3.5 μM) to the solution of LD02 (10 μM) in 10 mM PBS buffer (pH = 7.4). The dissociation constant of a competitor to α-glucosidase can be determined by titrating it against binding complexes of α-glucosidase with LD02, and can be calculated
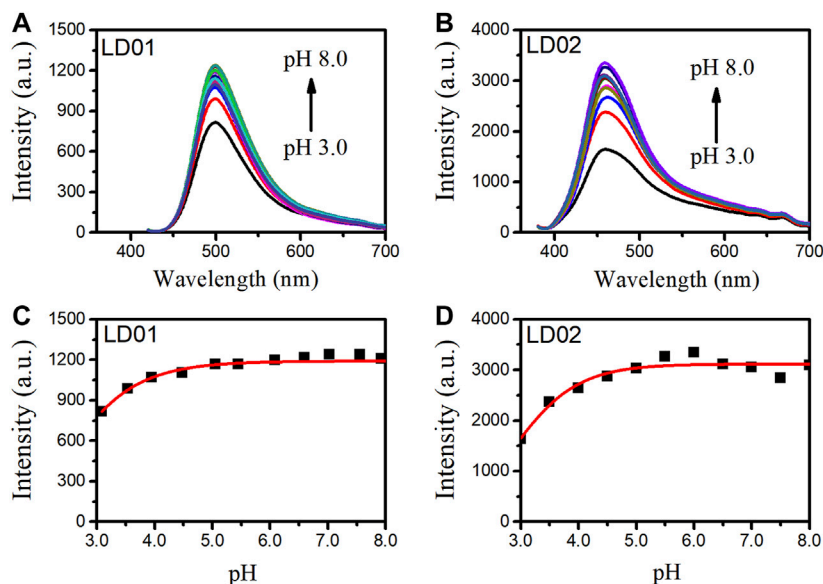
FIGURE 3 | Fluorescence spectra of LD01 **(A)** (λ_{ex} = 410 nm) and LD02 **(B)** (λ_{ex} = 365 nm) in buffers of various pH. Scatterplots of the most intense fluorescence emission by LD01 **(C)** and LD02 **(D)** in **(A, B)**.
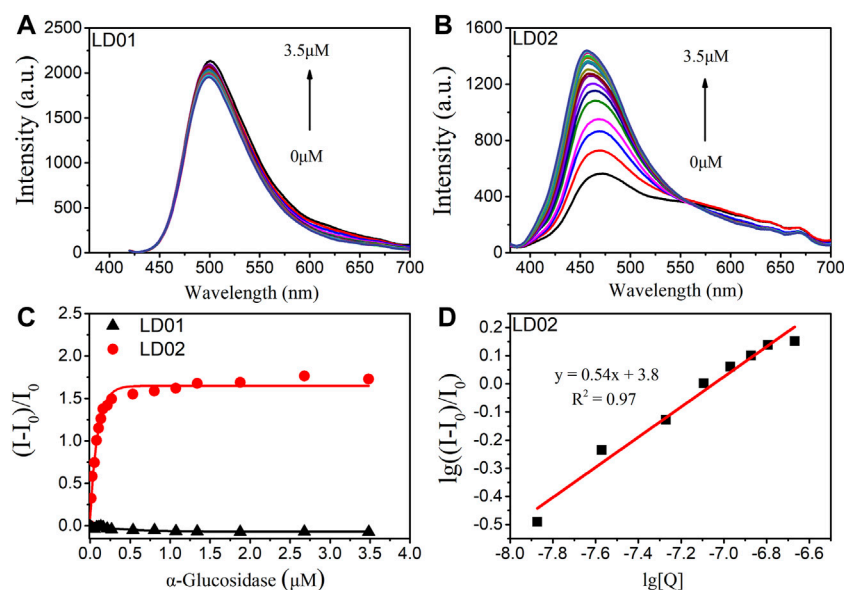
FIGURE 4 | Fluorescence spectra of LD01 **(A)** and LD02 **(B)** (10 μM) in the presence of various concentrations of α-glucosidase (0–3.5 μM) in PBS buffer. **(C)** Changes in (I-I$_0$/I$_0$) of LD01 (λ_{ex} = 410 nm, λ_{em} = 500 nm) and LD02 (λ_{ex} = 365 nm, λ_{em} = 457 nm) on addition of α-glucosidase. **(D)** The linear regression line of lg ((I-I$_0$)/I$_0$) to lg [Q], [Q] is the concentration of α-glucosidase (mol/L).

according to the Cheng–Prusoff equation (Cheng and Prusoff, 1973).

α-Glucosidase Inhibition Efficiency Test of LD01 and LD02

The inhibition efficiency of LD01 and LD02 were determined according to the procedures Xu et al. reported previously (Xu

et al., 2019). Stock solutions of testing compounds were prepared in DMSO. Enzyme solution of α-glucosidase (2 U/mL) was prepared in 0.1 M PBS buffer. Nitrophenol-α-D-glucoside (PNPG) was dissolved in 0.1 M PBS buffer (pH 6.8) to obtain the substrate solution (4 mM). In total, 10 μL of α-glucosidase (final concentration 0.1 U/mL), 130 μL of PBS buffer, and 10 μL of the sample solution were added into 96-well plates in succession and incubated at 37°C for 10 min. Then 50 μL of substrate solution (PNPG final
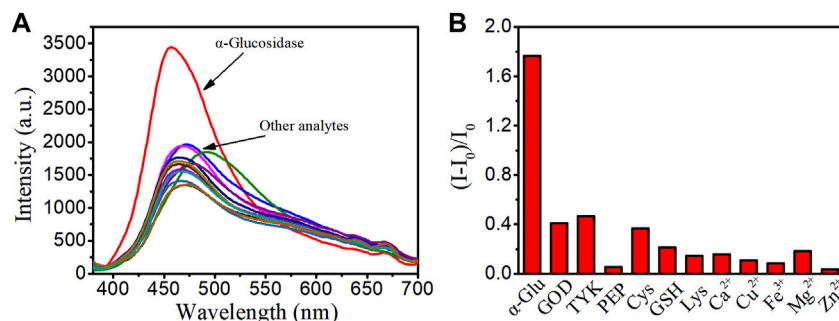
FIGURE 5 | (A) Fluorescence spectra of LD02 (10 μM) in the presence of various species: α-glucosidase (α-Glu) (3.5 μM), GOD (3.5 μM), TKY (3.5 μM), PEP (3.5 μM), Cys (1 mM), GSH (1 mM), Lys (1 mM), Ca^{2+} (1 mM), Cu^{2+} (1 mM), Fe^{3+} (1 mM), Mg^{2+} (1 mM), and Zn^{2+} (1 mM) in PBS buffer. **(B)** The plot of $(I-I_0)/I_0$ in A (λ_{ex} = 365 nm, λ_{em} = 457 nm).
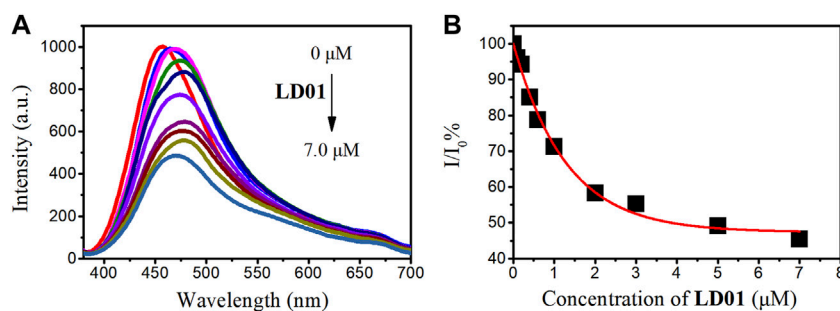
FIGURE 6 | (A) Fluorescent emission spectra of α-glucosidase–LD02 binding complex (10 μM of LD02 with 3.5 μM of α-glucosidase, λ_{ex} = 365 nm) in the presence of various concentrations of LD01. **(B)** Scatterplots of the relative intensity I/I_0 in A (λ_{em} = 457 nm).
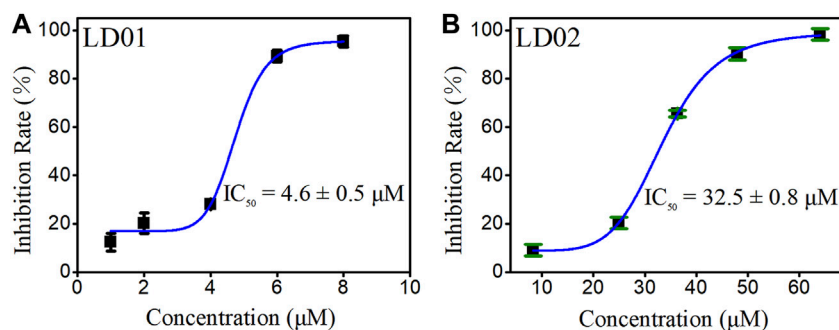
FIGURE 7 | Plot of the inhibition rate of LD01 **(A)** and LD02 **(B)** against α-glucosidase concentration.

concentration 1 mmol/L) was added, followed by incubation at 37°C for another 30 min. The enzymatic activity was quantified by measuring the absorbance of the reaction mixture at 405 nm using a multimodel reader. The inhibition rate was calculated using the following equation:

$$\text{Inhibition rate (\%)} = [(A_1 - A_0)/A_0] \times 100\%,$$

where A_1 and A_0 are the absorbance values of testing samples and blank control, respectively. The IC_{50} value was obtained from a plot of the inhibition rate *versus* the sample concentration curve. The assays were carried out in triplicate and the mean values were given.

RESULT AND DISCUSSION

Synthesis and Characterization of LD01 and LD02

LD01 and LD02 could be obtained through a two-step synthesis as shown in **Scheme 1**. In brief, substituted 3-acetylcoumarin

derivatives reacted with hydroxylamine hydrochloride under the basic condition to give the substituted coumarin-based oxime product, followed by acylation with corresponding cinnamic acid to produce the designed molecular probes **LD01** and **LD02**, which were well characterized by ^{1}H NMR, ^{13}C NMR, and HRMS (supporting information, **Supplementary Figures S1–6**).

Photophysical Properties' Studies

Absorption spectra of LD01 and LD02 were measured at room temperature in PBS buffer (pH = 7.4). LD01 has two absorption bands at 410 nm (ε = 14,800 M cm^{-1}) and 290 nm (ε = 9800 M cm^{-1}) assigned to $\pi \rightarrow \pi^\star$ transitions from diethylamino-coumarin and bromo cinnamic ester moiety, respectively. LD02 has an absorption band at around 365 nm (ε = 4900 M cm^{-1}) resulting from the mixed $\pi \rightarrow \pi^\star$ transitions of coumarin and cinnamic ester moieties. For the emission spectra, LD01 and LD02 show one emission band with maximum emission at 500 and 457 nm, respectively, while exhibiting very low emission quantum yield, 5.3% for LD01, and 3.2% for LD02 in PBS buffer (pH = 7.4). It has been well documented that dialkyl amine-substituted coumarin or cinnamic acid derivatives are ICT-based dyes, and their emission band or intensity is affected by the surrounding polarity. We first determined the emission spectra of LD01 and LD02 in various solvents of different polarities, such as water, methanol, acetonitrile, N,N-dimethylformamide, and dioxane (**Figures 2A–D**). The emission intensity of LD01 accrues in an increasing order of polarity. LD02 shows a similar tendency except for the emission of dioxane, which may result from the poor solubility of LD02 in it. Moreover, the emission band of LD02 shows a 40-nm blue shift in dioxane as compared to that in an aqueous buffer. We then measured the fluorescence of LD01 and LD02 in solvents with water and dioxane mixed at different ratios, representing different degrees of solvent polarity. As shown in **Figures 2E–H**, in the mixed solvent system, both LD01 and LD02's fluorescent emission shows a similar tendency in response to polarity change from different solvents, which suggests both LD01 and LD02 can be potentially used to detect α-glucosidase *via* responsive emission. In the meantime, the pH effect on the emission of LD01 and LD02 was investigated. The emission spectra of LD01 and LD02 are less sensitive to pH variation (**Figure 3**) from 3.0 to 8.0 than the polarity changes; the pKa values of LD01 and LD02 were worked out to be 4.2 and 4.6 for LD01 and LD02, respectively.

Fluorescence Titration of LD01 and LD02 Toward α-Glucosidase

To confirm the α-glucosidase-targeted binding interaction, fluorescence titrations were carried out by determining the emission spectra of LD01 and LD02 as a function of the concentration of α-glucosidase. As shown in **Figure 4A**, there are no obvious emission changes observed for LD01 after the gradual addition of α-glucosidase protein up to 3.5 μM. However, a significant enhancement of responsive fluorescence emission can be achieved for LD02 under the

same experimental condition (**Figures 4B, C**). After the addition of 3.5 μM α-glucosidase, the maximum emission intensity increased by 2.7 times, and the emission maximum of LD02 was detected of a ~7 nm blue shift from 457 to 450 nm, which suggests that the dimethylamine group in LD02 may locate in the binding pocket of relative lower polarity inside α-glucosidase than the aqueous surroundings. The binding constant and the rate of LD02 to α-glucosidase were obtained by the double logarithm regression curve as shown in **Figure 4D**. The value of log K_a of LD02 to α-glucosidase was calculated to be 3.8, and the binding ratio was approximately 0.5.

Binding Selectivity of LD02 Toward α-Glucosidase

To verify the binding specificity of LD02 toward α-glucosidase, emission spectra of LD02 in the presence of α-glucosidase or various potential competitors such as other enzymes (including glucose oxidase (GOD), polyphenol oxidase (TKY), and pepsin (PEP)), and small molecules of interest (including Cys, GSH, Lys, Ca^{2+}, Cu^{2+}, Fe^{3+}, Mg^{2+}, and Zn^{2+}), were collected in 10 mM PBS buffer (pH = 7.4) at room temperature. As shown in **Figure 5**, all potential competitors tested have no obvious effect on the emission band and intensity of LD02 compared with α-glucosidase, suggesting the highly specific selectivity of LD02 toward α-glucosidase.

Competitive Fluorescence Titration

For competitive fluorescence titration, different amounts of LD01 were added to a solution of α-glucosidase/LD02 complex. After the addition of LD01, it was found that the emission of α-glucosidase/LD02 complex decreased as a function of increasing the concentration of LD01, indicating LD01's competitive binding to the same binding pocket as LD02 (**Figure 6**). The binding constant (K_a) of LD01 to α-glucosidase was calculated, and the value of lgK_a was 5.2 for LD01, which means LD01 has a much stronger affinity for α-glucosidase than LD02 does. This result encouraged us to determine the inhibition efficiency of LD01 and LD02 against α-glucosidase.

α-Glucosidase Inhibitory Effect of LD01 and LD02

α-Glucosidase inhibitory efficiency of LD01 and LD02 was obtained from the inhibition rate vs. concentration curves of LD01 and LD02 (**Figure 7**). The results showed that coumarin derivatives LD01 and LD02 demonstrated excellent and potent inhibitory activity against α-glucosidase with the IC$_{50}$ values of 4.6 ± 0.5 and 32.5 ± 0.8 μM, respectively, as compared to the standard acarbose (IC$_{50}$ = 856.45 ± 5.60 μM). In particular, LD01 and LD02 have a relatively stronger inhibition effect against α-glucosidase than the coumarin derivatives that Xu et al. reported previously (Xu et al., 2019). In particular, the IC$_{50}$ values of LD01 and LD02 have a positive correlation with the binding affinities observed from the fluorescence titration experiments, which

indicates that our fluorescent probe LD02 can be used as an applicable tool helpful in the development and screening of pharmacologically active α-glucosidase inhibitors based on the candidate molecules' binding strength.

CONCLUSION

In summary, two environmentally sensitive fluorescence agents, LD01 and LD02, based on the conjugates of substituted coumarin and cinnamic acid, were designed and synthesized. Both LD01 and LD02's fluorescent emissions show a polarity-dependent enhancement feature, as demonstrated in various solvents of different polarities, and the solvent mixture of dioxane and water. When coming to fluorescence titration, LD02 shows responsive emission changes featured with 2.7 times emission enhancement upon its binding to α-glucosidase. However, LD01 does not have such changes under the same experimental conditions as LD02 does. The competitive fluorescence titration of LD01 to the α-glucosidase/LD02 complex shows a gradually reduced emission as a function of increasing concentration of LD01, which suggests that LD01 can competitively bind to the same pocket of α-glucosidase targeted by LD02. The binding constants of LD01 and LD02 toward α-glucosidase were worked out by the fluorescence titration experiments, from which the values of lg K_a were found to be 5.2 and 3.8 for LD01 and LD02, respectively, and positively correlated with IC_{50} values (4.6 ± 0.5 and $32.5 \pm 0.8\,\mu M$ for LD01 and LD02, respectively) as observed from the enzyme inhibitory assays. This research not only lays out a new strategy for quantitative detection of α-glucosidase but also offered a potential tool for binding affinity evaluation between α-glucosidase and its inhibitors, which may provide guidance for developing new α-glucosidase inhibitors treating diabetes.

DATA AVAILABILITY STATEMENT

The original contributions presented in the study are included in the article/**Supplementary Material**; further inquiries can be directed to the corresponding authors.

AUTHOR CONTRIBUTIONS

DL: Synthesis, photophysical properties' measurement, writing—original draft, and data curation. XZ: Synthesis and analysis. XL: Investigation and analysis. Y-YZ and XZ: Enzyme inhibition test. YZ: Supervision and writing—revise and editing. ZX: Supervision, methodology, and writing—review and editing. HL: Conceptualization, formal analysis, data curation, writing—review and editing, supervision, project administration, and funding acquisition.

FUNDING

SUPPLEMENTARY MATERIAL

The Supplementary Material for this article can be found online at: https://www.frontiersin.org/articles/10.3389/fchem.2022.927624/full#supplementary-material

REFERENCES

Adisakwattana, S. (2017). Cinnamic Acid and its Derivatives: Mechanisms for Prevention and Management of Diabetes and Its Complications. *Nutrients* 9, 163. doi:10.3390/nu9020163

Annunziata, F., Pinna, C., Dallavalle, S., Tamborini, L., and Pinto, A. (2020). An Overview of Coumarin as a Versatile and Readily Accessible Scaffold with Broad-Ranging Biological Activities. *Ijms* 21, 4618. doi:10.3390/ijms21134618

Ao, H., Feng, H., Huang, X., Zhao, M., and Qian, Z. (2017). A Reversible Fluorescence Nanoswitch Based on Dynamic Covalent B-O Bonds Using Functional Carbon Quantum Dots and its Application for α-Glucosidase Activity Monitoring. *J. Mat. Chem. C* 5, 2826–2832. doi:10.1039/C7TC00223H

Calcio Gaudino, E., Tagliapietra, S., Martina, K., Palmisano, G., and Cravotto, G. (2016). Recent Advances and Perspectives in the Synthesis of Bioactive Coumarins. *RSC Adv.* 6, 46394–46405. doi:10.1039/C6RA07071J

Chen, H., Zhang, J., Wu, H., Koh, K., and Yin, Y. (2015). Sensitive Colorimetric Assays for α-Glucosidase Activity and Inhibitor Screening Based on Unmodified Gold Nanoparticles. *Anal. Chim. Acta* 875, 92–98. doi:10.1016/j.aca.2015.02.022

Cheng, X., Huang, Y., Yuan, C., Dai, K., Jiang, H., and Ma, J. (2019). Colorimetric Detection of α-Glucosidase Activity Based on the Etching of Gold Nanorods and Its Application to Screen Anti-Diabetic Drugs. *Sensors Actuators B Chem.* 282, 838–843. doi:10.1016/j.snb.2018.11.097

Cheng, Y., and Prusoff, W. H. (1973). Relationship Between the Inhibition Constant (K1) and the Concentration of Inhibitor Which Causes 50 Per Cent Inhibition (I50) of an Enzymatic Reaction. *Biochem. Pharmacol.* 22, 3099–3108. doi:10.1016/0006-2952(73)90196-2

Dai, Y., Zhan, Z., Li, Q., Liu, R., and Lv, Y. (2020). Simultaneous Monitoring of Polarity Changes of Lipid Droplets and Lysosomes with Two-Photon Fluorescent Probes. *Anal. Chim. Acta* 1136, 34–41. doi:10.1016/j.aca.2020.08.033

Dhameja, M., and Gupta, P. (2019). Synthetic Heterocyclic Candidates as Promising α-Glucosidase Inhibitors: An Overview. *Eur. J. Med. Chem.* 176, 343–377. doi:10.1016/j.ejmech.2019.04.025

Dong, G., He, S., Qin, X., Liu, T., Jiang, Y., Li, X., et al. (2020). Discovery of Nonpeptide, Environmentally Sensitive Fluorescent Probes for Imaging P53-MDM2 Interactions in Living Cell Lines and Tissue Slice. *Anal. Chem.* 92, 2642–2648. doi:10.1021/acs.analchem.9b04551

Finikova, O., Galkin, A., Rozhkov, V., Cordero, M., Hägerhäll, C., and Vinogradov, S. (2003). Porphyrin and Tetrabenzoporphyrin Dendrimers: Tunable Membrane-Impermeable Fluorescent pH Nanosensors. *J. Am. Chem. Soc.* 125, 4882–4893. doi:10.1021/ja0341687

Guo, F.-N., Wang, Y.-T., Wu, N., Feng, L.-X., Zhang, H.-C., Yang, T., et al. (2021). Carbon Nitride Nanoparticles as Ultrasensitive Fluorescent Probes for the Detection of α-Glucosidase Activity and Inhibitor Screening. *Analyst* 146, 1016–1022. doi:10.1039/D0AN02079F

Gutiérrez-González, J. A., Pérez-Vásquez, A., Torres-Colín, R., Rangel-Grimaldo, M., Rebollar-Ramos, D., and Mata, R. (2021). α-Glucosidase Inhibitors from Ageratina Grandifolia. *J. Nat. Prod.* 84, 1573–1578. doi:10.1021/acs.jnatprod.1c00105

Kong, W., Wu, D., Xia, L., Chen, X., Li, G., Qiu, N., et al. (2017). Carbon Dots for Fluorescent Detection of α-Glucosidase Activity Using Enzyme Activated Inner Filter Effect and its Application to Anti-Diabetic Drug Discovery. *Anal. Chim. Acta* 973, 91–99. doi:10.1016/j.aca.2017.03.050

Li, J., He, G., Wang, B., Shi, L., Gao, T., and Li, G. (2018). Fabrication of Reusable Electrochemical Biosensor and Its Application for the Assay of α-Glucosidase Activity. *Anal. Chim. Acta* 1026, 140–146. doi:10.1016/j.aca.2018.04.015

Liu, Z., and Ma, S. (2017). Recent Advances in Synthetic α-Glucosidase Inhibitors. *ChemMedChem* 12, 819–829. doi:10.1002/cmdc.201700216

Pal, K., Kumar, P., and Koner, A. L. (2020). Deciphering Interior Polarity of Lysosome in Live Cancer and Normal Cells Using Spectral Scanning Microscopy. *J. Photochem. Photobiol. B Biol.* 206, 111848. doi:10.1016/j.jphotobiol.2020.111848

Prattichizzo, F., La Sala, L., Rydén, L., Marx, N., Ferrini, M., Valensi, P., et al. (2019). Glucose-Lowering Therapies in Patients with Type 2 Diabetes and Cardiovascular Diseases. *Eur. J. Prev. Cardiol.* 26, 73–80. doi:10.1177/2047487319880040

Ruwizhi, N., and Aderibigbe, B. A. (2020). Cinnamic Acid Derivatives and Their Biological Efficacy. *Ijms* 21, 5712. doi:10.3390/ijms21165712

Shvadchak, V. V., Kucherak, O., Afitska, K., Dziuba, D., and Yushchenko, D. A. (2017). Environmentally Sensitive Probes for Monitoring Protein-Membrane Interactions at Nanomolar Concentrations. *Biochimica Biophysica Acta (BBA) - Biomembr.* 1859, 852–859. doi:10.1016/j.bbamem.2017.01.021

Tang, C., Qian, Z., Qian, Y., Huang, Y., Zhao, M., Ao, H., et al. (2017). A Fluorometric and Real-Time Assay for α-Glucosidase Activity Through Supramolecular Self-Assembly and its Application for Inhibitor Screening. *Sensors Actuators B Chem.* 245, 282–289. doi:10.1016/j.snb.2017.01.150

Teng, H., and Chen, L. (2017). α-Glucosidase and α-Amylase Inhibitors from Seed Oil: A Review of Liposoluble Substance to Treat Diabetes. *Crit. Rev. Food Sci. Nutr.* 57, 3438–3448. doi:10.1080/10408398.2015.1129309

Trang, N. T. H., Tang, D. Y. Y., Chew, K. W., Linh, N. T., Hoang, L. T., Cuong, N. T., et al. (2021). Discovery of α-Glucosidase Inhibitors from Marine Microorganisms: Optimization of Culture Conditions and Medium Composition. *Mol. Biotechnol.* 63, 1004–1015. doi:10.1007/s12033-021-00362-3

Wei, X. L., Xiao, J. B., Wang, Y., and Bai, Y. (2010). Which Model Based on Fluorescence Quenching Is Suitable to Study the Interaction Between Trans-Resveratrol and BSA? *Spectrochimica Acta Part A Mol. Biomol. Spectrosc.* 75, 299–304. doi:10.1016/j.saa.2009.10.027

Xu, X.-T., Deng, X.-Y., Chen, J., Liang, Q.-M., Zhang, K., Li, D.-L., et al. (2020). Synthesis and Biological Evaluation of Coumarin Derivatives as α-Glucosidase Inhibitors. *Eur. J. Med. Chem.* 189, 112013. doi:10.1016/j.ejmech.2019.112013

Zhang, J., Liu, Y., Lv, J., and Li, G. (2015). A Colorimetric Method for α-Glucosidase Activity Assay and its Inhibitor Screening Based on Aggregation of Gold Nanoparticles Induced by Specific Recognition Between Phenylenediboronic Acid and 4-Aminophenyl-α-D-Glucopyranoside. *Nano Res.* 8, 920–930. doi:10.1007/s12274-014-0573-1

Zhou, X., Dong, G., Song, T., Wang, G., Li, Z., Qin, X., et al. (2020). Environment-Sensitive Fluorescent Inhibitors of Histone Deacetylase. *Bioorg. Med. Chem. Lett.* 30, 127128. doi:10.1016/j.bmcl.2020.127128

Design, Synthesis, and Biological Evaluation of N-Acyl-Homoserine Lactone Analogs of Quorum Sensing in *Pseudomonas aeruginosa*

Zhenyu Wei[1], Ting Li[1], Yan Gu[2], Qian Zhang[1], Enhui Wang[1], Wenbo Li[1], Xin Wang[2], Yang Li[2]* and Hongyu Li[1,2]

[1]International Scientific and Technological Cooperation Base of Biopharmaceutical, School of Life Sciences, Institute of Microbiology, Lanzhou University, Lanzhou, China, [2]Gansu High Throughput Screening and Creation Center for Health Products, School of Pharmacy, Lanzhou University, Lanzhou, China

Quorum sensing plays a necessary role in the production of virulence factors and the formation of biofilm on *Pseudomonas aeruginosa*. Thus, the development of inhibition of quorum sensing is one of the most promising methods to control bacterial infection and antibiotic resistance. In this work, nine novel AHL analogs were designed, synthesized, and evaluated as potential quorum sensing inhibitors. The results depicted that structural modifications have significant effects on quorum sensing inhibition activity of AHL molecules. Without inhibiting the growth of *P. aeruginosa*, 2-(4-bromophenyl)-N-(2-oxotetrapyridinefuran-3-yl) butanamide (compound no.10) showed the excellent performance in inhibiting biofilm formation and virulence factor production among all the compounds through robustly suppressing the expression of QS related genes. In a molecular docking study, compound no.10 exhibited a higher affinity toward LasR than other AHL analogs. In addition, compound no.10 also exhibits the best inhibition effect on virulence production in the *Caenorhabditis elegans* infection model.

Keywords: AHL analogs, quorum sensing, *Pseudomonas aeruginosa*, anti-virulence, antibiofilm

1 INTRODUCTION

Pseudomonas aeruginosa as an important nosocomial pathogen could threaten those who are long-term intubated and immunocompromised, and patients suffering from cystic fibrosis, traumatized cornea, burns, Gustilo open fractures, and lead to lethal infections (Hogardt and Heesemann, 2013; Moradali et al., 2017). A previous study reported that biofilm formation and virulence factor production are the major causes of *P. aeruginosa* infections (Schuster and Greenberg, 2006). At present, antibiotics such as tobramycin, meropenem, or ciprofloxacin, are considered the first choice in treating infections of *P. aeruginosa*. However, the wild use of antibiotics to treat infections of *P. aeruginosa* has led to the generation of multidrug-resistant pathogens (Abbas et al., 2017). Thus, combating *P. aeruginosa* infections need a new target.

Quorum sensing (QS) is a bacteria-to-bacteria communication system. Also, QS is moderated by the production of different kinds of signal molecules known as autoinducers, which are usually N-acyl-homoserine lactones (AHLs) in Gram-negative bacteria (Ng and Bassler, 2009). In *P. aeruginosa*, the QS system is composed of four interconnected systems (Las, Rhl, PQS, and IQS), among them, the LasI/LasR system is the most representative and primary (Hançer
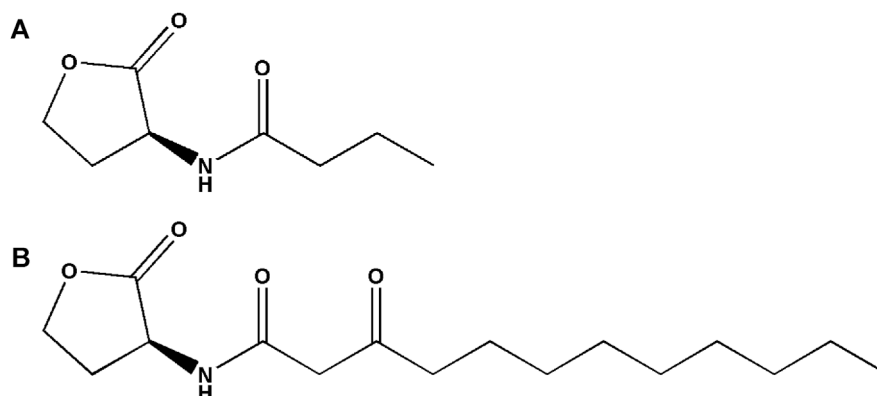
FIGURE 1 | Chemical structure of P. aeruginosa PAO1 natural signal molecule. **(A)** Structure of BHL and **(B)** structure of OdDHL.

Aydemir et al., 2018). In addition, each system utilizes a particular signal molecule such as N-(3-oxododecanoyl)-L-homoserine lactone (OdDHL), N-butanoyl-L-homoserine lactone (BHL), 2-heptyl-3-hydroxy-4-quinolone, and 2-(2-hydroxyphenyl)-thiazole-4-carbaldehyde (Hao et al., 2021). Typically, the accumulation of signal molecules interacts with a transcriptional activator protein (Abbas et al., 2017), and then the expression of QS-regulated genes were activated (Schuster and Greenberg, 2006).

It is reported that pathogenicity of *P. aeruginosa* is generally related to virulence production and biofilm formation (Bassler and Losick, 2006; Hançer Aydemir et al., 2018). As QS inhibitors (QSIs) had no influence on bacterial growth, they are believed to generate weaker selection for antibiotic resistance than conventional antibiotics. Thus, QSIs can be a novel and promising way to attenuate *P. aeruginosa* infection (Hançer Aydemir et al., 2018). Nowadays, numerous QS signal molecule analogs and plant-derived natural substances have been reported as QSIs to interfere with the QS system of *P. aeruginosa* (Qu et al., 2016; Abbas et al., 2020; Hao et al., 2021; Saqr et al., 2021). Unfortunately, its dose-dependent toxicity and a weak effect significantly limit clinical applications. Therefore, development of novel safe and effective QSIs is urgently needed for the treatment of *P. aeruginosa* infections.

In this study, nine novel AHL analogs were designed, synthesized, and evaluated as potential QSIs against *P. aeruginosa*. The effects of AHL analogs on biofilm formation and virulence factor production *in vitro* were evaluated. Furthermore, the mechanism was studied by related gene expression and molecular docking.

2 MATERIALS AND METHODS

2.1 Strains and Media
Pseudomonas aeruginosa PAO1 and *Escherichia coli* OP50 were stored in our laboratory. *Caenorhabditis elegans* N2 were obtained from the Caenorhabditis Genetics Center (CGC). *P. aeruginosa* PAO1 was cultured using Luria–Bertani broth (LB) at 37 °C and maintained on a nutrient agar plate (Solarbio,

Beijing, China) at 4 °C. *C. elegans* was cultured using the nematode growth medium (NGM) at 20 °C and *E. coli* OP50 was used as the standard food source. 4-Br-PHL (compound no.1) and other AHL analogs (compound no.2 to compound no.10) were dissolved in DMSO before treatment (Solarbio, Beijing, China).

2.2 Synthesis of Acyl-Homoserine Lactone (AHL) Analogs
Based on the structures of OdDHL and BHL (**Figure 1**), we synthesized a series of novel AHL-based QSIs, in which the natural homoserine lactone ring is present but the natural acyl group was substituted. The structures of analogs were modified from three aspects: 1) the acyl group, 2) the length of the acyl side chain, and 3) the type and position of the substituents on the benzene ring. The synthesis method is shown in **Figure 2**. Those AHL analogs used in this study were synthesized by us and characterized by NMR, and MS with a purity of ≥95% (**Supplementary Table S1**). To circumvent the issues of different assessment results, we also synthesized N-(4-bromophenylacetanoyl)-L-homoserine lactone (4-Br-PHL, no. 1) as a positive control (Geske et al., 2005).

2.3 Initial Screening of Analogs
To initial screen compounds with QS-inhibited activity, QS-regulated biofilm formation was tested as the screening indicator. As described previously (Luo et al., 2017), biofilm mass was measured using a crystal violet assay.

2.4 Planktonic Cell Growth
The planktonic cell growth assay was slightly modified (Qu et al., 2016). Overnight cultures of *P. aeruginosa* PAO1 were diluted in LB broth. The suspension was supplemented with two compounds (no.3 and no.10) with concentrations ranging from 10 to 400 μM and incubated at 37 °C. Then, 1 ml samples were obtained every 2 h, and the turbidity was recorded at 600 nm using a spectrophotometer (Thermo scientific, Finland), then a growth curve was generated.
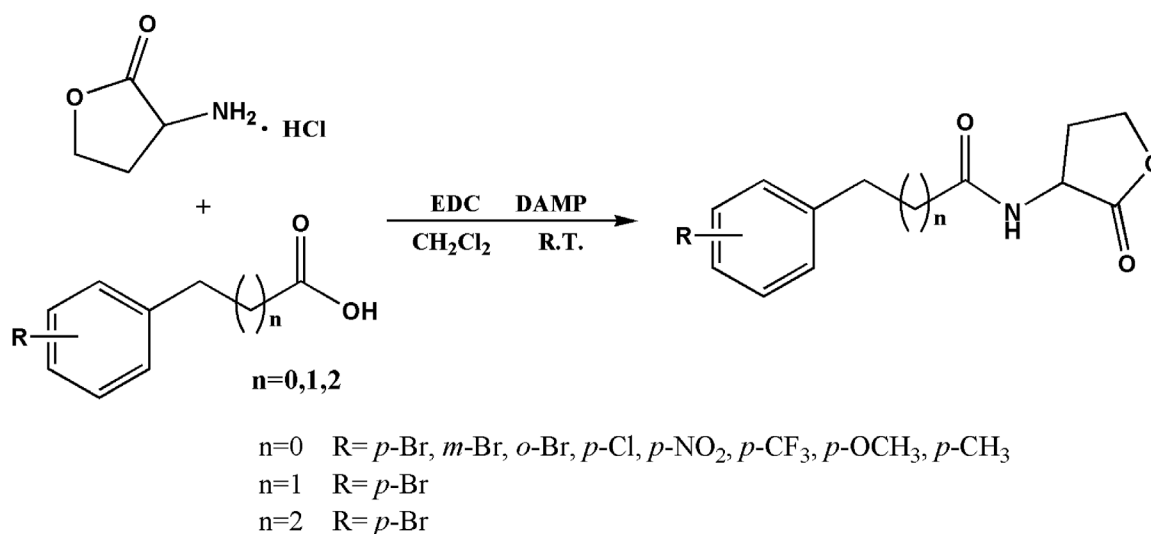
FIGURE 2 | Synthesis of AHL analogs. RT = room temperature.

2.5 Biofilm Inhibition Analyses

In this assay, the inhibitory effects of compound no.3 and compound no.10 on biofilm formation were further identified at different concentrations ranging from 50 to 400 μM. The method of this assay is similar to the method of initial screening of analogs. In addition, cover slides were incubated statically with or without 200 μM compound no.3 and compound no.10 at 37 ℃ to facilitate cell attachment and biofilm formation. Also, compound no.1 was conducted as a positive control. Finally, the structures of biofilm were observed using an upright microscope (BX53, Olympus, Japan) at ×20 magnification.

2.6 Motility Assay

2.6.1 Swimming

The swimming assay method was modified from Rashid and Kornberg (2000). Swimming agar plates (10 g/L peptone, 5 g/L NaCl, and 0.3% agarose) with compound no.3 and no.10 (200 μM) and blank control plates were center stabbed with *P. aeruginosa* PAO1 using sterile toothpick. Also, compound no.1 was conducted as a positive control. After incubating at 30 ℃ for 12–14 h, swimming zones were determined by measuring the diameter of circular expansion.

2.6.2 Swarming

The swarming plate was composed of nutrient agar (8 g/L) and glucose (5.0 g/L). Then, swarming plates with and without supplementation of 200 μM compound no.3 and no.10 were added 5 μl overnight culture of *P. aeruginosa* PAO1. In addition, compound no.1 was conducted as a positive control. Then, the swarming plates were placed at 30 ℃ and incubated for 18–24 h (Kumar et al., 2013), and swarming zones were determined by measuring the diameter of circular expansion.

2.6.3 Twitching

Twitching motility of *P. aeruginosa* PAO1 was modified from Saqr et al. (2021). A measure of 1% of LB agar with or without compounds (compound no.3 and compound no.10, 200 μM) stabbed with a toothpick up to bottom of the Petri dish from overnight culture *P. aeruginosa* PAO1 in order to evaluate twitching motility inhibition. Compound no.1 was conducted as a positive control, the agar was removed after incubation at 37 ℃ for 48 h, and then the plates were dried in air and stained with crystal violet. The dye was washed off with sterile water and the twitching zones were measured.

2.7 Pyocyanin Analyses

The assay of the inhibitory effect of compound no.3 and compound no.10 on pyocyanin production was conducted using previous methods (O'Loughlin et al., 2013). Overnight, *P. aeruginosa* PAO1 cultures were subcultured into LB broth with the compound no.3 and compound no.10 at the concentration of 200 μM for endpoint assays following 24 h of aerobic growth with shaking at 37 ℃. Also, compound no.1 was conducted as a positive control. Finally, the production of pyocyanin was measured by recording the absorbance of this pink layer at 520 nm.

2.8 Elastase Analysis

The skim milk agar method (Hao et al., 2021) was used to determine the effect of compound no.3 and compound no.10 on elastase activity. Also, compound no.1 was conducted as a positive control. After overnight culturing, *P. aeruginosa* PAO1 with or without compound no.3 and compound no.10 were incubated at 37 ℃ for 24 h at 180 rpm. After 24 h, the cultures were centrifuged at 10,000 rpm for 15 min. A measure of 100 μl of supernatant was added to the wells of skim milk agar

and then plates were incubated for 24 h at 37 °C. The elastase activity was determined by measuring the diameter of clear zone.

2.9 *C. elegans* Life Span Assays

To further investigate the anti-virulence effect of compound no.3 and compound no.10, we used a *C. elegans* life span assay. Also, compound no.1 was conducted as a positive control. This assay was modified from a previous study (Cezairliyan et al., 2013; O'Loughlin et al., 2013). After synchronization, *C. elegans* was grown to the L4 stage at 20 °C. In addition, an equivalent volume of compound no.1, compound no.3, and compound no.10 were mixed to the *P. aeruginosa* PAO1 cultures during growth and DMSO was added as a blank control. Then, an overnight culture of *P. aeruginosa* PAO1 was poured on Petri plates, containing PGS agar (1% peptone, 1% NaCl, 1% glucose, 150 mM sorbitol, and 1.7% agar) and kept for 24 h incubation at 37 °C. After 8–24 h, 25–30 L4 stage *C. elegans* were seeded with each plate. Then, live or dead worms were scored every 3 h at 25 °C and again at 24 h.
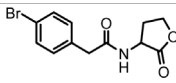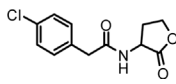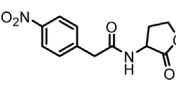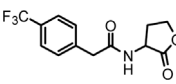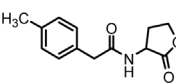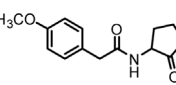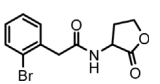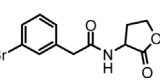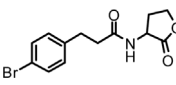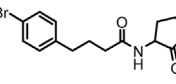
2.10 Gene Expression Analysis

According to the previous study (Qu et al., 2016), the expression of key QS regulatory genes (*lasI*, *lasR*, *rhlI*, *rhlR*, and *mvfR*) of *P. aeruginosa* PAO1 was monitored in the presence of compound no.3 and compound no.10. Also, compound no.1 was conducted as a positive control. The primers for the genes are shown in **Supplementary Table S2**. The 16S rRNA housekeeping gene was served as an internal control. Total RNA was isolated with an Ultrapure RNA kit (CWBIO, Beijing, China), and the first-strand cDNA was synthesized with a Hifair® III 1st Strand cDNA Synthesis SuperMix for qPCR (Yeasen, Beijing, China) according to the manufacturer's instructions. The reaction was carried out with Hieff UNICON® Universal Blue qPCR SYBR Green Master Mix (Yeasen, Beijing, China) also according to the manufacturer. The relative gene expression was calculated using the $2^{-\Delta\Delta Ct}$ method.

2.11 Molecular Docking Study

Molecular docking was conducted to analyze the interaction of compound no.3 and compound no.10 with the LasR receptor of *P. aeruginosa* PAO1. The crystal structure of *P. aeruginosa* PAO1 LasR was obtained from the Protein Data Bank (PDB ID:2UV0) (Bottomley et al., 2007). Hydrogen atoms were added according to the hydrogen network optimization and then minimized with an Amber19SB force field with UCSF Chimera. Finally, the protein structure was converted to a pdbqt file by prepare_receptor4.py script using AutoDockTools, and all the hydrogen atoms were kept. The ligands structures were built with UCSF Chimera, minimized with the GAFF force field, and converted to a pdbqt format by using the prepare_ligand4.py script with all hydrogen atoms. The docking site was determined by the *P. aeruginosa* PAO1 binding pocket. Finally, the molecular docking was performed by watvina (https://www.github.com/biocheming/watvina), which was optimized with new scorning function, with van der Waals, hydrogen bond, polar repulsion, and weak hydrogen bonds contribution. Conformation searching was performed by a simplified genetic algorithm and simulated annealing mixed with BFGS local optimization. Finally, the docking pose was optimized while the protein was kept fixed.

TABLE 1 | Inhibitory rate of AHL analogs.

Compound	Structure	Concentration (μM)	Inhibitory rate
No.1		100	6.22 ± 2.77%
No.2		100	17.04 ± 2.56%
No.3		100	36.78 ± 0.18%
No.4		100	10.54 ± 3.51%
No.5		100	5.11 ± 1.65%
No.6		100	−20.09 ± 0.29%
No.7		100	7.78 ± 1.46%
No.8		100	5.47 ± 1.67%
No.9		100	17.46 ± 1.25%
No.10		100	37.46 ± 2.31%

2.12 Statistical Analysis

All experiments were conducted in triplicate to validate the reproducibility. All values are presented as the mean ± standard error. One-way ANOVA was performed using SPSS 23.0 software. The significance was accepted when the *p*-value was less than 0.05. Graphs were constructed using GraphPad Prism 7.0 software.

3 RESULTS

3.1 AHL and Its Analogs

A series of novel AHL-based QS inhibitors are presented in **Table 1**. All compounds were characterized by NMR, MS with a purity of ≥95% (**Supplementary Table S1**).

3.2 Preliminary Screening of Analogs

The biofilm formation inhibition activity of compounds 1–10 was assessed. As shown in **Table 1**, all compounds showed inhibitory activity against biofilm formation of *P. aeruginosa* PAO1, except for compound no.6. Among all analogs, compound no.3 and

FIGURE 3 | Inhibitory effect of compound no.3 and compound no.10 on **(A)** pyocyanin and **(B)** elastase productions of P. aeruginosa PAO1.

compound no.10 exhibited the best inhibition activity and were identified as the potential QS-inhibitor to further evaluate in the following experiments.

3.3 Planktonic Cell Growth

The growth curves were drawn to identify the influence on the growth of *P. aeruginosa* PAO1. As shown in **Figure 3**, compound no.3 and compound no.10 had no inhibition effect on growth of *P. aeruginosa* PAO1 at the concentrations ranging from 10 to 400 μM.

3.4 Biofilm Inhibition Analyses

As shown in **Figures 4A–C**, inhibitory activities of compound no.3 and compound no.10 on biofilm formation were dose-dependent. Compound no.1 had slightly reduced biofilm formation at the concentration of 200 μM. By contrast, compound no.3 and compound no.10 had more obvious inhibitory effect on biofilm formation at the concentrations ranging from 200 to 400 μM. In the presence of compound no.3, the biofilm formation of *P. aeruginosa* PAO1 was decreased to nearly 35% at the concentration ranging from 50 to 400 μM. Remarkedly, compound no.10 inhibited more than 60% of biofilm formation at above 200 μM.

The aforementioned results were further revealed under a microscope. From **Figure 4D**, reduction of biofilm attached to the surface of plates was observed in treated groups. Compared with compound no.1, the reduction of biofilms was more obvious in compound no.3 and compound no.10 treated groups.

3.5 Motility Assay

As shown in **Figure 5**, in the absence of compounds, the swimming, swarming, and twitching zones for *P. aeruginosa* PAO1 are 2.53 ± 0.08 cm, 1.88 ± 0.20 cm, and 5.62 ± 0.16 cm, respectively. Compound no.1 exerted a weak inhibitory effect that the swimming, swarming, and twitching zones are 1.5 ± 0.05 cm, 1.58 ± 0.13 cm, and 4.32 ± 0.28 cm. In the presence of compound no.3, it resulted in a significant decrease in motility zones to 0.87 ± 0.07 cm, 1.35 ± 0.13 cm, and 2.38 ± 0.16 cm. Moreover, compound no.10 also reduce the motility zones to 0.98 ± 0.10 cm, 1.40 ± 0.05 cm, and 3.43 ± 0.16 cm, respectively.

3.6 Pyocyanin Analyses

Pyocyanin is a green exotoxin generated by *P. aeruginosa* governed by the QS system. The effect of compounds on pyocyanin production was studied using the chloroform extraction assay. As shown in **Figure 6A**, compound no.1 and compound no.3 exhibited a weak inhibitory effect. By contrast, compound no.10 robustly lowered pyocyanin production by 65.29%.

3.7 Elastase Analysis

The effect of compounds on elastase activity was assessed with the skim milk agar method. As shown in **Figure 6B**, all the compounds can effectively inhibit the activity of elastase compared with the control group. Compared with compound no.1, significant reduction in the diameter of the clear zone was produced in compound no.3 and no.10 treated groups on a skim milk plate.

3.8 Effect on the *C. elegans* Life Span

As shown in **Figure 7**, at 0–6 h, compound no.3 and compound no.10 exhibited an excellent effect on the survival rate compared with compound no.1. Then, the effect of compound no.10 was more obvious in improving the survival rate of infected *C. elegans* than no.3 at the 6–24 h. Compared with the untreated group, the survival rate of *C. elegans* of the compound no.10 group reaches nearly 80% within 6 h of incubation and can still be reached to 52% within 24 h.

3.9 Effect on Expression of QS-Regulated Genes

To further determine the inhibition mechanism of compounds on *P. aeruginosa* PAO1 virulence and biofilm formation, the expression level of key QS-related genes was assessed using qPCR. From **Figure 8**, it shows that compound no.3 and no.10 downregulated the expression of *lasI*, *lasR*, *rhlI*, *rhlR*, and *mvfR*. Compared with the untreated group, compound no.1 slightly inhibited the expression of *lasI*, *rhlI*, and *rhlR*. The relative expression of QS regulatory gene treatment with compound no.3 decreased by 87% for *lasI*, 59% for *lasR*, 66% for *rhlI*, 80% for *rhlR*, and 17% for *mvfR*,
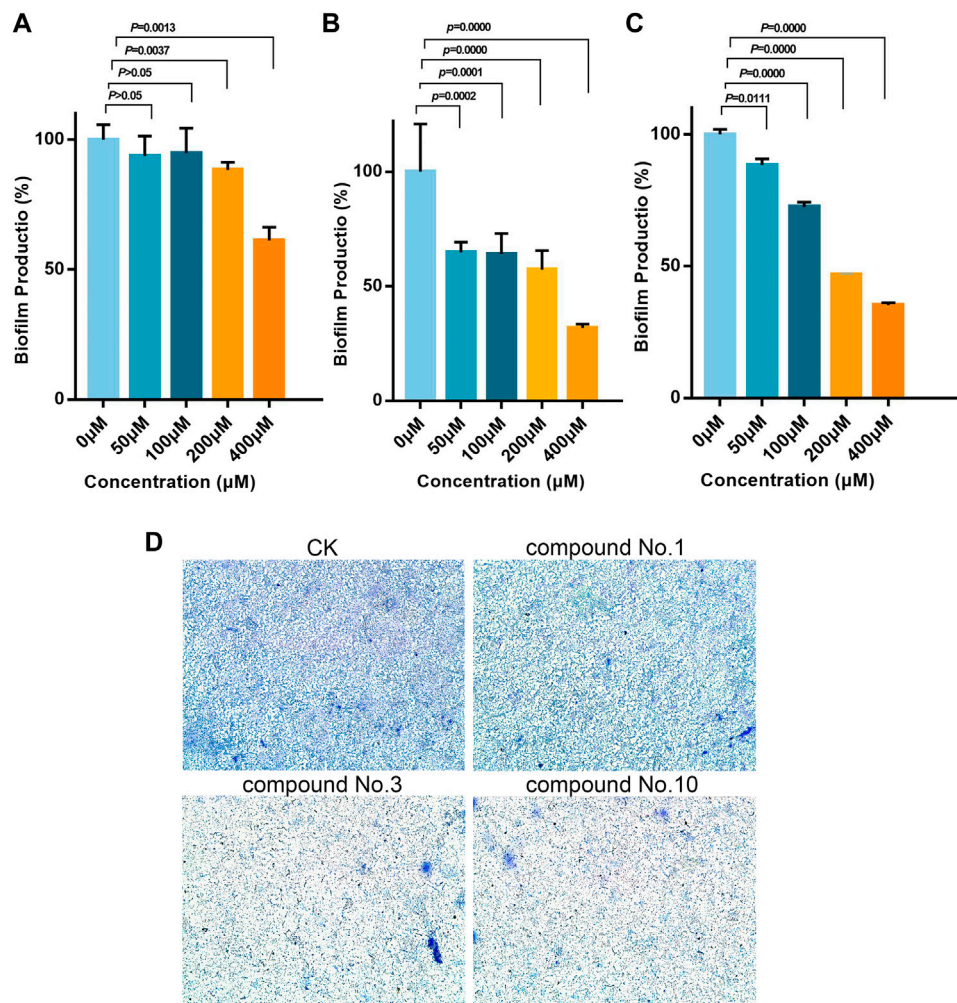
FIGURE 4 | Inhibitory effect of compound no.3 and compound no.10 on *P. aeruginosa* biofilm formation. Biofilm was stained by crystal violet and measured as absorbance at 570 nm. **(A)** Compound no.1, **(B)** compound no.3, **(C)** and compound no.10. **(D)** Representative microscope images of treated with compounds at 200 µM.

respectively, and compound no.10 decreased 82% for *lasI*, 77% for *lasR*, 57% for *rhlI*, 91% for *rhlR*, and 61% for *mvfR*, respectively.

3.10 Molecular Docking

To further explore the binding mode of compounds to the LasR, molecular docking analysis of compounds no.1, no.3, and no.10 was performed. As shown in **Figure 9**, the interaction between compound no.1 and LasR by formation of H-bonding with Try 56, Trp 60, and Asp 73. It may be the reason that compound no.1 had weaker effects on biofilm formation, motility, and virulence production of *P. aeruginosa* PAO1. By contrast, the interaction between compounds (no.3 and no.10) and LasR receptor by formation of H-bonding with the Try 56, Trp 60, Asp 73, and Ser 129, is consistent with the binding sites of OdDHL (Abbas et al., 2017). The Lavina scores indicated a higher affinity of compound no.10 to bind with LasR than compound no.3

resulting in a more considerable inhibition activity of biofilm formation and virulence production.

4 DISCUSSION

It is known that the pathogenicity of *P. aeruginosa* is contributed to the virulence factor production and the biofilm formation, which could lead to lethal infection and antibiotics defense (Costerton, 2001; Clatworthy et al., 2007; Zhao and Liu, 2010). Research evidence indicated that QS of *P. aeruginosa* was closely related to these phenomena (Lee and Zhang, 2015; Hegazy et al., 2021). Indeed, the structures of natural autoinducers have often served as an intermediate for the synthesis of the QS inhibitor (Galloway et al., 2011; O'Loughlin et al., 2013). In this study, we designed and synthesized nine novel AHL analogs and evaluated their inhibition activities and revealed their mechanism in the QS system of *P. aeruginosa*.
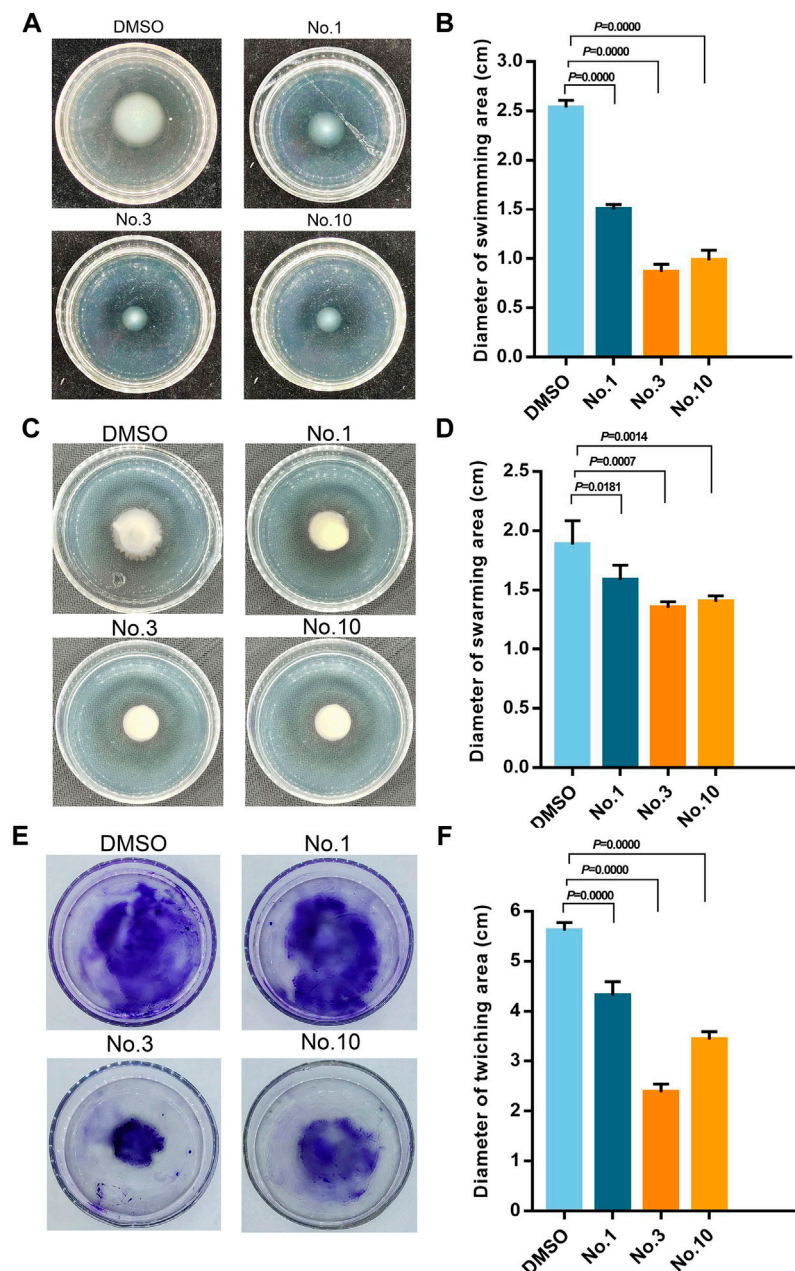
FIGURE 5 | Inhibitory effect of compound no.3 and compound no.10 on *P. aeruginosa* motility. **(A)** and **(B)** represent swimming motility of *P. aeruginosa* PAO1, **(C)** and **(D)** represent swarming motility of *P. aeruginosa* PAO1, **(E)** and **(F)** represent twitching motility of *P. aeruginosa* PAO1. DMSO and compound no.1 represent negative and positive control, respectively.

As described previously, subtle alterations to substituents and their placement on the AHL acyl group dramatically influenced analog inhibitory activity (Hodgkinson et al., 2012). Also then, the inhibitory activity of AHL analogs is highly dependent on the structure and position of substituents in the benzene group (Geske et al., 2008; Abbas et al., 2017). In this study, the chemical modification of AHL analogs is initiated by the replacement of the hydrocarbon chain length and by replacing substituents on the benzene ring, then nine novel AHL analogs were designed and synthesized.

In the initial screening assay, by using the QS-regulated production of biofilm as the screening indicator, compound no.3 and compound no.10 were selected to conduct further investigation. Consistent with the biofilm inhibition results, compound no.3 and compound no.10 also significantly inhibited the swimming, swarming, and twitching ability compared with compound no.1 at the concentration of 200 μM. In a previous study, the biofilm
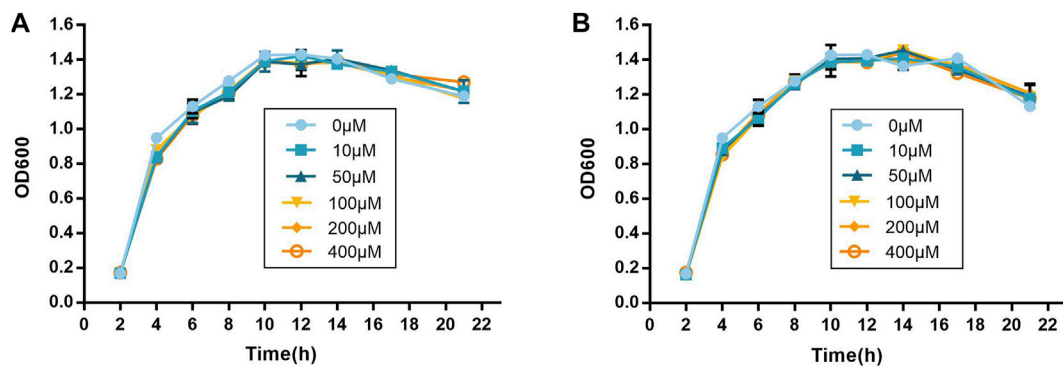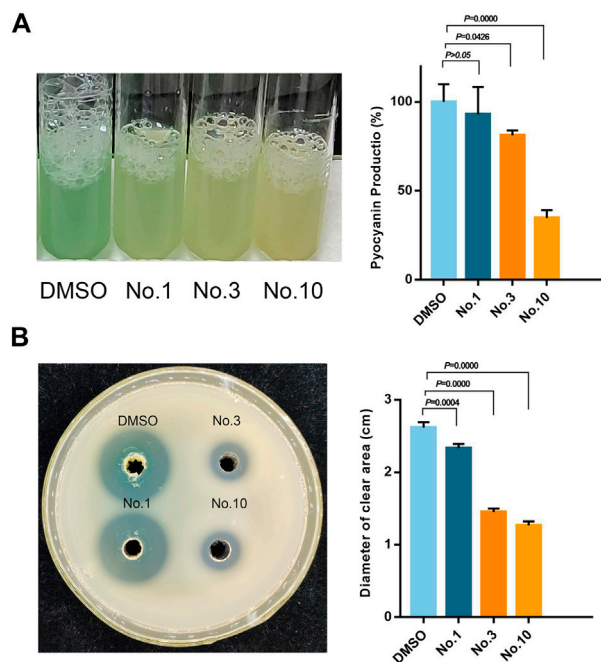
FIGURE 6 | Inhibitory effect of compound no.3 and compound no.10 on **(A)** pyocyanin and **(B)** elastase productions of *P. aeruginosa* PAO1.

formation and adhesion to tissue related to the motility of bacteria were confirmed (Landry et al., 2006). Furthermore, it is reported that thin and dispersed biofilm was formed by QS deficient *P. aeruginosa* (Lee et al., 2018; Mayer et al., 2020). Therefore, we supposed that the inhibition in motility is one of the reasons for biofilm formation inhibition by compound no.3 and compound no.10.

P. aeruginosa is armed by an armory rich in virulence factors that are regulated by QS and pyocyanin and elastase are

representative virulence of *P. aeruginosa* (Chatterjee et al., 2016). After being treated with compound no.3 and compound no.10, the production of pyocyanin was reduced by nearly 19 and 66%, respectively. The activity of elastase was also inhibited by 44 and 52%. Compound no.10 had a more obvious effect on inhibiting the virulence production of PAO1 *in vitro*. To further illustrate the inhibitory effect of those compound no.1, compound no.3, and compound no.10 on virulence production, *C. elegans* life span assays were conducted (Utari and Quax, 2013). Compared with compound no.3, compound no.10 had a more continuous and significant effect on improving the survival rate of infected *C. elegans*.

Moreover, compound no.10 exhibited more inhibition activity on pyocyanin production compared with other AHL analogs with a non-native tail region and native head group reported by previous studies (Morkunas et al., 2012). Chlorolactone (CL) was synthesized by Swem et al. (2009), and it exhibited 50% QS inhibition activity against *C. violaceum* at a concentration of 295 nM. However, O'Loughlin et al. (2013) proved that it had a weak QS inhibition effect in *P. aeruginosa* (Swem et al., 2009; O'Loughlin et al., 2013). Compared with 1,3-benzoxazol-2(3 H)-one derivatives, compound no.10 was able to achieve the similar QS-inhibition activity at lower concentrations (Miandji et al., 2012).

Based on aforementioned results, we supposed that the phenotype of QS system inhibition was attributed to the interaction between compounds and LasR. Molecular docking results have shown that compound no.1 interacted with LasR by formation of hydrogen bonds with three sites: Try 56, Trp 60, and
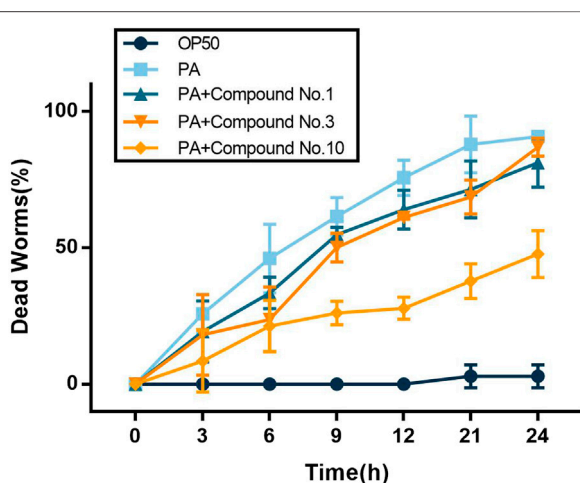
FIGURE 7 | Compound no.3 and compound no.10 decreased toxicity of *P. aeruginosa* PAO1 in the *C. elegans* model.
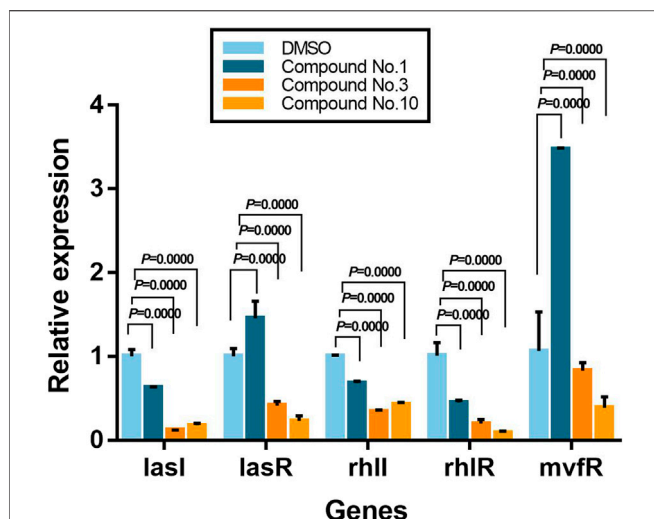
FIGURE 8 | Relative expression levels of QS-regulated genes in the presence of compound no.1, compound no.3, and compound no.10 as determined by real-time quantitative PCR.

provided as follows: 1) AHL analog aromatic functionality with electron-withdrawing groups had stronger QS inhibition activity. 2) AHL analogs with electron-withdrawing and lipophilic substituents in the 4th position on the phenyl group displayed the stronger antagonistic activities than other analogs. 3) AHL analogs with an elastic spacer flexible carbon spacer of at least one carbon between the homoserine lactone ring and the benzene ring showed optimal inhibition activity.

In addition, our work proved that the substitutes of natural acyl group can be used as the strategy for synthesizing QS inhibitor. Moreover, our compounds had no stress on neither bacterial nor normal mammalian cell growth (**Supplementary Figure S1**); it is safe and can avoid the development of drug resistance.

In conclusion, 2-(4-bromophenyl)-N-(2-oxotetrapyridinefuran-3-yl) butanamide (compound no.10) could be considered as the most promising anti-QS compound against *P. aeruginosa*. Nevertheless, further experiments are conducted to evaluate the effect of compound no.10 on

Asp 73. While both the compound no.3 and compound no.10 interacted with receptors at four sites: Try 56, Trp 60, Asp 73, and Ser 129, consistent with the binding site of the natural ligand (Abbas et al., 2017). A previous study has shown that the absence of the hydrogen bonds donated by Ser 129 in the LasR ligand-binding pocket may result in the reduction of QS inhibition activity of ligands (Manson et al., 2020). It was proved that Ser 129 of LasR may be an essential site for QS inhibitor binding to LasR. Moreover, the Lavina scores of compound no.3 and no.10 are −9 and −7, respectively, which indicated a high affinity of compound no.10 to bind with LasR, and it could contribute to its anti-QS activity.

In a previous study, biofilm formation related to the LasI/R system and RhlI/R system was confirmed, which is responsible for biofilm differentiation and optimal biofilm formation, respectively (Favre-Bonté et al., 2003). While virulence factors, such as pyocyanin and elastase, also were controlled by PQS and RhlI/R system (Oliveira et al., 2016; McCready et al., 2019). To further explore the compounds' mechanism, the relative expressions of QS-regulated (*lasI*, *lasR*, *rhlI*, *rhlR*, and *mvfR*) genes were selected to be tested (Kim et al., 2015). It has shown that compound no.3 and compound no.10 effectively downregulate *lasI*, *lasR*, rhlI, *rhlR*, and *mvfR*, while compound no.1 slightly inhibited the expression of *lasI*, *rhlI*, and *rhlR*. These results illustrated the possible causes that compound no.3 and compound no.10 had more significant bioactivity of anti-biofilm and anti-virulence at the gene level. In addition, compound no.10 has shown the more significant effect on downregulating the expression of QS-regulated genes than compound no.3, especially reduction in the expression of *mvfR*, which is the most important regulator of virulence production (Cao et al., 2001).

Based on aforementioned results, the structure–activity relationship trends influencing inhibitory activity are

FIGURE 9 | Molecular docking of **(A)** compound no.1, **(B)** compound no.3, and **(C)** compound no.10 into the active site of LasR. Both compound no.3 and compound no.10 interacted with LasR by formation of H-bonding with the Try 56, Trp 60, Asp 73, and Ser 129. Compound no.1 interacted with LasR with Try 56, Trp 60, and Asp 73 by H-bonding.

clinical drug-resistant strains and assess the therapeutic effect of compound no.10 on the infected animal model. In addition, further experiments are conducted to explore the QS inhibition mechanism of compound no.10.

DATA AVAILABILITY STATEMENT

The original contributions presented in the study are included in the article/**Supplementary Material**; further inquiries can be directed to the corresponding author.

AUTHOR CONTRIBUTIONS

Conceptualization, ZW and YL; methodology, TL, YG, EW, and WL; formal analysis, QZ; funding acquisition, HL; grammar correction, XW. All authors have read and agreed to the published version of the manuscript.

FUNDING

ACKNOWLEDGMENTS

SUPPLEMENTARY MATERIAL

The Supplementary Material for this article can be found online at: https://www.frontiersin.org/articles/10.3389/fchem.2022.948687/full#supplementary-material

REFERENCES

Abbas, H. A., Elsherbini, A. M., and Shaldam, M. A. (2017). Repurposing Metformin as a Quorum Sensing Inhibitor in *Pseudomonas A*. *Afr. Health Sci.* 17 (3), 808–819. doi:10.4314/ahs.v17i3.24

Abbas, H. A., Shaldam, M. A., and Eldamasi, D. (2020). Curtailing Quorum Sensing in *Pseudomonas A* by Sitagliptin. *Curr. Microbiol.* 77 (6), 1051–1060. doi:10.1007/s00284-020-01909-4

Bassler, B. L., and Losick, R. (2006). Bacterially Speaking. *Cell* 125 (2), 237–246. doi:10.1016/j.cell.2006.04.001

Bottomley, M. J., Muraglia, E., Bazzo, R., and Carfì, A. (2007). Molecular Insights into Quorum Sensing in the Human Pathogen *Pseudomonas A* from the Structure of the Virulence Regulator LasR Bound to its Autoinducer. *J. Biol. Chem.* 282 (18), 13592–13600. doi:10.1074/jbc.M700556200

Cao, H., Krishnan, G., Goumnerov, B., Tsongalis, J., Tompkins, R., and Rahme, L. G. (2001). A Quorum Sensing-Associated Virulence Gene of *Pseudomonas A* Encodes a LysR-Like Transcription Regulator with a Unique Self-Regulatory Mechanism. *Proc. Natl. Acad. Sci. U. S. A.* 98 (25), 14613–14618. doi:10.1073/pnas.251465298

Cezairliyan, B., Vinayavekhin, N., Grenfell-Lee, D., Yuen, G. J., Saghatelian, A., and Ausubel, F. M. (2013). Identification of *Pseudomonas Aeruginosa* Phenazines that Kill *Caenorhabditis Elegans*. *PLoS Pathog.* 9 (1), e1003101. doi:10.1371/journal.ppat.1003101

Chatterjee, M., Anju, C. P., Biswas, L., Anil Kumar, V., Gopi Mohan, C., and Biswas, R. (2016). Antibiotic Resistance in *Pseudomonas A* and Alternative Therapeutic Options. *Int. J. Med. Microbiol.* 306 (1), 48–58. doi:10.1016/j.ijmm.2015.11.004

Clatworthy, A. E., Pierson, E., and Hung, D. T. (2007). Targeting Virulence: A New Paradigm for Antimicrobial Therapy. *Nat. Chem. Biol.* 3 (9), 541–548. doi:10.1038/nchembio.2007.24

Costerton, J. W. (2001). Cystic Fibrosis Pathogenesis and the Role of Biofilms in Persistent Infection. *Trends Microbiol.* 9 (2), 50–52. doi:10.1016/s0966-842x(00)01918-1

Favre-Bonte, S., Köhler, T., and Van Delden, C. (2003). Biofilm Formation by *Pseudomonas A*: Role of the C4-HSL Cell-To-Cell Signal and Inhibition by Azithromycin. *J. Antimicrob. Chemother.* 52 (4), 598–604. doi:10.1093/jac/dkg397

Galloway, W. R. J. D., Hodgkinson, J. T., Bowden, S. D., Welch, M., and Spring, D. R. (2011). Quorum Sensing in Gram-Negative Bacteria: Small-Molecule Modulation of AHL and AI-2 Quorum Sensing Pathways. *Chem. Rev.* 111 (1), 28–67. doi:10.1021/cr100109t

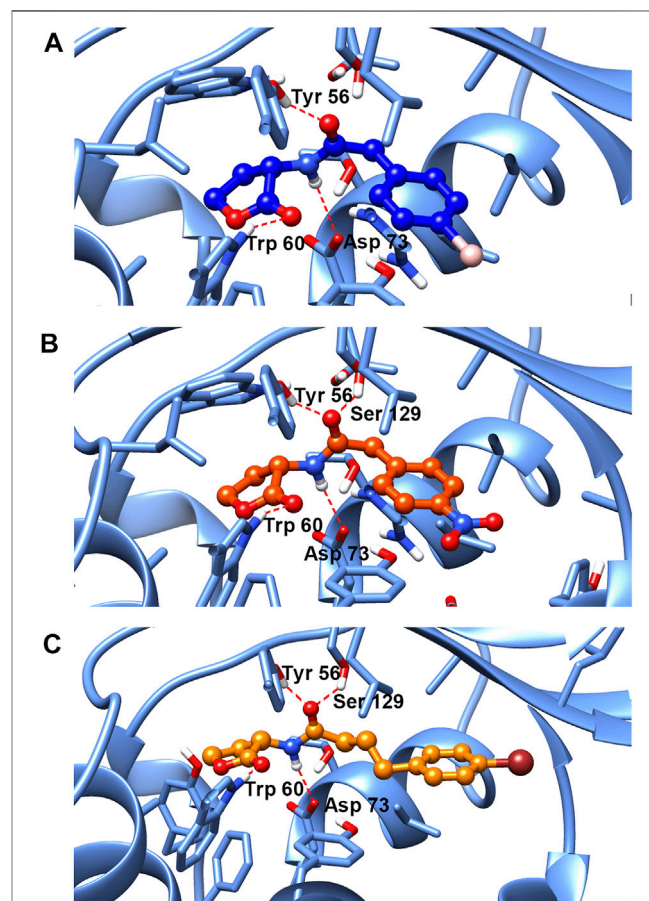Geske, G. D., O'Neill, J. C., Miller, D. M., Wezeman, R. J., Mattmann, M. E., Lin, Q., et al. (2008). Comparative Analyses of N-Acylated Homoserine Lactones Reveal Unique Structural Features that Dictate Their Ability to Activate or Inhibit Quorum Sensing. *Chembiochem* 9 (3), 389–400. doi:10.1002/cbic.200700551

Geske, G. D., Wezeman, R. J., Siegel, A. P., and Blackwell, H. E. (2005). Small Molecule Inhibitors of Bacterial Quorum Sensing and Biofilm Formation. *J. Am. Chem. Soc.* 127 (37), 12762–12763. doi:10.1021/ja0530321

Hançer Aydemir, D., Çifci, G., Aviyente, V., and Boşgelmez-Tinaz, G. (2018). Quorum-sensing Inhibitor Potential of Trans-Anethole Aganist *Pseudomonas A*. *J. Appl. Microbiol.* 125 (3), 731–739. doi:10.1111/jam.13892

Hao, S., Yang, D., Zhao, L., Shi, F., Ye, G., Fu, H., et al. (2021). EGCG-Mediated Potential Inhibition of Biofilm Development and Quorum Sensing in *Pseudomonas A*. *Int. J. Mol. Sci.* 22 (9), 4946. doi:10.3390/ijms22094946

Hegazy, W. A. H., Khayat, M. T., Ibrahim, T. S., Youns, M., Mosbah, R., and Soliman, W. E. (2021). Repurposing of Antidiabetics as *Serratia M* Virulence Inhibitors. *Braz J. Microbiol.* 52 (2), 627–638. doi:10.1007/s42770-021-00465-8

Hodgkinson, J. T., Galloway, W. R. J. D., Wright, M., Mati, I. K., Nicholson, R. L., Welch, M., et al. (2012). Design, Synthesis and Biological Evaluation of Non-Natural Modulators of Quorum Sensing in *Pseudomonas A*. *Org. Biomol. Chem.* 10 (30), 6032–6044. doi:10.1039/c2ob25198a

Hogardt, M., and Heesemann, J. (2013). Microevolution of *Pseudomonas A* to a Chronic Pathogen of the Cystic Fibrosis Lung. *Curr. Top. Microbiol. Immunol.* 358, 91–118. doi:10.1007/82_2011_199

Kim, H.-S., Lee, S.-H., Byun, Y., and Park, H.-D. (2015). 6-Gingerol Reduces *Pseudomonas A* Biofilm Formation and Virulence via Quorum Sensing Inhibition. *Sci. Rep.* 5, 8656. doi:10.1038/srep08656

Kumar, L., Chhibber, S., and Harjai, K. (2013). Zingerone Inhibit Biofilm Formation and Improve Antibiofilm Efficacy of Ciprofloxacin against *Pseudomonas A* PAO1. *Fitoterapia* 90, 73–78. doi:10.1016/j.fitote.2013.06.017

Landry, R. M., An, D., Hupp, J. T., Singh, P. K., and Parsek, M. R. (2006). Mucin-Pseudomonas aeruginosa Interactions Promote Biofilm Formation and Antibiotic Resistance. *Mol. Microbiol.* 59 (1), 142–151. doi:10.1111/j.1365-2958.2005.04941.x

Lee, D. J., Jo, A. R., Jang, M. C., Nam, J., Choi, H. J., Choi, G.-W., et al. (2018). Analysis of Two Quorum Sensing-Deficient Isolates of *Pseudomonas A*. *Microb. Pathog.* 119, 162–169. doi:10.1016/j.micpath.2018.04.014

Lee, J., and Zhang, L. (2015). The Hierarchy Quorum Sensing Network in *Pseudomonas A*. *Protein Cell* 6 (1), 26–41. doi:10.1007/s13238-014-0100-x

Luo, J., Dong, B., Wang, K., Cai, S., Liu, T., Cheng, X., et al. (2017). Baicalin Inhibits Biofilm Formation, Attenuates the Quorum Sensing-Controlled Virulence and Enhances *Pseudomonas A* Clearance in a Mouse Peritoneal Implant Infection Model. *PLoS One* 12 (4), e0176883. doi:10.1371/journal.pone.0176883

Manson, D. E., O'Reilly, M. C., Nyffeler, K. E., and Blackwell, H. E. (2020). Design, Synthesis, and Biochemical Characterization of Non-Native Antagonists of the

Pseudomonas A Quorum Sensing Receptor LasR with Nanomolar IC(50) Values. *ACS Infect. Dis.* 6 (4), 649–661. doi:10.1021/acsinfecdis.9b00518

Mayer, C., Muras, A., Parga, A., Romero, M., Rumbo-Feal, S., Poza, M., et al. (2020). Quorum Sensing as a Target for Controlling Surface Associated Motility and Biofilm Formation in Acinetobacter Baumannii ATCC(®) 17978(TM). *Front. Microbiol.* 11, 565548. doi:10.3389/fmicb.2020.565548

McCready, A. R., Paczkowski, J. E., Cong, J.-P., and Bassler, B. L. (2019). An Autoinducer-Independent RhlR Quorum-Sensing Receptor Enables Analysis of RhlR Regulation. *PLoS Pathog.* 15 (6), e1007820. doi:10.1371/journal.ppat.1007820

Miandji, A., Ulusoy, S., Dündar, Y., Özgen, S., Onurdağ, F., Boşgelmez-Tınaz, G., et al. (2012). Synthesis and Biological Activities of Some 1,3-Benzoxazol-2(3H)-One Derivatives as Anti-Quorum Sensing Agents. *Arzneimittelforschung* 62 (7), 330–334. doi:10.1055/s-0032-1312590

Moradali, M. F., Ghods, S., and Rehm, B. H. A. (2017). *Pseudomonas A* Lifestyle: A Paradigm for Adaptation, Survival, and Persistence. *Front. Cell. Infect. Microbiol.* 7, 39. doi:10.3389/fcimb.2017.00039

Morkunas, B., Galloway, W. R. J. D., Wright, M., Ibbeson, B. M., Hodgkinson, J. T., O'Connell, K. M. G., et al. (2012). Inhibition of the Production of the *Pseudomonas A* Virulence Factor Pyocyanin in Wild-Type Cells by Quorum Sensing Autoinducer-Mimics. *Org. Biomol. Chem.* 10 (42), 8452–8464. doi:10.1039/c2ob26501j

Ng, W.-L., and Bassler, B. L. (2009). Bacterial Quorum-Sensing Network Architectures. *Annu. Rev. Genet.* 43, 197–222. doi:10.1146/annurev-genet-102108-134304

Oliveira, B. D. Á., Rodrigues, A. C., Cardoso, B. M. I., Ramos, A. L. C. C., Bertoldi, M. C., Taylor, J. G., et al. (2016). Antioxidant, Antimicrobial and Anti-Quorum Sensing Activities of Rubus Rosaefolius Phenolic Extract. *Industrial Crops Prod.* 84, 59–66. doi:10.1016/j.indcrop.2016.01.037

O'Loughlin, C. T., Miller, L. C., Siryaporn, A., Drescher, K., Semmelhack, M. F., and Bassler, B. L. (2013). A Quorum-Sensing Inhibitor Blocks *Pseudomonas A* Virulence and Biofilm Formation. *Proc. Natl. Acad. Sci. U. S. A.* 110 (44), 17981–17986. doi:10.1073/pnas.1316981110

Qu, L., She, P., Wang, Y., Liu, F., Zhang, D., Chen, L., et al. (2016). Effects of Norspermidine on *Pseudomonas A* Biofilm Formation and Eradication. *Microbiologyopen* 5 (3), 402–412. doi:10.1002/mbo3.338

Rashid, M. H., and Kornberg, A. (2000). Inorganic Polyphosphate is Needed for Swimming, Swarming, and Twitching Motilities of *Pseudomonas A. Proc. Natl. Acad. Sci. U. S. A.* 97 (9), 4885–4890. doi:10.1073/pnas.060030097

Saqr, A. A., Aldawsari, M. F., Khafagy, E.-S., Shaldam, M. A., Hegazy, W. A. H., and Abbas, H. A. (2021). A Novel Use of Allopurinol as A Quorum-Sensing Inhibitor in *Pseudomonas A. Antibiotics* 10 (11), 1385. doi:10.3390/antibiotics10111385

Schuster, M., and Greenberg, E. P. (2006). A Network of Networks: Quorum-Sensing Gene Regulation in *Pseudomonas A. Int. J. Med. Microbiol.* 296 (2-3), 73–81. doi:10.1016/j.ijmm.2006.01.036

Swem, L. R., Swem, D. L., O'Loughlin, C. T., Gatmaitan, R., Zhao, B., Ulrich, S. M., et al. (2009). A Quorum-Sensing Antagonist Targets Both Membrane-Bound and Cytoplasmic Receptors and Controls Bacterial Pathogenicity. *Mol. Cell* 35 (2), 143–153. doi:10.1016/j.molcel.2009.05.029

Utari, P. D., and Quax, W. J. (2013). *Caenorhabditis E* Reveals Novel *Pseudomonas A* Virulence Mechanism. *Trends Microbiol.* 21 (7), 315–316. doi:10.1016/j.tim.2013.04.006

Zhao, T., and Liu, Y. (2010). N-Acetylcysteine Inhibit Biofilms Produced by *Pseudomonas A. BMC Microbiol.* 10, 140. doi:10.1186/1471-2180-10-140

Chemical Constituents With Antiproliferative Activity From *Pogostemon cablin* (Blanco) Benth.

Xingjia Peng[1†], Song Ang[1,2,3†], Yizi Zhang[1], Fenling Fan[1], Mengshuo Wu[1,2], Peiting Liang[1], Yan Wen[1,2], Lishe Gan[1,2], Kun Zhang[1,3]*, Dongli Li[1,2]* and Jianmin Yue[1,4]

[1]School of Biotechnology and Health Sciences, Wuyi University, Jiangmen, China, [2]International Healthcare Innovation Institute (Jiangmen), Jiangmen, China, [3]School of Chemical Engineering and Light Industry, Guangdong University of Technology, Guangzhou, China, [4]Key Laboratory of Drug Research, Shanghai Institute of Materia Medica, Chinese Academy of Sciences, Shanghai, China

Two new patchoulene sesquiterpenoid glycosides (**1–2**), a natural patchoulane-type sesquiterpenoid (**3**) and a natural cadinene-type sesquiterpenoid (**4**), were isolated from the aerial parts of *Pogostemon cablin* (Blanco) Benth., together with eleven known sesquiterpenoids (**5–15**) and eleven known flavonoids (**16–26**). Their chemical structures were elucidated on the basis of spectroscopic methods, including NMR, HRESIMS, IR, and CD spectroscopic data analysis, as well as chemical hydrolysis. The isolated compounds **1–13** and **15–26** were tested for inhibitory effects on the proliferation of HepG2 cancer cells. Among them, compounds **17** and **19** displayed anti-proliferative effects against HepG2 cells with IC_{50} values of 25.59 and 2.30 μM, respectively. Furthermore, the flow cytometry analysis and Western blotting assays revealed that compound **19** significantly induced apoptosis of HepG2 cells by downregulating the ratio of Bcl-2/Bax and upregulating the expression of cleaved caspase-3 and cleaved caspase-9. Therefore, the potential pharmaceutical applications of *P. cablin* would be applied according to our study findings.

Keywords: *Pogostemon cablin*, sesquiterpenoid, flavonoid, antiproliferative activity, apoptosis

INTRODUCTION

Pogostemon cablin (Blanco) Benth. is an annual herb known as patchouli, a form of traditional Chinese medicine for the treatment of upset stomach, vomiting, diarrhea, headache, and fever. The plant, a member of the genus *Pogostemon*, Lamiaceae family, was native to South and Southeast Asia, such as Indonesia, Malaysia, Philippines, and India, and was introduced to China in the 9th century as a spice. It was fostered in Guangdong, Guangxi, Fujian, and Taiwan provinces in China (Feng et al., 1994). In recent years, a large number of phytochemical studies on *P. cablin* had been carried out to concentrate on the constituents of this plant, which showed the presence of various monoterpenes and sesquiterpenoids (Hikino et al., 1968; Terhune et al., 1973), triterpenoids (Huang et al., 2009), steroids (Kongkathip et al., 2009), flavonoids (Ding et al., 2009), alkaloids (Büchi et al., 1966), and glycosides (Wang et al., 2010). The reported constituents from *P. cablin* possessed marked activities such as antibacterial activity, anti-influenza virus, anti-inflammation, cytotoxicity, antimutagenic activity, antiplatelet aggregation, and insecticidal activity (Li et al., 2013). In our continuous phytochemical studies on the constituents of this medicinal herb, two new patchoulene sesquiterpenoid glycosides (**1–2**), a natural patchoulane-type sesquiterpenoid (**3**) and a

natural cadinene-type sesquiterpenoid (**4**), as well as eleven known sesquiterpenoids (**5–15**) and eleven known flavonoids (**16–26**), were isolated and characterized. In addition, the antiproliferative activities of the isolated compounds (**1–13** and **15–26**) against HepG2 cancer cells were assessed in this article. Furthermore, the apoptosis-inducing effects of compound **19** in HepG2 cells were also investigated in the current study. To the best of our knowledge, the apoptosis-induced activity of compound **19** is reported for the first time.

EXPERIMENT

General Experimental Procedures

Column chromatographies (CC) were carried out with silica gel (200–300 mesh, Qingdao Marine Chemical Factory), silica gel for chromatography C_{18} SMB 100–20/45 (Fuji Silysia Chemical Ltd), and Sephadex LH-20 (Pharmacia Biotech AB). TLC was performed using precoated silica gel GF_{254} plates (Yantai Chemical Industry Research Institute). MPLC (medium pressure liquid chromatography) was carried out on a Buchi Pure C-815 apparatus. High-performance liquid chromatography (HPLC) was carried out on a Waters 1500-Series system. The semi-preparative C_{18} column used was the SunFire® C_{18} OBD (250 × 10 mm) apparatus. UPLC was carried out on a Waters Acquity UPLC-Class instrument. IR data were obtained with a KBr pellet on a Thermo Scientific Fourier Transform NICOLET iS5 Infrared Spectrometer (Waltham, USA). High-resolution electrospray ion mass (HRESIMS) was performed on a Thermo Scientific Q-Exactive mass spectrometer (Waltham, USA). 1D and 2D NMR data were recorded on a Bruker AVANCE NEO 500 spectrometer (Bremen, Germany) with chloroform-*d* and methanol-*d4* as solvents. Chemical shift values were expressed in δ (ppm) relative to tetramethylsilane (TMS) as the internal standard. An Anton Paar MCP 200 automatic polarimeter (Graz, Austria) was used to determine optical rotations in ACN at 25°C. CD spectra were obtained on a Chirascan spectrometer (England, United Kingdom) at room temperature using a 0.2-cm standard cell. All solvents used in column chromatography and HPLC were of analytical grade (Guangzhou Chemical Reagents Company Ltd., Guangzhou, China) and chromatographic grade (Thermo Fisher), respectively.

Plant Material

The aerial parts of *P. cablin* were collected in September 2019, GuangXi Province, China. The plant material was identified by Professor Xiaoji Zheng, and a voucher specimen (201909PC) was deposited at Wuyi University, Jiangmen, China.

Extraction and Isolation

The air-dried aerial parts of *P. cablin* (13.0 kg) were powdered and extracted with 95% ethanol (3 × 30 L) at room temperature for 6 days. The extract was evaporated under reduced pressure (45°C) to afford a brown residue (2.0 kg), which was suspended in water (5 L) and extracted sequentially with petroleum ether, EtOAc (ethyl acetate), and *n*-BuOH at room temperature. The EtOAc fraction (178 g) was subjected to a silica gel (200–300 mesh) column using a gradient petroleum ether (PE)-EtOAc system (100:1, 50:1, 30:1, 10:1, 5:1, 1:1, and 0:1, each 15 L) as eluents to afford 19 fractions (Fr. 1–Fr. 19). Fr. 4 (2.8 g) was subjected to Sephadex LH-20 and yielded two subfractions, namely, (Fr. 4.1- Fr. 4.2) and Fr. 4.2 (1.2 g), which were further purified by using a reversed phase (C_{18} SMB 100–20/45, 30 g, H_2O-MeOH: 40:1 to 0:100) column to obtain compound **10** (432 mg). Fr. 7 (4.5 g) was submitted to a silica gel (200–300 mesh) column using PE and EtOAc as eluents (50:1 to 0:1) to afford five subfractions (Fr. 7.1–Fr. 7.5); Fr. 7.4 (950 mg) was submitted to Sephadex LH-20 and eluted with the $CHCl_2$–CH_3OH (1:1) system to obtain compound **12** (7 mg), Fr. 7.3 (530 mg) was submitted to Sephadex LH-20 and eluted with the $CHCl_2$–CH_3OH (1:1) system to afford compounds **18** (77 mg) and **24** (44 mg). Fr. 8 (5.5 g) was subjected to Sephadex LH-20 and eluted with the $CHCl_2$–CH_3OH (1:1) system to afford two subfractions (Fr. 8.1 and Fr. 8.2), and Fr. 8.2 (1.6 g) was further purified by using a silica gel (200–300 mesh) column using PE and EtOAc as eluents (100:1 to 0:1) to obtain compound **23** (373 mg). Fr. 9 (15.5 g) was subjected to a reversed phase (C_{18} SMB 100–20/45, 30 g, H_2O-MeOH: 30:1 to 0:100) column, and four subfractions (Fr. 9.1–Fr. 9.4) were yielded, and Fr. 9.1 (200 mg) was further purified by semi-preparative HPLC (0–60 min: isocratic 80% CH_3CN in water) to yield compounds **4** (25 mg) and **5** (15 mg); Fr. 9.2 (330 mg) was purified by semi-preparative HPLC (0–60 min: isocratic 80% CH_3CN in water) to obtain **6** (27 mg) and **9** (20 mg); Fr. 9.4 (500 mg) was subjected to semi-preparative HPLC (0–60 min: isocratic 80% CH_3CN in water) to afford compounds **16** (4 mg), **20** (14 mg), and **25** (48 mg). Fr. 10 (4.1 g) was submitted to a silica gel (200–300 mesh) column using PE and EtOAc as eluents (30:1 to 0:1) to obtain Fr. 10.1–Fr. 10.3, and then, Fr. 10.3 (2.0 g) was further purified by Sephadex LH-20 to obtain compound **19** (75 mg). Fr. 12 (5.4 g) was subjected to Sephadex LH-20 to afford two subfractions (Fr. 12.1 and Fr. 12.2). Fr. 12.1 (1.3 g) was further purified using a reversed phase (C_{18} SMB 100–20/45, 30 g, H_2O-MeOH: 30:1 to 0:100) column to obtain compounds **3** (20 mg) and **22** (5 mg). Fr. 12.2 (150 mg) was subjected to semi-preparative HPLC (0–60 min: isocratic 60% CH_3CN in water) to afford compounds **7** (1 mg), **13** (1 mg), **14** (1 mg), and **17** (41 mg). Fr. 13 (1.3 g) was submitted to a silica gel (200–300 mesh) column using PE and EtOAc as eluents (50:1 to 0:1) to yield two subfractions (Fr. 13.1 and Fr. 13.2), and Fr. 13.1 (300 mg) was subjected to Sephadex LH-20 and a reversed phase (C_{18} SMB 100–20/45, 30 g, H_2O-MeOH: 30:1 to 0:100) column to obtain compounds **11** (5 mg), **21** (8 mg), **8** (26 mg), and **26** (12 mg). Fr. 15 (6.3 g) was submitted to a silica gel (200–300 mesh) column using PE and EtOAc as eluents (30:1 to 0:1) and further purified by using a reversed phase (C_{18} SMB 100–20/45, 30 g, H_2O-MeOH: 40:1 to 0: 100) column to obtain compound **15** (5 mg). Fr. 19 (11.5 g) was subjected to a silica gel column (200–300 mesh, 5 × 40 cm, 120 g) using a gradient CH_2Cl_2-MeOH system (10:1, 5:1, 1:1, 0:1) to obtain two subfractions (Fr. 19.1 and Fr. 19.2). Fr. 19.1 (2.0 g) was submitted to a reversed phase (C_{18} SMB 100–20/45, 30 g, H_2O-MeOH: 50:1 to 0:100) column and semi-preparative HPLC (0–60 min: isocratic 40% CH_3CN in water) to yield compounds **1** (6 mg) and **2** (6 mg).

Compound Characterization

Compound **1**: an amorphous white powder; $[\alpha]^{25}$ D = −35.5 (*c* 0.1, MeOH); IR (KBr) ν_{max} 3,449, 1,638, 1,075, and 536 cm^{-1};

TABLE 1 | ^{1}H NMR data of compounds **1** and **2** in CD$_3$OD and of compounds **3** and **4** in CDCl$_3$ (500 MHz).

Position	1	2	3	4
1	—	—	—	—
2	5.02, m	2.25, m	1.77, dd (14.0, 5.7)	2.20, m
	—	—	1.51, m	1.38, d (2.6)
3	2.44, ddt (16.5, 7.9, 2.2)	1.99, m	1.59, dd (12.6, 5.7)	2.24, m
	2.33, dq (16.5, 2.4)	1.72, m	1.40, td (12.6, 5.8)	1.64, m
4	2.58, m	2.71, m	2.17, m	2.54, m
5	2.94, m	—	1.20, m	—
6	1.73, d (12.7)	1.93, m	1.85, m	3.01, d (12.1)
	1.42, ddd (12.7, 7.7, 3.6)	1.28, d (9.6)	1.25, m	—
7	1.78, m	1.76, m	1.64, m	2.38, td (12.1, 4.3)
8	1.96, m	2.36, m	1.48, dd (5.8, 3.0)	1.27, overlapped
	1.54, m	1.71, m	1.32, m	—
9	1.66, m	1.73, m	1.87, m	1.95, tt (13.7, 3.8)
	1.52, m	1.70, m	1.06, m	1.38, m
10	—	—	—	1.73, m
11	—	—	—	1.10, d (7.2)
12	0.80, s	0.91, s	1.07, s	—
13	0.90, s	0.91, s	1.07, s	4.65, m
	—	—	—	4.50, s
14	4.01, dd (9.0, 6.0)	3.97, dd (9.2, 4.9)	0.84, s	1.80, s
	3.26, d (6.0)	3.27, m	—	—
15	1.02, s	0.93, s	3.89, dd (14.0, 7.7)	1.20, d (7.3)
	—	—	3.87, dd (14.0, 7.0)	—
16	—	—	—	—
17	—	—	2.04, s	—
1′	4.22, d (7.9)	4.23, d (7.9)	—	—
2′	3.16, dd (9.0, 7.9)	3.16, dd (9.0, 7.9)	—	—
3′	3.27, dd (7.9, 4.0)	3.26, dd (7.9, 4.0)	—	—
4′	3.26, m	3.27, m	—	—
5′	3.35, m	3.34, m	—	—
6′	3.86, dd (11.8, 1.7)	3.86, dd (11.9, 1.8)	—	—
	3.66, dd (11.8, 5.2)	3.66, dd (11.9, 5.3)	—	—

^{1}H and ^{13}C NMR data, see **Table 1** and **Table 2**; HRESIMS *m/z* 427.2318 [M + HCOO]$^-$ (calcd for C$_{22}$H$_{35}$O$_8$, 427.2326).

Compound **2**: an amorphous white powder; [α]^{25} D = −25.3 (*c* 0.1, MeOH); IR (KBr) ν_{max} 3,449, 2,947, 1,638, 1,384, 1,077, and 536 cm^{-1}; ^{1}H and ^{13}C NMR data, see **Table 1** and **Table 2**; HRESIMS *m/z* 427.2320 [M + HCOO]$^-$ (calcd for C$_{22}$H$_{35}$O$_8$, 427.2326).

Compound **3**: colorless oil; [α]^{25} D = −37.0 (*c* 0.1, MeOH); IR (KBr) ν_{max} 3,449, 2,964, 2,956, 2,922, 2,851, 1,685, 1,603, 1,261, 1,166, 1,105 and 1,026 cm^{-1}; ^{1}H and ^{13}C NMR data, see **Table 1** and **Table 2**; HRESIMS *m/z* 281.2109 [M + H]$^+$ (calcd for C$_{17}$H$_{29}$O$_3$, 281.2111).

Compound **4**: an amorphous white powder; [α]^{25} D = −38.0 (*c* 0.1, MeOH); IR (KBr) ν_{max} 3,474, 2,962, 2,923, 2,856, 1707, 1,644, 1,451, and 1,394 cm^{-1}; ^{1}H and ^{13}C NMR data, see **Table 1** and **Table 2**; HRESIMS *m/z* 237.1849 [M + H]$^+$ (calcd for C$_{15}$H$_{25}$O$_2$, 237.1849).

Quantum Chemical ECD Calculation

Electronic circular dichroism (ECD) was applied to establish the absolute configurations of **1′** and **2′**, according to the reported method (Stephens and Harada, 2010). According to the key correlations observed in the NOESY spectrum, CHEM3D

TABLE 2 | ^{13}C NMR data of compounds **1** and **2** in CD$_3$OD and of compounds **3** and **4** in CDCl$_3$ (125 MHz).

Position	1	2	3	4
1	154.0	146.7	75.8	80.1
2	116.5	31.3	31.8	31.3
3	36.9	28.1	23.5	28.5
4	40.0	50.0	33.3	44.8
5	42.6	131.9	38.9	214.6
6	29.8	30.0	24.2	50.3
7	47.9	46.1	39.1	38.5
8	27.4	34.4	24.7	26.8
9	36.7	41.5	28.7	28.1
10	47.8	44.2	37.2	39.8
11	45.3	46.4	40.2	16.1
12	20.7	19.7	26.8	150.8
13	24.2	23.9	24.3	107.2
14	72.7	73.8	20.6	22.7
15	17.0	15.5	66.9	15.8
16	—	—	171.4	—
17	—	—	21.1	—
1′	104.8	104.7	—	—
2′	75.2	75.2	—	—
3′	77.9	77.9	—	—
4′	71.7	71.7	—	—
5′	78.2	78.2	—	—
6′	62.8	62.8	—	—

FIGURE 1 | Key ^1H-^1H and HMBC correlations.
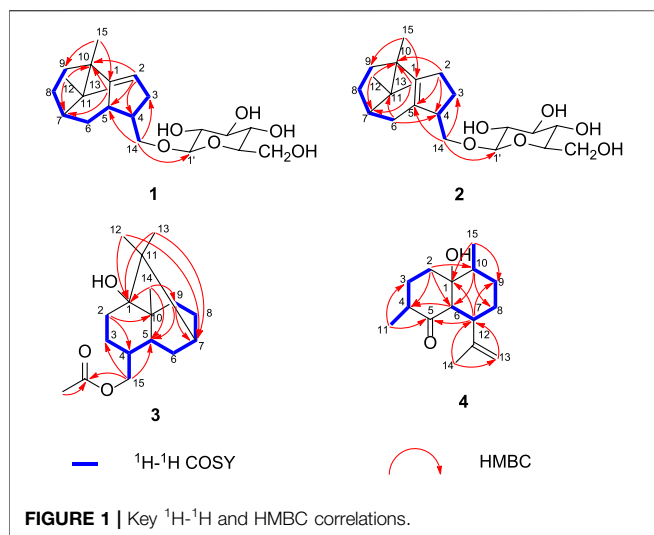
software with the MM2 force field was applied to search the preliminary conformational distribution. Geometric optimization of compounds **1′** and **2′** was calculated with the density functional theory (DFT) method and time-dependent DFT (TDDFT) *via* the Gaussian 09 program (Gaussian, Inc., Wallingford CT, USA). The optimized conformers obtained were submitted to CD calculation by the TDDFT [B3LYP/6-31G(d)] method. The computational data were fitted in the Origin 2021 (OriginLab Corporation, Northampton, MA, USA).

Acid Hydrolysis

Each compound (1–2 mg) was hydrolyzed with 1 M HCl (4 mL) for 4 h at 80°C. The reaction mixture was extracted with ethyl acetate 3 times (Zhang et al., 2020). The water layer was evaporated repeatedly under reduced pressure with MeOH until dryness, giving a monosaccharide residue. It was dissolved in anhydrous pyridine (1 mL), and L-cysteine methyl ester hydrochloride (3 mg) was added. The mixture was kept at 60°C for 1 h. Then, 5 μL (0.5 mg) O-tolylisothiocyanate was added and stirred at 60°C for another 1 h. The reaction mixture was directly analyzed by reversed-phase HPLC. The absolute configurations of sugars of compounds **1** and **2** were determined by comparing the retention times with derivatives of standard sugars prepared in a similar manner. Retention times for derivatives were 12.2 min (L-glucose) and 12.9 min

(D-glucose), respectively. Meanwhile, compounds **1** and **2** were hydrolyzed to obtain compounds **1′** and **2′**, respectively.

Anti-Proliferative Activity Assay (MTT Assay)

The antiproliferative activity of the isolated compounds was evaluated against the growth of hepatocellular carcinoma cells HepG2 (cells were grown in Dulbecco's modified Eagle medium containing 10% FBS at 37°C) using an MTT assay. HepG2 cells were seeded in 96-well plates at a density of 5,000 cells per well and cultured in a 37°C incubator for 24 h (Tang et al., 2020). After 24 h, the medium was removed, and a fresh medium containing different compounds with a series of concentration gradients was added to each well and cultured in a 37°C incubator for 72 h. A measure of 20 μL (5 mg/mL) of the MTT solution was added to each well and cultured in a 37°C incubator for 4 h. Then, the supernatant was removed, and DMSO (100 μL) was added to each well. The optical density was measured at a wavelength of 490 nm after 15 min of shaking. The IC_{50} values of each compound were calculated with GraphPad Prism 8.0 software (GraphPad Software Inc., San Diego, CA, USA).

Flow Cytometry

HepG2 cells were seeded in 6-well plates (1×10^6 cells/well) for 24 h. Then, the medium was removed, and a fresh medium containing different concentrations of compound **19** (1, 2.5, and 5 μM) was added and cultured again for 48 h. Gemcitabine (GEM) was used as a positive control. After culture, the cells were collected and washed twice with cold PBS; binding buffer solution was added to the collected cell precipitate to make the cell concentration reach 1×10^6/mL. Then, 100 μL of the cell suspension was reabsorbed into the new centrifuge tube, and 5 μL Annexin V-FITC and 5 μL PI were added. After incubation at room temperature for 15 min (in a dark place), 400 μL binding buffer was added to each well. Fluorescence of cells was immediately detected with a flow cytometer and used for quantitative analysis.

Western Blotting

HepG2 cells were seeded in 6-well plates (1×10^6 cells/well) for 24 h. Then, the medium was removed, and a fresh medium containing different concentrations of compound **19** (1, 2.5, and 5 μM) was cultured for another 48 h. The medium was

FIGURE 2 | Key NOESY correlations of compounds **1** and **2**.
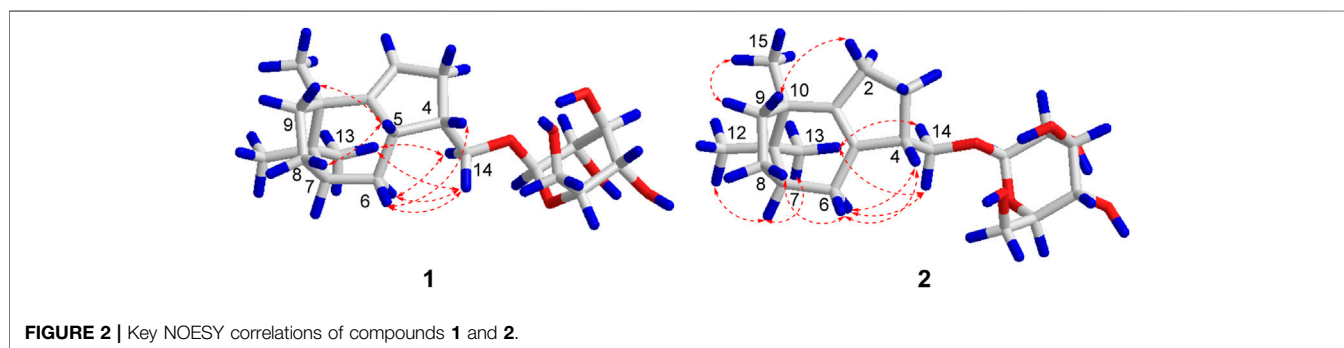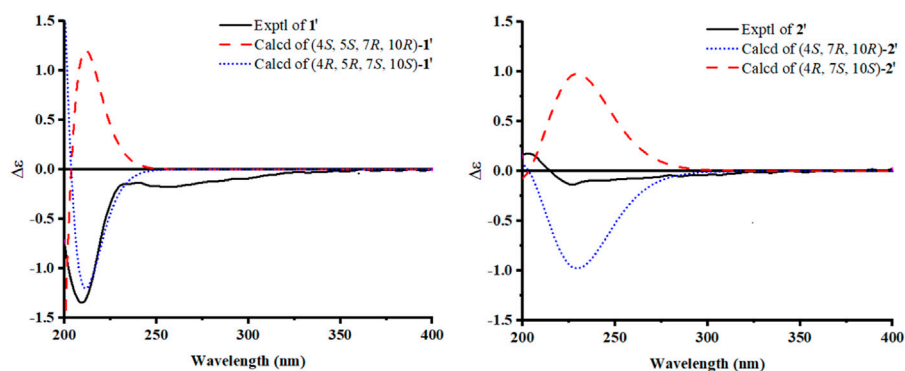
FIGURE 3 | Experimental and calculated CD spectra for compounds **1′** and **2′**.
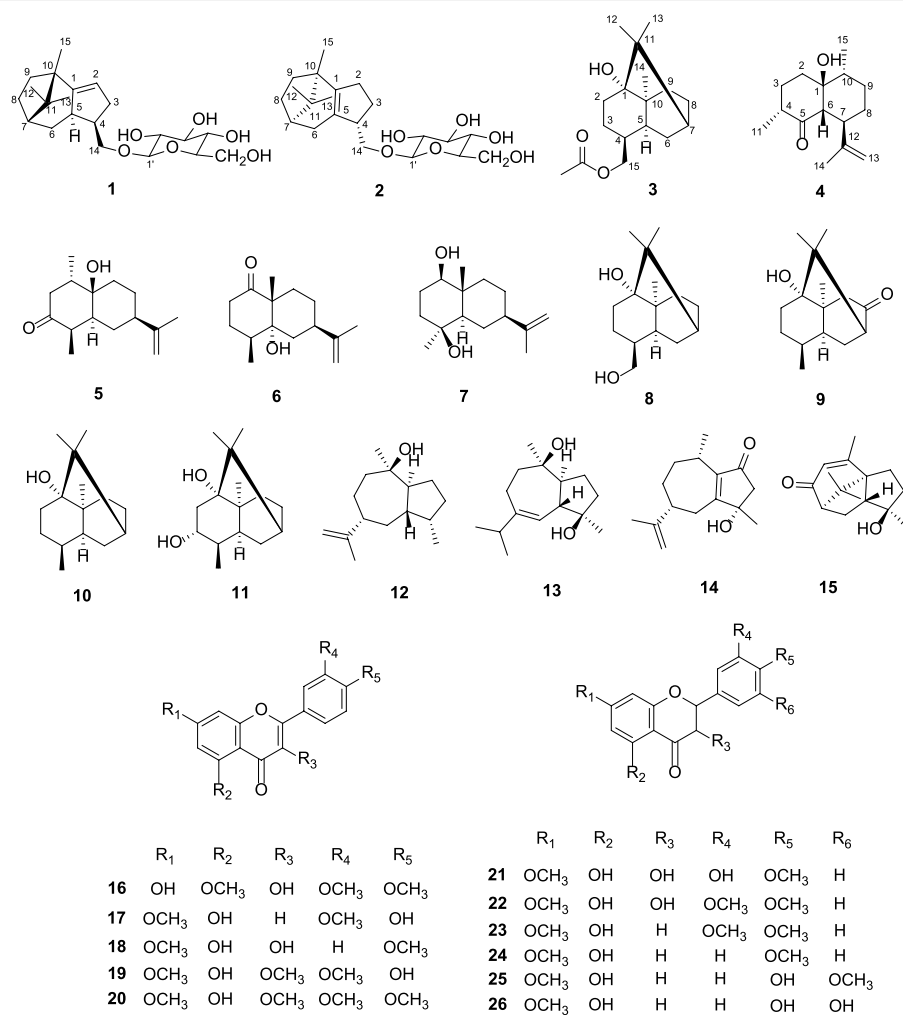
FIGURE 4 | Chemical structures of compounds **1-26**.

removed and washed with cold PBS; cells were collected and lysed with RIPA buffer, left to stand in an ice bath for 30 min, and centrifuged at 4°C for 20 min at the highest speed. The protein concentration was detected by using the BCA protein assay kit. Proteins were separated by SDS-PAGE gels and transferred to the PVDF membrane. The membrane was blocked with 5% non-fat

TABLE 3 | Anti-proliferative activity of compounds **1–13** and **15–26** against HepG2 cells.

Compound	IC$_{50}$ (μM)	Compound	IC$_{50}$ (μM)
1	>50	**15**	>50
2	>50	**16**	>50
3	>50	**17**	25.59 ± 0.41
4	>50	**18**	>50
5	>50	**19**	2.30 ± 0.30
6	>50	**20**	>50
7	>50	**21**	>50
8	>50	**22**	>50
9	>50	**23**	>50
10	>50	**24**	>50
11	>50	**25**	>50
12	>50	**26**	>50
13	>50	—	—

Gemcitabine (GEM) was used as a positive control with an IC$_{50}$ value of 2.32 ± 0.99 μM.

milk for 2 h. Then, specific primary antibodies were used to bind to the corresponding proteins and left for incubation at 4°C overnight, after washing thrice with TBST (5 min), followed by incubation with a second antibody at room temperature for 50 min. The protein bands were detected using the ECL detection kit, and the gray intensities of the bands were measured by ImageJ software.

Statistical Analysis

All data are presented as the mean ± SD of at least three independent experiments. The means were compared by one-way ANOVA, followed by Dunnett's test by GraphPad Prism 8.0 software. When the *p*-value was less than 0.05, the difference between groups was considered statistically significant.

RESULTS AND DISCUSSION

Structure Elucidation of New Compounds

Compound **1** was afforded as an amorphous white powder. The molecular formula of compound **1** was determined to be $C_{21}H_{34}O_6$ based on its HRESIMS data (*m/z* 427.2318 [M + HCOO]$^-$, calcd for $C_{22}H_{35}O_8$ 427.2326), indicating the existence of five degrees of unsaturation. The IR spectrum showed characteristic absorptions attributable to a cyclic olefinic bond (1,638 cm^{-1}) and a hydroxyl (3,449 cm^{-1}) bond. The ^{1}H NMR spectrum (**Table 1**) of compound **1** revealed the presence of an olefinic proton [δ_H 5.02 (1H, m)] and three methyl groups [δ_H 0.80 (3H, s), 0.90 (3H, s), and 1.02 (3H, s)]. The ^{13}C NMR and DEPT spectra (**Table 2**) showed 21 carbon signals due to three methyls, six methylenes, nine methines, and three quaternary carbons. Comprehensive interpretation of the 1D and 2D NMR spectral data allowed full assignment of the ^{1}H and ^{13}C NMR signals of compound **1** (**Table 1** and **Table 2**). The aforementioned data indicated the presence of a *β*-D-glucopyranosyl moiety (Xiao et al., 2011) [δ_C 104.8, 78.2, 77.9, 75.2, 71.7, and 62.8]. Acid hydrolysis of compound **1** with 1 mol/L HCl afforded compound **1′** and *β*-D-glucose that was identified by direct comparison with an authentic sample.

Analysis of ^{1}H–^{1}H COSY in combination with HSQC showed correlations from H-2 to H-9, as shown by bold lines in **Figure 1**. In the HMBC spectrum, as shown in **Figure 1**, the correlations were observed from H-15 to C-1/C-9, H-2 to C-10/C-5/C-4, H-12 to C-10/C-7, H-13 to C-10/C-7, and H-14 to C-5/C-3/C-1′. Comprehensive interpretation of 1D and 2D NMR spectra of compound **1** revealed the presence of a patchoulene-type sesquiterpene unit in **1**, which was similar to *δ*-patchoulene (Faraldos et al., 2010). However, its carbon spectrum NMR data have not been reported in the literature. The observed key HMBC correlations between H-14 and C-1′, as well as between H-1′ and C-14, indicated that the two units were linked *via* the C-14–O–C-1′ bond to form a patchoulene-type sesquiterpenoid glycoside. Thus, the planar structure of compound **1** was established (**Figure 1**).

The relative configuration of compound **1** was established by the NOESY interactions (**Figure 2**). The correlations between H-14a and H-6a/H-6b and between H-14a/H-14b and H-13 indicated the *β*-orientation of H-4, H-5, H-7, and CH$_3$-15. Thus, the relative configuration of the sesquiterpenoid unit in compound **1** was determined.

Finally, according to the quantum chemical electronic circular dichroism (ECD) calculation, as shown in **Figure 3**, the absolute configuration of compound **1** was deduced to be 4*R*, 5*R*, 7*S*, and 10*S* by a comparison of the experimental ECD spectrum of compound **1′** with the calculated one. Therefore, compound **1** was determined to be (4*R*, 5*R*, 7*S*, 10*S*)-14-hydroxypatchoulene-14-*O*-*β*-D-glucopyranoside, and named Pogopatchoulene A.

Compound **2** was afforded as an amorphous white powder. The molecular formula of compound **2** was deduced to be $C_{21}H_{34}O_6$ by its HRESIMS [M + HCOO]$^-$ ion at *m/z* 427.2320 (calcd for $C_{22}H_{35}O_8$ 427.2326), corresponding to five degrees of unsaturation. The UV and IR spectra of compound **2** displayed similar signals to those of **1**. The ^{13}C NMR spectrum revealed the presence of 21 carbon signals including three methyls, seven methylenes, seven methines, and four quaternary carbons. The 1D NMR signals of compound **2** closely resembled those of **1**, indicating that they possessed a similar structure except for the presence of a tetrasubstituted double-bond group in compound **2** instead of a trisubstituted double-bond group in compound **1**. A comprehensive comparison of their 2D NMR data revealed that the tetrasubstituted double-bond group in compound **2** was in positions 1 and 5 instead of positions 1 and 2 in compound **1**. Furthermore, compound **2** was hydrolyzed with 1 mol/L HCl to obtain compound **2′** and *β*-D-glucose. Hence, the planar structure of compound **2** was established.

The relative configuration of compound **2** could be suggested by the interpretation of the NOESY data, as shown in **Figure 2**; the cross peaks between H-14a/H-14b and H-13 and between H-14a and H-6a indicated that H-4, H-7, and CH$_3$-15 were in *β*-orientation. Finally, the absolute configuration of compound **2** was determined to be 4*S*, 7, and 10*R*, according to the quantum chemical ECD calculation presented in **Figure 3**. In conclusion, compound **2** was determined as (4*S*, 7*R*, 10*R*)-14-hydroxypatchoulene-14-*O*-*β*-D-glucopyranoside, and named Pogopatchoulene B.
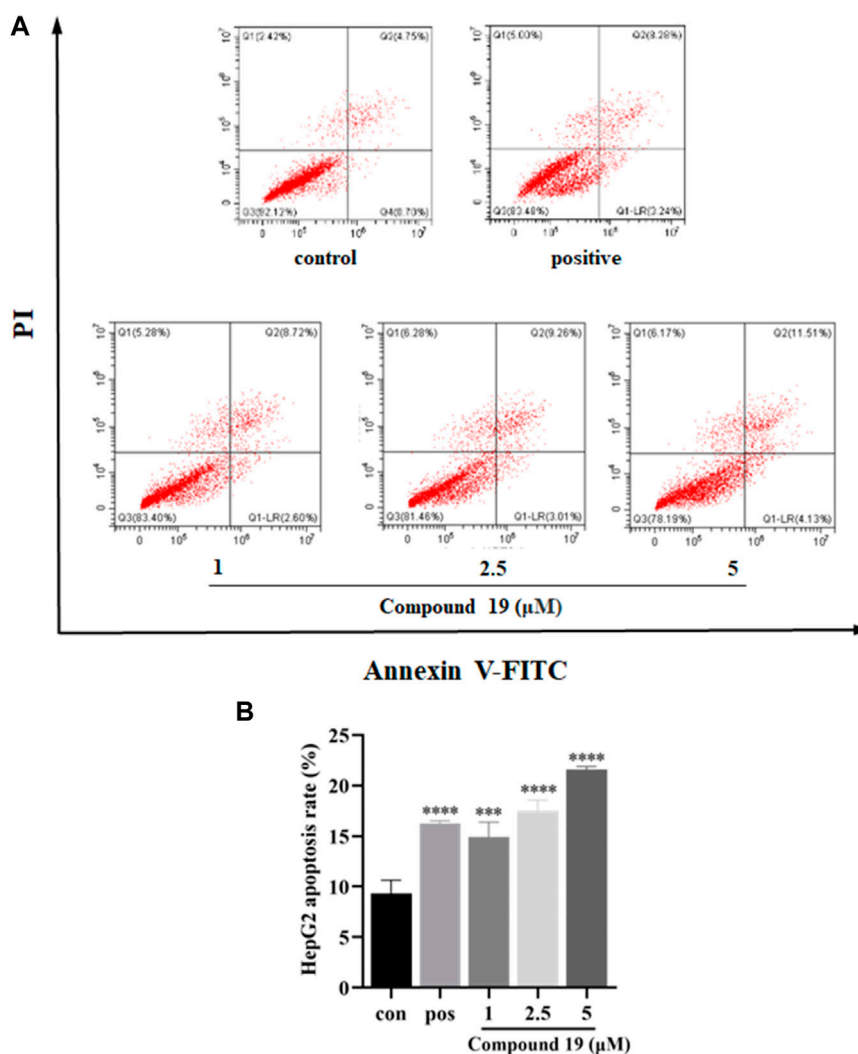
FIGURE 5 | Impact of compound **19** on apoptosis of HepG2 cells. Cells were seeded in 6-well plates (1 × 10^6 cells/well) and treated with compound **19** (1, 2.5, and 5 μM) for 48 h. Gemcitabine (GEM) was used as a positive control. Annexin V-FITC/PI staining flow cytometry was used to analyze the apoptosis of HepG2 cells after treatment with compound **19**; analysis is shown in **(A)**. The experiments were run in triplicate. Data were presented as mean ± SD. The explicit analysis is shown in **(B)**. $^{*}p < 0.05$, $^{**}p < 0.01$, and $^{***}p < 0.001$ *vs.* the control group.

Compound **3** was shown to have the molecular formula $C_{17}H_{28}O_3$ by its HRESIMS data (m/z 281.2109 [M + H]$^+$, calcd for $C_{17}H_{29}O_3$: 281.2111). The UV spectrum showed maximal absorption at 286 nm. The IR spectra revealed the characteristic absorptions for hydroxyl (3,449 cm^{-1}) and carbonyl (1,685 cm^{-1}) bonds. The ^{1}H NMR spectrum displayed the signals for four methyl protons [δ_H 0.84 (3H, s, H-14), 1.07 (6H, overlapped, H-13 and H-12), and 2.04 (3H, s, H-17)]. The ^{13}C NMR and DEPT spectra displayed 17 carbon signals including four methyls, six methylenes, three methines, and four quaternary carbons. Comparison of the NMR data of compound **3** with the known compound patchoulan-1, 15-diol (**8**) suggested that their NMR signals were similar except for extra acetyl [δ_H 2.04 (3H, s), δ_C 21.1, 171.4] in compound **3**. With the aid of ^{1}H-^{1}H COSY, HSQC, and HMBC experiments, all the ^{1}H and ^{13}C NMR signals were assigned, as shown in **Table 1** and the

relative configuration is shown in **Figure 4**, which was in accordance with a reaction product named patchouli alcohol acetate (Niwa et al., 1987). However, no relevant nuclear magnetic data on patchouli alcohol acetate had been reported in the literature. Therefore, we reported its carbon spectrum for the first time.

The molecular formula of compound **4** was established as $C_{15}H_{24}O_2$ by a quasi-molecular ion peak at m/z 237.1849 [M + H]$^+$ (calcd for $C_{15}H_{25}O_2$: 237.1849) in its HRESIMS. IR spectra showed the characteristic absorptions for hydroxyl (3,474 cm^{-1}), carbonyl (1707 cm^{-1}), and olefinic bonds (1,644 cm^{-1}). The ^{1}H NMR spectrum displayed two olefinic protons [δ_H 4.65 (1H, m) and 4.50 (1H, s)] and three methyl groups [δ_H 1.10 (3H, d), 1.20 (3H, d), and 1.80 (3H, s)]. We compared the NMR data on compound **4** with those of the synthetic compound (+)-[2R-(2α, 4aβ, 5α, 8β, 8aβ)]-octahydro-4a-hydroxy-2, 5-dimethyl-8-(1-
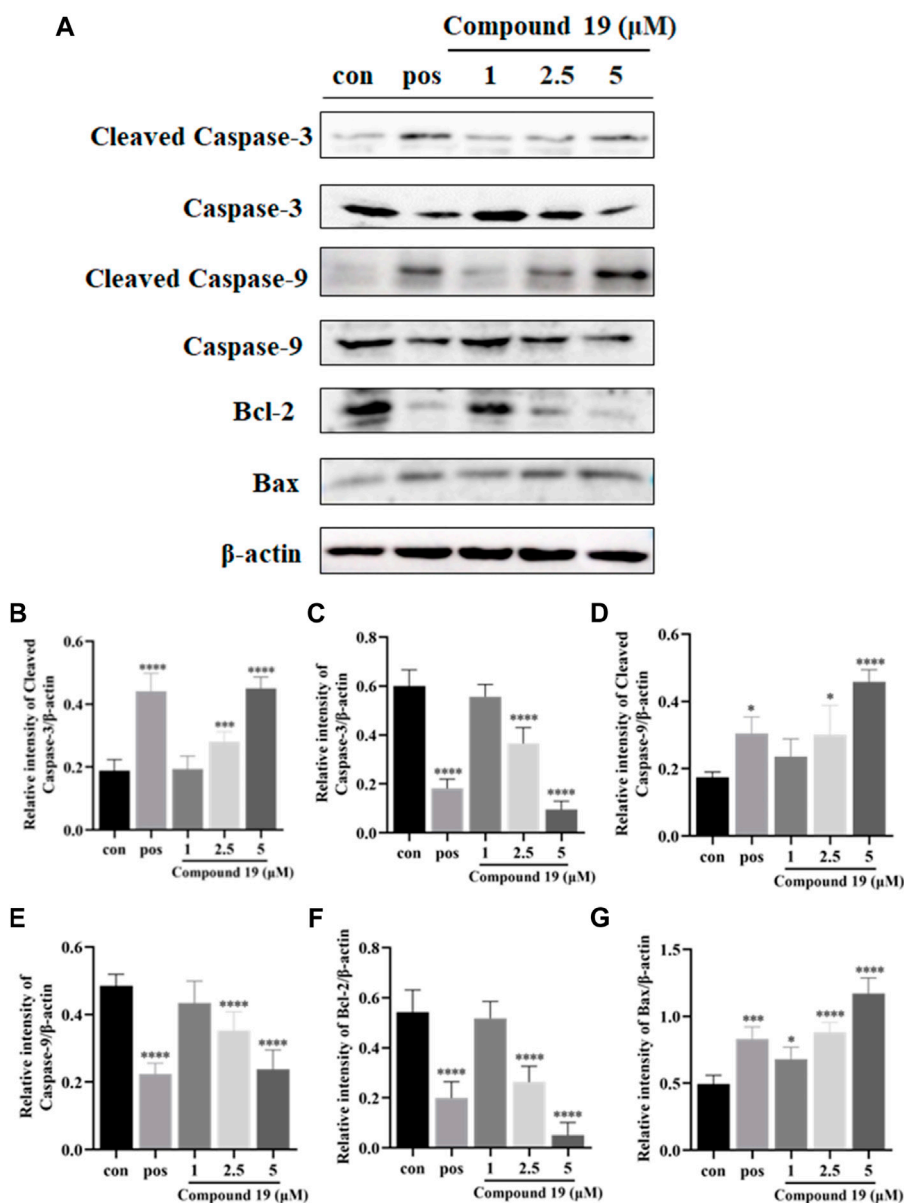
FIGURE 6 | Impact of compound **19** on the protein expressions of cleaved caspase-3, cleaved caspase-9, caspase-3, caspase-9, Bcl-2, and Bax in HepG2 cells. Cells were seeded in 6-well plates (1×10^6 cells/well) and treated with different concentrations of compound **19** (1, 2.5, and 5 μM) for 48 h. Western blotting was used to detect the protein expression levels after compound 19 was applied to HepG2 cells **(A)**. The ratio of the corresponding protein to β-actin is calculated in **(B–G)**. The experiments were run in triplicate. Data were presented as mean ± SD. $^*p < 0.05$, $^{**}p < 0.01$, and $^{***}p < 0.001$ *vs.* the control group.

methylethenyl)-1(2H)-naphthalenone (Gijsen et al., 1994), which were exactly the same. Hence, compound **4** was determined.

In a summary, two new patchoulene sesquiterpenoid glycosides (**1–2**), a natural patchoulane-type sesquiterpenoid (**3**) and a natural cadinene-type sesquiterpenoid (**4**) were isolated and determined from *P. cablin*. Other known compounds, as rel-(1*S*, 4*R*, 5*R*, 7*R*, 10*R*)-10-desmethyl-10-hydroxy-1-methyl-3-oxo-11-eudesmene (**5**) (Chavez et al., 1995), corymbolone (**6**) (Garbarino et al., 1985), 1*β*, 4*β*-dihydroxyeudesman-11-ene (**7**) (Li et al., 2005), patchoulan-1, 15-diol (**8**) (Ding et al., 2011), 2, 3, 4, 4*α*, 5, 6, 8, 8*α*-octayhydro-1-

hydroxy-4, 8*α*, 9, 9-tetramethyl-1, 6-methanonaphthalen-7(1H)-one (**9**) (Barton et al., 1987), patchouli alcohol (**10**) (Barton et al., 1987), 3*R*-3-hydroxypatchoulol (**11**) (Aleu et al., 2001), pogostol (**12**) (Stierle et al., 2003), 1*S*, 4*R*, 5*S*, 6*R*, 7*S*, 10*S*-1 (5), 6 (7)-diepoxy-4-guaiol (**13**) (Chen et al., 2020), (5*R*, 8*S*)-3-hydroxy-3, 8-dimethyl-5-(prop-1-en-2-yl)-3, 4, 5, 6, 7, 8-hexahydroazulen-1(2H)-one (**14**) (Huang et al., 2015), 8-keto-9 (10)-*α*-patchoulene-4*α*-ol (**15**) (Li et al., 2013), 3,7-dihydroxy-5, 3′, 4′-trimethoxyflavone (**16**) (Dong et al., 1999), velutin (**17**) (Zahir et al., 1996), 3, 5-dihydroxy-7, 4′-dimethoxy flavone (**18**) (Zhang et al., 2001), 5, 4′-dihydroxy-7-methoxyflavone

(**19**) (Zhang et al., 2001), 5-hydroxy-3, 7, 3′, 4′-tetramethoxyflavone (**20**) (Wang et al., 2020), (2R, 3R)-(+)-4′, 7-di-O-methyldihydroquercetin (**21**) (Yoon et al., 2019), 7, 3′, 4′-tri-O-methyldhq (**22**) (Kiehlmann and Slade, 2003), 5-hydroxy-7, 3′, 4′-trimethoxyflavanone (**23**) (Zhang et al., 2001), 7, 4′-dimethylapigenin (**24**) (Chen et al., 2017), ereiodictyol-7, 3′-dimethyl ether (5, 4′-dihydroxy-7, 3′-dimethoxyflavanone) (**25**) (Vasconcelos et al., 1998), and (2S)-5, 3′, 4′ trihydroxy-7-methoxy-flavanone (**26**) (Vasconcelos et al., 1998) were also obtained and established by comparing with reported spectroscopic data in the literature reports. Compounds **5–7**, **9**, **13**, **16**, **21**, **22**, and **26** were isolated from this plant for the first time.

Anti-Proliferative Effects of Isolates

An ethanol crude extract of *P. cablin* displayed *in vitro* anti-tumor potential in our preliminary experiments. Herein, most isolates (**1–13** and **15–26**) were evaluated for antiproliferative activities in HepG2 cells. Among the tested samples, compounds **17** and **19** displayed anti-proliferative effects against HepG2 cells with IC_{50} values of 25.59 and 2.30 µM, respectively. This observation was in agreement with reported data (Huong et al., 2005), in which the IC_{50} value of compound **19** against HepG2 cells was 1.60 µM. Previous studies have revealed that flavonoids with 2 and 3 double bonds have a higher ability to induce cell apoptosis than flavonols (Wang et al., 1999; Hui et al., 2014; Isoda et al., 2014). In addition, the presence of hydroxyl groups at the 4′ positions of the B ring is important for granulocyte differentiation (Takahashi et al., 1998; Isoda et al., 2014). According to our data, flavone compound **19** showed the best antiproliferative effects against HepG2 cells than other flavonoids; it can be concluded that 3-methoxy and 4′- hydroxyl might be important for its activity. The other compounds including sesquiterpenoids and dihydroflavones were inactive, as shown in **Table 3**. Our data suggest that the anti-tumor effects of *P. cablin* might be attributed, at least partially, to its bioactive flavonoids.

Compound 19 Induce Apoptosis in HepG2 Cells

Apoptosis plays an important role in maintaining tissue homeostasis (Ma, et al., 2018). Induction of apoptosis in tumor cells is an important survival strategy against cancer pathologic progression (Rejhová, et al., 2018), and many natural products have been shown to have anticancer effects through the mitochondrial-mediated apoptosis pathway (Friedman, 2015). The cytotoxic effects of compound **19** on HepG2 have been reported, but the mechanism of action has not been studied. Therefore, the apoptosis-inducing effects of compound **19** in HepG2 cells were also investigated in the current study. As shown in **Figure 5**, after treatment with compound **19** (1, 2.5, and 5 µM) for 48 h, the flow cytometric apoptosis experiment showed a dose-dependent increase in the percentage of early apoptotic cells when compared with the control group, which showed significant difference ($p < 0.001$).

Additionally, caspase-9 is an important initiator caspase within the cascade of apoptosis transduction in the mitochondrial-mediated apoptosis pathway. Upon proapoptotic factor release into the cytosol, procaspase-9 is recruited at apoptosome and self-cleaved to caspase-9 and then stimulates downstream executioner caspases, such as caspase-3, which subsequently cause apoptotic cell death (Brentnall et al., 2013; Sadeghi et al., 2019). Our results showed that compared with the control group, compound **19** significantly upregulated the expressions of cleaved caspase-9 and cleaved caspase-3 and significantly downregulated the expressions of caspase-3 and caspase-9. Moreover, both Bcl-2 (an anti-apoptotic protein) and Bax (a proapoptotic protein) belong to the B-cell lymphoma (Bcl-2) family and are critical in the mitochondrial-mediated apoptotic pathway. Western blotting results are shown in **Figure 6**; compared with the control group, compound **19** significantly upregulated the expressions of Bax and downregulated the expressions of Bcl-2. Thus, compound **19** may induce apoptosis in HepG2 cells and activate the mitochondrial-mediated apoptotic pathway. Our results showed for the first time that compound **19** exerted anti-proliferative effects by inducing apoptotic cell death.

CONCLUSION

In conclusion, this study was a phytochemical investigation that explored the chemical profiles and pharmacological properties of active constituents from *P. cablin*. Twenty-six compounds including two new patchoulene sesquiterpenoid glycosides and two natural sesquiterpenoids were isolated from the aerial parts of *P. cablin*, and the absolute configurations of new compounds (**1–2**) were established. The antiproliferative activities against the human tumor cell line (HepG2) of the isolated compounds (**1–13** and **15–26**) were examined by the MTT assay. Compounds **17** and **19** displayed anti-proliferative effects with IC_{50} values of 25.59 and 2.30 µM against HepG2 cells, respectively. In this article, the related mechanism of the anti-proliferative activity of compound **19** has been further studied, and it was found to induce the apoptosis of HepG2 cells by downregulating the ratio of Bcl-2/Bax and upregulating the expressions of cleaved caspase-3 and cleaved caspase-9. Therefore, findings from the current study supported that the chemical constituents from *P. cablin* were multitudinous, which were beneficial for the further fundamental and development research of *P. cablin*.

DATA AVAILABILITY STATEMENT

The original contributions presented in the study are included in the article/**Supplementary Material**; further inquiries can be directed to the corresponding authors.

AUTHOR CONTRIBUTIONS

XP: data curation, validation, and writing—original draft preparation. SA: software and writing—original draft preparation. YZ: data curation and software. FF: data curation and software. MW: data curation. PL: data curation. YW: software. LG: software and methodology. KZ: supervision and

SUPPLEMENTARY MATERIAL

The Supplementary Material for this article can be found online at: https://www.frontiersin.org/articles/10.3389/fchem.2022.938851/full#supplementary-material

REFERENCES

Aleu, J., Hanson, J. R., Hernández Galán, R., and Collado, I. G. (2001). Biotransformation of the Fungistatic Sesquiterpenoids Patchoulol, Ginsenol, Cedrol and Globulol by *Botrytis Cinerea*. *J. Mol. Catal. B Enzym.* 11, 329–334. doi:10.1016/S1381-1177(00)00014-X

Barton, D. H. R., Bel?il, J.-C., Billion, A., Boivion, J., Lallemand, J.-Y., and Mergui, S. (1987). Functionalisation of Saturated Hydrocarbons. Part 9. Oxidation of Patchouli Alcohol by the 'gif System': Isolation and Organoleptic Properties of Three New Ketonic Derivatives. *Helv. Chim. Acta* 70, 273–280. doi:10.1002/hlca.19870700202

Brentnall, M., Rodriguez-Menocal, L., De Guevara, R. L., Cepero, E., and Boise, L. H. (2013). Caspase-9, Caspase-3 and Caspase-7 Have Distinct Roles during Intrinsic Apoptosis. *BMC Cell. Biol.* 14 (1), 1–9. doi:10.1186/1471-2121-14-32

Büchi, G., Goldman, I. M., and Mayo, D. W. (1966). The Structures of Two Alkaloids from Patchouli Oil. *J. Am. Chem. Soc.* 88, 3109–3113. doi:10.1021/ja00965a040

Chavez, J. P., Gottlieb, O. R., and Yoshida, M. (1995). 10-Desmethyl-1-methyl-eudesmanes from *Ocotea Corymbosa*. *Phytochemistry* 39, 849–852. doi:10.1016/0031-9422(94)00977-2

Chen, Y. M., Cao, N. K., Tu, P. F., and Jiang, Y. (2017). Chemical Constituents from *Murraya Euchrestifolia*. *Zhongguo Zhong Yao Za Zhi* 42, 1916–1921. doi:10.19540/j.cnki.cjcmm.20170228.002j

Chen, Y. W., Dong, F. W., Qin, T. L., Zhang, F., Wu, S. L., Yang, M. Y., et al. (2020). Terpenoids from Stems and Leaves of *Aphanamixis Grandifolia*. *Chin. J. Exp. Traditional Med. Formulae* 26, 168–173. doi:10.13422/j.cnki.syfjx.20201311

Dahai, W., Yin, Z., Zhang, Q., Ye, W., Zhang, X., and Zhang, J. (2010). Nonvolatile Chemical Constituents from *Pogostemon Cablin*. *Cjcmm* 35, 2704–2707. doi:10.4268/cjcmm20102014

Ding, W.-B., Lin, L.-D., Liu, M.-F., and Wei, X.-Y. (2011). Two New Sesquiterpene Glycosides from*Pogostemon Cablin*. *J. Asian Nat. Prod. Res.* 13, 599–603. doi:10.1080/10286020.2011.577424

Ding, W., Liu, M., Wei, X., and Lin, L. (2009). Strong Polarity Components of *Pogostemon Cablin* (Blance) Benth. *J. Trop. Subtropical Bot.* 17, 610–616. doi:10.3969/j.issn.1005-3395.2009.06.017

Dong, H., Gou, Y.-L., Cao, S.-G., Chen, S.-X., Sim, K.-Y., Goh, S.-H., et al. (1999). Eicosenones and Methylated Flavonols from *Amomumkoenigii*. *Phytochemistry* 50, 899–902. doi:10.1016/S0031-9422(98)00622-0

Faraldos, J. A., Wu, S., Chappell, J., and Coates, R. M. (2010). Doubly Deuterium-Labeled Patchouli Alcohol from Cyclization of Singly Labeled [2-2H1]Farnesyl Diphosphate Catalyzed by Recombinant Patchoulol Synthase. *J. Am. Chem. Soc.* 132, 2998–3008. doi:10.1021/ja909251r

Feng, C., Sui, C., and Wu, H. (1994). Synthesizing Site and Storing Position of Essential Oil in *Pogostemon Cablin*. *Chin. Traditional Herb. Drugs* 38, 116–119.

Friedman, M. (2015). Chemistry and Anticarcinogenic Mechanisms of Glycoalkaloids Produced by Eggplants, Potatoes, and Tomatoes. *J. Agric. Food Chem.* 63 (13), 3323–3337. doi:10.1021/acs.jafc.5b00818

Garbarino, J. A., Gambaro, V., and Chamy, M. C. (1985). The Structure of Corymbolone, an Eudesmane Sesquiterpenoid Keto-Alcohol from *Cyperus Corymbosus*. *J. Nat. Prod.* 48, 323–325. doi:10.1021/np50038a023

Gijsen, H. J. M., Wijnberg, J. B. P. A., and de Groot, A. (1994). Thermal Rearrangement of Bicyclogermacrane-1,8-Dione. Synthesis of Humulenedione and (−)-cubenol, Starting from Natural (+)-Aromadendrene-V. *Tetrahedron* 50, 4745–4754. doi:10.1002/chin.19943323510.1016/s0040-4020(01)85013-4

Hikino, H., Ito, K., and Takemoto, T. (1968). Structure of Pogostol. *Chem. Pharm. Bull.* 16, 1608–1610. doi:10.1248/cpb.16.1608

Huang, A.-C., Sefton, M. A., Sumby, C. J., Tiekink, E. R. T., and Taylor, D. K. (2015). Mechanistic Studies on the Autoxidation of α-Guaiene: Structural Diversity of the Sesquiterpenoid Downstream Products. *J. Nat. Prod.* 78, 131–145. doi:10.1021/np500819f

Huang, L., Mu, S., Zhang, J., Deng, B., Song, Z., and Hao, X. (2009). Chemical Constituents from Involatile Moiety of Pogostemon Cablin. *Zhongguo Zhong Yao Za Zhi* 34, 410–413. doi:10.3321/j.issn:1001-5302.2009.04.010

Hui, H., Chen, Y., Yang, H., Zhao, K., Wang, Q., Zhao, L., et al. (2014). Oroxylin A Has Therapeutic Potential in Acute Myelogenous Leukemia by Dual Effects Targeting PPARγ and RXRα. *Int. J. Cancer* 134 (5), 1195–1206. doi:10.1002/ijc.28435

Huong, D. T., Luong, D. V., Thao, T. T., and Sung, T. V. (2005). A New Flavone and Cytotoxic Activity of Flavonoid Constituents Isolated from *Miliusa Balansae* (Annonaceae). *Pharmazie* 60, 627–629. doi:10.1002/chin.200550192

Isoda, H., Motojima, H., Onaga, S., Samet, I., Villareal, M. O., and Han, J. (2014). Analysis of the Erythroid Differentiation Effect of Flavonoid Apigenin on K562 Human Chronic Leukemia Cells. *Chemico-Biological Interact.* 220, 269–277. doi:10.1016/j.cbi.2014.07.006

Kiehlmann, E., and Slade, P. W. (2003). Methylation of Dihydroquercetin Acetates: Synthesis of 5-O-Methyldihydroquercetin. *J. Nat. Prod.* 66, 1562–1566. doi:10.1021/np034005w

Kongkathip, N., Sam-ang, P., Kongkathip, B., Pankaew, Y., Tanasombat, M., and Udomkusonsri, P. (2009). Development of Patchouli Extraction with Quality Control and Isolation of Active Compounds with Antibacterial Activity. *Agric. Nat. Resour.* 43, 519–525.

Li, F., Li, C.-J., Ma, J., Yang, J.-Z., Chen, H., Liu, X.-L., et al. (2013). Four New Sesquiterpenes from the Stems of *Pogostemon Cablin*. *Fitoterapia* 86, 183–187. doi:10.1016/j.fitote.2013.03.010

Li, X., Yang, M., Han, Y.-F., and Gao, K. (2005). New Sesquiterpenes from*Erigeron Annus*. *Planta Med.* 71, 268–272. doi:10.1055/s-2005-837827

Ma, Z.-J., Lu, L., Yang, J.-J., Wang, X.-X., Su, G., Wang, Z.-l., et al. (2018). Lariciresinol Induces Apoptosis in HepG2 Cells via Mitochondrial-Mediated Apoptosis Pathway. *Eur. J. Pharmacol.* 821, 1–10. doi:10.1016/j.ejphar.2017.12.027

Niwa, H., Hasegawa, T., Ban, N., and Yamada, K. (1987). Stereocontrolled Total Synthesis of (±)-norpatchoulenol and Two Metabolites of Patchouli Alcohol, (±)-hydroxy Patchouli Alcohol and the Corresponding (±)-carboxylic Acid. *Tetrahedron* 43, 825–834. doi:10.1016/S0040-4020(01)90019-5

Rejhová, A., Opattová, A., Čumová, A., Slíva, D., and Vodička, P. (2018). Natural Compounds and Combination Therapy in Colorectal Cancer Treatment. *Eur. J. Med. Chem.* 144, 582–594. doi:10.1016/j.ejmech.2017.12.039

Sadeghi, S., Davoodvandi, A., Pourhanifeh, M. H., Sharifi, N., ArefNezhad, R., Sahebnasagh, R., et al. (2019). Anti-cancer Effects of Cinnamon: Insights into its Apoptosis Effects. *Eur. J. Med. Chem.* 178, 131–140. doi:10.1016/j.ejmech.2019.05.067

Stephens, P. J., and Harada, N. (2009). ECD Cotton Effect Approximated by the Gaussian Curve and Other Methods. *Chirality* 22, 229–233. doi:10.1002/chir.20733

Stierle, A. A., Stierle, D. B., Goldstein, E., Parker, K., Bugni, T., Baarson, C., et al. (2003). A Novel 5-HT Receptor Ligand and Related Cytotoxic Compounds from an Acid Mine Waste Extremophile. *J. Nat. Prod.* 66, 1097–1100. doi:10.1021/np030044w

Takahashi, T., Kobori, M., Shinmoto, H., and Tsushida, T. (1998). Structure-activity Relationships of Flavonoids and the Induction of Granulocytic- or Monocytic-Differentiation in HL60 Human Myeloid Leukemia Cells. *Biosci. Biotechnol. Biochem.* 62 (11), 2199–2204. doi:10.1271/bbb.62.2199

Tang, S., Zhang, X.-T., Ma, Y.-B., Huang, X.-Y., Geng, C.-A., Li, T.-Z., et al. (2020). Artemyrianolides A-S, Cytotoxic Sesquiterpenoids from Artemisia Myriantha. *J. Nat. Prod.* 83, 2618–2630. doi:10.1021/acs.jnatprod.0c00396

Terhune, S. J., Hogg, J. W., and Lawrence, B. M. (1973). Cycloseychellene, a New Tetracyclic Sesquiterpene from. *Tetrahedron Lett.* 14, 4705–4706. doi:10.1016/S0040-4039(01)87315-9

Vasconcelos, J. M. J., Silva, A. M. S., and Cavaleiro, J. A. S. (1998). Chromones and Flavanones from *Artemisia Campestris* Subsp. *Maritima*. *Phytochemistry* 49, 1421–1424. doi:10.1002/chin.19991127010.1016/s0031-9422(98)00180-0

Wang, I.-K., Lin-Shiau, S.-Y., and Lin, J.-K. (1999). Induction of Apoptosis by Apigenin and Related Flavonoids through Cytochrome C Release and Activation of Caspase-9 and Caspase-3 in Leukaemia HL-60 Cells. *Eur. J. Cancer* 35 (10), 1517–1525. doi:10.1016/S0959-8049(99)00168-9

Wang, Z.-H., Li, Q., Huang, M., Xu, P.-F., Yang, L.-P., Zhai, Y.-Y., et al. (2020). Chemical Constituents of *Callicarpa Macrophylla*. *Chem. Nat. Compd.* 56, 1125–1127. doi:10.1007/s10600-020-03243-4

Xiao, H. M., Zu, L. B., Li, S. P., Wang, K. J., and Li, N. (2011). Chemical Constituents from Dried Fruits of *Rubus Chingii*. *Chin. J. Med. Chem.* 21, 220–226. doi:10.1007/s10570-010-9464-0

Yoon, K. D., Lee, J.-Y., Kim, T. Y., Kang, H., Ha, K.-S., Ham, T.-H., et al. (2019). *In Vitro* and *In Vivo* Anti-hyperglycemic Activities of Taxifolin and its Derivatives Isolated from Pigmented Rice (*Oryzae Sativa* L. Cv. Superhongmi). *J. Agric. Food Chem.* 68, 742–750. doi:10.1021/np034005w10.1021/acs.jafc.9b04962

Zahir, A., Jossang, A., Bodo, B., Provost, J., Cosson, J.-P., and Sévenet, T. (1996). DNA Topoisomerase I Inhibitors: Cytotoxic Flavones from *Lethedon Tannaensis*. *J. Nat. Prod.* 59 (7), 701–703. doi:10.1021/np960336f

Zhang, G. W., Ma, X. Q., and Su, J. Y. (2001). Flavonoids Isolated from *Pogostemon Cablin* (In English). *Chin. Traditional Herb. Drugs* 32, 870–873. doi:10.7501/j.issn.0253-2670.2001.10.2001010478

Zhang, Y., Zhou, W.-Y., Song, X.-Y., Yao, G.-D., and Song, S.-J. (2020). Neuroprotective Terpenoids from the Leaves of *Viburnum Odoratissimum*. *Nat. Prod. Res.* 34, 1352–1359. doi:10.1080/14786419.2018.1514400

Check for updates

Design, Synthesis, and Bioactivities of Novel Trifluoromethyl Pyrimidine Derivatives Bearing an Amide Moiety

Wenjun Lan[1†], Xuemei Tang[1†], Jia Yu[2], Qiang Fei[1], Wenneng Wu[1]*, Pei Li[3]* and Heng Luo[2]*

[1]Food and Pharmaceutical Engineering Institute, Guiyang University, Guiyang, China, [2]State Key Laboratory of Functions and Applications of Medicinal Plants, Guizhou Medical University, Guiyang, China, [3]Qiandongnan Engineering and Technology Research Center for Comprehensive Utilization of National Medicine, Kaili University, Kaili, China

Twenty-three novel trifluoromethyl pyrimidine derivatives containing an amide moiety were designed and synthesized through four-step reactions and evaluated for their antifungal, insecticidal, and anticancer properties. Bioassay results indicated that some of the title compounds exhibited good *in vitro* antifungal activities against *Botryosphaeria dothidea* (*B. dothidea*), *Phompsis* sp., *Botrytis cinereal* (*B. cinerea*), *Colletotrichum gloeosporioides* (*C. gloeosporioides*), *Pyricutaria oryzae* (*P. oryzae*), and *Sclerotinia sclerotiorum* (*S. sclerotiorum*) at 50 μg/ml. Meanwhile, the synthesized compounds showed moderate insecticidal activities against *Mythimna separata* (*M. separata*) and *Spdoptera frugiperda* (*S. frugiperda*) at 500 μg/ml, which were lower than those of chlorantraniliprole. In addition, the synthesized compounds indicated certain anticancer activities against PC3, K562, Hela, and A549 at 5 μg/ml, which were lower than those of doxorubicin. Notably, this work is the first report on the antifungal, insecticidal, and anticancer activities of trifluoromethyl pyrimidine derivatives bearing an amide moiety.

Keywords: amide, trifluoromethyl pyrimidine, design, synthesis, bioactivity

INTRODUCTION

In recent years, in the field of agricultural production, drug resistance and cross-resistance of existing pesticides continue to develop, and the development of efficient and new pesticides is still an urgent task for scientific researchers (Wei et al., 2021). Due to their unique biological structure, nitrogen-containing heterocyclic compounds have the characteristics of high target specificity and good environmental compatibility, which have become a research hotspot in the creation of new pesticides (Mermer et al., 2021). Among them, pyrimidine is an important lead molecule and an active fragment in the design of biologically active molecules, which is widely used in the design of pesticides and pharmaceutical molecules (Abbas et al., 2021), plant growth regulation (Tsygankova et al., 2018), and other biological activities. Many pyrimidine pesticide molecules are on the market, such as azoxystrobin, fluoxastrobin, pyrimethamine sulfonate, pyrimfen, cyclopropenyl, sulfluramid, and sulfonylureas. Especially in the prevention and treatment of plant fungal diseases, pyrimidine fungicides have become one of the hot spots in the research on new pesticides (Borthakur et al., 2020). In the medicine field, pyrimidine has broad-spectrum biological activity including anti-viral, anti-inflammatory, anti-cancer, and anti-HIV activities (Abdel-Aziz et al., 2021; Abu-Zaied et al., 2021; Ding et al., 2022; Li et al., 2022). Therefore, the molecular design, synthesis, and biological activity of pyrimidine derivatives are still one of the hot research topics in pesticide chemistry (Zhang et al., 2020).
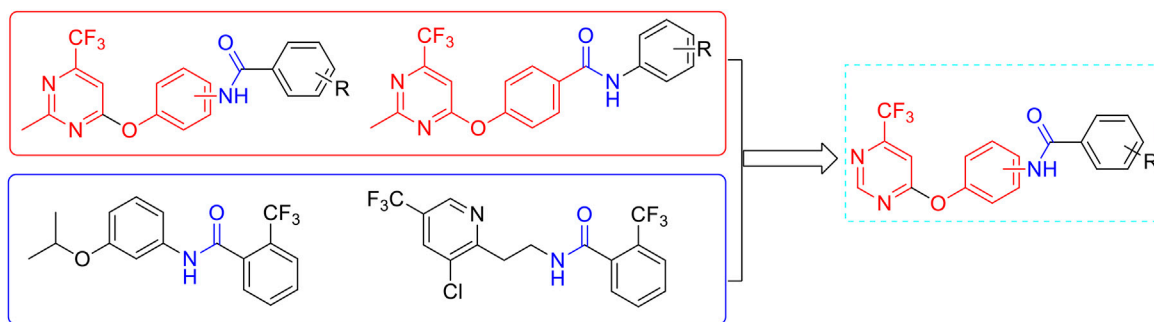
FIGURE 1 | Design of the target molecules.
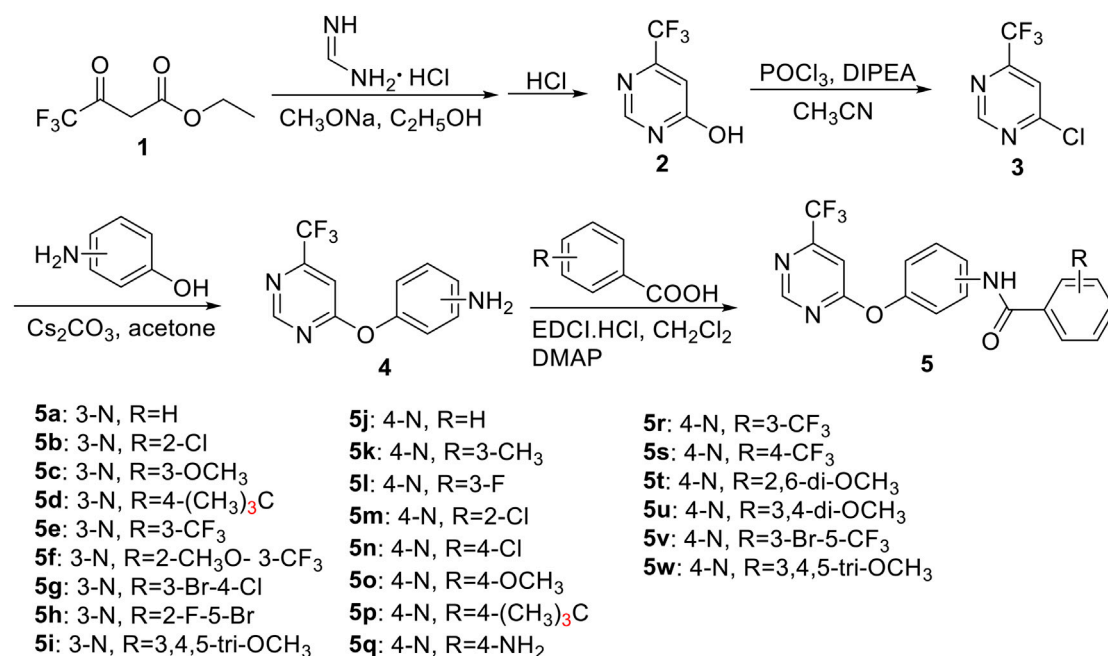
SCHEME 1 | Synthetic routes of the target compounds **5a–5w**.

Amide, an important negatively charged organic functional group, was widely present in active compounds, which has a broad spectrum of biological activities and is widely used in the field of pesticides and medicine (Maftei et al., 2015; Bhat et al., 2017). According to statistics, 25% of small-molecule drugs currently in the market contain at least one amide bond in their molecular structure (Kumari et al., 2020). At present, the fungicides of amide compounds have been used for decades, and the application of fungicides is the most effective measure to control phytopathogenic fungi. The use of fungicides can restore a lot of losses every year (Simkhada and Thapa, 2021; Wang R.-X. et al., 2021). The commercial varieties that have been developed include fentanyl, fluopicolide, flutolanil penthiopyrad, boscalid, etc. Amide fungicides can effectively prevent and control sheath blight, scab, and sclerotinia on crops such as wheat, corn, rapeseed, and rice. It can also effectively prevent and control fusarium wilt on tomato and potato diseases (AL-

Shammri et al., 2022). In our previous work, a series of synthesized pyrimidine-containing substituted amide derivatives exhibited good antifungal activity.

Based on the aforementioned considerations and our previous works (Wu et al., 2019; Wu et al., 2020; Wu et al., 2021; Yu et al., 2021), the amide is linked to the trifluoromethyl pyrimidine backbone through an oxygen ether. Finally, we designed and synthesized a novel series of trifluoromethyl pyrimidine derivatives containing an amide moiety due to the molecularly active splicing strategy (**Figure 1**).

MATERIALS AND METHODS

General Information

Melting points (m.p.) of the target compounds were tested on an XT-4 binocular microscope (Beijing Tech Instrument Co.,
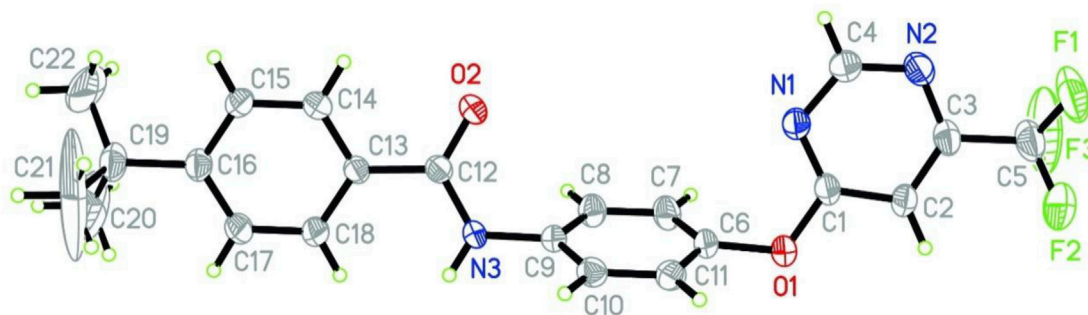
FIGURE 2 | X-ray crystal structure of **5p**.

China). [1]H nuclear magnetic resonance (NMR) and ^{13}C nuclear magnetic resonance (NMR) (solvent DMSO-d_6) spectral analyses were performed on a Bruker AvanceNEO spectrometer (600 MHz, Bruker, Germany) at room temperature. High-resolution mass spectrometry (HRMS) data were obtained on a Thermo Scientific Q Exactive Focus instrument (Thermo Fisher Scientific, Unites States). Analytical thin-layer chromatography (TLC) was prepared on silica gel GF$_{254}$.

Preparation of the Intermediates 2–4
Intermediates **2** and **3** were prepared using our previous research method in **Scheme 1** (Wu et al., 2019).

To a 100-ml three-necked bottle, intermediate **3** (20 mmol), KI (0.2 mmol), Cs$_2$CO$_3$ (30 mmol), and acetone (50 ml) were stirred under ice bath conditions. Then, dissolved 3-aminophenol or 4-aminophenol (20 mmol) in acetone (10 ml) was added dropwise, which continued to react for 7–8 h at 25°C. The chromatographic column was installed and eluted with petroleum ether and ethyl acetate in different proportions to gain intermediate **4**.

3-((6-(Trifluoromethyl)pyrimidin-4-yl)oxy)aniline (**4a**). White solid; yield 62.5%; m. p. 65–67°C; ^{1}H NMR (600 MHz, DMSO-d$_6$, ppm) δ: 8.94 (s, 1H, pyrimidine-H), 7.29 (s, 1H, pyrimidine-H), 7.06 (t, 2H, J = 7.8 Hz, Ph-H), 6.62 (d, 1H, J = 7.8 Hz, Ph-H), 6.42 (t, 1H, J = 2.4 Hz, Ph-H), 6.38 (d, 1H, J = 7.8 Hz, Ph-H), 5.40 (s, 2H, NH$_2$); ^{13}C NMR (125 MHz, DMSO-d$_6$, ppm)δ: 171.50, 169.88, 156.13 (q,J = 35.4 Hz), 147.42, 142.18, 122.26, 121.82 (q, J = 273.3 Hz), 114.96, 102.48; HRMS (ESI) calculated for C$_{11}$H$_9$ON$_3$F$_3$ [M + H]$^+$: 256.06839, found: 256.06922.

4-((6-(Trifluoromethyl)pyrimidin-4-yl)oxy)aniline (**4b**). White solid; yield 70.6%; m. p. 85–87°C; ^{1}H NMR (600 MHz, DMSO-d$_6$, ppm)δ: 8.96 (s, 1H, pyrimidine-H), 7.55 (s, 1H, pyrimidine-H), 6.93 (d, 2H, J = 9.0 Hz, Ph-H), 6.65 (d, 2H, J = 8.5 Hz, Ph-H), 5.17 (s, 2H, NH$_2$); ^{13}C NMR (125 MHz, DMSO-d$_6$, ppm) δ: 171.41, 159.88, 156.09 (q, J = 35.1 Hz), 147.45, 142.06, 122.17, 121.82 (q,J = 272.7 Hz), 114.83, 105.83; HRMS (ESI) calculated for C$_{11}$H$_9$ON$_3$F$_3$ [M + H]$^+$: 256.06839, found: 256.06910.

Preparation of the Target Compounds 5a–5w
To a 50-ml three-necked bottle, the key intermediate **4** (0.02 mol), aromatic acid (0.024 mol), and dimethylaminopyridine (DMAP, 0.0004 mol), dissolved in dichloromethane (20 ml), and 1-(3-dimethylaminopropyl)-3-ethylcarbodiimide hydrochloride

(EDCI, 0.03 mol) were added. The reactions were stirred at 25°C for 8–10 h. Then, the solvent was evaporated under vacuum and the residue was purified by column chromatography (ethyl acetate/petroleum ether = 10/1) to obtain the target compounds **5a–5w**.

N-(3-((6-(trifluoromethyl)pyrimidin-4-yl)oxy)phenyl)benzamide (**5a**). White solid; yield 53.4%; m. p. 125–127°C; ^{1}H NMR (600 MHz, DMSO-d$_6$, ppm) δ: 10.46 (s, 1H, -CONH-), 8.99 (s, 1H, pyrimidine), 7.83 (d, 2H, J = 7.2 Hz, Ph-H), 7.71 (t, 1H, J = 1.8 Hz, Ph-H), 7.78 (s, 1H, Ph-H), 7.72 (d, 1H, J = 8.4 Hz, Ph-H), 7.62 (t, 1H, J = 7.8 Hz, Ph-H), 7.56 (t, 1H, J = 7.8 Hz, Ph-H), 7.49 (t, 1H, J = 7.8 Hz, Ph-H), 7.04 (dd, 1H, J_1 = 1.8 Hz, J_2 = 8.4 Hz, Ph-H); ^{13}C NMR (150 MHz, DMSO-d$_6$, ppm) δ: 170.61, 166.25, 159.84, 156.13 (q, J = 35.6 Hz), 152.21, 141.21, 135.17, 132.19, 130.37, 128.88, 128.15, 121.81 (q, J = 273.3 Hz), 120.35, 118.30, 117.88, 117.13, 113.70, 106.66, 60.58, 55.79; HRMS (ESI) calculated for C$_{18}$H$_{12}$O$_2$N$_3$F$_3$ [M + Na]$^+$: 382.07681, found: 382.07725.

Crystal Data and Structure Determination
Single crystals of compound **5q** (deposition CCDC1965888) (DOI: 10.5517/ccdc.csd.cc23znrj) for X-ray diffraction were acquired from absolute ethanol by slow evaporation at 25°C. The crystallographic parameters are displayed in **Supplementary Table S1**. **Supplementary Table S1** showed that 3,107 independent reflections with the range of $2.072° \leq \theta \leq 22.729°$ were obtained. Compound **5q** crystallized in the monoclinic system and the space group is P2 (1)/c. The crystallographic parameters are as follows: a = 17.2341 (15) Å, b = 12.1803 (11) Å, c = 10.5015 (9) Å, α = 90°, β = 97.021 (2)°, γ = 90°, μ = 0.106 mm^{-1}, V = 2187.9 (3) Å^3, Z = 4, D_c = 1.316 g cm^{-3}, F (000) = 904.0, goodness of fit on F^2 = 1.000, R_1 = 0.1469, and wR_2 = 0.2676. Meanwhile, the crystal structure of **5q** was shown in **Figure 1**. **Figure 2** showed that the crystal structure of compound **5q** is monoclinic and contains two plane subunits of 6-(trifluoromethyl)pyrimidine and benzamide.

In Vitro Antifungal Activity Test
The antifungal activities against *Botryosphaeria dothidea* (*B. dothidea*), *Phompsis* sp., *Botrytis cinereal* (*B. cinerea*), *Colletotrichum gloeosporioides* (*C. gloeosporioides*), *Pyricutaria oryzae* (*P. oryzae*), and *Sclerotinia sclerotiorum* (*S. sclerotiorum*) of compounds **5a–5w** at 50 μg/ml were determined by the typical

TABLE 1 | The antifungal activities of the title compounds **5a–5w** at 50 µg/ml.

Compound	Inhibition rate (%)					
	B. dothidea	*Phomopsis* sp	*B. cinerea*	*C. gloeosporioides*	*P. oryzae*	*S. sclerotiorum*
5a	77.25 ± 3.15	59.22 ± 1.39	92.43 ± 3.25	53.89 ± 1.09	38.92 ± 1.86	72.18 ± 3.02
5b	88.72 ± 3.83	54.37 ± 1.67	96.76 ± 3.83	51.88 ± 3.61	43.64 ± 1.99	75.82 ± 2.08
5c	76.82 ± 3.22	70.73 ± 2.93	89.88 ± 2.89	64.12 ± 2.26	41.34 ± 2.31	76.28 ± 2.05
5d	67.34 ± 1.39	58.17 ± 1.94	71.35 ± 2.45	46.53 ± 1.23	36.05 ± 2.94	72.73 ± 1.12
5e	78.60 ± 3.70	75.19 ± 3.55	87.68 ± 3.17	49.11 ± 1.08	63.91 ± 1.34	75.45 ± 1.64
5f	73.87 ± 2.48	70.37 ± 3.03	89.04 ± 3.15	69.75 ± 1.53	52.49 ± 2.07	79.21 ± 2.30
5g	87.95 ± 4.47	85.70 ± 3.87	88.17 ± 1.61	43.17 ± 2.07	47.82 ± 2.64	74.00 ± 1.22
5h	71.81 ± 2.24	62.42 ± 2.71	89.51 ± 3.24	41.98 ± 3.51	61.48 ± 1.69	77.82 ± 1.29
5i	77.96 ± 3.42	64.14 ± 1.35	87.97 ± 3.58	43.56 ± 1.64	42.69 ± 2.81	57.27 ± 2.40
5j	89.89 ± 1.64	77.48 ± 2.63	96.84 ± 2.01	60.01 ± 1.09	41.65 ± 1.38	76.18 ± 1.05
5k	75.62 ± 2.18	65.34 ± 1.87	81.54 ± 1.25	41.98 ± 1.37	51.23 ± 3.05	70.36 ± 2.14
5l	88.84 ± 1.76	70.34 ± 2.25	100.00	39.21 ± 2.50	44.02 ± 1.96	65.45 ± 3.24
5m	74.26 ± 1.18	64.20 ± 2.35	90.40 ± 2.16	35.12 ± 1.79	30.11 ± 1.61	64.28 ± 2.18
5n	82.35 ± 1.15	68.23 ± 1.72	94.63 ± 3.46	41.58 ± 3.01	35.67 ± 3.81	73.27 ± 3.24
5o	86.49 ± 1.29	79.70 ± 1.53	92.84 ± 1.83	66.87 ± 1.94	40.16 ± 1.28	79.26 ± 3.58
5p	71.61 ± 2.34	58.81 ± 2.65	65.87 ± 1.32	52.15 ± 1.38	31.06 ± 2.54	58.27 ± 1.75
5q	60.48 ± 1.15	63.82 ± 2.83	76.48 ± 1.37	52.48 ± 2.00	49.70 ± 1.42	61.82 ± 1.09
5r	83.65 ± 1.70	79.69 ± 1.58	90.56 ± 1.17	41.58 ± 3.52	35.67 ± 2.62	73.27 ± 2.48
5s	90.12 ± 1.37	81.26 ± 1.19	93.47 ± 2.54	40.20 ± 1.08	37.33 ± 1.34	69.09 ± 2.81
5t	81.21 ± 1.20	79.65 ± 3.49	93.67 ± 1.67	50.05 ± 1.69	61.10 ± 2.20	72.64 ± 1.84
5u	76.82 ± 3.22	70.73 ± 2.93	89.88 ± 2.89	55.05 ± 2.22	47.25 ± 3.04	60.00 ± 2.19
5v	82.80 ± 1.44	82.34 ± 1.06	92.64 ± 1.13	51.88 ± 1.52	60.15 ± 1.11	82.73 ± 1.84
5w	75.86 ± 1.23	68.56 ± 2.35	92.31 ± 2.46	50.28 ± 0.98	47.36 ± 1.56	64.13 ± 2.27
Tebuconazole	100.00	100.00	96.45 ± 1.82	100.00	100.00	83.34 ± 1.18

mycelium growth rate method (Du et al., 2021; Wang W. et al., 2021), and tebuconazole was used as a positive control.

Insecticidal Activity Test

The insecticidal activities against *Spdoptera frugiperda* (*S. frugiperda*) and *Mythimna separata* (*M. separata*) of compounds **5a–5w** at 500 µg/mL were conducted according to the research method in the literature (Wang et al., 2020). Chlorantraniliprole was used as a positive control. Three replicates were performed for each treatment. The corrected mortality rate of compounds **5a–5w** were evaluated by the Abbott's formula.

$$\text{Corrected mortality rate (\%)} = (\text{Mortality rate of treatment group}$$
$$- \text{Mortality rate of control group})$$
$$/ (1 - \text{Mortality rate of control group}) \times 100$$

Anticancer Activity Test

The anticancer activities against the cells of compounds **5a–5w** at 5 µg/mL were conducted based on the MTT method (El-Dydamony et al., 2022). Doxorubicin was used as a positive control. Each treatment was repeated 3 times. The corrected mortality rates for compounds **5a–5w** were determined using the aforementioned formula.

RESULTS AND DISCUSSION

Chemistry

Using ethyl trifluoroacetoacetate as the initial reagent, as shown in **Scheme 1**, a series of novel trifluoromethyl

TABLE 2 | The insecticidal activities of the title compounds **5a–5w** at 500 µg/ml.

Compound	Mortality rate (%)	
	S. frugiperda	*M. separata*
5a	30.00 ± 1.60	16.70 ± 1.50
5b	13.33 ± 1.00	36.67 ± 1.80
5c	70.00 ± 1.50	60.00 ± 2.20
5d	50.00 ± 2.00	36.67 ± 2.00
5e	46.67 ± 1.50	30.00 ± 1.30
5f	60.00 ± 2.80	56.67 ± 1.20
5g	46.67 ± 1.00	30.00 ± 1.00
5h	50.00 ± 2.20	20.00 ± 1.50
5i	53.33 ± 1.20	33.33 ± 1.20
5j	26.67 ± 1.40	26.67 ± 1.80
5k	40.00 ± 2.00	50.00 ± 1.00
5l	26.67 ± 1.50	70.00 ± 2.20
5m	30.00 ± 1.00	16.67 ± 1.80
5n	40.00 ± 1.30	20.00 ± 1.20
5o>	80.00 ± 2.10	67.67 ± 2.50
5p	56.67 ± 1.00	46.67 ± 1.60
5q	43.33 ± 1.20	30.00 ± 2.00
5r	50.00 ± 1.80	27.00 ± 1.50
5s	66.67 ± 2.47	33.33 ± 1.30
5t	83.33 ± 1.56	20.00 ± 2.30
5u	73.33 ± 1.31	80.00 ± 1.50
5v	73.33 ± 2.03	43.33 ± 1.35
5w	90.00 ± 1.80	86.67 ± 2.42
Chlorantraniliprole	100	100

pyrimidine derivatives bearing an amide moiety were designed and synthesized via four-step reactions with the yields of 20.2–60.8% and the target compounds were

TABLE 3 | The anticancer activities of the title compounds 5a–5w at 5 µg/ml.

Compound	Mortality rate (%)			
	PC3	K562	Hela	A549
5a	0	10.03 ± 1.03	3.82 ± 2.64	15.76 ± 1.30
5b	15.53 ± 1.08	0	2.42 ± 1.06	13.65 ± 2.43
5c	0	19.59 ± 1.30	5.98 ± 1.09	13.74 ± 1.76
5d	5.80 ± 2.13	4.73 ± 2.15	11.37 ± 2.15	13.60 ± 2.80
5e	0	5.30 ± 1.16	0.55 ± 2.24	9.23 ± 1.32
5f	4.08 ± 1.67	21.88 ± 2.24	4.23 ± 1.25	12.47 ± 2.35
5g	0	15.52 ± 1.61	2.75 ± 1.60	14.51 ± 2.35
5h	0	10.98 ± 1.14	0	0.22 ± 1.05
5i	3.98 ± 1.22	3.53 ± 1.95	3.58 ± 1.69	15.15 ± 2.64
5j	31.01 ± 1.90	30.99 ± 2.06	25.22 ± 2.37	22.75 ± 2.94
5k	34.20 ± 2.01	37.80 ± 1.95	34.50 ± 1.89	28.50 ± 2.22
5l	54.94 ± 1.51	15.47 ± 1.38	32.20 ± 2.10	37.35 ± 2.00
5m	0	0	0	0
5n	51.71 ± 1.20	17.11 ± 1.52	30.78 ± 1.45	40.78 ± 1.09
5o	50.52 ± 1.22	19.40 ± 1.64	39.54 ± 2.22	38.78 ± 2.26
5p	9.20 ± 1.45	7.30 ± 2.01	20.40 ± 1.70	16.80 ± 3.26
5q	46.11 ± 1.54	31.40 ± 3.12	37.90 ± 3.01	42.42 ± 1.33
5r	55.32 ± 1.35	15.63 ± 0.96	34.65 ± 1.87	41.36 ± 1.51
5s	22.35 ± 1.16	5.28 ± 1.38	25.14 ± 2.03	15.24 ± 1.67
5t	0.37 ± 1.23	12.46 ± 2.26	6.87 ± 2.07	8.41 ± 2.83
5u	31.01 ± 1.64	30.99 ± 1.34	25.22 ± 2.35	22.75 ± 2.90
5v	64.20 ± 1.12	24.00 ± 1.92	48.25 ± 1.17	34.20 ± 2.31
5w	36.20 ± 1.36	35.40 ± 1.83	32.20 ± 2.62	31.80 ± 2.08
Doxorubicin	94.68 ± 1.05	72.81 ± 1.54	80.43 ± 1.36	89.57 ± 2.07

characterized by ^{1}H NMR, ^{13}C NMR, X-ray diffraction, and HRMS.

The ^{1}H NMR signals for compound 5a, a singlet appears 10.46 ppm indicates the presence of the -CONH- group. The CH proton of the 6-trifluoromethyl pyrimidine ring is located as two singlets at 8.99 and 7.78 ppm. Meanwhile, in the ^{13}C NMR data of compound 5a, two quartets at 156.13and121.81 ppm indicated the presence of -CF$_3$and C-CF$_3$ as characteristic peaks in the pyrimidine fragment. In addition, compound 5a was confirmed correctly with the [M + Na]$^+$ peaks by HRMS data.

Antifungal Activity Test In Vitro
Table 1 shows that compounds 5b, 5j, and 5l revealed excellent in vitro antifungal activity against B. cinerea, with the inhibition rates of 96.76, 96.84, and 100%, respectively, which were equal to or even better than that of tebuconazole (96.45%). Meanwhile, compound 5v had an inhibitory effect (82.73%) against S. sclerotiorum equal to that of tebuconazole (83.34%). Nevertheless, compounds 5a–5w revealed lower in vitro antifungal activities against B. Dothidea (60.48–90.12%), Phomopsis sp. (54.37–82.34%), C. gloeosporioides (35.12–69.75%), and P. oryzae (30.11–63.91%) than those of tebuconazole.

Insecticidal Activity Test
Table 2 shows that compounds 5a–5w indicated certain insecticidal activities against S. frugiperda and M. separata at 500 µg/ml, with the mortality rates of 13.3–90.0% and 16.7–86.7%, respectively, which were lower than those of chlorantraniliprole. Especially, compound 5w revealed fine insecticidal activities against Spdoptera frugiperda and Mythimna separata with the mortality rates of 90.0% and

86.7%, respectively. Meanwhile, compound 5o and 5t demonstrated moderate mortality rates of 80.0% and 83.3% against Spdoptera frugiperda.

Anticancer Activity Test
Table 3 shows that compounds 5a–5w indicated certain anticancer activities against PC3 (0–64.20%), K562 (0–37.80%), Hela (0–48.25%), and A549 (0–40.78%) at 5 µg/ml which were lower than those of doxorubicin. Particularly, compounds 5l, 5n, 5o, 5r, and 5v expressed moderate anticancer activities against PC3 with the inhibition rates of 54.94, 51.71, 50.52, 55.32, and 64.20%, respectively.

The preliminary structure–activity relationship showed that most compounds exhibited good activities against B. dothidea, Phomopsis sp., and B. cinerea. Especially for B. cinerea., majority of the compounds revealed inhibition rates higher than 80%. The inhibition rate of compound 5l was even up to 100%, which was exceeded by the control drug tebuconazole (96.45%). Excellent inhibitory activities also indicated the potential of these compounds as candidates or leading structure against B. cinerea.

CONCLUSION
In summary, twenty-three novel trifluoromethyl pyrimidine derivatives including an amide moiety were prepared based on amide and pyrimidine pharmacophore, and their structures were confirmed by ^{1}H NMR, ^{13}C NMR, X-ray diffraction, and HRMS determination. The preliminary biological activity screening indicated that most of the title compounds exhibited moderate to excellent antifungal and insecticidal activities. This study demonstrated the potential of trifluoromethyl pyrimidine derivatives including an amide moiety as the effective antifungal and insecticidal agents for crop protection and should be used as the reference for future research.

DATA AVAILABILITY STATEMENT
The original contributions presented in the study are included in the article/Supplementary Material; further inquiries can be directed to the corresponding authors.

AUTHOR CONTRIBUTIONS
WL, XT, JY, and QF contributed to the synthesis, purification, and characterization of all compounds, the activity research, and prepared the original manuscript. WW, PL, and HL designed and supervised the research and revised the manuscript. All authors have read and agreed to the published version of the manuscript.

REFERENCES

Abbas, N., Swamy, P. M. G., Dhiwar, P., Patel, S., and Giles, D. (2021). Development of Fused and Substituted Pyrimidine Derivatives as Potent Anticancer Agents (A Review). *Pharm. Chem. J.* 54 (12), 1215–1226. doi:10. 1007/s11094-021-02346-8

Abdel-Aziz, S. A., Taher, E. S., Lan, P., Asaad, G. F., Gomaa, H. A. M., El-Koussi, N. A., et al. (2021). Design, Synthesis, and Biological Evaluation of New Pyrimidine-5-Carbonitrile Derivatives Bearing 1,3-Thiazole Moiety as Novel Anti-Inflammatory EGFR Inhibitors with Cardiac Safety Profile. *Bioorg. Chem.* 111, 104890. doi:10.1016/j.bioorg.2021.104890

Abu-Zaied, M. A., Elgemeie, G. H., and Mahmoud, N. M. (2021). Anti-Covid-19 Drug Analogues: Synthesis of Novel Pyrimidine Thioglycosides as Antiviral Agents against SARS-COV-2 and Avian Influenza H5N1 Viruses. *ACS Omega* 6 (26), 16890–16904. doi:10.1021/acsomega.1c01501

AL-Shammri, K. N., Elkanzi, N. A. A., Arafa, W. A. A., Althobaiti, I. O., Bakr, R. B., and Moustafa, S. M. N. (2022). Novel Indan-1,3-Dione Derivatives: Design, Green Synthesis, Effect against Tomato Damping-Off Disease Caused by Fusarium Oxysporum and In Silico Molecular Docking Study. *Arab. J. Chem.* 15 (5), 103731. doi:10.1016/j.arabjc.2022.103731

Bhat, A. R., Dongre, R. S., Naikoo, G. A., Hassan, I. U., and Ara, T. (2017). Proficient Synthesis of Bioactive Annulated Pyrimidine Derivatives: A Review. *J. Taibah Univ. Sci.* 11 (6), 1047–1069. doi:10.1016/j.jtusci.2017.05.005

Borthakur, S. K., Kalita, P. K., and Borthakur, S. (2020). Synthesis and Antifungal Activities of 3,5-Diphenyl-7-Amino-[1,3]-Thiazolo[3,2-A]pyrimidine-6-Nitrile Derivatives. *J. Heterocycl. Chem.* 57 (3), 1–5. doi:10.1002/jhet.3863

Ding, L., Pannecouque, C., De Clercq, E., Zhuang, C., and Chen, F.-E. (2022). Discovery of Novel Pyridine-Dimethyl-Phenyl-DAPY Hybrids by Molecular Fusing of Methyl-Pyrimidine-DAPYs and Difluoro-Pyridinyl-DAPYs: Improving the Druggability toward High Inhibitory Activity, Solubility, Safety, and PK. *J. Med. Chem.* 65 (3), 2122–2138. doi:10.1021/acs.jmedchem.1c01676

Du, S., Yuan, Q., Hu, X., Fu, W., Xu, Q., Wei, Z., et al. (2021). Synthesis and Biological Activity of Novel Antifungal Leads: 3,5-Dichlorobenzyl Ester Derivatives. *J. Agric. Food Chem.* 69 (51), 15521–15529. doi:10.1021/acs.jafc.1c04022

El-Dydamony, N. M., Abdelnaby, R. M., Abdelhady, R., Ali, O., Fahmy, M. I., R. Fakhr Eldeen, R., et al. (2022). Pyrimidine-5-Carbonitrile Based Potential Anticancer Agents as Apoptosis Inducers through PI3K/AKT Axis Inhibition in Leukaemia K562. *J. Enzym. Inhib. Med. Chem.* 37 (1), 895–911. doi:10.1080/14756366.2022.2051022

Kumari, S., Carmona, A. V., Tiwari, A. K., and Trippier, P. C. (2020). Amide Bond Bioisosteres: Strategies, Synthesis, and Successes. *J. Med. Chem.* 63 (21), 12290–12358. doi:10.1021/acs.jmedchem.0c00530

Li, W., Zhang, J., Wang, M., Dong, R., Zhou, X., Zheng, X., et al. (2022). Pyrimidine-Fused Dinitrogenous Penta-Heterocycles as a Privileged Scaffold for Anti-Cancer Drug Discovery. *Curr. Top. Med. Chem.* 22 (4), 284–304. doi:10.2174/1568026622666220111143949

Maftei, C. V., Fodor, E., Jones, P. G., Freytag, M., Franz, M. H., Kelter, G., et al. (2015). N-Heterocyclic Carbenes (NHC) with 1,2,4-Oxadiazole-Substituents Related to Natural Products: Synthesis, Structure and Potential Antitumor Activity of Some Corresponding Gold(I) and Silver(I) Complexes. *Eur. J. Med. Chem.* 101, 431–441. doi:10.1016/j.ejmech.2015.06.053

Mermer, A., Keles, T., and Sirin, Y. (2021). Recent Studies of Nitrogen Containing Heterocyclic Compounds as Novel Antiviral Agents: A Review. *Bioorg. Chem.* 114, 105076. doi:10.1016/j.bioorg.2021.105076

Simkhada, K., and Thapa, R. (2021). Rice Blast, A Major Threat to the Rice Production and its Various Management Techniques. *Turk. JAF Sci.Tech.* 10 (2), 147–157. doi:10.24925/turjaf.v10i2.147-157.4548

Tsygankova, V., Andrusevich, Y., Shtompel, O., Kopich, V., Solomyanny, R., Bondarenko, O., et al. (2018). Phytohormone-Like Effect of Pyrimidine Derivatives on Regulation of Vegetative Growth of Tomato. *Int. J. Bot. Stud.* 2 (3), 91–102. Available at: https://www.researchgate.net/publication/324123283.

Wang, B., Wang, H., Liu, H., Xiong, L., Yang, N., Zhang, Y., et al. (2020). Synthesis and Structure-Insecticidal Activity Relationship of Novel Phenylpyrazole Carboxylic Acid Derivatives Containing Fluorine Moiety. *Chinese Chemical Letters.*. doi:10.1016/j.cclet.2019.07.064

Wang, R.-X., Du, S.-S., Wang, J.-R., Chu, Q.-R., Tang, C., Zhang, Z.-J., et al. (2021). Design, Synthesis, and Antifungal Evaluation of Luotonin A Derivatives against Phytopathogenic Fungi. *J. Agric. Food Chem.* 69 (48), 14467–14477. doi:10.1021/acs.jafc.1c04242

Wang, W., Cheng, X., Cui, X., Xia, D., Wang, Z., and Lv, X. (2021). Synthesis and Biological Activity of Novel Pyrazolo[3,4-d]pyrimidin-4-one Derivatives as Potent Antifungal Agent. *Pest Manag. Sci.* 77 (7), 3529–3537. doi:10.1002/ps.6406

Wei, L., Zhang, J., Tan, W., Wang, G., Li, Q., Dong, F., et al. (2021). Antifungal Activity of Double Schiff Bases of Chitosan Derivatives Bearing Active Halogeno-Benzenes. *Int. J. Biol. Macromol.* 179, 292–298. doi:10.1016/j.ijbiomac.2021.02.184

Wu, W., Chen, M., Fei, Q., Ge, Y., Zhu, Y., Chen, H., et al. (2020). Synthesis and Bioactivities Study of Novel Pyridylpyrazol Amide Derivatives Containing Pyrimidine Motifs. *Front. Chem.* 8, 522. doi:10.3389/fchem.2020.00522

Wu, W.-N., Chen, M.-H., Wang, R., Tu, H.-T., Yang, M.-F., and Ouyang, G.-P. (2019). Novel Pyrimidine Derivatives Containing an Amide Moiety: Design, Synthesis, and Antifungal Activity. *Chem. Pap.* 73, 719–729. doi:10.1007/s11696-018-0583-7

Wu, W.-N., Lan, W. J., Wu, C.-Y., and Fei, Q. (2021). Synthesis and Antifungal Activity of Pyrimidine Derivatives Containing an Amide Moiety. *Front. Chem.* 9, 695628. doi:10.3389/fchem.2021.695628

Yu, X., Lan, W., Chen, M., Xu, S., Luo, X., He, S., et al. (2021). Synthesis and Antifungal and Insecticidal Activities of Novel N-Phenylbenzamide Derivatives Bearing a Trifluoromethylpyrimidine Moiety. *J. Chem.* 2021, 8370407. doi:10.1155/2021/8370407

Zhang, N., Huang, M.-Z., Liu, A.-P., Liu, M.-H., Li, L.-Z., Zhou, C.-G., et al. (2020). Design, Synthesis, and Insecticidal/Acaricidal Evaluation of Novel Pyrimidinamine Derivatives Containing Phenyloxazole Moiety. *Chem. Pap.* 74, 963–970. doi:10.1007/s11696-019-00932-5

SUPPLEMENTARY MATERIAL

The Supplementary Material for this article can be found online at: https://www.frontiersin.org/articles/10.3389/fchem.2022.952679/full#supplementary-material

Comparison on Bioactivities and Characteristics of Polysaccharides From Four Varieties of *Gastrodia elata* Blume

Ning Ji[1,2], Peng Liu[3], Ni Zhang[2], Shengyan Yang[2] and Mingsheng Zhang[1]*

[1]*Key Laboratory of Plant Resource Conservation and Germplasm Innovation in Mountainous Region (Ministry of Education), Collaborative Innovation Center for Mountain Ecology & Agro-Bioengineering(CICMEAB), College of Life Sciences/Institute of Agro-bioengineering, Guizhou University, Guiyang, China, [2]Food and Pharmaceutical Engineering Institute, Guiyang University, Guiyang, China, [3]Dejiang Lvtong Gastrodia elata Development Co., Ltd., Tongren, China*

The composition, physicochemical properties, *in vitro* biological activity, and hypoglycemic activity exhibited by polysaccharides from four varieties of *G. elata* were investigated in this study; the four extracted GaE polysaccharides were termed as GaE-B (*G. elata Bl. f. glauca S. chow* polysaccharides), GaE-R (*G. elata Bl. f. elata* polysaccharides), GaE-Hyb (hybridization of *G. elata Bl. f. glauca S. chow* and *G. elata Bl. f. elata* polysaccharides), and GaE-G (*G. elata Bl. f. viridis Makino* polysaccharides). As revealed by the results, the GaE polysaccharides were found with the same monosaccharide composition, primarily including glucose, whereas the content of each variety was significantly different. In addition, different degrees of differences were found in the *in vitro* antioxidant and hypoglycemic activity, molecular weight, yield, and chemical composition exhibited by the abovementioned varieties. However, GaE-B and GaE-Hyb were found with similar physical properties, chemical composition, and antioxidant and hypoglycemic activity. GaE-R had the lowest yield, total sugar content, and molecular weight, whereas it involved higher xylose, binding protein, and polyphenols as well as higher antioxidant and hypoglycemic activity. In contrast, GaE-G was found with the highest yield, total sugar content, and molecular weight, whereas it contained the lowest xylose, binding protein, and polyphenols, as well as the weakest antioxidant and hypoglycemic activity. In brief, the polysaccharide of *G. elata*, a plant resource for homology of medicine and food, could more significantly enhance the biological activity of *G. elata* as it was released in the process of decocting and stewing. To be specific, the assessment of polysaccharide activity alone suggested that GaE-R was the best.

Keywords: *Gastrodia elata* blume., polysaccharide, variety, physicochemical property, biological activity

1 INTRODUCTION

Over the past few years, increasing studies have been conducted on various physiological and biochemical characteristics of plant polysaccharides. Plant polysaccharides, a natural polymer, have less irritation to the body when exerting their pharmacological properties. The bioactivities of plant polysaccharides are largely manifested in anti-inflammatory, antioxidation, anti-tumor, anti-virus, anti-diabetes, immune regulation, etc. (Yue et al., 2017; Chen L. et al., 2018; Chen Y. et al., 2018; Fan

et al., 2018; Ma et al., 2018). The above mentioned characteristics of plant polysaccharides are capable of facilitating the development and utilization of a range of health foods and medicines. The physical and chemical properties exhibited by polysaccharides take on a critical significance to their physiological and functional properties. In particular, the chemical composition, molecular weight and distribution, monosaccharide composition, and functional group differences in polysaccharides have effects on the physiological and biochemical properties exhibited by polysaccharides (Nie et al., 2017). Accordingly, studying the physical and chemical properties exhibited by plant polysaccharides can assess the biological activity and application value of the abovementioned plants from one side.

G. eleta (Orchidaceae) refers to an orchid plant, a fully mycoheterotrophic plant, forming a symbiotic relationship with Armillaria mellea (Cha and Igarashi, 1995) during its growth. It is a traditional Chinese herbal medicine (Yuan et al., 2018). It has been recorded in ancient China, and its dry tubers are commonly used as medicine (Chinese Pharmacopoeia Commission, 2015). It is currently planted in East Asian nations (e.g., China, Japan, South Korea, and India) (Lee et al., 2014). *G. elata* is largely adopted to treat dizziness, cancer, depression, epilepsy, convulsion, inflammation, liver protection, anti-aging, neuroprotection, and other diseases (Chen J. et al., 2016; Chen L. et al., 2016; Zhan et al., 2016; Kim et al., 2017; Lin et al., 2018; Wang et al., 2018; Zhang et al., 2018; Ma et al., 2020). The major medicinal components of *G. elata* are gastrodin p-hydroxybenzyl alcohol and p-hydroxybenzaldehyde (Chinese Pharmacopoeia Commission, 2015; Li et al., 2019). Second, *G. elata* also contains polyphenols, polysaccharides, organic acids, and other active components (Ojemann et al., 2006). In China, different varieties of *G. elata* have been employed for cultivation under forest (Zhan et al., 2016). The major difference of *G. elata* varieties refers to the not consistent color of the stem after the process of bolting and flowering. At present, *G. elata Bl. f. glauca S. chow*, *G. elata Bl. f. elata*, *G. elata Bl. f. viridis Makino*, and Hybrid *G. elata Bl.* (Hybridization of *G. elata Bl. f. glauca S. chow* and *G. elata Bl. f. elata*) have been primarily planted in Guizhou, China, whereas the adaptability and growth trend of the varieties of *G. elata* are different, thus resulting in the differences of biological activities (Zhan et al., 2016). Over the past few years, *G. elata* polysaccharides have aroused wide attention for their various physiological activities and functions (e.g., anticancer, bioactivity on gut microbiota, anti-aging, immunomodulation, neuroprotection, and prevention of cardiovascular and cerebrovascular diseases, as well as other activities) (Chen et al., 2011; Kim et al., 2012; ; Chen L. et al., 2016; Zhou et al., 2017; Chen L. et al., 2018; Huo et al., 2021). As revealed by the abovementioned activity results, *G. elata* polysaccharides play a vital role in the whole pharmacological activity of *G. elata*. Although a considerable number of reports on the structure, composition, and activity of *G. elata* polysaccharide have been conducted, the focus has been placed on a single variety, and there have been rare relevant research reports on the differences in physical properties, chemical properties, and biological activities between different varieties.

In this study, the selection of varieties in the cultivation process has been controversial in the experimental *G. elata* planting area, Dejiang County, Guizhou Province, China. At this stage, *G. elata* polysaccharides have also been recognized as one of the key natural compounds in the study of active components of *G. elata*. Thus, this study aimed to compare the physicochemical properties and biological activities of non-starch polysaccharides in different varieties of *G. elata* from the perspective of *G. elata* polysaccharides, so as assess the differences of polysaccharides between different varieties of *G. elata*. Indeed, the differences of polysaccharides do not represent the differences of the overall quality of *G. elata*, and the differences of varieties cannot represent the differences between regions. Impacted by the different natural conditions (e.g., weather, altitude, soil, and rainfall in the planting area), the physical and chemical indicators of *G. elata* planted will be different. As an ancient saying in China goes, "A side water and soil raises a side person" (i.e., the unique features of a local environment always give special characteristics to its inhabitants). We consider that this ancient saying is also suitable for plants. The difference of polysaccharide in different varieties of *G. elata* planted in our experimental area does not represent the variety difference in the entire Chinese region, whereas they can serve as an assessment of variety selection and application value of locally planted *G. elata*.

2 MATERIALS AND METHODS

2.1 Materials

The fresh tubers of four varieties of *G. elata* (*G. elata* Bl. f. glauca S. chow, *G. elata* Bl. f. elata, Hybridization of *G. elata* Bl. f. glauca S. chow, and *G. elata* Bl. f. elata (*G. elata Bl. f. elata* was the female parent and *G. elata Bl. f. glauca S. chow* was the male parent) and G. elata Bl. f. viridis Makino, the extracted polysaccharides were termed GaE-B, GaE-R, GaE-Hyb, and GaE-G) were collected from the planting base of Dejiang Lvtong *G. elata* Blume. Development Co., Ltd. ($108°8'49.36''$E, $28°8'1.12''$N, and the altitude was 1091.32 m, the annual average temperature was 16.0°C, and the annual average rainfall was 1237 mm), Guizhou Province, China, and they were planted at the same time. The fresh *G. elata* tubers were washed and cut into slices. Subsequently, the tubers were dried at 50°C, and the moisture content was controlled in a range of 3%–5% (determination of moisture content by the constant weight method). Next, the tubers were crushed into powder and passed through a 60-mesh sieve. The sieved powder was stored in sealed bags for standby. The treated powder was soaked in petroleum ether (material liquid ratio was 1:3), and the mixture was stirred continuously with a mechanical stirrer (boiling point range: 60–90°C). The petroleum ether was replaced every 8 h for a total of 3 times. The powder soaked in petroleum ether was dried and then soaked in 95% ethanol (v/v) for 3 times (material liquid ratio was 1:3). In the soaking period, a mechanical agitator was used for continuous stirring. After the filtration, the sample was dried at 40°C for later use (termed GaEs). Monosaccharides,

pigments, lipids, oligosaccharides, and small molecular impurities could be removed through soaking in petroleum ether and ethanol.

The reagents applied in this study consisted of ascorbic acid (Vc), acarbose, bovine serum albumin (BSA), 1-pheny-3-methyl-5-pyrazolone (PMP), trifluoroacetic acid (TFA), 3-phenylphenol, 2,2-diphenyl-1-picrylhydrazyl (DPPH), phenazine methosulfate, β-nicotinamide adenine dinucleotide (NADH), 2,2-diphenyl-1-picrylhydrazyl (DPPH), nitrotetrazolium blue chloride (NBT), 2,2′-azino-bis(3-ethylbenzothiazoline-6-sulfonic acid) diammonium salt (ABTS), 3-(2-pyridyl)-5,6-bis(4-phenylsulfonicacid)-1,2,4-triazine monosodium salt, α-glucosidase (50 U/mg, BR), α-amylase (50 U/mg, BR), salicylic acid, ethylenediaminetetraacetic acid (EDTA), 4-nitrophenyl α-D-galacto-pyran-oside (PNGP), 3,5-dinitrosalicylic acid, and standard dextran (10, 40, 70, 100, 150, 270, and 410 Kda). Standard monosaccharides (Purity ≥ 99%), consisting of D-mannose (Man), L-rhamnose (Rha), D-glucuronic acid (GlcA), D-galacturonic acid (GalA), D-lactose (Lac), D-glucose (Glc), D-galactose (Gal), D-xylose (Xyl), and L-arabinose (Ara) originated from Shanghai Macklin Biochemical Technology Co., Ltd. (Shanghai, China), and other used chemical reagents were of analytical grade and purchased locally. Dialysis bags (molecular weight cut-off, 8000–14,000 Da) were provided by Union Carbide Co., Ltd. (United States).

2.2 Polysaccharide Extraction and Isolation

The GaE polysaccharide was extracted using the water extraction method (Yan et al., 2018) and modified slightly. 25.0 g of pretreated *G. elata* powder was poured into 500 ml distilled water and extracted in a 90°C water bath for 4 h. After the extraction, the mixture was subjected to vacuum decompression filtration. Next, the filter residue was extracted and filtered using the same method, and the two filtrates were combined. Subsequently, the filtrate was concentrated to 1/5 of the original volume using a rotary evaporator (RV10, IKA, Germany) in a 50°C water bath. The concentrated solution was precipitated with anhydrous ethanol (ethanol: concentrated solution = 5:1, v/v) and then placed at 4°C for 12 h, so it could be sufficiently precipitated. Afterward, the mixed solution was centrifuged at 6500 rpm for 10 min, and the precipitates of combining were washed 3 times with anhydrous ethanol, anhydrous ether, and acetone. In the following, the precipitate was dissolved with a small amount of distilled water. The following used sevag reagent (n-butanol: trichloromethane = 1:4, v/v) to remove the associated protein (Sevag et al., 1938). The aqueous layer after the removal of the protein was placed into dialysis bag (molecular weight cut-off 8000–14,000 Da) and then dialyzed for 72 h in flowing distilled water. After the dialysis, the solution was placed in a vacuum freeze dryer (BenchTop Pro-EL, Virtis, United States) for vacuum freeze-drying, all extraction steps were repeated 3 times, and the average value was taken. The partially purified *G. elata* polysaccharides were termed below: GaE-B (*G. elata Bl. f. glauca S. chow polysaccharides*), GaE-R (*G. elata Bl. f. elata*

polysaccharides), GaE-Hyb (Hybridization of *G. elata Bl. f. glauca S. chow and G. elata Bl. f. elata polysaccharides*), and GaE-G (*G. elata Bl. f. viridis Makino polysaccharides*). The yield (%) of *G. elata* polysaccharides was obtained by:

$$\text{Yield}\,(\%, \text{w/w}) = \frac{\text{weight of dried polysaccharides}\,(g)}{\text{weight of extracted GaEs powder}\,(g)} \times 100.$$

2.3 Chemical Composition Determination

The total sugar content of the GaE polysaccharide was obtained using the phenol–sulfuric acid method (DuBois et al., 1956) with D-glucose as the standard. The protein content was obtained using the Bradford method (Bradford, 1976) with bovine serum albumin (BSA) as the standard, uronic acid content was obtained using the m-hydroxybiphenyl method (Blumenkrantz and Asboe-Hansen, 1973), total phenol content was obtained using the Folin–Ciocalteu method (Chen et al., 2014) with gallic acid as the standard, and sulfate was obtained using the barium chloride–gelatin method (Tabatabai, 1974), and total flavonoids were obtained by colorimetry (Zhishen et al., 1999) with rutin as the standard. All indicators were measured 3 times.

2.4 Determination of Molecular Weight

The molecular weight (Mw) of the GaE polysaccharide was measured using the high-performance gel permeation chromatography (HPGPC) method in accordance with a previous report (He et al., 2018). A Shimadzu LC-2010A HPLC system (Shimadzu Co., Ltd., Japan) was used as the experimental instrument, the detector was refractive index detector (RID-10A, Shimadzu Co., Ltd., Japan), and TSK-Gel G4000 SWXL column (7.8 mm × 300 mm, Tosoh Biosep, Japan) was adopted as the chromatographic column. The experimental methods are elucidated below. The sample solution (1.5 mg/ml) was first filtered with a pore size of 45 μm aqueous membrane, and 25 μL was injected into the chromatographic column each time, 0.02 mol/L KH_2PO_4 served as the mobile phase, and the elution process was performed at a flow rate of 0.7 ml/min. The chromatographic column temperature was maintained at 35°C. The same method for dextran was employed as a standard (Macklin Biochemical Technology Co., Ltd., Shanghai, China) with different molecular weights (10, 40, 70, 100, 150, 270, and 410 kDa).

2.5 Monosaccharide Composition Analysis

First, 10 mg of the GaE polysaccharide sample was dissolved in 4 ml of trifluoroacetic acid solution (4 mol/L), sealed and hydrolyzed at 120°C for 4 h. Subsequently, PMP derivatization was performed using the method of Nie et al. (2017). The derivatized samples were investigated through HPLC with the use of a Shimadzu LC-2010A HPLC system (Shimadzu Co., Ltd., Japan) and a detector: UV analysis detector. A Wonda Sil C18-WR (4.6 mm × 150 mm×5 μm, Shimadzu Co., Ltd., Japan) was used as the chromatographic column. The specific method is elucidated below: the mobile phase was a mixture of 80% of 0.06 M phosphate buffer (pH 6.5) and 20% acetonitrile, at a flow rate of 0.8 ml/min

with a UV detection wavelength of 250 nm, an injection volume of 10 μL and at a column temperature of 28°C. The monosaccharide standards were studied using the same method.

2.6 Fourier-Transform Infrared Spectroscopy Analysis

First, 1.5 mg of the dried GaE polysaccharide powder and 150 mg of the dried potassium bromide powder were mixed, ground, and pressed into granules. Subsequently, the granules were scanned in the range of 4000–400 cm^{-1} through Fourier transform infrared (FT-IR) spectroscopy (Nicolet iS5, Thermo Fisher Scientific Co., Ltd., United States).

2.7 Thermal Analysis

The GaE polysaccharide sample was fixed in a platinum crucible, and the thermal characteristics were studied with a thermogravimetric analyzer TGA, DTG-60A (Shimadzu Co., Ltd., Japan). The specific experimental operation is elucidated below. The nitrogen gas was maintained at a flow rate of 50 ml/min in the measurement. The initial temperature ranged from 30°C to 800°C, and the temperature increased at 10°C/min.

2.8 Measurement of Zeta Potential and Particle Size

The sample of the GaE polysaccharide was dissolved in distilled water to prepare the solution (1 mg/ml). A Phase Analysis Light Scattering analyzer (90 Plus PALS, Brookhaven Instruments Co., Ltd., United States) was employed to determine the zeta potential and particle size of the GaE polysaccharide. The respective sample was measured 3 times, and the average value was taken.

2.9 Scanning Electron Microscopy Analysis

The dried *G. elata* polysaccharide samples were sprayed with gold–palladium alloy and scanned using a scanning electron microscope (Gemini 300, ZEISS, Germany). Scanning electron microscopy (SEM) images were captured at a magnification of 300× and 1500× based on a voltage of 2 kV acceleration under high vacuum conditions.

2.10 Determination of Antioxidant Activities

2.10.1 Superoxide Radical Scavenging Activity

The superoxide radical scavenging activity of the GaE polysaccharide was assessed using a method described previously (Bi et al., 2013) with slight modifications. The GaE polysaccharide samples of different concentrations (0.25–5.00 mg/L) consisted of 100 μL and 100 μL phenazine methosulfate (PMS) solutions (120 μmol/L), nitrotetrazolium blue chloride (NBT) solution (300 μmol/L), and β-nicotinamide adenine dinucleotide (NADH) solution (936 μmol/L). A 100 μmol/L phosphate buffer (PBS, pH 7.4) was added. Subsequently, the mixture was stirred and placed in the dark environment at 25°C for reaction for 5 min. Furthermore, PBS (0.1 mol/L, pH 7.4) solution served as a control, the absorbance value of the mixture was measured at

560 nm, and the Vc solution was employed as a positive control. The scavenging activity is expressed as:

$$\text{Scavenging activity}(\%) = \left(1 - \frac{A_1 - A_2}{A_0}\right) \times 100,$$

where A_0 denotes the absorbance value of control (PBS instead of sample); A_1 represents the absorbance value of the mixed sample; and A_2 expresses the absorbance value of only sample without NBT (PBS instead of NBT).

2.10.2 DPPH Radical Scavenging Activity

The DPPH radical scavenging activity of the GaE polysaccharide was measured using the method of Chen et al. with slight modification (Chen et al., 2019a). DPPH was dissolved in anhydrous ethanol to prepare 0.4 mmol/L solution. It was used right after it was ready. One milliliter of sample solutions was mixed with different concentrations (0.25–5.00 mg/L), and 1 ml of DPPH (0.4 mmol/L) solution was mixed. The solution was stirred and then incubated at a dark environment at 25°C for 30 min. The absorbance value of the mixture was measured at 517 nm, and the Vc solution served as a positive control. The scavenging activity is expressed as

$$\text{Scavenging activity}(\%) = \left(1 - \frac{A_1 - A_2}{A_0}\right) \times 100,$$

where A_0 denotes the absorbance value of control (distilled water instead of sample); A_1 is the absorbance value of the mixed sample; and A_2 is the absorbance value of only sample without DPPH (anhydrous ethanol instead of DPPH).

2.10.3 Hydroxyl Radical Scavenging Activity

The hydroxyl radical scavenging activity of the GaE polysaccharide was measured using the method reported by Qiao et al. with slight modification (Qiao et al., 2009). The GaE polysaccharide solution (0.5 ml) of different concentrations (0.25–5.00 mg/L) was mixed with 0.5 ml of salicylic acid solution (9 mmol/L), 0.5 ml of FeSO$_4$ solution (9 mmol/L), and 0.5 ml of H$_2$O$_2$ solution (9 mmol/L). Subsequently, the mixture was stirred and incubated at 37°C for 40 min. The absorbance value of the mixture was measured at 510 nm, and the Vc solution was employed as a positive control. The scavenging activity is expressed as

$$\text{Scavenging activity}(\%) = \left(1 - \frac{A_1 - A_2}{A_0}\right) \times 100,$$

where A_0 denotes the absorbance value of control (distilled water instead of sample and H$_2$O$_2$); A_1 is the absorbance value of the mixed sample; and A_2 represents the absorbance value of only sample without H$_2$O$_2$ (distilled water instead of H$_2$O$_2$ solution).

2.10.4 ABTS Radical Scavenging Activity

The ABTS radical scavenging activity of the GaE polysaccharide was measured using the method described by Erel (2004) with minor modification. In brief, the reaction solution was prepared, 9.9 mg potassium persulfate was mixed with 15 ml of 5.55 mmol/L ABTS

aqueous solution, stirred, and then incubated in a dark environment at 25°C for 15 h to form a blue-green solution. Subsequently, the mixture was diluted with PBS (100 μmol/L, pH 7.4) solution, and the absorbance value was determined at 734 nm. When the absorbance value of the mixture reached 0.70 ± 0.03, it could be employed for the GaE polysaccharide scavenging ABTS radial scavenging assay in 3 h. Afterward, the GaE polysaccharide samples of different concentrations (0.25–5.00 mg/L) were reacted with 0.2 and 8 ml ABTS solutions for 25 min, and then the absorbance value of the mixture was measured at 734 nm. The Vc solution served as a positive control. The scavenging activity is expressed as:

$$Scavenging\ activity\ (\%) = \left(1 - \frac{A_1 - A_2}{A_0}\right) \times 100,$$

where A_0 denotes the absorbance value of control (distilled water instead of sample); A_1 represents the absorbance value of the mixed sample; and A_2 is the absorbance value of only sample without ABTS (distilled water instead of ABTS solution).

2.10.5 Ferrous Ion-Chelating Ability

The ferrous ion-chelating activity of the GaE polysaccharide was measured using the method reported by Wang et al. with some modifications (Wang et al., 2012). First, 3 ml of distilled water was mixed with 75 μL of $FeCl_2$ solution (2 mmol/L), and then 1.5 ml of the GaE polysaccharide solution with different concentrations (0.25–5.00 mg/L) was added. The mixed solution was maintained at 25°C for 3 min, and then 0.15 ml of ferrozine solution (5 mmol/L) was added. Subsequently, the mixture was shaken and incubated at 25°C for 10 min. The absorbance value of the mixture was measured at 562 nm, and the ethylenediaminetetraacetic acid (EDTA) solution was employed as a positive control. The chelating ability is expressed as:

$$Scavenging\ activity\ (\%) = \left(1 - \frac{A_1 - A_2}{A_0}\right) \times 100,$$

where A_0 denotes the absorbance value of control (distilled water instead of sample); A_1 represents the absorbance value of the mixed sample; and A_2 expresses the absorbance value of only sample without $FeCl_2$ (distilled water instead of $FeCl_2$ solution).

2.10.6 Reducing Power

The reducing power of the GaE polysaccharide was measured using the reported method of Yuan et al. with slight modified (Yuan et al., 2005). First, 1.2 ml of the GaE polysaccharide of different concentrations (0.25–5.00 mg/L) was mixed with 3 ml of phosphate buffer (0.2 mol/L, pH 6.6) and 3 ml of $K_3Fe(CN)_6$ solution (1%, w/v), and then it was placed in a 50°C environment and incubated for 20 min. After the reaction was complete, 1.2 ml of TCA solution (10%, w/v) was added, and then the mixture was centrifuged at 3,500 rpm for 10 min. Subsequently, 2 ml of supernatant was mixed with 2 ml of distilled water and 1.2 ml of $FeCl_3$ (0.1%, w/v), and the absorbance of the mixture was measured at 700 nm after 10 min. The Vc solution served as a positive control. The reducing power is expressed as:

$$Reducing\ power = A_1 - A_0$$

where A_0 denotes the absorbance value of control (distilled water instead of $FeCl_3$ solution) and A_1 represents the absorbance value of the mixed sample.

2.11 Hypoglycemic Activity Assay Analysis

2.11.1 α-Glucosidase Inhibitory Activity

The α-glucosidase inhibitory activity of the GaE polysaccharide was measured using the previous method with slight modification (Jia et al., 2017). First, 1.2 ml of the GaE polysaccharide of different concentrations (0.25–5.00 mg/L) was mixed with 75 μL of α-glucosidase solution (2 U/mL) and then incubated at 37°C for 10 min. Subsequently, 75 μL of pNPG (6 mmol/L) was added, and the mixture was incubated at 37°C for 20 min. After the reaction time was completed, 100 μL of Na_2CO_3 solution (1 mol/L) was added, and the reaction was terminated. The mixture was placed for 10 min, and the absorbance value was measured at 400 nm. The acarbose solution was employed as a positive control. The inhibition activity is expressed as:

$$Inhibitory\ activity\ (\%) = \left(1 - \frac{A_1 - A_2}{A_0}\right) \times 100,$$

where A_0 denotes the absorbance value of mixture without sample (distilled water instead of sample solution); A_1 represents the absorbance value of the mixed sample; and A_2 expresses the absorbance value of mixture without α-glucosidase (distilled water instead of α-glucosidase solution)

2.11.2 α-Amylase Inhibitory Activity

The α-amylase inhibitory activity of the GaE polysaccharide was measured using the method of Duan with slight modification (Duan et al., 2018). First, 0.2 ml of the GaE polysaccharide of different concentrations (0.25–5.00 mg/L) was mixed with 0.2 ml of phosphate buffer (0.2 mol/L, pH 6.9) and 0.2 ml of α-amylase solution (0.5 mg/ml). The mixture was incubated at 37°C for 10 min. Subsequently, 0.2 ml of soluble starch solution (1%, w/v) was added to the mixture for 10 min. After the reaction, 0.4 ml of DNS reagent was added to the mixture and kept in a 90°C water bath for 5 min. When the mixture was cooled to an ambient temperature, the absorbance value of the mixture was measured at 540 nm. The acarbose solution served as a positive control. The inhibition activity is expressed as:

$$Inhibitory\ activity\ (\%) = \left(1 - \frac{A_1 - A_2}{A_0}\right) \times 100,$$

where A_0 denotes the absorbance value of mixture without sample (distilled water instead of the polysaccharide sample solution); A_1 represents the absorbance value of the mixed sample; and A_2 expresses the absorbance value of mixture without α-amylase (distilled water instead of α-amylase solution).

2.12 Statistical Analysis

The three repeated experiments with the respective group of data are expressed as mean ± standard deviation (SD) and were plotted using origin 2018. Analysis of variance (ANOVA) was conducted through Dunnett's multiple-range tests (SPSS Statistics 24 software); p-value < 0.05 was considered statistically

Varieties	GaE-B	GaE-R	GaE-Hyb	GaE-G
Yield (%)[1]	5.67 ± 0.31^c	4.21 ± 0.25^d	6.63 ± 0.22^b	7.82 ± 0.35^a
Chemical composition (W%)[1]				
Total sugar	65.62 ± 1.24^b	60.21 ± 0.96^c	67.18 ± 1.82^b	73.85 ± 2.36^a
Protein	2.72 ± 0.18^c	4.11 ± 0.29^a	3.21 ± 0.11^b	1.34 ± 0.08^d
Total polyphenol	0.62 ± 0.004^b	0.84 ± 0.006^a	0.53 ± 0.003^c	0.32 ± 0.002^d

[1]*The values are presented as mean ± SD (standard deviation).*
Values with a different letter of superscripts (a, b, c, and d) are significantly different (p < 0.05).

TABLE 2 | Monosaccharide composition of the *Gastrodia elata* polysaccharide with four different varieties.

Monosaccharide compositions (mol%)	GaE-B	GaE-R	GaE-Hyb	GaE-G
Mannose	5.36	5.07	4.83	3.64
Rhamnose	2.64	3.18	3.02	2.96
Glucose	77.35	71.01	77.58	81.88
Galactose	5.33	6.41	4.76	3.11
Xylose	9.34	14.32	9.81	8.40

significant. To be specific, the IC_{50} values of radical scavenging and enzyme inhibitory activities by multiple comparisons of means were studied through the least significance difference (LSD) test of differences between the groups.

3 RESULTS AND DISCUSSION

3.1 Chemical Composition of the GaE Polysaccharide

Table 1 lists the yields and chemical compositions of the GaE polysaccharides. The yield of GaE-G was found as the highest (7.82%), the yield of GaE-R was the lowest (4.21%), and GaE-B and GaE-Hyb were between them, which were 5.67% and 6.63%, respectively. The total sugar content of GaE-G was significantly higher than those of the other three groups ($p < 0.05$), and the content of GaE-R was found as the lowest (60.21%). Binding proteins and phenols could affect the functional properties exhibited by polysaccharides (Peng et al., 2012). Among the GaE polysaccharides, the content of binding proteins and total phenol of GaE-R was significantly higher than that of GaE-B, GaE-Hyb, and GaE-G, so GaE-R might exhibit stronger biological activity than the other three groups. Moreover, uronic acid, flavonoids, and sulfate radicals in polysaccharides had an effect on the biological activity exhibited by polysaccharides (Sun et al., 2008; Peng et al., 2012), whereas no uronic acid (detected by Blumenkrantz et al.'s method, Farhadi, 2017), flavonoids (Zhishen et al.'s method detection, Oliveira et al., 2016), and sulfate (Tabatabai's method detection, Thaipong et al., 2006) were detected in the GaE polysaccharides. In brief, obvious differences were found in the chemical composition of the GaE polysaccharides, which might lead to differences in their biological activities.

3.2 Monosaccharide Composition of the GaE Polysaccharide

The composition and content of monosaccharides often had an effect on the characteristic of polysaccharides. The monosaccharide composition of the GaE polysaccharides hydrolyzed after PMP derivatives were confirmed through comparison with the retention time of the HPLC chromatogram of the standard. As depicted in **Table 2** and **Figure 1**, the GaE polysaccharides were heteropolysaccharides, and the GaE polysaccharides comprised mannose (Man), rhamnose (Rha), glucose (Glc), galactose (Gal), and xylose (Xyl). However, the content of each monosaccharide was different among various varieties. The GaE polysaccharides are primarily composed of glucose and xylose. To be specific, the content of glucose was found as the highest, higher than 50% in the respective group. The contents of GaE-B and GaE-Hyb glucose were close, and the content of glucose in GaE-G was found as the highest, reaching 81.88%, and the content of GaE-R was the lowest, only 71.01%. Second, the xylose content ranked second in the monosaccharide composition of the GaE polysaccharides. The GaE-R achieved the highest content of xylose, reaching 14.32%, and GaE-G achieved the lowest content of 8.4%, while the xylose contents of GaE-B and GaE were still close. It was found that the higher the content of Gal in polysaccharides, the stronger its antioxidant activity would be (Xing et al., 2005; Fan et al., 2014). Among the GaE polysaccharides, the Gal content in GaE-R was found as the highest at 6.41%, followed by GaE-B and GaE-Hyb, and the lowest was found as GaE-G, with a content of 3.11%. Accordingly, the content of Gal and Xyl might be one of the factors affecting the activity of the GaE polysaccharides.

3.3 Molecular Weight of the GaE Polysaccharide

As depicted in **Figure 2**, the HPGPC curves suggested that the GaE polysaccharides showed a wide molecular weight (*Mw*) distribution, which revealed that the GaE polysaccharides were heterogeneous polysaccharides, and they all had four main peaks. The molecular weights of the respective group arranged from large to small, and GaE-B was 381.46 KDa (9.36%, Peak1), 264.51 KDa (7.07%, Peak2), 167.36 KDa (12.78%, Peak3), and 48.63 KDa (70.78%, Peak4); GaE-R was 289.45 kDa (16.29%, peak1), 181.32 kDa (11.64%, peak2),
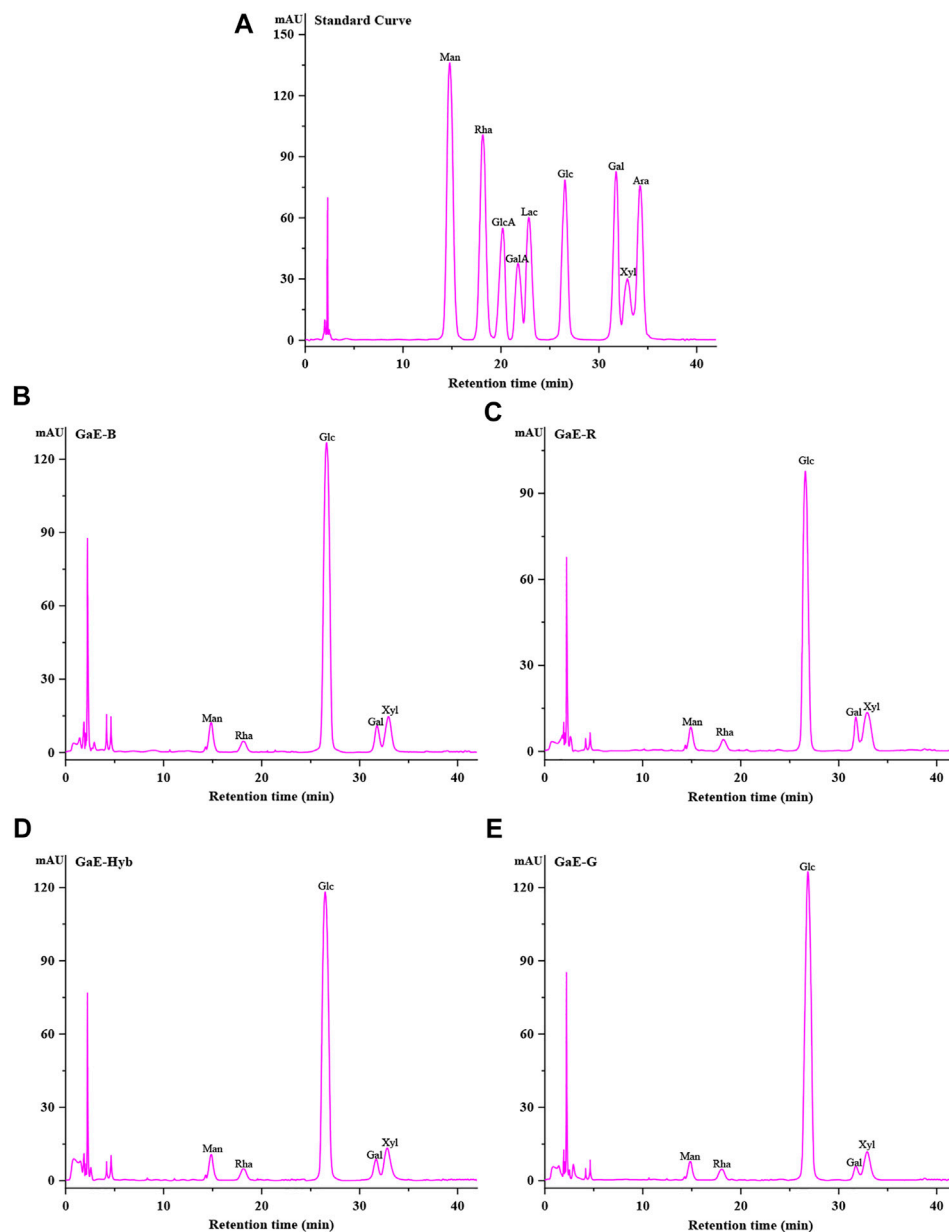
FIGURE 1 | Monosaccharide composition of the polysaccharide with four different varieties of *Gastrodia elata*. **(A)** Standard curve; **(B)** GaE-B; **(C)** GaE-R; **(D)** GaE-Hyb; and **(E)** GaE-G.

95.61 kDa (22.21%, peak3), and 28.6 kDa (49.87%, peak4); GaE-Hyb was 354.46 kDa (11.69%, peak1), 222.01 kDa (4.14%, peak2), 153.45 kDa (27.55%, peak3), and 50.67 kDa (56.62%, peak4); GaE-G was 491.04 kDa (28.67%, peak1), 292.63 kDa (18.40%, peak2), 129.751 kDa (32.31%, peak3), and 89.65 kDa (20.62%, peak4). As revealed by the comparison, the molecular weight of GaE-R was smaller than that of the other three groups, and the molecular weights of the four peaks were lower than 300 kDa. There was a slight difference in molecular weight between GaE-B and GaE-Hyb, whereas the content difference

was significant. GaE-B low-molecular-weight polysaccharide content (70.78%) and GaE-Hyb intermediate-molecular-weight polysaccharide content were both higher. In comparison with the first three groups, the maximum molecular weight of GaE-G (491.04 kDa) was higher than that of the other three groups, the content was higher (28.67%), whereas the low-molecular-weight content (20.62%) was relatively lower. As compared with high-molecular-weight polysaccharides, the low-molecular-weight polysaccharides could more easily penetrate via the cell
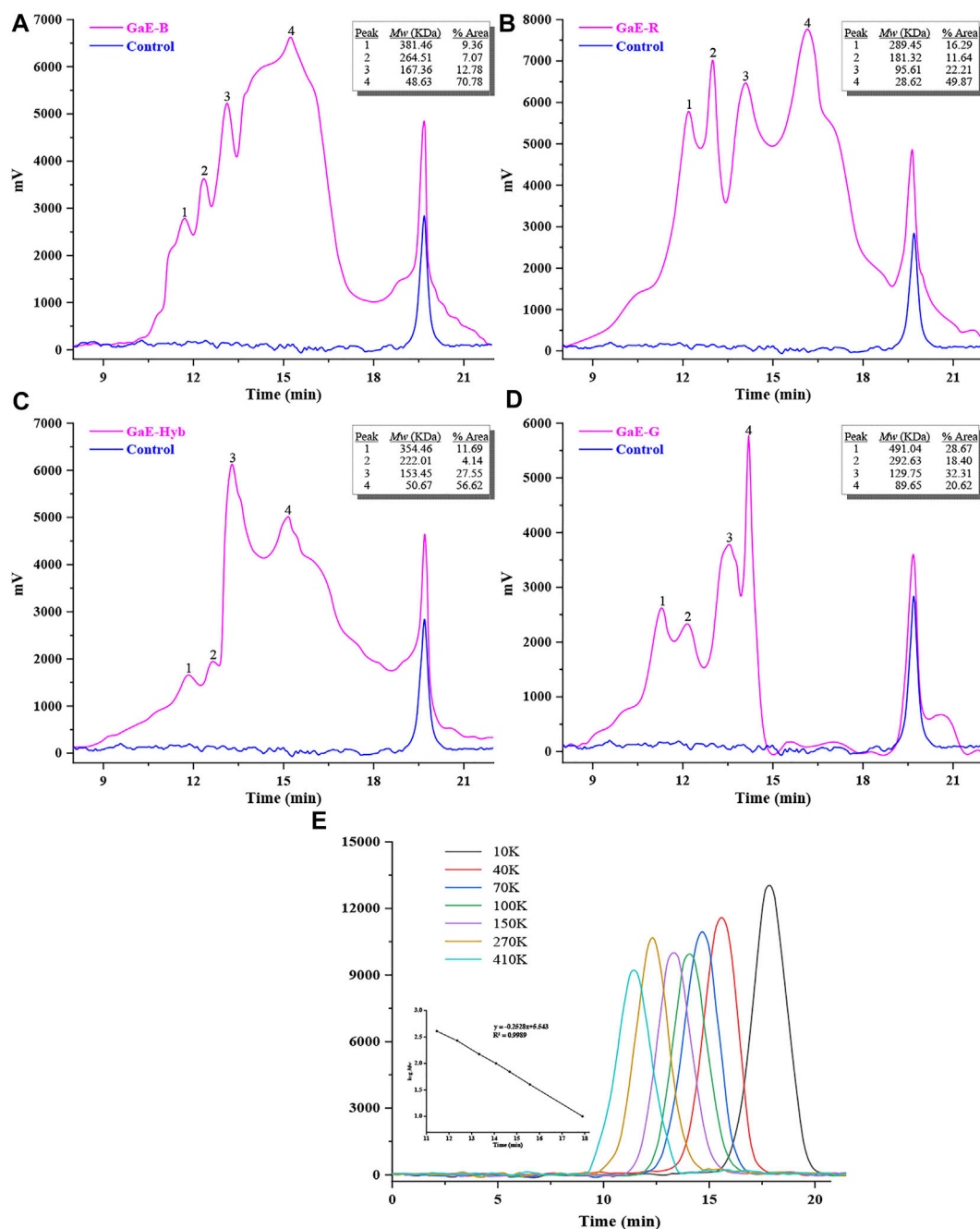
FIGURE 2 | Molecular weight of the *Gastrodia elata* polysaccharide with four varieties. **(A)** GaE-B; **(B)** GaE-R; **(C)** GaE-Hyb; **(D)** GaE-G; and **(E)** standard curve.

membrane, thus exhibiting higher physiological activities (Li et al., 2016; Zhang et al., 2016) (e.g., better ability to scavenge free radicals) (Cai et al., 2018). Some studies have found that polysaccharides with a molecular weight of 10–200 kDa usually showed better water solubility and biological activity (Chen and Kan, 2018; Chen et al., 2019b). Thus, in the further study, the biological activities of the GaEs polysaccharides will be assessed (e.g., antioxidant and hypoglycemic ability).

3.4 FT-IR Spectra of the GaE Polysaccharide

As depicted in **Figure 3**, no significant difference was identified in the FT-IR spectra of polysaccharides extracted from each of the GaEs, whereas there were typical signal peaks of polysaccharides. As revealed by the peak vibrating strongly close to $3400 cm^{-1}$, there are stretching vibrations of O–H and N–H between molecules, or within the molecule (Zhang et al., 2013). The peak with a vibration close to
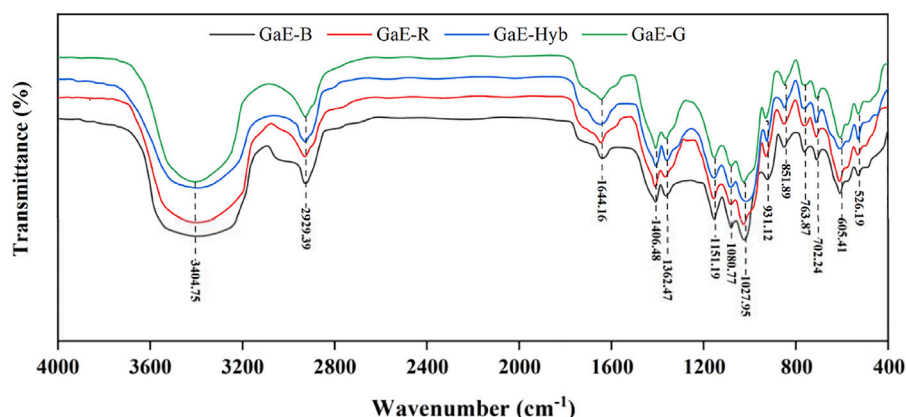
FIGURE 3 | FT-IR spectra of the *Gastrodia elata* polysaccharides with four different varieties.

$2925 cm^{-1}$ suggested the existence of the stretching vibration of C–H between CH_3, CH_2, and CH (Yu et al., 2017), and the vibration peak close to $1640 cm^{-1}$ was attributed to the asymmetric stretching vibration of C=O and C-O=O, which was the characteristic absorption peak of -CONH- (Zhang et al., 2013); the reason might be the existence of glycoprotein. The peak close to $1400 cm^{-1}$ indicated the existence of the C–H bending vibration, the vibration peak close to $1360 cm^{-1}$ indicates the existence of the O–H bending vibration, and the three peaks close to $900–1150 cm^{-1}$ indicated the existence of C–O–C and C–O–H of the pyranose ring bond asymmetric stretching vibration. To be specific, close to $1020 cm^{-1}$ was the C–O stretching vibration peak of sugar primary alcohols, and close to $1080 cm^{-1}$ was the C–O stretching vibration peak of sugar secondary alcohols (Yan et al., 2018). The peak close to $920 cm^{-1}$ indicated the existence of D-type glucopyranose asymmetric ring stretching vibration characteristic absorption (Farhadi, 2017), and the peaks close to $850 cm^{-1}$ indicate that the hemiacetal hydroxyl group of the GaE polysaccharides was largely α-configuration. As revealed by the FT-IR results, no significant difference was found in the spectra of the GaE polysaccharides, and they were found to contain similar principal components and chemical groups.

3.5 Thermal Characteristic of the GaE Polysaccharide

Thermogravimetric analysis (TGA) can indicate the thermal stability of a substance in a certain temperature range. The analysis of the thermal stability of polysaccharides can explore the correlation between the chemical composition of polysaccharides and other properties. As depicted in **Figure 4**, with the gradual increase of the temperature, the weight of the GaE polysaccharides tended to decrease, whereas the thermal decomposition curves of the GaEs were almost identical. The first weight loss occurred from 30°C to 110°C, primarily caused by the loss of free water and bound water of the GaE polysaccharides. When the temperature increased from 110°C to 200°C, the weight loss of GaE-Hyb was found as the highest and the GaE-G was the lowest. The second substantial weight loss was reported between

200°C and 600°C, largely due to the thermal melt degradation of the respective group of polysaccharides. The second degradation of the respective group's weight loss exceeded 50%. In the second degradation temperature range, the weight loss of GaE-R and GaE-Hyb was higher than that of GaE-B and GaE-G, with GaE-R achieved the largest loss and GaE-G achieved the smallest loss. At a temperature of 600°C, the residual amount of the respective group of polysaccharides from high to low was GaE-G > GaE-B > GaE-R > GaE-Hyb, thus suggesting that the thermal stability of GaE-G was higher than that of the other three groups, probably correlated with the monosaccharide composition and molecular weight of GaE-G. At a test temperature of 800°C, the weight loss rate of the GaE polysaccharides continued to decrease, and the final residual content was 20.55% (GaE-G), 17.07% (GaE-B), 10.98% (GaE-R), and 12.52% (GaE-Hyb). As revealed by the results of thermogravimetric analysis, there might exist differences in structure, molecular composition, size, and other aspects of polysaccharides between the GaEs.

3.6 Particle Sizes and Zeta Potentials of the GaE Polysaccharide

The stability and solubility of polysaccharides can be assessed by investigating the particle size and zeta potential. Particle size refers to the hydrodynamic radius of molecules in the solution, and zeta potential is a measure strength of mutual repulsion or attraction between particles. The smaller the particle size, the higher the absolute value (positive or negative) of zeta potential would be, the larger the specific surface area of polysaccharide would be, the more uniform the dispersion in the solution would be, the higher the solubility would be, and the stability of the solution system would be (Dickinson, 2009). As depicted in **Figure 5**, the GaE polysaccharides were negatively charged, which suggested that the particles were mutually exclusive and difficult to aggregate into super molecules. The particle size of the four groups of polysaccharides showed a positive correlation with the molecular weight of the major components. GaE-G containing more macromolecules (491.04 kDa, 28.67%; 292.63 kDa, 18.40%) achieved the largest particle size (422.68 ± 10.11 nm). In contrast, GaE-R containing more small
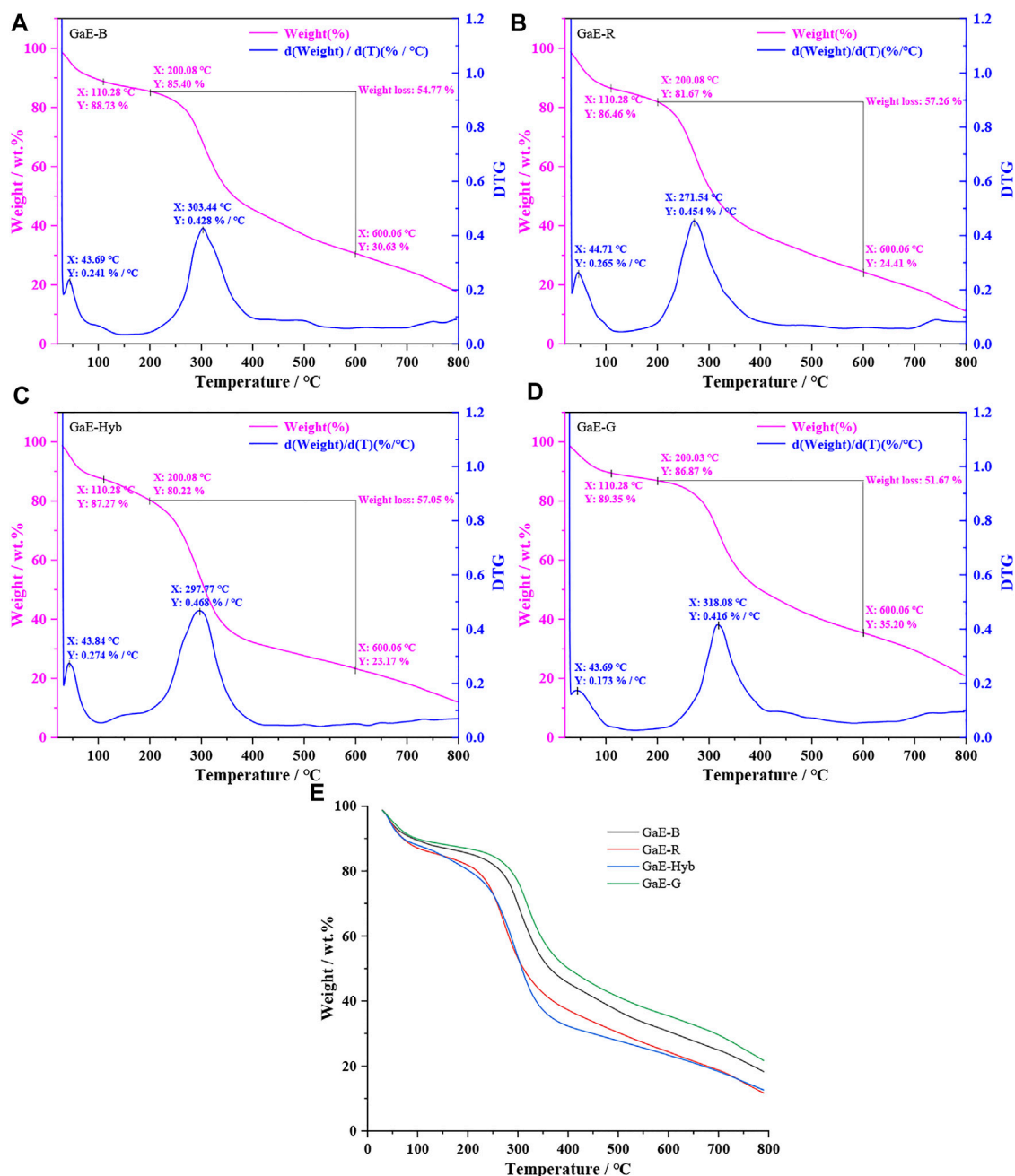
FIGURE 4 | TGA thermogram of *Gastrodia elata* with four different varieties. **(A)** GaE-B; **(B)** GaE-R; **(C)** GaE-Hyb; **(D)** GaE-G; and **(E)** the four varieties of *Gastrodia elata*.

molecular weights (95.61 kDa, 22.21%; 28.6 kDa, 49.87%) achieved the smallest particle size (212.94 ± 7.22 nm). The absolute value of GaE-G zeta potential was found as the largest, which might arise from the small molecular weight, a considerable number of molecules of GaE-G, and more charged groups. As revealed by the abovementioned results, the size and stability of polysaccharide particles might account for the differences in the properties exhibited by the GaE polysaccharides in the four groups.

3.7 Scanning Electron Microscopy Images of *G. elata* Polysaccharide Microstructures

The bioactivity of polysaccharides is generally correlated with their three-dimensional (3D) structure. **Figure 6**. presents the microstructure of four varieties of *G. elata* polysaccharides. As depicted in the images, the 3D structure of each variety of *G. elata* showed certain differences. GaE-B, GaE-R, and GaE-Hyb were primarily sheet-like structures, while GaE-B and GaE-Hyb
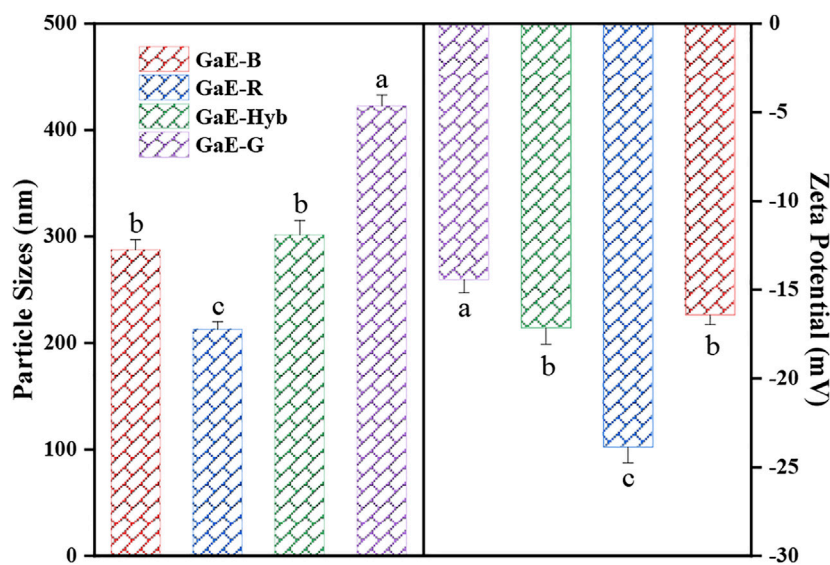
FIGURE 5 | Particle sizes and zeta potentials of the *Gastrodia elata* polysaccharides with four different varieties.

exhibited more pores and rough surfaces, which suggested that the 3D structure of the two was more similar. Although GaE-R also had a sheet-like structure, the surface was relatively smooth without small pores. GaE-G had a considerable number of particles and filamentous structures, and the 3D structure was relatively loose, which suggested that GaE-G polysaccharide particles might be mutually exclusive. As revealed by the biological activity of *G. elata* polysaccharide, the 3D structure of GaE-R could more significantly contribute to the improvement of polysaccharide activity.

3.8 Antioxidant Activity of the GaE Polysaccharide

3.8.1 DPPH Radical Scavenging Activity
DPPH refers to a stable nitrogen-centered free radical. Its solution has been commonly employed to measure the *in vitro* antioxidant capacity of a substance. The antioxidant activity of the substance can be assessed by measuring the change in absorbance (Oliveira et al., 2016). As depicted in **Figure 7A**, as the polysaccharide concentration increased, the DPPH free radical scavenging activity of the GaE polysaccharides was enhanced and dependent on concentration. GaE-R exhibited the higher scavenging activity than other varieties in the experimental concentration range, while the scavenging ability exhibited by GaE-G was always the weakest. Before the experimental concentration was 4 mg/ml, no significant difference was identified in the scavenging capacity of GaE-B and GaE-Hyb ($p > 0.05$), but the scavenging activity of the respective group was lower than that of the positive control group, vitamin C. The IC_{50} values of the respective group were obtained by curve fitting and found that the IC_{50} value of GaE-R was 3.112 mg/ml, which was the lowest in four varieties but still significantly higher than the positive control groups,

vitamin C IC_{50} values (0.031 mg/ml). Through the LSD analysis, it was found that there were significant differences in IC_{50} values between GaE-R, GaE-G, and other groups, while no significant difference was found between GaE-B and GaE-Hyb. Accordingly, among the GaE polysaccharides, the DPPH scavenging ability of GaE-R was higher than other varieties.

3.8.2 ABTS Radical Scavenging Activity
The ABTS radical scavenging method can be assessed for the antioxidant capacity of the substance by measuring the hydrophilic or lipophilic substances to scavenging the cationic free radical $ABTs^+$ that cause changes in the absorbance of the system (Thaipong et al., 2006). As depicted in **Figure 7B**, with the increase in concentration, the ability of the GaE polysaccharides to scavenge ABT^+ radicals gradually increased and showed concentration dependence. At the same experimental concentration, the scavenging ability of GaE-R was higher than that of the other groups, while the scavenging ability of GaE-G was the weakest, and no significant difference was identified between GaE-B and GaE-Hyb. By comparing the IC_{50} values of the respective group, it was found that GaE-R IC_{50} was the lowest (1.486 mg/ml) and GaE-G IC_{50} was the highest (2.475 mg/ml), while GaE-B and GaE-Hyb were somewhere in between but were higher than the IC_{50} values of vitamin C. Thus, among the four samples, the GaE-R has the strongest scavenging ability for ABT^+ radicals, but it was still lower than that of vitamin C at the same concentration.

3.8.3 Superoxide Radical Scavenging Activity
As a free radical produced in the process of biological metabolism, superoxide anion free radical can attack biological macromolecules, which are closely correlated to the body's aging and pathological changes (Zhang et al., 2016). Thus, the
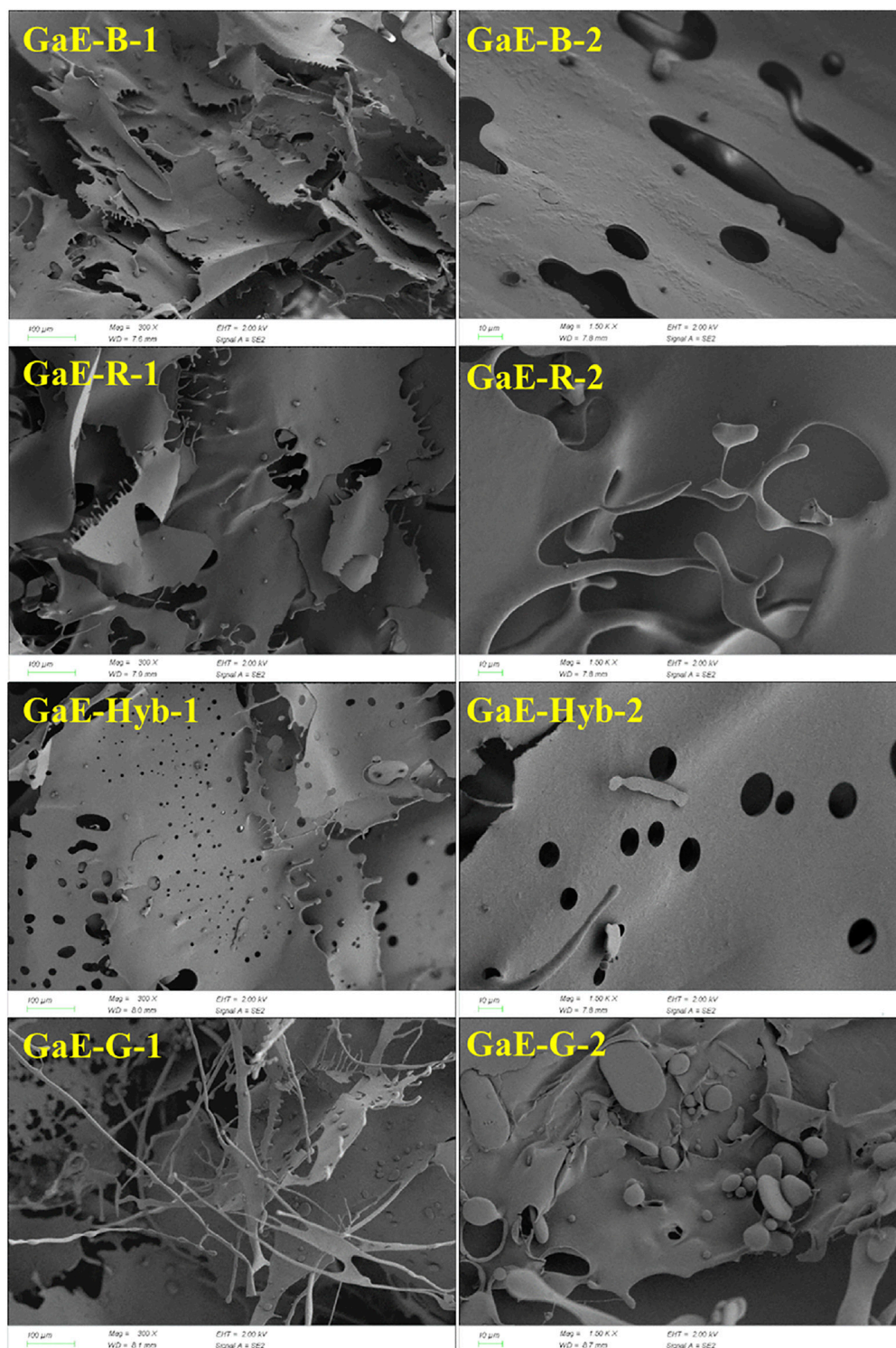
FIGURE 6 | SEM photographs of polysaccharides obtained from different varieties of *Gastrodia elata* (1 for 300× and 2 for 1500×).

determination of superoxide anion free radical scavenging ability can reflect the antioxidant activity of substances from another way. As depicted in **Figure 7C**, with the increase of polysaccharide concentration, the ability of the GaE

polysaccharides to scavenge superoxide free radicals also gradually increased and showed the same concentration dependence as scavenging DPPH and ABT$^+$ radicals. In the experimental concentration range, the scavenging capacity of

GaE-R was always higher than that of other groups, and the difference was significant. No significant difference was found between GaE-B and GaE-Hyb but they were higher than that of GaE-G. When the concentration reached 0.5 mg/ml, the scavenging capacity of ascorbic acid increased sharply, and the scavenging ability was significantly different from the GaE polysaccharides. Among the IC_{50} values of superoxide radical scavenging by the GaE polysaccharides, GaE-R achieved the lowest IC_{50} values (1.026 mg/ml) and GaE-G achieved the highest IC_{50} values (1.636 mg/ml). Accordingly, the superoxide radical scavenging capacity of the GaE polysaccharides was ranked as GaE-R > (GaE-B and GaE-Hyb) > GaE-G, whereas the IC_{50} values of the four groups were higher than that of ascorbic acid (0.158 mg/ml).

3.8.4 Hydroxyl Radical Scavenging Activity

Hydroxyl radical (OH) refers to a type of free radical with strong oxidation ability. It is capable of easily oxidizing various biological macromolecules with a high oxidation efficiency and fast reaction rate. It is an active oxygen free radical causing tissue lipid peroxidation, nucleic acid breaking, and protein and polysaccharide breakdown (Fan et al., 2014). As depicted in **Figure 7D**, with the increase in the polysaccharide concentration, the scavenging capacity of hydroxyl radicals in the respective group tended to increase, and the concentration dependence was indicated. At the experimental maximum concentration of 5 mg/ml, the scavenging capacity of GaE-R was higher than that of other groups, but no significant difference was identified among GaE-B, GaE-Hyb, and GaE-G. Comparing the IC_{50} values of the GaE polysaccharide samples, GaE-R had the lowest IC_{50} values (2.08 mg/ml), GaE-G had the highest IC_{50} values (2.08 mg/ml), GaE-B and GaE-Hyb have no significant difference, and no significant difference was found between GaE-B and GaE-HyB, whereas all of them were higher than that of ascorbic acid (0.203 mg/ml). As revealed by the results, among the GaE polysaccharides, GaE-R exhibited the strongest ability to scavenge hydroxyl free radicals.

3.8.5 Ferrous Ion Chelating Capacity

Fe^{2+} refers to the active center of numerous oxidation reaction catalysts. In the body, Fe^{2+} is capable of reacting with O_2 to generate superoxide radical and hydroxyl radical. When chelated, Fe^{2+} can reduce the generation of reactive oxygen species, thus indirectly playing a certain antioxidant role. As depicted in **Figure 7E**, the ferrous ion chelating capacity of each of the GaE polysaccharides tended to be enhanced as the concentration of the GaE polysaccharides increased in the experiment. The Fe^{2+} chelating capacity of GaE-R was the highest, and that of GaE-G was found as the weakest. The GaE polysaccharides' chelating Fe^{2+} activity (y) was employed as a quadratic function of concentration (x) ($p < 0.05$), and the linear equation was yielded as $y = -1.4749x2 + 20.897x + 1.794$ ($R^2 = 0.9988$) for GaE-B, $y = -2.8178x2 + 29.131x + 0.3111$ ($R^2 = 0.9985$) for GaE-R, $y = -1.9059x2 + 23.657x + 1.3267$ ($R^2 = 0.9985$) for GaE-Hyb, and $y = -1.1649x2 + 18.25x + 1.7959$ ($R^2 = 0.997$) for GaE-G. As revealed by the abovementioned quadratic fitting equations, the Fe^{2+} chelating activity of the GaE

polysaccharides was dependent on concentration. Existing studies reported that the C=O functional group in the polysaccharide could form a cross-bridge with Fe^{2+} (Wang C. C. et al., 2010) to enhance the chelating ability of the polysaccharide to Fe^{2+}. Compared with the other three groups, GaE-R exhibited a stronger chelating ability of Fe^{2+}. The comprehensive comparison of the zeta potential, particle size, and molecular weight of the respective group suggested that GaE-R might contain more C = O functional groups since it formed a larger specific surface area in the solution and contained more molecular quantitative. As indicated by the comparison of the IC_{50} values of the Fe^{2+} chelating ability of the GaE polysaccharides, GaE-R achieved the lowest IC_{50} value (2.073 mg/ml), and the IC_{50} value of GaE-G was the highest (3.306 mg/ml), higher than those of EDTA in the positive control group. However, the GaE polysaccharides still had high practicability in chelating Fe^{2+} relative to polysaccharide macromolecules.

3.8.6 Reducing Power

Iron reducing ability refers to the reaction of removing free radicals by reducing Fe^{3+} to Fe^{2+}, and Fe^{3+} electrons are obtained from antioxidants (reducing agents). The reducing capacity and the antioxidant capacity were stronger, the latter of which has been commonly employed as an index to assess the antioxidant activity of polysaccharides. As depicted in **Figure 7F**, the reduction capacity of the GaE polysaccharides tended to be enhanced (the absorbance value gradually increased) as the experimental concentration of polysaccharides increased, which suggested that the antioxidant capacity of the GaE polysaccharides gradually increased as well. At the maximum experimental concentration of 5 mg/ml, the reducing ability of GaE-R was found as the strongest, that of GaE-G was the weakest, and that of GaE-B and GaE-Hyb were between GaE-R and GaE-G. However, the reducing ability of the GaE polysaccharides was lower than that of ascorbic acid in the positive control group at the same concentration. As revealed by the results, the GaE polysaccharides exhibited an electron-donating ability to scavenge free radicals and terminate the chain reaction of free radicals. To be specific, the Fe^{3+} reduction of GaE-R was slightly stronger than that of the other three groups, whereas there was slight difference in the Fe^{3+} reducing ability among the groups.

Excessive production of free radicals in the body can damage biofilms and biological macromolecules, accelerate aging, and cause diseases. In this study, the antioxidant activity of the GaE polysaccharides was obtained using a series of methods (e.g., DPPH radical scavenging ability, ABTS radical scavenging ability, superoxide radical scavenging ability, hydroxyl radical scavenging ability, Fe^{2+} chelating ability, and Fe^{3+} reducing ability). As revealed by the comparison of the antioxidant activity of the GaE polysaccharides, GaE-R was stronger than the other three groups in terms of DPPH radical, superoxide radical, hydroxyl radical, ABTS radical scavenging ability, Fe^{3+} reducing ability, and Fe^{2+} chelating ability; GaE-G exhibited the weakest capability relatively. Studies have shown that the antioxidant activity of polysaccharides was correlated with numerous factors (e.g., monosaccharide composition,
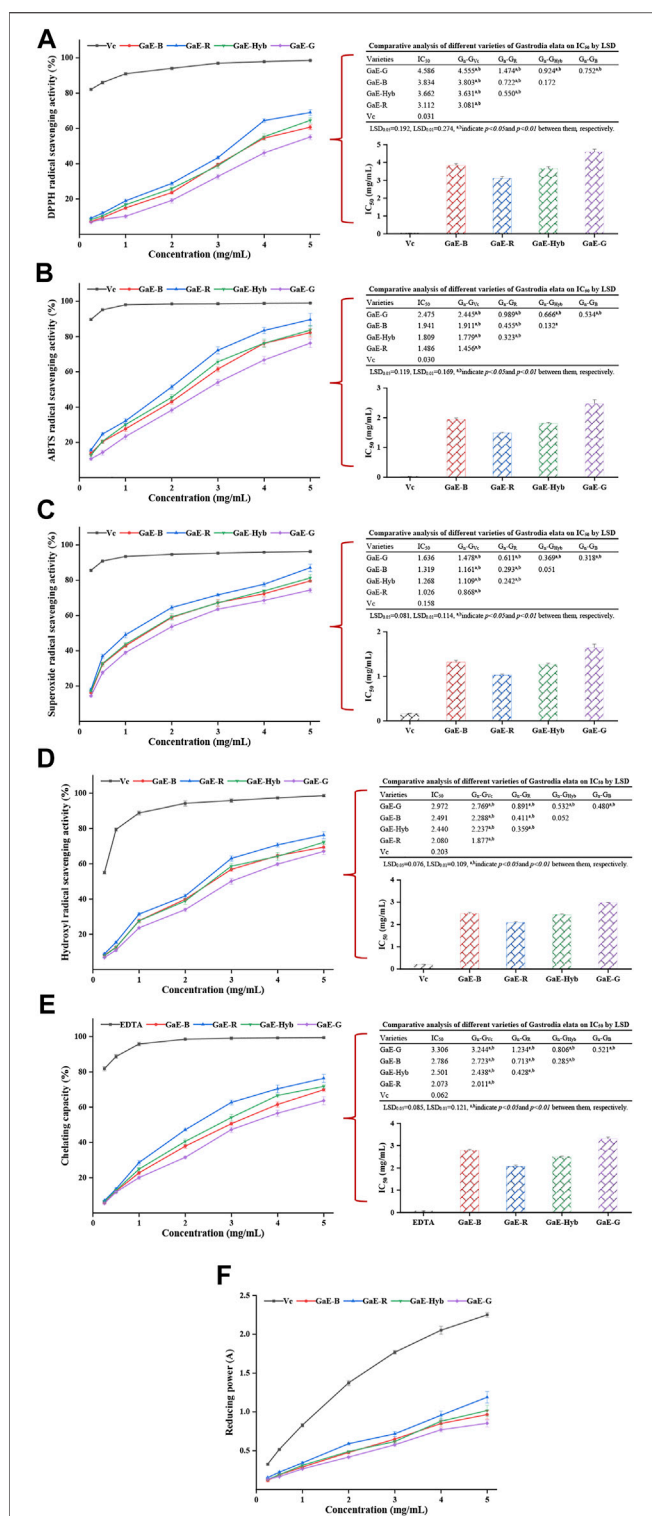
FIGURE 7 | Antioxidant activities of the different varieties of *Gastrodia elata* polysaccharides at different concentrations *in vitro* and IC$_{50}$ values: **(A)** DPPH radical scavenging activity and IC$_{50}$ values; **(B)** ABTS radical scavenging activity and IC$_{50}$ values; **(C)** superoxide radical scavenging activity and IC$_{50}$ values; **(D)** hydroxyl radical scavenging activity and IC$_{50}$ values; **(E)** chelating activity on ferrous ion and IC$_{50}$ values; and **(F)** reducing power. The respective value is expressed as the means ± standard deviation (SD) of triplicate measurements.

molecular weight, the existence form and content of -C=O groups, the distribution of charge, and the contents of protein, sulfate, and phenols). The low quality polysaccharides exhibited higher free radical scavenging activity (Cai et al., 2018), which was probably because at the same concentration, low-molecular-weight polysaccharides contained more terminal hydroxyl and carbonyl groups, and a larger specific surface area was combined with free radicals in solution (Zhang et al., 2016). In this study, GaE-R had a lower molecular weight compared with the other three groups of the GaE polysaccharides, probably explaining why its biological activity was higher than the other groups. Second, the carboxyl and phenolic hydroxyl groups in proteins and polyphenols exhibited reducibility, which could enhance the antioxidant capacity of polysaccharides (Liao et al., 2014; Yan et al., 2018). GaE-R exhibited high free radical scavenging activity and reducing ability, which might be correlated with the factor that GaE-R contained more binding proteins and polyphenols. In addition, the composition and content of monosaccharides had an effect on the antioxidant activity of polysaccharides. In the abovementioned monosaccharides, more acidic sugars were contained, which significantly affected the free radical scavenging ability of polysaccharides since acidic sugars could more easily release H$^+$ to be combined with reactive oxygen species (Yuan et al., 2019). Furthermore, existing research suggested that the lower the glucose content in the monosaccharides of polysaccharides, the higher the antioxidant activity of polysaccharides would be (Chen et al., 2010). In this study, the glucose content of GaE-R was found as the lowest and that of GaE-G was found as the highest, which might also account for the difference in antioxidant activities.

3.9 Hypoglycemic Activity *In Vitro*
3.9.1 *α*-Glucosidase Inhibitory Activity *In Vitro*
The body-ingested carbohydrates are largely hydrolyzed by α-amylase and α-glucosidase (Ali et al., 2006). If the activity of α-amylase and α-glucosidase can be inhibited, the blood sugar concentration in the body can be effectively reduced. Commonly used in clinic, α-amylase and α-glycosidase inhibitors include orlistat, acarbose, and miglitol (Kim et al., 1999), but taking the abovementioned inhibitors may cause damage to various viscera (Sall et al., 2014). However, natural macromolecular compounds inhibited enzyme activity more gently and had less toxic side effects than synthetic drugs (Bustanji et al., 2011). Plant polysaccharides can reduce blood glucose concentration by inhibiting the activity of related enzymes and promoting the secretion of insulin (Wang Y. et al., 2010). Thus, studying the α-amylase and α-glucosidase inhibitory activities of polysaccharides had practical significance for those patients suffering from hyperglycemia. As depicted in **Figure 8A**, with the increase in the concentration of the GaE polysaccharides, the inhibitory activity of the respective group to α-glucosidase also tended to increase and was dependent on concentration. In the experimental concentration range, the inhibitory activity of GaE-R was higher than that of other the GaE groups, and that of GaE-G was found as the lowest, which might be correlated with their size of molecular weight,
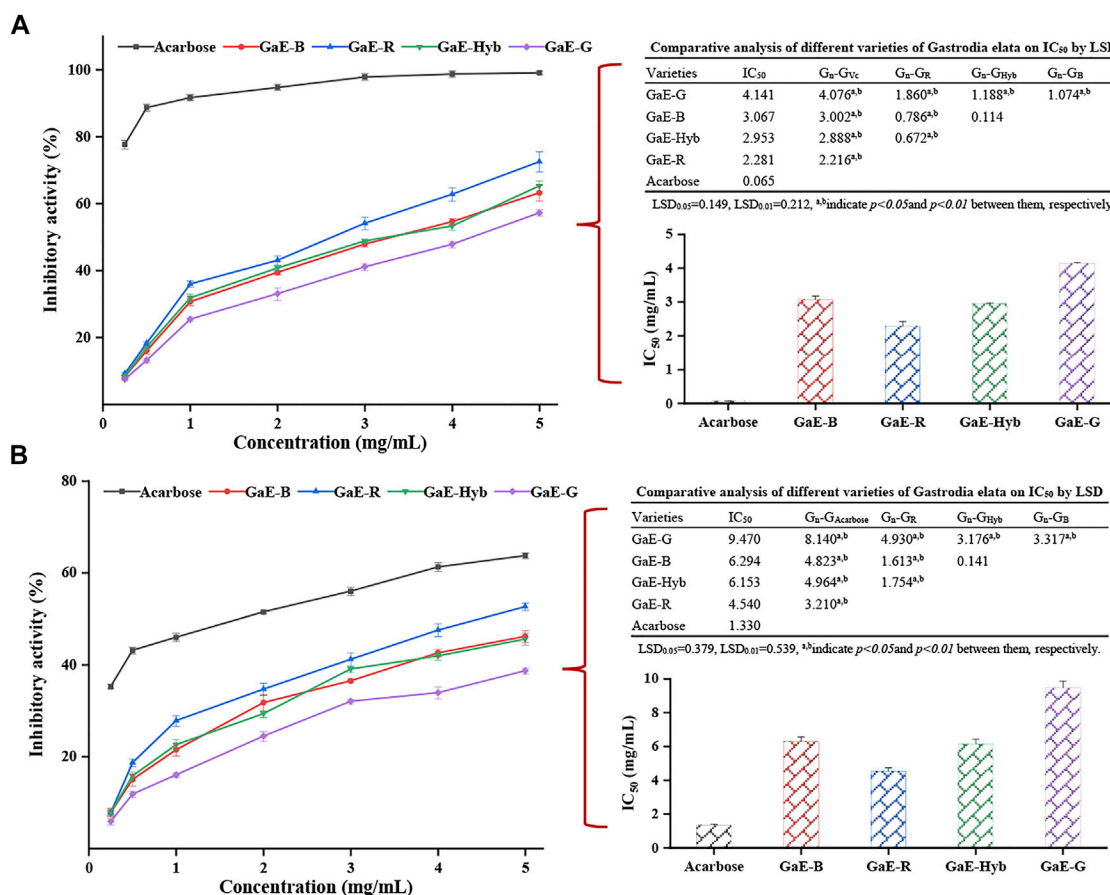
FIGURE 8 | Hypoglycemic activities of the different varieties of *Gastrodia elata* polysaccharides at different concentrations *in vitro*: **(A)** α-amylase inhibitory activity and IC_{50} values and **(B)** α-glucosidase inhibitory activity and IC_{50} values. Each value is expressed as means ± standard deviation (SD) of triplicate measurements.

whereas the inhibitory activity of the GaEs was significantly lower than that of the positive control of acarbose. The calculation of the IC_{50} value of the respective group after fitting curves suggested that the IC_{50} value of GaE-R was the lowest (2.281 mg/ml), and the IC_{50} value of GaE-G was the highest (4.14 mg/ml). No significant difference was identified between GaE-B and GaE-Hyb, whereas the IC_{50} value of the GaEs was significantly higher than the IC_{50} value of the positive control acarbose (0.065 mg/ml, $p < 0.01$). Nevertheless, the abovementioned natural polysaccharide macromolecules could still be sufficient to be developed and employed as hypoglycemic health food. In brief, the inhibitory activity of GaE-R on α-glucosidase was higher than that of the other three GaE polysaccharides.

3.9.2 α-Amylase Inhibitory Activity *In Vitro*

Starch in food is primarily decomposed into glucose by α-amylase, which enters the blood to increase blood sugar concentration, inhibit the activity of α-amylase, and reduce the absorption of glucose by the body; as a result, the increase of blood sugar concentration in diabetic patients is delayed (Liu et al., 2017). In this study, the inhibitory activity of the GaE polysaccharides on α-amylase was investigated to explore

the application value of the GaE polysaccharides in hypoglycemic drugs. As depicted in **Figure 8B**, the α-amylase inhibitory activity of the GaE polysaccharides in the respective group increased as the experimental concentration increased. In the concentration range of 2–3 mg/ml, the inhibition rates of GaE-R, GaE-B, and GaE-Hyb were close; in the concentration range of 4–5 mg/ml, the inhibition rate of GaE-R was higher than that of GaE-B and GaE-Hyb. The experimental concentration of 0.5–5 mg/ml suggested that the inhibition rate of GaE-G was significantly lower than that of other groups ($p < 0.05$), and almost no significant difference was found between GaE-B and GaE-Hyb. At the experimental concentration of 5 mg/ml, GaE-R exhibited the inhibitory activity of 52.62% ± 0.81%, the highest among the GaE polysaccharides, and the activity of GaE-G was found as the lowest at 38.63% ± 0.62%. The IC_{50} values of the GaE polysaccharides in the four groups were found as the lowest in GaE-R (4.54 mg/ml) and the highest in GaE-G (9.47 mg/ml), whereas the values were significantly higher than those of acarbose in the positive control group (1.33 mg/ml, $p < 0.05$). Although the value was lower than the positive control, relative to the natural biological macromolecules, it still could serve as a better α-amylase

inhibitor. The hydroxyl or carboxyl groups in polysaccharides could be combined with amino acid residues in the active site of enzyme, thus competitively or non-competitively inhibiting the catalysis of the enzyme by the substrate (Wang et al., 2010 ; Wu et al., 2017).

In this study, the inhibitory activities of the GaE polysaccharides on enzymes were not exactly the same. Regardless of α-glucosidase or α-amylase, the inhibitory activity of GaE-R was higher than that of the other three groups, while no significant difference was found between GaE-B and GaE-Hyb (p > 0.05). In addition, GaE-G was always the lowest. It was found that the side-chain group of polysaccharides could be combined with the active site of enzyme, so as to reduce the catalytic activity of enzyme (Kim et al., 1999). Moreover, the charge on the polysaccharide could form a complex with α-glucosidase, thus reducing the activity of the enzyme (Jia et al., 2017). Accordingly, the differences in the activities of the respective group might arise from the different types and quantities of side-chain groups and charges of each of the GaE polysaccharide. In addition, the molecular weight and monosaccharide composition of polysaccharides might account for the abovementioned result (Zhang et al., 2010; Li et al., 2016; Chen et al., 2013). This is because the smaller the molecular weight, the more the side-chain groups would be at the same molar concentration, the more charges would carry, and the more binding to the active site of the enzyme would be. As revealed by the abovementioned results, the higher inhibitory activity of GaE-R than other groups might arise from the differences in molecular weight, structure, side-chain groups, and monosaccharide composition.

4 CONCLUSION

In this study, the characteristics of the GaE polysaccharides were investigated, which were largely described in accordance with structural characteristics, biological activity, and physicochemical properties. As revealed by the results, the GaE polysaccharides had different yields, chemical compositions, monosaccharide compositions, molecular weight distributions, physical properties, and biological activities, whereas most of the properties between GaE-B and GaE-Hyb were similar or showed no significant difference. The GaE polysaccharides were composed of the same type of monosaccharides, so they were heteropolysaccharides, and glucose was reported as the major component. However, differences in monosaccharide content were found among the varieties, and the GaE-R glucose content was found as the lowest. In general, GaE-R exhibited excellent antioxidant and glycosidase inhibitory activities *in vitro*, probably due to its lower molecular weight and glucose content, higher contents of binding protein, and polyphenols. In addition, the yield and total sugar content of GaE-R were lower than those of the other three varieties.

Although the GaE polysaccharides exhibited some physiological activities, the harvested *G. elata* polysaccharides would be impossible to extract and utilize, which is unacceptable in terms of cost. The efficacy of *G. elata*, a traditional Chinese medicine, could not be assessed only according to the physiological activity of polysaccharides, the content of the major medicinal components of *G. elata* (e.g., gastrodin, p-hydroxybenzyl alcohol, and p-hydroxybenzaldehyde) also directly affected the overall *G. elata* medicinal properties. This study only investigated the functions and properties exhibited by *G. elata* from the perspective of polysaccharide, which does not represent the overall medicinal value of *G. elata*. However, with the continuous expansion of the *G. elata* industry in China, *G. elata* has also been approved by the National Health Commission of the People's Republic of China as a homologous of medicine and food. Consumers often stew or boil *G. elata* as a food supplement with other ingredients, which will disperse *G. elata* polysaccharide and other medicinal components into the soup, as an attempt to achieve a synergistic therapeutic effect between different types of activity of components. Moreover, the water extraction method was chosen to extract polysaccharides in this study because the water extraction method was closer to the method of obtaining *G. elata* polysaccharide in life. In brief, comparing the physicochemical properties and antioxidant activities of polysaccharides among different *G. elata* varieties can lay a relevant theoretical basis for enterprise processing or consumer purchase.

DATA AVAILABILITY STATEMENT

The raw data supporting the conclusions of this article will be made available by the authors without undue reservation.

AUTHOR CONTRIBUTIONS

ACKNOWLEDGMENTS

REFERENCES

Ali, H., Houghton, P. J., and Soumyanath, A. (2006). α-Amylase Inhibitory Activity of Some Malaysian Plants Used to Treat Diabetes; with Particular Reference to Phyllanthus Amarus. *J. Ethnopharmacol.* 107, 449–455. doi:10.1016/j.jep.2006.04.004

Bi, H., Gao, T., Li, Z., Ji, L., Yang, W., Jeff Iteku, B., et al. (2013). Structural Elucidation and Antioxidant Activity of a Water-Soluble Polysaccharide from the Fruit Bodies of Bulgaria Inquinans (Fries). *Food Chem.* 138 (2-3), 1470–1475. doi:10.1016/j.foodchem.2012.11.039

Blumenkrantz, N., and Asboe-Hansen, G. (1973). New Method for Quantitative Determination of Uronic Acids. *Anal. Biochem.* 54 (2), 484–489. doi:10.1016/0003-2697(73)90377-1

Bradford, M. M. (1976). A Rapid and Sensitive Method for the Quantitation of Microgram Quantities of Protein Utilizing the Principle of Protein-Dye Binding. *Anal. Biochem.* 72 (1-2), 248–254. doi:10.1006/abio.1976.9999

Bustanji, Y., Mohammad, M., Hudaib, M., Tawaha, K., Almasri, I., Alkhatib, H., et al. (2011). Screening of Some Medicinal Plants for Their Pancreatic Lipase Inhibitory Potential. *Jordan J. Pharm. Sci.* 4, 81–88.

Cai, L., Zou, S., Liang, D., and Luan, L. (2018). Structural Characterization, Antioxidant and Hepatoprotective Activities of Polysaccharides from Sophorae Tonkinensis Radix. *Carbohydr. Polym.* 184, 354–365. doi:10.1016/j.carbpol.2017.12.083

Cha, J. Y., and Igarashi, T. (1995). Armillaria Species Associated with Gastrodia Elata in Japan. *For. Pathol.* 25 (6-7), 319–326. doi:10.1111/j.1439-0329.1995.tb01347.x

Chen, G.-L., Chen, S.-G., Zhao, Y.-Y., Luo, C.-X., Li, J., and Gao, Y.-Q. (2014). Total Phenolic Contents of 33 Fruits and Their Antioxidant Capacities before and after *In Vitro* Digestion. *Industrial Crops Prod.* 57, 150–157. doi:10.1016/j.indcrop.2014.03.018

Chen, G., Fang, C., Chen, X., Wang, Z., Liu, M., and Kan, J. (2019a). High-Pressure Ultrasonic-Assisted Extraction of Polysaccharides from Mentha Haplocalyx: Structure, Functional and Biological Activities. *Industrial Crops Prod.* 130, 273–284. doi:10.1016/j.indcrop.2018.12.086

Chen, G., and Kan, J. (2018). Characterization of a Novel Polysaccharide Isolated from Rosa Roxburghii Tratt Fruit and Assessment of its Antioxidant *In Vitro* and *In Vivo*. *Int. J. Biol. Macromol.* 107, 166–174. doi:10.1016/j.ijbiomac.2017.08.160

Chen, G., Li, C., Wang, S., Mei, X., Zhang, H., and Kan, J. (2019b). Characterization of Physicochemical Properties and Antioxidant Activity of Polysaccharides from Shoot Residues of Bamboo (Chimonobambusa Quadrangularis): Effect of Drying Procedures. *Food Chem.* 292, 281–293. doi:10.1016/j.foodchem.2019.04.060

Chen, H., Xu, X., and Zhu, Y. (2010). Optimization of Hydroxyl Radical Scavenging Activity of Exo-Polysaccharides from Inonotus Obliquus in Submerged Fermentation Using Response Surface Methodology. *J. Microbiol. Biotechnol.* 20, 835–843. doi:10.4014/jmb.0909.09017

Chen, J., Tian, S., Shu, X., Du, H., Li, N., and Wang, J. (2016). Extraction, Characterization and Immunological Activity of Polysaccharides from Rhizoma Gastrodiae. *Int. J. Mol. Sci.* 17 (7), 1011. doi:10.3390/ijms17071011

Chen, J., Liu, X., Wang, H., and Qu, M. (2016). Gastrodin Attenuates Pentylenetetrazole-Induced Seizures by Modulating the Mitogen-Activated Protein Kinase-Associated Inflammatory Responses in Mice. *Neurosci. Bull.* 33 (3), 264–272. doi:10.1007/s12264-016-0084-z

Chen, L., Zhang, Y. P., and Jin, L. X. (2018). Preparation, Characterization and Anti-Ageing Activity of Gastrodia Elata Blume Polysaccharide. *Acta Aliment.* 47 (2), 210–219. doi:10.1556/066.2018.47.2.10

Chen, S., Chen, H., Tian, J., Wang, Y., Xing, L., and Wang, J. (2013). Chemical Modification, Antioxidant and α-Amylase Inhibitory Activities of Corn Silk Polysaccharides. *Carbohydr. Polym.* 98 (1), 428–437. doi:10.1016/j.carbpol.2013.06.011

Chen, X., Cao, D., Zhou, L., Jin, H., Dong, Q., Yao, J., et al. (2011). Structure of a Polysaccharide from Gastrodia Elata Bl., and Oligosaccharides Prepared Thereof with Anti-Pancreatic Cancer Cell Growth Activities. *Carbohydr. Polym.* 86, 1300–1305. doi:10.1016/j.carbpol.2011.06.029

Chen, Y., Jiang, X., Xie, H., Li, X., and Shi, L. (2018). Structural Characterization and Antitumor Activity of a Polysaccharide from Ramulus Mori. *Carbohydr. Polym.* 190, 232–239. doi:10.1016/j.carbpol.2018.02.036

Chinese Pharmacopoeia Commission (2015). *Pharmacopoeia of the People's Republic of China, Part I*. Beijing: Chinese Medical Science and Technology Press, 58–59.

Dickinson, E. (2009). Hydrocolloids as Emulsifiers and Emulsion Stabilizers. *Food Hydrocoll.* 23 (6), 1473–1482. doi:10.1016/j.foodhyd.2008.08.005

Duan, M., Shang, H., Chen, S., Li, R., and Wu, H. (2018). Physicochemical Properties and Activities of Comfrey Polysaccharides Extracted by Different Techniques. *Int. J. Biol. Macromol.* 115, 876–882. doi:10.1016/j.ijbiomac.2018.04.188

DuBois, M., Gilles, K. A., Hamilton, J. K., Rebers, P. A., and Smith, F. (1956). Colorimetric Method for Determination of Sugars and Related Substances. *Anal. Chem.* 28 (3), 350–356. doi:10.1021/ac60111a017

Erel, O. (2004). A Novel Automated Direct Measurement Method for Total Antioxidant Capacity Using a New Generation, More Stable ABTS Radical Cation. *Clin. Biochem.* 37 (4), 277–285. doi:10.1016/j.clinbiochem.2003.11.015

Fan, J., Wu, Z., Zhao, T., Sun, Y., Ye, H., Xu, R., et al. (2014). Characterization, Antioxidant and Hepatoprotective Activities of Polysaccharides from Ilex Latifolia Thunb. *Carbohydr. Polym.* 101, 990–997. doi:10.1016/j.carbpol.2013.10.037

Fan, S., Yu, G., Nie, W., Jin, J., Chen, L., and Chen, X. (2018). Antitumor Activity and Underlying Mechanism of Sargassum Fusiforme Polysaccharides in CNE-Bearing Mice. *Int. J. Biol. Macromol.* 112, 516–522. doi:10.1016/j.ijbiomac.2018.01.168

Farhadi, N. (2017). Structural Elucidation of a Water-Soluble Polysaccharide Isolated from Balangu Shirazi (Lallemantia Royleana) Seeds. *Food Hydrocoll.* 72, 263–270. doi:10.1016/j.foodhyd.2017.05.028

He, K., Mergens, B., Yatcilla, M., Zheng, Q., Bao, Z., Zhang, Y., et al. (2018). Molecular Weight Determination of Aloe Polysaccharides Using Size Exclusion Chromatography Coupled with Multi-Angle Laser Light Scattering and Refractive Index Detectors. *J. AOAC Int.* 101 (6), 1729–1740. doi:10.5740/jaoacint.18-0121

Huo, J., Lei, M., Li, F., Hou, J., Zhang, Z., Long, H., et al. (2021). Structural Characterization of a Polysaccharide from Gastrodia Elata and its Bioactivity on Gut Microbiota. *Molecules* 26 (15), 4443. doi:10.3390/molecules26154443

Jia, X., Hu, J., He, M., Zhang, Q., Li, P., Wan, J., et al. (2017). α-Glucosidase Inhibitory Activity and Structural Characterization of Polysaccharide Fraction from Rhynchosia Minima Root. *J. Funct. Foods* 28, 76–82. doi:10.1016/j.jff.2016.10.026

Kim, K.-J., Lee, O.-H., Han, C.-K., Kim, Y.-C., and Hong, H.-D. (2012). Acidic Polysaccharide Extracts from Gastrodia Rhizomes Suppress the Atherosclerosis Risk Index through Inhibition of the Serum Cholesterol Composition in Sprague Dawley Rats Fed a High-Fat Diet. *Int. J. Mol. Sci.* 13 (2), 1620–1631. doi:10.3390/ijms13021620

Kim, M.-J., Lee, S.-B., Lee, H.-S., Lee, S.-Y., Baek, J.-S., Kim, D., et al. (1999). Comparative Study of the Inhibition of α-Glucosidase, α-Amylase, and Cyclomaltodextrin Glucanosyltransferase by Acarbose, Isoacarbose, and Acarviosine-Glucose. *Archives Biochem. Biophysics* 371, 277–283. doi:10.1006/abbi.1999.1423

Kim, N.-H., Xin, M. J., Cha, J.-Y., Ji, S.-J., Kwon, S.-U., Jee, H.-K., et al. (2017). Antitumor and Immunomodulatory Effect of Gastrodia Elata on Colon Cancer *In Vitro* and *In Vivo*. *Am. J. Chin. Med.* 45 (02), 319–335. doi:10.1142/s0192415x17500203

Lee, D.-K., Lim, D., Um, J., Lim, C., Hong, J., Yoon, Y., et al. (2014). Evaluation of Four Different Analytical Tools to Determine the Regional Origin of Gastrodia Elata and Rehmannia Glutinosa on the Basis of Metabolomics Study. *Molecules* 19 (5), 6294–6308. doi:10.3390/molecules19056294

Li, X., Wang, L., Wang, Y., and Xiong, Z. (2016). Effect of Drying Method on Physicochemical Properties and Antioxidant Activities of Hohenbuehelia Serotina Polysaccharides. *Process Biochem.* 51 (8), 1100–1108. doi:10.1016/j.procbio.2016.05.006

Li, Y., Liu, X.-Q., Liu, S.-S., Liu, D.-H., Wang, X., and Wang, Z.-M. (2019). Transformation Mechanisms of Chemical Ingredients in Steaming Process of Gastrodia Elata Blume. *Molecules* 24 (17), 3159. doi:10.3390/molecules24173159

Liao, N., Chen, S., Ye, X., Zhong, J., Ye, X., Yin, X., et al. (2014). Structural Characterization of a Novel Glucan from *Achatina F* and its Antioxidant Activity. *J. Agric. Food Chem.* 62 (11), 2344–2352. doi:10.1021/jf403896c

Lin, Y.-E., Chou, S.-T., Lin, S.-H., Lu, K.-H., Panyod, S., Lai, Y.-S., et al. (2018). Antidepressant-Like Effects of Water Extract of Gastrodia Elata Blume on Neurotrophic Regulation in a Chronic Social Defeat Stress Model. *J. Ethnopharmacol.* 215, 132–139. doi:10.1016/j.jep.2017.12.044

Liu, S., Ai, Z., Qu, F., Chen, Y., and Ni, D. (2017). Effect of Steeping Temperature on Antioxidant and Inhibitory Activities of Green Tea Extracts against α-Amylase, α-Glucosidase and Intestinal Glucose Uptake. *Food Chem.* 234, 168–173. doi:10.1016/j.foodchem.2017.04.151

Ma, J.-Q., Sun, Y.-Z., Ming, Q.-L., Tian, Z.-K., Zhang, Y.-J., and Liu, C.-M. (2020). Effects of Gastrodin against Carbon Tetrachloride Induced Kidney Inflammation and Fibrosis in Mice Associated with the AMPK/Nrf2/HMGB1 Pathway. *Food Funct.* 11, 4615–4624. doi:10.1039/d0fo00711k

Ma, Q., Yuan, L., and Zhuang, Y. (2018). Preparation, Characterization and *In Vivo* Antidiabetic Effects of Polysaccharides from Pachyrrhizus Erosus. *Int. J. Biol. Macromol.* 114, 97–105. doi:10.1016/j.ijbiomac.2018.03.099

Nie, C., Zhu, P., Wang, M., Ma, S., and Wei, Z. (2017). Optimization of Water-Soluble Polysaccharides from Stem Lettuce by Response Surface Methodology and Study on its Characterization and Bioactivities. *Int. J. Biol. Macromol.* 105, 912–923. doi:10.1016/j.ijbiomac.2017.07.125

Ojemann, L. M., Nelson, W. L., Shin, D. S., Rowe, A. O., and Buchanan, R. A. (2006). Tian Ma, an Ancient Chinese Herb, Offers New Options for the Treatment of Epilepsy and Other Conditions. *Epilepsy Behav.* 8 (2), 376–383. doi:10.1016/j.yebeh.2005.12.009

Oliveira, G. K. F., Tormin, T. F., Sousa, R. M. F., de Oliveira, A., de Morais, S. A. L., Richter, E. M., et al. (2016). Batch-Injection Analysis with Amperometric Detection of the DPPH Radical for Evaluation of Antioxidant Capacity. *Food Chem.* 192, 691–697. doi:10.1016/j.foodchem.2015.07.064

Peng, Z., Liu, M., Fang, Z., and Zhang, Q. (2012). *In Vitro* antioxidant Effects and Cytotoxicity of Polysaccharides Extracted from Laminaria Japonica. *Int. J. Biol. Macromol.* 50 (5), 1254–1259. doi:10.1016/j.ijbiomac.2012.04.006

Qiao, D., Ke, C., Hu, B., Luo, J., Ye, H., Sun, Y., et al. (2009). Antioxidant Activities of Polysaccharides from Hyriopsis Cumingii. *Carbohydr. Polym.* 78 (2), 199–204. doi:10.1016/j.carbpol.2009.03.018

Sall, D., Wang, J., Rashkin, M., Welch, M., Droege, C., and Schauer, D. (2014). Orlistat-Induced Fulminant Hepatic Failure. *Clin. Obes.* 4, 342–347. doi:10.1111/cob.12075

Sevag, M. G., Lackman, D. B., and Smolens, J. (1938). The Isolation of the Components of Streptococcal Nucleoproteins in Serologically Active Form. *J. Biol. Chem.* 124 (2), 425–436. doi:10.1016/s0021-9258(18)74048-9

Sun, W. D., Melton, L. D., O'Connor, C. J., Kilmartin, P. A., and Smith, B. G. (2008). Effect of Apple Cell Walls and Their Extracts on the Activity of Dietary Antioxidants. *J. Agric. Food Chem.* 56 (1), 289–295. doi:10.1021/jf072670v

Tabatabai, M. A. (1974). A Rapid Method for Determination of Sulfate in Water Samples. *Environ. Lett.* 7 (3), 237–243. doi:10.1080/00139307409437403

Thaipong, K., Boonprakob, U., Crosby, K., Cisneros-Zevallos, L., and Hawkins Byrne, D. (2006). Comparison of ABTS, DPPH, FRAP, and ORAC Assays for Estimating Antioxidant Activity from Guava Fruit Extracts. *J. Food Compos. Analysis* 19 (6-7), 669–675. doi:10.1016/j.jfca.2006.01.003

Wang, C. C., Chang, S. C., Inbaraj, B. S., and Chen, B. H. (2010). Isolation of Carotenoids, Flavonoids and Polysaccharides from Lycium Barbarum L. And Evaluation of Antioxidant Activity. *Food Chem.* 120, 184–192. doi:10.1016/j.foodchem.2009.10.005

Wang, M., Zhu, P., Jiang, C., Ma, L., Zhang, Z., and Zeng, X. (2012). Preliminary Characterization, Antioxidant Activity *In Vitro* and Hepatoprotective Effect on Acute Alcohol-Induced Liver Injury in Mice of Polysaccharides from the Peduncles of Hovenia Dulcis. *Food Chem. Toxicol.* 50 (9), 2964–2970. doi:10.1016/j.fct.2012.06.034

Wang, Y., Yang, Z., and Wei, X. (2010). Sugar Compositions, α-Glucosidase Inhibitory and Amylase Inhibitory Activities of Polysaccharides from Leaves and Flowers of Camellia Sinensis Obtained by Different Extraction Methods. *Int. J. Biol. Macromol.* 47 (4), 534–539. doi:10.1016/j.ijbiomac.2010.07.007

Wang, Z.-W., Li, Y., Liu, D.-H., Mu, Y., Dong, H.-J., Zhou, H.-L., et al. (2018). Chemical Constituents from the Rhizomes of Gastrodia Elata F. Glauca and Their Potential Neuroprotective Effects. *Phytochem. Lett.* 24, 167–171. doi:10.1016/j.phytol.2018.02.010

Wu, S., Lai, M., Luo, J., Pan, J., Zhang, L.-M., and Yang, L. (2017). Interactions between α-Amylase and an Acidic Branched Polysaccharide from Green Tea. *Int. J. Biol. Macromol.* 94, 669–678. doi:10.1016/j.ijbiomac.2016.09.036

Xing, R., Liu, S., Guo, Z., Yu, H., Wang, P., Li, C., et al. (2005). Relevance of Molecular Weight of Chitosan and its Derivatives and Their Antioxidant Activities *In Vitro*. *Bioorg. Med. Chem.* 13 (5), 1573–1577. doi:10.1016/j.bmc.2004.12.022

Yan, J.-K., Ding, Z.-C., Gao, X., Wang, Y.-Y., Yang, Y., Wu, D., et al. (2018). Comparative Study of Physicochemical Properties and Bioactivity of Hericium erinaceus Polysaccharides at Different Solvent Extractions. *Carbohydr. Polym.* 193, 373–382. doi:10.1016/j.carbpol.2018.04.019

Yu, X.-H., Liu, Y., Wu, X.-L., Liu, L.-Z., Fu, W., and Song, D.-D. (2017). Isolation, Purification, Characterization and Immunostimulatory Activity of Polysaccharides Derived from American Ginseng. *Carbohydr. Polym.* 156, 9–18. doi:10.1016/j.carbpol.2016.08.092

Yuan, Q., Lin, S., Fu, Y., Nie, X.-R., Liu, W., Su, Y., et al. (2019). Effects of Extraction Methods on the Physicochemical Characteristics and Biological Activities of Polysaccharides from Okra (Abelmoschus Esculentus). *Int. J. Biol. Macromol.* 127, 178–186. doi:10.1016/j.ijbiomac.2019.01.042

Yuan, Y., Jin, X., Liu, J., Zhao, X., Zhou, J., Wang, X., et al. (2018). The Gastrodia Elata Genome Provides Insights into Plant Adaptation to Heterotrophy. *Nat. Commun.* 9 (1), 1615. doi:10.1038/s41467-018-03423-5

Yuan, Y. V., Carrington, M. F., and Walsh, N. A. (2005). Extracts from Dulse (Palmaria Palmata) Are Effective Antioxidants and Inhibitors of Cell Proliferation *In Vitro*. *Food Chem. Toxicol.* 43, 1073–1081. doi:10.1016/j.fct.2005.02.012

Yue, Y., Li, Z., Li, P., Song, N., Li, B., Lin, W., et al. (2017). Antiviral Activity of a Polysaccharide from Laminaria Japonica against Enterovirus 71. *Biomed. Pharmacother.* 96, 256–262. doi:10.1016/j.biopha.2017.09.117

Zhan, H.-D., Zhou, H.-Y., Sui, Y.-P., Du, X.-L., Wang, W.-H., Dai, L., et al. (2016). The Rhizome of Gastrodia Elata Blume - An Ethnopharmacological Review. *J. Ethnopharmacol.* 189, 361–385. doi:10.1016/j.jep.2016.06.057

Zhang, D., Li, S., Xiong, Q., Jiang, C., and Lai, X. (2013). Extraction, Characterization and Biological Activities of Polysaccharides from Amomum Villosum. *Carbohydr. Polym.* 95 (1), 114–122. doi:10.1016/j.carbpol.2013.03.015

Zhang, Y., Wang, C., Yu, B., Jiang, J.-D., and Kong, W.-J. (2018). Gastrodin Protects against Ethanol-Induced Liver Injury and Apoptosis in HepG2 Cells and Animal Models of Alcoholic Liver Disease. *Biol. Pharm. Bull.* 41 (5), 670–679. doi:10.1248/bpb.b17-00825

Zhang, Y., Zhang, J., Mo, X., Lu, X., Zhang, Y., and Qin, L. (2010). Modification, Characterization and Structure-Anticoagulant Activity Relationships of Persimmon Polysaccharides. *Carbohydr. Polym.* 82 (2), 515–520. doi:10.1016/j.carbpol.2010.05.008

Zhang, Z., Wang, X., Liu, C., and Li, J. (2016). The Degradation, Antioxidant and Antimutagenic Activity of the Mucilage Polysaccharide from Dioscorea Opposita. *Carbohydr. Polym.* 150, 227–231. doi:10.1016/j.carbpol.2016.05.034

Zhishen, J., Mengcheng, T., and Jianming, W. (1999). The Determination of Flavonoid Contents in Mulberry and Their Scavenging Effects on Superoxide Radicals. *Food Chem.* 64 (4), 555–559. doi:10.1016/s0308-8146(98)00102-2

Zhou, B., Tan, J., Zhang, C., and Wu, Y. (2017). Neuroprotective Effect of Polysaccharides from Gastrodia Elata Blume against Corticosterone-Induced Apoptosis in PC12 Cells via Inhibition of the Endoplasmic Reticulum Stress-Mediated Pathway. *Mol. Med. Rep.* 17, 1182–1190. doi:10.3892/mmr.2017.7948

Complanatuside alleviates inflammatory cell damage induced by pro-inflammatory cytokines in skin keratinocytes

Xiao Wang[1], Xuetao Xu[1,2], Panpan Wu[1,2], Mengshuo Wu[1], Lishe Gan[1,2], Jingwei Jin[1], Rihui Wu[1], Wenfeng Liu[1], Kun Zhang[1], Dongli Li[2]* and Xi Zheng[3]*

[1]School of Biotechnology and Health Sciences, Wuyi University, Jiangmen City, China, [2]International Healthcare Innovation Institute (Jiangmen), Jiangmen, China, [3]Department of Chemical Biology, Ernest Mario School of Pharmacy, Rutgers, the State University of New Jersey, Piscataway, NJ, United States

Cytokine-mediated inflammatory response is considered a cause of skin lesion in COVID-19 patients. Complanatuside is a flavonol glycoside isolated from *Astragalus complanatus*. Flavonoids from *Astragalus complanatus* were reported to have anti-inflammatory and anticancer activities but the potential protective effect of complanatuside on cytokine-induced inflammatory damage in skin keratinocytes is not known. The aim of this study is to explore the inhibitory effect of complanatuside on inflammation and its underlying mechanisms in skin epithelial HaCaT cells treated with inflammatory cytokines. The combination of IFN-γ, TNF-α, and IL-6 decreased cell viability, increased cell death, and pyroptosis in HaCaT cells. Treatment with complanatuside alleviated the effects of the cytokine combination on HaCaT cells. Complanatuside down-regulated pyroptosis related to NLRP3, GSDMD, and ASC. The effects of complanatuside were related to vast reductions in the levels of iNOS, COX-2, and ROS. Results of the present study indicate that complanatuside inhibited inflammation and protected the cells from inflammatory cell damage in HaCaT cells treated with the combination of IFN-γ, TNF-α, and IL-6. Complanatuside may be a promising candidate for inhibiting COVID-19 related skin inflammatory damage.

KEYWORDS
HaCaT cells, skin inflammatory damage, complanatuside, pyroptosis, COVID-19
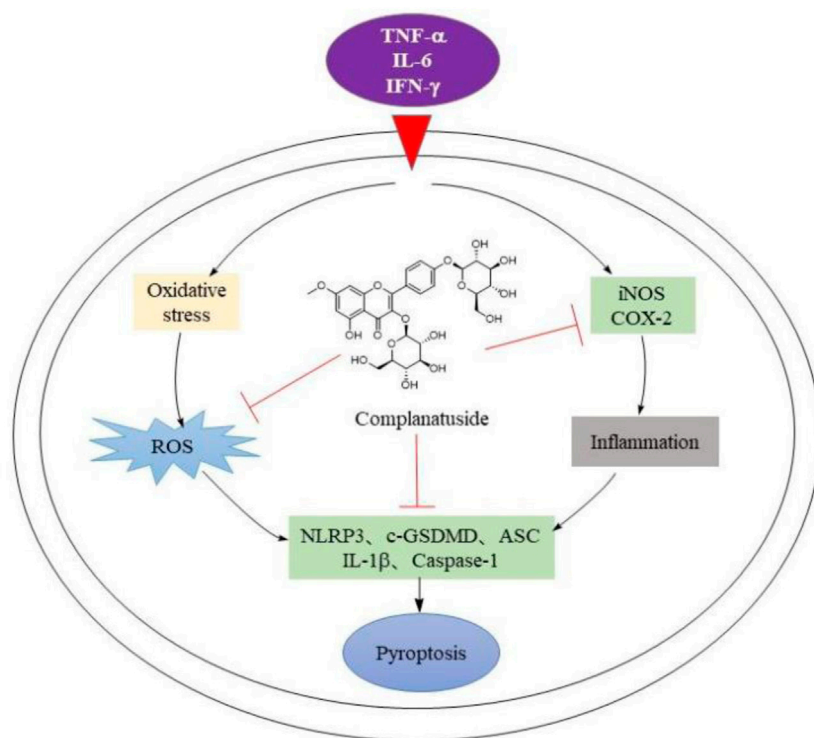
Graphical Abstract

Introduction

Severe acute respiratory syndrome coronavirus 2 (SARS-CoV-2) is the cause of Coronavirus disease-19 (COVID-19), which is a worldwide epidemic (Huang et al., 2020). The COVID-19 pandemic has affected many countries and caused an overwhelming of health care systems and both psychological and economic burdens. Although COVID-19 is best known to cause interstitial pneumonia and respiratory failure (Novak et al., 2021), skin manifestations as extrapulmonary signs associated with COVID-19 have been increasingly reported (Marzano et al., 2020; Matar et al., 2020). According to the recent classification, as shown by a study from Spain, the most typical presentations of skin lesions include chilblain-like lesions, ischemic-livedoid/necrotic lesions, and varicelliform-like/vesicular eruptions. Vacuolar interface dermatitis with scattered dead keratinocytes has been found in chilblain-like lesions. Histopathology of ischemic-livedoid/necrotic lesions related to COVID-19 is characterized by epidermal necrosis and thrombotic vascular lesions (Rongioletti et al., 2021). The COVID-19 skin lesions are plausibly associated with the excessive inflammation response of the patients characterized by pathological cytokine levels. However, the pathogenesis of the skin lesions in COVID-19 patients is not clear. It has been hypothesized that the increase in COVID-19 related release of interferon and inflammatory cell damage induced by cytokines may cause the skin lesions (Grimm et al., 2021).

Coronavirus, especially SARS-CoV-2, can cause a "cytokine storm" by increasing the production and release of pro-inflammatory cytokines (Barnes et al., 2020). Studies have shown that the cytokine storm is directly related to lung injury, multiple organ failure, and death of COVID-19 (Gao et al., 2020; Sun et al., 2020). TNF-α, IL-6, IFN-γ, IL-18, IL-15, IL-1α, IL-1β, and IL-2 are among the most highly upregulated pro-inflammatory cytokines in COVID-19 (Lucas et al., 2020; Karki et al., 2021).

Studies indicate that IL-6, TNF-α, and IFN-γ has become a significant feature of COVID-19 patient deterioration (Fara et al., 2020; Gubernatorova et al., 2020). Inflammatory cell death may be a possible mechanistic link between cytokine storm and organ damage. A recent study showed that among the eight cytokines tested, TNF-α in combination with IFN-γ strongly induced inflammatory cell death, and administration of this cytokine combination to mice resulted in lethal cytokine shock which resembles COVID-19 related tissue damage and inflammation (Karki et al., 2021).

Results of this study indicated that pathological levels of multiple cytokines can cause inflammatory cell death and contribute to tissue damage in COVID-19 patients. It is of great interest to investigate the effects of multiple cytokines on skin keratinocytes and explore the possible mechanistic link between cytokine storm and skin lesions in COVID-19 patients.
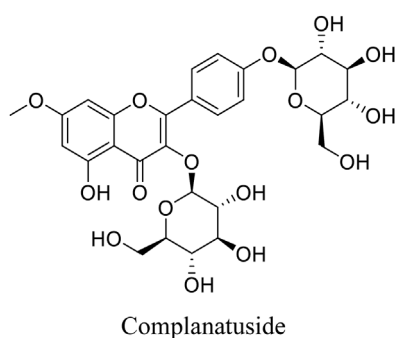
FIGURE 1
Structure of complanatuside.

Complanatuside is a flavonol glycoside (Figure 1) present in *Astragalus complanatus*. That is commonly used as a traditional Chinese medicine in clinics. Flavonoids from *Astragalus complanatus* have been reported to exert inhibitory effects on inflammation and cancer (Ng et al., 2014; Yao et al., 2018). In this study, IL-6, TNF-α, and IFN-γ were used to simulate "cytokine storm" to induce inflammatory injury in HaCaT cells. We utilized this model to determine the inhibitory effect of complanatuside on inflammation and explore the mechanisms underlying its actions.

Materials and methods

Cell line and cell culture

HaCaT cells were obtained from the American Type Culture Collection (ATCC, Rockville, MD, United States). Dulbecco's Modified Eagle Medium (DMEM) medium supplemented with 10% fetal bovine serum (FBS), penicillin (100 units/mL), and streptomycin (100 mg/ml) (all from Gibco, Grand Island, NY, United States) was used for the culture of HaCaT cells. The cells were grown at 37°C in a humidified atmosphere of 5% CO_2. IFN-γ was purchased from Beijing T&L Biotechnology Co., Ltd. TNF-α and IL-6 were obtained from Shanghai Bohu Biotech Co., Ltd. Complanatuside was obtained from Meilunbio (Dalian, China). The compounds were dissolved in dimethyl sulfoxide (DMSO, Sigma-Aldrich, St. Louis, MO, United States) as a stock solution and stored at −20°C and the final concentration of DMSO in all experiments was 0.2%.

Cell viability assay

HaCaT cells were grown in 96-well plates at a cell density of 5×10^3 cells/well and incubated for 24 h to allow the attachment of the cells to the culture plates. The cells were treated with serum-free

DMEM medium for 24 h, then treated with various concentrations of complanatuside and incubated in the absence or presence of cytokine combinations (80 ng/ml IFN-γ, 40 ng/ml TNF-α, and 20 ng/ml IL-6) for 24 h. At the end, MTT solution (200 μl; 0.5 mg/ml in DMEM medium without serum) was added to each of the wells. The plate was incubated at 37°C for 4 h. After carefully removing the medium, 200 μl DMSO was added to each well. The absorbance at 570 nm was measured by a microplate reader.

Trypan blue exclusion assay

HaCaT cells (5×10^5 cells/mL) were grown in 35-mm cell culture dishes (2 ml/dish) and incubated in DMEM +10% FBS for 24 h. The cells were treated with serum-free DMEM medium for 24 h, the media were subsequently changed to different concentrations of complanatuside with a cytokine combination of IFN-γ (80 ng/ml), TNF-α (40 ng/ml), and IL-6 (20 ng/ml) alone or in cytokine combination for 24 h. After treatment, the cells were digested by trypsin to make a single cell suspension. 10 μl of cell suspension was mixed with 10 μl of 0.4% trypan blue solution for 2 min. The number of viable and dead cells was counted by the countess automatic cell counter (Countess®, AMQAX1000, Thermo, United States).

ROS measurement

ROS were examined using 2′,7′-dichlorfluoroescein diacetate (DCFH-DA) and ROS ELISA Kit (Shanghai Enzyme-linked Biotech Co., Ltd, China). HaCaT cells (1×10^6 cells/well) were plated in 35-mm cell culture dishes for 24 h. After HaCaT cells were treated with cytokine combinations and complanatuside, the supernatants were gathered and subjected to the analysis of ROS by using the ROS ELISA Kit. After washing with PBS buffer, cells were incubated with 10 μM DCFH-DA in the culture medium at 37°C for 30 min in the dark. After washing, the fluorescent signals (excitation at 488 nm and emission at 525 nm) in the cells were determined by a fluorescence microplate reader.

IL-1β assay

To determine IL-1β, HaCaT cells (1×10^6 cells/well) were plated in 6-well plates and incubated for 24 h to allow the attachment of cells to the culture plates. The cells were treated with serum-free DMEM medium for 24 h, then treated with various concentrations of complanatuside and incubated in the absence or presence of cytokine combination (80 ng/ml IFN-γ, 40 ng/ml TNF-α, and 20 ng/ml IL-6) for 24 h. After treatment, the culture supernatants were gathered and subjected to the analysis of IL-1β by using the IL-1β ELISA Kit (ab214025).
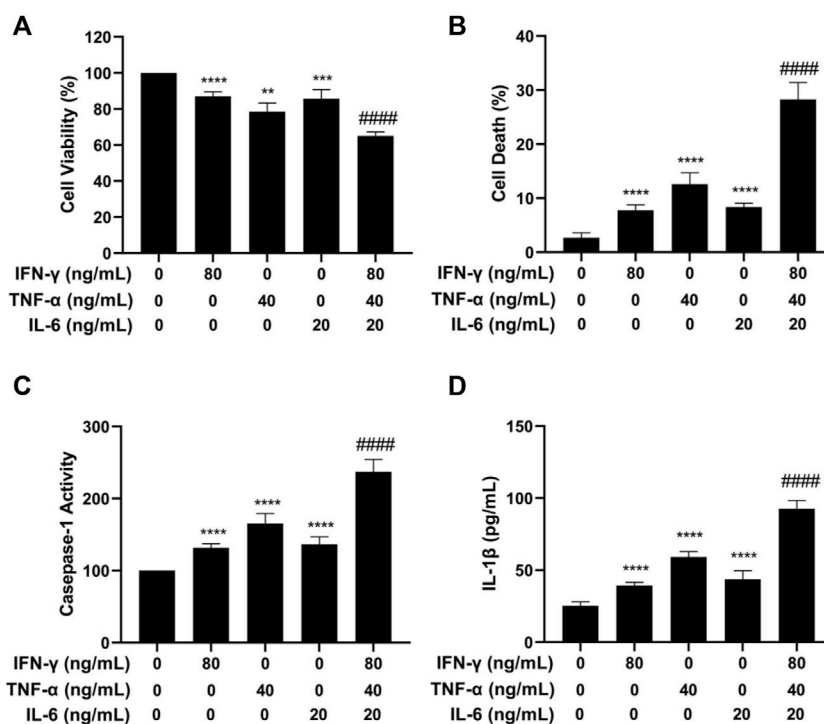
FIGURE 2
Effects of IFN-γ, TNF-α, and IL-6 on cell viability, cell death, caspase-1 activation, and IL-1β level of HaCaT cells. HaCaT cells were exposed to IFN-γ, TNF-α, and IL-6 alone or in combination for 24 h. **(A)** The MTT assay was used to determine the cell viability. **(B)** The Trypan blue exclusion assay was used to determine cell death. **(C)** Caspase-1 activity was detected by the caspase-1 assay kit. **(D)** IL-1β level was measured by ELISA. The data were presented as mean $\pm$ SD (n = 3), **** = $p < 0.01$, **** = $p < 0.001$, and **** = $p < 0.0001$ as compared with the cells treated with IFN-γ, TNF-α, or IL-6 alone.

Caspase-1 assay

Caspase-1 fluorescence staining was done using the Caspase-1 (active) Staining Kit-Green Fluorescence (#ab219935, Abcam Ltd., Waltham, MA). HaCaT cells were treated with various concentrations of complanatuside in the presence or absence of cytokine combination (80 ng/ml IFN-γ, 40 ng/ml TNF-α, and 20 ng/ml IL-6). After treatment, FAM-YVAD-FMK was added into the cell solution and incubated for 1 h at 37°C. Caspase-1 staining was analyzed in cells by a fluorescence microscope. For the caspase-1 activity assay, the Caspase-1 assay kit (Fluorometric) (#ab39412, Abcam) was used. In brief, cell lysates were prepared after treatment. Reaction buffer and YVAD-AFC substrate were mixed with cell lysates and incubated for 1 h at 37°C. Samples were analyzed using a fluorescence microplate reader at an excitation wavelength of 400 nm and an emission wavelength of 505 nm.

Western blot

At the end of the experiment, the cells were lysed to prepare cell lysates. Proteins were loaded and separated by sodium dodecyl sulfate polyacrylamide gel electrophoresis (SDS-PAGE) and transferred to a nitrocellulose membrane. After blocking nonspecific binding sites with blocking buffer, the membranes were incubated overnight at 4°C with primary antibodies. β-Actin (#8457, CST) was used as a loading control. After the removal of the primary antibodies (COX-2, #12282, CST; iNOS, AF0199, Affinity; ASC, #13833, CST; GSDMD, AF4012, Affinity; NLRP3, AG-20B-0014-C100, AdipoGen), the membranes were then washed three times with TBST buffer (100 mM NaCl, 10 mM Tris-HCl, pH 7.5, and 0.1% Tween-20) at room temperature and incubated with secondary antibody. Next, the membrane was washed with TBST buffer three times. Finally, protein bands were detected using the Pierce™ ECL Western Blotting Substrate (Thermo Scientific, United States).

Statistical analysis

Statistical analyses were done by using the software Graphpad Prism. All data were presented as mean ± SD. One-way ANOVA was performed to evaluate the difference between groups. The differences were considered statistically significant at $p < 0.05$.
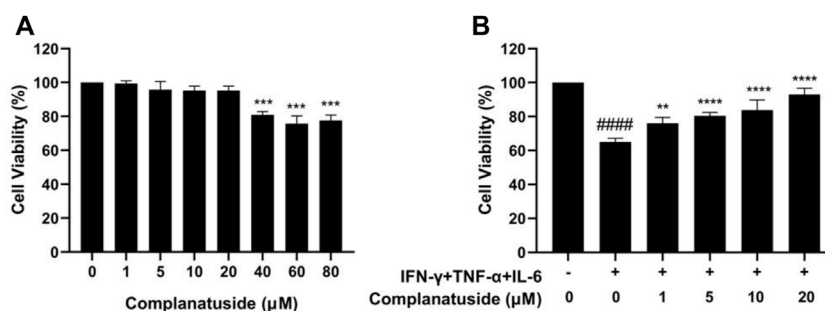
FIGURE 3
Effects of complanatuside on the viability of HaCaT cells with or without the cytokine combination treatment. **(A)** HaCaT cells were treated with various concentrations of complanatuside for 24 h. The MTT assay was used to determine cell viability. The results were shown as mean $\pm$ SD (n = 3), ******* = p < 0.001 as compared with control cells. **(B)** HaCaT cells were treated with various concentrations of complanatuside in the absence or presence of cytokine combination and the cell viability was determined by MTT assay. Mean $\pm$ SD from three separate experiments were shown. **\#\#\#\#** = p < 0.0001 as compared with control group, ******* = p < 0.001, and ******** = p < 0.0001 as compared with cells treated with cytokine combination.

Results

Effect of IFN-γ, TNF-α and IL-6 on the viability of HaCaT cells

Initial experiments were carried out by treating HaCaT cells with cytokines of IFN-γ, TNF-α, and IL-6 alone or in combination. After a 24 h-treatment, the MTT assay was used to determine cell viability. As shown in Figure 2A, after treatment with IFN-γ, TNF-α, and IL-6 separately or in combination, the average survival rate of HaCaT cells was 87.1%, 78.1%, 85.6%, and 65.1%, respectively. The combined effect of IL-6, TNF-α, and IFN-γ on cell viability was more obvious than that of single factor alone, and the survival rate was obviously lower in the combination-treated cells than that in the single cytokine-treated cells. The result of the study described above indicated that the combination of IFN-γ, TNF-α, and IL-6 strongly decreased the HaCaT cell viability.

IFN-γ, TNF-α, and IL-6 induce cell death in HaCaT cells

We next investigated the effect of the cytokines separately or in combination on HaCaT cell death using the trypan blue exclusion assay. As shown in Figure 2B, the combination of IFN-γ, TNF-α, and IL-6 strongly increased the number of dead cells. The combination of IFN-γ, TNF-α, and IL-6 had a more potent effect on inducing cell death than each cytokine used alone (p < 0.0001). To further investigate if the cytokine combination induced pyroptosis, caspase-1 activation and IL-1β were examined in HaCaT cells after treatment with IFN-γ, TNF-α, and IL-6. Caspase-1 activation contributes to the maturation of cytokines and membrane pore forming protein

gasdermine during the process of pyroptosis and can be used as a marker of pyroptosis. As displayed in Figure 2C, treatment of HaCaT cells with the cytokine combination strongly increased the activity of caspase-1. Statistical analysis showed that the cells treated with the cytokine combination had a significantly higher level of caspase-1 activity (p < 0.0001) as compared to the cells treated with a single cytokine.

IL-1β is a proinflammatory cytokine that is released by the host cells and is involved in the process of pyroptosis. The effects of IFN-γ, TNF-α, and IL-6 alone or in combination on increasing the levels of IL-1β were determined using the ELISA assay. As illustrated in Figure 2D, treatment of HaCaT cells with the cytokine combination strongly increased the level of IL-1β. The differences in the level of IL-1β between the single cytokine-treated group and the cytokine combination-treated group were statistically significant (p < 0.0001). The results of caspase-1 and IL-1β experiments indicated that the IFN-γ, TNF-α, and IL-6 in combination induced pyroptosis in the HaCaT cells.

Complanatuside alleviates the effect of IFN-γ, TNF-α, and IL-6 on decreasing cell viability

Cytotoxicity of complanatuside was evaluated using the MTT assay before the evaluation of its potential protective effect on cytokine-induced cell damage in HaCaT cells. In these experiments, HaCaT cells were treated with different concentrations of complanatuside for 24 h, and the cell viability was measured using the MTT assay. As shown in Figure 3A, complanatuside did not alter the cell viability significantly at concentrations up to 20 μM. Statistical analysis exhibited that the differences in cell viability between the control
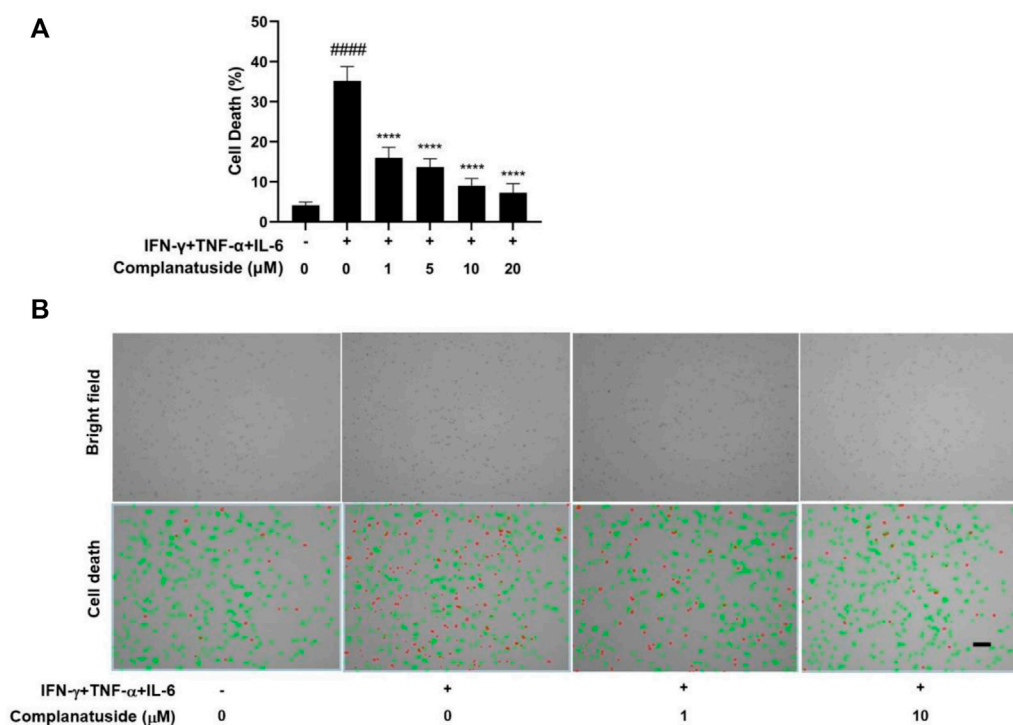
FIGURE 4
Protective effect of complanatuside on HaCaT cell death induced by the cytokine combination. HaCaT cells were treated with various concentrations of complanatuside in the absence or presence of cytokine combination and cell death was determined by the Trypan blue exclusion assay. **(A)** Percentage of cell death in HaCaT cells treated with the cytokine combination in the presence or absence of complanatuside. The data were presented as mean $\pm$ SD ($n = 3$), **####** = $p < 0.0001$ as compared with the control group, ******** = $p < 0.0001$ as compared with the cytokine combination-treated group. **(B)** Images of control cells, cytokine combination-treated cells, cells treated with cytokine combination, and complanatuside (1 or 10 μM) were taken by the Countess® automatic cell counter. Red color represents dead cells and green represents living cells (Size bar = 50 μm).

group and different concentrations of complanatuside-treated groups (1, 5, 10, and 20 μM) were not statistically significant ($p > 0.05$). Higher concentrations of complanatuside (40, 60, and 80 μM) significantly reduced the cell viability ($p < 0.0001$). The results indicated that complanatuside had no toxicity to the skin keratinocytes at a concentration range of 1–20 μM. Therefore, all subsequent experiments were conducted using these non-toxic concentrations.

As shown in Figure 3B, treatment with the combination of IFN-γ, TNF-α, and IL-6 significantly decreased the viability of HaCaT cells. It was noticed that complanatuside increased the cell viability of HaCaT cells treated with the cytokine combination. When HaCaT cells were treated with complanatuside at 1, 5, 10, and 20 μM, the cell survival rates as compared to the cytokine combination-treated cells were increased by 11.0, 15.3, 18.7, and 28.0%, respectively. Results of our study suggested that complanatuside at non-toxic concentrations protected HaCaT cells from the cytokine combination-induced decrease in cell viability.

Protective effect of complanatuside on HaCaT cell death induced by TNF-α, IFN-γ, and IL-6

The potential protective effect of complanatuside on HaCaT cell death induced by the combination of TNF-α, IFN-γ, and IL-6 was examined using the trypan blue exclusion assay and the result was shown in Figure 4. The cytokine combination strongly induced cell death in HaCaT cells (Figure 4A). Treatment with complanatuside reduced the number of dead cells. Complanatuside at 1, 5, 10, and 20 μM decreased the dead cells by 19.2, 21.5, 26.2, and 27.9%, respectively. Representative graphs of the trypan blue assay by the Countess II cell counter were shown in Figure 4B. Cells labeled with green are alive cells, and those labeled red are dead cells. As illustrated in Figure 4B, the number of red cells increased in cytokine-induced cells as compared with the negative control. Treatment with complanatuside markedly decreased the red cells, indicating that complanatuside could protect HaCaT cells from cytokine-induced cell death in HaCaT cells.
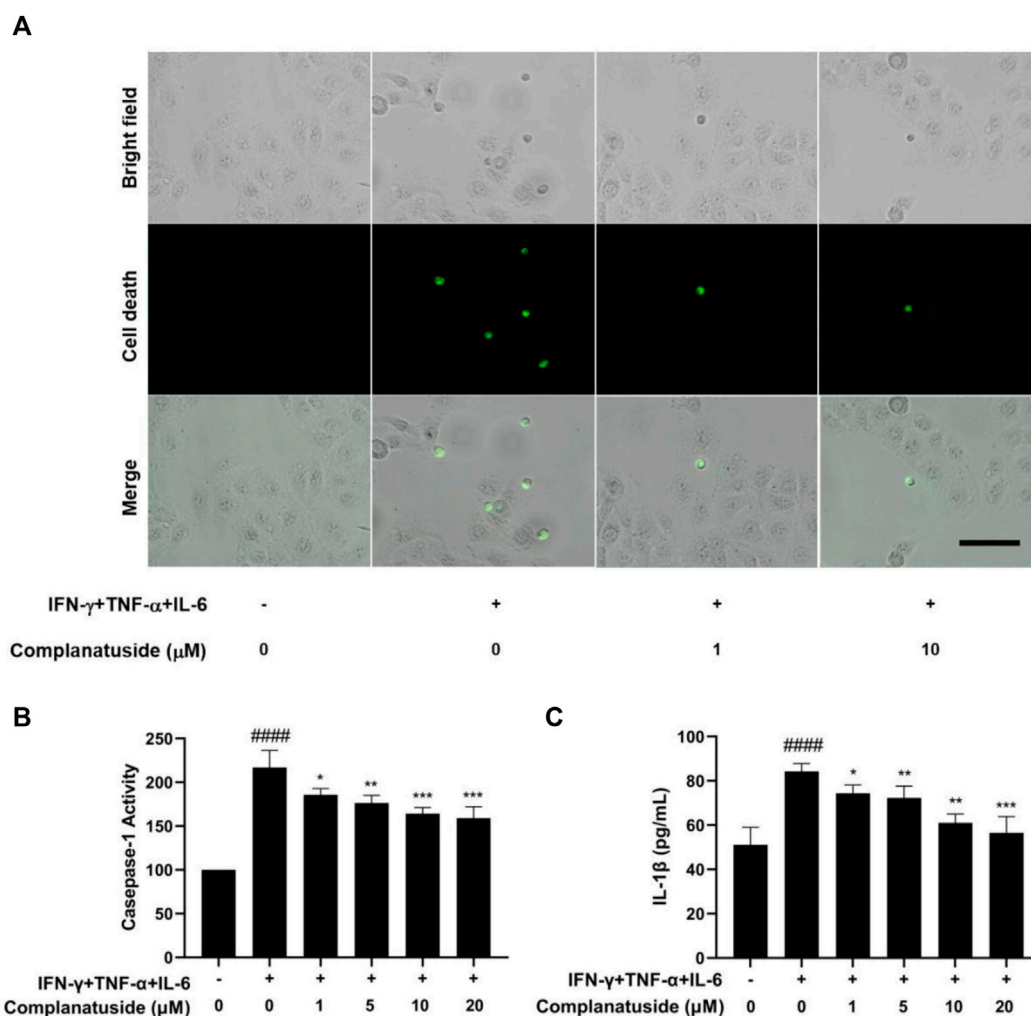
FIGURE 5
Protective effect of complanatuside on pyroptosis in HaCaT cells induced by the cytokine combination. **(A)** Representative micrographs of caspase-1 staining in HaCaT cells treated with complanatuside in the presence or absence of the cytokine combination (Size bar = 25 μm). **(B)** Caspase-1 activity in HaCaT cells was measured using the caspase-1 assay kit. **(C)** ELISA was used to measure the levels of IL-1β. The data were presented as mean $\pm$ SD ($n = 3$), **####** = $p < 0.0001$ as compared with control group, ***** = $p < 0.05$, ****** = $p < 0.01$, and ******* = $p < 0.001$ as compared with the cells treated with cytokine combination.

We further explored the effect of complanatuside on cytokine-induced inflammatory cell death, pyroptosis, in HaCaT cells. Figure 5 showed the results of pyroptosis in HaCaT cells as indicated by the increase in caspase-1 and IL-1β. Treatment of the cells with complanatuside decreased the activation of caspase-1 induced by the cytokine combination. Representative micrographs of caspase-1 fluorescence staining in HaCaT cells are shown in Figure 5A. More caspase-1 positive cells were found in HaCaT cells treated with the cytokine combination as compared with the negative control. Treatment with complanatuside decreased the number of caspase-1 positive cells (Figure 5A). Caspase-1 was also tested using the caspase-1 activity assay kit. As shown in Figure 5B, treatment of the cells with complanatuside significantly decreased the caspase-1 activity induced by the cytokine combination ($p < 0.001$). ELISA was used to determine the effect of complanatuside on the levels of IL-1β in HaCaT cells. As shown in Figure 5C, treatment with complanatuside reduced the elevated level of IL-1β caused by the cytokine combination. Treatment with complanatuside at 1, 5, 10, and 20 μM decreased the levels of IL-1β by 11.7, 14.2, 27.6, and 32.9%, respectively. The results of these experiments indicated that complanatuside strongly alleviated pyroptosis induced by the combination of TNF-α, IFN-γ, and IL-6 in HaCaT cells.

FIGURE 6
Effects of complanatuside on the levels of NLRP3, ASC, and cleaved GSDMD in HaCaT cells treated with the cytokine combination. HaCaT cells were treated with various concentrations of complanatuside with or without co-treatment with the cytokine combination for 24 h. The levels of NLRP3, ASC, and cleaved GSDMD were determined by Western blot analysis.

Effects of complanatuside on NLRP3 GSDMD ASC

Studies have shown that pyroptosis in COVID-19 may be associated with activation of the NLRP3 associated pyroptosis pathway (Song et al., 2020). Therefore, we measured the levels of NLRP3, ASC, and GSDMD in HaCaT cells. As shown in Figure 6, the levels of NLRP3, ASC, and cleaved GSDMD markedly increased in the cells exposed to the cytokine combination. Treatments with complanatuside strongly inhibited cytokine combination-induced NLRP3, ASC, and cleaved GSDMD expression, indicating that complanatuside had a potent inhibitory effect on the activation of pyroptosis pathway in HaCaT cells exposed to the combination of TNF-α, IFN-γ, and IL-6.

Effects of complanatuside on cytokines combination-induced iNOS, COX-2 and ROS

To further explore the mechanisms for inhibition of the NLRP3 pathway by complanatuside, we determined its effect on iNOS and COX-2, which have been shown to be associated with the activation of NLRP3 inflammasome (Kundu et al., 2018; Cinelli et al., 2020; Liao et al., 2021). As shown in Figure 7A, the cytokine combination strongly increased the levels of iNOS and COX-2 in HaCaT cells. Treatment of the cells with different concentrations of complanatuside dose-dependently reduced the elevated levels of iNOS and COX-2 in HaCaT cells induced by the cytokine combination. The results of these experiments suggested that inhibition of iNOS and COX-2 was involved in mediating the effect of complanatuside in cytokine-induced pyroptosis.

In additional experiments, we investigated the effects of cytokine combination and complanatuside on the levels of ROS in HaCaT cells. As shown in Figure 7B, the cytokine combination induced a distinct increase in the level of ROS, and treatment with complanatuside dose-dependently decreased the elevated level of ROS induced by the cytokine combination. The average inhibition rates in the cells treated with 1, 5, 10, and 20 μM of complanatuside were 10.1, 20.6, 25.1, and 29.5%, respectively. Representative micrographs of ROS fluorescence staining in the cells are shown in Figure 7C. The fluorescence intensity of ROS in HaCaT cells treated with the cytokine combination was visibly increased as compared with that in the control group, and treatment with complanatuside reduced the fluorescence intensity in the cells. The result of this study indicated that inhibition of inflammatory cell death by complanatuside in HaCaT cells was associated with strong suppression of ROS.

Discussion

According to current research, we demonstrated that the combination of IFN-γ, TNF-α, and IL-6 strongly decreased the viability of HaCaT skin keratinocytes. This cytokine combination also strongly increased the death of HaCaT cell. Our study further indicated that the HaCaT cell death induced by the cytokine combination involved inflammatory cell death and pyroptosis. In addition, we found that complanatuside effectively alleviated inflammatory cell death in HaCaT cells induced by the cytokine combination. As far as we know, this is the first study reporting the combined effect of IFN-γ, TNF-α, and IL-6 on pyroptosis in skin keratinocytes and the protective effect of complanatuside on cytokine-induced pyroptosis in HaCaT cells.
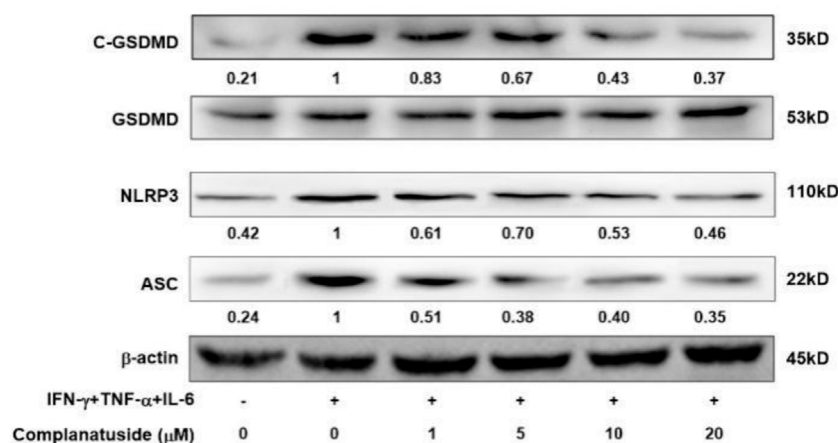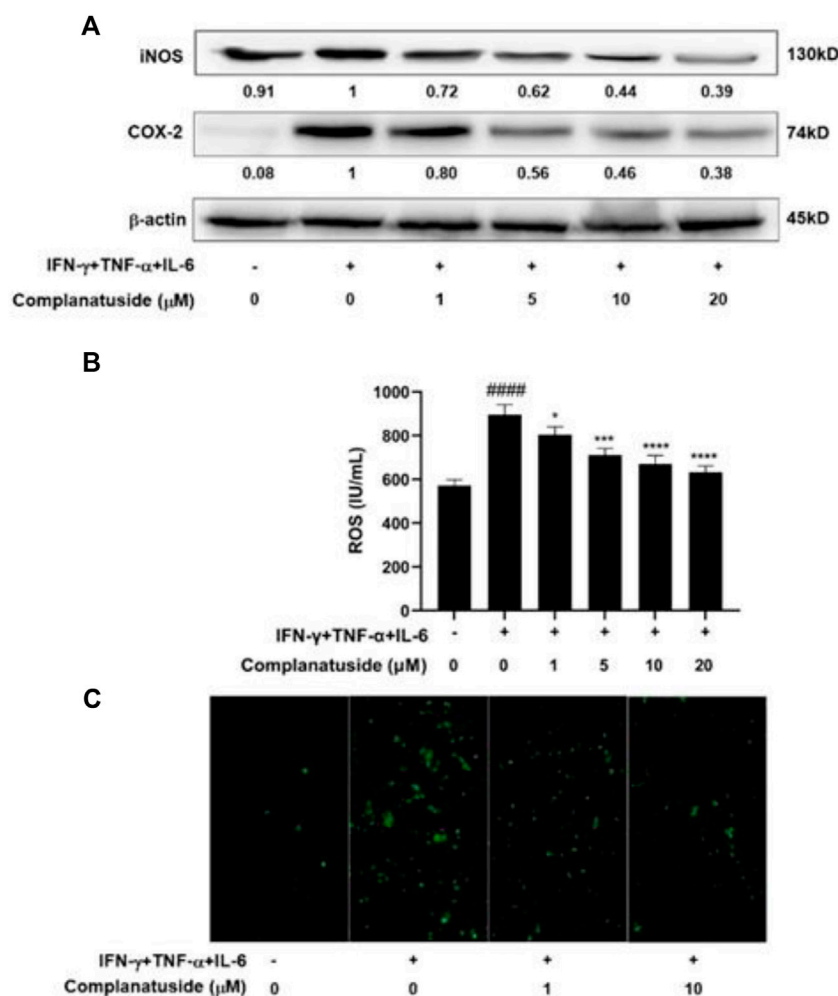
FIGURE 7

Effects of complanatuside on the levels of iNOS, COX-2, and ROS in HaCaT cells treated with the cytokine combination. HaCaT cells were treated with various concentrations of complanatuside with or without co-treatment with the cytokine combination for 24 h. **(A)** The levels of iNOS and COX-2 were determined by Western blot analysis. **(B)** ROS was detected using the fluorescence dye DCFH-DA and ELISA. ROS levels in HaCaT cells treated with complanatuside with or without co-treatment with the cytokine combination. The data were presented as mean $\pm$ SD. Asterisk indicates comparison between the cytokine combination–treated group and complanatuside-treated groups (***** = $p < 0.05$, ******* = $p < 0.001$, and ******** = $p < 0.0001$). The number sign # indicates comparison between the cells treated with cytokine combination and the cells in control group (**\#\#\#\#** = $p < 0.0001$). **(C)** Representative micrographs of ROS fluorescence staining of HaCaT cells treated with complanatuside in the presence or absence of the cytokine combination (Size bar = 50 μm).

Recent studies have indicated that IL-6, TNF-α, and IFN-γ were intensely elevated in COVID-19 patients and had become a significant feature of COVID-19 diseases deterioration (Diorio et al., 2020; Lucas et al., 2020; Karki et al., 2021). A recent study demonstrated that IFN-γ combined with TNF-α had a strong effect on inducing inflammatory cell death (Karki et al., 2021). Since IL-6 was found elevated in COVID-19, it is of great interest to explore the combined effect of IFN-γ, TNF-α, with IL-6 on inflammatory cell damage. We found that the cytokine combination strongly decreased cell viability and increased cell death in HaCaT cells. Utilizing caspase-1 and IL-1β as markers, we found that the cytokine combination induced pyroptosis in HaCaT cells. Caspase-1 activation contributes to the maturation of

cytokines and membrane pore forming protein gasdermine during the process of pyroptosis and can be used as a marker of pyroptosis. The proinflammatory cytokine IL-1β is released by the host cells and is involved in the process of pyroptosis. Results of our study demonstrated that the combination of IFN-γ, TNF-α, and IL-6 strongly increased caspase-1 activation and elevated the level of IL-1β, indicating that this cytokine combination induced pyroptosis in HaCaT cells.

In our continuing search for effective anti-inflammatory agents, a series of natural compounds were screened for their potential effect on alleviating cytokine-induced inflammatory response in skin keratinocytes. We found that complanatuside had protective

effect on HaCaT cells treated with IFN-γ, TNF-α and IL-6. Complanatuside is a flavonol glycoside isolated from *Astragalus complanatus*, which is commonly used in traditional Chinese medicine clinics. Studies have shown that flavonoids from *Astragalus complanatus* exert anti-inflammatory, anticancer, and immuno-modulating activities (Ng et al., 2014; Li et al., 2018; Yao et al., 2018). However, the anti-inflammatory effect and the protective effect of complanatuside on skin keratinocytes have not been reported. In our study, we found that complanatuside alleviated the effect of the cytokine combination on decreasing HaCaT cell viability. We also found that complanatuside decreased HaCaT cell pyroptosis induced by the cytokine combination. These results indicate that complanatuside protect HaCaT cells from cytokine-induced inflammatory cell damage.

To further investigate the mechanisms underlying the protective effect of complanatuside, we determined the effects of complanatuside on the NOD-like receptor, protein 3 (NLRP3), apoptosis-associated speck-like protein containing a caspase recruitment domain (ASC), and gasdermin D (GSDMD). Studies have shown that pyroptosis in COVID-19 may be associated with activation of NLRP3, ASC, and GSDMD (Song et al., 2020). The NLRP3 inflammasome is a complex platform involved in the activation of caspase-1 and the maturation of IL-1β in pyroptosis. NLRP3 activation elevates the release of the inflammatory cytokine IL-1β and induces pyroptosis (Wang et al., 2019). Downstream of NLRP3, ASC plays a crucial role in the formation of inflammasomes and the recruitment of caspase-1 (Satoh et al., 2013). GSDMD is a crucial component of the NLRP3 inflammasome and is required for IL-1β secretion and pyroptosis (He et al., 2015). Our study showed that pyroptosis in HaCaT cells resulted from the treatment with IFN-γ, TNF-α, and IL-6 and was associated with the increase in NLRP3, ASC, and GSDMD, and treatment with complanatuside strongly decreased the levels of these proteins. The results of the present study suggest that the combination of IFN-γ, TNF-α, and IL-6 induces pyroptosis through the NLRP3 inflammasome pathway, and inhibition of this pathway by complanatuside can effectively reduce pyroptosis in skin keratinocytes.

The mechanisms for activation of the NLRP3 inflammasome are not entirely clear. Inducible nitric oxide synthase (iNOS), one of the important inflammation regulators, has recently been found to be involved in NLRP3 activation and pyroptosis (Cinelli et al., 2020; Liao et al., 2021). COX-2 is an inflammatory mediator factor, which plays an important role in inducing inflammation-related diseases (Kundu et al., 2018). It was shown that COX-2 enhanced the activation of NLRP3 inflammasome and pyroptosis (Hua et al., 2015). Results of our study showed that treatment with complanatuside resulted in decreases in the levels of iNOS and COX-2 in HaCaT cells treated with the combination of IFN-γ, TNF-α, and IL-6. This result supports the notion that the effect of complanatuside on inhibiting NLRP3 inflammasome is partly mediated via inhibition of iNOS and COX-2.

ROS is a second messenger that regulates the inflammatory response. Inflammation can increase the level of ROS, and overexpression of ROS can also aggravate the inflammatory response (Forrester et al., 2018). ROS is involved in the inflammatory response in COVID-19 (Morris et al., 2020) and activation of NLRP3 (Abais et al., 2015). In our study, we found that that the elevated level of ROS in HaCaT cells treated with the combination of IFN-γ, TNF-α, and IL-6 was strongly reduced upon treatment with complanatuside. This result, together with the inhibitory effect of complanatuside on iNOS and COX-2 as described above, suggests that multiple mechanisms may contribute to the protective effect of complanatuside on cytokine-induced pyroptosis. Simultaneously inhibition of iNOS, COX-2, and ROS may be an effective strategy for alleviating cytokine storm induced skin lesion in COVID-19 patients.

Conclusion

To sum up, our results demonstrated that complanatuside alleviated inflammatory cell damage induced by the IFN-γ, TNF-α, and IL-6 combination in skin keratinocytes. Complanatuside protected HaCaT cells from cytokine-induced pyroptosis as evidenced by decreased caspase-1 and IL-1β. Mechanistic studies showed that the pyroptosis related NLRP3 pathway was inhibited by complanatuside. The suppression of NLRP3 activation and pyroptosis was associated with inhibition of iNOS, COX-2, and ROS. Complanatuside may be a promising candidate for inhibiting COVID-19 related skin inflammatory damage.

Data availability statement

The original contributions presented in the study are included in the article/Supplementary Material, further inquiries can be directed to the corresponding authors.

Author contributions

XZ and DL managed the whole project and founding support, XW conducted the experiments and drafted the manuscript. XX, PW, MW, LG, and JJ managed the data selection and analysis, and RW, WL, and KZ managed the modification of manuscript.

Funding

Jiangmen Program for Innovative Research Team (No: 2018630100180019806).

Conflict of interest

The authors declare that the research was conducted in the absence of any commercial or financial relationships that could be construed as a potential conflict of interest.

Publisher's note

All claims expressed in this article are solely those of the authors and do not necessarily represent those of their affiliated organizations, or those of the publisher, the editors and the reviewers. Any product that may be evaluated in this article, or claim that may be made by its manufacturer, is not guaranteed or endorsed by the publisher.

References

Abais, J. M., Xia, M., Zhang, Y., Boini, K. M., and Li, P.-L. (2015). Redox Regulation of NLRP3 Inflammasomes: ROS as Trigger or Effector? *Antioxidants Redox Signal.* 22, 1111–1129. doi:10.1089/ars.2014.5994

Barnes, B. J., Adrover, J. M., Baxter-Stoltzfus, A., Borczuk, A., Cools-Lartigue, J., Crawford, J. M., et al. (2020). Targeting Potential Drivers of COVID-19: Neutrophil Extracellular Traps. *J. Exp. Med.* 217, e20200652. doi:10.1084/jem.20200652

Cinelli, M. A., Do, H. T., Miley, G. P., and Silverman, R. B. (2020). Inducible Nitric Oxide Synthase: Regulation, Structure, and Inhibition. *Med. Res. Rev.* 40, 158–189. doi:10.1002/med.21599

Diorio, C., Henrickson, S. E., Vella, L. A., McNerney, K. O., Chase, J., Burudpakdee, C., et al. (2020). Multisystem Inflammatory Syndrome in Children and COVID-19 Are Distinct Presentations of SARS-CoV-2. *J. Clin. Invest.* 130, 5967–5975. doi:10.1172/jci140970

Fara, A., Mitrev, Z., Rosalia, R. A., and Assas, B. M. (2020). Cytokine Storm and COVID-19: A Chronicle of Pro-inflammatory Cytokines. *Open Biol.* 10, 200160. doi:10.1098/rsob.200160

Forrester, S. J., Kikuchi, D. S., Hernandes, M. S., Xu, Q., and Griendling, K. K. (2018). Reactive Oxygen Species in Metabolic and Inflammatory Signaling. *Circ. Res.* 122, 877–902. doi:10.1161/circresaha.117.311401

Gao, Y., Li, T., Han, M., Li, X., Wu, D., Xu, Y., et al. (2020). Diagnostic Utility of Clinical Laboratory Data Determinations for Patients with the Severe COVID-19. *J. Med. Virol.* 92, 791–796. doi:10.1002/jmv.25770

Grimm, C., Dickel, S., Grundmann, J., Payen, D., Schanz, J., Zautner, A. E., et al. (2021). Case report: Interferon- γ rescues Monocytic human leukocyte antigen receptor (mHLA-DR) function in a COVID-19 patient with ARDS and superinfection with multiple MDR 4MRGN bacterial strains. *Front. Immunol.* 12, 753849. doi:10.3389/fimmu.2021.753849

Gubernatorova, E. O., Gorshkova, E. A., Polinova, A. I., and Drutskaya, M. S. (2020). IL-6: Relevance for Immunopathology of SARS-CoV-2. *Cytokine & Growth Factor Rev.* 53, 13–24. doi:10.1016/j.cytogfr.2020.05.009

He, W.-t., Wan, H., Hu, L., Chen, P., Wang, X., Huang, Z., et al. (2015). Gasdermin D Is an Executor of Pyroptosis and Required for Interleukin-1β Secretion. *Cell. Res.* 25, 1285–1298. doi:10.1038/cr.2015.139

Hua, K.-F., Chou, J.-C., Ka, S.-M., Tasi, Y.-L., Chen, A., Wu, S.-H., et al. (2015). Cyclooxygenase-2 regulates NLRP3 inflammasome-derived IL-1β production. *J. Cell. Physiol.* 230, 863–874. doi:10.1002/jcp.24815

Huang, C., Wang, Y., Li, X., Ren, L., Zhao, J., Hu, Y., et al. (2020). Clinical Features of Patients Infected with 2019 Novel Coronavirus in Wuhan, China. *Lancet* 395, 497–506. doi:10.1016/s0140-6736(20)30183-5

Karki, R., Sharma, B. R., Tuladhar, S., Williams, E. P., Zalduondo, L., Samir, P., et al. (2021). Synergism of TNF-α and IFN-γ triggers inflammatory cell death, tissue damage, and Mortality in SARS-CoV-2 infection and cytokine shock syndromes. *Cell* 184, 149–168. e17. doi:10.1016/j.cell.2020.11.025

Kundu, J., Kim, D.-H., Chae, I. G., Lee, J. K., Lee, S., Jeong, C.-H., et al. (2018). Silicon Dioxide Nanoparticles Induce COX-2 Expression through Activation of STAT3 Signaling Pathway in HaCaT Cells. *Toxicol. Vitro* 52, 235–242. doi:10.1016/j.tiv.2018.06.008

Li, Y., Hao, N., Zou, S., Meng, T., Tao, H., Ming, P., et al. (2018). Immune Regulation of RAW264.7 Cells *In Vitro* by Flavonoids from *Astragalus*

Complanatus via Activating the NF-κB Signalling Pathway. *J. Immunol. Res.* 2018, 7948068. doi:10.1155/2018/7948068

Liao, K., Lv, D.-Y., Yu, H.-L., Chen, H., and Luo, S.-X. (2021). iNOS Regulates Activation of the NLRP3 Inflammasome through the sGC/cGMP/PKG/TACE/TNF-α axis in Response to Cigarette Smoke Resulting in Aortic Endothelial Pyroptosis and Vascular Dysfunction. *Int. Immunopharmacol.* 101, 108334. doi:10.1016/j.intimp.2021.108334

Lucas, C., Wong, P., Klein, J., Castro, T. B. R., Silva, J., Sundaram, M., et al. (2020). Longitudinal Analyses Reveal Immunological Misfiring in Severe COVID-19. *Nature* 584, 463–469. doi:10.1038/s41586-020-2588-y

Marzano, A. V., Cassano, N., Genovese, G., Moltrasio, C., and Vena, G. A. (2020). Cutaneous Manifestations in Patients with COVID-19: A Preliminary Review of an Emerging Issue. *Br. J. Dermatol.* 183, 431–442. doi:10.1111/bjd.19264

Matar, S., Oulès, B., Sohier, P., Chosidow, O., Beylot-Barry, M., Dupin, N., et al. (2020). Cutaneous Manifestations in SARS-CoV-2 Infection (COVID-19): A French Experience and a Systematic Review of the Literature. *J. Eur. Acad. Dermatol. Venereol.* 34, e686–e689. doi:10.1111/jdv.16775

Morris, G., Bortolasci, C. C., Puri, B. K., Olive, L., Marx, W., O'Neil, A., et al. (2020). The Pathophysiology of SARS-CoV-2: A Suggested Model and Therapeutic Approach. *Life Sci.* 258, 118166. doi:10.1016/j.lfs.2020.118166

Ng, Y.-F., Tang, P. C.-T., Sham, T.-T., Lam, W.-S., Mok, D. K.-W., and Chan, S.-W. (2014). *Semen Astragali Complanati*: An Ethnopharmacological, Phytochemical and Pharmacological Review. *J. Ethnopharmacol.* 155, 39–53. doi:10.1016/j.jep.2014.06.013

Novak, N., Peng, W., Naegeli, M. C., Galvan, C., Kolm-Djamei, I., Brüggen, C., et al. (2021). SARS-CoV-2, COVID-19, Skin and Immunology - what Do We Know So Far? *Allergy* 76, 698–713. doi:10.1111/all.14498

Rongioletti, F., Ferreli, C., Sena, P., Caputo, V., and Atzori, L. (2021). Clinicopathologic Correlations of COVID-19-Related Cutaneous Manifestations with Special Emphasis on Histopathologic Patterns. *Clin. Dermatology* 39, 149–162. doi:10.1016/j.clindermatol.2020.12.004

Satoh, T., Kambe, N., and Matsue, H. (2013). NLRP3 Activation Induces ASC-dependent Programmed Necrotic Cell Death, Which Leads to Neutrophilic Inflammation. *Cell. death. Dis.* 4, e644. doi:10.1038/cddis.2013.169

Song, P., Li, W., Xie, J., Hou, Y., and You, C. (2020). Cytokine Storm Induced by SARS-CoV-2. *Clin. Chim. Acta* 509, 280–287. doi:10.1016/j.cca.2020.06.017

Sun, D., Li, H., Lu, X.-X., Xiao, H., Ren, J., Zhang, F.-R., et al. (2020). Clinical Features of Severe Pediatric Patients with Coronavirus Disease 2019 in wuhan: A Single Center's Observational Study. *World. J. Pediatr.* 16, 251–259. doi:10.1007/s12519-020-00354-4

Wang, S., Yuan, Y.-H., Chen, N.-H., and Wang, H.-B. (2019). The Mechanisms of NLRP3 Inflammasome/pyroptosis Activation and Their Role in Parkinson's Disease. *Int. Immunopharmacol.* 67, 458–464. doi:10.1016/j.intimp.2018.12.019

Yao, Y.-F., Lin, C.-Z., Liu, F.-L., Zhang, R.-J., Zhang, Q.-Y., Huang, T., et al. (2018). Identification and Pharmacokinetic Studies on Complanatuside and its Major Metabolites in Rats by UHPLC-Q-TOF-MS/MS and LC-MS/MS. *Molecules* 24, 71. doi:10.3390/molecules24010071

Check for updates

Green synthesis, structure optimization and biological evalution of Rhopaladins' analog 2−styryl−5-oxopyrrolidine-2-carboxamide RPDPRH on CaSki cells

Li-Na Ke[1,2†], Ling-Qi Kong[1,2†], Xiu-Lian Zhu[3†], Feng-Xu Wu[2], Qin-Hua Chen[4], Bin Li[2], Yun Dong[1,2]*, Hong-Mei Wang[1,2]* and Xiao-Hua Zeng[1,2]*

[1]Sinopharm Dongfeng General Hospital, Hubei University of Medicine, Shiyan, China, [2]Hubei Key Laboratory of Wudang Local Chinese Medicine Research, School of Pharmaceutical Sciences, Hubei University of Medicine, Shiyan, China, [3]Animal Laboratory, The 924th Hospital of the Joint Logistics Support Force of Chinese PLA, Guilin, China, [4]Shenzhen Baoan Authentic TCM Therapy Hospital, Shenzhen, China

We have synthesized Rhopaladins' analog (2E,4E)-4-chlorobenzylidene-2-(4-chlorostyryl)-N-cyclohexyl-1-(4-fluorophenyl)-5-oxopyrrolidine-2-carboxamide (RPDPRH) via a highly facile, inexpensive and green approach and verified the structural superiority of compound RPDPRH through molecular docking. Moreover, we further detected the anti-proliferation, apoptosis and HPV E6/E7 effects of RPDPRH on CaSki cells. Finally, we confirmed that compared with the previous compound (E)-N-(tert-butyl)-2-(4-chlorobenzoyl)-4-(4-fluorobenzylidene)-1-isopropyl-5-oxopyrrolidine-2-carboxamide (RPDPB), RPDPRH could better inhibit proliferation, induce apoptosis, and down-regulate HPV E6/E7 mRNA expression on Caski cells. And preliminary RT-PCR experiments have demonstrated that RPDPRH also could affect the expression of Bcl-2, Bax and Caspase-3 mRNA in Caski cells. In summary, RPDPRH has potential as an effective agent against cervical cancer and will play an important role in our subsequent research.

KEYWORDS

4-arylidene-5-oxopyrrolidine, green synthesis, molecular docking, anti-tumor activity, apoptosis

Introduction

Cancer is among the severest diseases threatening human health in the 20th century, which is considered to be a major cause of death (Roy and Saikia, 2016; Bray et al., 2018). For women, cervical cancer has become one of the top ten cancers in women, with morbidity and mortality ranking fourth, posing a serious threat to women's life and health

(Canfell, 2019; Wang et al., 2020a). As a classical treatment, drug therapy plays an important role in different stages of tumor cell growth (An et al., 2021). But because of the widespread resistance of anti-tumor drugs, it is necessary to find or synthesize new anti-cervical cancer drugs.

Marine natural products have novel structures and a variety of physiological activities, especially the marine alkaloids containing pyrrolidone structure have unique chemical structure and strong antifungal and antibacterial biological characteristics (Nijampatnam et al., 2015). Among them, alkaloid Rhopaladins A-D isolated from marine natural products has obvious anti-tumor activity (Sato et al., 1998). Hence, Rhopaladins' analogs (E)-2-aroyl-4-arylidene-5-oxopyrrolidine (RPDP serial chemicals) have been synthesized by one-pot method using Ugi condensation and intramolecular S_N Cyclization (Zeng et al., 2013; Wang et al., 2020b), and (E)-N-(tert-butyl)-2-(4-chlorobenzoyl)-4-(4-fluorobenzylidene)-1-isopropyl-5-oxopyrrolidine-2-carboxamide (RPDPB for short) effects on proliferation, apoptosis and E6/E7 mRNA of cervical cancer CaSki cells were studied (Zhu et al., 2020). Further, in order to obtain compounds with better apoptosis inducing activity of tumor cells, analogs of Rhopaladins (2E,4E)-4-arylidene-2-styryl-5-oxopyrrolidine (RPDPR serial chemicals) were synthesized after structural optimization (Kong et al., 2021). Among them (2E,4E)-4-chlorobenzylidene-2-(4-chlorostyryl)-N-cyclohexyl-1-(4-fluorophenyl)-5-oxopyrrolidine-2-carboxamide (RPDPRH for short, see Scheme 1) has better anti-hepatoma activity and low hepatotoxicity (Zeng et al., 2020; Zhu et al., 2022). Thus, we further explored the effect of RPDPRH on CaSki cell apoptosis.

Nowadays, traditional synthetic chemistry has caused a serious impact on the environment. The use of non-toxic and harmless raw materials, catalysts and solvents is the development trend of synthetic chemistry. However, the solvent used in the preliminary synthesis step is methanol, which is toxic and not friendly to the environment. Therefore, in this study, the experimental conditions were optimized on the basis of previous studies, and the environment-friendly one-pot method was adopted to synthesize RPDPRH with ethanol-water as solvent, which was more green and efficient. Moreover, the structural superiority of RPDPRH was verified by molecular docking, and in order to better compare its anti-tumor activity with RPDPB in vitro, we continued to select cervical cancer cells and further study the anti-proliferation activity, apoptosis and E6/E7 mRNA expression of RPDPRH on CaSki cells.

Experimental protocol

Melting points were measured with an X-4 melting point instrument (uncorrected thermometer) produced by Beijing Ruili Analytical Instrument Co., Ltd. Mass spectrometry was performed with a Finnigan trace MS analyzer (direct injection method). Elemental analysis was determined was performed using a Vario EL III analyzer. ^{1}H NMR and ^{13}C NMR spectra

were measured at 400 MHz using spectrometers. The solvent was $CDCl_3$ with TMS is the internal standard.

Molecular docking experiments

The 2D structure of the compound was drawn in the ChemOffice Pro 16 suite and converted to 3D structure with minimal energy in Discovery Studio 2016 Visualizer. The crystal structure of FKBP12-MTOR (PDB ID: 1FAP) was obtained from Protein Data Bank (https://www.rcsb.org/). Ligand molecules, water molecules and residues are removed from the complex structure, where the active site is identified. Hydrogen atom of FKBP12-MTOR was performed through Discovery Studio 2016 Visualizer. Molecular docking was performed with GOLD 3.0. The active site radius is set to 10°A for 300 cycles using a genetic algorithm (GA). The highest level of confirmation is chosen as representative. Molecular graphics were generated by PyMOL.

One-pot synthesis of Rhopaladins' analog RPDPRH

The synthesis procedure was based on our previous research (Zhu et al., 2022). First, a mixture of 4-fluoroaniline **2** (1 mmol) and substituted (E)-3-(4-chlorophenyl) acrylaldehyde **3** (1 mmol) was stirred in ethanol-water (3:1, vol/vol, 8 ml) at room temperature for 30 min. After precipitation was produced, Baylis-Hillman acid (Z)-2-(chloromethyl)-3-(4-chlorophenyl) acrylic acid **1** (1 mmol) and cyclohexyl isocyanide **4** (1 mmol) were added successively, and the mixture was stirred at room temperature for 2 h. Then 2 ml K_2CO_3 (0.5 mmol) solution was used to adjust pH value 10 times, once every 2 h, and the reaction was continued for 2 h after dropping. After the reaction was monitored and completed by thin layer chromatography (TLC), the mixture was chilled overnight and the precipitate was filtered, washed by water, recrystallized from ether, then (2E,4E)-4-chlorobenzylidene-2-(4-chlorostyryl)-N-cyclohexyl-1-(4-fluorophenyl)-5-oxopyrrolidine-2-carboxamide (RPDPRH, see Scheme 2) was obtained.

Cell culture and treatment

Human cervical cancer cell lines of CaSki, HeLa and normal hepatocyte LO2 were attained from Experiment Center of Medicine, Sinopharm Dongfeng General Hospital, Hubei University of Medicine. CaSki and LO2 cells were cultured in RPMI Medium 1640 basic (1640, Gibco), HeLa cells were cultured in Dulbecco's modified Eagle medium (DMEM, Gibco), meanwhile, 10% fetal bovine serum (FBS,
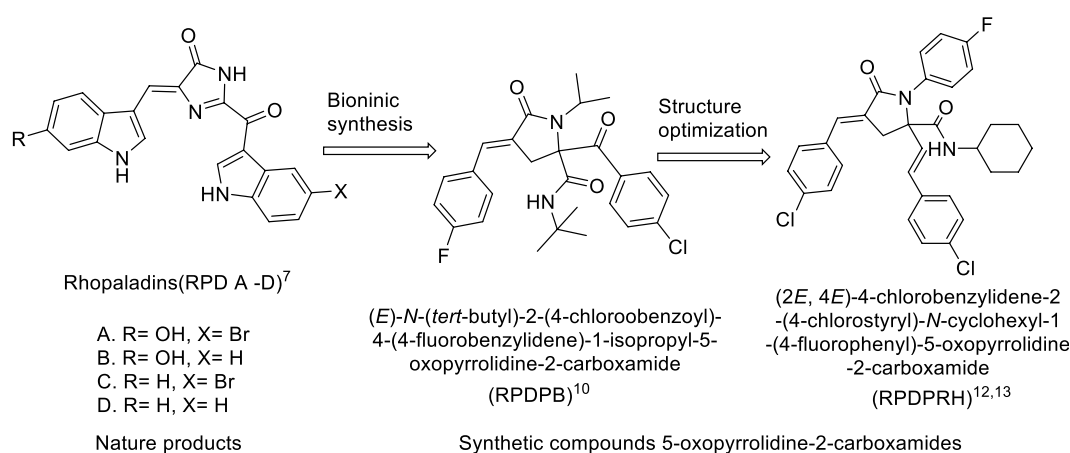
SCHEME 1
The strategies leading to Rhopaladins' analog RPDPRH as target.

CORNING). All of cells were fostered in an incubator with a humidified atmosphere of 5% CO_2 at 37°C. Cisplatin was purchased from Shanghai Aladdin, China. The compounds were dissolved by dimethyl sulfoxide (DMSO, MP Biomedicals). Control group (0 μM) was treated with DMSO only under the same conditions, and the content of DMSO in each group was less than 0.1%.

Cell viability assay *in vitro*

Following previous studies (Zhu et al., 2022), cell activity was determined by 3-(4,5-dimethylthiazol-2-yl)-2,5-diphenyltetrazolium bromide (MTT, MultiSciences) assay. The logarithmic growth phase cells were digested and inoculated into 96 well cell culture plates with 5×10^3 cells per well. Then, the cells were treated with different concentrations of RPDPRH (0, 3.125, 6.25, 12.5, 25, 50, 100 μM) for 24 h or 48 h. Control group (0 μM) was treated with DMSO, while the blank group contained only culture medium without cells. Cisplatin was used as positive control. Cells in each well were incubated with MTT 20 μL (5 mg/ml) at 37°C for 4 h. The absorbance value (A) at 490 nm wavelength was detected by enzyme-labeled meter (Biotek MQX200) after adding 150 μL of DMSO to each hole. Cell viability rate of each compound on different cells were calculated. Cell viability rate (%) = (A experimental-A blank)/(A control-A blank) × 100%.

Morphological observation of CaSki cells

CaSki cell suspensions in logarithmic growth phase were inoculated into 6-well plates at a density of 3×10^5 cells per well.

TABLE 1 Primer sequences used in RT-qPCR gene expression analysis.

Primers	Primer sequence
Bcl-2—forward	5′-GGATGCCTTTGTGGAACTGT-3′
Bcl-2—reverse	5′-AGCCTGCAGCTTTGTTTCAT-3
Bax—forward	5′-TTTGCTTCAGGGTTTCATCC-3′
Bax—reverse	5′-CAGTTGAAGTTGCCGTCAGA-3′
Caspase-3—forward	5′-TTTTTTCAGAGGGGGATCGTTG-3′
Caspase-3—reverse	5′-CGGCCTCCACTGGTATTTTA-3′
E6—forward	5′-TTGCTTTTCGGGATTTATGC-3′
E6—reverse	5′-CAGGACACAGTGGCTTTTGA-3′
E7—forward	5′-GAACCGGACAGAGCCCATTA-3′
E7—reverse	5′AGAACAGATGGGGCACACAAT-3′
GAPDH—forward	5′-CCATGTTCGTCATGGGTGTGAACCA-3′
GAPDH—reverse	5′-GCCAGTAGAGGCAGGGATGATGTTC-3′

After cell adherence, RPDPRH (0, 5, 10, 15 μM) was added and treated for 24 h. Morphological changes of CaSki cells were observed under an inverted microscope.

Cell apoptosis assay

Effect of RPDPRH on apoptosis was evaluated using the Annexin V-FITC/PI Apoptosis kit (MULTI SCIENCES). CaSki cells were seeded into 6-well plates, and exposed to different dosages of RPDPRH (0, 5, 10, 15 μM) for 24 h. After treatment, cells were collected and washed twice with precooled phosphate buffered solution (PBS, Gibco), and re-suspended in 500 μL
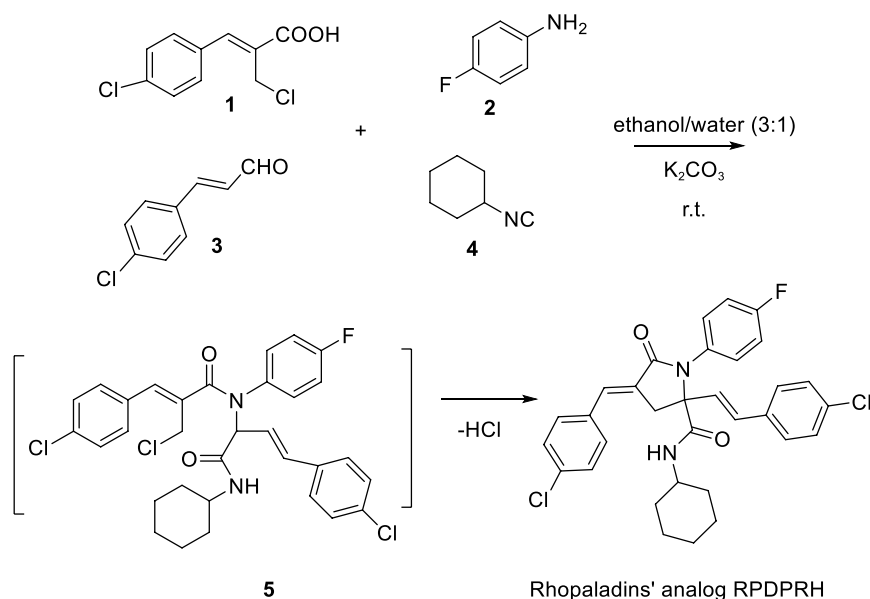
SCHEME 2
Synthesis of Rhopaladins' analog RPDPRH.

binding buffer. Annexin V-FITC (5 μL) and PI (10 μL) were added to the cell suspension followed by incubation at room temperature for 5 min in the dark. Cells were analyzed by flow cytometry (Agilent NovoCyte).

Reverse transcriptase-polymerase chain reaction

RT-qPCR analysis was performed as follows. Briefly, CaSki cells were treated with RPDPRH (0, 5, 10, 15 μM) for 24 h. Total RNA was extracted with TRIzol Reagent (MRC-Holland). Reverse

transcription of cDNA is carried out according to Fermentas' reverse transcription kit instructions. The cDNA was synthesized from 2 μg of RNA using RevertAid First Strand cDNA Synthesis kit (Thermo Fisher Scientific). Amplifications were using the FastStart universal SYBR® Green Master (Roche). The amplification conditions were initial denaturation at 95°C for 5 min, followed by 40 cycles of denaturation at 94°C for 30 s, annealing at 58°C for 30 s, and extension at 72°C for 30 s $2^{-\Delta\Delta CT}$ method was used for the evaluation of the reaction results. GAPDH was an internal reference gene. The primers were designed using Primer-Blast and Primer Premier 6.0 software and synthesized by the Shanghai Biotechnology Company. The sequence of primers was shown in Table 1.
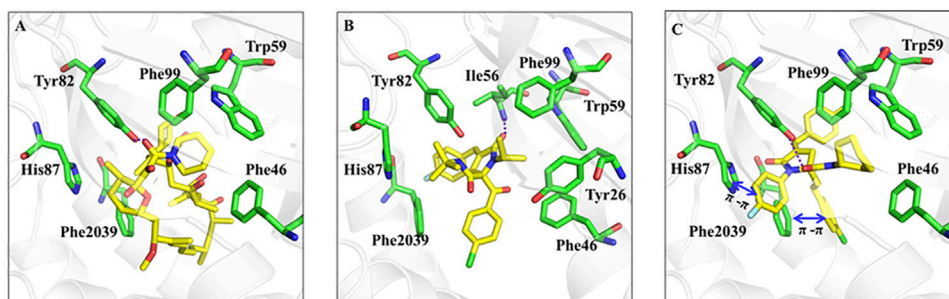
FIGURE 1
Rapamycin, RPDPB and RPDPRH were docked into the complex of FKBP12-mTOR (PDB ID: 1FAP), respectively. Note: **(A)**: Rapamycin docked into FKBP12-mTOR; **(B)**: RPDPB docked into FKBP12-mTOR; **(C)**: RPDPRH docked into FKBP12-mTOR.
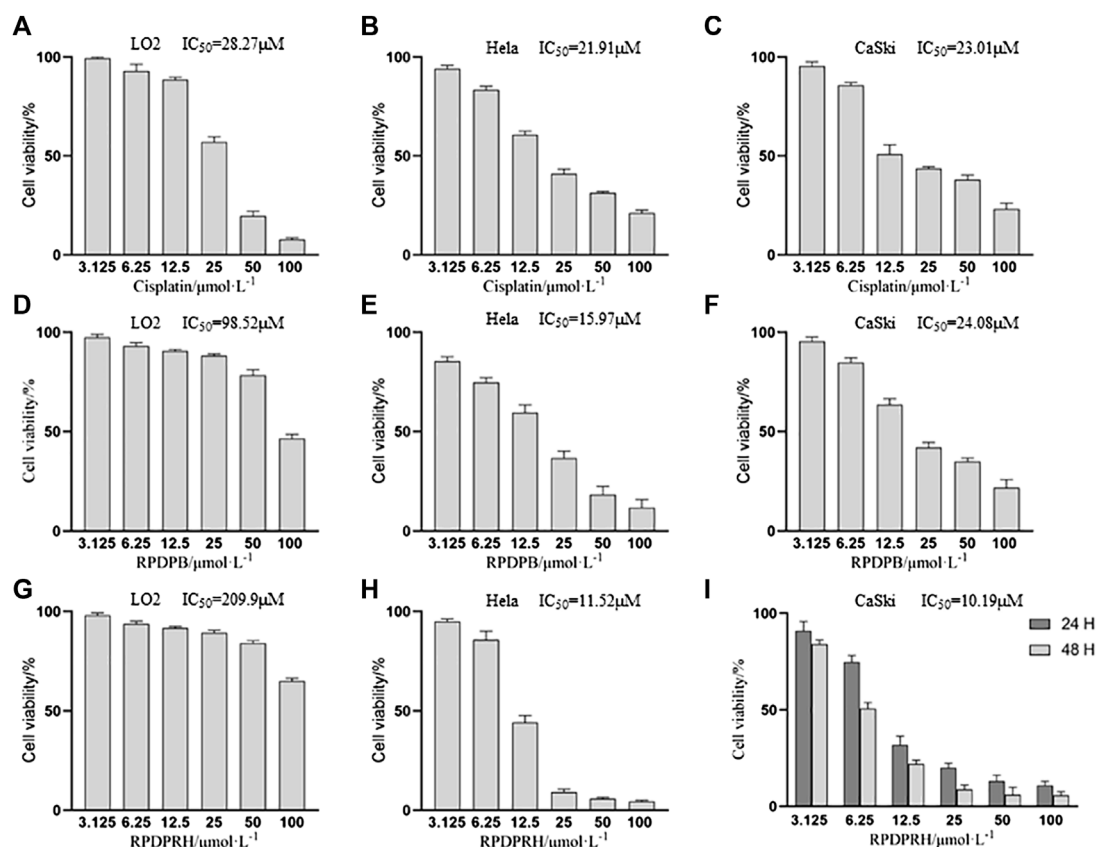
FIGURE 2
Anti-proliferative activities of Cisplatin, RPDPB and RPDPRH on Hela, LO2 and CaSki cells, respectively. Note: **(A–C)**: Cell activity of LO2, Hela and CaSki cells treated with Cisplatin for 48 h **(D–F)**: Cell activity of LO2, Hela and CaSki cells treated with RPDPB for 48 h **(G, H)**: Cell activity of LO2 and Hela cells treated with RPDPRH for 48 h **(I)**: Cell activity of CaSki cells treated with RPDPRH for 24 and 48 h.

Statistical methods

The apoptosis was analyzed by FlowJo 10.6.2 software. All data were processed and analyzed by GraphPad Prism 8.0.1 software. The significance of differences was evaluated by one-way variance (ANOVA). $p < 0.05$, the difference was statistically significant. All experiments were repeated three times, and data shown in Mean ± SD.

Results

One-pot synthesis of Rhopaladins' analog RPDPRH

The (2*E*,4*E*)-4-chlorobenzylidene-2-(4-chlorostyryl)-*N*-cyclohexyl-1-(4-fluorophenyl)-5-oxopyrrolidine-2-carboxamide (RPDPRH, Melt point 128–130°C) was produced in good yields about 93%. The structure of RPDPRH was confirmed by spectroscopic data (Zeng et al., 2020). For instance, the ^{1}H NMR

spectrum of RPDPRH shows that the signals of the CH_2 in the pyrrolidinone core appear at 3.44 and 3.35 ppm as two doublets. The signal due to CONH appears at 5.64 ppm as a singlet. The signal attributable to CH_3 of the *tert*-butyl group is found at 1.21 ppm as a singlet. The signals of the Ar-Hs and vinyl-Hs appear at 7.57–7.27 ppm and 7.02 as mutiplets and doublets. The ^{13}C NMR spectrum data in RPDPRH showed that the two CON carbons absorb at 169.9 and 169.0 ppm. The signal of the quaternary carbon in the pyrrolidinone core absorbs at 69.7 ppm. The MS spectrum of RPDPRH shows molecular ion peak and M$^+$-CONHBu-*t* at m/z 518 and 418 with 5 and 100% abundance.

Molecular docking

As we all know, rapamycin is a kind of cancer chemotherapy drug with good anti-tumor effect. Thus, we validated the binding mode of rapamycin and RPDPB with FKBP12-mTOR (PDB ID: 1FAP) by molecular docking experiments. The result was shown in Figure 1, there were hydrogen bonds between in the two complexes, but the
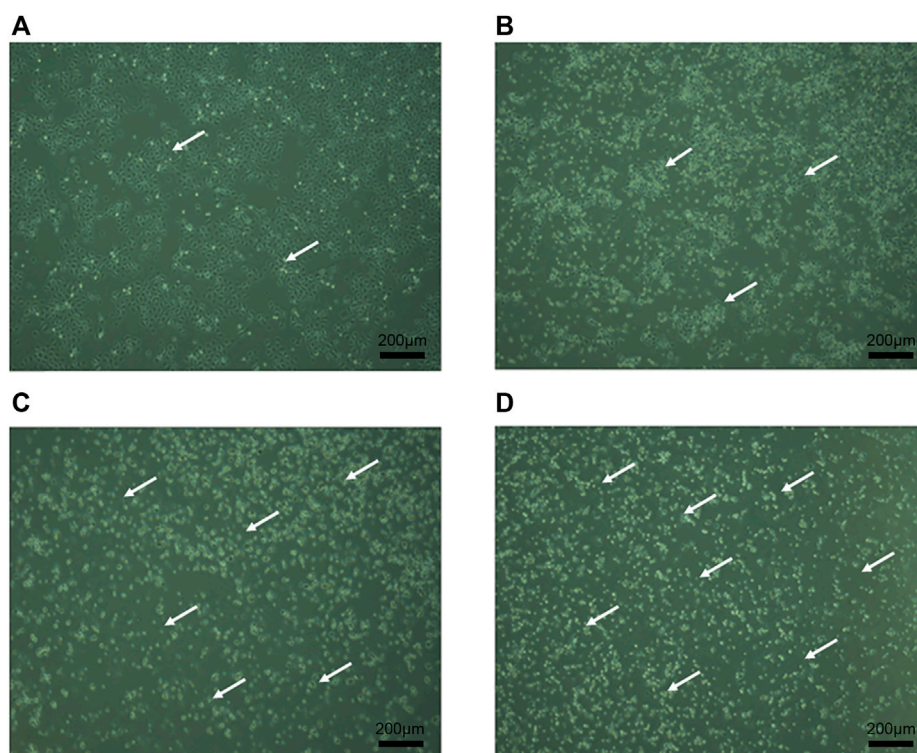
FIGURE 3
Morphological observation of CaSki cells. Note: **(A)**: Control group was treated for 24 h with CaSki cell morphology. **(B)**: 5 μM RPDPRH was treated for 24 h with CaSki cell morphology. **(C)**: 10 μM RPDPRH was treated for 24 h with CaSki cell morphology. **(D)**: 15 μM RPDPRH was treated for 24 h with CaSki cell morphology. Scale bar: 200 μm.

molecular size of RPDPB was small and the effect of RPDPB with FKBP12-mTOR was not strong. In order to optimize Rhopaladins' analog (*E*)-2-aroyl-4-(4-fluorobenzylidene)-5-oxopyrrolidines, the Rhopaladins' analog (2*E*,4*E*)-4-arylidene-2-styryl-5-oxopyrrolidines (RPDPR serial chemicals) were designed by using 2-styryl group instead of 2-benzoyl group, and the longer the length of the aryl group to the pyrilidinone core, the stronger the π-π effect of the aryl group with the Phe 2039. At the same time, the fitting degree of RPDPRH and FKBP12-mTOR complex was calculated. From the docking experiment result (shown in Figure 1), we may find that RPDPRH formed a hydrogen bond with Tyr82, which also exists in the binding mode between rapamycin and FKBP12-mTOR complex. RPDPRH could also form π-π interactions with His87 and Phe 2039, as well as hydrophobic interactions with Phe99, Trp59 and Phe46. However, these interactions were not observed in the binding of rapamycin to FKBP12-mTOR complex. According to the analysis, we may infer that RPDPRH has the potential better ability to inhibit the passageway between FKBP12-mTOR than rapamycin.

In vitro anti-proliferative activities assay

MTT assays were carried out to determine the growth inhibitory effects of Cisplatin, RPDPB and RPDPRH on one normal hepatocyte cells (LO2 cells) and two types of cervical cancer cells (Hela and CaSki cells). The results (Figure 2) were showed that RPDPRH has obvious anti-cervical cancer activities and low cytotoxicity to normal liver LO2 cells compared with cisplatin and RPDPB, which also indicated that our structure optimization has an obvious effect. Therefore, we also studied the effects of RPDPRH on HPV16 positive CaSki cells proliferation for 24 and 48 h, and the cells viability was showed in Figure 2I. The survival rate of CaSki cells treated with 12.5 and 25 μM RPDPRH for 24 h was 31.93 ± 4.81% and 20.01 ± 2.45%, respectively. When treated with RPDPRH for 48 h, the cell survival rate was 22.13 ± 1.88% and 8.93 ± 2.36%, respectively. In conclusion, RPDPRH also has a dose-dependent and time-dependent inhibitory effect on CaSki cell proliferation, which is superior to RPDPB.
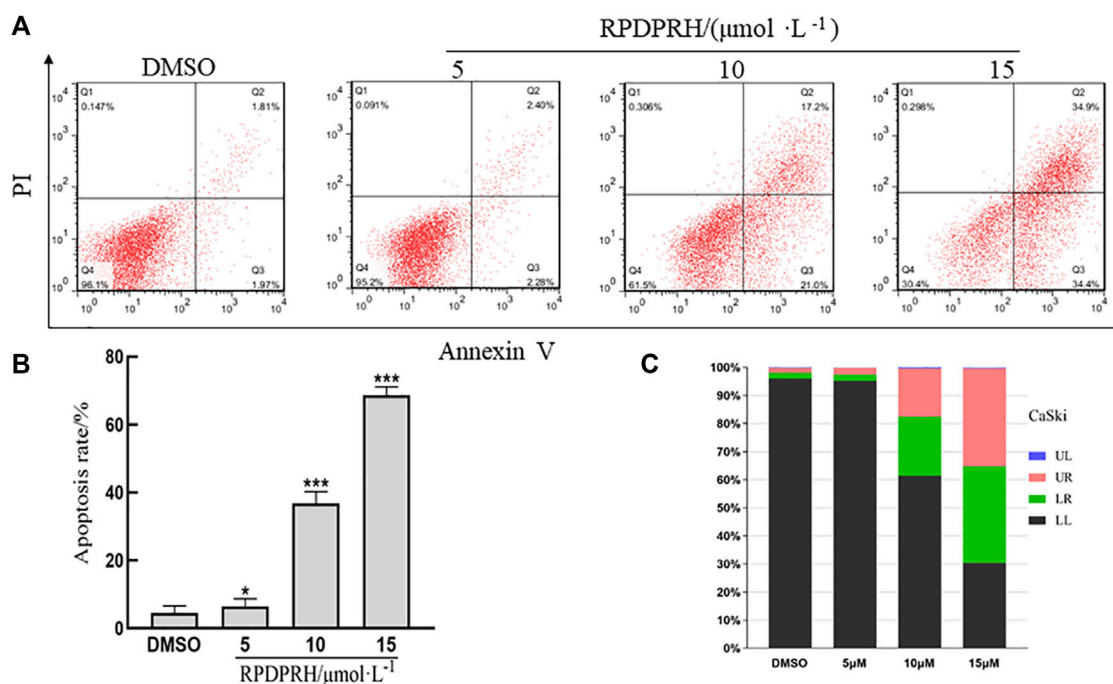
FIGURE 4
Effects of RPDPRH on cell-apoptosis progression in CaSki cells. Note: **(A)**: Flow cytometry analyses of apoptosis induction in CaSki cells after treated by RPDPRH for 24 h **(B)**: the total apoptosis rate. Compared with the DMSO control group, $**p < 0.01$, $***p < 0.001$, ($\bar{x} \pm$ s, $n = 3$). **(C)**: The living cells (LL), early apoptotic cells (LR), late apoptotic (UR), and necrotic cells/fragments (UL) rate of CaSki were analysed.
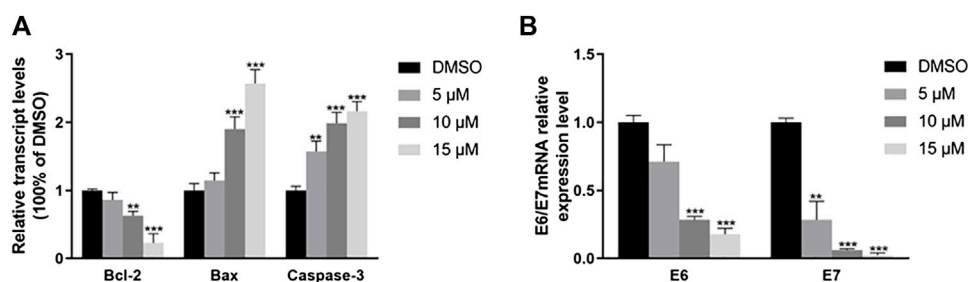
FIGURE 5
The effect of RPDPRH on the expression of mRNA in CaSki cells. Note: **(A)**: The mRNA expression of Bcl-2, Bax, and Caspase-3. **(B)**: The mRNA expression of E6/E7. Compared with the DMSO control group, $*p < 0.05$, $**p < 0.01$, ($\bar{x} \pm$ s, $n = 3$).

Effect of RPDPRH on human cervical cancer CaSki cell morphology

The growth of CaSki cells was observed under inverted microscope. In the normal control group, cells were round or oval, adhered to the wall, with complete morphology and tight connection, as shown in Figure 3. After treatment with different concentrations of RPDPRH (5, 10, 15 μM) for 24 h, the growth of CaSki cells was inhibited, cell morphology changed, light transmittance increased, and adhesion ability decreased. Meanwhile, cell density decreased significantly and floating cells increased. Therefore, the results showed that RPDPRH could significantly inhibit the proliferation and change the cell morphology of cervical cancer CaSki cells.

RPDPRH could induce apoptosis of cervical cancer CaSki cells *in vitro*

Annexin V and PI staining assay was used to detect cells apoptosis. The result was shown in Figure 4, when CaSki cells were treated with different concentration of RPDPRH (0, 5, 10, 15 μM) for 24 h, the apoptosis rates were increased. Compared with the control group, which had $3.78 \pm 0.57\%$, at the treatment groups, the apoptosis rate increased up to $4.66 \pm 0.64\%$, $38.20 \pm 2.62\%$ and $69.30 \pm 1.78\%$, respectively. The results indicated that RPDPRH induced cells apoptosis in a concentration-dependent manner. In addition, compared with RPDPB (Zhu et al., 2020) in our previous experiment, the CaSki cell apoptosis induced by RPDPRH at a lower concentration was better than which induced by RPDPB at the same treatment for 24 h.

Effects of RPDPRH on the expression of Bcl-2, Bax, Caspase-3, and HPV E6/E7 mRNA in human cervical cancer CaSki cells

Reverse transcription PCR (RT-PCR) assay was used to analysis gene expression difference in cervical cancer cells. The mRNA expression of pro-apoptosis and anti-apoptosis cytokines, such as Bcl-2, Bax and Caspase-3 were different compared with control (Figure 5A). When CaSki cell treated with 10 and 15 μM of RPDPRH, the fold changes of Bcl-2 were 0.786 ± 0.092 and 0.081 ± 0.029, respectively. For the Bax, the treated with 5 μM, the fold change was 1.394 ± 0.198. The mRNA expression of HPV E6 and E7 was decreased in CaSki cells (Figure 5B), the fold changes of HPV E6 mRNA were 0.710 ± 0.102、0.186 ± 0.01765 and 0.176 ± 0.036, respectively. And the HPV E7 mRNA was 0.283 ± 0.112、0.062 ± 0.0069 and 0.023 ± 0.0126, respectively. These decreases were statistically significant, $p < 0.05$. In conclusion, RPDPRH can reduce the expression of E6/E7 mRNA and affect the expression of related apoptotic genes.

Discussion and conclusion

Multicomponent reactions, which combine three or more starting substances into a single product by one pot under very mild conditions, are important and effective synthetic tools for the preparation of complex molecules (Cimarelli, 2019; Graebin et al., 2019). One of the advantages of multicomponent synthesis is the generation of complex molecules in a few synthesis steps (Touré and Hall, 2009). Among the multicomponent reactions, the Passerini and Ugi reactions play an important role in combinatorial chemistry, high-throughput screening and assembly of important pharmacological structures (Serafin and Priest, 2015; Oelmann et al., 2019). Both two reactions are

completely in line with the green chemistry standard, displaying an excellent atom economy: there is no by-product in the Passerini reaction, while in the Ugi reaction, water is the only waste product (Pirali et al., 2019). Marine alkaloids are widely found in marine organisms and have diverse physiological activities (Delfourne, 2008; Dyshlovoy et al., 2016; Tanaka et al., 2016). Thus, a series of Rhopaladins analogs were previously synthesized by a multi-component tandem one-pot method. However, the solvent used in the synthesis is methanol, which is the same as that used in the common four-component Ugi reaction. As we all know, the four-component Ugi reaction is most thorough in methanol (Gerokonstantis et al., 2019; Sasaki et al., 2020), but methanol is more toxic and not friendly to human health and environment. In this study, we substituted (Z)-2-(chloromethyl)-3-(4-chlorophenyl) acrylic acid for before (Z)-2-(bromomethyl)-3-(4-chlorophenyl) acrylic acid, reducing the cost of synthesis. Moreover, we use ethanol-water mixed solution as the reaction solvent, which makes the synthesis process more beneficial to human health, more friendly to the environment, and more in line with the development direction of green chemistry.

Cell apoptosis is a momentous biological process involving a large number of molecules and pathways, including exogenous and endogenous pathways linking to death receptors, which are closely related to the occurrence and development of tumors (Ye et al., 2017; Obeng, 2021). Consistent evidences indicate that persistent infection with human papillomavirus (HPV) is the main cause in triggering the development of cervical cancer (Arbyn et al., 2020). The modification of E6 and E7 oncoproteins can regulate cell cycle and apoptosis, lead to genomic instability and eventually cancer, then E6/E7 play an important role in the occurrence and development of cervical cancer (Pal and Kundu, 2019). Hence, in this paper, we evaluated the anti-proliferative activities of RPDPRH in CaSki cells, Hela cells and LO2 cells. Moreover, we found that RPDPRH inhibited CaSki cell proliferation in a time and dose dependent manner, induced CaSki cell apoptosis and down-regulated HPV E6/E7 mRNA expression, all of which were superior to RPDPB. Meanwhile, we verified the structural advantages of compound RPDPRH by molecular docking, and continued to explore the effects of RPDPRH on apoptosis factors, and found that RPDPRH can down-regulate the expression of anti-apoptotic factor Bcl-2 mRNA, and up-regulate the expression of pro-apoptotic factors Bax and caspase-3 mRNA.

In conclusion, we improved the previous synthesis method to synthesize RPDPRH in a more economical and green way, and verified that RPDPRH was superior to RPDPB by molecular docking experiment and *in vitro* cell experiment. And through this experiment, we hope to provide some ideas for more efficient, green and economic compounds in the future, and provide some help for further expanding and optimizing this series of compounds to synthesize better anti-tumor compounds. At the same time, our experiment is still in the very preliminary

pharmacological research stage, and we will verify its molecular mechanism at the protein level and further study its potential as an anti-tumor drug *in vivo* through animal model experiments.

Data availability statement

The raw data supporting the conclusion of this article will be made available by the authors, without undue reservation.

Author contributions

L-NK: Conceptualization, investigation, methodology, resources, and writing-review and editing. L-QK: Investigation, software, validation and writing-original draft. X-LZ: Investigation, data curation, formal analysis, software, visualization. F-XW: Software, formal analysis and visualization. Q-HC: Formal analysis, and validation. BL: Investigation, and funding acquisition. YD: Conceptualization, funding acquisition, and project administration. H-MW: Conceptualization, methodology, and resources. X-HZ: Conceptualization, investigation, methodology, resources, supervision, and writing-review and editing.

Funding

Conflict of interest

The authors declare that the research was conducted in the absence of any commercial or financial relationships that could be construed as a potential conflict of interest.

Publisher's note

All claims expressed in this article are solely those of the authors and do not necessarily represent those of their affiliated organizations, or those of the publisher, the editors and the reviewers. Any product that may be evaluated in this article, or claim that may be made by its manufacturer, is not guaranteed or endorsed by the publisher.

Supplementary material

The Supplementary Material for this article can be found online at: https://www.frontiersin.org/articles/10.3389/fchem.2022.975559/full#supplementary-material

References

An, L., Wang, C., Zheng, Y. G., Liu, J. D., and Huang, T. H. (2021). Design, synthesis and evaluation of calix[4]arene-based carbonyl amide derivatives with antitumor activities. *Eur. J. Med. Chem.* 210, 112984. doi:10.1016/j.ejmech.2020.112984

Arbyn, M., Weiderpass, E., Bruni, L., de Sanjosé, S., Saraiya, M., Ferlay, J., et al. (2020). Estimates of incidence and mortality of cervical cancer in 2018: A worldwide analysis. *Lancet Glob. Health* 8, e191–e203. doi:10.1016/s2214-109x(19)30482-6

Bray, F., Ferlay, J., Soerjomataram, I., Siegel, R. L., Torre, L. A., and Jemal, A. (2018). Global cancer statistics 2018: GLOBOCAN estimates of incidence and mortality worldwide for 36 cancers in 185 countries. *CA A Cancer J. Clin.* 68, 394–424. doi:10.3322/caac.21492

Canfell, K. (2019). Towards the global elimination of cervical cancer. *Papillomavirus Res.* 8, 100170. doi:10.1016/j.pvr.2019.100170

Cimarelli, C. (2019). Multicomponent reactions. *Molecules* 24 (13), 2372. doi:10.3390/molecules24132372

Delfourne, E. (2008). Analogues of marine pyrroloiminoquinone alkaloids: Synthesis and antitumor properties. *Anticancer. Agents Med. Chem.* 8, 910–916. doi:10.2174/187152008786847710

Dyshlovoy, S. A., Tabakmakher, K. M., Hauschild, J., Shchekaleva, R. K., Otte, K., Guzii, A. G., et al. (2016). Guanidine alkaloids from the marine sponge monanchora pulchra show cytotoxic properties and prevent EGF-induced neoplastic transformation *in vitro*. *Mar. Drugs* 14, 133. doi:10.3390/md14070133

Gerokonstantis, D. T., Nikolaou, A., Magkrioti, C., Afantitis, A., Aidinis, V., Kokotos, G., et al. (2019). Synthesis of novel 2-pyrrolidinone and pyrrolidine derivatives and study of their inhibitory activity against autotaxin enzyme. *Bioorg. Med. Chem.* 28 (2), 115216. doi:10.1016/j.bmc.2019.115216

Graebin, C. S., Ribeiro, F. V., Rogério, K. R., and Kümmerle, A. E. (2019). Multicomponent reactions for the synthesis of bioactive compounds: A review. *Curr. Org. Synth.* 16 (6), 855–899. doi:10.2174/1570179416666190718153703

Kong, L. Q., Zhu, X. L., Chen, Q. H., Wu, L., Wang, H. M., Ke, L. N., et al. (2021). One-pot synthesis and biological evaluation of (2E, 4E)-4-arylidene-2-styryl-5-oxopyrrolidine derivatives. *J. Chem. Res.* 45 (11-12), 1042–1046. doi:10.1177/17475198211051910

Nijampatnam, B., Dutta, S., and Velu, S. E. (2015). Velu, Recent advances in isolation, synthesis, and evaluation of bioactivities of bispyrroloquinone alkaloids of marine origin. *Chin. J. Nat. Med.* 13, 561–577.

Obeng, E. (2021). Apoptosis (programmed cell death) and its signals- A review. *Braz. J. Biol.* 81 (4), 1133–1143. doi:10.1590/1519-6984.228437

Oelmann, S., Travanut, A., Barther, D., Romero, M., Howdle, S. M., Alexander, C., et al. (2019). Biocompatible unimolecular micelles obtained via the Passerini reaction as Versatile nanocarriers for potential medical applications. *Biomacromolecules* 20 (1), 90–101. doi:10.1021/acs.biomac.8b00592

Pal, A., and Kundu, R. (2019). Human papillomavirus E6 and E7: The cervical cancer hallmarks and targets for therapy. *Front. Microbiol.* 10, 3116. doi:10.3389/fmicb.2019.03116

Pirali, T., Galli, U., Serafini, M., Griglio, A., Genazzani, A. A., and Tron, G. C. (2019). Drug Discovery for soft drugs on TRPV1 and TRPM8 channels using the Passerini reaction. *Methods Mol. Biol.* 1987, 207–221. doi:10.1007/978-1-4939-9446-5_13

Roy, P. S., and Saikia, B. J. (2016). Cancer and cure: A critical analysis. *Indian J. Cancer* 53, 441–442. doi:10.4103/0019-509X.200658

Sasaki, Y., Tokuhara, H., Ohba, Y., Okabe, A., Nakayama, M., Nakagawa, H., et al. (2020). Efficient synthesis of tert-butyl 3-cyano-3-cyclopropyl-2-oxopyrrolidine-4-carboxylates: Highly functionalized 2-pyrrolidinone enabling access to novel macrocyclic Tyk2 inhibitors. *Bioorg. Med. Chem. Lett.* 30 (5), 126963. doi:10.1016/j.bmcl.2020.126963

Sato, H., Tsuda, M., Watanabe, K., and Kobayashi, J. (1998). Rhopaladins A ~ D, new indole alkaloids from marine tunicate Rhopalaea sp. *Tetrahedron* 54, 8687–8690. doi:10.1016/s0040-4020(98)00470-0

Serafin, M., and Priest, O. P. (2015). Identifying Passerini products using a green, guided-inquiry, collaborative approach combined with spectroscopic lab techniques. *J. Chem. Educ.* 92, 579–581. doi:10.1021/ed5007184

Tanaka, N., Kusama, T., Kashiwada, Y., and Kobayashi, J. (2016). Bromopyrrole alkaloids from okinawan marine sponges agelas spp. *Chem. Pharm. Bull.* 64, 691–694. doi:10.1248/cpb.c16-00245

Touré, B. B., and Hall, D. G. (2009). Natural product synthesis using multicomponent reaction strategies. *Chem. Rev.* 109 (9), 4439–4486. doi:10.1021/cr800296p

Wang, H., Zhu, X., Deng, S., Chen, Q., and Zeng, X. (2020). Synthesis and cytotoxic effects on HeLa cervical cancer cells of (E)-2-aroyl-4-(4-fluorobenzylidene)-5-oxopyrrolidine. *J. Chem. Res.* 44, 576–579. doi:10.1177/1747519820911849

Wang, R., Pan, W., Jin, L., Huang, W., Li, Y., Wu, D., et al. (2020). Human papillomavirus vaccine against cervical cancer: Opportunity and challenge. *Cancer Lett.* 471, 88–102. doi:10.1016/j.canlet.2019.11.039

Ye, K., Wei, Q., Gong, Z., Huang, Y., Liu, H., Li, Y., et al. (2017). Effect of norcantharidin on the proliferation, apoptosis, and cell cycle of human mesangial cells. *Ren. Fail.* 39, 458–464. doi:10.1080/0886022x.2017.1308257

Zeng, X. H., Zhu, X. L., M Wang, H., and Chen, Q. H. (2020). *Cyclopolypeptide 2-styrene-5-pyrrolidone 2-amide derivatives, preparation method and application*. China Patent CN 110885307A. Shiyan,Hubei: Hubei university of medicine

Zeng, X., Wang, H., Wu, L., and Ding, M. (2013). One-pot synthesis of 5-Oxopyrrolidine-2-carboxamides via a tandem Ugi 4CC/S_N cyclization starting from baylis-hillman bromides. *Tetrahedron* 69, 3823–3828. doi:10.1016/j.tet.2013.03.058

Zhu, J., Kong, L. Q., Chen, Q. H., Li, B., Wu, L., Ran, F. Y., et al. (2022). Design, synthesis, and apoptosis-promoting effect evaluation of Rhopaladins' analog 4-arylidene-5-oxopyrrolidine derivatives. *Front. Chem.* 10, 898436. doi:10.3389/fchem.2022.898436

Zhu, X. L., Tian, X. Q., Xu, H. H., Wang, H. M., Chen, Q. H., and Zeng, X. H. (2020). Rhopaladins' analogue (E)-2-aroyl-4-(4-fluorobenzylidene)-5-oxopyrrolidines inhibit proliferation, promote apoptosis and down-regulation of E6/E7 mRNA in cervical cancer. *Bioorg. Med. Chem. Lett.* 30, 127554. doi:10.1016/j.bmcl.2020.127554

Neuroprotective and antioxidant activities of different polarity parts of the extracts of the *Ginkgo biloba* leaf and *Zingiber officinale* rhizome from Yongzhou

Zuoying Huang[1,2,3†], Tingting Yuan[1,2,3†], Jiayi Chen[1,2,3], Mihan Jiang[1,2,3], Rongling Yan[1,2,3]*, Wencai Yang[1,2,3], Liqian Wang[1,2,3], Yang Liao[1,2,3]* and Guowen Huang[1,2,3]

[1]College of Life Sciences and Chemistry Engineering, Hunan University of Science and Engineering, Yongzhou, Hunan, China, [2]Key Laboratory of Comprehensive Utilization of Dominant Plant Resources in Southern Hunan, Yongzhou, Hunan, China, [3]Hunan Provincial Engineering Research Center for Ginkgo Biloba, Yongzhou, Hunan, China

In order to make better use of the two local dominant plant resources of *Ginkgo biloba* and *Zingiber officinale* from Yongzhou in Hunan province, the *in vitro* neuroprotective and antioxidant activities of extracts from the *G. biloba* leaf and *Z. officinale* rhizome, and the correlation between these two kinds of activities, were analyzed. The *in vivo* effects of these two plant extracts on aged mice blood physiology and central neuron cell activity were then determined after continuous gavage with the best polarity part at different concentrations (2, 4, 8 mg/ml). The results showed that the cell survival rate and superoxide dismutase (SOD) activity of the induced injury central neurons increased, although the malondialdehyde (MDA) content decreased gradually with the extract concentrations increasing in a certain range. Different polarity parts performed differently, even though they had the same concentration, with *G. biloba* always performing better than the *Z. officinale* rhizome at the same concentration and polarity. The order of *G. biloba* extract from superior to inferior was ethanol, ethyl acetate, n-butanol, chloroform, water, and petroleum ether (except that the petroleum ether part performed slightly better than the water part at 0.4 and 0.5 mg/ml), while the order of *Z. officinale* rhizome extract from superior to inferior was ethanol, chloroform, n-butanol, ethyl acetate, water, and petroleum ether. These two plant extracts demonstrated good *in vitro* effect against oxygen free radicals; the scavenging rate of superoxide free radicals had a significant positive correlation with the cell survival rate. The *in vivo* central nerve cell activity and SOD, glutathione peroxidase (GSH-PX) activity in aged mice blood serum increased while the MDA content decreased with treatment with these two extracts ($p < 0.05$). There were no significant changes in the number of leukocytes, lymphocytes, red blood cells, hemoglobin content, blood urine nitrogen, uric acid, creatinine, and the enzyme activity of glutamic oxaloacetic transaminase (GOT) and

glutamic pyruvic transaminase (GPT) ($p > 0.05$). *G. biloba* had a better *in vivo* effect than *Z. officinale* rhizome even though their concentration and polarity part were same. These results could provide some references for better development of these two plant extracts from Yongzhou in the field of neuroprotection.

1 Introduction

Aging and central nervous system diseases all exhibit pathological processes such as neuron injury and cell apoptosis, so improving and repairing neuronal injury is an important strategy for preventing aging and treating central nervous system diseases (Zhou et al., 2010). Plant extracts are playing an increasingly important role in neuroprotection and neurological disease treatment. Many plant extracts such as glossy ganoderma, pine bark, and purslane have been found to have excellent neuroprotective bioactivity—free radical scavenging and oxidative stress alleviation are considered important reasons for the neuroprotective functions of these plant extracts (Lu et al., 2014; Guo et al., 2016; Li, 2018).

Ginkgo biloba and *Zingiber officinale* are two dominant plant resources in Yongzhou, Hunan Province. Extract of *G. biloba* leaf is widely used in treatment of cardiovascular and cerebrovascular diseases for containing flavonoids, esters, and other active components. Research in recent years has found that it also demonstrates activities of free radical scavenging, cerebral blood flow improvement, apoptosis process inhibition, and cell survival rate improvement for injured neurons, and shows significant potential for development in treating Alzheimer's disease and acute cerebral infarction (Rojas et al., 2012; Liu et al., 2016; Vellas et al., 2012; El-Borm et al., 2021). *Z. officinale* rhizome also contains volatile oil, gingerol, and other active components; it has a series of medicinal and health care functions—antibacterial, antioxidant, anti-aging, and decreasing blood pressure—and has a protective effect on central neurons injured by cerebral ischemia and ischemia-reperfusion. It significantly improved the learning and memory ability of Alzheimer's disease model rats (Zeng et al., 2013; Pannangrong et al., 2020).

Climate and environment factors affect the composition and content of the active components in plants organs, and the activity of different polarity parts of a certain plant extract may be different. Therefore, comparing the activity of different polarity parts of plant extracts from specific producing areas and analyzing their physiological impact could provide a basis for precise clarification of medication and pharmacological mechanisms (Luo et al., 2018; Xu et al., 2018; Ren et al., 2017). Until now, there have been few reports on neuroprotective and antioxidant activity and their correlation between the two kinds of bioactivity regarding the extracts of *G. biloba* leaf and *Z. officinale* rhizome from Yongzhou, as well as whether their activities are polarity part and concentration dependent. Therefore, this study focused on these issues in order to provide some references for the development of these two plant extracts in the field of neuroprotection.

2 Materials and methods

2.1 Materials

G. biloba leaves were collected in Yongzhou base in August 2019, and fresh *Z. officinale* rhizomes were purchased from the local market. These leaves and rhizomes were brought back to laboratory in an ice box, dried to constant weight at 60°C after washing, then powdered and screened at 80 mesh. The two kinds of plant were identified by Dr. Huang Guowen in the School of Chemistry and Bioengineering.

2.2 Main instruments

Ultraviolet visible spectrophotometer (Shanghai spectrum instrument Co., Ltd., SP-756P); cell incubator (Shengke Instrument Equipment Co., Ltd.); microplate reader (Type 1510, Thermofisher); high-speed tissue grinder (KZ-II, Wuhan Servicebio Co., Ltd.); automatic biochemical analyzer (Chemray 800, Redu Life Technology Co., Ltd.); automatic blood cell analyzer (BC-2800vet, Mindray Medical Instrument Co., Ltd.).

2.3 Main reagent

N-methyl-D-aspartic acid (NMDA, Shanghai Yuanye Biology company); DMEM medium (Sigma-Aldrich company); trypsin (Amresco company); D-Hank's solution (Sigma-Aldrich company); cytarabine (Ara-C, Sigma-Aldrich company); CCK-8 Kit (Shanghai Bogu Biotechnology Co., Ltd.); malondialdehyde kit (Nanjing Jiancheng Bioengineering Research Institute); superoxide dismutase kit (SOD, Nanjing Jiancheng Biology); GSH-PH Kit (Nanjing Jiancheng Bioengineering Institute); DMEM/F-12 medium (Hyclone company); PBS solution (1x, Solarbio company); trypan blue

(Solarbio company); collagenase I (Solarbio company); cytarabine (Solarbio company); L-glutamine (Solarbio company).

2.4 Methods

2.4.1 Extraction

Powder of *G. biloba* leaf or *Z. officinale* rhizome was put into ten beakers (100 g each beaker), 500 ml 75% ethanol was added, then continuously treated in a 400 W microwave for 5 min.0 Stand for 24 h, suction filtration, concentrate with reduced pressure to get the extraction paste, then bake it to a constant weight at 60℃.

2.4.2 Preparation of different polarity part of the extracts

Dry the extract to constant weight and dissolve in an appropriate amount of distilled water to make a suspension. Five different polar reagents—petroleum ether, chloroform, ethyl acetate, n-butanol, and ethanol—are successively added to the suspension at a 1:1 volume ratio. Repeat three times for each reagent and then add the next reagent to obtain the correspondingly different polarity parts of petroleum ether, chloroform, ethyl acetate, n-butanol, and ethanol; the remaining part after all the above organic solvents extraction is the water part. Each extraction solution is evaporated and dried in water bath, then baked to a constant weight at 60℃.

2.4.3 Preparation and *in vitro* neuronal cells culture

The thalamus of mice born less than 24 h was separated under sterile conditions with the aid of anatomical microscope, cut into about 0.5 mm^3, washed twice with D-Hank's solution, digested in 0.125% trypsin, incubated at 37℃ for 10 min; add the culture medium containing 10% fetal bovine serum to terminate trypsin digestion, centrifuge to remove the supernatant, and then add the buffer and gently blow to make the cell suspension. Dilute the cell suspension with DMEM culture medium to the appropriate concentration, then inoculate into the culture plate, place it in the CO_2 incubator at 37℃, replace the solution in half amount after 24 h and add 10 μMol/L Ara-C to inhibit glial cells. Replace whole solution 48 h later, and then half solution replaced every three days; observe cell growth dynamically. Newborn mice are produced by adult mice fed in the laboratory which were purchased from Hunan Silaike Jingda Laboratory Animal Co., Ltd. Animal experiments were carried out after being approved by the ethics committee of the college.

2.4.4 *In vitro* neuron injury and neuroprotective activity and antioxidant activity test

The cell suspension was inoculated into 96 well culture plates at 0.2 ml per well after five days' culture. Except for a part of the cell culture wells left as the blank control group without NMDA added, NMDA is added to other culture wells at 50 μ Mol/L final concentration for induced neuronal injury. After NMDA treatment for the hypoxia injury group (no extract added), different concentrations of extract treatment groups of *G. biloba* leaf and *Z. officinale* rhizome in each polarity part were set. Added to each treatment group 0.2 ml were different concentration extracts, with 0.2 ml of 1% sodium carboxymethyl cellulose added to the blank control group and hypoxia injury group. The cell survival rate (CCK8 method), malondialdehyde (MDA) content, and superoxide dismutase (SOD) activity were then tested 24 h later (Xu et al., 2015; Yuan et al., 2016).

Take Tris-HCl buffer 8.0 ml (PH8.2) in a water bath at 25℃ for 20 min, add 1.0 ml extract solution of each polarity part with different concentrations, and 0.5 ml 25 nmol/L pyrogallol hydrochloric acid solution preheated to 25℃; shake quickly, terminate reaction accurately with 0.5 ml concentrated HCl 4 min later, then determine the absorption value A_1 at 320 nm. The absorption value (A_0) was measured following the same steps except for replacing the extract solution with the same volume of distilled water; the absorption value A_2 was measured following the some steps except for replacing pyrogallol hydrochloric acid solution with the same volume of distilled water. Each determination was repeated thrice to calculate the average value. The O_2^{-} scavenging capacity (%) of the extract solution can then be calculated with the formula $[A_0 − (A_1 − A_2)] * 100/A_0$ (Kong et al., 2015).

2.4.5 Effect of the best polarity part on blood physiology and neuron cell activity of aged mice

Dissolve 0.2, 0.4 and 0.8 g of the best polarity part determined by *in vitro* experiment of the two extracts with normal saline and fix the volume to 100 ml to achieve three different concentration levels of 2 mg/ml (low), 4 mg/ml (medium), and 8 mg/ml (high). A total of 70 aged mice (20 months) were randomly divided into seven groups (ten mice each group) after five days adaptive feeding. The seven groups, including control group, were treated in groups with low, medium, and high concentrations of *G. biloba* and *Z. officinale* extract. Each mouse was fed with same amount every day, maintained a 25℃ feeding environment temperature and 60% relative humidity. Extract solutions of 5 ml with low, medium, and high concentration were gavaged at 9 a.m. every day. The control group was fed with the same amount of normal saline. On the 20th day of gavage treatment, blood was collected from the tail after anesthesia, and blood physiological and biochemical indexes were determined by automatic biochemical analyzer and automatic blood cell analyzer (Chen et al., 2019). MDA content, SOD, and GSH-Px activity were determined according to the kit instructions.

After anesthesia and blood collection, the necks were broken and brain tissue was extracted and immediately immersed in the precooled DMEM/F_{12} serum-free medium. The hippocampus
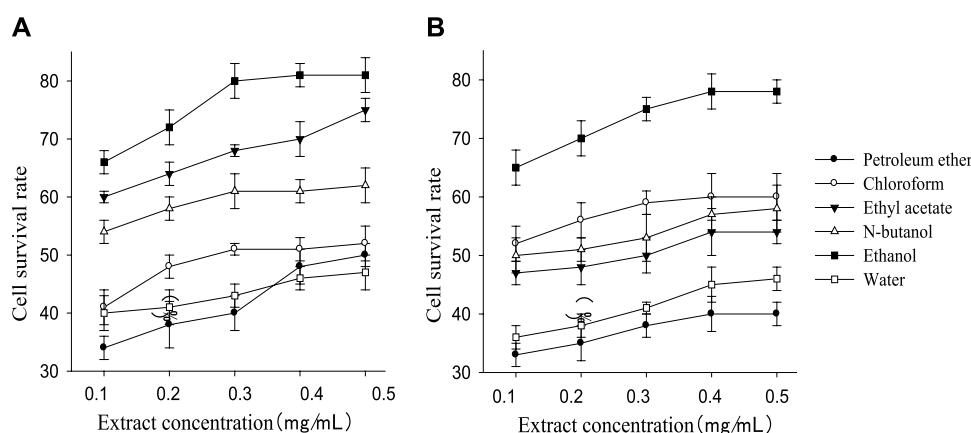
FIGURE 1
Survival rate of nerve cells in different polarity parts of extract of *G. biloba* leaf **(A)** and *Z. officinale* rhizome **(B)** at different concentration.

was then separated into the PBS buffer under an ice bath on an ultra-clean workbench. After washing with PBS five times, cut the hippocampus into small blocks, and then digest with 0.25% trypsin + 0.1% type I collagenase at 37°C for 40 min. Terminate digestion with FBS, mix gently, filter with 100 μm membrane, centrifuge the filtrate at 1,500 rpm for 5 min to remove the supernatant, then re-suspend with the complete medium (89% DMEM/F$_{12}$ + 10% fetal bovine serum + 1% cyanine/streptomycin) and culture in an incubator. Update the solution by a half amount every two days, then add 8 μ cytarabine three days later to inhibit the proliferation of non-neural cells and primary glia. After that, add 10 μl CCK-8 solution per well on the fifth day, determine absorption value at 450 nm with the microplate reader after 2 h incubation, and then calculate the cell activity (%) (Wang et al., 2021).

3 Results and analysis

3.1 *In vitro* neuroprotective activity of different polarity parts of two kinds of extract

The cell survival rate of the treatment groups was higher than the injury group (32%) although still lower than the control group (94%). The cell survival rate of each treatment group increased with the rising extract concentration within a certain range and then kept stable (Figure 1). The order of the cell survival rate of the different polarity part of the extract of *G. biloba* leaf from high to low was ethanol, ethyl acetate, n-butanol, chloroform, water, and petroleum ether (petroleum ether part performed slightly better than water part at 0.4 mg/ml and 0.5 mg/ml), while the order of *Z. officinale* extract was

ethanol, chloroform, n-butanol, ethyl acetate, water, and petroleum ether. Both kinds of extract performed best in ethanol part, and *G. biloba* always performed better than *Z. officinale* in all polarity parts except the chloroform part.

3.2 *In vitro* effect of the two extracts on the SOD activity and MDA content of the neuron cells

The SOD activity of the control group (161.20 ± 30.34) was higher than the injury group (103.36 ± 24.12), while MDA content (9.76 ± 0.35) was lower than the injury group (15.23 ± 1.16). Like the cell survival rate, SOD activity and MDA content increased or decreased with a rising extract concentration, then remained stable when the concentration reached a certain value (Figures 2, 3). The best performance concentration in ethanol part of the two extracts was different from other polarity parts, while all different polarity parts showed a similar overall law of change with increasing concentration. Both kinds of extract performed best in the polarity part of ethanol, and the performed order from superior to inferior of different polarity parts was consistent with the cell survival rate.

3.3 *In vitro* antioxidant activity of different polarity parts of the two extracts

All polarity parts of the two plant extracts displayed different antagonistic effects on superoxide free radicals. The scavenging rate to free radicals increased with the rise in extract concentration in a certain range, and the order of different

FIGURE 2
SOD activity in different polarity parts of the two plant extracts with different concentrations [**(A)**: *G. biloba* leaf; **(B)** *Z. officinale* rhizome].
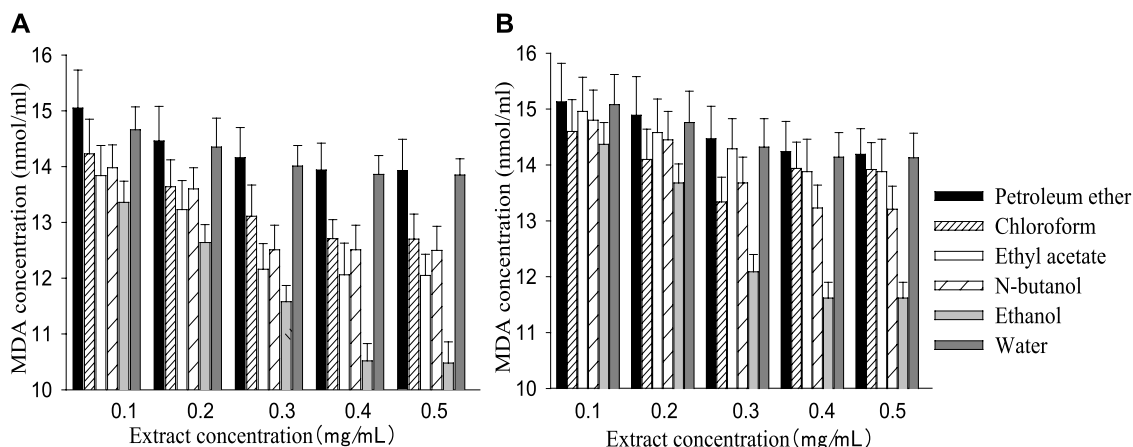
FIGURE 3
MDA concentration in different polarity parts of the two extracts with different concentrations [**(A)**: *G. biloba* leaf; **(B)** *Z. officinale* rhizome].

polar segments performing from superior to inferior was also consistent with the resulting cell survival rate (Figure 4). *G. biloba* performed better than *Z. officinale* if they had a same concentration and polarity part. As shown in Figure 5, there was a significant positive relationship between cell survival rate and superoxide radical scavenging rate under treatment with both *G. biloba* and *Z. officinale* extracts ($p < 0.01$).

3.4 *In vivo* effect of the best polarity part of the two extracts on the central neuron cell activity and blood physiology of aged mice

After continuous gavage with ethanol polarity part of extracts of *G. biloba* leaf or *Z. officinale* rhizome, the

activity of thalamic neurons (Figure 6A), SOD (Figure 6C), and GSH-Px (Figure 6D) in the serum of aged mice were higher than the control group ($p < 0.05$), while the MDA content decreased compared with the control group (Figure 6B). *G. biloba* performed better than *Z. officinale* when they had the same concentration level.

There were no significant differences in the number of white blood cells (WBC), lymphocytes, red blood cells (RBC), and hemoglobin content between the control and treatment groups ($p > 0.05$, Table 1), as well as the activities of glutamic oxaloacetic transaminase (GOT), glutamic pyruvic transaminase (GPT), and the contents of blood urine nitrogen (BUN), uric acid (UA), and creatinine (CEEA), which were closely related to liver and renal functioning ($p > 0.05$, Table 1).
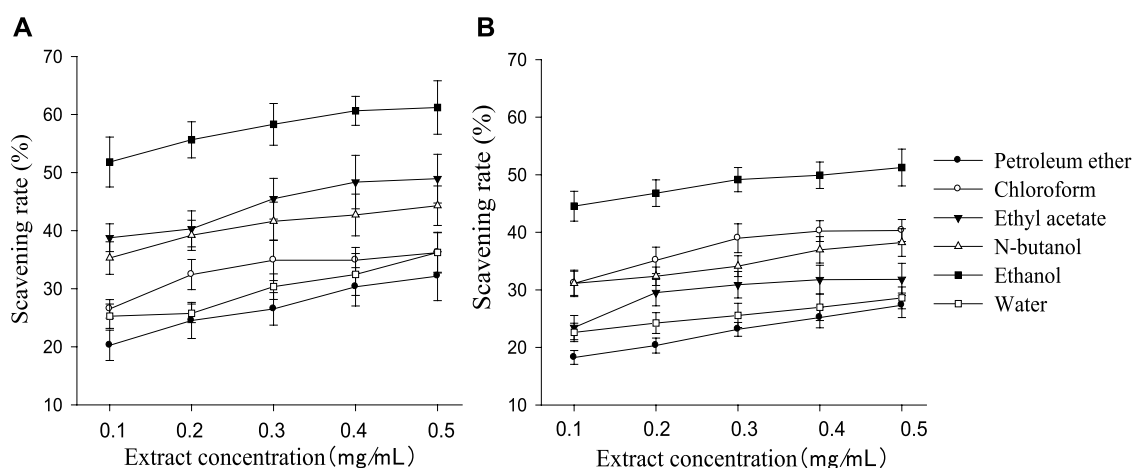
FIGURE 4
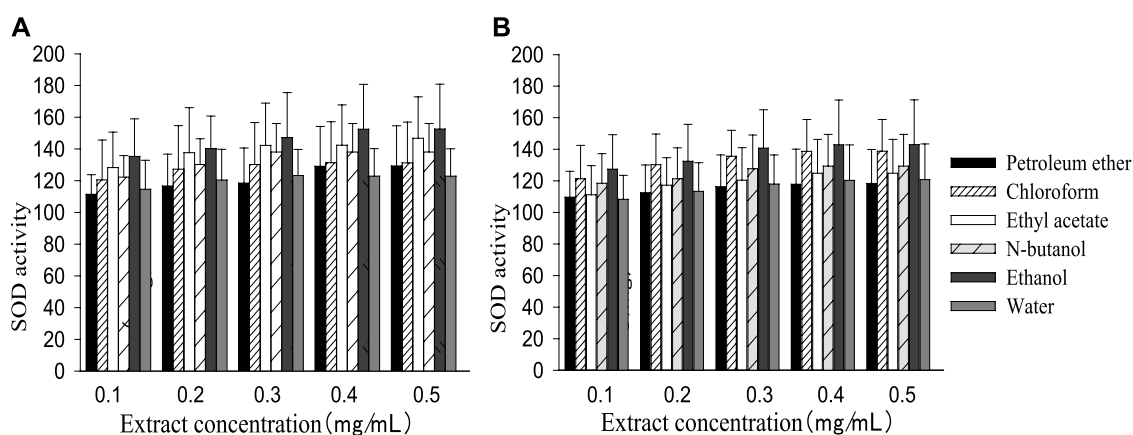Scavening rate to superoxide radical in different polarity parts of the extracts with different concentrations [**(A)**: *G. biloba* leaf; **(B)** *Z. officinale* rhizome].
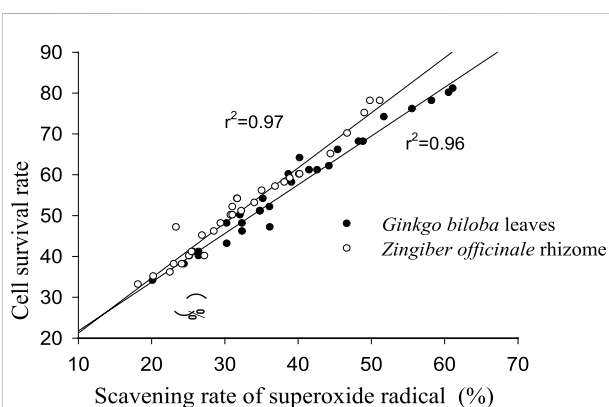
FIGURE 5
Correlation between cell survival rate and superoxide radical scavenging rate under treatment by the two plant extracts.

3 Discussion

Neurodegenerative diseases such as Parkinson's and Alzheimer's diseases are closely related to neuron damage in specific central neuron parts, and clinical symptoms will appear when the number of injured neuron cells reaches a certain proportion (dopamine neuron numbers in the substantia nigra of Alzheimer's disease patients reduces more than half). It is, therefore, of great importance to screen the natural active ingredients with neuroprotective effects to prevent neurodegenerative processes and treat corresponding diseases. Local dominant and characteristic plant resources

are important sources for active substance screening; these natural active substances with neuroprotective activity are mainly concentrated in glycosides, flavonoids, saponins, and so on (He et al., 2017). *G. biloba* leaf contains flavonoids and esters, while *Z. officinale* rhizomes contain curcumin, flavonoids, polyphenols, saponins, These two plant resource thus have the substance bases of neuroprotective function (Wang et al., 2011; Shang et al., 2018; Small et al., 2018).

This study found that all the polarity parts of the extracts of *G. biloba* leaf and *Z. officinale* rhizomes produced in Yongzhou had the effect of increasing the cell survival rate and SOD activity of central nerve cells while reducing the MDA content, meaning that the two plant extracts performed positively in central neuron survival and showed excellent neuroprotective activity. However, the composition and content difference of these active components in each polarity part led to a different presentation of protective effect, so it is necessary to separate, purify, and identify the components of the high activity polarity part of the two plant extracts. Coincidentally, both the extracts show the best activity in ethanol polarity part—the non-toxicity, low boiling point, and easy removal of ethanol are beneficial for its large-scale extraction and application.

Antagonizing oxidative stress and oxidative damage are considered important reasons for the neuroprotective activity of plant extracts. If oxidation and antioxidation are out of balance in cells, the predomination of oxidation could lead to free radicals enrichment which would damage cell membrane structures and cause a series of adverse consequences, including metabolic disorder, abnormal protein expression and mitochondrial function, and the failure of physiological activities (Rhein et al., 2010; Jia et al., 2011; Yan et al., 2014). In this study, the *in vitro* changes of SOD activity
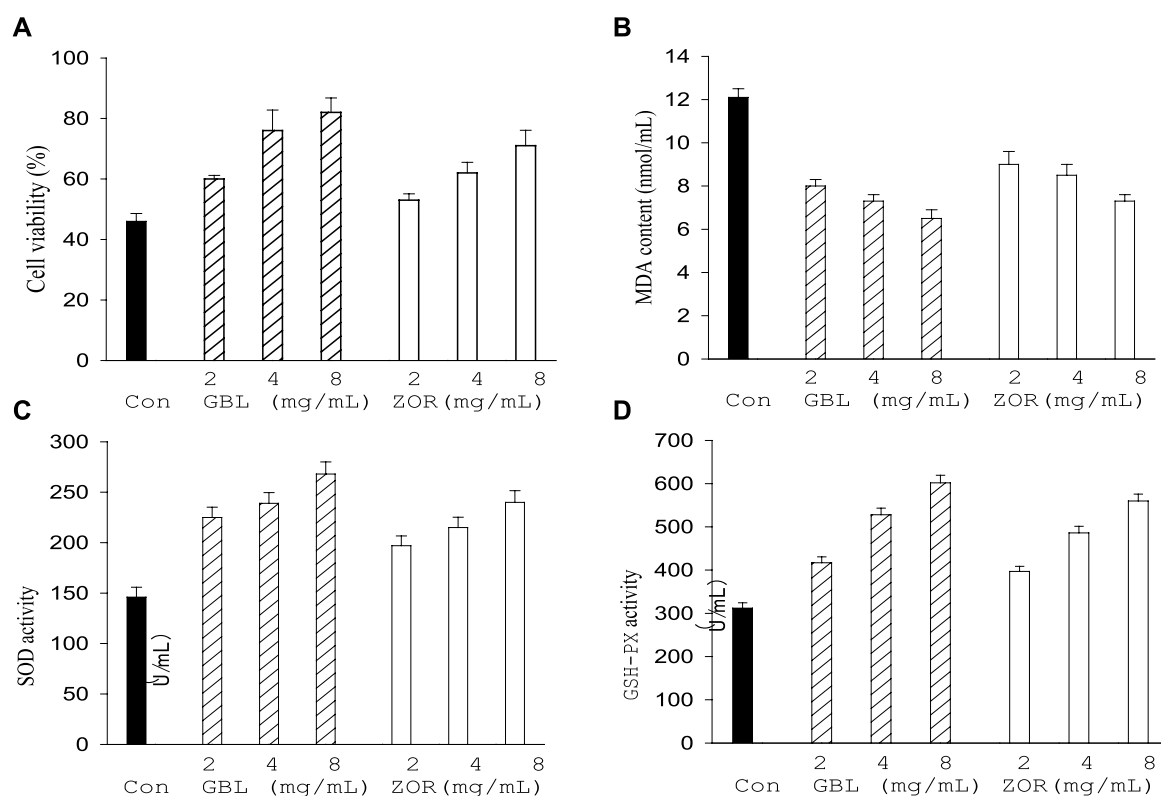
FIGURE 6
Effect of *G. biloba* leaf (GBL) and *Z. officinale* rhizome extracts (ZOR) from Yongzhou on central neuron cell viability **(A)** and serum antioxidant indexes **(B–D)** in aged mice.

TABLE 1 Effects of extracts of *G. biloba* leaves (GBL) and *Z. officinale* rhizome (ZOR) on aged mice' blood physiology.

Indexes	GBL (mg/ml)			ZOR (mg/ml)			Con
	8	**4**	**2**	**8**	**4**	**2**	
WBC (10^9/L)	10.0	10.3	10.6	10.4	10.4	10.2	10.3
Lymphocyte (10^9/L)	6.6	6.7	6.8	6.9	6.8	6.8	6.8
RBC (10^9/L)	7.2	7.2	7.2	7.2	7.1	7.1	7.2
Hemoglobin (10^{12}/L)	142	140	140	140	140	141	140
GOT (U/L)	47.6	47.1	46.5	47.3	47.3	46.8	46.8
GPT (U/L)	167.8	160.4	161.8	165.8	165.6	161.7	166.5
BUN (mmol/L)	8.6	8.4	8.3	8.3	8.3	8.2	8.2
UA (μmol/L)	2.7	2.6	2.6	2.6	2.6	2.5	2.5
CREA (μmol/L)	75.6	74.1	74.5	75.1	73.6	72.8	72.3

and MDA content with the concentration and scavenging ability to super-oxidize the free radicals of the two plant extracts indicate their excellent antioxidant activity. The positive correlation between cell survival rate and free radical clear rate indicate that antioxidant activity is an important underlying mechanism for the neuroprotective function of the two plant extracts.

Oxidative stress is considered an important cause of aging, while effective anti-oxidation can delay the aging process. *G. biloba* extract can inhibit the intracellular oxidative stress level of central neurons; *Z. officinale* extract can reduce lipid peroxidation in the brain tissue of Alzheimer's model rats (Xia et al., 2014; Song et al., 2015). The ethanol polarity part improves body antioxidant function by affecting the MDA content and the activity of SOD, GSH-Px in blood serum. This indicates that the two plant extracts have neuroprotective efficacy and can slow the central nervous degeneration process by improving elderly individuals' antioxidant capacity. There is no significant change in the aged mice blood cells numbers, the content of hemoglobin, uric acid and creatinine, and the activities of GOT and GPT in serum ($p > 0.05$). This indicates that the two extracts are very safe and will not cause a stress response to or damage the body's immune system and the organ functions of the liver and kidney. *G. biloba* always performs better than *Z. officinale* when they have same concentration and polarity part; the activity of the two plant extracts shows an obvious concentration dependence within a certain range, providing important references for future neuroprotection formulation development based on

these two plant extracts from Yongzhou (Rojas et al., 2012; Xin et al., 2015; Ren et al., 2017).

Data availability statement

The original contributions presented in the study are included in the article/supplementary material, further inquiries can be directed to the corresponding authors.

Ethics statement

The animal study was reviewed and approved by the Ethics Committee of the College of Life Sciences and Chemistry Engineering.

Author contributions

ZH and TY contributed to the *in vitro* neuroprotective and antioxidant ability and JC, MJ, and RY contributed to *in vivo* effect of the best polarity part on central neuron cell activity. WY, LW, and GH contributed to the *in vivo* effect of the best polarity part on blood physiology of aged mice. YL supervised the work and prepared the manuscript.

Conflict of interest

The authors declare that the research was conducted in the absence of any commercial or financial relationships that could be construed as a potential conflict of interest.

Publisher's note

All claims expressed in this article are solely those of the authors and do not necessarily represent those of their affiliated organizations, or those of the publisher, the editors and the reviewers. Any product that may be evaluated in this article, or claim that may be made by its manufacturer, is not guaranteed or endorsed by the publisher.

References

Chen, L. X., Wang, J. B., Li, Y. Y., Xu, H. J., Yu, W. H., Ma, J., et al. (2019). Effects of astragalus polysaccharides on growth performance, blood physiological and biochemical indexes and incidence of diarrhea in breeding rhesus monkeys[J]. *Laboratory Animal Sci.* 36 (6), 44–49. doi:10.3969/j.issn.1006-6179.2019.06.009

El-Borm, H. T., Gobara, M. S., and Badawy, G. M. (2021). Ginger extract attenuates labetalol induced apoptosis, DNA damage, histological and ultrastructural changes in the heart of rat fetuses. *Saudi J. Biol. Sci.* 28 (1), 440–447. doi:10.1016/j.sjbs.2020.10.027

Guo, K., Miu, H., Wang, S. S., Cheng, J. J., and Shang, Y. Z. (2016). Scutellaria barbata flavonoids inhibits NFT aggregation and regulatory mechanism in rats induced by composited Aβ[J]. *Chin. J. Pathophysiol.* 32 (12), 2147–2156.

Jia, S. Q., Wang, J., Zhang, H. X., Huang, X., Sun, W., and Man-hua, F. U. (2011). Effects of *Zingiberis Rhizoma* recens on neuronal apoptosis and related prote in expression in focal cerebral Ischemia-reperfusion in rats[J]. *Chin. J. Exp. Traditional Med. Formulae* 17 (3), 163–166. doi:10.13422/j.cnki.syfjx.2011.03.056

Kong, L. X., Liang, X. X., He, M., Aga, E. B., and Fan, Q. J. (2015). Study on antioxidant activities of different polarity fractions of ethanol extract of *Gentiana urnula* H. Smith[J]. *Nat. Prod. Res. Dev.* 27 (4), 651–654. doi:10.16333/j.1001-6880.2015.04.01

Li, L. Y. (2018). *Research on neuroprotective and anti-inflammatory effects of oleracein E and extracts from* Portulaca oleracea L.[D]. Jinan: Shandong University.

Liu, L., Zhang, C. Y., Kalionis, B., Wan, W. B., Murthi, P., Chen, C., et al. (2016). EGb761 protects against Aβ1-42 oligomer-induced cell damage via endoplasmic reticulum stress activation andHsp70 protein expression increase in SH-SY5Y cells. *Exp. Gerontol.* 75, 56–63. doi:10.1016/j.exger.2016.01.003

Lu, F. B., Wang, R., Chen, L., Chen, L. N., Zhang, L. P., and Liu, C. B. (2014). Protective effect of pine bark extract on impaired neuron in rotenone induced Parkinson's disease mouse model[J]. *Mod. Prev. Med.* 41 (8), 1468–1471.

Luo, A. Y., Nong, J. D., Jin-ping, L., Luo, Q. L., Lu, L. Q., and Huang, S. Y. (2018). Antioxidant activity of different polar fractions from Guangxi Jasmine leaves [J]. *Chin. J. Clin. Pharmacol.* 34 (6), 703–706.

Pannangrong, W., Welbat, J. U., Chaichun, A., and Sripanidkulchai, B. (2020). Effect of combined extracts of aged garlic, ginger, and chili peppers on cognitive performance and brain antioxidant markers in Aβ-induced rats. *Exp. Anim.* 69 (3), 269–278. doi:10.1538/expanim.19-0123

Ren, L. H., He, S., and Xu, Y. L. (2017). Research progress in studies on mechanism of traditional Chinese medicine active ingredients with neuroprotective effect[J]. *Chin. J. Exp. Traditional Med. Formulae* 23 (3), 229–234. doi:10.3969/j:issn.2095-1191.2015.4.675

Rhein, V., Giese, M., Baysang, G., Meier, F., Rao, S., Schulz, K. L., et al. (2010). Ginkgo biloba extract ameliorates oxidative phosphorylation performance and rescues aβ-induced failure. *PLoS One* 5 (8), e12359. doi:10.1371/journal.Pone.0012359

Rojas, P., Ruiz-Sanchez, E., Rojas, C., and Ogren, S. O. (2012). *Ginkgo biloba* extract (EGb761) modulates the expression of dopamine-related genes in 1-methyl-4-phenyl-1, 2, 3, 6 -tetrahydropyridine-induced Parkinsonism in mice[J]. *Neuroscice* 223 (30), 246–257. doi:10.1016/j.neuroscience.2012.08.004

Shang, H., Ren, X. H., Yang, H. X., and Xu, F. (2018). Effects of curcumin on expression of caspase-3, caspase-8 and caspase-9in PC12 cells induced by Aβ25-35 [J]. *Chin. J. Pathophysiol.* 34 (1), 168–172. doi:10.3969/j.issn.1000-4718.2018.01.029

Small, G. W., Siddarth, P., Li, Z. P., Miller, K. J., Ercoli, L., Emerson, N. D., et al. (2018). Memory and brain amyloid and tau effects of a bioavailable form of curcumin in non-demented adults: A double-blind, placebo-controlled 18-month trial. *Am. J. Geriatr. Psychiatry* 26 (3), 266–277. doi:10.1016/j.jagp.2017.10.010

Song, L. L., Sha, J. Q., Zhang, L., and Zhang, Y. X. (2015). Study on extraction of ginger polysaccharide and its protecting effect on cerebral ischemia-reperfusion injury[J]. *Liaoning J. Traditional Chin. Med.* 42 (12), 2433–2435. doi:10.13192/j.issn.1000-1719.2015.12.063

Vellas, B., Coley, N., Ousset, P. J., Berreut, G., Dartigues, J. F., Dubois, B., et al. (2012). Long-term use of standardised *Ginkgo biloba* extract for the prevention of alzheimer's disease (GuidAge): A randomised placebo-

controlled trial[J]. *Lancet Neurology* 11 (10), 851–859. doi:10.1016/s1474-4422(12)70206-5

Wang, D. K., Zhang, H. Y., Liu, H. Y., Sun, Z., Han, J. L., Zhang, L. X., et al. (2011). The neural protection of leave *Ginkgo Biloba* extract injection in intracerebral hemorrhage rats[J]. *Chin. J. Neuroanat.* 27 (3), 316–320.

Wang, Z. Y., Ma, Y. R., Yan, Q. Y., Zhang, X. R., Liu, S. Y., and Zhu, L. (2021). Pterostilbene improves learning and memory impairment in AD mice[J]. *J. Shenyang Pharm. Univ.* 38 (6), 596–601.

Xia, C. Y., Dong, X. W., Zhao, Y., Xu, Y., Hao, L., and Zhang, Z. X. (2014). [Ginkgo biloba extract 50 inhibited beta-amyloid-induced oxidative stress in rats' hippocampal neurons: An experimental study]. *Chin. J. Integr. Traditional West. Med.* 34 (7), 833–838. doi:10.7661/cjim.2014.07.0833

Xin, R. H., Peng, W. J., Wang, G. B., Luo, Y. J., Luo, C. Y., Xie, J. Y., et al. (2015). Comparison on efficacy of different polarity section extract from Aster tataricus[J]. *J. South. Agric.* 46 (4), 675–679. doi:10.3969/j:issn.2095-1191.2015.4.675

Xu, Y. Z., Liu, S., Li, Y. C., Li, L., Yu, Y., Zhao, W. X., et al. (2015). Protective effect of *Ginkgo biloba* extract on dopaminergic neurons in rats with Parkinson's disease

[J]. *Pharmacol. Clin. Chin. Materia Medica* 31 (2), 131–132. doi:10.13412/j.cnki.zyyl.2015.02.055

Xu, X. M., Li, M. Z., Huang, J. R., and Wang, Q. H. (2018). Antibacterial activity study of different polar extractings of *Eleutherine americana*[J]. *Nat. Prod. Res. Dev.* 30 (9), 1621–1626.

Yan, J., Zheng, M. D., and Zhang, D. S. (2014). Chrysophanol liposome preconditioning protects against cerebral ischemia-reperfusion injury by inhibiting oxidative stress and apoptosis in mice. *Int. J. Pharmacol.* 10 (1), 55–68. doi:10.3923/ijp.2014.55.68

Yuan, H. Y., Wang, Z. S., and Wang, Y. Q. (2016). Protective effect of gastrodin on hypoxic injury of cortical neurons in rats[J]. *Pract. J. Med. Pharm.* 33 (7), 625–626. doi:10.14172/j.issn1671-4008.2016.07.020

Zeng, G. F., Zong, S. H., and He, J. M. (2013). Effect and its mechanism of ginger root extract on cognitive dysfunction in rats with Alzheimer disease[J]. *J. Clin. Neurology* 26 (5), 362–365.

Zhou, Z. Y., Tang, Y. P., Jin, H. M., Gao, J. P., Zhang, J. P., Wang, Z., et al. (2010). Ganoderma lucidum extract protects rat cerebral cortical neurons from hypoxia/reoxygenation injury *in vitro*[J]. *Chin. J. Pathophysiol.* 26 (11), 2229–2234. doi:10.3969/jissn.1000-4718.2010.11.029

A comparative study of three chemometrics methods combined with excitation–emission matrix fluorescence for quantification of the bioactive compounds aesculin and aesculetin in Cortex Fraxini

Ze Ying Li[1], Xin Kang Li[1], Yuan Lin[1], Na Feng[1], Xiang-Zhi Zhang[1], Qing-Lin Li[2] and Bao Qiong Li[1]*

[1]School of Biotechnology and Health Sciences, Wuyi University, Jiangmen, China, [2]Agricultural Science Research Institute of Yiyang, Yiyang, China

Cortex Fraxini is an important traditional Chinese herbal medicine with various medical functions. Aesculin and aesculetin are the main effective components of Cortex Fraxini. The fluorescence signals of the two compounds have a high degree of overlap with each other, making quantitative analysis difficult with conventional analytical methods. In the present study, different chemometrics methods, including lasso regression (LAR), interval partial least squares (iPLS), and multidimensional partial least squares (N-PLS) methods, were employed and combined with excitation–emission matrix (EEM) fluorescence for the purpose of accurate quantification of aesculin and aesculetin in Cortex Fraxini samples. The most satisfactory results were obtained by using the N-PLS method based on the EEM spectra without scatterings, with correlation coefficient of calibration and prediction values higher than 0.9972 and 0.9962, respectively, root mean squared errors for calibration and prediction values lower than 0.0304 and 0.1165, respectively, and recovery values in the range of 83.32%–104.62%. The obtained credible models indicated that the N-PLS method combined with EEM spectra has the advantages of being green, low cost, and accurate and it is a good strategy for the determination of active compounds in complex samples. To further confirm the accuracy of the obtained results, the same samples were analyzed by the recognized ultra-performance liquid chromatography method.

KEYWORDS

Cortex Fraxini, excitation-emission matrix fluorescence, second-order calibration, machine learning, quantitative analysis, UPLC

1 Introduction

Chinese herbal medicine is a natural resource with abundant sources. It is widely used in the treatment of diseases in China and neighboring countries. Compared with western medicine, Chinese herbal medicine is popular with people because of its low toxicity and few side effects. Cortex Fraxini (Chinese name Qin-pi) is an important traditional Chinese herbal medicine that has been used to treat gout, arthritis, hyperuricemia, and other diseases (Wang et al., 2016a) for over 2000 years. Coumarin compounds are the main chemical active ingredients in Cortex Fraxini medicinal materials, which have obvious effect in the treatment of primary hyperuricemia (Zhou et al., 2018).

Nowadays, numerous methods exist for the quantitative analysis of target ingredients of Chinese herbal medicines or their formulas, including high-performance liquid chromatography (HPLC), ultra-performance liquid chromatography (UPLC), liquid chromatography–mass spectrometry (LC-MS), gas chromatography–mass spectrometry (GC-MS), ultra-high-performance supercritical fluid chromatography (UHPSFC), Fourier-transform infrared (FTIR) spectroscopy, excitation–emission matrix (EEM) fluorescence spectroscopy, terahertz (THz) spectroscopy, and proton nuclear magnetic resonance (^{1}H NMR) spectroscopy. Among these methods, EEM spectroscopy has the advantages of rapidity, simplicity, low cost, high sensitivity, and non-destructiveness. At present, a large number of reports on the analysis of ingredients in foods and medicines by fluorescence spectroscopy combined with chemometrics methods have been reported, and a few examples include those of Bai et al. (2018), Liu et al. (2019), Wang et al. (2017), and Li et al. (2021). These successful examples demonstrated that fluorescence spectroscopy combined with chemometrics methods can be regarded as an effective way to quantitatively analyze target components in complex systems.

Aesculin and aesculetin are the main effective components of Cortex Fraxini. At present, many analytical methods have been applied to analyze one or both components of aesculin and aesculetin, including HPLC (Wang et al., 2019), LC-MS (Li et al., 2013), capillary electrophoresis (CE) (Li et al., 2005), GC-MS (Wang et al., 2016b), and electrochemical analysis (Sheng et al., 2020). In our research, we intend to quantitatively analyze these two components based on EEM spectra because of its advantages of simplicity, low cost, and high sensitivity. Owing to the complexity of the Cortex Fraxini samples, unknown interferences may be present in the measured data, and the fluorescence signals of aesculin and aesculetin have a high degree of overlap with each other, making simultaneous quantitative analysis difficult by using conventional fluorescence methods. To realize the accurate quantitative analysis purposes, appropriate algorithms should be explored and employed.

The aim of this work was to explore different chemometrics strategies, such as lasso regression (LAR), interval partial least squares (iPLS), and multidimensional partial least squares (N-PLS) methods, in combination with EEM spectra for the quantitative determination of aesculin and aesculetin in Cortex Fraxini samples. Among these three methods, LAR is an important machine learning technique that can be applied for analyzing data suffering from multicollinearity (Gao et al., 2022), iPLS is a feature interval extraction method on the basis of PLS that aims to minimize multicollinearity problems to improve the accuracy of the PLS model (Abreu et al., 2015), and N-PLS is a second-order multivariate calibration algorithm that can be used for three-way data modeling even in the presence of multicollinearity problems (Lopez-Fornieles et al., 2022). To the best of our knowledge, there exist no published reports of the analysis of the aesculin and aesculetin in Cortex Fraxini samples by using the above-mentioned methods. The obtained results of each method were fully validated by statistical parameters, and the potentials of the methods were evaluated and compared. The comparison results showed that the N-PLS method gave the most satisfactory quantitative analysis results. Furthermore, we compared the most satisfactory results achieved from the N-PLS method with those obtained by the UPLC method, which further proved the reliability and accuracy of the explored method.

2 Theory

2.1 Chemometrics methods

In the following subsections, a brief introduction is given to the three employed methods, LAR, iPLS, and N-PLS.

2.1.1 Lasso regression (LAR)

The LAR method is an important machine learning technique for analyzing data suffering from multilinearity (Yang and Wen, 2018). The basic idea of LAR is to minimize the sum of squared residuals under the constraint that the sum of the absolute values of the regression coefficients is less than a constant, so that some regression coefficients strictly equal to zero can be generated and an interpretable model can be obtained (Tkachenko et al., 2021) when the regression coefficients are zero and the corresponding variables are not selected, thus eliminating irrelevant information variables and improving the predictive accuracy of the model and its interpretability.

2.1.2 Interval partial least squares (iPLS) algorithm

The iPLS algorithm can be used to extract the feature bands and remove a large amount of useless information and noisy variables. It divides the entire spectral region into several subintervals of equal width. For each interval, a local PLS is established. If a subinterval contains more information and less noise, the performance of the

corresponding model will be better (Wu et al., 2015). Therefore, in each subinterval, the root mean squared errors for cross-validation (RMSECV) are calculated, and the subinterval with the minimum RMSECV value is taken as the characteristic band and selected for further use. For cross-validation, an individual sample is taken from the calibration set and a model is established by the remaining samples. Then, the model is applied to predict the removed sample. The calculation formula of RMSECV is as follows (Zhang et al., 2021):

$$RMSECV = \sqrt{\frac{\sum_{i=1}^{m}(y_i - \tilde{y}_i)^2}{m}}, \tag{1}$$

where m is the sample numbers of the calibration set, y_i is the reference value of sample i, and $\tilde{y}_i$ is the calculated value of the removed sample i.

2.1.3 Multidimensional partial least squares (N–PLS)

N-PLS (Bro, 1996) is an extension of partial least squares (PLS) regression to higher-order arrays; it has been used in many quantitative analysis studies (Bro, 1996; Luo et al., 2016). During the construction of the N-PLS models, it is important to choose the proper number of latent variables (LVs). Some necessary and useful information may be missed if the number of LVs is too small, whereas some useless information or even interferences will be involved in the model if the number of LVs is more than required (Yang et al., 2018). Therefore, the proper number of LVs should be determined carefully. In this study, the proper number of LVs was chosen on the basis of the minimum predicted residual error sum of squares (PRESS) for each model (Thomas, 2003). The calculation formula of PRESS is as follows (Khajehsharifi and Eskandari, 2011):

$$PRESS = \sum_{i=1}^{m}(y_i - \hat{y}_i)^2, \tag{2}$$

where m is the sample numbers of the calibration set and y_i and $\hat{y}_i$ are the reference and calculated values, respectively, of sample i in the calibration samples.

2.2 Validation of model performance

The performance of the established models should be validated by statistical parameters. For the above purpose, the following parameters have been employed: the correlation coefficient for calibration (Rc) and prediction (Rp) and the root mean squared errors for calibration (RMSEC) and prediction (RMSEP). The correlation coefficient is a measure of the linearity between the calculated and actual values of the model, and the root mean squared error is a commonly used index to measure the error in quantitative models. A successful calibration model should have higher values of Rc and Rp and lower values of RMSEC and RMSEP.

3 Experimental

3.1 Reagents and solutions

Aesculin and aesculetin were purchased from Chengdu MUST BIO-TECHNOLOGY CO., LTD. (purity higher than 98%). The molecular structures of the two compounds are illustrated in Figure 1. Ultra-pure water was purchased from Watsons. Methanol was of HPLC grade and other chemicals were of analytical grade.

Six Cortex Fraxini samples were purchased from local drug stores (Jiangmen, Guangdong, China) and then pulverized with a traditional Chinese medicine grinder.

3.2 Apparatus

Fluorescence data of all samples were measured by a fully automatic and integrated FluoroMax-4 instrument with a 150 w ozone-free xenon light source, excitation monochromator, reference detector, sample cell, emission monochromator, and signal detector. The spectral data were obtained by scanning the samples at excitation wavelengths ranging from 200 nm to 600 nm and emission wavelengths ranging from 200 nm to 600 nm with steps of 10 nm.

The multifunctional ultrasonic cleaner (GS-060A) was purchased from Shenzhen Keneng Cleaning Equipment Co., Ltd.

The UPLC chromatograms were carried out on Waters UPLC H-class instrument coupled with a PAD e λ detector, a sample manager, a quaternary solvent manager, and a BEH C18 column (2.1 × 100 mm, 1.7 μm). The gradient elution program used 0.1% v/v formic acid in water (A) and acetonitrile (B) as the eluents, and the program was as follows: 0–1.00 min, 13%–15% B; 1.00–5.00 min, 15%–20% B; 6.00–9.00 min 100% B; 9.00–10.00 min 100%–13.00% B; 10.00–12.00 min 13% B. The column temperature was at room temperature, the scan wavelength ranged from 210 to 400 nm, the flow rate was set at 0.5 ml/min, and the injection volume was 10 μl (Preeti Chandra et al., 2016).

The implementation of the N-PLS and iPLS algorithms was on the eclipse platform, and the version number was 4.19.0; the jdk version was 1.7.0_13-b20, the tomcat version was 7.0, and the computer language was java. The implementation of the LAR algorithm was on the pycharm platform, and the computer language was python.
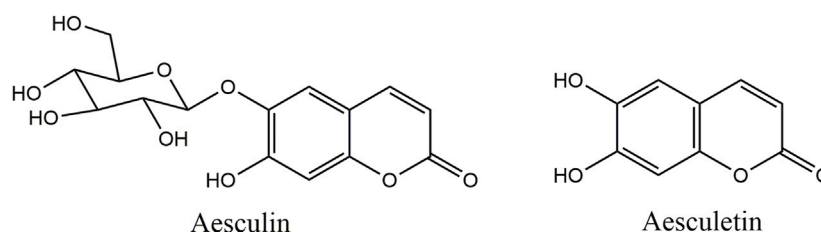
FIGURE 1
Molecular structures of aesculin and aesculetin.

3.3 Sample preparation

Stock solutions of aesculin (745 μg/ml) and aesculetin (1,060 μg/ml) were prepared by dissolving the standards in methanol, and they were stored at 4°C in the freezer. Working solutions were prepared by appropriate dilution of the stock solutions with methanol. Britton–Robinson buffer solution (BR buffer) (0.2 mol/L, pH = 9) was used to stabilize the fluorescence intensity of aesculin and aesculetin.

A series of 21 mixed standard solution samples was prepared. The concentrations of aesculin and aesculetin were in the range of 0.002–1.020 μg/ml and 0.009–4.000 μg/ml, respectively, and the detailed concentrations of the aesculin and aesculetin are shown in Supplementary Tables S1, S2, respectively (in the Supporting information).

The purchased Cortex Fraxini samples were crushed into powder by a pulverizer for better extraction of aesculin and aesculetin. We referred to some Chinese literature and found that the active substances in Cortex Fraxini can be better extracted by soaking the sample in methanol for 24 h and then extracting by ultrasonication for 30 min. Thus, in this study, the powdered Cortex Fraxini samples were soaked in methanol for 24 h at room temperature and then treated with ultrasonication for 30 min. They were then filtered and transferred to a 50.0 ml volumetric flask, left at room temperature, and appropriately diluted with methanol during use.

For the recovery test, the six actual samples were all spiked with a certain amount of aesculin and aesculetin, respectively. The recovery values were calculated as $(Con_1 - Con_0)/Con_s$, where Con_1 was the calculated concentration of spiked samples, Con_0 was the calculated concentration of unspiked samples, and Con_s was the concentration of the target compounds added to real samples.

For all of the above samples, 2 ml of BR buffer was added and then the samples were diluted to the mark in 10.0 ml volumetric flasks with ultra-pure water. Each mixed standard sample was measured once, and each spiked and actual sample was measured three times to obtain the average value.

4 Results and discussion

4.1 Spectral characters

In EEM spectra, Raman and Rayleigh scatterings are unrelated to the chemical sample composition (Andersen and Bro, 2003), and the existence of Raman and Rayleigh scatterings may have some influence on the final analytical results. The EEM spectra of aesculin and aesculetin are presented in Figure 2; Figure 2A is with Raman and Rayleigh scatterings, and Figure 2B is without scatterings. Moreover, one can see that there is a high degree of overlap between the two signals. Therefore, it is difficult to determine the concentration of the two components by the ordinary fluorescence method. In the present study, the scatterings are first removed and then the missing data is filled by interpolation by using new data consistent with the rest of the EEM spectrum (Bahram et al., 2006). As can be seen from Figure 2B, the scatterings have been removed successfully. In order to obtain satisfactory analytical results, in the present study, three well-known chemometrics methods, namely LAR, iPLS, and N-PLS, were employed, and the results obtained are compared and discussed herein.

The EEM spectra matrices without scatterings were arranged in a three-way array with the dimensions of 41 (emission wavelength points) × 41 (excitation wavelength points) × sample numbers. To explore the main characteristics of the employed methods, the mixed standard samples were divided into calibration and prediction sets; three quarters of the samples were selected as the calibration set and used to establish the calibration model, and the remaining ones were selected as the prediction set and applied to validate the performance of the established model. For the calibration set, the matrix size was 41 × 41 × 16, and for the prediction set the matrix size was 41 × 41 × 5.

4.2 Results and discussion

A suitable method was the vital factor for model establishment. Three algorithms, namely LAR, iPLS, and N-PLS, were applied individually to build calibration models.
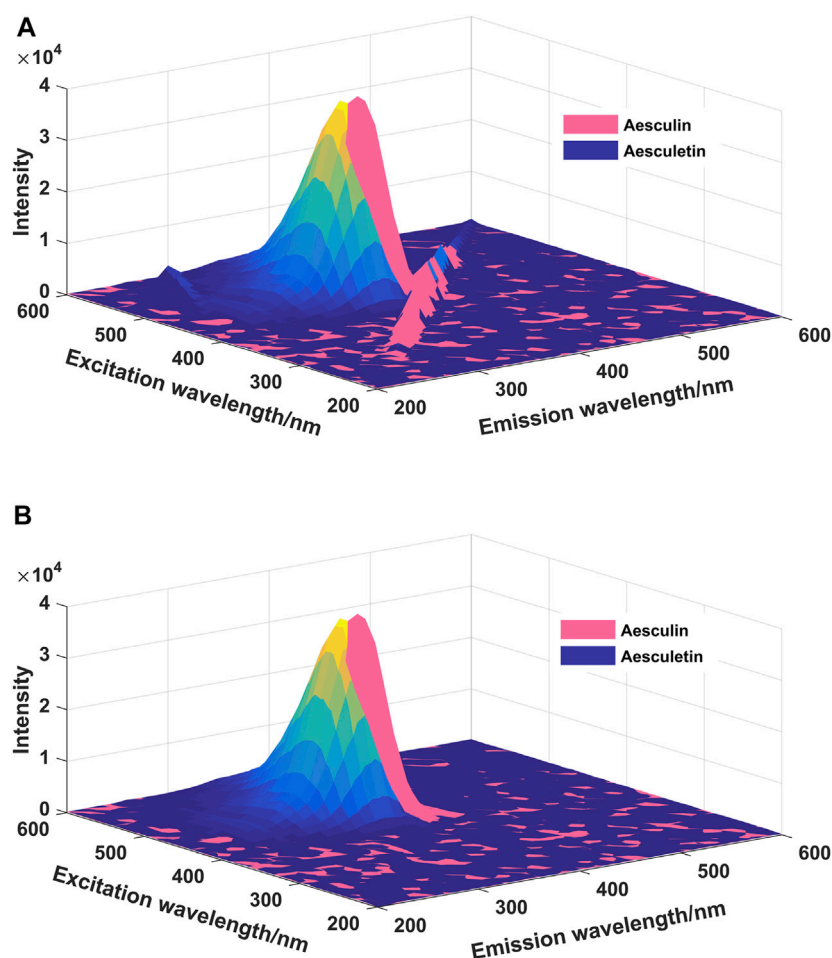
FIGURE 2
The EEM spectra of aesculin (0.16 μg/ml) and aesculetin (1 μg/ml). **(A)**: Scatterings are not eliminated; **(B)**: Scatterings are eliminated.

The performances of the established models were compared with each other by evaluation of *Rc*, *Rp*, *RMSEC*, and *RMSEP*.

4.2.1 LAR models

The first method explored was the LAR method. The existence of multicollinearity may cause the model to shift greatly and cannot simulate the overall view of data. LAR is an important machine learning technique for analyzing data that suffer from multilinearity. Before the LAR model establishment, the contour values (Li et al., 2015) of the EEM spectra of all samples were extracted for dimensionality reduction purposes. The process of extracting the contour values is equivalent to the process of extracting the emission wavelength values by fixing the excitation wavelength. A plot of the contour values of the EEM spectrum of a sample is presented in Supplementary Figure S2. After extraction of the contour values, the data matrix of the calibration set had a size of 16 (sample number) × 41 (emission wavelength points). For the prediction set, the matrix had a size

of 5 (sample number) × 41 (emission wavelength points). By application of this method, the irrelevant information variables was eliminated and a regression model was obtained for each target compound. In this case, the LAR model for each target compound was described as follows:

The LAR model for aesculin:

$$
\begin{aligned}
C_{Aesculim} = &-2.89 \times 10^{-2} + 8.10 \times 10^{-2} \times V_{200} + 3.00 \times 10^{-6} \times V_{210} - 8.00 \times 10^{-6} \times V_{220} \\
&+ 3.90 \times 10^{-5} \times V_{250} + 5.20 \times 10^{-5} \times V_{280} + 2.00 \times 10^{-6} \times V_{410} + 1.10 \times 10^{-5} \times V_{450} \\
&- 3.29 \times 10^{-4} \times V_{470} + 1.34 \times 10^{-4} \times V_{480} + 6.00 \times 10^{-6} \times V_{520} + 8.70 \times 10^{-5} \times V_{530} \\
&- 3.57 \times 10^{-4} \times V_{560} + 3.80 \times 10^{-4} \times V_{570}
\end{aligned}
$$

(3)

The LAR model for aesculetin:

$$
\begin{aligned}
C_{Aesculetin} = &-4.02 + 1.50 \times 10^{-5} \times V_{260} + 4.60 \times 10^{-5} \times V_{270} + 4.19 \times 10^{-4} \times V_{430} \\
&+ 9.29 \times 10^{-4} \times V_{490}
\end{aligned}
$$

(4)

In the above models, $C_{Aesculin}$ and $C_{Aesculetin}$ were the concentrations of aesculin and aesculetin, respectively, V_{200} was the contour value at an emission wavelength of 200 nm,
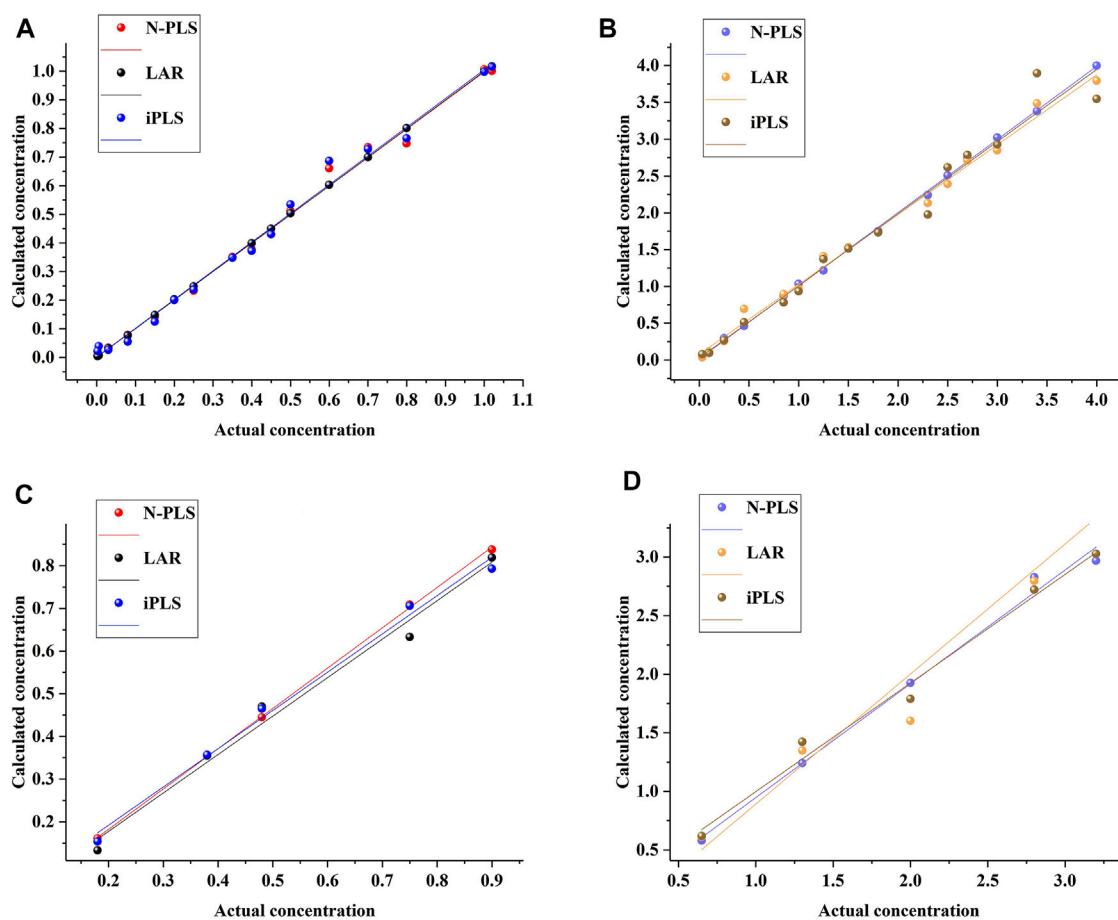
FIGURE 3
The relationship between the actual concentrations and calculated concentrations by using different methods for aesculin **(A)** and aesculetin **(B)** in the calibration set and aesculin **(C)** and aesculetin **(D)** in the prediction set.

TABLE 1 Statistical parameters related to the calibration and prediction models of aesculin and aesceletin established by different methods.

Analytical method	Analyte	Calibration set		Prediction set	
		Rc	*RMSEC*	*Rp*	*RMSEP*
LAR	Aesculin	1.0000	0.0023	0.9921	0.0680
iPLS		0.9958	0.0307	0.9962	0.0544
N-PLS		0.9972	0.0243	0.9998	0.0392
LAR	Aesculetin	0.9967	0.1174	0.9767	0.2507
iPLS		0.9875	0.1969	0.9940	0.1386
N-PLS		0.9997	0.0304	0.9962	0.1165

LAR: lasso regression.
iPLS: interval partial least squares.
N-PLS: multidimensional partial least squares.

TABLE 2 Recovery values obtained by different methods.

Samples	Analyte	Spike (µg/ml)	Recovery (%)			
			LAR	iPLS	N-PLS	UPLC
Cortex Fraxini 1	Aesculin	0.48	103.36	96.68	90.53	102.35
Cortex Fraxini 2		0.50	96.80	99.52	99.56	92.14
Cortex Fraxini 3		0.48	102.13	100.17	99.95	81.96
Cortex Fraxini 4		0.48	80.04	82.36	88.16	96.96
Cortex Fraxini 5		0.25	99.57	105.45	103.99	86.43
Cortex Fraxini 6		0.40	89.12	90.60	87.22	89.42
Cortex Fraxini 1	Aesculetin	2.00	89.35	87.9	90.25	86.59
Cortex Fraxini 2		2.30	93.74	84.57	89.84	99.55
Cortex Fraxini 3		2.00	103.47	92.13	83.32	95.31
Cortex Fraxini 4		2.00	76.65	74.88	104.62	89.14
Cortex Fraxini 5		1.00	106.03	99.87	92.55	84.88
Cortex Fraxini 6		1.50	95.32	91.53	101.53	89.62

and the remaining parameters followed the same pattern in their definitions.

To assess the prediction ability of the established models, they were estimated by prediction sets; the statistical results are shown in Table 1. As can be seen, the values of R_c were 1.0000 and 0.9967 and of $RMSEC$ were 0.0023 and 0.1174 for aesculin and aesculetin, respectively, demonstrating that the established models have good linearity and can be applied to the prediction set. For prediction purposes, R_p values of 0.9921 and 0.9767 (Figure 3) and $RMSEP$ values of 0.0680 and 0.2507 were obtained for aesculin and aesculetin, respectively.

In addition, as can be seen from Table 2, the recovery values were in the range of 80.04%–103.36%, and 76.65%–106.03% for aesculin and aesculetin, respectively. One can conclude that not all recovery results were satisfactory, such as the recovery of aesculetin (76.65%) obtained from Cortex Fraxini 4. We suspect the possible reason is that the unknown interference and useless information in the spectra has an impact on the final analysis results. Therefore, as described in the following section, a method that can be used to extract characteristic variables to improve the accuracy of the analytical results was explored.

4.2.2 iPLS models

The iPLS method can be used to extract the characteristic intervals from the given spectral data to obtain more accurate analytical results. In the present study, the iPLS method was also performed on the contour values, and 8 intervals were determined for further analysis. Then, one optimum interval and corresponding PLS component was determined according to the minimum $RMSECV$ value. In the present study, the interval

in the emission wavelength range of 310–350 nm is determined for both aesculin and aesculetin, and the optimization numbers of the PLS component are 2 and 1, respectively. The corresponding statistical parameters of the established iPLS models are summarized in Table 1.

As can be seen from Table 1, the iPLS models have higher R_p values and lower $RMSEP$ values than that of LAR models, demonstrating that the iPLS method has good feature extraction ability and can be applied to improve the accuracy of the established models.

After model evaluation, the recovery values were also calculated; as can be seen from Table 2, the recovery values were in the range of 82.36%–105.45%, and 74.88%–99.87% for aesculin and aesculetin, respectively. The same phenomenon occurred as with the LAR method in that the recovery of aesculetin (74.88%) in Cortex Fraxini 4 was not satisfactory. From this perspective, we suspect that one possible reason was that some important information from the contour values might be lost, so a high-order chemometrics method was considered to deal with the EEM spectral data.

4.2.3 N-PLS models

The calibration set with the size of $41 \times 41 \times 16$ was applied to establish the calibration model, and the performance of the established models was evaluated by using the prediction set. In the process of establishing the N-PLS models, the optimal number of LVs should first be determined. In the present study, the optimum number of LVs for the N-PLS models was indicated by the minimum $PRESS$ value versus the number of LVs (Supplementary Figure S1). For aesculin (Supplementary Figure S1A), the minimum $PRESS$ value can be determined

TABLE 3 Analytical results related to the calibration and prediction results for aesculin and aesculetin based on the UPLC method.

Analyte	Calibration set			Prediction set	
	R_c	RMSEC	Equation	R_p	RMSEP
Aesculin	0.9923	0.0274	$y = 36228x-797.31$	0.9957	0.0816
Aesculetin	0.9858	0.1414	$y = 53779x-6536.4$	0.9965	0.0222

y: peak area.

x: concentration (μg/ml).

with 2 LVs, and for aesculetin (Supplementary Figure S1B), the local minimum *PRESS* value can be determined with 5 LVs. The statistical parameters of the N-PLS models are summarized in Table 1.

As can be seen from Table 1, the results from the calibration set show that the N-PLS method yielded satisfactory *Rc* values of 0.9972 and 0.9997 and *RMSEC* values of 0.0243 and 0.0304 for aesculin and aesculetin, respectively, demonstrating that the established models have the ability to accurately calculate the prediction set. The established models were then applied to the prediction set, and values were obtained for *Rp* of 0.9998 and 0.9962, and *RMSEP* of 0.0392 and 0.1165 for aesculin and aesculetin, respectively, which proved that good predictions were obtained.

Next, the spike recovery experiment was performed. As can be seen from Table 2, the recovery values were in the range of 87.22%–103.99% for aesculin, and 83.32%–104.62% for aesculetin. Compared with the results of the previous LAR and iPLS methods, the linearity, predictive ability, and accuracy of the N-PLS models were improved. However, owing to the same phenomenon that occurred with the LAR and iPLS methods, the recovery values of aesculetin in Cortex Fraxini 4 were nearly the same and not satisfactory, so we decided that it was necessary to further verify which method gives the most reliable recovery values.

4.3 UPLC method for validation

A UPLC method was developed to further confirm the accuracy and reliability of the presented strategies. The two analytes and the backgrounds can be separated properly and completely under the chromatographic conditions mentioned above, and thus they can be quantified accurately based on peak areas. The chromatograms of aesculin, aesculetin, and a Cortex Fraxini sample are shown in Supplementary Figure S3. For a comprehensive comparison, the concentrations of aesculin and aesculetin used for UPLC and fluorescence were the same. In the measurement process, the samples with lower concentrations were not detected (Supplementary Tables S1, S2); thus, the calibration

equations of aesculin and aesculetin were established from samples 1 to 14 in the calibration set. The statistical parameters of the calibration equations are summarized in Table 3; the low *RMSEC* and *RMSEP* values and high *R_c* and *R_p* values illustrate the accuracy of the UPLC method. The recoveries of aesculin and aesculetin by UPLC are shown in Table 2. First, we can see that the recovery rates of aesculin (81.96%–102.35%) and aesculetin (84.88%–99.55%) were satisfactory. One can then conclude that the accuracy of the UPLC and N-PLS methods is comparable. The separation of complex samples with UPLC requires some effort to find suitable conditions. A comparison of the comprehensive results of the N-PLS and UPLC methods shows that EEM fluorescence coupled with the chemometrics method can be regarded as a reliable and accurate approach to determine the two components in Cortex Fraxini samples simultaneously.

4.4 Further discussion

The above comparisons show that the analytical results of the N-PLS method on the EEM spectra are more accurate and reliable than the LAR and iPLS methods on the contour values. The reason may be that the higher-order N-PLS algorithm is less disturbed by the noise of the analysis system, so the quantitative analysis results obtained are more accurate (Pierce et al., 2011). Although the LAR and iPLS methods have not yielded satisfactory results, these strategies still have application values in proper analytical systems.

5 Conclusion

The present study reported a comparative study of three different algorithm (LAR, iPLS, and N-PLS) methods in combination with EEM spectroscopy for the determination of aesculin and aesculetin in traditional Chinese medicine. Satisfactory results were obtained with the N-PLS method on the basis of the EEM spectra despite the strong overlaps of the two analytes. The results presented herein show that the methodology proposed has the advantages of being simple, sensitive, and low cost. Consequently, EEM with the aid of proper chemometrics methods is a useful tool in processing the serious problem of overlapping and can be extended to other complex systems in the fields of food and the environment, such as body fluids.

Data availability statement

The original contributions presented in the study are included in the article/Supplementary Materials; further inquiries can be directed to the corresponding author.

Author contributions

Z-Y L: Investigation, visualization, writing-original draft, writing-review and editing; X-K L: Investigation, visualization; YL: Visualization; NF: Supervision, review and editing, funding acquisition; X-Z Z: Supervision, review and editing, funding acquisition; Q-L L: Visualization; B-Q L: Investigation, resources, supervision, review and editing, funding acquisition, project administration.

Acknowledgments

Conflict of interest

The authors declare that the research was conducted in the absence of any commercial or financial relationships that could be construed as a potential conflict of interest.

Publisher's note

All claims expressed in this article are solely those of the authors and do not necessarily represent those of their affiliated organizations, or those of the publisher, the editors, and the reviewers. Any product that may be evaluated in this article, or claim that may be made by its manufacturer, is not guaranteed or endorsed by the publisher.

Supplementary material

The Supplementary Material for this article can be found online at: https://www.frontiersin.org/articles/10.3389/fchem.2022.984010/full#supplementary-material

References

Abreu, R. E. L., Paz, J. E. M., Silva, A. C., Pontes, M. J. C., and Lemos, S. G. (2015). Ethanol fuel adulteration with methanol assessed by cyclic voltammetry and multivariate calibration. *Fuel* 156, 20–25. doi:10.1016/j.fuel.2015.04.024

Andersen, C. M., and Bro, R. (2003). Practical aspects of PARAFAC modeling of fluorescence excitation-emission data. *J. Chemom.* 17 (4), 200–215. doi:10.1002/cem.790

Bahram, M., Bro, R., Stedmon, C., and Afkhami, A. (2006). Handling of Rayleigh and Raman scatter for PARAFAC modeling of fluorescence data using interpolation. *J. Chemom.* 20 (3-4), 99–105. doi:10.1002/cem.978

Bai, X. M., Liu, T., Liu, D. L., and Wei, Y. J. (2018). Simultaneous determination of alpha-asarone and beta-asarone in Acorus tatarinowii using excitation-emission matrix fluorescence coupled with chemometrics methods. *Spectrochimica Acta Part A Mol. Biomol. Spectrosc.* 191, 195–202. doi:10.1016/j.saa.2017.10.011

Bro, R. (1996). Multiway calibration. Multilinear PLS. *J. Chemom.* 10, 47–61. doi:10.1002/(sici)1099-128x(199601)10:1<47::aid-cem400>3.0.co;2-c

Gao, W., Shu, T., Guan, Y., Ling, S., Liu, S., and Zhou, L. (2022). Novel strategy for establishment of an FT-Raman spectroscopy based quantitative model for poplar holocellulose content determination. *Carbohydr. Polym.* 277, 118793. doi:10.1016/j.carbpol.2021.118793

Khajehsharifi, H., and Eskandari, Z. (2011). Potentiality of partial least-squares multivariate calibration in the spectrophotometric analysis of binary mixtures of purine bases. *Monatsh. Chem.* 142 (8), 773–778. doi:10.1007/s00706-011-0513-7

Li, B. Q., Chen, J., Li, J. J., Wang, X., Zhai, H. L., and Zhang, X. Y. (2015). High-performance liquid chromatography with photodiode array detection and chemometrics method for the analysis of multiple components in the traditional Chinese medicine Shuanghuanglian oral liquid. *J. Sep. Sci.* 38 (24), 4187–4195. doi:10.1002/jssc.201500712

Li, C., Chen, A., Chen, X., Ma, X., Chen, X., and Hu, Z. (2005). Non-aqueous capillary electrophoresis for separation and simultaneous determination of fraxin, esculin and esculetin in Cortex fraxini and its medicinal preparations. *Biomed. Chromatogr.* 19 (9), 696–702. doi:10.1002/bmc.497

Li, M.-X., Li, Y.-Z., Chen, Y., Wang, T., Yang, J., Fu, H.-Y., et al. (2021). Excitation-emission matrix fluorescence spectroscopy combined with chemometrics methods for rapid identification and quantification of adulteration in Atractylodes macrocephala Koidz. *Microchem. J.* 171, 106884. doi:10.1016/j.microc.2021.106884

Li, Y., Guo, H., Wu, Y., Geng, Q., Dong, D., Wu, H., et al. (2013). A sensitive and selective method for determination of aesculin in Cortex fraxini by liquid chromatography quadrupole time-of-flight tandem mass spectrometry and application in pharmacokinetic study. *J. Anal. Methods Chem.* 2013, 1–6. doi:10.1155/2013/432465

Liu, T., Li, X. G., Wang, J. Y., Liu, D. L., and Wei, Y. J. (2019). Time-resolved fluorescence and chemometrics-assisted excitation-emission fluorescence for qualitative and quantitative analysis of scopoletin and scopolin in Erycibe obtusifolia Benth. *Spectrochimica Acta Part A Mol. Biomol. Spectrosc.* 219, 96–103. doi:10.1016/j.saa.2019.04.019

Lopez-Fornieles, E., Brunel, G., Rancon, F., Gaci, B., Metz, M., Devaux, N., et al. (2022). Potential of multiway PLS (N-PLS) regression method to analyse time-series of multispectral images: A case study in agriculture. *Remote Sens.* 14 (1), 216. doi:10.3390/rs14010216

Luo, L., Bao, S., Mao, J., and Tang, D. (2016). Quality prediction and quality-relevant monitoring with multilinear PLS for batch processes. *Chemom. Intell. Lab. Syst.* 150, 9–22. doi:10.1016/j.chemolab.2015.11.004

Pierce, K. M., Schale, S. P., Le, T., and Larson, J. C. (2011). An advanced analytical Chemistry experiment using gas ChromatographyMass spectrometry, MATLAB, and chemometrics to predict biodiesel blend percent composition. *J. Chem. Educ.* 88, 806–810. doi:10.1021/ed100917x

Preeti Chandra, R. K., Saxena, A., Srivastava, M., Bahadur, L., Pal, M., Pratap Singh, B., et al. (2016). Quantitative determination of multi markers in five varieties of Withania somnifera using ultra-high performance liquid chromatography with hybrid triple quadrupole linear ion trap mass spectrometer combined with multivariate analysis: Application to pharmaceutical dosage forms. *J. Pharm. Biomed. Anal.* 129 (10), 419–426. doi:10.1016/j.jpba.2016.07.032

Sheng, K., Li, L., Zhang, Q., and Wang, Y. (2020). A highly sensitive sensor based on electropolymerization for electrochemical detection of esculetin. *Microchem. J.* 159, 105368. doi:10.1016/j.microc.2020.105368

Thomas, E. V. (2003). Non-parametric statistical methods for multivariate calibration model selection and comparison. *J. Chemom.* 17 (12), 653–659. doi:10.1002/cem.833

Tkachenko, S. N., Tkachenko, I. A., Shpilevaya, S. G., and Dedkov, V. P. (2021). Modelling the production process of Roman snail using RIDGE and LASSO regression. *J. Phys. Conf. Ser.* 1902, 012134. doi:10.1088/1742-6596/1902/1/012134

Wang, L., Wu, H. L., Yin, X. L., Hu, Y., Gu, H. W., and Yu, R. Q. (2017). Simultaneous determination of umbelliferone and scopoletin in Tibetan medicine Saussurea laniceps and traditional Chinese medicine Radix angelicae pubescentis using excitation-emission matrix fluorescence coupled with second-order

calibration method. *Spectrochimica Acta Part A Mol. Biomol. Spectrosc.* 170, 104–110. doi:10.1016/j.saa.2016.07.018

Wang, Y., Han, F., Song, A., Wang, M., Zhao, M., and Zhao, C. (2016b). Rapid characterization of the chemical constituents of Cortex Fraxini by homogenate extraction followed by UHPLC coupled with Fourier transform ion cyclotron resonance mass spectrometry and GC-MS. *J. Sep. Sci.* 39 (22), 4325–4334. doi:10.1002/jssc.201600851

Wang, Y., Xu, Q., Shen, Z., Wang, Y., Dong, L., Fu, S., et al. (2019). Simultaneous determination of eight active compounds in baitouweng decotion and its single herbs. *J. Chromatogr. Sci.* 57 (6), 502–510. doi:10.1093/chromsci/bmz022

Wang, Y., Zhao, M., Xin, Y., Liu, J., Wang, M., and Zhao, C. (2016a). ^{1}H NMR and MS based metabolomics study of the therapeutic effect of Cortex Fraxini on hyperuricemic rats. *J. Ethnopharmacol.* 185, 272–281. doi:10.1016/j.jep.2016.03.043

Wu, X., Yang, Z., Ji, G., Chen, X., and Yuan, M. (2015). Using consensus interval partial least square in near infrared spectra analysis. *Chemom. Intell. Lab. Syst.* 144 (15), 56–62. doi:10.1016/j.chemolab.2015.03.008

Yang, R., Dong, G., Sun, X., Yang, Y., Yu, Y., Liu, H., et al. (2018). Feasibility of the simultaneous determination of polycyclic aromatic hydrocarbons based on two-dimensional fluorescence correlation spectroscopy. *Spectrochimica Acta Part A Mol. Biomol. Spectrosc.* 190, 342–346. doi:10.1016/j.saa.2017.09.061

Yang, X., and Wen, W. (2018). Ridge and lasso regression models for cross-version defect prediction. *IEEE Trans. Reliab.* 67, 885–896. doi:10.1109/tr.2018.2847353

Zhang, L.-p., Li, Z.-y., Geng, X., Zhang, Y.-f., Tie, D., Chen, X., et al. (2021). Analysis of Chinese herbal compound preparations by ballpoint connector supported solvent microextraction and high-performance liquid chromatography with ultraviolet detection. *Instrum. Sci. Technol.* 50 (1), 69–82. doi:10.1080/10739149.2021.1955708

Zhou, Y., Zhang, X., Li, C., Yuan, X., Han, L., Li, Z., et al. (2018). Research on the pharmacodynamics and mechanism of Fraxini Cortex on hyperuricemia based on the regulation of URAT1 and GLUT9. *Biomed. Pharmacother.* 106, 434–442. doi:10.1016/j.biopha.2018.06.163

frontiers | Frontiers in Chemistry

Green synthesis, crystal structure, and antifungal activities of (*E*)-4-arylidene-5-oxotetrahydrofuran

Yun Dong[1,2†], Ling-Qi Kong[1,2†], Qin-Hua Chen[3], Bin Li[1],
Xiao-Hua Zeng[1,2]*, Li-Na Ke[1,2]* and Hong-Mei Wang[1,2]*

[1]Sinopharm Dongfeng General Hospital, Hubei University of Medicine, Shiyan, China, [2]Hubei Key
Laboratory of Wudang Local Chinese Medicine Research, School of Pharmaceutical Sciences, Hubei
University of Medicine, Shiyan, China, [3]Shenzhen Baoan Authentic TCM Therapy Hospital, Shenzhen,
China

A series of γ-lactone derivatives (*E*)-4-arylidene-5-oxotetrahydrofuran
derivatives were synthesized *via* a tandem Passerini 3CC/S_N cyclization
microwave-assisted one-pot method efficiently starting from Baylis Hillman
acids, aryl glyoxals and isocyanides, and using ionic liquid as reaction medium.
The products were characterized by hydrogen nuclear magnetic resonance
spectroscopy (^{1}H-NMR), carbon nuclear magnetic resonance spectroscopy
(^{13}C-NMR). Single crystal X-ray analysis of the compound RPDFB clearly
confirmed its assigned chemical structures. Meanwhile, the effects of four
compounds (RPDFB, RPDFC, RPDFI, RPDFJ) on the growth inhibition activity
of *Gibberella zeae* were detected, and found that the compound RPDFB has
significant growth inhibition activity to *Gibberella zeae*.

1 Introduction

The synthesis of heterocyclic compounds plays an important role in organic synthesis, because heterocyclic compounds have a large number and are widely used in pesticide, medicine and industry (El-Sayed and Althagafi, 2016). Among heterocyclic compounds, especially those containing pyrrole ring, pyridine ring, furan ring and β-lactam ring have attracted the attention of organic synthesis scientists because of their high efficiency, low toxicity and broad spectrum of physiological activities (Butin et al., 2010; Hafez and El-Gazzar, 2020; Shiri, 2021; Zhang et al., 2022). At present, numerous anti-inflammatory, antitumor, antiviral, antibacterial, insecticide, and herbicide containing these heterocyclic rings have been developed by synthetic methods (Burriss et al., 2018; Bari et al., 2019; Jiang et al., 2021; Manaithiya et al., 2021). Therefore, the structural modification and synthesis method optimization of heterocyclic compounds are very important for more efficient and green synthesis of new agents.
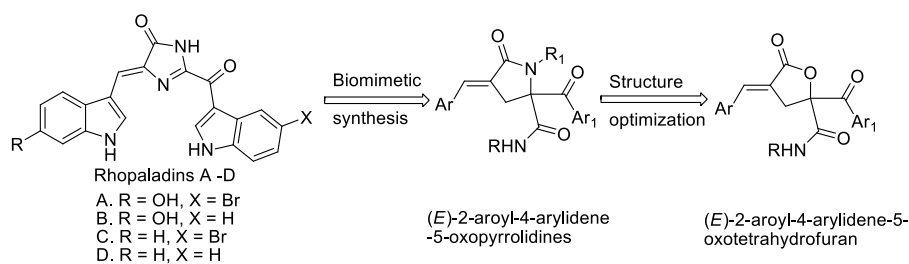
SCHEME 1
The strategy for the choice of (E)-2-arylidene-4-arylidene-5-oxotetrahydrofurans as targets.

The development prospect of pharmaceutical and pesticide products is to synthesize agents which are environmentally friendly, safe and harmless to human beings, with high selectivity and ultra-low dosage by using green synthesis process (Sharma et al., 2020; Zhang et al., 2020). Therefore, green synthesis method will also be a mandatory requirement of green pesticides. Following this concept, we applied the efficient multi-component tandem one-pot method to synthesize heterocyclic compounds with potential biological activity, such as pyrrole, pyridine, furan, and β-lactam.

Studies have shown that rhopaladins A-D alkaloids (Janosik et al., 2002; Méndez et al., 2018) (Scheme 1) present in marine cysts have significantly biological activities. We have previously synthesized several different series of rhopaladins' analogs, such as (E)-2-aroyl-4-arylidene-5-oxopyrrolidines (Scheme 1), and (2E, 4E)-2-styryl-4-arylidene-5-oxopyrrolidines, *via* multi-component one-pot method starting from Baylis-Hillman acid, and found that these compounds showed good anti-proliferation and apoptosis-inducing effects on cervical cancer cells and liver cancer cells, respectively (Zeng et al., 2013; Zhu et al., 2020; Wang et al., 2021; Wang et al., 2021; Kong et al., 2021; Zhu et al., 2022). Baylis Hillman (B-H) reaction is a coupling reaction between active alkenes and electrophiles under catalyst, which can be used to synthesize compounds with polyfunctional groups under mild reaction conditions (Huang and Cui, 2018). Moreover, B-H reaction is also an important synthetic transition reaction in the formation of carbon-carbon bond, which can provide highly substituted allyl alcohol and amine in one step reaction (Nelson et al., 2018). γ-Lactone is a common chemical skeleton in many synthetic and natural products, mainly composed of five-member lactone heterocycles, which possess many biological properties and are key intermediates in the synthesis of major antiviral and anticancer nucleoside analogs (Julien et al., 2018). Therefore, by combining Passerini reaction with Baylis Hillman reaction, γ-lactone derivatives of (E)-4-arylidene-5-oxotetrahydrofuran derivatives (RPDF serial chemicals, which are other analogs of rhopaladins, Scheme 1) were synthesized *via* a tandem Passerini 3CC/S_N cyclization one pot method (Wang et al., 2021).

Herein, we optimized the synthesis method, using ionic liquid as a green medium and microwave radiation as a heating method to synthesize (E)-N-tert-butyl-4-(4-chlorobenzylidene)-2-(4-nitrobenzoyl)-5-oxotetrahydrofuran-2-carboxamide (RPDFB) and other three new compounds (RPDFC, RPDFI, RPDFJ). Next, the single crystal of RPDFB was cultured and analyzed. Meanwhile, the effects of the four compounds (RPDFB, RPDFC, RPDFI, RPDFJ) on the growth inhibition activity of *Gibberella zeae* were detected.

2 Results and discussion

2.1 Chemistry

The realization of environmentally friendly organic synthesis has become an important topic of organic synthesis. Such as solvent-free reaction, or reaction with water as the medium and using room temperature ionic liquid as the reaction solvent (Welton, 1999). Ionic liquid has the advantages of low vapor pressure, non-flammable, good thermal stability, recyclable, compared with other organic solvents (Sowmiah et al., 2009; Çınar et al., 2016; Bystrzanowska et al., 2019). On the other hand, assisted by microwave radiation, the rate of organic reaction is also greatly improved, and simple operation, high yield, simple post-treatment characteristics (Santagada et al., 2009; Sharma et al., 2012). Meanwhile, study has shown that ionic liquid [BMIM][PF_6] has a good role in the one-pot synthesis of tetrahydropyran ring in series Barbier-Prins reaction (Batista et al., 2019). Therefore, we tried to synthesize RPDFB RPDFC, RPDFI, RPDFJ in ionic liquid [BMIM][PF_6] and microwave-assisted as the continuation of previous research.

The results showed that using Baylis-Hillmanic acid 1, aryl glyoxals 2, and isocyanide 3 as starting materials and ionic liquid [BMIM][PF_6] as reaction medium, a series of γ-lactone derivatives (E)-2-aroyl-4-arylidene-5-oxotetrahydrofuran derivatives (see Scheme 2) were synthesized via a tandem Passerini $3CC/S_N$ cyclization microwave-assisted one-pot method efficiently, which provided a new green synthesis
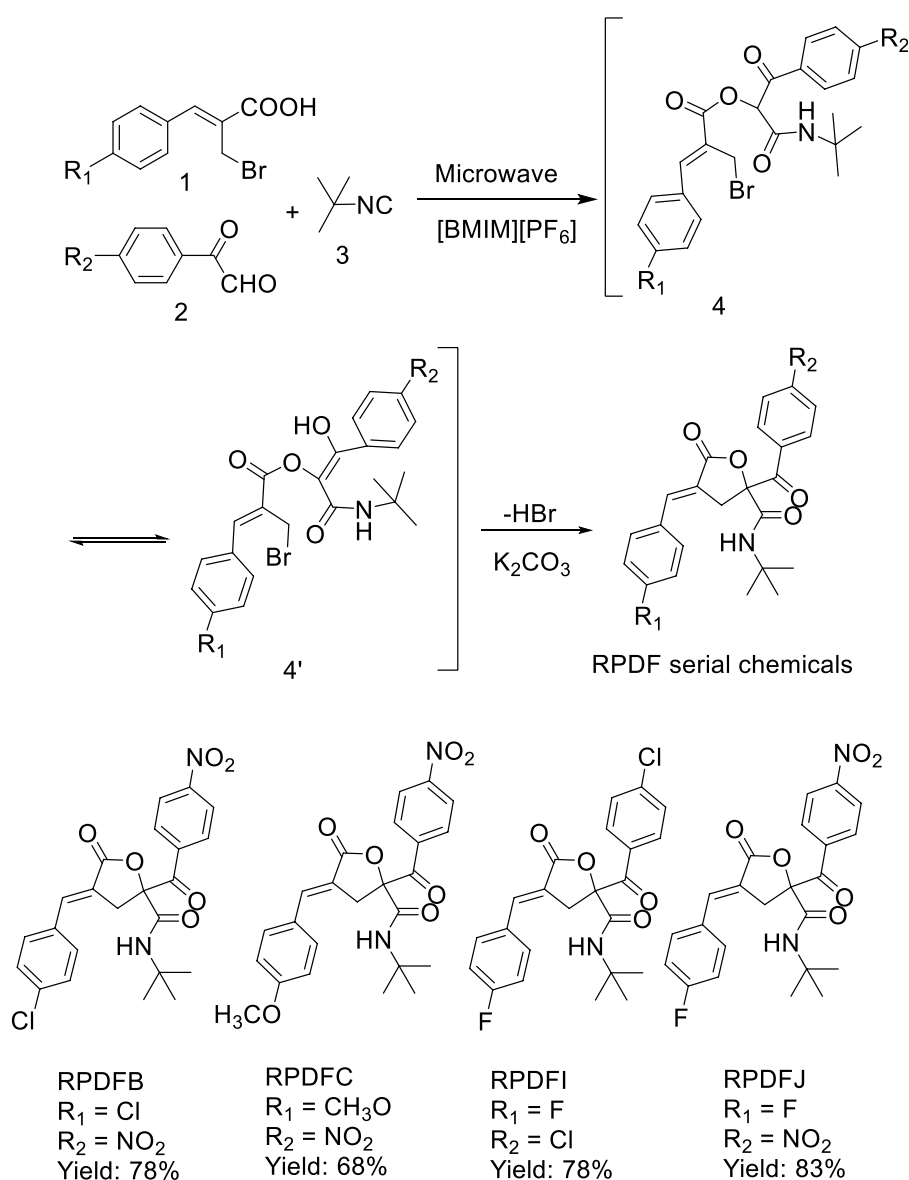
SCHEME 2
Synthesis of (*E*)-2-aroyl-4-arylidene-5-oxotetrahydrofuran derivatives.

strategy for the synthesis of (*E*)-4-arylidene-5-oxotetrahydrofuran derivatives.

2.2 Crystal structure description of (E)-N-tert-butyl-4-(4-chlorobenzylidene)-2-(4-nitrobenzoyl)-5-oxotetrahydrofuran-2-carboxamide (RPDFB)

In order to determine the structure of RPDFB, the single crystal of compound RPDFB was cultured. The crystal belongs to triclinic system and the space group were P-1, a = 8.155 (3)Å, b = 9.732 (3)Å, c = 14.809 (5)Å, α = 97.446 (5)°, β = 98.874 (5)°, γ = 101.753 (5)°, V = 1,121.1 (6)Å^3, Z = 2, Dc = 1.353 Mg/m^3, μ(MoKa) = 0.212 mm^{-1}, F (000) = 476. The crystal structure was solved by the direct method (SHELXL-97), and all the non hydrogen atoms were obtained by multi round Fourier synthesis. The hydrogen atoms were acquired by direct hydrogenation after theoretical calculation. The coordinates of all non hydrogen atoms and heterogeneous thermal parameters were corrected to convergence by the full matrix least square method. The final deviation factor was R = 0.0298, wR = 0.1444. On the final difference Fourier diagram, the
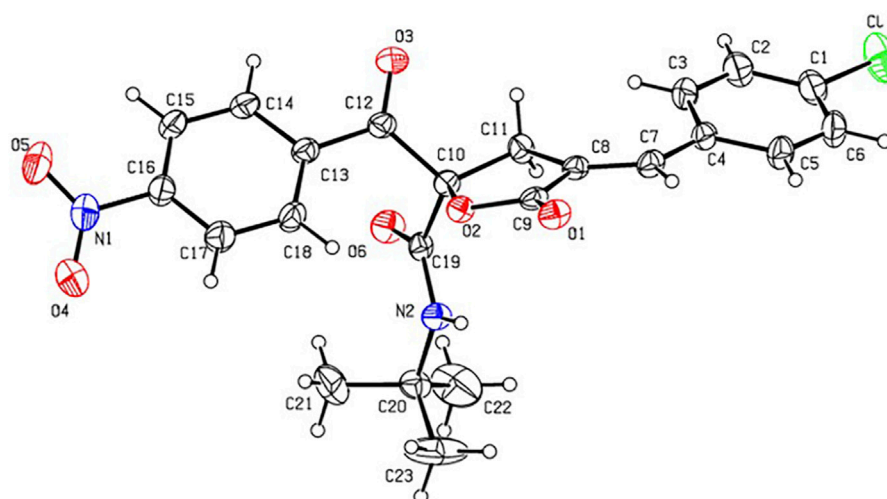
FIGURE 1
Crystal structure diagram of compound RPDFB (CCDC 2179210). Note: black, carbon; white, hydrogen; red, oxygen; purple, nitrogen; green, chlorine.

heights of the maximum and minimum electron density peaks were 0.392, −0.392 e/Å^3, respectively. The single crystal diffraction pattern and the crystal packing pattern of compound RPDFB were showed in Figure 1 and Figure 2, respectively.

2.3 Antifungal effect of (E)-2-aroyl-4-arylidene-5-oxotetrahydrofuran derivatives RPDFB, RPDFC, RPDFI, RPDFJ

The growth inhibition activity of the target compounds RPDFB, RPDFC, RPDFI, RPDFJ against *Gibberella zeae* were tested by toxic medium method. The results (Figure 3) showed that at the concentration of 50 μg/ml, the four compounds showed certain inhibitory effects on *Gibberella zeae*, but the inhibitory activities were significantly different. Among them, the inhibition rate of RPDFB was as high as 98%, while the inhibitory effect of other compounds was close to 50%. Under the same control conditions, the growth inhibition rate of diniconazole on *Gibberella zeae* was 96%.

Then, the compound RPDFB with better inhibitory activity was selected for concentration gradient control experiment with diniconazole. The results (Figure 4) showed that when the concentration of diniconazole was 30 μg/ml, the growth inhibition rate was as high as 96%, and with the increase of the concentration, the inhibition rate was almost unchanged, even if the concentration decreased to 15 μg/ml, the growth inhibition rate was still up to 90%. When the concentration of RPDFB was 50 μg/ml, the inhibition rate was higher than that of diniconazole. However, when the concentration decreased, the inhibition rate decreased to 58% at 40 μg/ml, and the inhibition activity was not obvious at 30 μg/ml. Our results showed that the

compound RPDFB showed a good inhibitory effect on *Gibberella zeae* at 50 μg/ml, and its inhibitory effect was better than that of diniconazole with the concentration more than 50 μg/ml, which is worth further exploration.

3 Materials and methods

3.1 General information

The melting point was measured by X-4 melting point instrument (uncorrected thermometer) produced by Beijing Rayleigh Analytical Instrument Company. MS was determined by Finnigan-trace-MS analyzer (direct injection method). Elemental analysis was performed by vario-EL-III analyzer. ^{1}H NMR and ^{13}C NMR were determined by a 600 MHz high resolution nuclear magnetic resonance spectrometer (Varian-Mercury-Plus 600) or 150 MHz high resolution nuclear magnetic resonance spectrometer (Varian-Mercury-Plus 150). The solvent was deuterium chloroform (CDCl$_3$) with TMS internal standard. Single crystal diffraction was determined by Bruker-Smart-AXS-CCD X-ray single crystal diffractometer. The reagent used is sinopharm group (or imported) analytical pure.

3.2 One-pot synthesis of (E)-2-aroyl-4-arylidene-5-oxotetrahydrofuran derivatives RPDFB, RPDFC, RPDFI, RPDFJ

Dry Baylis-Hillmanic acid (1 mmol) and 2 ml [BMIM][PF$_6$] were added to a 25 ml round-bottom flask. After stirring, aryl
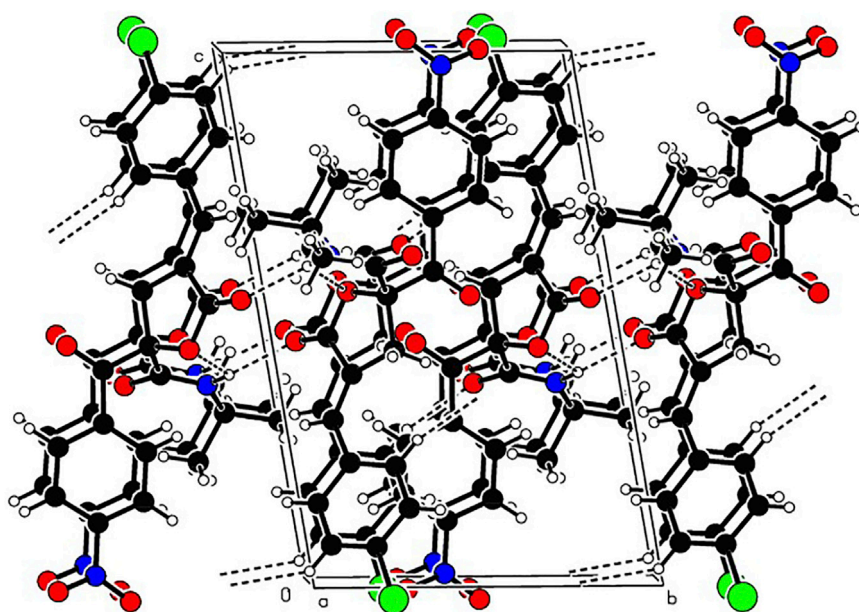
FIGURE 2
Packing of the crystal structure of compound RPDFB. Note: black, carbon; white, hydrogen; red, oxygen; purple, nitrogen; green, chlorine.

glyoxals (1 mmol) and isocyanide (1 mmol) were added successively. After shaking, the flask was placed into a microwave reactor with a power of 300 w. Magnetic stirring and interval heating, heating every 8 s, stop 8 s. Repeat several times, and the reaction time is 16 min. Then 2 ml K_2CO_3 (0.5 mmol) aqueous solution was divided into 10 parts, and the pH value of the system was adjusted 10 times. Each reaction time is 96 s (heating for 8 s, stopping for 8 s, a total of 6 times). After the reaction was complete (TLC detection), the mixture was chilled overnight and the precipitate was filtered, washed by water, recrystallized from ethanol, then (E)-4-arylidene-5-oxotetrahydrofuran derivatives (RPDF serial chemicals) was obtained.

3.2.1 (*E*)-*N*-*tert*-butyl-4-(4-chlorobenzylidene)-2-(4-nitrobenzoyl)-5-oxotetrahydrofuran-2-carboxamide (RPDFB) (Wang et al., 2021)

White crystals (0.35 g, yield 78%), mp 143–144°C; ^{1}H NMR (CDCl$_3$, 600 MHz) δ (ppm) 8.31 (d, J = 8.4 Hz, 2H, Ar-H), 8.22 (d, J = 7.8 Hz, 2H, Ar-H), 7.58–7.46 ((m, 5H, Ar-H and = CH), 6.55 (s, 1H, NH), 4.40 (d, J = 18.6 Hz, 1H, CH$_2^a$), 3.40 (d, J = 18.0 Hz, 1H, CH$_2^b$), 1.36 (s, 9H, 3CH$_3$); ^{13}C NMR (CDCl$_3$, 150 MHz) δ (ppm) 189.2, 169.0, 167.0, 150.5, 138.7, 138.2, 137.1, 132.0, 131.7, 130.6, 129.4,123.6, 120.5, 85.7, 52.6, 29.0, 28.4. MS (*m/z*, %) 456 (M$^+$, 4), 356 (66), 306 (95), 250 (100), 150 (66), 57 (74). Anal. Calcd for C$_{23}$H$_{21}$ClN$_2$O$_6$: C, 60.46; H, 4.63; N, 6.13. Found: C, 60.21; H, 4.68; N, 6.19.
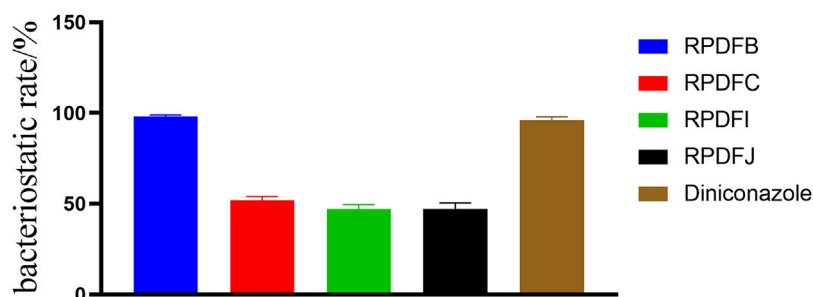
FIGURE 3
Antifungal activity of (E)-2-aroyl-4-arylidene-5-oxotetrahydrofuran derivatives, against-*Gibberella zeae*.
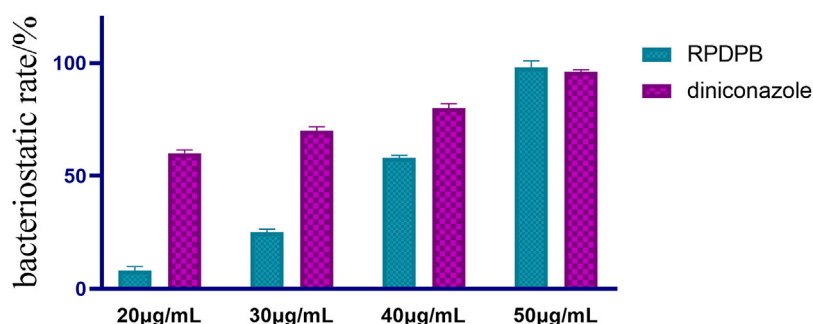
FIGURE 4
Comparison of inhibitory activities of RPDFB and diniconazole against-*Gibberella zeae*.

3.2.2 (*E*)-*N*-*tert*-butyl-4-(4-methoxybenzylidene)-2-(4-nitrobenzoyl)-5-oxotetrahydrofuran-2-carboxamide (RPDFC)

White crystals (0.30 g, yield 68%), mp 222–223°C; ^{1}H NMR (CDCl$_3$, 600 MHz) δ (ppm) 8.30 (d, J = 8.4 Hz, 2H, Ar-H), 8.23 (d, J = 9.0 Hz, 2H, Ar-H), 7.57 (s, 1H, =CH), 7.52 (d, J = 8.4 Hz, 2H, Ar-H),6.99 (d, J = 8.4 Hz, 2H, Ar-H), 6.64 (s, 1H, NH), 4.41 (d, J = 18.0 Hz, 1H, CH$_2$[a]), 3.88 (s, 3H, CH$_3$),3.33 (d, J = 18.0 Hz, 1H, CH$_2$[b]), 1.36 (s, 9H, 3CH$_3$); ^{13}C NMR (CDCl$_3$, 150 MHz) δ (ppm) 189.4, 169.7,167.3, 161.7, 150.4, 140.0, 138.4, 132.5, 132.5, 131.3, 123.5, 116.7, 114.5, 85.7, 55.6, 52.4, 33.7, 28.4. MS (*m/z*, %) 452 (M[+], 4), 352 (24), 302 (100), 246 (86), 150 (25), 57 (23). Anal. Calcd for C$_{24}$H$_{24}$N$_2$O$_7$:C, 63.71; H, 5.35; N, 6.19. Found: C, 63.94; H, 5.38; N, 6.04.

3.2.3 (*E*)-*N*-*tert*-butyl-2-(4-chlorobenzoyl)-4-(4-fluorobenzylidene)-5-oxotetrahydrofuran-2-carboxamide (RPDFI)

White crystals (0.33 g, yield 78%), mp 180–181°C; ^{1}H NMR (CDCl$_3$, 600 MHz) δ (ppm) 8.04 (d, J = 8.4 Hz, 2H, Ar-H), 7.53–7.12 (m, 7H, Ar-H and = CH), 6.69 (s, 1H, NH), 4.39 (d, J = 18.0 Hz, 1H, CH$_2$[a]), 3.37 (d, J = 18.0 Hz, 1H, CH$_2$[b]), 1.35 (s, 9H, 3CH$_3$); ^{13}C NMR (CDCl$_3$, 150 MHz) δ (ppm) 189.2,169.4, 167.2, 163.7 (d, J = 250 Hz), 140.4, 138.0, 132.4, 131.5, 130.9, 129.9, 128.7, 120.2, 116.2, 86.0,52.2, 33.8, 28.2. MS (*m/z*, %) 429 (M[+], 3), 329 (47), 290 (51), 234 (56), 139 (100), 57 (26). Anal. Calcd for C$_{23}$H$_{21}$ClFNO$_4$: C, 64.26; H, 4.92; N, 3.26. Found: C, 64.16; H, 4.94; N, 3.42.

3.2.4 (*E*)-*N*-*tert*-butyl-4-(4-fluorobenzylidene)-2-(4-nitrobenzoyl)-5-oxotetrahydrofuran-2-carboxamide (RPDFJ)

White crystals (0.36 g, yield 83%), mp 226–227°C; ^{1}H NMR (CDCl$_3$, 600 MHz) δ (ppm) 8.31 (d, J = 8.4 Hz, 2H, Ar-H), 8.23 (d, J = 8.4 Hz, 2H, Ar-H), 7.59–7.18 (m, 5H, Ar-H and = CH), 6.61 (s, 1H, NH), 4.41 (d, J = 18.6 Hz, 1H, CH$_2$[a]), 3.35 (d, J = 18.0 Hz, 1H, CH$_2$[b]), 1.36 (s, 9H, 3CH$_3$); ^{13}C NMR (CDCl$_3$, 150 MHz) δ (ppm) 189.3, 169.2, 167.0, 163.9 (d, J = 250 Hz), 150.4, 138.9, 138.2, 132.5,130.5, 129.9, 123.5, 119.5, 116.3, 85.7, 52.5, 33.6, 28.5. MS (*m/z*, %) 440 (M[+], 3), 340 (47), 290 (89), 234 (100), 123 (46), 57 (59). Anal. Calcd for C$_{23}$H$_{21}$FN$_2$O$_6$: C, 62.72; H, 4.81; N, 6.36. Found: C, 62.69; H, 4.93; N, 6.13.

3.3 Single crystal structure detection

A crystal with an external size of 0.10 mm^3 × 0.10 mm^3 × 0.10 mm^3 was selected for X-ray single crystal diffraction experiment and placed on a BRUKER SMART APEX-CCD diffractometer for detection. MoKα rays (wavelength λ = 0.71073Å) monochromatized by a graphite monochromator are used as incident radiation. In the range 2.00<θ < 26.55°, a total of 8,168 reflection points were collected by ω-2θ scanning at 298 (2) K, of which 5,150 were independent observable reflections [I ≥ 2σ(I)], R (int) = 0.0247. All the intensity data were corrected by SADABS software.

3.4 Antifungal assay

The antifungal activity of the compound RPDFB, RPDFC, RPDFI, RPDFJ at 50 μg/ml was determined against *Gibberella Zeae* by the poison plate technique. The medium was prepared by dissolving 43 g of potato dextrose agar powder (PAD. BR, Solarbio) in 1 L of distilled water and sterilized in autoclave at 125°C for 0.5 h. Next, the 2.0 mg drug was dissolved with 0.2 ml DMSO (AR, Sinopharm) and emulsified with a drop of tween-80 (AR, Sinopharm), then diluted to 2.0 ml with distilled water to obtain intermediate solutions of 1 mg/ml. Add 500 μL intermediate solution, while hot, to a Petri dish containing 9.5 ml PDA medium. After evenly mixing, a working solutions with a concentration of 50 μg/ml is obtained. As in

the above method, enazole and enazolone were added as positive control group, and no drug was added as blank control group. Then a blank PDA with a diameter of about 5 mm containing *Gibberella Zeae* was selected by the inoculation ring, and the mycelium was placed in the middle of the PDA containing the above-mentioned drugs. The lid of the Petri dish was immediately covered. The Petri dish was placed in a constant temperature incubator and cultured at 25°C for 3 days. The inhibition effect on the growth of *Gibberella Zeae* was observed and the diameter of plaque was measured. Three parallel experiments were performed. Inhibition rate (%) = (control colony diameter - treatment colony diameter)/ (control colony diameter - initial plaque diameter).

4 Conclusion

We improved the synthesis method of (*E*)-*N*-*tert*-butyl-4-(4-chlorobenzylidene)-2-(4-nitrobenzoyl)-5-oxotetrahydrofuran-2-carboxamide (RPDFB) by using ionic liquid as medium and microwave assisted method, which made the synthesis process more green and efficient. Meanwhile, three new compounds were synthesized by this method, and the chemical structures of four compounds were verified by spectroscopic method. The single crystal structure of RPDFB was also cultured and analyzed. Moreover, all the four compounds had inhibitory effects on *Gibberella Zeae*, and RPDFB had better anti-fungal effect. However, compared with enazole, the antibacterial effect of RPDFB still lags behind, which is worthy of further structural optimization. In conclusion, we synthesized a series of γ-lactone derivatives with a new synthesis strategy that is more environmentally friendly and efficient, hoping to provide a little help for the "greening" of organic synthesis.

Data availability statement

The datasets presented in this study can be found in online repositories. The names of the repository/repositories and accession number(s) can be found in the article/Supplementary Material.

Author contributions

YD: Conceptualization, investigation, methodology, resources, and writing-review and editing. L-QK: Investigation, software, validation, and writing-original draft.

Funding

Conflict of interest

The authors declare that the research was conducted in the absence of any commercial or financial relationships that could be construed as a potential conflict of interest.

Publisher's note

Supplementary material

The Supplementary Material for this article can be found online at: https://www.frontiersin.org/articles/10.3389/fchem. 2022.997095/full#supplementary-material

References

Bari, A., Grenier, D., Azelmat, J., Syed, S. A., Al-Obaid, A. M., and Hosten, E. C. (2019). Synthesis and anti-inflammatory activity of diversified heterocyclic systems. *Chem. Biol. Drug Des.* 94 (4), 1750–1759. doi:10. 1111/cbdd.13576

Batista, P. K., de O Ferreira, J. M. G., Silva, F. P. L., Vasconcellos, M. L. A. A., and Vale, J. A. (2019). The role ionic liquid [BMIM] [PF$_6$] in one-pot synthesis of tetrahydropyran rings through tandem barbier-prins reaction. *Molecules* 24 (11), 2084. doi:10.3390/molecules24112084

Huang, B., and Cui, S. (2018). Homologation of Ugi and Passerini reactions using ynamides. *Drug Discov. Today Technol.* 29, 43–49. doi:10.1016/j.ddtec.2018.09.001

Burriss, A., Edmunds, A. J., Emery, D., Hall, R. G., Jacob, O., and Schaetzer, J. (2018). The importance of trifluoromethyl pyridines in crop protection. *Pest Manag. Sci.* 74 (6), 1228–1238. doi:10.1002/ps.4806

Butin, A. V., Nevolina, T. A., Shcherbinin, V. A., Trushkov, I. V., Cheshkov, D. A., and Krapivin, G. D. (2010). Furan ring opening-pyrrole ring closure: A new synthetic route to aryl(heteroaryl)-annulated pyrrolo[1, 2-a] [1, 4]diazepines. *Org. Biomol. Chem.* 8 (14), 3316–3327. doi:10.1039/c002994g

Bystrzanowska, M., Pena-Pereira, F., Marcinkowski, Ł., and Tobiszewski, M. (2019). How green are ionic liquids? - a multicriteria decision analysis approach. *Ecotoxicol. Environ. Saf.* 174, 455–458. doi:10.1016/j.ecoenv.2019.03.014

Çınar, S., Schulz, M. D., Oyola-Reynoso, S., Bwambok, D. K., Gathiaka, S. M., and Thuo, M. (2016). Application of ionic liquids in pot-in-pot reactions. *Molecules* 21 (3), 272. doi:10.3390/molecules21030272

El-Sayed, R., and Althagafi, I. (2016). Potential biosignificant interest and surface activity of efficient heterocyclic derivatives. *J. Oleo Sci.* 65 (2), 177–192. doi:10.5650/jos.ess15193

Hafez, H. N., and El-Gazzar, A. B. A. (2020). Synthesis of novel pyridine bearing biologically active imidiazolyl, pyrazolyl, oxa/thiadiazolyl and urea derivatives as promising anticancer agents. *Curr. Org. Synth.* 17 (1), 55–64. doi:10.2174/1570179417666191223163225

Janosik, T., Johnson, A. L., and Bergman, J. (2002). Synthesis of the marine alkaloids rhopaladins A, B, C and D. *Tetrahedron* 58 (14), 2813–2819. doi:10.1016/S0040-4020(02)00171-0

Jiang, J., Hou, Y., Duan, M., Wang, B., Wu, Y., Ding, X., et al. (2021). Design, synthesis and antibacterial evaluation of novel oxazolidinone derivatives nitrogen-containing fused heterocyclic moiety. *Bioorg. Med. Chem. Lett.* 32, 127660. doi:10.1016/j.bmcl.2020.127660

Julien, D., Abdellatif, T., and Stephane, V. (2018). Efficient and regioselective synthesis of γ-lactone glycosides through a novel debenzylative cyclization reaction. *Chem. Commun.* 54, 9845–9848. doi:10.1039/c8cc05523h

Kong, L. Q., Zhu, X. L., Chen, Q. H., Wu, L., Wang, H. M., Ke, L. N., et al. (2021). One-pot synthesis and biological evaluation of (2E, 4E)-4-arylidene-2-styryl-5-oxopyrrolidine derivatives. *J. Chem. Res.* 45 (11-12), 1042–1046. doi:10.1177/17475198211051910

Manaithiya, A., Alam, O., Sharma, V., Naim, M. J., Mittal, S., Azam, F., et al. (2021). Current status of novel pyridine fused derivatives as anticancer agents: An insight into future perspectives and structure activity relationship (SAR). *Curr. Top. Med. Chem.* 21 (25), 2292–2349. doi:10.2174/1568026621666210916171015

Méndez, Y., Chang, J., Humpierre, A. R., Zanuy, A., Garrido, R., Vasco, A. V., et al. (2018). Multicomponent polysaccharide-protein bioconjugation in the development of antibacterial glycoconjugate vaccine candidates. *Chem. Sci.* 9 (9), 2581–2588. Published 2018 Jan 19. doi:10.1039/c7sc05467j

Nelson, G. L., Williams, M. J., Jonnalagadda, S., Alam, M. A., Mereddy, G., Johnson, J. L., et al. (2018). Synthesis and evaluation of baylis-hillman reaction derived imidazole and triazole cinnamates as antifungal agents. *Int. J. Med. Chem.*, 2018, 1–8. doi:10.1155/2018/5758076

Santagada, V., Frecentese, F., Perissutti, E., Fiorino, F., Severino, B., and Caliendo, G. (2009). Microwave assisted synthesis: A new technology in drug discovery. *Mini Rev. Med. Chem.* 9 (3), 340–358. doi:10.2174/1389557510909030340

Sharma, A., Appukkuttan, P., and Van der Eycken, E. (2012). Microwave-assisted synthesis of medium-sized heterocycles. *Chem. Commun.* 48 (11), 1623–1637. doi:10.1039/c1cc15238f

Sharma, S., Das, J., Braje, W. M., Dash, A. K., and Handa, S. (2020). A glimpse into green Chemistry practices in the pharmaceutical industry. *ChemSusChem* 13 (11), 2859–2875. doi:10.1002/cssc.202000317

Shiri, P. (2021). Novel hybrid molecules based on triazole-β-lactam as potential biological agents. *Mini Rev. Med. Chem.* 21 (5), 536–553. doi:10.2174/1389557520666201027160436

Sowmiah, S., Srinivasadesikan, V., Tseng, M. C., and Chu, Y. H. (2009). On the chemical stabilities of ionic liquids. *Molecules* 14 (9), 3780–3813. doi:10.3390/molecules14093780

Wang, H. M., Zhu, X. L., Chen, Q. H., Ding, M., Zeng, X., et al. (2021). An efficient one-pot synthesis and biological evaluation of novel (E)-2-aroyl-4-arylidene-5-oxotetrahydrofuran derivatives. *J. Chem. Res.* 45 (5-6), 395–399. doi:10.1177/1747519820911849

Welton, T. (1999). Room-temperature ionic liquids. Solvents for synthesis and catalysis. *Chem. Rev.* 99 (8), 2071–2084. doi:10.1021/cr980032t

Zeng, X. H., Wang, H. M., Wu, L., and Ding, M. W. (2013). One-pot synthesis of 5-oxopyrrolidine-2-carboxamides via a tandem Ugi 4CC/SN cyclization starting from Baylis-Hillman bromides. *Tetrahedron* 69 (19), 3823–3828. doi:10.1016/j.tet.2013.03.058

Zhang, B., Yu, G., Li, J., Liu, Y., Zhou, Y., Li, Y., et al. (2020). Optimization of extraction technology of poly-mannuronic acid to a green delivery system for the water-insoluble pesticide, λ-Cyhalothrin. *Int. J. Biol. Macromol.* 153, 17–25. doi:10.1016/j.ijbiomac.2020.02.228

Zhang, X., Zheng, Y. Y., Hu, C. M., Wu, X. Z., Lin, J., Xiong, Z., et al. (2022). Synthesis and biological evaluation of coumarin derivatives containing oxime ester as α-glucosidase inhibitors. *Arabian J. Chem.* 9 (15), 104072. doi:10.1016/j.arabjc.2022.104072

Zhu, J., Kong, L. Q., Chen, Q. H., Li, B., Wu, L., Ran, F. Y., et al. (2022). Design, synthesis, and apoptosis-promoting effect evaluation of rhopaladins' analog 4-arylidene-5-oxopyrrolidine derivatives. *Front. Chem.* 10, 898436. doi:10.3389/fchem.2022.898436

Zhu, X. L., Tian, X. Q., Xu, H. H., Wang, H. M., Chen, Q. H., and Zeng, X. H. (2020). Rhopaladins' analogue (E)-2-aroyl-4-(4-fluorobenzylidene)-5-oxopyrrolidines inhibit proliferation, promote apoptosis and down-regulation of E6/E7 mRNA in cervical cancer. *Bioorg. Med. Chem. Lett.* 30 (23), 127554. doi:10.1016/j.bmcl.2020.127554

Check for updates

Brønsted acid catalyzed remote C6 functionalization of 2,3-disubstituted indoles with β,γ-unsaturated α-ketoester

You-Ya Zhang, Lin Li, Xiang-Zhi Zhang and Jin-Bao Peng*

School of Biotechnology and Health Sciences, Wuyi University, Jiangmen, China

A metal-free catalytic approach for the remote C6-functionalization of 2,3-disubstituted indoles has been developed. In the presence of catalytic amounts of Brønsted acid, the β,γ-unsaturated α-ketoesters react with 2,3-disubstituted indoles at the C6 position selectively. Under mild reaction conditions, a range of C6-functionalized indoles were prepared with good yields and excellent regioselectivity. This methodology provides a concise and efficient route for the synthesis of C6-functionalized indole derivatives.

Introduction

Indole and its homologues and derivatives widely exist in nature, mainly in natural flower oils, such as jasmine, bitter orange flower, daffodil, vanilla, etc. This structure also ubiquitously exists as key structural framework in numerous natural products, functional materials, and medicines (Ishikura et al., 2015; Sherer and Snape, 2015; Zhang et al., 2015; Sravanthi and Manju, 2016; Gao et al., 2020) (Scheme 1A). For example, tryptophan is an essential amino acid of animals. Trikentrins, which have a fused cyclopenta[*g*]indole structures, were isolated from sponges and showed antimicrobial activity and cytotoxicity against KB cells (Capon et al., 1986; Herb et al., 1990). ABT-299 is a prodrug that is highly potent and specific platelet activating factor (PAF) antagonist (Vaden et al., 1996). Nintedanib is an oral tyrosine kinase inhibitor approved for the treatment of idiopathic pulmonary fibrosis (Wind et al., 2019).

Due to their important biological activities, the synthesis of functionalized indoles has received continuous attention. Although traditional methods for the indole synthesis can lead to indoles with different functionalizations (Fischer and Jourdan, 1883; Sugasawa et al., 1979; Gassman et al., 1984; Street et al., 1993; Fukukyama et al., 1994; Furstner and Ernst, 1995) these methods require multi-step substrate synthesis and the introduction of functional groups in many cases are less efficient. An alternative approach to access functionalized indoles is the direct C-H functionalization of indoles, (Wang et al., 2016; Fan et al., 2017; Gandeepan et al., 2019; Rej et al., 2020), which allows for the rapid and efficient introduction of specific
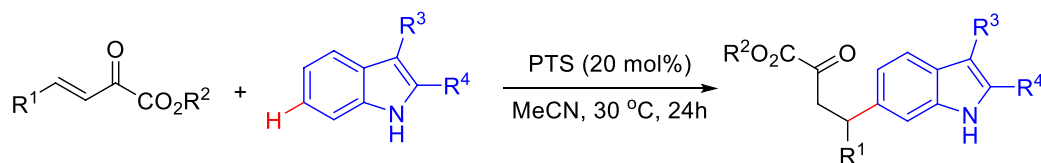
● Remote C6 Functionalization of Indoles   ● Mild conditions

GRAPHICAL ABSTRACT

groups into the indole backbone, thus providing a most straightforward and atom-economical access to the target indoles. Numerous efforts have been made in recent years to achieve selective functionalization of indoles. One of the major challenges of this area is the controlling of the site-selectivity of indole (Cacchi and Fabrizi, 2005; Humphrey and Kuethe, 2006; Sandtorv, 2015; Yang and Shi, 2018). Due to its inherent nucleophilic characteristics, the reaction of indoles

usually take place at their very reactive N1, C3 and C2 positions. (Scheme 1B) various methods have been developed for the C3, C2, and N1-functionalization of indoles via organo- and transition-metal-catalysis.

Comparatively, the functionalization at the C4−C7 position of indoles has been less reported, most of them were based on transition metal catalysis using directing groups to achieve C-H bond activation (Poulsen et al., 2015;

SCHEME 1
Selected bioactive molecules and natural products containing indole skeleton and selective C-H functionalization of indoles.

Rostoll-Berenguer et al., 2018; Xiao et al., 2018; Huang et al., 2019; Wen and Shi, 2021). Among them, the C6 position of indole is far away from the possible directing group, which makes the C6 functionalization of indole even more difficult (Liu et al., 2014; Zhou et al., 2014; Wu et al., 2019; Ling et al., 2019; Yan et al., 2020). In 2014, Yu and co-workers developed a removable "U-shaped" template to enable the orientation of indole C6-H to carry out alkenylation reactions (Yang et al., 2014) (Scheme 2A). In 2016, Larrosa developed a new strategy for indole C7 carboxyl group as a guiding group, causing indole C6 to undergo arylation (Scheme 2B). Simonetti et al. (2017) Frost's group used C3 ester groups with auxiliary coordination orientation and strong coordination orientation of pyrimidine groups on N atoms as the reaction substrate, and achieved selective C-H bond alkylation of indole C6 in Ru catalysis (Scheme 2C). (Leitch et al. (2017) Recently, the groups of Zhang (Zhou et al., 2019) (Scheme 2D) and Zhou (Huang et al., 2021) (Scheme 2E) have independently developed C6-

enantioselective C–H functionalization of 2,3-disubstituted indoles via chiral phosphoric acid catalysis. However, the development of efficient methods for the facile access to metal-free and highly selective C6 functionalization of indole in a sustainable fashion under mild conditions is still highly desirable. Herein, we developed a Brønsted acid catalyzed remote C6 functionalization of 2,3-disubstituted indoles with β,γ-unsaturated α-ketoester (Scheme 2F).

Initially, we examined this indole C6 functionalization reaction using β,γ-unsaturated α-ketoester 1a and 2,3-dimethyl-1H-indole 2a as model substrates. To our delight, when a mixture of 1a and 2a in toluene were treated with benzenesulfonic acid (BSA) at 30°C, the expected reaction proceeds smoothly and produced the desired C6 functionalized product 3aa in 42% yield (Table 1, entry 1). Inspired by this exciting result, we studied different reaction parameters for this reaction. Firstly, we screened the acid catalysts, including both Brønsted acids and Lewis acids (Table 1, entries 2–7). When p-toluenesulfonic

TABLE 1 Optimization of the reaction conditions[a].

Entry	Catalyst	Sol	Temp. (°C)	1a:2a	Yield (%)[b]
1	BSA	Toluene	30	1.2:1	42
2	PTS	Toluene	30	1.2:1	54
3	diphenyl phosphite	Toluene	30	1.2:1	13
4	PPTS	Toluene	30	1.2:1	47
5	4-Cl-BSA	Toluene	30	1.2:1	37
6	FeCl$_3$	Toluene	30	1.2:1	40
7	Sc(OTf)$_3$	Toluene	30	1.2:1	41
8	PTS	DCM	30	1.2:1	30
9	PTS	DCE	30	1.2:1	39
10	PTS	THF	30	1.2:1	trace
11	PTS	DMSO	30	1.2:1	10
12	PTS	MeCN	30	1.2:1	85
13	PTS	MeOH	30	1.2:1	16
14	PTS	MeCN	0	1.2:1	69
15	PTS	MeCN	40	1.2:1	65
16	PTS	MeCN	50	1.2:1	33
17	PTS	MeCN	30	1:1.2	74
18	**PTS**	**MeCN**	**30**	**1:1.5**	**92**
19	PTS	MeCN	30	1:1	34
20	PTS	MeCN	30	1.5:1	83

[a]Reaction conditions: 1a (0.2 mmol), 2a, Catalyst (20 mol%), solvent (2 ml), 24 h, [b]Isolated yields. BSA: benzenesulfonic acid. PTS: p-toluenesulfonic acid. PPTS: pyridinium p-toluenesulfonate. 4-Cl-BSA: 4-chlorobenzenesulfonic acid.
The optimized reaction conditions.
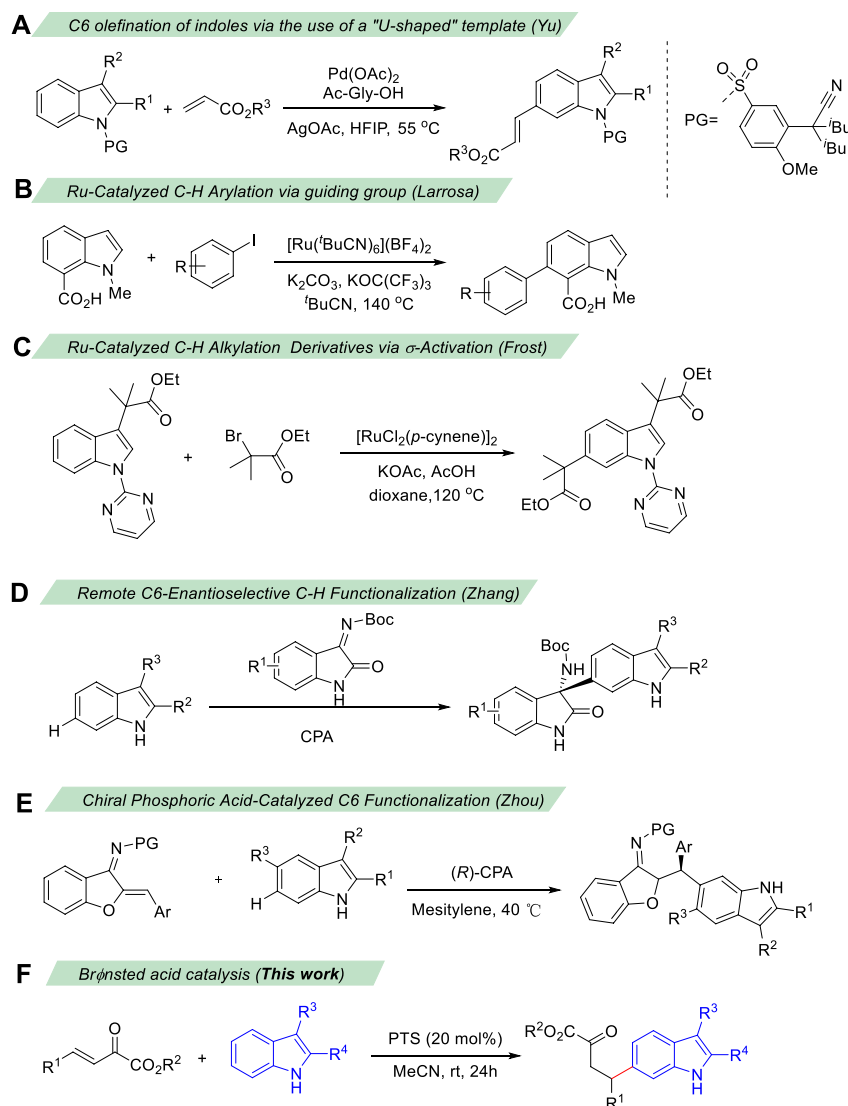
SCHEME 2
Transition-Metal Catalyzed C6 selective C−H Functionalization of Indoles.

acid (PTS) was used as the catalyst, the product **3aa** could be obtained in a yield of 54% (Table 1, entry 2). Subsequently, different solvents were examined. DCM and DCE provided the desired product **3aa** in moderate yields (Table 1, entries ht and 9). Other solvents such as THF and DMSO were ineffective for this reaction and only trace amounts of product were detected (Table 1, entries 10 and 11). MeCN was found to be the optimal solvent and the product **3aa** was obtained in 85% yield (Table 1, entry 12). Then, the influence of the reaction temperature to this transformation was investigated. When the reaction was performed at 0°C, the yield of **3aa** was decreased to 69% (Table1, entry 14). However, higher temperature also led to

decreased yields (Table 1, entries 15 and 16). Finally, the ratio of the starting materials was screened (Table 1, entries 16–20). When 1.5 equivalent of 2,3-dimethyl indole was used, the desired product was obtained in an excellent yield of 92% (Table 1, entry 18).

With the optimal reaction conditions in hand, we turned our attention to examining the generality of that reaction. Firstly, as shown in Scheme 3, under optimal reaction conditions, various substituted β,γ-unsaturated α-ketoesters reacted with 2,3-dimethyl indole **2a** and produced the corresponding products in good to excellent yields. Both electron-donating and electron-withdrawing group
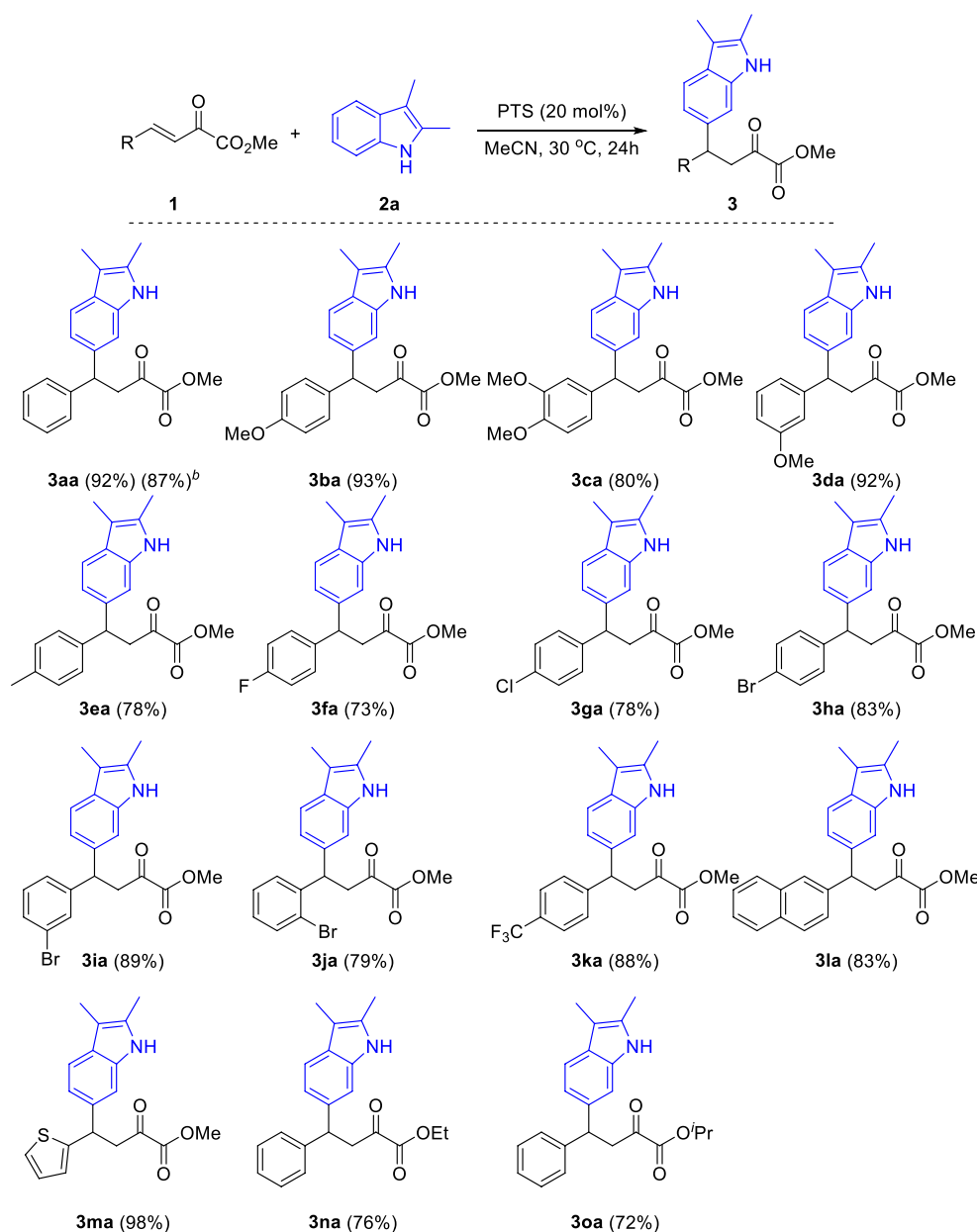
SCHEME 3

Substrate scope of β,γ-unsaturated α-ketoesters. aReaction conditions: β,γ-unsaturated α-ketoester **1** (0.2 mmol), Indoles **2a** (0.3 mmol), PTS (20 mol%), 30°C, 24 h, isolated yields. b**1a** (3 mmol), Indoles **2a** (4.5 mmol).

substituted β,γ-unsaturated α-ketoesters were tolerated in this reaction. The electronic properties of the substituents affect the efficiency of this reaction. Generally, β,γ-unsaturated α-ketoesters with electron-donating groups (**3ba-3ea**) gave higher yields than that with electron-withdrawing groups (**3fa-3ka**). The steric effect of the substituents has little influence to the yield of this reaction (**3ba** *vs.* **3da**, **3ha** *vs.* **3ja**). Notably, halides including fluoro-, chloro- and bromo- groups were compatible in this reaction. Furthermore,

heteroarenes such as 2-naphthyl (**3la**) and thienyl (**3ma**) substituted enoneates were also compatible in this reaction and produced the corresponding products in 83% and 98% yields, respectively. In addition, the reaction also gave good yields when ethyl and isopropyl esters were used (**3na**, **3oa**).

Then, we examined the scope of indoles for this reaction. As shown in Scheme 4, a range of 2,3-disubstituted indoles were successfully applied in this reaction, providing the corresponding C6 functionalized products in moderate to
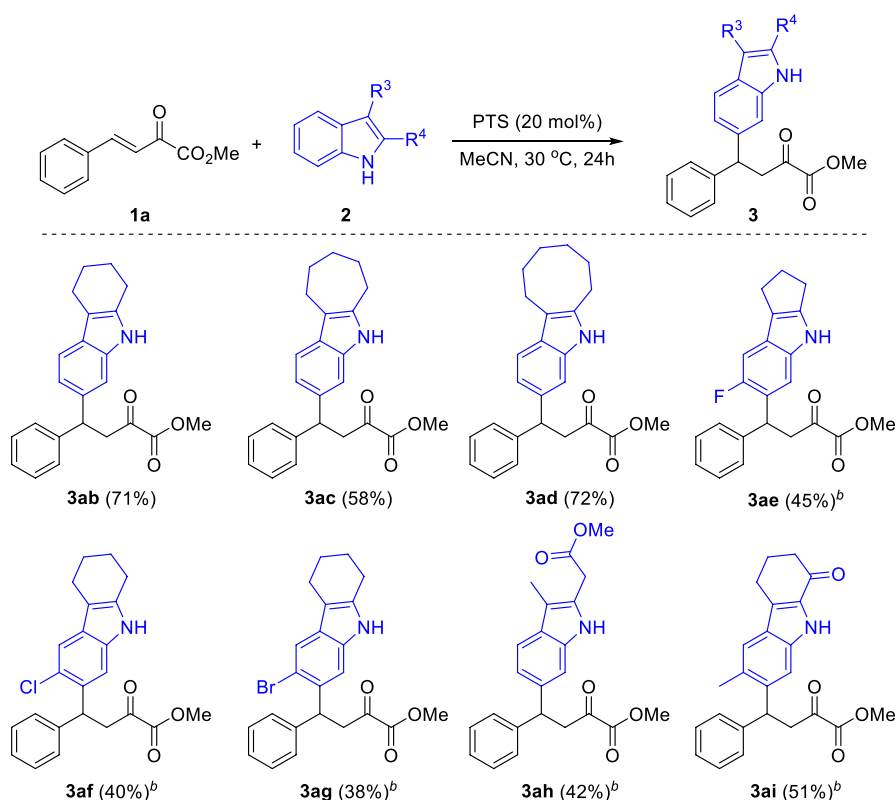
SCHEME 4
Substrate Scope of Indoles. [a]Reaction conditions: β,γ-unsaturated α-ketoester **1a** (0.2 mmol), Indoles **2** (0.3 mmol), PTS (20 mol%), 30°C, 24 h, isolated yields. [b]60°C.
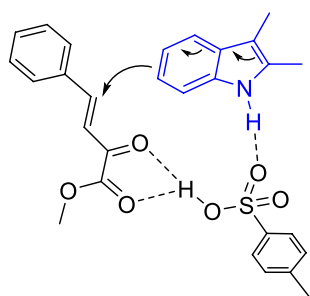
SCHEME 5
Proposed Reaction Modela.

good yields. When tetrahydro-1H-carbazole was subjected to the optimized conditions, the desired product **3 ab** was obtained in 71% yield. Other analogues with six-, seven- and five-membered fused rings were also tolerated in this reaction (**3ac-3ae**). Besides, several functional groups including halides (**3ae-3ag**), ester (**3ah**) and ketone (**3ai**) were compatible in this reaction. It should be noted that

the substitution at both C2 and C3 positions of indole were essential for this reaction. When 2-methyl-1H-indole was used in this reaction, a mixture of isomers were obtained, while 3-methyl-1H-indole led to the formation of 9H-pyrrolo [1,2-a]indole (Sun et al., 2016). Other heterocycles such as benzofuran, benzothiophene, carbazole and quinoline were failed in this reaction.

On the basis of these results and the previous literatures, we proposed a plausible reaction model to illustrate the regioselectivity of this reaction. The Brønsted acid served as a bifunctional catalyst to activate both the indole and the β,γ-unsaturated α-ketoesters (Scheme 5).

In summary, we have developed a metal-free catalytic approach for the remote C6-functionalization of 2,3-disubstituted indoles. In the presence of catalytic amounts of Brønsted acid, the β,γ-unsaturated α-ketoesters react with 2,3-disubstituted indoles at the C6 position selectively. Under mild reaction conditions, a range of C6-functionalized indoles were prepared with good yields and excellent regioselectivity. This methodology provides a concise and efficient route for the synthesis of C6-functionalized indole derivatives.

Data availability statement

The original contributions presented in the study are included in the article/Supplementary Materials, further inquiries can be directed to the corresponding author.

Author contributions

J-BP conceived and directed the project. YY-Z performed the experiments. LL and X-ZZ participated in substrates synthesis and discussions. Y-YZ and J-BP wrote the manuscript and ESI.

Funding

Conflict of interest

The authors declare that the research was conducted in the absence of any commercial or financial relationships that could be construed as a potential conflict of interest.

Publisher's note

All claims expressed in this article are solely those of the authors and do not necessarily represent those of their affiliated organizations, or those of the publisher, the editors and the reviewers. Any product that may be evaluated in this article, or claim that may be made by its manufacturer, is not guaranteed or endorsed by the publisher.

Supplementary material

The Supplementary Material for this article can be found online at: https://www.frontiersin.org/articles/10.3389/fchem.2022.992398/full#supplementary-material

References

Cacchi, S., and Fabrizi, G. (2005). Synthesis and functionalization of indoles through palladium-catalyzed reactions. *Chem. Rev.* 105, 2873–2920. doi:10.1021/cr040639b

Capon, R. J., Macleod, J. K., and Scammells, P. J. (1986). The trikentrins : Novel indoles from the sponge. *Tetrahedron* 42, 6545–6550. doi:10.1016/s0040-4020(01)88117-5

Fan, Z., Lu, H., Li, W., Geng, K., and Zhang, A. (2017). Rhodium-catalyzed redox-neutral coupling of phenidones with alkynes. *Org. Biomol. Chem.* 15, 5701–5708. doi:10.1039/c7ob01271c

Fischer, E., and Jourdan, F. (1883). Ueber die Hydrazine der Brenztraubensäure. *Ber. Dtsch. Chem. Ges.* 16, 2241–2245. doi:10.1002/cber.188301602141

Fukuyama, T., Chen, X., and Peng, G. (1994). A novel tin-mediated indole synthesis. *J. Am. Chem. Soc.* 116, 3127–3128. doi:10.1021/ja00086a054

Furstner, A., and Ernst, A. (1995). Syntheses of camalexin, indolopyridocoline and flavopereirine. *Tetrahedron* 51, 773–786. doi:10.1016/0040-4020(94)00987-6

Gandeepan, P., Müller, T., Zell, D., Cera, G., Warratz, S., and Ackermann, L. (2019). 3d transition metals for C–H activation. *Chem. Rev.* 119 (4), 2192–2452. doi:10.1021/acs.chemrev.8b00507

Gao, Y., Wang, X. N., Wei, Z. L., Cao, J. G., Liang, D. P., Lin, Y. J., et al. (2020). Asymmetric synthesis of spirooxindole-pyranoindole products via Friedel–Crafts alkylation/cyclization of the indole carbocyclic ring. *New J. Chem.* 44, 9788–9792. doi:10.1039/d0nj00074d

Gassman, P. G., Roos, J. J., and Lee, S. J. (1984). Use of [2, 3]-sigmatropic rearrangements in a one-step conversion of tetrahydroquinoline to substituted 1, 2, 5, 6-tetrahydro-4N-pyrrolo[3, 2, 1-ij]quinolin-2-one and 5, 6-dihydro-4H-pyrrolo[3, 2, 1-ij]quinoline. *J. Org. Chem.* 49 (4), 717–718. doi:10.1021/jo00178a033

Herb, R., Carroll, A. R., Yoshida, W. Y., Scheuer, P. J., and Paul, V. J. (1990). Polyalkylated cyclopentindoles: Cytotoxic fish antifeedants from a sponge, Axinella sp. *Tetrahedron* 46, 3089–3092. doi:10.1016/s0040-4020(01)88399-x

Huang, T., Zhao, Y., Meng, S., Chan, A. S. C., and Zhao, J. (2019). C7-Functionalization of indoles via organocatalytic enantioselective friedel-crafts alkylation of 4-aminoindoles with 2-butene-1, 4-diones and 3-aroylacrylates. *Adv. Synth. Catal.* 361, 3632–3638. doi:10.1002/adsc.201900377

Huang, W. J., Ma, Y. Y., Liu, L. X., Wu, B., Jiang, G. F., and Zhou, Y. G. (2021). Chiral phosphoric acid-catalyzed C6 functionalization of 2, 3-disubstituted indoles

for synthesis of hetero-triarylmethanes. *Org. Lett.* 23, 2393–2398. doi:10.1021/acs.orglett.0c04002

Humphrey, G. R., and Kuethe, J. T. (2006). Practical methodologies for the synthesis of indoles. *Chem. Rev.* 106, 2875–2911. doi:10.1021/cr0505270

Ishikura, M., Abe, T., Choshi, T., and Hibino, S. (2015). Simple indole alkaloids and those with a nonrearranged monoterpenoid unit. *Nat. Prod. Rep.* 32, 1389–1471. doi:10.1039/c5np00032g

Leitch, J. A., McMullin, C. L., Mahon, M. F., Bhonoah, Y., and Frost, C. G. (2017). Remote C6-selective ruthenium-catalyzed C–H alkylation of indole derivatives via σ-activation. *ACS Catal.* 7 (4), 2616–2623. doi:10.1021/acscatal.7b00038

Ling, Y., An, D., Zhou, Y., and Rao, W. (2019). Ga(OTf)$_3$-Catalyzed temperature-controlled regioselective friedel-crafts alkylation of trifluoromethylated 3-indolylmethanols with 2- substituted indoles: Divergent synthesis of trifluoromethylated unsymmetrical 3, 3′-and 3, 6′-Bis(indolyl)methanes. *Org. Lett.* 21, 3396–3401. doi:10.1021/acs.orglett.9b01135

Liu, H., Zheng, C., and You, S.-L. (2014). Catalytic C6 functionalization of 2, 3-disubstituted indoles by scandium triflate. *J. Org. Chem.* 79, 1047–1054. doi:10.1021/jo402511b

Poulsen, P. H., Feu, K. S., Paz, B. M., Jensen, F., and Jørgensen, K. A. (2015). Organocatalytic asymmetric 1, 6-addition/1, 4-addition sequence to 2, 4-dienals for the synthesis of chiral chromans. *Angew. Chem. Int. Ed. Engl.* 54, 8321–8325. doi:10.1002/ange.201503370

Rej, S., Ano, Y., and Chatani, N. (2020). Bidentate directing groups: An efficient tool in C–H bond functionalization Chemistry for the expedient construction of C–C bonds. *Chem. Rev.* 120 (3), 1788–1887. doi:10.1021/acs.chemrev.9b00495

Rostoll-Berenguer, J., Sanchez-García, R., Blay, G., Fernandez, I., Muñoz, M. C., and Pedro, J. R. (2018). Enantioselective synthesis of 2-amino-1, 1-diarylalkanes bearing a carbocyclic ring substituted indole through asymmetric catalytic reaction of hydroxyindoles with nitroalkene. *J. Org. Chem.* 83, 6397–6407.

Sandtorv, A. H. (2015). Transition metal-catalyzed C–H activation of indoles. *Adv. Synth. Catal.* 357, 2403–2435. doi:10.1002/adsc.201500374

Sherer, C., and Snape, T. J. (2015). Heterocyclic scaffolds as promising anticancer agents against tumours of the central nervous system: Exploring the scope of indole and carbazole derivatives. *Eur. J. Med. Chem.* 97, 552–560. doi:10.1016/j.ejmech.2014.11.007

Simonetti, M., Cannas, D. M., Panigrahi, M., Kujawa, S., Kryjewski, M., Xie, P., et al. (2017). Ruthenium-ruthenium-catalyzed C–H arylation of benzoic acids and indole carboxylic acids with aryl halides. *Chem. Eur. J.* 23 (3), 549–553. doi:10.1002/chem.201605068

Sravanthi, T. V., and Manju, S. L. (2016). Indoles-A promising scaffold for drug development. *Eur. J. Pharm. Sci.* 91, 1–10. doi:10.1016/j.ejps.2016.05.025

Street, L. J., Baker, R., Castro, J. L., Chambers, M. S., Guiblin, A. R., Hobbs, S. C., et al. (1993). Synthesis and serotonergic activity of 5-(oxadiazolyl)tryptamines: Potent agonists for 5-ht1d receptors. *J. Med. Chem.* 36 (11), 1529–1538. doi:10.1021/jm00063a003

Sugasawa, T., Adachi, M., Sasakura, K., and Kitagawa, A. (1979). Aminohaloborane in organic synthesis. 2. Simple synthesis of indoles and 1-acyl-3-indolinones using specific ortho .alpha.-chloroacetylation of anilines. *J. Org. Chem.* 44 (4), 578–586. doi:10.1021/jo01318a021

Sun, Y., Qiao, Y., Zhao, H., Li, B., and Chen, S. (2016). Construction of 9*H*-Pyrrolo[1, 2-*a*]indoles by a copper-catalyzed Friedel–Crafts alkylation/annulation cascade reaction. *J. Org. Chem.* 81, 11987–11993. doi:10.1021/acs.joc.6b02143

Vaden, S. L., Page, R. L., and Riviere, J. E. (1996). An *in vitro-in vivo* validation of the isolated perfused tumor and skin flap preparation as a model of cisplatin delivery to tumors. *J. Pharmacol. Toxicol. Methods* 35, 173–177. doi:10.1016/1056-8719(96)00044-5

Wang, H., Moselage, M., González, M. J., and Ackermann, L. (2016). Selective synthesis of indoles by cobalt(III)-Catalyzed C–H/N–O functionalization with nitrones. *ACS Catal.* 6 (4), 2705–2709. doi:10.1021/acscatal.5b02937

Wen, J., and Shi, Z. (2021). From C4 to C7: Innovative strategies for site-selective functionalization of indole C–H bonds. *Acc. Chem. Res.* 54 (7), 1723–1736. doi:10.1021/acs.accounts.0c00888

Wind, S., Schmid, U., Freiwald, M., Marzin, K., Lots, R., Ebner, T., et al. (2019). Clinical pharmacokinetics and pharmacodynamics of Nintedanib. *Clin. Pharmacokinet.* 58, 1131–1147. doi:10.1007/s40262-019-00766-0

Wu, Q., Li, G. L., Yang, S., Shi, X. Q., Huang, T.-A., Du, X.-H., et al. (2019). A chemo- and regioselective C6-functionalization of 2, 3-disubstituted indoles: Highly efficient synthesis of diarylindol-6-ylmethanes. *Org. Biomol. Chem.* 17, 3462–3470. doi:10.1039/c9ob00283a

Xiao, M., Xu, D., Liang, W., Wu, W., Chan, A. S. C., and Zhao, J. (2018). Organocatalytic enantioselective friedel-crafts alkylation/lactonization reaction of hydroxyindoles with methyleneoxindoles. *Adv. Synth. Catal.* 360, 917–924. doi:10.1002/adsc.201701089

Yan, J., Zhang, Z., Chen, M., Lin, Z., and Sun, J. (2020). A study of the reactivity of (Aza-)Quinone methides in selective C6-alkylations of indoles. *ChemCatChem* 12, 5053–5057. doi:10.1002/cctc.202000850

Yang, Y., and Shi, Z. (2018). Regioselective direct arylation of indoles on the benzenoid moiety. *Chem. Commun.* 54, 1676–1685. doi:10.1039/c7cc08752g

Yang, G. Q., Lindovska, P., Zhu, D. J., Kim, J., Wang, P., Tang, R. Y., et al. (2014). Pd(II)-Catalyzed meta-C-H olefination, arylation, and acetoxylation of indolines using a U-shaped template. *J. Am. Chem. Soc.* 136 (30), 10807–10813. doi:10.1021/ja505737x

Zhang, M. Z., Chen, Q., and Yang, G. F. (2015). A review on recent developments of indole containing antiviral agents. *Eur. J. Med. Chem.* 89, 421–441. doi:10.1016/j.ejmech.2014.10.065

Zhou, L. J., Zhang, Y. C., Zhao, J. J., Shi, F., and Tu, S. J. (2014). Organocatalytic arylation of 3-indolylmethanols via chemo- and regiospecific C6-functionalization of indoles. *J. Org. Chem.* 79, 10390–10398. doi:10.1021/jo501989x

Zhou, J., Zhu, G. D., Wang, L., Tan, F. X., Jiang, W., Ma, Z. G., et al. (2019). Remote C6-Enantio-selective C-H functionalization of 2, 3-disubstituted indoles through the dual H-bonds and π-π interaction strategy enabled by CPAs. *Org. Lett.* 21, 8662–8666. doi:10.1021/acs.orglett.9b03276

Studies toward synthesis of the core skeleton of spiroaspertrione A

Zhong-Hui Shen, Si-Yuan Lu, Jing-Yun Zheng, Xiang-Zhi Zhang, Jin-Bao Peng and Ai-Jun Ma*

School of Biotechnology and Health Sciences, Wuyi University, Jiangmen, China

Bioassay-guided isolation of spiroaspertrione A from cultures of *Aspergillus sp.* TJ23 in 2017 demonstrated potent resensitization of oxacillin against methicillin-resistant *Staphylococcus aureus* by lowering the oxacillin minimal inhibitory concentration up to 32-fold. To construct this unique spiro[bicyclo [3.2.2]nonane-2,1′-cyclohexane] system, a protocol for ceric ammonium nitrate-induced intramolecular cross-coupling of silyl enolate is disclosed.

Introduction

The expansion of multidrug-resistant pathogens is a threat to human health that can effectively take us back to the pre-antibiotic era for many infectious diseases (Walsh et al., 2011). Considering its grave roles in hospital and community-acquired infections, methicillin-resistant *Staphylococcus aureus* (MRSA) is a "superbug" with an extreme array of resistance and virulence factors (Gonzales, et al., 2015). Drug-resistance gene mutations of MRSA are exemplified by *mecA*, the disruption of which can produce inducible resistance to β-lactam antibiotics because it encodes penicillin-binding protein 2a (Fuda et al., 2005). With the rapid acquisition of resistance restricting therapeutic options for MRSA, many scientists have explored treatment methods combining the use of small molecules to render MRSA sensitive to the effects of conventional β-lactam antibiotics (Van Hal et al., 2011; Long et al., 2014; Bush, 2015; Gonzales et al., 2015).

In 2017, Zhang group used a bioassay-guided approach to isolate a novel terpene-polyketide hybrid spiromero-terpenoid from a culture of *Aspergillus sp.* TJ23, spiroaspertrione A (**1**), which bears a unique spiro[bicyclo[3.2.2]nonane-2,1′-cyclohexane] carbocyclic skeleton (Figure 1) (He et al., 2017). Spiroaspertrione A demonstrated potent resensitization of oxacillin against MRSA by lowering the oxacillin minimal inhibitory concentration (MIC) up to 32-fold from 32 μg/mL to 1 μg/mL (He et al., 2017). This promising bioactivity together with a unique spiro [bicyclo[3.2.2]nonane-2,1-cyclohexane] carbocyclic skeleton renders spiroaspertrione A an interesting and challenging target for total synthesis. To date, no synthesis method for spiroaspertrione A has been reported.

Here, we analyzed and constructed the core skeleton of this spiromeroterpenoid, culminating in a strategy of intramolecular enol oxidative coupling (Figure 2). When
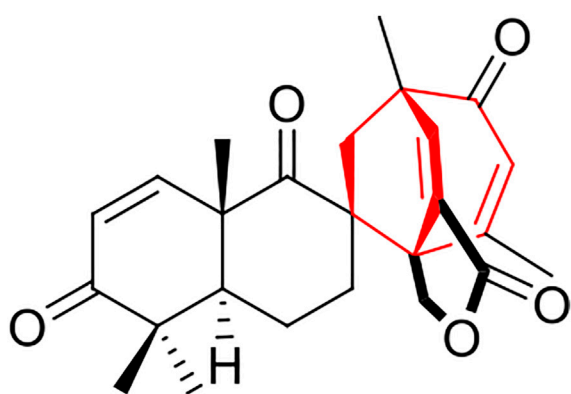
FIGURE 1
Structure of spiroaspertrione A (1).

designing this synthetic strategy for spiroaspertrione A, we noticed that the E lactone ring can be obtained by simple lactonization during later synthesis. Construction of the spiro [bicyclo[3.2.2]nonane] system of the ABCD rings exhibits a high degree of ring tension and rigidity–the most interesting and challenging feature of spiroaspertrione A synthesis. The core skeleton of spiroaspertrione A could be constructed through *Birch* reduction followed by methylation of the naphthene compound 2. This synthetically significant and more tractable spiro-ring system can then be built by an intramolecular enol oxidative coupling (EOC) reaction of precursor 3, which can then

be traced back to a 1,4-conjugate addition of western fragment 5 and eastern fragment 4.

As an efficient synthetic method to directly construct C-C bonds, the oxidative coupling reaction of enol derivatives has been applied in the syntheses of polyketides, alkaloids, and other natural products. (Murarka and Antonchick 2018). Although the first oxidative coupling reaction of enol derivatives dates back to 1935, it did not receive widespread attention from chemists until the 1970s because the efficiency and practicality of this reaction were less than satisfactory (Fujii et al., 1992; Kohno and Narasaka 1995; Ryter and Livinghouse 1998; Ekebergh et al., 2011; Rathke and Lindert 1971; Dessau and Heiba 1974; Xie and Huang 2010; Renaud and Fox 1998). In 2005, Baran group began to conduct in-depth research on the oxidative coupling reaction of enolates and successfully applied their findings to the total synthesis of multiple complex natural products (Baran et al., 2005; Richter et al., 2007; DeMartino et al., 2008). To date, the oxidative coupling reaction of enol derivates remains under constant development and optimization. The EOC reaction can be broadly divided into two categories: direct oxidation, involving the construction of C-C bonds under single-electron oxidants (e.g., ketones, carboxylic acids, esters, and amides) bound to the corresponding enols or enolates; and indirect oxidation, in which single-electron oxidants are converted to the corresponding enol (e.g., silanes and enamines) prior to construction of the C-C bonds (Figure 3). The EOC reaction has been reviewed by Plumet (Csákÿ and Plumet 2001), Baran (Baran 2006), Dong (Yeung Dong 2011), Thomson (Guo et al., 2012), Ma (Nagaraju and Ma 2018), Chen (Chen and Liu 2021), and others.

In recent years, intermolecular and intramolecular EOC reactions have been applied to many natural products as an efficient method of constructing C-C bonds (Figure 4). Baran
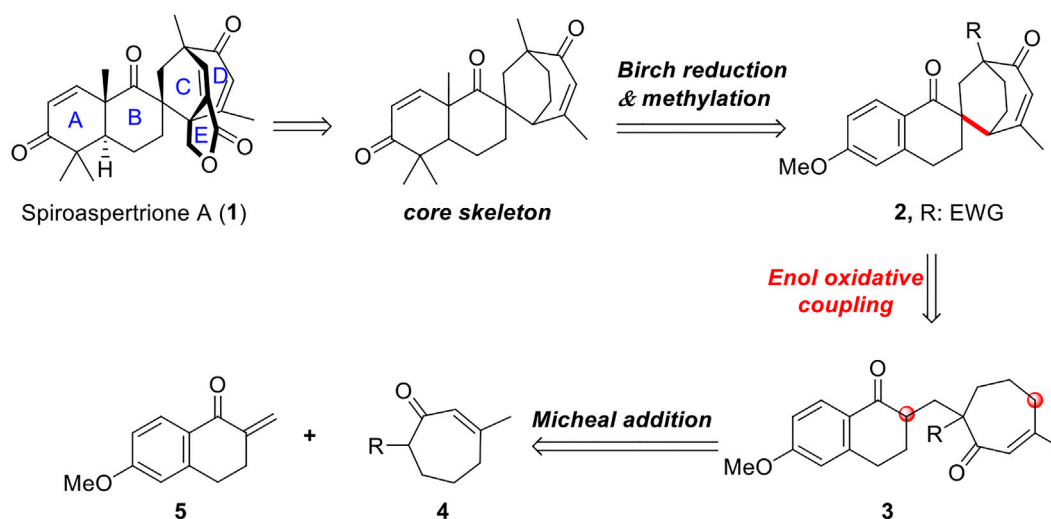
FIGURE 2
Retrosynthetic analysis.
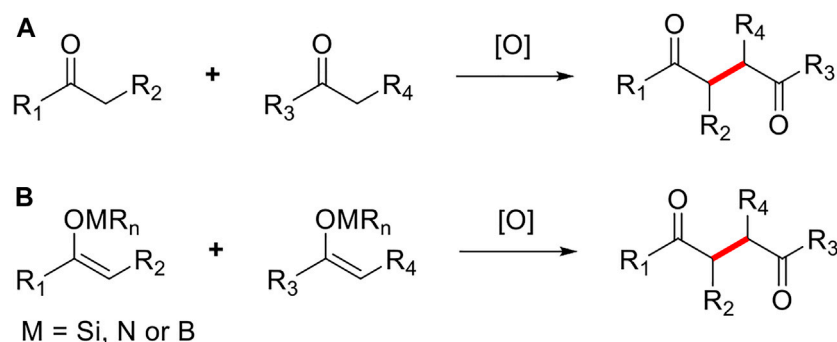
FIGURE 3
Types of enol oxidative coupling reaction.
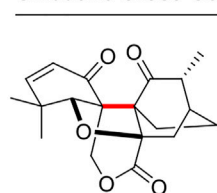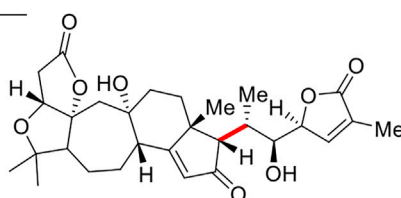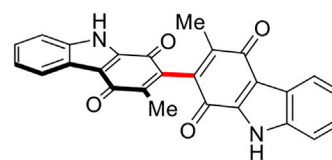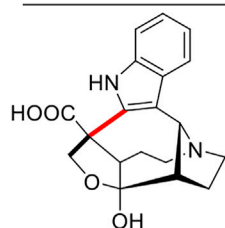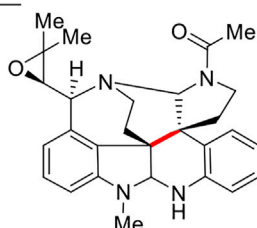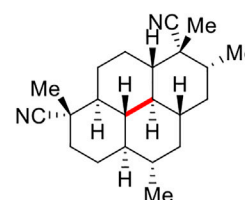
FIGURE 4
Application of EOC reaction in the synthesis of natural products.

group completed the construction of the core skeleton of the natural product *maoecrystal* V using intermolecular EOC reactions (Krawczuk et al., 2009). Furthermore, Yang group (You et al., 2015) used enol silyl ethers substrates to realize the enantioselective synthesis of *propindilactone* G from the Schisandra family by cross-oxidative coupling reaction. Moreover, Thomson groups disclosed a method of *self-*

intermolecular EOC reactions applied to the synthesis of dimerized natural product *bis-murrayaquinone* A (Konkol et al., 2011).

Using intramolecular EOC reactions, Overman group (Martin et al., 2008; Martin et al., 2010) made important progress toward the total synthesis of the indole alkaloids (±)-*actinophyllic acid*. From 2010 to 2014, Ma group (Zuo

FIGURE 5
Synthesis of precursor 3.
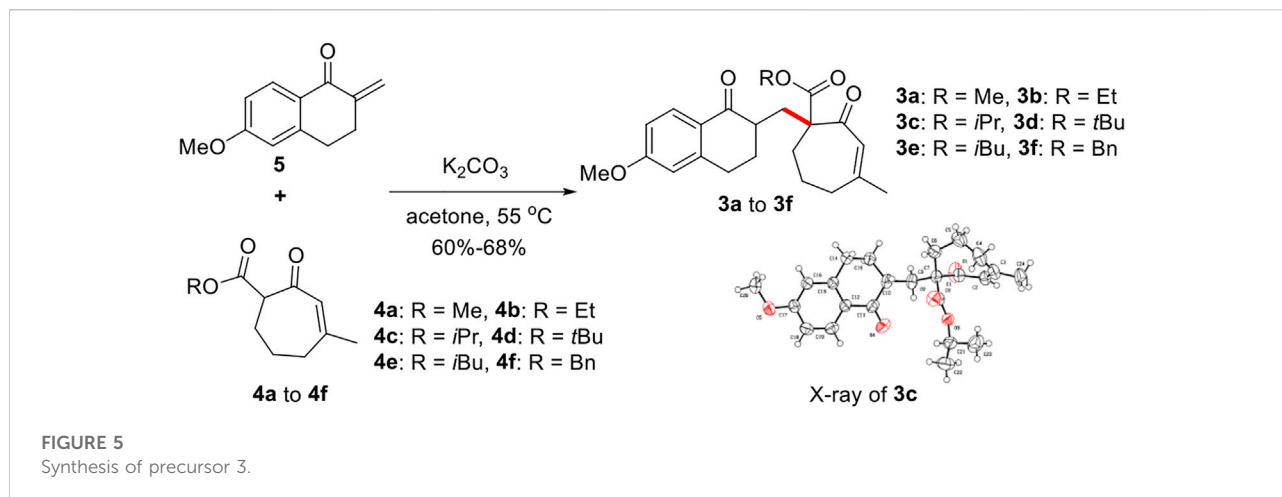
TABLE 1 Optimization of the reaction conditions[a].

Entry	Conditions	Yield (2a+2a′)
1	LHMDS, CuCl$_2$	<5%, 60% (brsm)[b]
2	LHMDS, FeCl$_3$	<5%, 53% (brsm)[b]
3	LDA, CuCl$_2$	complex mixture
4	KHMDS, CuCl$_2$	9%
5	NaHMDS, CuCl$_2$	11%
6[c]	NaHMDS, CuCl$_2$, O$_2$	--
7[d]	NaHMDS, CuCl$_2$, air	--
8	NaHMDS, Cu(acac)$_2$	8%
9	NaHMDS, FeCl$_3$	9%
10	NaHMDS, I$_2$	--
11[e]		--

[a]Reactions were carried out with 3a (30 mg, 0.081 mmol), metal base (0.243 mmol), and single-electricity oxidant (0.162 mmol) in THF (2.0 ml) under N$_2$.
[b]Brsm = based on the recovered starting material.
[c]Reactions were carried out with CuCl$_2$ (20% mmol) under O$_2$.
[d]Reactions were carried out with CuCl$_2$ (20% mmol) under air.
[e]Reactions were carried out with 10 mol% catalyst and Cu(acac)$_2$ (20 mol%).

et al., 2010; Zuo and Ma 2011; Zi et al., 2012; Wei et al., 2013; Teng et al., 2014) realized the efficient construction of the core skeleton of indole alkaloids and synthesized several indole alkaloids such as (+)-*communesins* A. In 2018, Thomson group (Guo et al., 2012; Jones et al., 2014; Robinson and Thomson, 2018) reported the strategy of *intra*-EOC reaction using enol *di*-silyl ether to realize the formal synthesis of natural products (+)-7,20-*diisocyanoadociane* and other derived products.

TABLE 2 Optimization of silyl bis-enol etherification conditions[a].
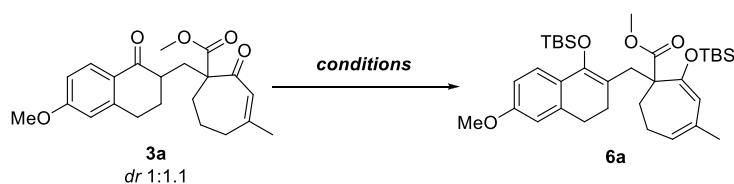
Entry	Conditions	Yield %	
		Bis-silyl	**Mono-silyl**
1	LDA, TBSOTf, THF	complex mixture	
2	LHMDS, TBSOTf, THF	21	75
3[b]	LHMDS, HMPA, TBSCl, THF	24	74
4	KHMDS, TBSOTf, THF	35	60
5	NaHMDS, TBSOTf, THF	58	30
6[c]	Et$_3$N, TBSOTf, DCM	0	90

[a]Reactions were carried out with 3a (30 mg, 0.081 mmol), base (0.243 mmol), and TBSOTf (0.162 mmol) in THF (2.0 ml) at -78°C under N$_2$.
[b]Reactions were carried out with 3a (30 mg, 0.081 mmol), LHMDS (0.243 mmol), TBSCl (0.162 mmol) and HMPA (0.162 mmol) in THF (2.0 ml) at -78°C under N$_2$.
[c]Reactions were carried out with 3a (30 mg, 0.081 mmol), Et$_3$N (0.243 mmol), TBSOTf (0.162 mmol) in DCM (2.0 ml) at room temperature under N$_2$.

TABLE 3 Optimization of intramolecular EOC reaction conditions[a].
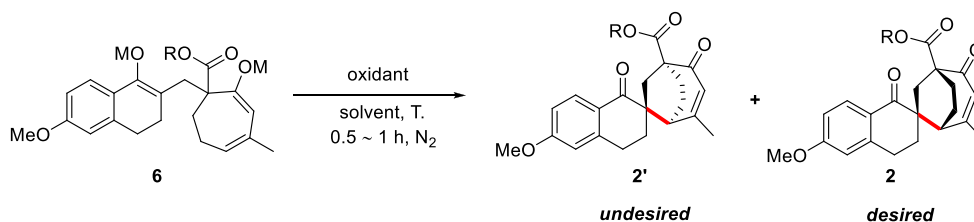
Entry	R	M	Oxidant	Solvent	T (°C)	dr[b]	Yield[c]
1	Me	TBS	CAN	CH$_3$CN/THF	0	8.7:1	77%
2	Et	TBS	CAN	CH$_3$CN/THF	0	8:1	74%
3	**iPr**	**TBS**	**CAN**	**CH$_3$CN/THF**	**0**	**4.9:1**	**69%**
4	tBu	TBS	CAN	CH$_3$CN/THF	0	12:1	68%
5	iBu	TBS	CAN	CH$_3$CN/THF	0	6.4:1	62%
6	iPr	TES	CAN	CH$_3$CN/THF	0	5.8:1	64%
7	iPr	TIPS	CAN	CH$_3$CN/THF	0	6.8:1	64%
8	iPr	TBS	CuCl$_2$	CH$_3$CN/THF	−78 to rt	--	21% (50%)[d]
9	iPr	TBS	Cu(acac)$_2$	CH$_3$CN/THF	−78 to rt	--	--
10	iPr	TBS	FeCl$_3$	CH$_3$CN/THF	−78 to rt	--	23% (54%)[d]
11	iPr	TBS	AgF, PhBr	CH$_3$CN	Rt	--	no reaction
12	iPr	TBS	PhI(OH)OTs	DCM	−78	12:1	61%

[a]Reactions were carried out with 6 (0.08 mmol), CAN (0.24 mmol), and NaHCO$_3$ (0.48 mmol) in CH$_3$CN/THF (0.1 M, 4:1) at 0°C under N$_2$.
[b]Determined ratio of 2′ and 2 by ^{1}H NMR.
[c]Isolated yields of 2 and 2′ after purification by column chromatography.
[d]Isolated yields of 3 after purification by column chromatography.

Materials and methods

Unless otherwise noted, all reactions were carried out under N$_2$ atmosphere. All reagents were from commercial sources and used as received without further purification. All solvents were dried by standard techniques and distilled prior to use. Column chromatography was performed on silica gel (200–300 meshes) using petrol etherand ethyl acetate as eluent. NMR spectra were recorded on a Bruker Avance operating at for ^{1}H NMR at 500 MHz, ^{13}C NMR at 126 MHz and spectral data were reported in ppm relative to tetramethylsilane (TMS) as internal standard and CDCl$_3$ (^{1}H NMR δ 7.26, ^{13}C NMR δ 77.0) as solvent. All high-resolution mass spectra (HRMS) were obtained by Thermo Scientific's UltiMate 3,000 Series liquid system and Thermo Scientific Q-Exactive combined quadrupole Orbitrap mass spectrometer.

According to our retrosynthetic analysis, we chose known compound 5 (Li et al., 2019) and 4 self-prepared from 3-methylcyclohept-2-en-1-one as substrates to form the important precursor 3. Following screening of various conditions, we obtained compound 3 as a minor product with a yield of 30% under NaH and MeOH, and compound 5's *O*-1,4-addition byproduct as the major product. Subsequent screening of several Lewis acids, such as BF$_3$·OEt and TiCl$_4$, yielded substrate 5's *O*-DA reaction byproduct as the major product. To our delight, conducting the reaction in acetone at 55°C in the presence of K$_2$CO$_3$(2 eq) afforded the desired 1,4-addition product 3 with 60%–68% yield (Figure 5).

With precursor 3a in hand, we intended to construct the desired C-C bond by single-electron oxidation under conditions including a metal base (Table 1). In the presence of LHMDS and cupric chloride (CuCl$_2$) or ferric chloride (FeCl$_3$), we obtained a very small amount of the EOC product 2a and 2a′, although the recovery yield was 60% (Table 1, entries 1 and 2). We assumed that LHMDS conditions were not conducive to the formation of stable enolates, thus, screened various metal bases. When using LDA as the base, the reaction only provided a complex mixture and trace amount of product with the oxidant CuCl$_2$ (Table 1, entry 3). The substrate was completely consumed under conditions including KHMDS or NaHMDS (Table 1, entries 4 and 5). Although we tried numerous oxidative conditions, the yield of oxidative coupling products was not significantly improved (Table 1, entries 6 to 11).

Results and discussion

According to the unsatisfactory experimental results described above, we assumed that substrate 3a may form more stable metal complexes with Cu(II) or Fe(III) ions

under the alkaline system, thereby inhibiting the process of oxidative coupling. Therefore, we envisaged the replacement of this stable complex by enol silyl ether (Table 2). We chose compound 3a as a substrate to first optimize the silyl bis-enol etherification condition. The desired silyl bis-enol ether product 6a was obtained with 21% yield in THF (2.0 ml) at -78°C under N$_2$ in the presence of LHMDS (0.243 mmol) and TBSOTf (0.162 mmol) (Table 2, entry 2). As previously mentioned, it was not conducive to obtain silyl enol ethers and could be broken down using LDA as the base (Table 2, entry 1). Encouraged by this result, we surveyed other bases including NaHMDS, KHMDS and Et$_3$N, and found that NaHMDS generated the best yield (58%) while Et$_3$N only generated monosilyl product (Table 2, entries 3–6).

With the enol bis-silyl ether 6a in hand, we intended to optimize the intramolecular enol oxidative coupling reaction (Table 3). Conducting the reaction in CH$_3$CN/THF at 0°C in the presence of CAN (0.24 mmol) and NaHCO$_3$ (0.48 mmol) exclusively afforded the coupling products in 77% isolated yield after 0.5 h (Table 3, entry 1). However, the main product 4a′ identified by X-ray analyses was an undesired stereoisomer. We intended to optimize the diastereomeric ratio (*dr*) by changing the ester group of 6 (Table 3, entries 2–5) and found that the isopropyl *dr* of ester substrate (3c) reached 4.9:1. We also explored the effect of different silicon groups (Table 3, entries 6–7). Unfortunately, changing the silicon groups did not decisively progress the EOC reaction. Finally, we evaluated different oxidants to optimize the *dr* of products (Table 3, entries 8–12). Cu(II) chloride and Fe(III) chloride produced the coupling products with 21% and 23% yields, but even more of the desilylation product 3 (Table 3, entries 8 and 10). Other metal oxidants, including Cu(acac)$_2$ and AgF, provided a complex mixture of product and raw product 6c (Table 3, entries 9 and 11), and the result of Koser's reagent (PhI(OH)OTs) was also unsatisfactory (Table 3, entry 12).

Conclusion

In conclusion, we developed an efficient method of constructing the spiro[bicyclo[3.2.2]nonane] system by intramolecular enol oxidative coupling reaction. Although the diastereomeric ratio of products is embarrassing, the high yield of this remote oxidative coupling reaction to build rigid spiro[bicyclo[3.2.2]nonane] structures is encouraging. Our findings once again confirm the practicality of enol oxidative coupling reactions in natural products and provide a new strategy for the synthesis of spiroaspertrione A. Further study for the total synthesis of spiroaspertrione A is underway in our laboratory.

Data availability statement

Author contributions

AM and ZS designed the project and wrote the manuscript. ZS, SL, JZ, XZ, JP, and JZ performed the experiments. All authors contributed to the article and approved the submitted version.

Funding

Acknowledgments

Conflict of interest

Publisher's note

Supplementary material

The Supplementary Material for this article can be found online at: https://www.frontiersin.org/articles/10.3389/fchem.2022.1022533/full#supplementary-material

References

Baran, P. S., Richter, J. M., and Lin, D. W. (2005). Direct coupling of pyrroles with carbonyl compounds: Short enantioselective synthesis of (S)-Ketorolac. *Angew. Chem.* 117, 615–618. doi:10.1002/ange.200462048

Baron, P. S. (2006). Enantioselective total synthesis of avrainvillamide and the stephacidins. *J. Am. Chem. Soc.* 128, 8678–8693. doi:10.1021/ja061660s

Bush, K. (2015). Synergistic MRSA combinations. *Nat. Chem. Biol.* 11, 832–833. doi:10.1038/nchembio.1935

Chen, W., and Liu, Q. (2021). Recent advances in the oxidative coupling reaction of enol derivatives. *Chin. J. Org. Chem.* 41, 3414–3430. doi:10.6023/cjoc202104058

Csáký, A. G., and Plumet, J. (2001). Stereoselective coupling of ketone and carboxylate enolates. *Chem. Soc. Rev.* 30, 313–320. doi:10.1039/B104000F

DeMartino, M. P., Chen, K., and Baran, P. S. (2008). Intermolecular enolate heterocoupling: Scope, mechanism, and application. *J. Am. Chem. Soc.* 130, 11546–11560. doi:10.1021/ja804159y

Dessau, R. M., and Heiba, E. A. I. (1974). Oxidation by metal salts. XII. Novel one-step synthesis of 1, 4-diketones. *J. Org. Chem.* 93, 3457–3459. doi:10.1021/jo00937a053

Ekebergh, A., Karlsson, I., Mete, R., Pan, Y., Börje, A., and Ma˚rtensson, J. (2011). Oxidative coupling as a biomimetic approach to the synthesis of scytonemin. *Org. Lett.* 13, 4458–4461. doi:10.1021/ol201812n

Fuda, C., Hesek, D., Lee, M., Morio, K. I., Nowak, T., and Mobashery, S. (2005). Activation for catalysis of penicillin-binding protein 2a from methicillin-resistant Staphylococcus a ureus by bacterial cell wall. *J. Am. Chem. Soc.* 127, 2056–2057. doi:10.1021/ja0434376

Fujii, T., Hirao, T., and Ohshiro, Y. (1992). Oxovanadium-induced oxidative desilylation for the selective synthesis of 1, 4-diketones. *Tetrahedron Lett.* 33, 5823–5826. doi:10.1016/0040-4039(92)89041-A

Gonzales, P. R., Pesesky, M. W., Bouley, R., Ballard, A., Biddy, B. A., Suckow, M. A., et al. (2015). Synergistic, collaterally sensitive β-lactam combinations suppress resistance in MRSA. *Nat. Chem. Biol.* 11, 855–861. doi:10.1038/nchembio.1911

Guo, F., Clift, M. D., and Thomson, R. J. (2012). Oxidative coupling of enolates, enol silanes, and enamines: Methods and natural product synthesis. *Eur. J. Org. Chem.* 2012, 4881–4896. doi:10.1002/ejoc.201200665

He, Y., Hu, Z., Sun, W., Li, Q., Li, X. N., Zhu, H., et al. (2017). Spiroaspertrione A, a bridged spirocyclic meroterpenoid, as a potent potentiator of oxacillin against methicillin-resistant *Staphylococcus aureus* from *Aspergillus* sp. TJ23. *J. Org. Chem.* 82, 3125–3131. doi:10.1021/acs.joc.7b00056

Jones, B. T., Avetta, C. T., and Thomson, R. J. (2014). Total synthesis of propolisbenzofuran B. *Chem. Sci.* 5, 1794–1798. doi:10.1039/C4SC00356J

Kise, N., Tokioka, K., Aoyama, Y., and Matsumura, Y. (1995). Enantioselective synthesis of 2, 3-disubstituted succinic acids by oxidative homocoupling of optically active 3-acyl-2-oxazolidones. *J. Org. Chem.* 60, 1100–1101. doi:10.1021/jo00110a003

Kohno, Y., and Narasaka, K. (1995). Oxidative generation of α-radicals of carbonyl compounds from the α-stannyl derivatives and their reactions with electron-rich olefins. *Bull. Chem. Soc. Jpn.* 68, 322–329. doi:10.1246/bcsj.68.322

Konkol, L. C., Guo, F., Sarjeant, A. A., and Thomson, R. J. (2011). Enantioselective total synthesis and studies into the configurational stability of bismurrayaquinone A. *Angew. Chem. Int. Ed.* 50, 9931–9934. doi:10.1002/anie.201104726

Krawczuk, P. J., Schöne, N., and Baran, P. S. (2009). A synthesis of the carbon skeleton of maoecrystal V. *Org. Lett.* 11, 4774–4776. doi:10.1021/ol901963v

Li, Y. P., Li, Z. Q., Zhou, B., Li, M. L., Xue, X. S., Zhu, S. F., et al. (2019). Chiral spiro phosphoric acid-catalyzed friedel–crafts conjugate addition/ enantioselective protonation reactions. *ACS Catal.* 9, 6522–6529. doi:10.1021/acscatal.9b01502

Long, S. W., Olsen, R. J., Mehta, S. C., Palzkill, T., Cernoch, P. L., Perez, K. K., et al. (2014). PBP2a mutations causing high-level ceftaroline resistance in clinical methicillin-resistant *Staphylococcus aureus* isolates. *Antimicrob. Agents Chemother.* 58, 6668–6674. doi:10.1128/AAC.03622-14

Martin, C. L., Overman, L. E., and Rohde, J. M. (2008). Total synthesis of (±)-actinophyllic acid. *J. Am. Chem. Soc.* 130, 7568–7569. doi:10.1021/ja803158y

Martin, C. L., Overman, L. E., and Rohde, J. M. (2010). Total synthesis of (±)-and (−)-actinophyllic acid. *J. Am. Chem. Soc.* 132, 4894–4906. doi:10.1021/ja100178u

Murarka, S., and Antonchick, A. P. (2018). Metal-catalyzed oxidative coupling of ketones and ketone enolates. *Synthesis* 50, 2150–2162. doi:10.1055/s-0037-1609715

Nagaraju, K., and Ma, D. (2018). Oxidative coupling strategies for the synthesis of indole alkaloids. *Chem. Soc. Rev.* 47, 8018–8029. doi:10.1039/C8CS00305J

Rathke, M. W., and Lindert, A. (1971). Reaction of ester enolates with copper (II) salts. Synthesis of substituted succinate esters. *J. Am. Chem. Soc.* 93, 4605–4606. doi:10.1021/ja00747a051

Renaud, P., and Fox, M. A. (1988). Reaction of dilithiated carboxylic acids with iodine: Evidence for the formation of a radical anion intermediate. *J. Org. Chem.* 53, 3745–3752. doi:10.1021/jo00251a015

Richter, J. M., Whitefield, B. W., Maimone, T. J., Lin, D. W., Castroviejo, M. P., and Baran, P. S. (2007). Scope and mechanism of direct indole and pyrrole couplings adjacent to carbonyl compounds: Total synthesis of acremoauxin A and oxazinin 3. *J. Am. Chem. Soc.* 129, 12857–12869. doi:10.1021/ja074392m

Robinson, E. E., and Thomson, R. J. (2018). A strategy for the convergent and stereoselective assembly of polycyclic molecules. *J. Am. Chem. Soc.* 140, 1956–1965. doi:10.1021/jacs.7b13234

Ryter, K., and Livinghouse, T. (1998). Dichloro (2, 2, 2-trifluoroethoxy) oxovanadium (V). A remarkably effective reagent for promoting one-electron oxidative cyclization and unsymmetrical coupling of silyl enol ethers. *J. Am. Chem. Soc.* 120, 2658–2659. doi:10.1021/ja973585e

Teng, M., Zi, W., and Ma, D. (2014). Total synthesis of the monoterpenoid indole alkaloid (±)-Aspidophylline A. *Angew. Chem. Int. Ed.* 53, 1814–1817. doi:10.1002/anie.201310928

Van Hal, S. J., Paterson, D. L., and Gosbell, I. B. (2011). Emergence of daptomycin resistance following vancomycin-unresponsive *Staphylococcus aureus* bacteraemia in a daptomycin-naïve patient—A review of the literature. *Eur. J. Clin. Microbiol. Infect. Dis.* 30, 603–610. doi:10.1007/s10096-010-1128-3

Walsh, T. R., Weeks, J., Livermore, D. M., and Toleman, M. A. (2011). Dissemination of NDM-1 positive bacteria in the New Delhi environment and its implications for human health: An environmental point prevalence study. *Lancet Infect. Dis.* 11, 355–362. doi:10.1016/S1473-3099(11)70059-7

Wei, Y., Zhao, D., and Ma, D. (2013). Total synthesis of the indole alkaloid (±)-and (+)-Methyl N-decarbomethoxychanofruticosinate. *Angew. Chem.* 125, 13226–13229. doi:10.1002/ange.201307788

Xie, J., and Huang, Z. Z. (2010). The cascade carbo-carbonylation of unactivated alkenes catalyzed by an organocatalyst and a transition metal catalyst: A facile approach to γ-diketones and γ-carbonyl aldehydes from arylalkenes under air. *Chem. Commun.* 46, 1947–1949. doi:10.1039/B921310D

Yeung, C. S., and Dong, V. M. (2011). Catalytic dehydrogenative cross-coupling: Forming carbon– carbon bonds by oxidizing two carbon-hydrogen bonds. *Chem. Rev.* 111, 1215–1292. doi:10.1021/cr100280d

You, L., Liang, X. T., Xu, L. M., Wang, Y. F., Zhang, J. J., Su, Q., et al. (2015). Asymmetric total synthesis of propindilactone G. *J. Am. Chem. Soc.* 137, 10120–10123. doi:10.1021/jacs.5b06480

Zi, W., Xie, W., and Ma, D. (2012). Total synthesis of akuammiline alkaloid (−)-vincorine via intramolecular oxidative coupling. *J. Am. Chem. Soc.* 134, 9126–9129. doi:10.1021/ja303602f

Zuo, Z., and Ma, D. (2011). Enantioselective total syntheses of communesins A and B. *Angew. Chem. Int. Ed.* 50, 12008–12011. doi:10.1002/anie.201106205

Zuo, Z., Xie, W., and Ma, D. (2010). Total synthesis and absolute stereochemical assignment of (−)-communesin F. *J. Am. Chem. Soc.* 132, 13226–13228. doi:10.1021/ja106739g

Phytochemical composition, antimicrobial activities, and cholinesterase inhibitory properties of the lichen *Usnea diffracta* Vain

Yi-Meng Hao[1], Yuan-Cong Yan[1], Qing Zhang[1], Bing-Qian Liu[1], Chang-Sheng Wu[2] and Li-Ning Wang[1]*

[1]School of Chinese Materia Medica, Tianjin University of Traditional Chinese Medicine, Tianjin, China, [2]State Key Laboratory of Microbial Technology, Institute of Microbial Technology, Shandong University, Qingdao, China

Lichens are important sources of versatile bioactive compounds. Two new dibenzofurans **(1–2)**, a multi-substituted single benzene ring **(3)**, and two organic acid compounds **(4–5)** along with 25 known compounds **(6–30)** were isolated from the lichen *Usnea diffracta* Vain. Their structures were identified by physicochemical properties and spectral analyses. Compounds **1–30** were tested for inhibitory activities against *Staphylococcus aureus, Escherichia coli*, and *Candida albicans* by the disk diffusion method and microdilution assay respectively. Compound **3** showed moderate inhibitory activities against *S. aureus* and *E. coli* with the inhibition zone (IZ) of 6.2 mm and 6.3 mm, respectively. Depside **10** exhibited good activity against *S.aureus* and *C. albicans* with 6.6 mm and 32 μg/ml, respectively. The acetylcholinesterase inhibitory activities of compounds **1, 2,** and **6−8** with the characteristic dibenzofuran scaffold were evaluated var anti-AChE assay and a molecular docking study. Compound **2** could better inhibit AChE at the concentration of 0.3 μmol/ml with a value of 61.07 $\pm$ 0.85%. The molecular docking study also demonstrated that compound **2** had the strongest binding affinity among the five dibenzofurans, and the "-CDOCKER Energy" value was 14.4513 kcal/mol.

1 Introduction

Lichens are autotrophic symbionts which are composed of mycobiontic fungi (mainly Ascomycetes) and one or more photosynthetic organisms (algae or cyanobacteria). Lichens have a remarkable ability to survive in extreme environmental conditions ranging from deserts to polar areas. Their specific secondary metabolites can protect them from physical and biological attacks (Reddy et al., 2019; Popovici et al., 2022). Lichens are not only ecologically important but also significant medicinal natural product resources, especially phenolic secondary metabolites, including phenols (orinol), dibenzofurans (usnic acid and its derivatives), depsidones (norstictic acid), depsides (diffractaic acid), depsones (picrolichenic acid), and pulvinic acid derivatives (vulpinic acid). There are about 26,000 species of lichens belonging to 500 genera in the world, among which more than 360 *Usnea* species are found (Salgado et al., 2018).

Usnea diffracta Vain, belonging to the genus *Usnea*, is widely used as a folk medicine for the treatment of diarrhea, stomachache, ulcer, tuberculosis, pneumonia, malaria, wounds, and

parasitic diseases (Singh B. et al., 2016; Zhao et al., 2019). Depsidones, depsides, depsones, quinones, polyphenolics, polysac-charides, and dibenzofurans are the main compounds of *Usnea* (Salgado et al., 2018). Previous studies have showed numerous good pharmacological activities of *U. diffracta*, such as antimicrobial, antioxidant, antitumor, antiviral, anti-inflammatory, cardiovascular protective, anti-genotoxic, and antiproliferative effects (Behera et al., 2012; Lai et al., 2013; Ceker et al., 2015; Koparal, 2015; Nishanth et al., 2015; Singh S. et al., 2016; Vanga et al., 2017; Yang et al., 2017). It is noteworthy that most of these pharmacological activities are attributed to the availability of bioactive depsides and dibenzofuran derivatives (especially usnic acid) (Sun et al., 2016). *Usnea diffracta* and its major constituent usnic acid are potent antimicrobial agents to inhibit growth of different planktonic bacteria and fungi strains (Helena et al., 2012).

Alzheimer's disease (AD) is a serious degenerative disorder of the central nervous system, characterized by a variety of symptoms, including memory loss, emotional behavior, and cognitive impairment (Singh et al., 2013). One of its pathogeneses mainly includes cholinergic system damage. The cholinergic system of AD patients involves two main cholinesterases (ChE), acetylcholin-esterase (AChE) and butyrylcholinesterase (BChE) (Colovic Mirjana et al., 2013). AChE inhibitors mainly act on the catalytic active site (CAS) at the bottom of AChE, which can relieve the symptoms of mild-to-moderate AD patients (Zhu et al., 2019). At present, cholinesterase inhibitors are mainly selective acetycholinesterase inhibitors (AChEIs) such as tacrine, donepezil, and galantamine (Greig et al., 2005; Furukawa-Hibi et al., 2011; Wu et al., 2016). These drugs have greater side effects or lower response rates in the long-term treatment of patients with mild-to-moderate AD. In order to find natural lead compounds for the treatment of Alzheimer's disease, benzofurans, as an important pharmacophore, have received extensive attention in the past few years because of their attractive cholinesterase inhibitory activity (Rizzo et al., 2012; Khanam

and Shamsuzzaman, 2015; Delogu et al., 2016; Wang et al., 2017). The bibenzofuran structures of usnic acid derivatives are similar to those of galantamine, an anticholinesterase drug for AD. Usnic acid enantiomers show antioxidant and anti-inflammatory activities, which are involved in AD pathogenesis (Araújo et al., 2015; Cazarin et al., 2020).

Hence, in the current research, 30 compounds including five new compounds were isolated and identified from *U. diffracta*. The complete isolation and structural elucidation of all compounds and their antimicrobial activities against two pathogenic bacteria including one Gram-positive strain (*Staphylococcus aureus*) and one Gram-negative bacterial strain (*Escherichia coli*) and fungus strain (*Candida albicans*) were described. Among them, the inhibitory activities on AChE of usnic acid derivatives **1**, **2**, and **6–8** were reported. The interaction between these compounds and the active centers of AChE were investigated by molecular docking.

2 Results

2.1 Isolated compounds from *Usnea diffracta* Vain

Thirty compounds (Figure 1) were separated and identified from the ethanol extract of the dry lichen body of *U. diffracta* Vain, including five dibenzofuran compounds (**1**, **2**, and **6–8**), eleven multi-substituted single benzene ring compounds (**3** and **13–22**) and four depsides compounds (**9–12**), four organic acid compounds (**4**, **5**, **24**, and **25**), one organic acid ester compound (**23**), two fatty acids containing furan ring (**26** and **27**), one furfural compound (**28**), one amino acid compound (**29**), and one nucleoside compound (**30**). After searching the SciFinder database, compounds **1–5** were identified as new compounds and their structural analysis as follows.
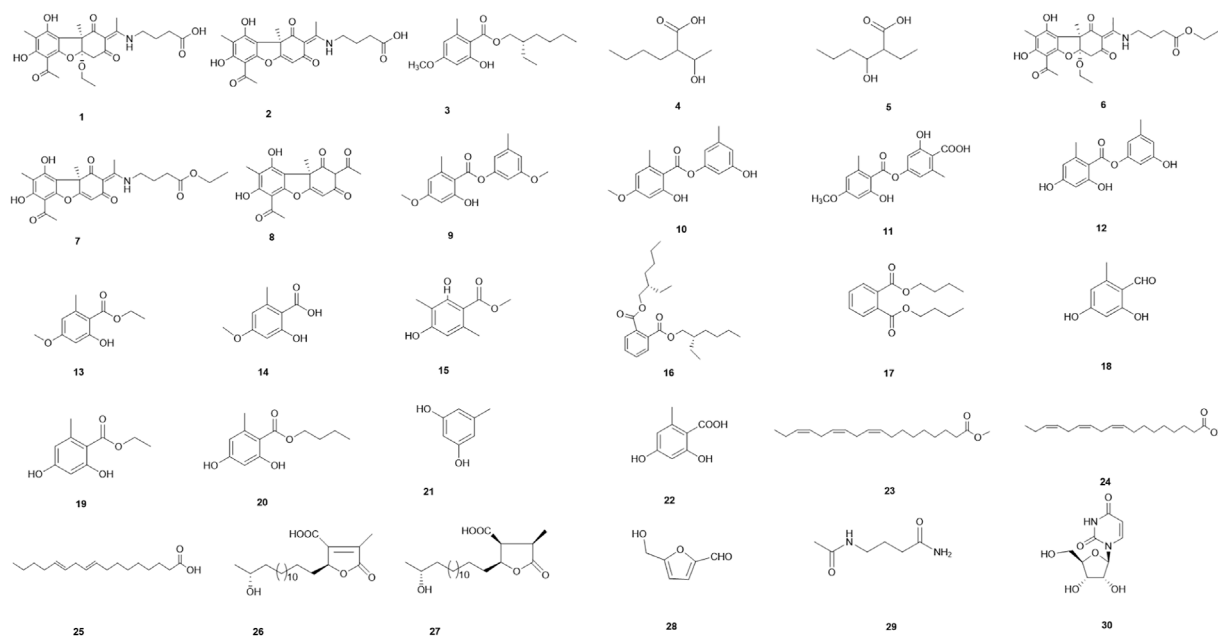
FIGURE 1
Chemical structures of compounds **1–30**.

TABLE 1 ^{1}H and ^{13}C NMR data (δ in ppm, J in Hz) for 1–5.

No.	1 δ_H	1 δ_C	2 δ_H	2 δ_C	3 δ_H	3 δ_C	4 δ_H	4 δ_C	5 δ_H	5 δ_C
1		200		196.2		105.5		179.6		179.2
2		106.8		100.6	11.95 (1H, s)	165.7	2.28 (1H, m)	55.4	2.27 (1H, m)	55.6
3		194.1		188	6.33 (1H, d, J = 2.4)	98.8	1.51 (1H, m)	29.6	3.67 (1H, m)	73.0
							1.58 (1H, m)			
4	3.10 (1H, d, J = 15.4)	43.7	5.87 (1H, s)	101.4		163.8	1.34 (2H, m)	31.0	1.50 (2H, m)	38.1
	3.15 (1H, d, J = 15.4)									
4a		111.6		172						
5a		158.5		154.8						
5					6.28 (1H, d, J = 2.4)	111.1	1.34 (2H, m)	23.8	1.38 (2H, m)	19.9
6		102.3		99.9		143.0	0.91 (3H, t, J = 6.9)	14.3	0.94 (3H, m)	14.3
7		163.8	13.40 (1H, s)	161.5	2.52 (3H, s)	24.6	3.86 (1H, m)	69.7	1.60 (2H, m)	23.1
8		106.5		105.3		172.2	1.19 (3H, d, J = 6.3)	21.3	0.94 (3H, m)	12.4
9		161.2	12.31 (1H, s)	156.7	4.27 (2H, m)	67.6				
9a		107.6		104.2						
9b		61.2		55.3						
10	1.55 (3H, s)	19.2	1.64 (3H, s)	30.7	1.71 (1H, m)	38.8				
11		176.1		174	1.39 (2H, m)	30.6				
12	2.52 (3H, s)	18.0	2.58 (3H, s)	17.1	1.32 (2H, m)	29.0				
13	1.96 (3H, s)	7.4	1.97 (3H, s)	6.5	1.32 (2H, m)	23.0				
14		202.8		199.9	0.90 (3H, t, J = 7.0)	14.0				
15	2.55 (3H, s)	31.4	2.63 (3H, s)	30	1.45 (2H, m)	24.0				
16	3.88 (1H, q, J = 7.0)	60.7			0.94 (3H, t, J = 7.5)	11.1				
	3.87 (1H, q, J = 7.0)									
17	1.23 (3H, t, J = 7.0)	15.7								
18										
1′	3.59 (2H, t, J = 7.3)	44.2	3.54–3.59 (2H, m)	41.8						
2′	1.94–2.01 (2H, m)	25.4	1.86 (2H, m)	23						
3′	2.43 (2H, t, J = 7.1)	31.7	2.35 (2H, t, J = 7.3)	29.7						
4′		176.2								
5′										
6′										
-OCH$_3$					3.80 (3H, s)	55.3				
-NH-			13.05 (1H, t, J = 5.2)							
-COOH				172.7						
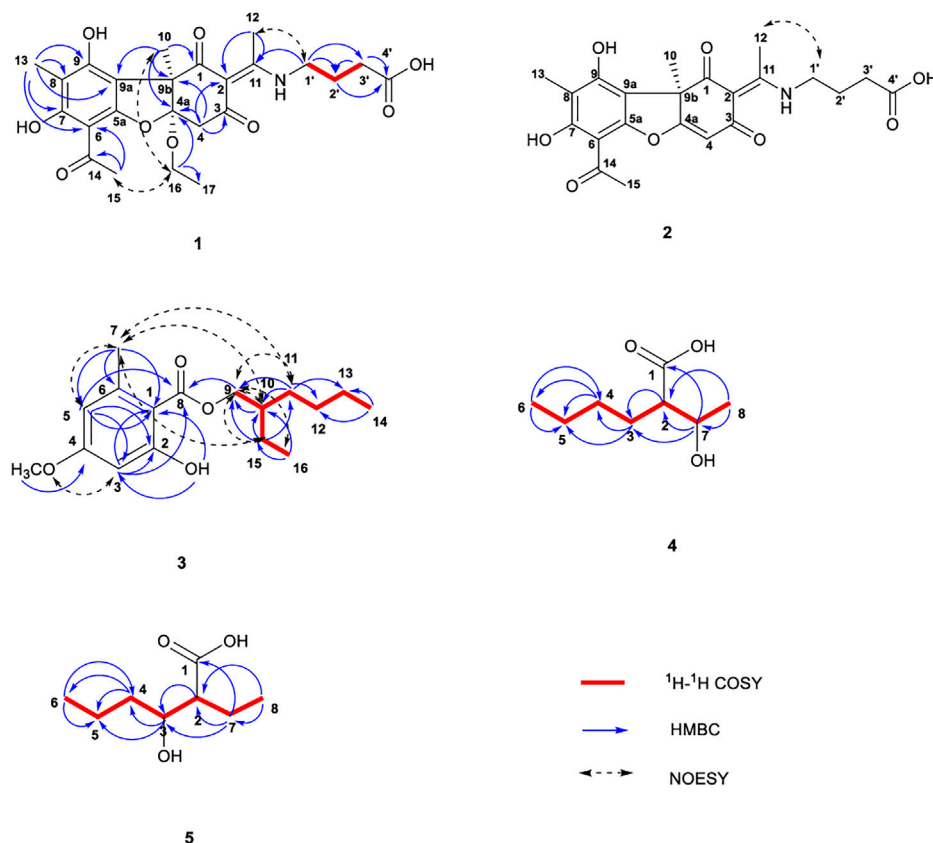
FIGURE 2
Chemical structures of compounds **1–5** along with the key ^{1}H-^{1}H COSY, HMBC, and NOESY interactions.

2.1.1 Usenamine G (1)

Pale yellow oil (CH$_3$OH). $[\alpha]_D^{25}$ -132.0° (c 0.05, CH$_3$OH); CD (0.59 mg/ml, CH$_3$OH) λmax ($\Delta\varepsilon$) 304 (−2.19) nm, 278 (+1.74) nm; UV (CH$_3$OH) λmax (log ε): 223 (3.92) nm, 296 (4.16) nm; IR (KBr): ν_{max} 3426, 1639, 1541, 1420, and 1015 cm^{-1}; ^{1}H NMR (500 MHz, CD$_3$OD) and ^{13}C NMR (125 MHz, CD$_3$OD) data; HR-ESI-MS m/z 476.1931 [M + H]$^+$ (Calcd. For C$_{24}$H$_{29}$NO$_9$, 476.1921) (Table 1; Supplementary Figures S1–S11).

The ^{1}H NMR data of **1** in CD$_3$OD showed signals for five methyl groups: δ 1.23 (3H, t), 1.55 (3H, s), 1.96 (3H, s), 2.52 (3H, s), and 2.55 (3H, s); four methylene groups: δ 2.43 (2H, t), 1.94–2.01 (2H, m), 3.59 (2H, t), 3.88 (1H, q) and 3.87 (1H, q); two single hydrogen signals: δ 3.10 (1H, d) and 3.15 (1H, d). The coupling constants at δ 3.10 and 3.15 are both 15.4 Hz, which is speculated to be a carbon coupling hydrogen signal. The ^{13}C NMR spectrum showed 24 carbon resonances that consisted of three carbonyl signals (δ 202.8, 200.0, and 194.1), aromatic carbon signals and alkene carbon signals (δ 161.2, 163.8, 158.5, 107.6, 106.8, 106.5, and 102.3), the chemical shifts 176.2 and 176.1 may contain carboxyl signals, as well as oxycarbon and aliphatic carbon signals. According to the DEPT 135 spectra (Supplementary Figure S11), five methylenes (δ 60.7, 44.2, 43.7, 31.7, and 25.4) were existed in compound **1**. The HSQCs (Supplementary Figure S8) indicated directly linked hydrocarbon correlations. Combined with ^{1}H-^{1}H COSY, the correlations (Figure 2; Supplementary Figure S7) from δ_H 3.10 to δ_H 3.15, δ_H 1.23 to δ_H 3.88/3.87, and δ_H 1.97 to δ_H 2.43/3.59 further verified the existence of

-CH$_2$-, -OCH$_2$CH$_3$, and -CH$_2$-CH$_2$-CH$_2$-. The HMBCs (Figure 2; Supplementary Figure S9) from δ_H 1.55 to δ_C 200.0/111.6/107.6/ 61.2 indicated that the angular methyl group was located at C-9b, while those from δ_H 2.55 to δ_C 102.3/202.8 suggested that C-14 was connected to C-6. The correlations from δ_H 2.52 to δ_C 106.8/ 176.1 established the connection of C-11 with C-2. The HMBCs from δ_H 3.88/3.87 to δ_C 15.7/111.6 suggested the connection of an ethoxy group at C-4a and from δ_H 2.43/1.94–2.01 to δ_C 176.2 and δ_H 3.59 to δ_C 176.1 revealed the presence of a C-2 enamine moiety in compound **1**. The configuration of the double bond was determined by the NOESY data (Figure 2; Supplementary Figure S10) δ_H (2.52) - δ_H (3.59) as *E*, analysis of the correlation between δ_H (1.55/2.55) and δ_H (3.88/3.87) dedicated that 9b-CH$_3$ and 4a-OCH$_2$CH$_3$ were on the same side. In addition, the CD spectrum (Supplementary Figure S2) of compound **1** was compared with the related literature previously published (Yu X. et al., 2016). Compound **1** presented one negative maximum at 298 nm and positive at 278 nm, which was consistent with the CD spectrum of Usenamine B, indicating that the absolute configuration of compound **1** was 4a*R*/9b*R*, as represented in Figure 2. Overall, compound **1** was identified as a new compound by SciFinder inquiry, named Usenamine G.

2.1.2 Usenamine H (2)

Pale yellow oil (CH$_3$OH). $[\alpha]_D^{25}$ +104.0° (c 0.05, CH$_3$OH); CD (0.59 mg/mL, CH$_3$OH) λmax ($\Delta\varepsilon$) 332 (+0.59) nm; ^{1}H NMR (600 MHz, DMSO-d$_6$) and ^{13}C NMR (150 MHz, DMSO-d$_6$) data;

HR-ESI-MS m/z 430.1518 [M + H]$^+$ (Calcd. For $C_{22}H_{23}NO_8$, 430.1502) (Table 1; Supplementary Figures S12–S16). A comparison of the ^{1}H and ^{13}C NMR data of compound **2** with the ^{1}H (500 MHz, CD_3OD) and ^{13}C NMR (125 MHz, CD_3OD) data of **1** revealed their structural similarities, except for the presence of alkene proton signal at δ_H 5.87 (1H, s)/δ_C 101.4 (C-4), and the absence of -OCH_2 - (C-16) and -CH_3 segments (C-17). The NOESY correlation (Supplementary Figure S16) between H-12 (δ 2.58) and H-1′ (δ 3.54–3.59) suggested an E-configuration for the double bond and it was the same as compound **1** (Figure 2). The similar sign of the specific rotation $[\alpha]_D^{25}$ +104.0° (c .05, CH_3OH) and positive at 333 nm, which was consistent with the CD spectrum of Usneamine A (Yu X. et al., 2016), indicating that the absolute configuration was 9bR, as represented in Figure 2. The spectroscopic data were in accord with the literature (Bruno et al., 2013), compound **2** was identified as a new compound by SciFinder inquiry, named Usneamine H.

2.1.3 2-Ethylhexyl-4-methoxy orsellinate (3)

White oil (CH_3OH). $[\alpha]_D^{25}$ -12.0° (c 0.05, CH_3OH); CD (0.09 mg/ml, CH_3OH) λmax (Δε) 227 (+0.28) nm, 253 (+0.08) nm, 266 (-0.06) nm, 227 (+0.03) nm; UV (CH_3OH) λmax (log ε): 215 (4.27) nm, 263 (4.03) nm, 301 (3.61) nm; IR (KBr): ν_{max} 3462, 2960, 2931, 1653, 1617, 1576, 1456, 1257, 1159 cm^{-1}; ^{1}H NMR (500 MHz, $CDCl_3$) and ^{13}C NMR (125 MHz, $CDCl_3$) data; HR-ESI-MS m/z 295.1897 [M + H]$^+$ (Calcd. For $C_{17}H_{26}O_4$, 295.1909) (Table 1; Supplementary Figures S17–S27).

The ^{1}H NMR data of **3** in $CDCl_3$ showed signals for a hydroxyl: δ 11.95 (1H, s); two m-position hydrogen of benzene ring: δ 6.33 (1H, d, J = 2.4 Hz) and 6.28 (1H, d, J = 2.4 Hz); a -O-CH_2- fragment: δ 4.27 (2H, m); a methoxy group: δ 3.80 (3H, s); a methyl attached to the benzene ring: δ 2.52 (3H, s); an aliphatic chain: δ 1.71 (1H, m), 1.45 (2H, m), 1.39 (2H, m), and 1.32 (4H, m); and two terminal methyl of aliphatic chain: δ 0.94 (3H, t, J = 7.5 Hz) and 0.90 (3H, t, J = 7.0 Hz). The ^{13}C NMR spectrum revealed 17 carbon resonances that consisted of a -COO- fragment signal (δ 172.2), a -O-CH_2- fragment signal (δ 67.6), a -O-CH_3 fragment signal (δ 55.3), six aromatic carbon signals (δ 105.5, 165.7, 98.8, 163.8, 111.1, and 143.0) and eight aliphatic carbon signals (δ 38.8, 30.6, 29.0, 24.6, 24.0, 23.0, 14.0, and 11.1). The DEPT spectra (Supplementary Figure S27) demonstrated five methylene signals: δ 67.6, 30.6, 29.0, 24.0, and 23.0. The HSQCs (Supplementary Figure S24) indicated directly linked hydrocarbon correlations. According to the HMBCs (Figure 2; Supplementary Figure S25), correlations from δ_H (0.94) to δ_C (24.0/38.8), δ_H (0.90) to δ_C (23.0/29.0), δ_H (1.32) to δ_C (14.0/23.0/29.0/30.6), and δ_H (1.39) to δ_C (23.0/29.0) showed the presence of -CH_2-CH_2-CH_2-CH_3 fragment in the aliphatic chain, and δ_H (0.94) to δ_H (1.45) showed -CH_2-CH_3. The correlations from δ_H (1.38) to δ_C (38.0/67.6), δ_H (1.45) to δ_C (67.6/38.8/11.1/30.6), δ_H (1.71) to δ_C (67.6/24.0/11.1/30.6), and δ_H (4.27) to δ_C (23.0/30.6/38.8/172.7) together indicated the fragment of CH_3-CH_2-CH-CH_2-OOC-, in which -CH- was linked to the butyl group. The δ_H (2.51)–δ_C (143.0/111.1/105.5) and δ_H (3.80)–δ_C (163.8) revealed that the methyl and oxymethyl existed on the benzene ring. At the same time combined with COSY correlations (Supplementary Figure S23), the planar structure of compound **3** was shown in Figure 2. The main hydrogen-related signals shown by the NOESY spectra (Figure 2; Supplementary Figure S26) were δ_H (4.27)–δ_H (0.94/1.32/1.39/1.45/1.71), δ_H (2.51)–δ_H (1.32/1.39/1.45/1.71), δ_H (6.33)–δ_H (3.80), and δ_H (6.28)–δ_H (2.52). In addition, the CD spectrum (Supplementary Figure S18) of compound **3** was compared with the related literature previously published (Nahrstedt

et al., 1990). Compound **3** presented one negative which was consistent with (S)-2-Methylbutan-1-yl-β-D-glucopyranoside, indicating that the absolute configuration of C-10 was S. Through SciFinder database query, it was confirmed that compound **3** was a new compound and shared the similar structure with 2-ethylhexyl orsellinate (Bui et al., 2020), named 2-ethylhexyl-4-methoxy orsellinate.

2.1.4 2-(1-Hydroethyl)-hexanoic acid (4)

White oil (CH_3OH). $[\alpha]_D^{25}$ -8.0° (c 0.07, CH_3OH); CD (0.56 mg/mLl CH_3OH) λmax (Δε) 199 (-0.22) nm; UV (CH_3OH) λmax (log ε): 202 (2.68) nm, 222 (2.35) nm, 274 (1.70) nm; IR (KBr): ν_{max} 3416, 2958, 2932, 1694, 1403, 1204, and 1119 cm^{-1}; ^{1}H NMR (600 MHz, CD_3OD) and ^{13}C NMR (150 MHz, CD_3OD) data; HR-ESI-MS m/z 159.1038 [M−H]$^-$ (Calcd. For $C_8H_{16}O_3$, 159.1021) (Table 1; Supplementary Figures S28–S38).

The ^{1}H NMR data of compound **4** in CD_3OD showed signals for 14 hydrogen atoms. According to the chemical shift, 1.19 (3H, d, J = 6.3 Hz), it is inferred that there is a -CH-CH_3 fragment in the structure, and the shift 0.91 (3H, t, J = 6.9 Hz) showed the existence of -CH_2-CH_3. The ^{13}C NMR spectrum showed eight carbon resonances that consisted of one carbonyl signals (δ 179.6), one -O-C- fragment signal (δ 69.7), one -O-CH_3 fragment signal (δ 55.4), and five aliphatic carbon signals (δ 31.0, 29.6, 23.8, 21.3, and 14.3). According to the DEPT 135 spectra (Supplementary Figure S38), three methylenes (δ 31.0, 29.6, and 23.8) were existed in compound **4**. The HSQC spectrum (Supplementary Figure S35) revealed directly linked hydrocarbon correlations. Correlations presented in ^{1}H-^{1}H COSY (Figure 2; Supplementary Figure S34) from δ_H (1.19) to δ_H (3.86), δ_H (3.86) to δ_H (2.28), δ_H (1.51/1.58) to δ_H (1.34/2.28), and δ_H (1.34) to δ_H (.91) further verified the existence of -CH-CH_3 and -CH_2-CH_2-CH_3. The HMBCs (Figure 2; Supplementary Figure S36) from δ_H (.91/1.51/1.58) to δ_C (23.8/31.0) and δ_H (1.34) to δ_C (14.3/23.8/31.0) indicated the presence of CH_3-CH_2-CH_2-CH_2-. The correlations from δ_H (2.28) to δ_C (21.3/29.6/69.7) and δ_H (3.86) to δ_C (29.6/55.4/179.6) showed the fragment of $COOH$-CH-CH-OH. The signal of δ_H (1.19) - δ_C (55.4/69.7) confirmed that the terminal methyl (C-8) was connected to C-7. The main hydrogen-related signals shown by the NOESY spectra (Supplementary Figure S37) were δ_H (2.28) - δ_H (3.86/1.51/1.58/1.34/1.21) and δ_H (3.86) - δ_H (1.51/1.58/1.21). The structure and spectroscopic data were shown in Figure 2 and Table 1. Overall, compound **4** was identified as a new compound by SciFinder inquiry, named 2-(1-hydroethyl)-hexanoic acid. Its configuration needs to be further determined.

2.1.5 2-Ethyl-3-hydroxyhexanoic acid (5)

White oil (CH_3OH). $[\alpha]_D^{25}$ -8.0° (c 0.05, CH_3OH); ^{1}H NMR (600 MHz, CD_3OD) and ^{13}C NMR (150 MHz, CD_3OD) data; HR-ESI-MS m/z 159.0546 [M−H]$^-$ (Calcd. For $C_8H_{16}O_3$, 159.1021) (Table 1; Supplementary Figures S39–S46).

A comparison of the ^{1}H and ^{13}C NMR data of compound **5** and compound **4** revealed their structural similarities, except for the presence of two proton signals at δ_H 1.60 (2H, m)/δ_C 23.1 (C-7) and one proton signal at δ_H 3.67 (1H, m)/δ_C 73.0 (C-3). According to the chemical shift, it is inferred that the hydroxyl group (C-7) of compound **4** was connected to the C-3 in compound **5**. Also, the ^{1}H NMR data of compound **5** showed signals for 14 hydrogen and the ^{13}C NMR spectrum showed eight carbon resonances. According to the

TABLE 2 Antimicrobial activities of compounds from *U. diffracta* Vain. (The IZ value indicated the diameter of the inhibition zone at 3.2 µg/disk. The MIC value indicated the minimal inhibitory concentration. "—" indicated no inhibitory activity in 3.2 µg/disk or 64 µg/ml.)

No.	IZ (mm)/S. aureus	No.	IZ (mm)/E. coli	No.	MIC(µg/ml)/C. albicans
1	—	1	—	1	64
2	—	2	—	2	64
3	6.2	3	6.3	3	—
4–8	—	4	—	4–5	No antifungal assay
9	6.4	5	—	6–9	64
10	6.6	6	—	10	32
11–17	—	7	—	11	—
18	6.6	8	—	12–15	64
19	—	9	—	16	—
20	—	10	—	17	64
21	—	11–29	—	18–25	—
22–30	—	30	6.3	26–27	64
DMSO	—	DMSO	—	28	—
Gentamicin sulfate	12.3	Gentamicin sulfate	12.4	29–30	64

DEPT 135 spectra (Supplementary Figure S46), three methylenes were existed in compound **5**. The HSQC spectrum (Supplementary Figure S43) revealed directly linked hydrocarbon correlations. Correlations presented in ^{1}H-^{1}H COSY (Supplementary Figure S42) from δ_H (1.50) to δ_H (3.67) and δ_H (1.60) to δ_H (0.94) further verified the existence of -CH$_2$-CH$_2$-CH-OH and -CH$_2$-CH$_3$. The relations of δ_H (0.94)–(1.60/3.67) showed that the -CH-COOH fragment was linked to -CH-OH and -CH$_2$-CH$_3$ fragment and δ_H (0.94)–(1.38) indicated that the terminal methyl was connected to the -CH$_2$-CH$_2$-. The correlations of H-2/C-1, 3, 4, 7, 8; H-3/C-1, 2, 4, 5; H-4/C-3, 5, 6; H-5/C-3, 4, 6; H-6/C-4, 5; H-7/C-1, 2, 3, 4, 8; and H-8/C-2, 7 were observed in HMBC (Supplementary Figure S44) and H-2/H-4, 7, 3 and H-6/H-4, 7, 5 in NOESY (Supplementary Figure S45). The structure and spectroscopic data were shown in Figure 2; Table 1. The configuration of the two chiral carbons could not be determined. Compound **5** was identified as a new compound by SciFinder inquiry, named 2-ethyl-3-hydroxyhexanoic acid (Wahl et al., 2001).

The known compounds isolated and identified by spectroscopic techniques were Usneamine F (**6**) (Yu X. et al., 2016), Usneamine E (**7**) (Yu X. et al., 2016), (+)-usnic acid (**8**) (Laxi et al., 2013), 2′-O-methylevernol (**9**) (Huneck et al., 1989), 3-hydroxy-5-methylphenyl-2-hydroxy-4-methoxy-6-methylbenzoate (**10**) (Yu X.L. et al., 2016), evernic acid (**11**) (Tang et al., 2015), lecanorin (**12**) (Bui et al., 2020), ethyl everninate (**13**) (Yu X.L. et al., 2016), evernesic acid (**14**) (Nishitoba et al., 1987), methyl-2,4-dihydroxy-3,6-dimethylbenzoate (**15**) (Feng et al., 2009), bis-(2S-ethylhexyl) benzene-1,2-dicarboxylate (**16**) (Su et al., 2009), dibutyl phthalate (**17**) (Li et al., 2009), orsellinaldehyde (**18**) (Zheng et al., 2012), ethyl orsellinate (**19**) (Tuan et al., 2020), *n*-butyl orsellinate (**20**) (Li et al., 2006), orcinol (**21**) (Eliwa et al., 2019), orsellinic acid (**22**) (Wang et al., 2009), α-linolenic acid methyl ester (**23**) (Zou et al., 2021), α-linolenic acid (**24**) (Qin et al., 2010), linoleic acid (**25**) (Zhao et al., 2020), constipatic acid (**26**) (Chester and Elix, 1979),

18R-hydroxy-dihydroalloprotolichesterinic acid (**27**) (Rezanka and Guschina, 2001), 5-hydromethyl furaldehyde (**28**) (Feng et al., 2011), 4-(acylamino)butyramides (**29**) (Graham et al., 1987), and uridine (**30**) (Gu et al., 2017); (Figure 1).

2.2 Antimicrobial activity

In this study, the antimicrobial activities of the isolated compounds were studied *in vitro*. The inhibition zone of the compounds against *S. aureus* and *E. coli* were determined by the disk diffusion method and the values of minimal inhibitory concentration (MIC) against *C. albicans* by microdilution assay. The results (Table 2) revealed that when the amount of compound was 3.2 µg/disk, the inhibition zone (IZ) of compounds **3**, **9**, **10**, and **18** were 6.2, 6.4, 6.6, and 6.6 mm, respectively, and others had no effect in the preliminary screening experiment of anti-*S. aureus*. Among them, **10** and **18** exhibited better antibacterial activities against *S. aureus* than other compounds, but lower than the positive control gentamicin sulfate. In addition, compounds **3** and **30** can better inhibit *E. coli* with IZ of 6.3 mm than other compounds at 3.2 µg/disk. The assay

TABLE 3 AChE inhibitory activities of five dibenzofurans from *U. diffracta* Vain.

Compound	AChE inhibition (% at 0.3 µmol/ml)
1	61.18 ± 1.16
2	67.56 ± 0.49
6	61.07 ± 0.85
7	57.61 ± 0.23
8	58.06 ± 0.73

TABLE 4 Binding interaction data of compounds **1**, **2**, and **6**–**8** docked into the active site gorge of AChE.

Ligand	-CDOCKER Energy (kcal/mol)	Interacting site	Residue	Type of interaction	Distance (Å)	Ligand interacting moiety
1	1.01935	Anionic subsite	Tyr133	H-bonded	2.12	C7-OH
		Anionic subsite	Tyr133	H-bonded	2.45	C14-C=O
			Val294	H-bonded	2.41	C4′-C=O
		Oxyanion hole	Gly120	H-bonded	2.82	C14-C=O
		Oxyanion hole	Gly120	Amide–Pi stacked	4.1	Benzene ring
		PAS	Tyr124	H-bonded	2.34	C1′-H
		PAS	Tyr124	H-bonded	2.49	C1′-H
		PAS	Tyr124	Pi–alkyl	4.49	C10
		PAS	Tyr341	Pi–cation	3.57	N
		PAS	Asp74	Attractive charge	5.58	N
		CAS	His447	Pi–alkyl	4.92	C17
		Anionic subsite	Tyr337	Pi–alkyl	4.09	C17
		Anionic subsite	Trp86	Pi–alkyl	5.44	C17
2	14.4513	Anionic subsite	Tyr133	H-bonded	2.33	C7-OH
		Oxyanion hole	Gly120	Amide–Pi stacked	4.02	Benzene ring
		PAS	Tyr124	H-bonded	2.45	C2′-H
		PAS	Tyr124	H-bonded	2.35	C2′-H
		Acyl pocket	Phe295	H-bonded	2.08	C4′-COOH
		PAS	Tyr341	Pi–cation	3.68	N
		Anionic subsite	Tyr337	Pi–alkyl	4.3	C10
		Anionic subsite	Trp86	Pi–alkyl	4.37	C10
6	−1.95894	Anionic subsite	Tyr133	H-bonded	2.28	C7-OH
		PAS	Tyr124	H-bonded	2.04	-NH-
		PAS	Tyr124	Pi–alkyl	5.2	C17
		PAS	Tyr341	H-bonded	2.57	C3-C=O
		PAS	Tyr341	Pi–cation	4.21	N
			Ser125	H-bonded	2.36	C16-H
			Ser125	H-bonded	2.2	C16-H
		Anionic subsite	Trp86	Pi–alkyl	4.28	C10
		Anionic subsite	Tyr337	Pi–alkyl	4.29	C10
		Oxyanion hole	Gly120	Amide–Pi stacked	4	Benzene ring
7	12.8461		Gly126	H-bonded	2.51	C4′-C=O
			Ser125	H-bonded	2.68	C4′-C=O
		Anionic subsite	Trp86	Pi–lone pair	2.88	C3-C=O
		Anionic subsite	Trp86	Pi–cation	4.54	N
		Anionic subsite	Glu202	Attractive charge	4.33	N
		PAS	Tyr124	Pi–lone pair	2.86	Benzene ring
		PAS	Tyr124	Pi–alkyl	4.34	C10

TABLE 4 (*Continued*) Binding interaction data of compounds 1, 2, and 6–8 docked into the active site gorge of AChE.

Ligand	-CDOCKER Energy (kcal/mol)	Interacting site	Residue	Type of interaction	Distance (Å)	Ligand interacting moiety
		PAS	Tyr341	Pi–Pi	4.67	Benzene ring
		Anionic subsite	Tyr337	Pi–Pi	5.73	Benzene ring
		Anionic subsite	Phe338	Pi–alkyl	4.99	C16
		Acyl pocket	Phe297	Pi–alkyl	4.78	C16
8	−3.65539	Oxyanion hole	Gly121	H-bonded	1.83	C14-C=O
		Oxyanion hole	Gly122	H-bonded	1.95	C14-C=O
		CAS	Ser203	H-bonded	2.24	C14-C=O
		Oxyanion hole	Ala204	H-bonded	2.14	C14-C=O
		Oxyanion hole	Gly120	H-bonded	2.68	C3-C=O
		CAS	His447	H-bonded	2.59	C1-C=O
		PAS	Tyr124	Pi–alkyl	5.86	Benzene ring
		PAS	Tyr341	Pi–alkyl	4.02	C16
		Anionic subsite	Tyr337	Pi–alkyl	3.99	C13
		Anionic subsite	Trp86	Pi–alkyl	4.87	C13

of anti-*C. albicans* showed that the MIC value of tested compound **10** was 32 μg/ml, which exhibited the strongest inhibitory activity among all compounds. In conclusion, the results of the preliminary screening demonstrated that compound **3** had certain inhibitory activities against *S. aureus* and *E. coli* but no anti-*C. albicans* activity at 64 μg/ml, compound **9** had certain inhibitory effect on *S. aureus* and *C. albicans* with MIC of 64 μg/ml. Furthermore, in this preliminary screening, compound **10** demonstrated the strongest inhibition against *S. aureus* and *C. albicans* among all compounds.

2.3 Acetylcholinesterase inhibitory activity

The activities of five dibenzofurans [Usneamine G (**1**), Usneamine H (**2**), Usneamine F (**6**), Usneamine E (**7**), and (+)-usnic acid (**8**)] against AChE were evaluated in the current work. Compound **2** (at the concentration of 0.3 μmol/ml) exhibited the strongest AChE inhibitory activity among the five compounds, with the inhibition value of 67.56 ± 0.49% (as shown in Table 3). Others also exhibited moderate AChE inhibition at the concentration of 0.3 μmol/ml with values of 61.18 ± 1.16%, 61.07 ± 0.85%, 57.61 ± 0.23%, and 58.06 ± 0.73%, respectively.

2.4 Molecular docking study

In order to study the binding affinity related to the inhibition of acetylcholinesterase, five compounds of dibenzofurans: Usneamine G (**1**), Usneamine H (**2**), Usneamine F (**6**), Usneamine E (**7**), and (+)-usnic acid (**8**) were simulated. The results of molecular docking revealed that the five compounds had good binding affinities with the active pockets of AChE, and the '-CDOCKER Energy' values were

1.01935 kcal/mol, 14.4513 kcal/mol, -1.95894 kcal/mol, 12.8461 kcal/mol, and -3.65539 kcal/mol, respectively, higher than that of the original ligand galantamine (-9.06147 kcal/mol). Among them, compound **2** exhibited the highest AChE inhibition, which was consistent with the previous work. The interactions data for compounds **1**, **2**, and **6–8** docked into the active site gorge of AChE is shown in Table 4.

Regarding AChE, the higher of '-CDOCKER Energy' meant interactions between the five compounds and the 4EY6 were stronger than galantamine. Hydrogen bonding, attractive charge, amide–Pi stacked, Pi–Pi, Pi–alkyl, Pi–cation, Pi–anion, Pi–lone pair interactions were found to be involved between the compounds and the active site residues Tyr133, Tyr337, Trp86, Glu202, and Phe338 in the anionic subsite; Tyr124, Tyr341, and Asp74 in the peripheral active site (PAS); His447 and Ser203 in the catalytic active site (CAS); Gly120, Gly121, Gly122, and Ala204 in the oxyanion hole; and Phe297 and Phe295 in the acyl pocket (Namdaung et al., 2018; Saenkham et al., 2020). Compound **2** was found with the highest AChE (PDB: 4EY6) inhibition, which showed eight tight bindings to key residues (Table 4). The 3D and 2D molecular interaction of compound **2** in the binding pocket of AChE are clearly explained in Figure 3 and Figure 4. The results suggested that compound **2** formed four hydrogen bondings to key residues, namely, two hydrogen atoms of C2' to Tyr124 (2.45 Å and 2.35 Å) at PAS, C4'-COOH to Phe295 (2.08 Å) at acyl pocket, C7-OH to Tyr133 (2.33 Å) at anionic subsite. Secondly, the benzene ring interacted with the Gly120 (4.02 Å) of the oxyanion hole to form amide–Pi stacked, and C10 interacted with Tyr337 (4.30 Å) and Tyr86 (4.37 Å) at anionic subsite to form Pi–alkyl interaction. In addition, the Pi–catinon interaction between the N atom and the Tyr341 (3.68 Å) located in PAS can also be observed. These interactions played a vital role for anti-AChE activity and may be useful to further explain the inhibition exhibited by compound **2**.
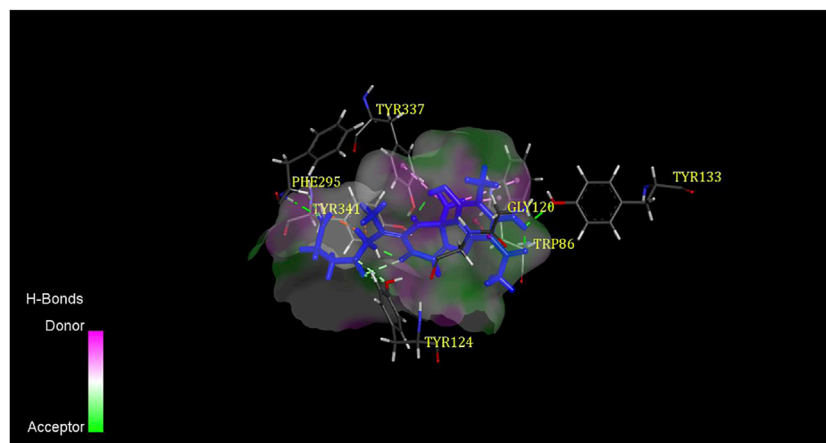
FIGURE 3
3D binding mode of compound **2** with AChE.
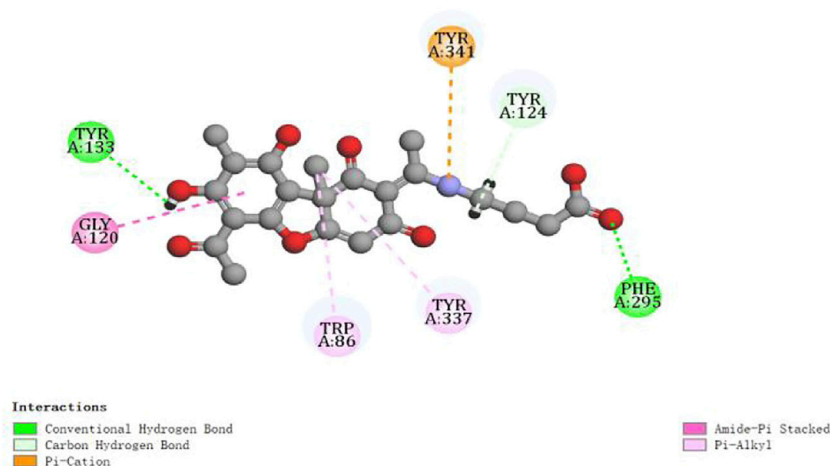
FIGURE 4
2D diagram of the ligand–protein interaction for compound **2** with AChE.

3 Discussion

Usnea is a kind of lichen traditional Chinese medicine with high-medicinal value, distributed in polar and tropical regions, and widely distributed in Sichuan, Inner Mongolia, Yunnan, Heilongjiang, and other places in China. There are more than 10 common species, such as *U. diffracta* Vain, *U. cavernosa* Tuck, and *U. longissima* Ach, among which *U. longissima* Ach is a large species studied widely (Salgado et al., 2018; Ullah et al., 2019). The phytochemistry of the *Usnea* genus show that it contains more than 60 compounds, which mainly belong to depsides, depsidones, depsones, lactones, quinones, phenolics, polysaccharides, fatty acids, and dibenzofurans (Salgado et al., 2018). Among them, depsides, depsidones, depsones, and dibenzofurans are the unique phenolic components of lichens. These representative aromatic products are compounds derived from the acetyl-polymalonyl pathway, the most characteristic being formed by the bonding of two or three orcinol or 3-orcinol-type phenolic units through ester, ether, and carbon–carbon linkages (Shukla et al., 2010).

The purpose of this study was to determine the chemical constituents from the dry lichen body of *Usnea diffracta* Vain. Following the isolation procedure in this article, we isolated 30 compounds including 16 phenols from *U. diffracta* Vain, which specifically belonged to dibenzofurans, multi-substituted single benzene ring, depsides, organic acid, organic acid ester, fatty acids containing furan ring, furfural, amino acid, and nucleoside compound. After searching the SciFinder database, compounds **1–5** were identified as new compounds. Most of the compounds were multi-substituted single benzene ring, dibenzofurans, and depsides, all of which were recognized as the main secondary metabolites of *Usnea*.

Usnea lichen has a long history of antimicrobial use as a folk medicine. Modern scientific research reveals that its crude extracts and monomer compounds have good progress in antimicrobial activities. Derivatives of depsides and dibenzofurans are the main

resources of its antimicrobial activities, especially the usnic acid is the most prominent which has a relatively wide antimicrobial spectrum. Several studies have confirmed that usnic acid can inhibit growth of different planctonic bacteria and fungi strains, such as *Klebsiella pneumoniae*, *Bacillus subtilis*, *Bacillus cereus*, *Bacillus mycoides*, *Staphylococcus aureus*, and *Escherichia coli* (Sultana and Afolayan, 2011; Helena et al., 2012; Rankovic et al., 2012). The antimicrobial activity of *Usnea diffracta* Vain ethyl acetate extracts against *Actinomyces viscosus* and *Streptococcus mutans* assays showed that ethyl acetate extracts were resistant to these strains (Qi et al., 2009). In this study, the disk diffusion method and the microdilution method were designed to screen the activities of the isolated compounds against *Staphylococcus aureus*, *Escherichia coli*, and *Candida albicans*. An anti-*C. albicans* assay was not performed due to the insufficient amount of compounds **4–5**. The results exhibited that compound **3** had certain inhibitory activities against *S. aureus* and *E. coli* but no anti-*C. albicans* activity at 64 μg/ml, compound **9** had certain an inhibitory effect on *S. aureus* and *C. albicans* with the MIC of 64 μg/ml, and compound **10** demonstrated the strongest inhibition against *S. aureus* and *C. albicans* among all compounds. Among them, compounds **9** and **10** belong to depsides. Although five dibenzofurans (**1**, **2**, and **6–8**) have no antibacterial effect, they can inhibit the growth of *C. albicans* with the MIC of 64 μg/ml. This further confirmed that derivatives of depsides and dibenzofurans were the main resources of its antimicrobial activities. The result that (+)-usnic acid (**8**) studied in this study showed no activity against *S. aureus* and *E. coli* does not mean that it is inconsistent with previous studies, but can only demonstrate that there is no bacteriostatic effect at this concentration. As this antimicrobial activity assay is only conducted in a certain concentration range for primary activity screening, and cannot be concluded that other compounds have no effect, the follow-up needs to be more detailed and in-depth study of the antimicrobial activities of these compounds.

Since benzofuran has been reported to be a pharmacophore with cholinesterase inhibitory activity, and dibenzofurans, such as (+)-usnic acid, are similar to galantamine in structure, an anticholinesterase drug for AD. We designed experiments to observe the cholinesterase inhibitory activity of the isolated dibenzofurans **1**, **2**, and **6–8** and to study whether they can be potential cholinesterase inhibitors or drugs for the treatment of AD. The assay of AChE inhibitory activity was determined by the improved spectrophotometric Ellman's method (Zhu et al., 2019; Saenkham et al., 2020). Results demonstrated that the five compounds also exhibited AChE inhibition at the concentration of 0.3 μmol/ml with values of 1.01935 kcal/mol, 14.4513 kcal/mol, −1.95894 kcal/mol, 12.8461 kcal/mol, and -3.65539 kcal/mol, respectively. To follow up our results and study the binding affinity related to the inhibition of acetylcholinesterase, molecular docking simulations were performed. The 3D crystal structure of recombinant human AChE complexed with galantamine (code ID: 4EY6) was obtained from the protein data bank (PDB) with a resolution of 2.4 Å and docked with the 3D structure of five compounds (Cheung et al., 2012). Docking analysis exhibited that the investigated compounds had a high affinity for the acetylcholinesterase's active sites and higher '–CDOCKER Energy' than the original ligand molecule ranged from -3.65539 kcal/mol ((+)-usnic acid) to 14.4513 kcal/mol (Usneamine H) for the target enzyme. Usneamine H exhibited the highest AChE inhibition, which was consistent with the assay of AChE inhibitory activity. It formed four hydrogen bonding, amide–Pi stacked, Pi–catinon interaction, two Pi–alkyl interactions to key residues at PAS, acyl pocket, anionic subsite, and oxyanion hole of AChE. These previous interactions assisted in the understanding of anti-AChE activity. However, considering the simplicity of our anti-acetylcholinesterase activity experiments, whether the isolated compounds can become potential cholinesterase inhibitors still needs further research, such as cell assays and *in vivo* assays.

4 Materials and methods

4.1 Plant collection

The dry lichens of *Usnea diffracta* Vain were collected from the Anguo traditional Chinese medicine market in Baoding (Hebei, China) in September 2018, and were identified by Professor Lijuan Zhang of Tianjin University of Traditional Chinese Medicine. The voucher specimen (UD-2018-C412-1) has been deposited at the College of Traditional Chinese Medicine, Tianjin University of Traditional Chinese Medicine.

4.2 Chemicals and reagents

Chromatographic grade methanol and acetonitrile were obtained from (Concord Technology (Tianjin) Co., Ltd.). Analytical grade petroleum ether, dichloromethane, ethyl acetate, methanol, trifluoroacetic acid, formic acid, and dimethyl sulfoxide were obtained from (Concord Technology (Tianjin) Co., Ltd.). 5,5-dithiobis [2-nitrobenzoic acid] (DTNB, CAS: 69-78-3), acetylthiocholine iodide (ATCI, CAS: 2260-50-6), and acetylcholinesterase (CAS: 9000-81-1) from *Electrophorus electricus* (Sigma Aldrich). Brain–Heart Infusion Agar and Broth were obtained from Qingdao Hope Bio-Technology Co., Ltd. Gentamicin sulfate (CAS: 1405-41-0) was obtained from Shanghai Aladdin Biochemical Technology Co., Ltd.

4.3 General

The CD spectrum was recorded by a J-1500 circular dichroic spectrometer (JASCO Co., Japan). NMR spectroscopy was performed on a Bruker AVANCE III NMR spectrometer operating at 600 MHz for (^{1}H), 150 MHz (^{13}C) or Bruker AVANCE III 500 NMR spectrometer (Bruker Co., Switzerland). The deuterated solvents used were DMSO-d$_6$ and CD$_3$OD and the chemical shifts were recorded in ppm. UV spectra were taken on a UV-6150S dual-beam UV-vis spectrophotometer (Shanghai MADAPA Instruments Co., Ltd.). The IR spectrum was detected using a Bruker ALPHA IR spectrophotometer (Bruker Co., Switzerland.). Specific optical rotations were measured using an AUTOPOLV polarimeter (Rudolph Co., United States). The relative molecular mass was measured on a Waters Xevo G2-SUPLC-Q/TOF spectrometer (Waters Co., United States). The samples were prepared by a LC-20AR system, LC-20AP system (Shimadzu, Kyoto, Japan), and Waters 2535 system (Waters Co., United States). Column

chromatography included silica gel (200–300 and 300–400 mesh, Qingdao Marine Chemical Co., Qingdao, China), ODS (5–50 μm, YMC Co., Japan), YMC-pack-A (5 μm, 10 × 250 mm, YMC Co., Japan), Shim Pack PRC (ODS 15 μm, 20 × 250 mm, Japan), Sephadex LH-20 (Pharmacia, Sweden), and Macroreticular absorbing resin AB-8 (Tianjin Saizhiwei Technology Co., Tianjin, China). TLC was performed on TLC plates pre-coated with silica gel GF-254 (Qingdao Marine Chemical Co., Qingdao, China). The antimicrobial activities were measured by an HJH-C1112B clean bench (Shanghai Zhicheng Analytical Instrument Manufacturing Co., Shanghai, China), an HNYC-2102C incubation oscillator (Tianjin Honour Instrument Co., Tianjin, China), a YXQ-LS-75S11 vertical pressure steam sterilization pot (Shanghai Boxun Industry & commerce Co., Shanghai, China), a GEN10SUV-Vis ultraviolet spectrophotometer (Thermo Fisher Scientific Co., United States).

4.4 Extraction and isolation

The dry lichens of *Usnea diffracta* Vain (4.0 Kg; sampling: September 2018) were extracted with 95% v/v EtOH/H$_2$O three times for 3 h each time and then 70% v/v EtOH/H$_2$O three times for 3 h each time. The extracts were concentrated to afford the crude extract (1.7 kg). The crude extract was dissolved in 5 L pure water to make suspension, and then successively extracted with petroleum ether, dichloromethane, and ethyl acetate. The filtered combined solution of each solvent extraction was evaporated to yield the petroleum ether (101.2 g), CH$_2$Cl$_2$ (672.5 g), EtOAC (218.1 g), and post-extraction (650.3 g) extracts. The post-extraction extract (650.3 g) was dissolved in pure water and passed through AB-8 macroporous resin (3.5 kg) column, which was divided into insoluble precipitation layer (250.4 g), water layer (149.6 g), 30% ethanol layer (90.3 g), 60% ethanol layer (41.4 g), and 100% ethanol layer (73.5 g).

The petroleum ether extract (2.0 g) was fractionated by column chromatography (CC) using silica gel (300–400 mesh) as the adsorbent. Eluting with a gradient system of petroleum ether–ethyl acetate (100:1–14:1–7:1–3:1) to afford 12 main fractions (Fr1-12) based on TLC investigations. Fraction Fr2 (100:1) was precipitated and crystallized, washed with petroleum ether, and filtered to obtain compound **13** (100.0 mg) as a white acicular crystal. Fraction Fr10 (14:1) was precipitated and crystallized, washed with petroleum ether and dichloromethane, and filtered to obtain compound **14** (40.0 mg) as a white acicular crystal. Fraction Fr7 (25.5 mg, 14:1) was further purified on a Sephadex LH-20 column with dichloromethane-methanol (1:1) to obtain Fr (7-1)–(7-8). Fr7-4 precipitated and crystallized, washed with dichloromethane, and filtered to obtain compound **8** (9.8 mg) as a yellow acicular crystal. Fr7-7 was further purified on a Sephadex LH-20 column with dichloromethane-methanol (1:1) and filtered crystallization to obtain compound **15** (4.7 mg) as a white acicular crystal.

The CH$_2$Cl$_2$ extract (50.0 g) was fractionated by CC (200–300 mesh) eluting with a gradient system of petroleum ether–ethyl acetate (300:1-1:1) to afford 13 main fractions (Fr1–13), CH$_2$Cl$_2$-CH$_3$OH (10:1-1:1) to afford Fr14. Fraction Fr13 (2.3 g, 1:1) was further purified on a Sephadex LH-20 column with dichloromethane-methanol (1:2) to obtain Fr (13-1)–(13-5). Fr13-4 (0.68 g) was subjected to the 5–50 μm ODS column chromatography and eluted with a gradient of methanol/water (5:95-100:0, v/v) to afford eight fractions Fr (13-4-1)–(13-4-8). The fraction Fr13-4-4 (213.0 mg) was precipitated and crystallized. The crystals (6.0 mg) were

filtered and prepared by Waters C18 preparation column (10 mm × 150 mm) in Waters 2535 preparative high performance liquid chromatography (210 nm, 280 nm). Compound **27** (3.2 mg, t_R 10 min) was obtained with acetonitrile/water (65:35, v/v, 2.0 mL/min) as eluent. The remaining fraction was also prepared by the same condition to afford compound **6** (48.2 mg, t_R 77 min), compound **26** (10.3 mg, t_R 71 min), and compound **7** (4.8 mg, t_R 86 min) were obtained with methanol/water (68:32, v/v, 2.0 mL/min) as eluent. The remaining Fr13 were combined into Fr14 and Fr13 + 14 (10.8 g). This fraction was subjected to 5–50 μm ODS column chromatography (11.5 × 3 cm, 38 g) and eluted with a gradient of methanol/water (5:95-100:0, v/v) to afford nine fractions Fr ((13 + 14)-1)-Fr ((13 + 14)-9). Fraction Fr ((13 + 14)-4 (1.2 g) was prepared by Shim Pack PRC (201 nm, 283 nm) with a gradient system of methanol/water (70:30, v/v, 6.0 mL/min) as eluent to afford 12 fractions Fr ((13 + 14)-4)-1-Fr ((13 + 14)-4–12). Fr (13 + 14)-4-11 (t_R 90–95 min, 50.7 mg) was further prepared by Waters C18 preparation column (10 mm × 150 mm) (201 nm, 283 nm) with a gradient system of acetonitrile/water (50:50, v/v, 2.0 mL/min) as eluent to yield compound **2** (t_R 20 min, 25.3 mg) and compound **1** (t_R 26 min, 10.0 mg).

The EtOAC extract (100.0 g) was fractionated by CC (200–300 mesh) eluting with a gradient system of petroleum ether–ethyl acetate (150:1-1:1) to afford 10 main fractions (Fr1-10). Fr2 (110:1, 470.2 mg) was subjected to the CC eluted with petroleum ether to afford Fr (2-1)-(2-4). Fr (2-3) (300.1 mg) was prepared by a YMC column (201 nm, 254 nm) with a gradient system of methanol/water (70%–100% 25 min, 100% 15 min, 100%–70% 10 min, 1.5 mL/min) as eluent to yield Fr (2-3-1)–(2-3-7). Compounds **16** (6.1 mg) and **23** (2.2 mg) were prepared by scraping thin layer silica gel with petroleum ether–ethyl acetate (25:1) from Fr2-3-7 (17.0 mg, t_R 42 min). Fr3 (40:1, 45.0 mg) was successively purified on a CC eluting with a gradient system of petroleum ether–ethyl acetate (120:1) and a YMC column (201 nm, 254 nm) with methanol/water (70%–95% 25 min, 95%–100% 5 min, 100%–70% 10 min, 1.5 mL/min) as eluent to afford compound **9** (3.0 mg, t_R 35 min). Fr4 (25:1) was successively purified on a CC eluting with a gradient system of petroleum ether–ethyl acetate (120:1-30:1) and a YMC column (201 nm, 254 nm) with methanol/water (70%–100% 25 min, 100% 15 min, 100%–70% 10 min, 1.5 mL/min) as eluent to afford compound **17** (8.0 mg, t_R 30 min). Fr4-4 (70:1, 90.0 mg) was prepared by a YMC column under the same condition, then scraper was prepared by thin layer silica gel, and compounds **24** (3.5 mg) and **25** (4.8 mg) were obtained by the expansion of petroleum ether–ethyl acetate 8-1 with 0.01% formic acid. Fr6 (5:1, 430.0 mg) was successively purified on a CC eluting with a gradient system of petroleum ether–ethyl acetate (30:1, 0.01% formic acid) and a YMC column (201 nm, 254 nm) under the same condition to afford compounds **18** (2.8 mg, t_R 13.5 min) and **10** (70.1 mg, t_R 25.5 min). Fr8 (5:1, 7.0 g) was successively purified on a CC, ODS column, and a YMC column (201 nm, 254 nm) with methanol/water (30%–70% 30 min, 70% 15 min, 70%–90% 15 min, 90%–100% 10 min, 100% 10 min, 100%–30% 10 min, 1.5 mL/min) as eluent to afford Fr (8-1)-(8-8). Compound **22** (12.8 mg) was obtained from Fr8-3 (t_R 29–39 min) by a YMC column with 40% elution of methanol/water. Fr8-6 (t_R 51–52 min, 20.0 mg) was further prepared by a YMC column with a gradient system of acetonitrile/water (60:40, v/v) as eluent to yield compound **12** (16.8 mg).

The 60% ethanol layer (2.7 g) was fractionated by 5–50 μm ODS column chromatography and eluted with a gradient of methanol/water (5:95-100:0, v/v) to afford 14 fractions (Fr1-14). Fraction Fr4 (33.1 mg, 30:

70) was further purified on a Sephadex LH-20 column with methanol to obtain Fr (4-1)-(4-4). Fr (4-2) was prepared by a YMC column (210 nm, 278 nm) with a gradient system of methanol/water (50:50, v/v, 1.5 mL/min) as eluent to yield four fractions Fr (4-2-1)-(4-2-4). Fr4-2-4 (t_R 17-24 min, 10.9 mg) was further prepared by a YMC semi-preparative column (210 nm, 278 nm) with a gradient system of methanol/0.05% trifluoroacetic acid water (50:50, v/v, 1.5 mL/min) as eluent to yield Fr (4-2-4-1)-(4-2-4-4). Fr4-2-4-3 (t_R 16–21 min, 7.5 mg) was further prepared by a YMC column (210 nm, 278 nm) with a gradient system of acetonitrile/0.07% trifluoroacetic acid water (25:75, v/v, 1.5 mL/min) as eluent to yield compound **5** (t_R 17 min, 3.0 mg) and compound **4** (t_R 18.5 min, 1.5 mg). Fr7 (49.1 mg, 50:50) was subjected to the Sephadex LH-20 column with methanol and CC (200–300 mesh) eluting with a gradient system of petroleum ether–ethyl acetate (15:1) to afford compound **19** (3.6 mg). Fr10 (162.1 mg, 70:30) was purified on a Sephadex LH-20 column with methanol to obtain Fr (10-1)-(10-7). Fr10-5 (13.8 mg) was fractionated by CC (200–300 mesh) eluting with a gradient system of petroleum ether–ethyl acetate (1:1) to afford compound **11** (6.7 mg). Fr10-4 (6.1 mg) was fractionated by CC (200–300 mesh) with petroleum ether–ethyl acetate (50:1) to yield compound **20** (1.7 mg). Fraction Fr14 was successively purified on a Sephadex LH-20 column with methanol and CC (200–300 mesh) eluting with a gradient system of petroleum ether–ethyl acetate (150:1) to afford compound **3** (14.5 mg).

The 30% ethanol layer (75.5 g) was fractionated by CC (200–300 mesh) eluting with a gradient system of dichloromethane-methanol (10:1-1:1) ~ methanol ~ methanol-water (1:1) to afford Fr1-6. Fr1 (10:1, 7.5 g) was further purified by CC with dichloromethane-methanol (80:1-8:1) to obtain Fr (1-1)-(1–5). Fr1-2 (80:1, 650.1 mg) was successively purified on a ODS column eluting with methanol/water (5:95-100:0), CC (petroleum ether-ethyl acetate (5:1-1:1) ~ dichloromethane-methanol (10:1-1:1)) and a YMC column (201 nm, 281 nm) with methanol/water (40:60, 1.5 mL/min) as eluent to afford compound **21** (6.7 mg, t_R 21 min). Fr1-3 (20:1) was subjected to a ODS column eluting with methanol/water (5:95-100:0) to obtain Fr (1-3-1)-(1-3-10). Fr1-3-1 (5:95, 1.58 g) was successively prepared by CC (petroleum ether–ethyl acetate (5:2-3:2) ~ dichloromethane-methanol (1:1)) and a YMC column with methanol/water (53:47) as eluent to afford compound **28** (5.8 mg, t_R 10 min). The remaining Fr1-3-1 were combined into Fr1-3-2 and Fr1-3-3 (1.4 g). This fraction was successively prepared by Shim Pack PRC (201 nm, 281 nm) with methanol/water (10:90, v/v, 7.0 mL/min) and a YMC column (201 nm, 281 nm) with methanol/water (5:95, 1.5 mL/min) as eluent to afford compounds **29** (3.0 mg, t_R 20 min) and **30** (2.0 mg, t_R 26 min).

The compounds were characterized by CD, UV, IR, HR-ESI-MS, ^{1}H NMR, ^{13}C NMR data, and 2D NMR.

4.5 *In vitro* antimicrobial activity

Referring to the disk diffusion method (Noumi et al., 2018), the inhibition zone of compounds against *Staphylococcus aureus* ATCC6358 and *Escherichia coli* BL21 were determined in order to preliminarily screen their antibacterial activities. RPMI1640 medium microdilution assay (M27-Ed4) (Clinical Laboratory Standard Institute, 2017) issued by the CLSI was performed to identify the minimal inhibitory concentration of compounds against *Candida albicans* ATCC90028. The antimicrobial effect was tested against two pathogenic bacteria including one Gram-positive strain (*S. aureus*) and one Gram-negative bacterial strain (*E. coli*) and fungus

strain (*C. albicans*). The detailed protocol can be found in Supplemental Materials.

4.6 Anti-AChE assay

The assay of AChE inhibitory activity was determined by the improved spectrophotometric Ellman's method (Zhu et al., 2019; Saenkham et al., 2020). In brief, 140 μL of 100 mM sodium phosphate buffer (pH 8.0), 20 μL of a solution of AChE (0.05 unit/mL), and 20 μL of test compound were mixed in 96-well plates, and then incubated at 30 °C for 15 min. The reaction was initiated by adding 20 μL of mixture solution of 10 μL 5,5′-dithio-bis-nitrobenzoic acid (DTNB) (10.0 mM) and 10 μL ATCl (7.5 mM), then catalyzed by enzymes at a wavelength of 412 nm and the absorbance was measured after 30 min of incubation at 37 °C. We replaced the test compound with 20 μL of phosphate buffer salt (100 mM) as a blank control. All reactions were performed in 96-well microplates in triplicate. Percentage of inhibition was calculated by the following equation:

$$\text{Inhibition activity}\,(\%) = \frac{\text{Absorbance of control} - \text{Absorbance of sample}}{\text{Absorbance of control}} \times 100.$$

Data were expressed as means ± SD and determined with SPSS 21.0 software.

4.7 Molecular docking

Molecular docking studies were generated by using the Discovery Studio 2019 Client program. The 3D crystal structure of recombinant human AChE complexed with galantamine (code ID: 4EY6) was obtained from the protein data bank (PDB) with a resolution of 2.4 Å (Cheung et al., 2012). The 4EY6 protein was optimized through the Prepare Protein function of DS software, and the active pocked was defined by the original ligand molecule. Before molecular docking, the original ligand galantamine was redocked to the AChE active pocket. Default settings were kept for parameters. The structural differences before and after molecular docking were compared. The results showed that the RMSD value was 0.5002 Å, indicating the rationality of the selected docking parameters and scoring function. Therefore, this parameter can be used for subsequent molecular docking research. The small molecules were introduced into DS software, and optimized by Prepare Ligands and Minimization. The CDOCKER module was used to simulate the molecular docking between small molecules and AChE. The docking results were analyzed using Discovery Studio Visualizer. Evaluation of the molecular docking was performed according to '–CDOCKEREnergy' value (Yu et al., 2018).

5 Conclusion

In this study, we exhibited how to isolate secondary metabolites from the dry lichen body of *Usnea diffracta* Vain and confirmed their structures by physicochemical properties and various spectral methods. We isolated 30 compounds which belonged to dibenzofurans, multi-substituted benzenes, depsides, organic acids, fatty acids, amino acid, furfural, and nucleoside. It contains five new

compounds (**1–5**). The results of preliminary screening experiments on antibacterial and antifungal activities revealed that the new compound **3** had certain inhibitory activities against *S. aureus* and *E. coli* with IZ of 6.2 mm and 6.3 mm, depsides **9** and **10** had certain inhibitory effect on *S. aureus* and *C. albicans*. Compound **10** demonstrated the strongest inhibition against *S. aureus* and *C. albicans* with 6.6 mm and 32 µg/ml, respectively. Five isolated dibenzofurans (**1**, **2**, and **6–8**) were evaluated for their biological properties toward specific target human AChE involved in AD. This study clearly demonstrated that they could effectively inhibit AChE at 0.3 µmol/ml. The most anti-AChE activity was demonstrated by the lichen secondary metabolite Usneamine H (**2**), which was identified as a new compound. Furthermore, the result of molecular docking was consistent with activity experimental data. This compound exhibited the strongest binding affinity and formed several tight bindings to key residues located in the peripheral active site, acyl pocket, anionic subsite, and the oxyanion hole of AChE. In addition, whether these compounds can be potential antimicrobial agents or drug candidate for the treatment of AD needs further study.

Data availability statement

The original contributions presented in the study are included in the article/Supplemental Material; further inquiries can be directed to the corresponding author.

Author contributions

Conceptualization: L-NW; methodology: L-NW, Y-MH, B-QL, and C-SW; validation: L-NW, Y-MH, B-QL, and C-SW; data curation: Y-MH and B-QL; writing—original draft preparation: Y-MH; writing—review and editing: L-NW, Y-MH, Y-CY, and QZ; supervision: L-NW; project administration: L-NW; and funding

acquisition: L-NW. All authors read and agreed to the published version of the manuscript.

Conflict of interest

The authors declare that the research was conducted in the absence of any commercial or financial relationships that could be construed as a potential conflict of interest.

The reviewer JZ declared a shared affiliation with the author C-SW to the handling editor at the time of review.

Publisher's note

All claims expressed in this article are solely those of the authors and do not necessarily represent those of their affiliated organizations, or those of the publisher, the editors, and the reviewers. Any product that may be evaluated in this article, or claim that may be made by its manufacturer, is not guaranteed or endorsed by the publisher.

Supplementary material

The Supplementary Material for this article can be found online at: https://www.frontiersin.org/articles/10.3389/fchem.2022.1063645/full#supplementary-material

References

Araújo, A. A., Melo, M. G., Rabelo, T. K., Nunes, P. S., Santos, S. L., Serafini, M. R., et al. (2015). Review of the biological properties and toxicity of usnic acid. *Nat. Prod. Res.* 29 (23), 2167–2180. doi:10.1080/14786419.2015.1007455

Behera, B. C., Mahadik, N., and Morey, M. (2012). Antioxidative and cardiovascular protective activities of metabolite usnic acid and psoromic acid produced by lichen species *Usnea complanata* under submerged fermentation. *Pharm. Biol.* 50, 968–979. doi:10.3109/13880209.2012.654396

Bruno, M., Trucchi, B., Burlando, B., Ranzato, E., Martinotti, S., Akkol, E. R., et al. (2013). (+)-Usnic acid enamines with remarkable cicatrizing properties. *Bioorgan Med. Chem.* 21 (7), 1834–1843. doi:10.1016/j.bmc.2013.01.045

Bui, V. M., Duong, T. H., Nguyen, T. A. M., Nguyen, T. N. V., Nguyen, N. H., Nguyen, H. H., et al. (2020). Two new phenolic compounds from the Vietnamese lichen *Parmotrema tinctorum*. *Nat. Prod. Res.* 36 (13), 3429–3434. doi:10.1080/14786419.2020.1864367

Cazarin, C. A., Dalmagro, A. P., Gonçalves, A. E., Boeing, T., Silva, L. M., Corrêa, R., et al. (2020). Usnic acid enantiomers restore cognitive deficits and neurochemical alterations induced by Aβ 1–42 in mice. *Behav. Brain Res.* 397, 112945. doi:10.1016/j.bbr.2020.112945

Ceker, S., Orhan, F., Kizil, H. E., Alpsoy, L., Gulluce, M., Aslan, A., et al. (2015). Genotoxic and antigenotoxic potentials of two *Usnea* species. *Toxicol. Ind. Health.* 31, 990–999. doi:10.1177/0748233713485889

Chester, D. O., and Elix, J. A. (1979). Three new aliphatic acids from lichens of genus *parmelia* (subgenus *xanthoparmelia*). *Aust. J. Chem.* 32 (11), 2565–2569. doi:10.1071/ch9792565

Cheung, J., Rudolph, M. J., Burshteyn, F., Cassidy, M. S., Cary, E. N., Love, J., et al. (2012). Structures of human acetylcholinesterase in complex with pharmacologically important ligands. *J. Med. Chem.* 55, 10282–10286. doi:10.1021/jm300871x

Clinical Laboratory Standard Institute (2017). *Reference method for broth dilution antifungal susceptibility testing of yeasts: Aproved standard.* 4th ed. Wayne, PA: American Clinical Laboratory Standard Institute (CLSI). M27-E4.

Colovic Mirjana, B., Krstic Danijela, Z., Lazarević-Pašti Tamara, D., Bondžić Aleksandra, M., and Vasić Vesna, M. (2013). Acetylcholinesterase inhibitors: Pharmacology and toxicology. *Curr. Neuropharmacol.* 11 (3), 315–335. doi:10.2174/1570159x11311030006

Delogu, G. L., Matos, M. J., Fanti, M., Era, B., Medda, R., Pieroni, E., et al. (2016). 2-Phenylbenzofuran derivatives as butyrylcholinesterase inhibitors: synthesis, biological activity and molecular modeling. *Bioorg. Med. Chem. Lett.* 26, 2308–2313. doi:10.1016/j.bmcl.2016.03.039

Eliwa, E., Abdel-Razek, A., Frese, M., Halawa, A., El-Agrody, A., Bedair, A., et al. (2019). New naturally occurring phenolic derivatives from marine *Nocardiopsis* sp. AS23C: Structural elucidation and *in silico* computational studies. *Vietnam J. Chem.* 57, 164–174. doi:10.1002/vjch.201900010

Feng, B.-M., Liu, J.-Y., Wang, H.-G., Shi, L.-Y., Tang, L., and Wang, Y.-Q. (2011). Isolation and identification of chemical constituents of root of *Girardinia suborbiculata*. C.J.Chen subsp.triloba. *J. Shenyang Pharm. Univ.* 28 (05), 364–367. doi:10.14066/j.cnki.cn21-1349/r.2011.05.004

Feng, J., Yang, X.-W., Su, S.-D., and He, C. (2009). Chemical constituents from *Usnea longgisima*. *China J. Chin. Mater. Med.* 34 (06), 708–711.

Furukawa-Hibi, Y., Alkam, T., Nitta, A., Matsuyamaet, A., Mizoguchi, H., Suzuki, K., et al. (2011). Butyrylcholinesterase inhibitors ameliorate cognitive dysfunction induced by amyloid-β peptide in mice. *Behav. Brain Res.* 225, 222–229. doi:10.1016/j.bbr.2011.07.035

Graham, D. W., Ashton, W. T., Barash, L., Brown, J. E., Brown, R. D., Canning, L. F., et al. (1987). Inhibition of the mammalian β-lactamase renal dipeptidase

(dehydropeptidase-I) by Z-2-(acylamino)-3-substituted-propenoic acids. *J. Med. Chem.* 30 (6), 1074–1090. doi:10.1021/jm00389a018

Greig, N. H., Utsuki, T., Ingram, D. K., Wang, Y., Pepeu, G., Scali, C., et al. (2005). Selective butyrylcholinesterase inhibition elevates brain acetylcholine, augments learning and lowers Alzheimer *β*-amyloid peptide in rodent. *Proc. Natl. Acad. Sci. U. S. A.* 102 (47), 17213–17218. doi:10.1073/pnas.0508575102

Gu, X.-L., Jin, Y., Zhang, L.-Y., Fan, J.-T., and Du, S.-H. (2017). Study on the chemical constituents from the n-Butanol extract of *Typhonii Rhizoma*. *Res. Pract. Chin. Med.* 31 (04), 30–32. doi:10.13728/j.1673-6427.2017.04.009

Helena, P. R., Rodrigo, L., and Soares, M.-G. M. J. (2012). Effect of usnic acid on *Candida orthopsilosis* and *C. parapsilosis*. *Antimicrob. agents Chemother.* 56 (1), 595–597. doi:10.1128/AAC.05348-11

Huneck, S., Schmidt, J., and Tabacchi, R. (1989). Thermal decomposition of lichen depsides. *Z. Naturforsch B* 44, 1283–1289. doi:10.1515/znb-1989-1023

Khanam, H., and Shamsuzzaman (2015). Bioactive benzofuran derivatives: a review. *Eur. J. Med. Chem.* 97, 483–504. doi:10.1016/j.ejmech.2014.11.039

Koparal, A. T. (2015). Anti-angiogenic and antiproliferative properties of the lichen substances (-) usnic acid and vulpinic acid. *Z. Naturforsch. C* 70, 159–164. doi:10.1515/znc-2014-4178

Lai, D., Odimegwu, D. C., Esimone, C., Thomas, G., and Peter, P. (2013). Phenolic compounds with *in vitro* activity against respiratory syncytial virus from the Nigerian lichen *Ramalina farinacea*. *Planta Med.* 79, 1440–1446. doi:10.1055/s-0033-1350711

Laxi, N., Tang, Y.-X., Bao, H.-Y., and Tuli, Q. (2013). Chemical constituents from *Usnea longgisima*, a traditional Mongolian medicine. *China J. Chin. Mater. Med.* 38 (13), 2125–2128.

Li, G.-H., Li, L., Duan, M., and Zhang, K.-Q. (2006). The chemical constituents of the fungus *stereum* sp. *Chem. Biodivers.* 3 (2), 210–216. doi:10.1002/cbdv.200690024

Li, J., Yin, B., Liu, Y., Wang, L.-Q., and Chen, Y.-G. (2009). Mono-aromatic constituents of *Dendrobium longicornu*. *Chem. Nat. Compd.* 45 (2), 234–236. doi:10.1007/s10600-009-9293-2

Nahrstedt, A., Economou, D., and Wray, V. (1990). 2-Methylbutan-l-yl-β/-D-glucoside, a hemiterpene glucoside from bystropogon plumosus. *J. Nat. Prod.* 53 (5), 1387–1389. doi:10.1021/np50071a045

Namdaung, U., Athipornchai, A., Khammee, T., Kuno, M., and Suksamrarn, S. (2018). 2-Arylbenzofurans from *Artocarpus lakoocha* and methyl ether analogs with potent cholinesterase inhibitory activity. *Eur. J. Med. Chem.* 143, 1301–1311. doi:10.1016/j.ejmech.2017.10.019

Nishanth, K. S., Sreerag, R. S., Deepa, I., Mohandas, C., and Nambisan, B. (2015). Protocetraric acid: an excellent broad spectrum compound from the lichen *Usnea albopunctata* against medically important microbes. *Nat. Prod. Res.* 29, 574–577. doi:10.1080/14786419.2014.953500

Nishitoba, Y., Nishimura, I., Nishiyama, T., and Mizutani, J. (1987). Lichen acids, plant growth inhibitors from *Usnea longissima*. *Phytochemistry* 6 (12), 3181–3185. doi:10.1016/S0031-9422(00)82466-8

Noumi, E., Merghni, A., Alreshidi, M. M., Haddad, O., Akmadar, G., Martino, M. D., et al. (2018). *Chromobacterium violaceum* and *Pseudomonas aeruginosa* PAO1: Models for evaluating anti-quorum sensing activity of *Melaleuca alternifolia* essential oil and its main component terpinen-4-ol. *Molecules* 23, 2672. doi:10.3390/molecules23102672

Popovici, V., Bucur, L., Gȋrd, C. E., Rambu, D., Calcan, S. I., Cucolea, E. I., et al. (2022). Antioxidant, cytotoxic, and rheological properties of canola oil extract of *Usnea barbata* (L.) weber ex F.H. Wigg from cǎlimani mountains, Romania. *Plants* 11, 854. doi:10.3390/PLANTS11070854

Qi, H. Y., Jin, Y. P., and Shi, Y. P. (2009). ChemInform abstract: A new depsidone from usnea diffracta. *Chin. Chem. Lett.* 20 (2), 187–189. doi:10.1002/chin.200924204

Qin, C.-P., Wang, X.-R., Tian, Y.-Q., and Wang, L. (2010). Study on the secondary metabolites from *Mariannaea camdospora* SIIA-F12361. *Chin. J. Antibiot.* 35 (11), 877–880. doi:10.13461/j.cnki.cja.004692

Rankovic, B., Kosanic, M., Stanojkovic, T., Vasiljević, P., and Manojlović, N. (2012). Biological activities of *Toninia candida* and *Usnea barbata* together with their norstictic acid and usnic acid constituents. *J. Mol. Sci.* 13 (2), 14707–14722. doi:10.3390/ijms131114707

Reddy, S. D., Siva, B., Kumar, K., Babu, V. S. P., Sravanthi, V., Boustie, J., et al. (2019). Comprehensive analysis of secondary metabolites in *Usnea longissima* (lichenized Ascomycetes, parmeliaceae) using UPLC-ESI-QTOF-MS/MS and pro-apoptotic activity of barbatic acid. *Molecules* 24 (12), 2270. doi:10.3390/molecules24122270

Rezanka, T., and Guschina, I. A. (2001). Glycoside esters from lichens of central Asia. *Phytochemistry* 58 (3), 509–516. doi:10.1016/S0031-9422(01)00261-8

Rizzo, S., Tarozzi, A., Bartolini, M., Costa, G. D., Bisi, A., Gobbi, S., et al. (2012). 2-arylbenzofuran-based molecules as multipotent Alzheimer's disease modifying agents. *Eur. J. Med. Chem.* 58, 519–532. doi:10.1016/j.ejmech.2012.10.045

Saenkham, A., Jaratrungtawee, A., Siriwattanasathien, Y., Boonsri, P., Chainok, K., Suksamrarn, A., et al. (2020). Highly potent cholinesterase inhibition of geranylated xanthones from *Garcinia fusca* and molecular docking studies. *Fitoterapia* 146, 104637. doi:10.1016/j.fitote.2020.104637

Salgado, F., Albornoz, L., Cortez, C., Stashenko, E., Urrea-Vallejo, K., Nagles, E., et al. (2018). Secondary metabolite profiling of species of the genus *Usnea* by UHPLC-ESI-OT-MS-MS. *Molecules* 23 (1), 54–69. doi:10.3390/molecules23010054

Shukla, V., Joshi, G. P., and Rawat, M. (2010). Lichens as a potential natural source of bioactive compounds: a review. *Phytochem. Rev.* 9 (2), 303–314. doi:10.1007/s11101-010-9189-6

Singh, B., Gangwar, P., Paliya, B., Bajpai, R., Singh, B. R., Kumar, J., et al. (2016). The genus *usnea*: A potent phytomedicine with multifarious ethnobotany, phytochemistry and pharmacology. *Rsc Adv.* 6 (26), 21672–21696. doi:10.1039/c5ra24205c

Singh, M., Kaur, M., Kukreja, H., Chugh, R., Silakari, O., and Singh, D. (2013). Acetylcholinesterase inhibitors as alzheimer therapy: from nerve toxins to neuroprotection. *Eur. J. Med. Chem.* 70, 165–188. doi:10.1016/j.ejmech.2013.09.050

Singh, S., Khatoon, S., Joshi, Y., Prgyadeep, S., Upreti, D. K., and Singh Rawat, A. K. (2016). A validated HPTLC densitometric method for simultaneous determination of evernic and usnic acids in four *usnea* species and comparison of their antioxidant potential. *J. Chromatogr. Sci.* 54, 1670–1677. doi:10.1093/chromsci/bmw118

Su, H., Zhu, X.-B., Yuan, Z.-H., Li, J., Guo, S.-J., Han, L.-J., et al. (2009). Studies on chemical constituents of. *Chondrophycus Papillous*. *Mar. Sci.* 33 (05), 33–35.

Sultana, N., and Afolayan, A. J. (2011). A new depsidone and antibacterial activities of compounds from *Usnea undulata Stirton*. *J. Asian Nat. Prod. Res.* 13 (12), 1158–1164. doi:10.1080/10286020.2011.622720

Sun, C., Liu, F., Sun, J., Li, J., and Wang, X. (2016). Optimisation and establishment of separation conditions of organic acids from *Usnea longissima* Ach. by pH-zone-refifining counter-current chromatography: Discussion of the eluotropic sequence. *J. Chromatogr. A* 1427, 96–101. doi:10.1016/j.chroma.2015.12.016

Tang, Y.-X., Laxi, N., and Bao, H.-Y. (2015). Chemical constituents and their antioxidant activities from thallus of Ramalina conduplicans. *Mycosystema* 34 (01), 169–176. doi:10.13346/j.mycosystema.130130

Tuan, N. T., Dam, N. P., Van Hieu, M., Trang, D. T. X., Danh, L. T., Men, T. T., et al. (2020). Chemical constituents of the lichen *parmotrema tinctorum* and their antifungal activity. *Chem. Nat. Compd.* 56 (2), 315–317. doi:10.1007/s10600-020-03017-y

Ullah, M., Uddin, Z., Song, Y. H., Li, Z. P., Kim, J. Y., Ban, Y. J., et al. (2019). Bacterial neuraminidase inhibition by phenolic compounds from U*snea longissima*. *S Afric J. Bot.* 120, 326–330. doi:10.1016/j.sajb.2018.10.020

Vanga, N. R., Kota, A., Sistla, R., and Uppuluri, M. (2017). Synthesis and anti-inflammatory activity of novel triazole hybrids of (+)-usnic acid, the major dibenzofuran metabolite of the lichen *Usnea longissima*. *Mol. Divers.* 21, 273–282. doi:10.1007/s11030-016-9716-5

Wahl, H., Hong, Q., Stube, D., Maier, M. E., Häring, H. U., and Liebich, H. M. (2001). Simultaneous analysis of the di(2-ethylhexyl)phthalate metabolites 2-ethylhexanoic acid, 2-ethyl-3-hydroxyhexanoic acid and 2-ethyl-3-oxohexanoic acid in urine by gas chromatography–mass spectrometry. *J. Chromatogr. B* 758 (2), 213–219. doi:10.1016/s0378-4347(01)00183-9

Wang, L.-D., Wu, S.-H., Chen, Y.-W., Yu, Y., Yang, L.-Y., Li, S.-L., et al. (2009). Studies on the secondary metabolites of endophytic fungus *Epicoccum* isolated from *Azadirachta indica*. *Nat. Prod. Res. Dev.* 21 (06), 916–918. doi:10.16333/j.1001-6880.2009.06.004

Wang, Y.-N., Liu, M.-F., Hou, W.-Z., Xu, R.-M., Gao, J., Lu, A.-Q., et al. (2017). Bioactive benzofuran derivatives from Cortex Mori Radicis, and their neuroprotective and analgesic activities mediated by mGluR1. *Molecules* 22, 236–248. doi:10.3390/molecules22020236

Wu, J., Tian, Y., Wang, S., Pistolozzi, M., Jin, Y., Zhou, T., et al. (2016). Design, synthesis and biological evaluation of bambuterol analogues as novel inhibitors of butyrylcholinesterase. *Eur. J. Med. Chem.* 126, 61–71. doi:10.1016/j.ejmech.2016.08.061

Yang, Y., Nguyen, T. T., Jeong, M. H., Crişan, F., Yu, H., Ha, H. H., et al. (2017). Inhibitory activity of (+)-usnic acid against nonsmall cell lung cancer cell motility. *PLoS One* 11, e0146575. doi:10.1371/journal.pone.0146575

Yu, X.-L., Yang, X.-Y., Gao, X. -L., Bai, R.-F., Yin, X., Su, G.-Z., et al. (2016). Phenolic constituents from *Usnea longgisima*. *China J. Chin. Mater, Med.* 41 (10), 1864–1869. doi:10.4268/cjcmm20161017

Yu, X., Guo, Q., Su, G., Yang, A., Hu, Z., Qu, C., et al. (2016). Usnic acid derivatives with cytotoxic and antifungal activities from the lichen *Usnea longissima*. *J. Nat. Prod.* 79 (5), 1373–1380. doi:10.1021/acs.jnatprod.6b00109

Yu, Z.-P., Wu, S.-J., Zhao, W.-Z., Ding, L., Fan, Y., Shiuan, D., et al. (2018). Anti-Alzheimers activity and molecular mechanism of albumin-derived peptides against AChE and BChE. *Food Funct.* 9 (2), 1173–1178. doi:10.1039/c7fo01462g

Zhao, C., Yao, Z., Yang, D., Ke, J., Wu, Q., Li, J., et al. (2020). Chemical constituents from *Fraxinus hupehensis* and their antifungal and herbicidal activities. *Biomolecules* 10 (1), 74–83. doi:10.3390/biom10010074

Zhao, X.-Q., Zhu, J.-L., Wang, L.-W., Li, Y.-B., Zhao, T.-T., Chen, X., et al. (2019). *U. diffracta* extract mitigates high fat diet and VD3-induced atherosclerosis and biochemical changes in the serum liver and aorta of rats. *Biomed. Pharmacother.* 120, 109446. doi:10.1016/j.biopha.2019.109446

Zheng, Y.-B., Lu, C.-H., Xu, L., Zheng, Z.-H., Su, W.-J., and Shen, Y.-M. (2012). Chemical components from surface liquid fermented *Hericium erinaceus* with cytotoxity investigations. *Nat. Prod. Res. Dev.* 24 (12), 1703–1706. doi:10.16333/j.1001-6880.2012.12.002

Zhu, J., Wang, L.-N., Cai, R., Geng, S.-Q., Dong, Y.-F., and Liu, Y.-M. (2019). Design, synthesis, evaluation and molecular modeling study of 4-N-phenylaminoquinolines for Alzheimer disease treatment. *Bioorg. Med. Chem. Lett.* 29 (11), 1325–1329. doi:10.1016/j.bmcl.2019.03.050

Zou, J., Mao, X.-X., He, K., Ye, J.-H., Tang, R.-T., Wang, Y.-X., et al. (2021). Chemical constituents from *Pteris insignis*. *Guihaia* 41 (07), 1046–1053.

Frontiers in
Chemistry

Explores all fields of chemical science across the periodic table

Advances our understanding of how atoms, ions, and molecules come together and come apart. It explores the role of chemistry in our everyday lives - from electronic devices to health and wellbeing.

Discover the latest Research Topics

See more →

frontiers | Research Topics